

Dipl.-Ing. Dr. mont. Tanja Lube

**Strength and
Fracture Toughness Testing
of Brittle Materials and
Components**

Habilitationsschrift

eingereicht an der Montanuniversität Leoben

zur Erreichung der *venia docendi* für das Fach Werkstoffprüfung

Leoben, Februar 2024

I declare on oath that I wrote this thesis independently, did not use any sources and aids other than those specified, have fully and truthfully reported the use of generative methods and models of artificial intelligence, and did not otherwise use any other unauthorized aids.

In order to enhance the readability, use of the translation service offered by <https://www.deepl.com> to obtain suggestions for the wording of phrases or paragraphs was occasionally made. On all of these occasions, the suggestions were carefully revised.

I declare that I have read, understood and complied with the "Good Scientific Practice" of the Montanuniversität Leoben.

Furthermore, I declare that the electronic and printed versions of the submitted thesis are identical in form and content.

Danksagung

Die Arbeiten, die in dieser Habilitationsschrift zusammengefasst sind, wurden über viele Jahre hinweg in nationalen und internationalen geförderten Projekten, im Rahmen von Diplom- oder Masterarbeiten, Dissertationen, Praktika oder in informellen Kooperationen durchgeführt. Sie sind das Ergebnis der Zusammenarbeit mit vielen verschiedenen motivierten, fleißigen und klugen Personen, denen ich hier dafür danken möchte, dass sie mich beim Erfinden und Verbessern von Methoden zum Zerstören von Keramik und bei meinen sonstigen Arbeiten als Werkstoffwissenschaftlerin an der Montanuniversität Leoben unterstützt, motiviert, gefordert und gefördert haben.

Einige Personen ragen heraus, darunter auch ein paar, die nicht zum Keramikforscherkreis gehören, und verdienen besondere Erwähnung.

Danke Robert - für die vielen Versuche, mir mit interessanten Aufgaben und Projekten den Weg zur Habilitation zu ermöglichen. Ich habe lieber immer wieder Neues begonnen als Bisheriges zusammenzufassen. Du hast dennoch dafür gesorgt, dass ich Wissenschaftlerin und akademische Lehrerin bleiben konnte.

Danke Sigrid und Manfred, Martin, Bernhard und Johanna - ihr habt mir durch Nicht-Zusammenbrechenlassen aller Aspekte des Familienlebens und völlig unproblematisches Kinder-, Schüler- und Maturantendasein den Rücken freigehalten, wenn ich forschen wollte.

Danke Gregor - für wiederholtes Motivieren und zielführendes Herunterspielen des Aufwandes für das Schreiben des dritten schwarzen Buches.

Danke Max - für den Wunsch nach einer Laudatio, den ich nicht erfüllen durfte. Das war das bisschen Motivation, das davor gefehlt hat.

Symbols and Abbreviations

Symbols

f_h	factor to determine h_{eq}
a	crack length, crack depth
A	point at the front of a surface crack
A	Auerbach constant
a_c	critical crack length
a_i	as-indented crack length
b	specimen width
b_1	width of a CharAM cantilever at the minimum fracture position
b_2	width of a CharAM cantilever at the maximum fracture position
b_{eq}	equivalent specimen half-width (rectangular cross section)
b_{max}	maximal width of a bulged cross section
c	surface crack length
C	intersection point of the crack front - specimen surface
$c_0 - c_6$	coefficients for f_{B3B}
c_i	as-indented surface crack length
D	specimen diameter (disc or ball)
D_{eff}	effective specimen diameter
D_L	load diameter
D_S	support diameter
D_{SB}	diameter of the support balls in the B3B test
E	Young's modulus of specimens
E_{LB}	Young's modulus of the load ball in a B3B test
F	probability of failure
f, f_b, f_ν, f_χ	factors to consider finite specimen width, Poisson's ratio and crack-front – surface angle in the geometry factor
f_{B3B}	dimensionless stress factor for the Ball-on-Three-Balls test
$f_{B3B,hex}$	dimensionless stress factor for the Ball-on-Three-Balls test on hexagonal plates
$f_{B3B,new}$	dimensionless stress factor for the Ball-on-Three-Balls test
f_{BoR}	dimensionless stress factor for the Ball-on-Ring test
f_{corr}	corrected dimensionless stress factor for Ball-on-Three-Balls tests

F_{des}	probability of failure – design goal
f_{NBT}	dimensionless stress factor for the Notched-Ball test
f_{piston}	dimensionless stress factor for the Piston-on-Three-Balls test
f_{RoR}	dimensionless stress factor for the Ring-on-Ring test
f_{test}	dimensionless stress factor for strength tests
f_{σ}	dimensionless correction factor
G	energy release rate
G_{Ic}	critical energy release rate
h	specimen thickness, ligament height
h_{eq}	equivalent thickness
h_{max}	maximal thickness of a bulged cross section
I	moment of inertia of a bulged cross section
I_{ideal}	moment of inertia of a rectangular cross section
J	J-integral
K_0	material intrinsic fracture toughness
k_1	dimensionless correction factor for $f_{B3B,new}$ for deflection (B3B test)
k_2	dimensionless correction factor for $f_{B3B,new}$ for large load contact (B3B test)
K_{appl}	applied stress intensity
K_{corr}	dimensionless correction factor
K_I	mode I stress intensity
K_{Ic}	mode I fracture toughness
K_R	crack length dependent fracture toughness, R-curve
K_{shield}	shielding stress intensity
K_{tip}	stress intensity at the crack tip
L	side length of a plate
L_{eff}	Weibull effective length
L_L	load span
L_N	length of a notch
L_S	support span
L_{test}	length of the testing region of a CharAM cantilever
m	Weibull modulus
$m_0 - m_3$	coefficients for the ligament stress in NBT- K_{Ic} tests
m_{ex}	Weibull modulus through size extrapolation
$n_0 - n_1$	coefficients for the ligament stress in NBT- K_{Ic} tests
P	fracture load
r	radial coordinate of a coordinate system at the crack tip
R	radius of a disc or ball specimen
R_{des}	design-reliability
R_{eff}	effective specimen radius
R_N	notch fillet radius
R_S	support radius
S_{eff}	Weibull effective area
t	specimen thickness (discs, plates)
V	volume

V_0	normalising volume
V_{eff}	Weibull effective volume
W_N	width of a notch
x, y, z	cartesian coordinates, coordinate system in a 3D-printer
Y	geometry factor
Y_A	geometry factor at the front of a surface crack
Y_C	geometry factor at the intersection point crack front - specimen surface
Y_{max}	maximal geometry factor along the crack front
Y_{NRF}	geometry factor for surface cracks according to Newman & Raju
Y_S	geometry factor for surface cracks according to Strobl et al.
$Y_{S,A}$	geometry factor for surface cracks at point A according to Strobl et al.
Δa	amount of crack growth
Δh	amount of ground-off material in SCF tests
Δx	offset of a crack in a B3B test
Δy	offset of a crack in a B3B test
α	rotation of a crack in a B3B test
β	opening angle of a constant moment cantilever beam
ξ	coordinate
χ	intersection angle crack front – specimen surface
δ	shift of the load introduction point on CharAM-cantilevers
ϕ	parameteric angle of a semi-elliptical surface crack
γ	thermodynamic surface energy
γ_f	surface energy
φ	angle in a coordinate system at the crack tip
ν	Poisson's ratio of specimens
ν_{LB}	Poisson's ratio of the load ball in a B3B test
ρ	notch root radius
σ	stress
σ_0	Weibull characteristic strength
$\sigma_{0,C}$	characteristic strength of components
$\sigma_{0,S}$	characteristic strength of specimens
σ_a	operating stress
σ_{des}	design stress

σ_f	strength
$\sigma_{f,corr}$	corrected strength of a CharAM cantilever
σ_{lim}	maximum threshold stress for application of $f_{B3B,new}$
σ_{NBT}	stress in a Notched-Ball test
σ_{ref}	reference stress
σ_y	component of a stress field in y -direction
$\sigma_{z,lig}$	ligament stress in NBT- K_{Ic} tests

Abbreviations

AM	additive manufacturing
B3B	Ball-on-three-Balls test
BoR	Ball-on-Ring test
CAD/CAM	computer aided design/computer aided manufacturing
DLP	digital light processing
FE	finite element
FEA	finite element analysis
VPP	vat photo-polymerization
LCM	lithography-based ceramic manufacturing
NBT	Notched-Ball test
RoR	Ring-on-Ring test
SCF	Surface-Crack-in-Flexure
SEPB	Single-Edge-Pre-cracked Beam
SEVNB	Single-Edge-V-Notched Beam
SOEC	Solid Oxide Electrolyzer Cell
SOFC	Solid Oxide Fuel Cell
TZP	tetragonal zirconia polycrystal

Contents

1	Introduction	1
2	Fracture Behavior of Ceramics and its Characterization	3
2.1	Brittle Fracture	3
2.2	Scatter of Strength	4
2.3	Measurement of Strength	7
2.3.1	Uniaxial Flexure Tests	7
2.3.2	Biaxial Flexure Tests	8
2.3.3	Tests on Components	11
2.4	Measurement of Fracture Toughness	12
2.4.1	Methods with Edge Cracks or Notches in Flexure Specimens	13
2.4.2	The Surface-Crack-in-Flexure Method	14
2.5	Material Aspects of Strength and Fracture Toughness	14
3	Challenges for Components and New Manufacturing Methods	18
3.1	Biaxial Strength Testing of Strong and Thin Specimens	18
3.2	Anisotropic Strength: AM Ceramic Components	19
3.3	Fracture Toughness: Pre-crack Shape and Measurements on Small Components	21
4	Improved Tests for Strength and Fracture Toughness	24
4.1	Extension of the Application Range of the Ball-on-Three-Balls Test	24
4.2	A Strength Test Methodology for AM Ceramics	29
4.3	Methods for Fracture Toughness Measurement on Components	33
4.3.1	Improved Treatment of Two-Dimensional Surface Cracks	33
4.3.2	Fracture Toughness of Balls, Discs and Plates	35
5	Summary and Outlook	39
6	Literature	41
7	Selected Publications	53

I Introduction

There is one decisive condition for all components that we manufacture from materials: they must not break. In case they are ceramic components, dealing with this requirement is a particular challenge due to their brittle failure behavior.

A ceramic component is the outcome of a sequence of shaping and processing steps during which strength-limiting defects may be introduced. Such defects can come into existence at any time, up to - and frequently during - component service. Thus, on one hand, in order to ensure the structural integrity of components, their properties must be known and compared with their in-service load profiles. On the other hand, it is also necessary to test the strength of materials with standardized specimens, in order to establish comparability between materials, select materials, define goals for material development and establish qualification profiles for materials for specific applications. In order to be able to make statements about the actual component behavior, however, for the reasons explained above, it is desirable to test components directly or to investigate specimens made from components [1-3].

This is particularly important for additively manufactured (AM) ceramics. This technology enables unprecedented designs and aims at avoiding machining. In additive manufacturing, there are only components and no "semi-finished" products. In this field too, either testing the components directly or making specimens that are close to components in their geometry (dimensions, orientation in the building space, ... [4, 5]) is a viable strategy. To arrive at reasonable procedures, it has to be considered which properties are typical and need to be represented and how the specimens can be skillfully designed, manufactured and consolidated using the possibilities a certain AM process offers.

When it comes to developing such qualified testing methods, it should be kept in mind that materials testing has to provide relevant and accurate values through validated and reproducible procedures [6]. This is particularly important if the data have to be used to perform for example calculations of service life or if size extrapolations according to Weibull strength statistics are to be carried out. The formal description derived to obtain the strength or fracture toughness from experimental quantities such as specimen dimensions and load at fracture must therefore reflect the testing reality sufficiently close. If this is not possible, deviations can be quantified and considered when evaluating tests.

In the following, activities will be reported and summarized which address some issues related to strength and fracture toughness testing of ceramic specimens and components. The text is organized as follows. Chapter 2 introduces the reader very briefly to the fracture behavior of

ceramics and the determination of relevant material properties such as strength and fracture toughness. Based on the current state of knowledge, the subsequent chapter 3 points out some areas in which questions remain unanswered. This is intended to explain the motivation for the work of this habilitation. Chapter 4 summarizes the results of the publications which are part of the presented thesis. The following topics are addressed: A first section, which is supported by papers A – C, deals with a thorough description of a biaxial strength test that can be applied to a wide range of specimen sizes. The following part, according to papers D – F, introduces a methodology to measure the strength of ceramics produced by the Lithography-based Ceramic Manufacturing (LCM) process. The final section, associated to papers G – K, is dedicated to various aspects of fracture toughness testing using indentation induced surface cracks. The text is concluded by a summary and outlook.

2 Fracture Behavior of Ceramics and its Characterization

Due to their manufacturing route from powders, ceramics - specimens or components - contain defects. A number of defects of different sizes is present at different locations in every single ceramic part [7]. One of them will be the most dangerous one for a given loading situation and trigger the brittle fracture. In this context it is common experience that tensile stresses are much more dangerous than compressive stresses. In order to deal with this behavior, it is necessary to understand its causes and characteristics, describe it with theoretical models and be able to measure the relevant material properties. Only then it may be possible to design reliable components using such materials.

2.1 Brittle Fracture

Brittle fracture occurs when acting stresses are high enough to break the atomic bonds in a material. Generally, the loads to achieve such high stresses would be extremely high if there were no ways to concentrate stresses. In ceramics this happens because they contain small defects that intensify stresses to sufficiently high levels. The failure is brittle, e.g. occurs without prior plastic deformation, because flow mechanisms to relieve the stress concentration are insufficient in ceramics [8]. Linear elastic fracture mechanics [9-15] offers insights into the conditions at which stress these defects might expand, based on knowledge of the part's geometry and the applied loads. For the ease of formal treatment, the actual defects occurring in a polycrystalline material can be described as small cracks in a continuum [14].

Three ways in which a stress can be applied to a crack can be envisaged, see Figure 1a.

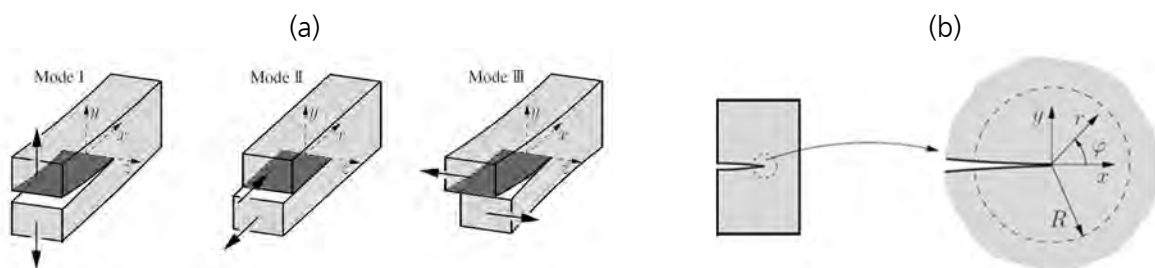


Figure 1: (a) Body with an edge crack and crack opening modes of fracture. (b) Coordinate system to describe stresses in front of cracks [15].

For mode I, "opening", which is the most dangerous one for brittle materials, the relevant stress component σ_y (cp. Figure 1b) of the general stress state is given by

$$\sigma_y = \frac{K_I}{\sqrt{2\pi r}} f(\varphi) \quad (1)$$

with r the distance of a point from the crack tip at an angle φ . The stress intensity K_I is a scaling term which relates the applied uniaxial stress σ (at the position of the crack if the crack was not present) to the crack size a through

$$K_I = \sigma Y \sqrt{\pi a} \quad (2)$$

where Y is a geometry factor that takes the crack geometry and location in the part into account as well as the loading details. Expressions for Y can be found in literature [16, 17]. Crack extension may take place if the stress intensity factor is high enough to produce stresses so that rupture of atomic bonds takes place at the crack tip:

$$K_I \geq K_{Ic} \quad (3)$$

The critical stress intensity factor K_{Ic} is called fracture toughness. This description of the condition for crack growth is based on the stresses near the crack tip. Alternatively, the involved energies can be considered. Thus, it is possible to relate the fracture toughness to the specific energy that is required to produce a unit area of crack surface, G_{Ic} , or the fracture surface energy γ_f :

$$K_{Ic} \equiv (E G_{Ic})^{1/2} \equiv (2E \gamma_f)^{1/2} \quad (4)$$

Since the yield stress of ceramics is very high, only small process zones at the crack tip will be present, so that in practically all cases of interest the crack will be in a state of plane strain. Then eq. (4) must be adjusted using $E' = E/(1 - \nu^2)$ with Poisson's ratio ν , when stress intensities (K_I , K_{Ic}) are converted to energy release rates (G , G_{Ic}).

Using eq. (2) and the failure criterion eq. (3) we can now relate the strength σ_f of a part to the material property K_{Ic} and the size of the critical crack a_c .

$$\sigma_f = \frac{K_{Ic}}{Y \sqrt{\pi a_c}} \quad (5)$$

Eq. (5) highlights the interplay between fracture toughness K_{Ic} as a material property, the critical defect size a_c influenced by processing, and strength σ_f , which remains the primary design objective for components.

2.2 Scatter of Strength

Different specimens or components typically contain defects of varying size at random locations, consequently leading to unique strengths, as becomes obvious from eq. (5). Thus, the "strength of ceramics" is not typically characterized by a single value but rather described using a distribution function. Particularly fitting has been the Weibull distribution, initially empirically substantiated

[18, 19] and subsequently associated with the fracture mechanical description of brittle failure of non-interacting defects with a specific crack-size frequency density through Extreme Value Statistics [20-22]. For uniaxial tension the probability of failure F of a Volume V at a stress σ is given by

$$F(\sigma, V) = 1 - \exp\left[-\frac{V}{V_0} \left(\frac{\sigma}{\sigma_0}\right)^m\right] \quad (6)$$

with the characteristic strength σ_0 , the Weibull modulus m and a normalizing volume V_0 . The characteristic strength is the stress at which a specimen with $V = V_0$ has $F \approx 63\%$ and is thus always linked to the choice of the value of V_0 .

For inhomogeneous uniaxial stress states $\sigma(x, y, z) = \sigma_{ref} \cdot g(x, y, z)$ eq. (6) can be generalized as

$$F(\sigma_{ref}, V_{eff}) = 1 - \exp\left[-\frac{V_{eff}}{V_0} \left(\frac{\sigma_{ref}}{\sigma_0}\right)^m\right] \quad (7)$$

with the effective volume V_{eff} given by

$$V_{eff} = \iiint_{\sigma > 0} [g(x, y, z)]^m dx dy dz \quad (8)$$

This representation considers that highly stressed regions have a much higher probability of failure than portions with low stresses. Situations with multiaxial stress states can be considered by defining an equivalent stress [23, 24]. So far, this approach holds for failure-causing defects that are located in the interior of the specimens or components. In the case that defects located at the surface or on edges are relevant for failure, the effective volume has to be replaced by an analogously calculated effective area (S_{eff}) or effective length (L_{eff}).

The strength distribution is usually determined by measuring the strengths of a set (ideally 30 pieces) of similar specimens [25-27]. From this, the parameters of the distribution, the characteristic strength σ_0 and the Weibull modulus m , can be estimated using statistical methods. As $V_0 = V_{eff}$ is used in this process, the value of σ_0 is unambiguously linked to the selected specimen geometry and loading situation (which determine the Weibull effective quantities V_{eff} , S_{eff} , L_{eff}). Measured strength values are often represented in a Weibull diagram, Figure 2, the axes of which are selected so that the cumulative distribution function appears as a straight line ("Weibull line") with slope m . A few important facts of the statistical strength behavior and the application to probabilistic design shall be noted:

- Every measured strength distribution also represents a crack-size frequency density according to eq. (5), where, depending on the covered stress levels, a corresponding range of critical defect sizes is empirically captured [28, 29].
- Eqs. (6) and (7) indicate a relationship between the loaded volume and the probability of failure. In practice, this is observed as a size dependence of strength. It manifests itself in the Weibull diagram as a parallel shift of the Weibull line. A formal description for this is

$$\sigma_1^m \cdot V_{eff,1} = \sigma_2^m \cdot V_{eff,2} \quad (9)$$

- The probabilistic design process that is used to estimate an allowable design stress (σ_{des}) for a desired reliability ($R_{des} = 1 - F_{des}$) or to predict the probability of failure ($R = 1 - F$) at a given operating stress (σ_a) relies on the existence of similar defect populations in specimens and components. Only in this case (i.e. if the material is a "Weibull material" [24]) it is guaranteed that the size extrapolation according to eq. (9) is correct and that the Weibull line can be extrapolated to smaller stresses/probabilities of failure than those measured with specimens. The process can be represented graphically as shown in Figure 2. Blue symbols indicate measured strength values and the blue line is the fitted strength distribution ($m, \sigma_{0,S}$). In this example, the components have a larger effective volume than the specimens and the green line indicates the extrapolated strength distribution for the components ($m, \sigma_{0,C}$) given by eq. (9). This line can be used to evaluate the design quantities σ_{des} or F (red arrows).

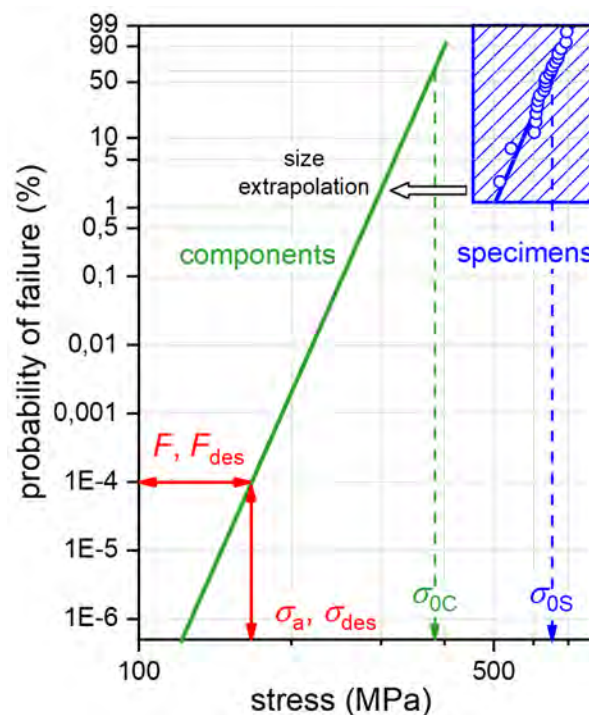


Figure 2: Weibull diagram showing a measured strength distribution (blue) and a graphical representation of the procedure to calculate the reliability or the design stress for components (green line, red arrows).

- In case that two or more distinct flaw types act as critical defects [30, 31], or if defects are not homogeneously distributed within the material [32], or if the material exhibits an R-curve behavior (see section 2.5) [33] or there are residual stresses acting on a scale similar to the defect size [34-36], the scatter of strength can no longer be described using the Weibull distribution and measured strength values will no longer lie on a straight line in the Weibull diagram. A more general approach has to be used to describe the statistical nature of strength [1, 2, 21, 37].

2.3 Measurement of Strength

A number of methods has been developed to measure the strength of ceramics [38-40]. Usually an increasing load is applied in a defined way to a specimen until fracture occurs. The maximum stress that occurs in the specimen at the moment of failure is equated to the strength. Therefore, it is essential for every test configuration to have a knowledge of the stress distribution as accurately as possible. Traditionally, the relationship between loading, specimen geometry, and the maximum stress occurring is provided in the form of analytically derived expressions for linear-elastic deformations. These expressions often rely on an idealized loading situation. Deviations from this, which always occur in reality, are either quantified through an error analysis [41], mitigated by specific provisions for test execution [42] or eliminated by restricting the specimen geometry [43]. It should be mentioned that strength tests have to be sufficiently accurate in order to allow for a meaningful estimation of the material's Weibull modulus. It has been shown that in order to determine a Weibull modulus of $m = 20$ (which is a desirable value for structural applications) the random error in any individual strength measurements must not exceed $\pm 5\%$ [44].

Another prerequisite for useful strength test for ceramics are specimen geometries which can be readily provided either in the form of as-sintered test bodies without the need for any hard machining or by simple cutting and grinding procedures to fabricate them out of larger blanks or even components. This is especially important when considering that the determination of a strength distribution and its parameters requires thirty or more measured strength values [25-27].

For the design of ceramic components according to the probabilistic methodology outlined in section 2.2 not only knowledge of the parameters of the strength distribution is indispensable, but also the Weibull effective volume, area or length are required and have to be provided [45-47].

In addition to delivering strength values, fractured strength specimens or components are the key to analyzing strength determining defects [48-51]. A critical defect must inevitably be present on the fracture surface of every broken specimen. These defects can be found and imaged using suitable fractographic methods, showing which defect type is the most dangerous. The fractographic examination of strength specimens is not only useful in order to better understand the material and its manufacturing process. It can additionally provide valuable information for refining the design of components and improving their reliability and mechanical performance [50, 52, 53]. During failure analysis, details of the fracture sequence and the stress at fracture can also be obtained from the specific characteristics of fractured parts and their fracture surfaces [54, 55].

2.3.1 Uniaxial Flexure Tests

Bending beams are most commonly used to measure the strength of ceramics. Either prismatic bars with cross section $b \times h$ (width \times thickness) [56-58] or cylindrical rods [59] with a thickness to length ratio > 10 are loaded in 3-point or 4-point bending, Figure 3. The maximum stress can be calculated from the load at fracture P using Euler beam theory, eq. (10). The simple stress distribution allows for a straightforward calculation of Weibull effective quantities [60]. Possible errors associated with these tests have been extensively analyzed [41, 61]. The most important complications arise when friction is present between the specimen and support and loading

rollers. Due to the concentration of the high stresses onto the tensile surfaces, these tests are quite sensitive to the state of the tensile surface and its edges.

$$\sigma_f = \frac{3P(L_S - L_L)}{2bh^2} \quad (10)$$

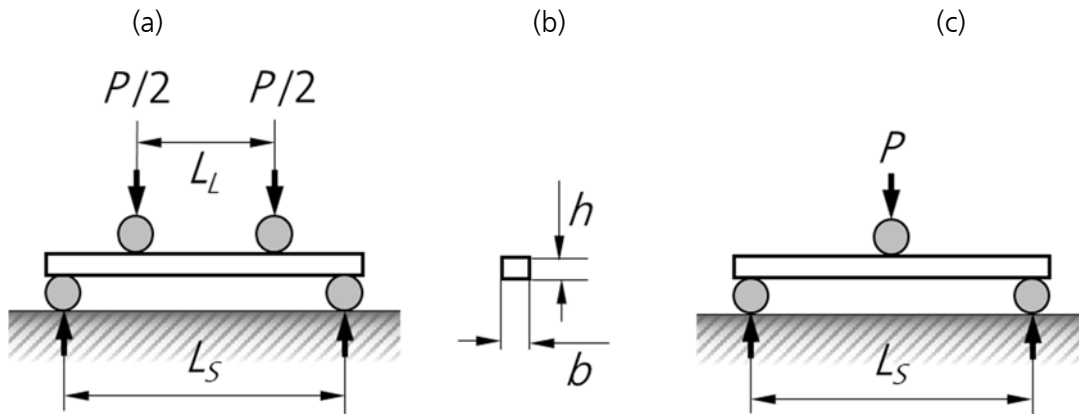


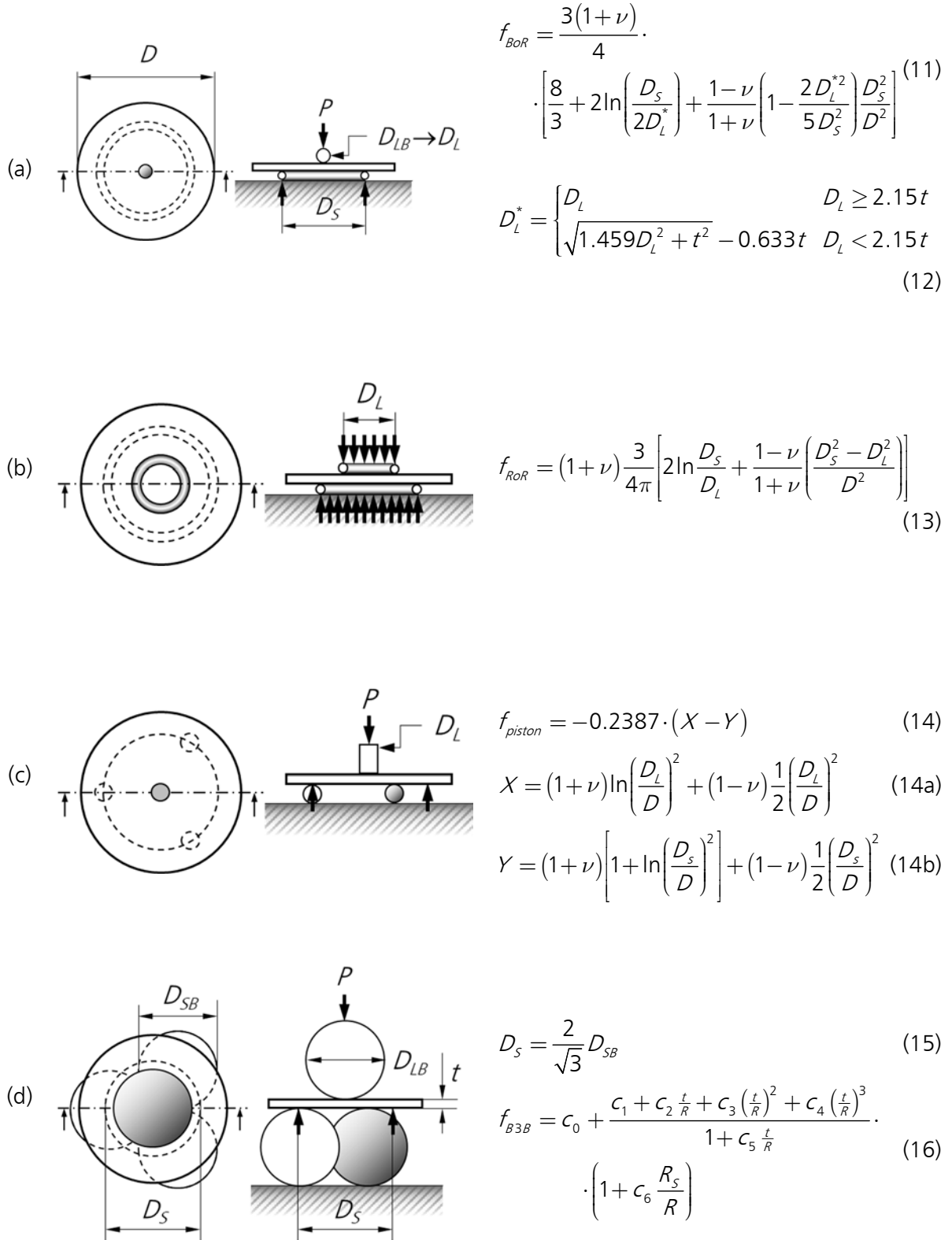
Figure 3: Schematics of uniaxial flexure tests for ceramics. (a) Four-point bend test. (b) Cross section of typical prismatic specimen. (c) Three-point bend test.

Dimensions of test set-ups are 40mm or 20mm for the support span L_S and load spans of $L_L = L_S/2$, respectively, on which prismatic specimens with a cross section of $b = 4\text{mm} \times h = 3\text{mm}$ or $2.5\text{mm} \times 2\text{mm}$ are tested [56-58]. An analysis was carried out to determine the minimum size of flexure tests with a claimed maximum error of $\pm 5\%$ (which is deemed sufficient for statistical analysis of strength data [25-27, 44]) considering typical manufacturing tolerances in metal working. The resulting miniature specimen with a cross section of $2\text{mm} \times 1.5\text{mm}$ tested on $13\text{mm}/4.33\text{mm}$ spans is still manageable on standard testing equipment yet in many cases too big to be harvested from components [62].

Standard flexure bars also serve as basic structures for fracture toughness tests due to their specimen geometry which is suitable for simple pre-crack introduction.

2.3.2 Biaxial Flexure Tests

While strength testing with uniaxial stress field provides easy-to-interpret results, the majority of components experience multi-axial stress states. Hence, there is a need for simple strength tests that use multi-axial stress states, in the simplest case equi-biaxial ones. Biaxial stressing is a more severe loading case than uniaxial stressing and provides data that are more useful for conservative strength design [24]. Common biaxial strength tests are performed on discs or plates which are supported on a ring or on three support points evenly distributed on a support diameter. The load can be introduced by a ring, a flat piston or a ball [39]. A few tests are shown in Figure 4.



The maximum stress in such specimens is calculated from the load at fracture P using the general relation

$$\sigma_f = f_{test} \cdot \frac{P}{t^2} \tag{17}$$

with a factor f_{test} that depends on the test configuration (support diameter D_s , load diameter D_l), specimen shape (diameter D , thickness t) and Poisson's ratio. For the Ring-on-Ring (RoR) [42, 65], Piston-on-Three-Balls [43, 66] and the Ball-on-Ring (BoR) [67-69, 63] configurations, analytical solutions exist for f_{test} . For the Ball-on-Three-Balls (B3B) test an expression fitted on FEA results covering a wide specimen geometry range has been provided [64, 70].

The Ring-on-Ring test is standardized [42] for a parameterized geometry which allows to maintain test conditions where small deflections and linear-elastic material behaviour prevail. This motivates limits in specimen thickness relative to the support diameter. Figure 5 indicates these limits graphically for some engineering and dental ceramics. Practical restrictions (due to manufacturing issues) in the size of the support diameter thus pose a lower bound to specimen thickness of approximately $t > 500\mu\text{m}$ [71, 72]. This limitation can prevent valid tests on thin specimens of strong, compliant materials. The test provides a large stressed region, but is strongly affected by friction. To mitigate this, low-friction or soft interlayers between specimen and loading and support rings are prescribed. Expressions for the Weibull effective quantities have been provided [42].

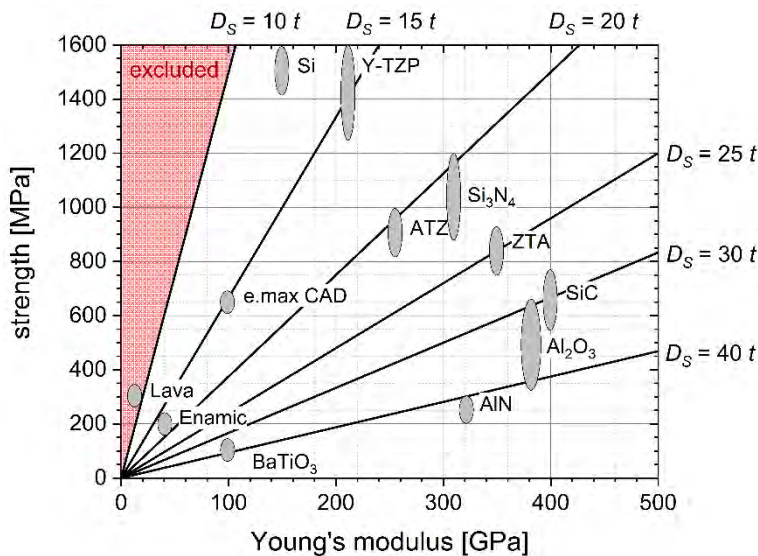


Figure 5: Approximate graphical representation of the geometrical restraints according to ASTM 1499 [42] for the RoR test to ensure linear-elastic deformations for various materials. Lines indicate combinations of support diameter D_s and thickness t . For a given material the grey "property bubble" must lie above a certain combination.

The Piston-on-Three-Balls test is only standardized for a very limited specimen size range because the analytical expression provided for the evaluation does not sufficiently accurately for other geometries [43]. Loading of a specimen with a flat piston is not well defined due to deflection of the specimen and possible wear of the piston. As with the RoR test, soft interlayers are frequently used as a remedy.

It is obvious that both of these tests suffer from a somewhat undefined load introduction situation due to the use of the interlayers. This problem, together with friction can be avoided altogether by supporting the specimen on three balls and loading it with a fourth ball. This is the Ball-on-Three-Balls test [64, 70]. For this test, the support is formed by three balls in contact with each other, so that the support diameter is defined by the diameter of these balls, eq. (15). By using a simple guide to arrange support balls, specimen and load ball, the test set-up is not confined anyhow during loading, so that friction can be ruled out [73]. Other than for the previously described tests, no sufficiently accurate analytical expression for the factor f_{B3B} can be obtained. Instead, it has been evaluated by a parametric FE analysis with a linear elastic model using point supports and a point load. The results have been provided as empirical function fitted to the FEA results and employing 7×6 constants for a range of seven different Poisson's ratios [64, 70]. Weibull effective quantities can only be obtained by multivariate interpolation of the FEA results. Due to its simple execution and robustness against systematic errors [73], it can be downscaled easily to maintain small-deflection conditions even for very thin specimens. It has been applied to disc and plate specimens with diameters or side lengths ranging from 3mm to 45mm and thicknesses from $130\mu\text{m}$ to 5mm made from various structural and functional ceramics, single crystals or hard metals [74-81].

2.3.3 Tests on Components

Components made from brittle materials have specific properties that result from the entire manufacturing process. Naturally, care is taken during manufacture to produce the best possible material condition. However, as already mentioned, defects can still occur during finishing, transportation, installation and operation [82-86]. It is therefore of great interest to be able to measure the strength directly on components. To do this, it is necessary to consider whether and how the component needs to be modified/machined in order to create a test specimen that can be subjected to a quantifiable stress field [3].

A prominent example for such a test is a strength test for ceramic bearing balls. Of course, discs or flexure specimens could be manufactured from balls if they are big enough. But with such specimens the interior of the ball would be tested and not the surface, which is on one hand the part of the ball that experienced machining and on the other hand the stressed location during service. The strength test for balls exists in two variations, the Notched-Ball test (NBT) [87-89], which has also been standardized [90, 91], and the C-sphere test [92].

Both variations of the test apply the same principle to apply a tensile stress to the surface of a sphere: a wide notch with a length L_N , exceeding the radius R of the sphere, is made in the equatorial plane of the sphere, Figure 6.

The sphere is then compressed perpendicular to this notch. A bending stress field develops in the circle-segment shaped ligament of the equatorial plane, with the tensile stress components at the surface of the sphere. Fracture usually occurs at the apex of the ball. The stress field has been evaluated by FEA for a variety of relative notch geometries. The maximum stress at fracture which is equated to the strength σ_f can be calculated from the fracture load P and the ligament thickness h by

$$\sigma_f = f_{NBT} \left(\frac{L_N}{D}, \frac{W_N}{D}, \frac{R_N}{W_N}, \nu \right) \cdot \frac{6P}{h^2} \quad (18)$$

with ball diameter $D = 2R$, the notch length L_N , the notch width W_N , the notch fillet radius R_N and Poisson's ratio ν .

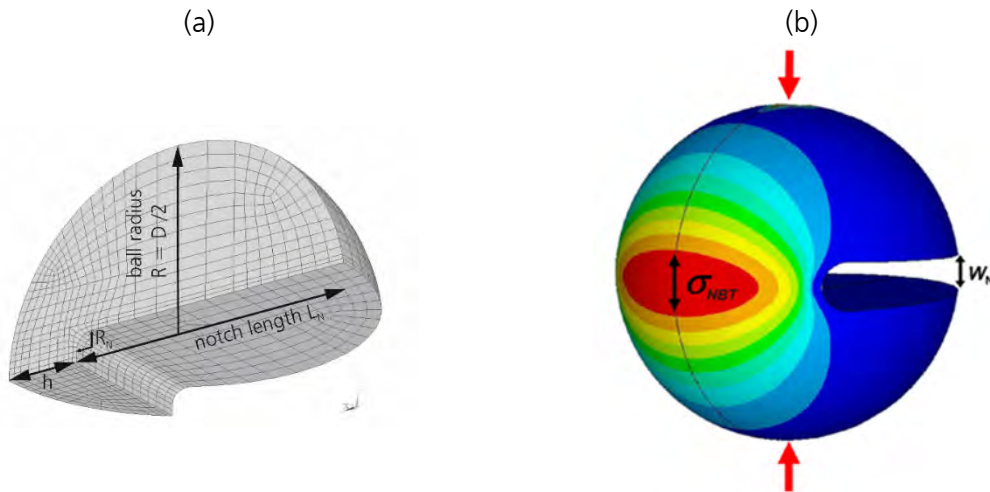


Figure 6: Schematic of the Notched-Ball test. (a) FE model. (b) 1st principal stress distribution on the ball surface [87].

The factor f_{NBT} is provided as analytical expression fitted to the FEA results [88, 90, 91]. The Weibull effective volume V_{eff} and effective area S_{eff} are provided as approximated expressions fitted to FEA results [90]. This test is probably the most accurate strength test for ceramics. The specimens (balls) are usually extremely accurate, the dimensions of the notches can be measured accurately to a level that only introduces a minor systematic error to the result. The load introduction happens far away from the location of the maximum stress and friction can be completely excluded by using test fixtures (flat plates) from the same materials as the balls.

2.4 Measurement of Fracture Toughness

The principle to determine fracture toughness is offered by Eq. (5). By knowing the size and configuration of a crack a in a specimen fractured under a quantified applied stress σ_f and with knowledge of the geometric factor Y , one can easily calculate the fracture toughness K_{Ic} . As for any mechanical testing method, in order to achieve accurate measurements, it is crucial to ensure that the real-world scenario follows closely the fracture mechanical model employed for evaluation. Hence, the essential prerequisites for a correct fracture toughness measurement include [93]:

- i. Fracture by fast crack propagation of
- ii. a well-defined crack a in
- iii. a well-defined stress field, for which
- iv. a well defined geometry factor Y is known.

Guidelines for implementing specimens and procedures that meet these conditions have been established for metals in ASTM E399 [94]. However, transferring these guidelines directly to ceramics presents challenges for several reasons:

- *Machining Complexity.* Ceramics pose challenges in machining due to their hardness and brittleness. While it is relatively straightforward to grind ceramics to achieve prismatic bodies with flat surfaces, tasks such as drilling holes or shaping cylinders are notably more challenging and expensive.
- *Pre-cracking Issues.* The fatigue pre-cracking techniques commonly recommended for metals are not feasible for ceramics.
- *Limited Material Availability.* Often, there is a restricted quantity of ceramic material available for testing purposes. Moreover, the properties of ceramics are intricately tied to the characteristics of their processing.
- *R-curves.* In ceramic microstructures, mechanisms may act that lead to an increasing resistance against crack propagation with crack extension (section 2.5). The R-curve behaviour has to be considered if results from different methods are compared [93, 95].

Consequently, the standardized techniques for determining the fracture toughness of ceramics use the test configurations for uniaxial flexure tests as described in section 2.3.1 to generate a well-defined stress field. They employ prismatic bars with dimensions $h = 4\text{mm}$ and $b = 3\text{mm}$ which undergo flexural loading either in 4-point or 3-point bending configurations. Pre-cracks or appropriate notches are incorporated into the bars' potential tensile surfaces using a range of methods. Some methods shall be introduced here as examples. Figure 7 offers an overview of the loading setup and some pre-crack configurations.

2.4.1 Methods with Edge Cracks or Notches in Flexure Specimens

In the standardized single edge pre-cracked beam (SEPB) method [96, 97], a pre-crack with a relative depth of $0.35 < a/h < 0.6$ is introduced into the tensile face of a standard bend bar, see Figure 7a. Subsequently, the specimen undergoes a bending fracture test at a rapid loading rate to determine σ_f . Typically, fracture in such a test takes place by unstable crack propagation. The length of the pre-crack, a , is measured on the fracture surface. Any specimens exhibiting pre-cracks that are excessively long, irregular, or tilt or twist away from the optimal plane are deemed unsuitable and rejected from the evaluation. Criteria for this are detailed in the respective standards. The method works with realistic, but very long pre-cracks. These cracks are not easy to introduce, which often leads to a high number of invalid specimens [98, 99].

A variation of this method is the single-edge V-notched beam (SEVNB) method [100]. This technique shares similarities with the SEPB method concerning fracture test procedures and the computation of fracture toughness. However, instead of employing a sharp pre-crack, a slender notch is introduced. Fracture toughness is determined based on the failure stress σ_f recorded in a 4-point bend test, the notch depth a , and the associated geometric factor. Ideally, the notch should exhibit a relative depth within the range $0.2 < a/h < 0.3$. Moreover, the radius ρ at the notch root should be less than twice the average grain size of the material being tested, ensuring $\rho < 10\mu\text{m}$ in all instances. To create such notches, one can sharpen a saw cut using a razor blade combined with $1\mu\text{m}$ diamond paste by a honing procedure. In materials with small grains, notch root radii around $\rho \approx 2\mu\text{m}$ can be achieved, as illustrated in Figure 7a. In materials with very fine grains such as TZPs, sufficiently sharp notches cannot be produced so that they are excluded from the application of the method [100].

This method replaces the sharp crack with a notch that has a slightly smaller stress intensity than a crack of the same length. Theoretical considerations backed-up by experimental evidence [101,

102] postulate the existence of small cracks in front of such notches, which mitigate the blunting effect. The system 'notch + small crack' then acts as an equivalent sharp crack, so that in most materials accurate measurements are possible. The method is much faster and more practicable than the SEPB method, easy to execute and delivers precise values.

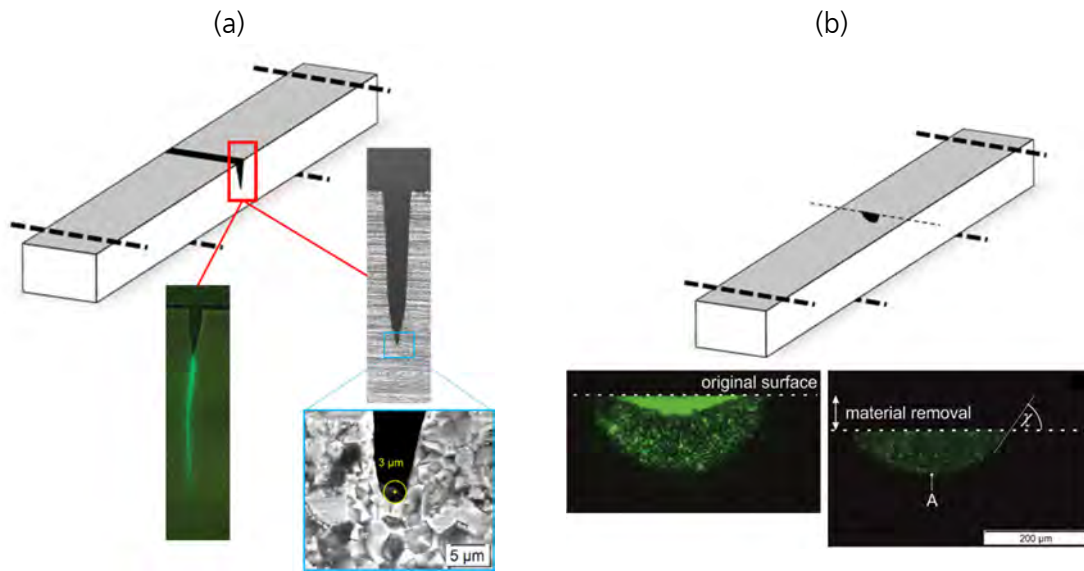


Figure 7: Schematics of fracture toughness tests and typical precracks. (a) Single-Edge-Pre-cracked beam with pre-crack emanating from a short notch and Single-Edge-V-Notched beam with sharp notch. (b) Surface-Crack-in-Flexure specimen with as-indentated pre-crack and ground-off pre-crack made visible by fluorescent penetration dye.

2.4.2 The Surface-Crack-in-Flexure Method

This approach is also a standardized method [97, 103]. In this test, a small semi-elliptical pre-crack is introduced into the bend bar using a Knoop indentation, typically executed with a load ranging between 5kg to 10kg. To eliminate the residual stresses linked with the hardness imprint, a layer Δh of approximately 4.5 to 5 times the depth of the indentation imprint must be ground away from the bar's indented surface, leaving a small nearly semi-elliptical surface crack, as depicted in Figure 7b. Subsequently, the bar is fractured in a standard 4-point bend test. The fracture toughness is calculated based on the fracture stress σ_f of the bar, the depth a and half-length c of the surface crack, and a geometric factor for semi-elliptical cracks as defined by Newman and Raju [104]. The dimensions of the pre-crack are measured on the fracture surface of the bar.

The SCF method used rather small cracks with a size comparable to natural material defects. However, locating the crack and measuring the pre-crack size is not straightforward and requires fractographic experience, especially in coarse grained ceramics. Consequently, also with this method a considerable number of invalid specimens is to be expected [98].

2.5 Material Aspects of Strength and Fracture Toughness

Considering eq. (5) it is obvious that the strength of ceramics is actually determined by two entities: the size of the critical defect a_c and the fracture toughness K_{Ic} . Defects in ceramic bodies

are present in a variety of sizes. They are not necessarily a result of errors made unintentionally during manufacture and should be considered as intrinsic characteristics of ceramic materials. Defects that come into existence during processing may be pores, inclusions, inhomogeneities or delaminations. Cracks may be generated by machining or polishing through localized contact loads as well as by a superposition of residual micro-stresses with external loads or by phase transformations. A few examples are shown in Figure 8. The region lacking glassy intergranular phase in Figure 8a comes into existence during powder processing, the delamination pore in Figure 8b is a results of the material flow during the injection molding process. Coarse grains in Figure 8c grow due to a chemical interaction with kiln furniture during sintering, and the contact crack in Figure 8d was generated during the final grinding step by careless part management.

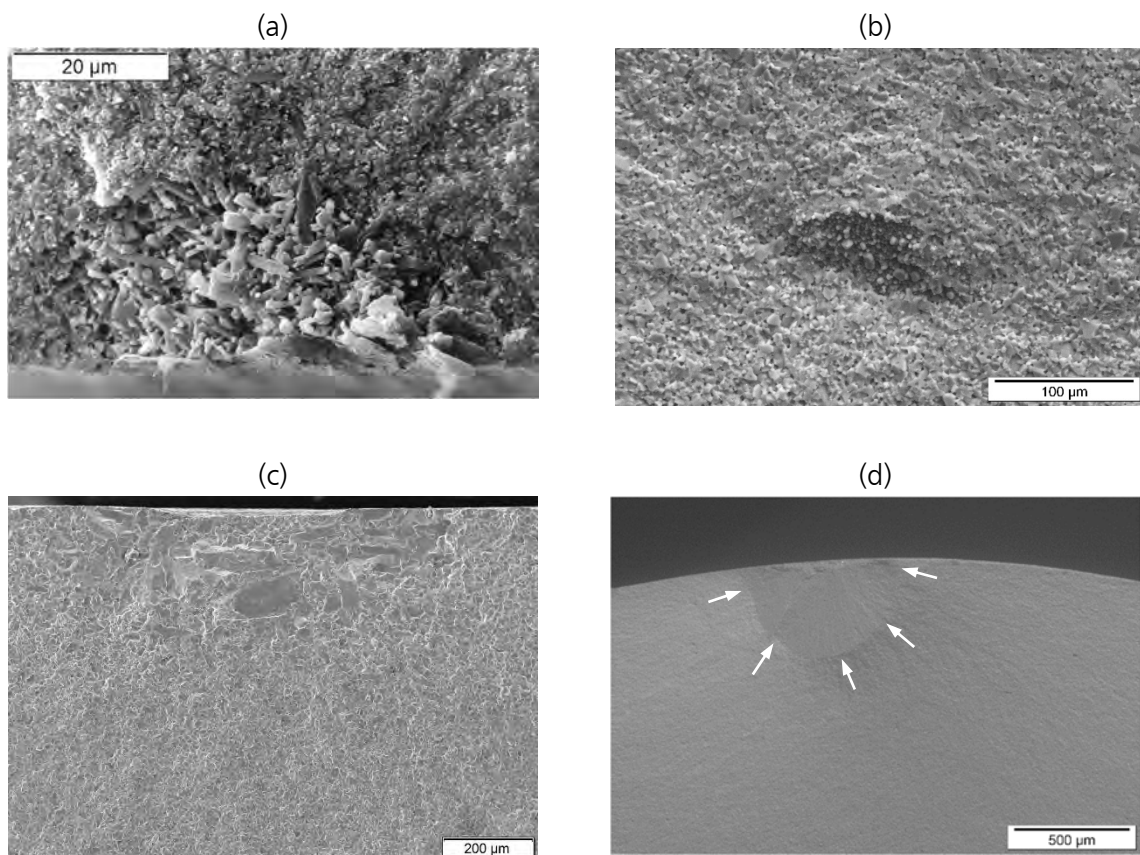


Figure 8: Defects in ceramics. (a) Microporous region lacking glassy intergranular phase in Si_3N_4 , (b) Delamination in injection molded Al_2O_3 [52], (c) Coarse grain zone and surface dimple in Al_2O_3 , (d) Contact crack in Al_2O_3 [52].

The fracture toughness is apparently related to the surface energy (eq. (4)), where the thermodynamic surface energy γ substantiates a lower boundary value for this property for a given material. In many polycrystalline materials, mechanisms can work during crack growth in addition to the formation of new crack surfaces, which require additional energy and make crack propagation "more difficult", i.e. they toughen the material. Such mechanisms may occur in front of the advancing crack or in the crack wake [95]. An example for the former is the phase transformation of tetragonal zirconia to its monoclinic phase [105-109]. Because of the volume increase associated with this transformation, the stress in front of the crack tip is reduced. Examples for the latter are interactions between the two faces of a crack behind the crack tip.

Such interactions may be interlocking bridging grains or frictional sliding grains which also reduce the stress acting at the crack tip [110-115]. Both mechanisms reach a saturation if either a steady state transformation zone is created or the crack opening is too large to maintain crack face tractions, respectively [95].

In the context of continuum mechanics and linear elastic fracture mechanics, these effects are modeled by superposition of the positive applied stress intensity $K_{appl}(\sigma_{appl})$ with a negative shielding stress intensity $K_{shield}(\Delta a)$, the value of which depends on the amount of crack propagation [14]. For such a situation, the stress intensity at the crack tip K_{tip} is

$$K_{tip} = K_{appl} - K_{shield} \quad . \quad (19)$$

The failure criterion given by eq. (3) is valid at the crack tip and is specified as

$$K_{tip} \geq K_0 \quad , \quad (20)$$

where K_0 is the material intrinsic toughness. The value for fracture toughness that we can measure with any experimental method follows from equating eqs. (19) and (20):

$$K_{appl} = K_0 + K_{shield} = K_R(\Delta a) \quad . \quad (21)$$

The quantity $K_R(\Delta a)$ now depends on the amount of crack growth Δa that a pre-crack has experienced during specimen preparation before it is fractured unstably in the fracture toughness test. The phenomenon is called rising crack growth resistance curve (R-curve). Materials differ in the crack growth range over which the R-curve increases (a few μm to several $100\mu\text{m}$) and how far the R-curve rises before it reaches its saturation value (a small percentage of K_0 to a doubling or more of K_0) [116, 115]. Both characteristics depend details of the actual crack and loading configuration [95].

In Figure 9, R-curves of a few ceramics are shown and the intervals, in which different methods for the determination K_{Ic} / K_R operate, are indicated by grey shaded areas. This states that knowledge about the used method as well as the analyzed material is necessary for the interpretation of measured fracture toughness values [14, 117].

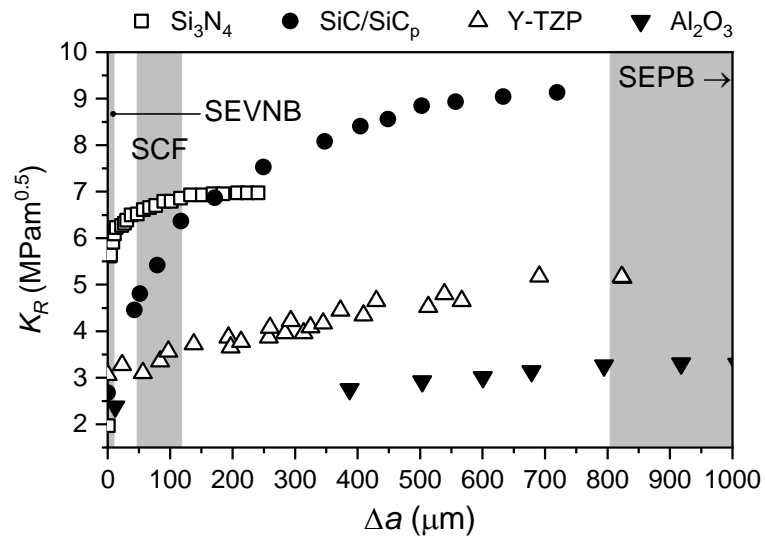


Figure 9: R-curves of some ceramics and crack length intervals which are covered with various fracture toughness test methods [118].

3 Challenges for Components and New Manufacturing Methods

Material development has led to a number of new ceramic materials, manufactured by new methods for new applications: highly porous materials or thin for SOFCs or SOECs [119], high strength ceramic substrates and single crystals for microelectronics [120, 121], scaffolds for medical applications fabricated by AM processes [122], to name only a few. Consequently, new challenges regarding the determination of strength and fracture toughness of these materials and components emerge. Some of them will be detailed in this section.

3.1 Biaxial Strength Testing of Strong and Thin Specimens

Biaxial strength testing methods are particularly important for components and in some areas of ceramic development and research. On one hand, components such as substrates for electronics, components for fuel or electrolyzer cells, watch glasses and semiconductors only exist as discs or plates. On the other hand, samples from available material batches can only be produced in this form, as for example when specimens are fabricated from dental ceramic-CAD/CAM blanks [79]. These discs are often very thin and/or the materials are particularly strong and/or compliant.

In biaxial flexure testing of thin plates, it is difficult to avoid excessive deflection, which may violate Euler/Bernoulli beam-bending theory employed to analytically derive the stress factors f_{test} , unless a very small support diameter is used. It has been shown that fixtures with a support diameter $D_s < 10\text{mm}$ for Ring-on-Ring tests are difficult to manufacture and handle. For such cases, the Ball-on-Three-Balls test offers an alternative, since even small support radii can be realized very precisely via the contacting spheres forming the support [75]. However, even in this test, large deflections may occur which means that the idealized assumptions for the stress calculation are no longer valid [70].

In the case of particularly strong specimens, high fracture forces occur which not only lead to high deformations prior to failure but also influence the contact situation between the specimen and the load ball. The area of load application is then no longer so small that it can be described with a point load, as was done for the calculation of the pre-factor f_{B3B} (section 2.3.2), but has to be described by a contact pressure distribution over a contact area [123-125]. For a given applied load, the applied bending moment as compared to the point load situation is then reduced and less tensile stress is generated on the tensile face. This effect becomes more prominent as the load increases. Thus, the factor f_{B3B} decreases with increasing load. This effect can only be captured

numerical by using elaborate 3D FE models which require long computation times. It is shown for a single specimen geometry and material and various specimen thicknesses in Figure 10.

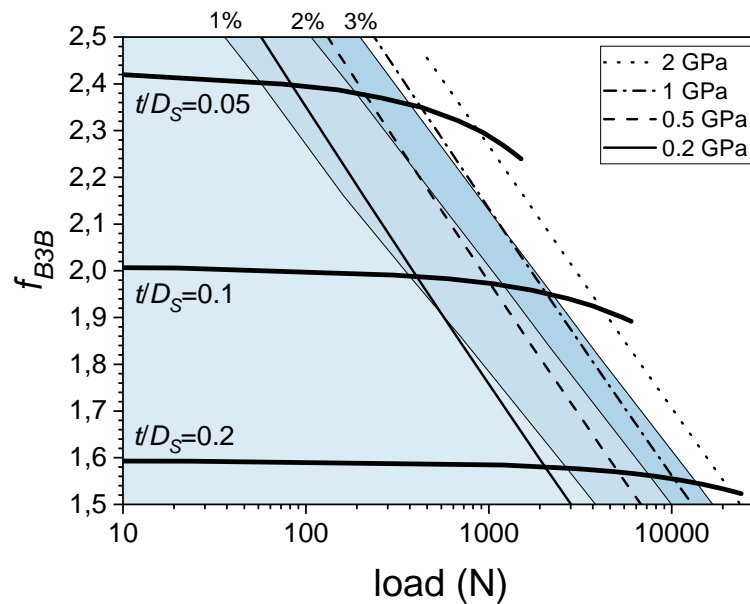


Figure 10: Load dependence of the factor f_{B3B} for the B3B test. The blue regions indicate loads at which the factor decreases by the indicated percentage compared to the point load situation. The lines indicate maximum stresses in the disc. Calculations were performed for discs with $D = 20\text{mm}$ ($E = 300\text{GPa}$, $\nu = 0.27$) tested on steel balls with $D_{SB} = 15.07\text{mm}$. Plot adapted from [70].

Strength tests on specimens are often used to estimate the reliability of components according to the statistical description of brittle fracture (section 2.2). For this purpose, and also to enable comparisons with measured values from other (standardized) strength test methods, it is necessary to know the Weibull effective quantities [45].

In order to make the B3B test applicable to many new ceramics and other brittle materials and to bring its application potential to the same level as that of standardized strength tests, it is necessary to

- provide an evaluation for square plates
- quantify the effects of large deflections and more realistic load introduction conditions for general cases, i.e. a variety of combinations of specimen geometries with material elastic properties,
- validate the FEA calculations for these situations,
- determine and provide the Weibull effective areas and volumes for relevant geometries.

3.2 Anisotropic Strength: AM Ceramic Components

Additive manufacturing (AM) technologies are increasingly used to manufacture ceramic components [126-128]. These technologies can be categorized according to the characteristics of the feedstock that provides the ceramic powder, in (i) powder-based, (ii) solid-based and (iii) slurry-based. They allow to fabricate parts of high complexity without the need of hard-machining thus reducing the risk of introducing strength-limiting surface defects. Even though hard

machining can be avoided for AM ceramic parts, specific process-related aspects of their mechanical performance can be observed due to the layer-by-layer build-up.

These aspects will be explained in more detail in the following for one additive manufacturing process, specifically the LCM method [129]. For other processes, analogous but potentially distinct issues may be expected, which may entail entirely different characteristics [130]. The LCM (Lithography-based Ceramic Manufacturing) process belongs to the VPP (Vat Photopolymerization) processes, specifically falling under the category of DLP (Digital Light Processing) methods. In this technique, to fabricate an individual layer, a polymer slurry containing ideally 50vol% - 60vol% ceramic particles is selectively solidified at desired locations through photopolymerization [131]. In DLP processes, the entire layer is exposed through a single projection. The positions to be polymerized are defined by an array of small mirrors, each of which can be individually on/off-controlled. These mirrors have a defined dimension, for instance, $40\mu\text{m} \times 40\mu\text{m}$. This dimension determines the lateral resolution of the process; however, it also results in an approximative realization of all edges that are not parallel to the mirrors, leading to an aliasing effect. This effect is not limited to a single exposed (x - y)-layer but also manifests itself in the build direction (z) [132]. Consequently, the surfaces of LCM components may not always be entirely smooth but could exhibit a wavy structure, Figure 11b. A similar effect can also be observed when particularly thick layers are fabricated to speed up the manufacturing process [133]. The high light intensities required for this purpose result in increased light scattering at the edges of the layers and polymerization in undesired areas [134]. In this scenario as well, wavy surfaces may be formed, even when the edges are parallel to the mirror array. Finally, when load is applied, these waves can act as stress concentrators similar to notches, potentially influencing the mechanical strength of the components.

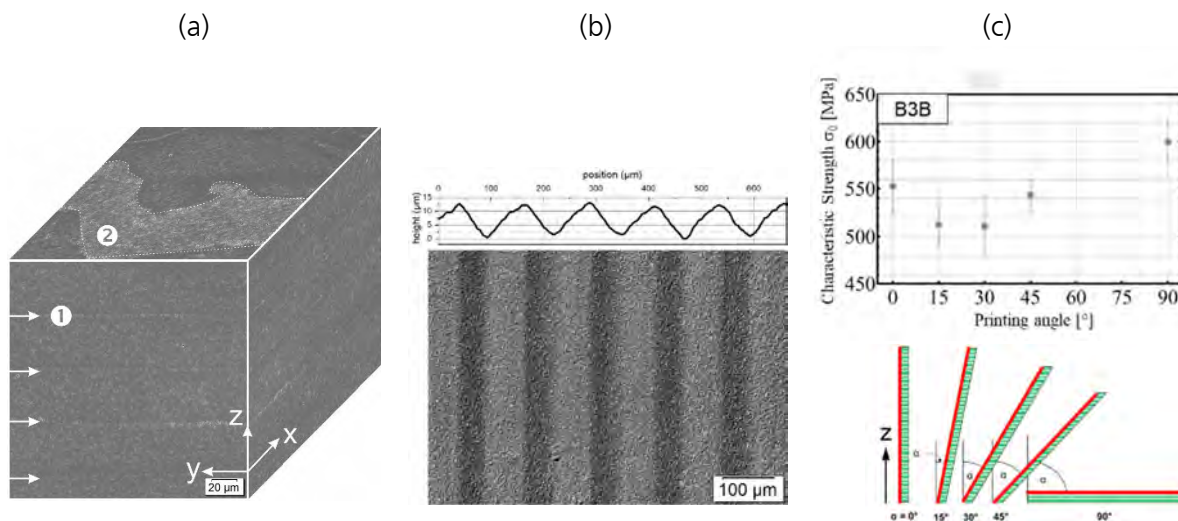


Figure 11 : Typical defects and surface structures in LCM-ceramics and their effect on strength. (a) Poorly bonded layer interfaces as cross sections ① and parallel view ②. (b) Surface structure due to aliasing. (c) Effect of surface structures on the characteristic strength measured using the B3B test [129].

In addition, insufficient bonding of two subsequent layers can cause another type of typical defect in such components. Interfaces may be systematically weakened by a higher degree of porosity or even by distinct delamination defects as has been shown for alumina specimens [133], Figure 11a.

Moreover, as the surface structures and internal defects are dependent on the orientation of a part in the building space, this can then lead to a change in the measured strength depending on the relation of loading direction and building direction [135]. The impact of aliasing on strength as measured with the B3B-test is represented in Figure 11c. Square plates were fabricated at varying inclinations (0° , 15° , 30° , 45° , 90°) relative to the vertical (z)- building direction under conditions avoiding overpolymerization. A correlation is evident between the printing orientation and the resultant characteristic strength. Specimens printed at 15° and 30° show reduced strength [129].

Apart from these effects on the produced ceramic itself, different AM processes for ceramics have distinctly different ranges of geometric resolution and possible part sizes [4, 5]. Standardized strength specimens [25] are not in all cases suitable for a given AM method. Prismatic bars of $4\text{mm} \times 3\text{mm}$ cross section and $> 45\text{mm}$ length as commonly used for strength assessment (cp. section 2.3) are for example quite large for the LCM process leading to problems with shape constancy, cracking or warpage. Additionally, they are thicker than most desirable structures in typical components fabricated by LCM.

When summarizing these aspects of the strength of AM ceramics and supplementing them with the required sample sizes for statistically significant conclusions (cf. section 2.2), requirements for customized strength measurement methods for AM ceramics emerge. Tailored strength test specimens for AM ceramics should:

- fully utilize the design options offered by additive manufacturing,
- use a test piece geometry with dimensions relevant to the specific ceramic AM method,
- have a tensile loaded face that is printable in different orientations with respect to the building direction z [132],
- deliver more than thirty individual test pieces for a statistical strength analysis, ideally produced in a time efficient single print job,
- provide test pieces with prospective tensile loaded faces that can be thermally processed without contact with kiln furniture to avoid contamination or friction effects on shrinkage.

3.3 Fracture Toughness: Pre-crack Shape and Measurements on Small Components

Similar to typical defects (section 2.5), the microstructure and thus K_{Ic} of ceramics are often influenced by manufacturing details [136]. On one hand, blanks specifically produced to obtain standard specimens for characterization purposes, have different sizes and shapes than actual components and may consequently exhibit different properties. On the other hand, typical components may be too small or too thin to extract standard specimens for applying corresponding testing methods. To give an example how to address such a scenario the approach for ceramic substrates can be mentioned: the materials of interest only exists as thin ($< 1\text{mm}$) sheets, thus a suitable standard [137] has been developed for determining their fracture toughness. The method is close to the SEPB-Method [96], but takes the small thickness into

account. In material development, processes such as uniaxial pressing, lamination of tapes [138, 139], Spark Plasma Sintering [140], and cold-sintering [141], among others, are employed to produce materials in the form of small discs. However, these processes typically do not yield discs which are big enough to provide standard specimens.

Determining fracture toughness in such scenarios remains a crucial task. For rolling elements for bearings, it is highly relevant to ensure that the pre-cracks used in the experiments are similar in size to defects that are failure-relevant during operation. This approach allows for the examination of a potentially occurring R-curve within the relevant range. Utilizing small initial cracks also facilitates measurements at various locations within a component or enables the use of very small or thin specimens.

To address this gap in material testing methods, there should be techniques available that utilize other test geometries than uniaxial bending specimens as the fundamental principle for generating the stress field. For instance, disks or plates in a Ball-on-Three-Balls test or spheres in the Notched-Ball test could be considered. Suitable pre-cracks for this purpose are surface cracks similar to those employed in the SCF-method (section 2.4), as they generally range in size from several $10\mu\text{m}$ to $100\mu\text{m}$ and are straightforward to induce.

The two mentioned loading geometries effectively meet the previously established requirement for a "well-defined stress field". However, when aiming for conditions such as a "well-defined crack" with a "well-defined geometry factor Y ", the pre-cracks warrant a more detailed examination.

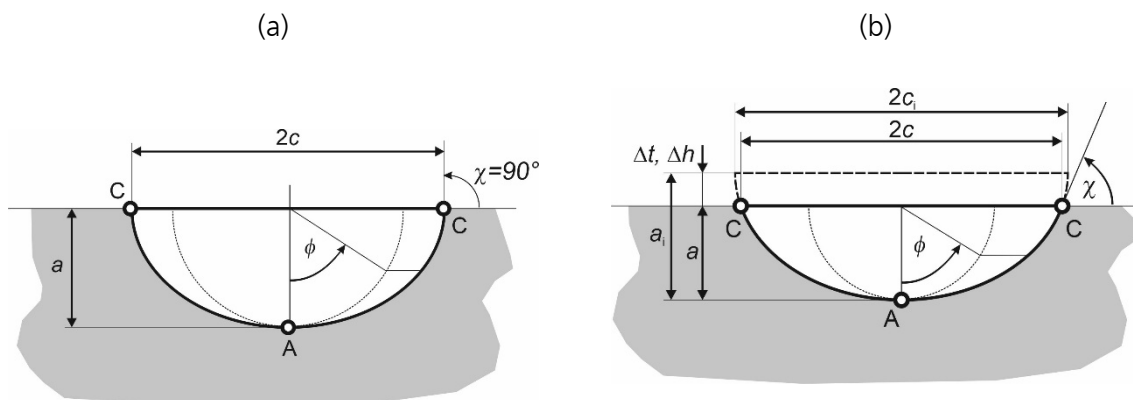


Figure 12: Schematics of surface cracks. (a) Semielliptical surface crack. (b) Surface crack with the shape of an ellipse segment [143].

As shown by Newman & Raju [104], semi-elliptical surface cracks like the one shown in Figure 12 have a stress intensity factor K that varies along their front in tensile or bending stress fields. Fracture is believed to start at the position with the highest stress intensity. Depending on their shape, characterized by a/c and size relative to the specimen's thickness a/h (or a/t) the maximum of K may either be at the deepest point A or at the intersection point of the crack front with the specimen surface, point C, cp. Figure 12. This gives rise to the definition of two distinct geometry factors Y_A and Y_C for such cracks. Moreover, at point C, the stress intensity is not proportional to $r^{-1/2}$ (with the distance from the crack tip, r) at angles χ of approximately

$80^\circ < \chi < 90^\circ$) [142]. The standard stress intensity factor description (such as the one given in eq. (2)) cannot be used for such cases and should be regarded as approximation only. Consequently, the standardised SCF-method prescribes to use only cracks for which $Y_A > Y_G$ i.e. which are critical at point A to generate valid data [97, 103]. Still, there are more details concerning such surface cracks. They are 2-dimensional cracks, implying that Poisson's ratio has an influence on their geometry factor Y . Moreover, they are not strictly semi-elliptical but rather take the form of segments of ellipses, cp. Figure 12. Both aspects need investigation since they are not considered in the existing solution [104].

When introducing these cracks using Knoop hardness indentations, not only are the desired surface cracks perpendicular to the indented surface created, but additional cracks beneath the specimens' surface develop that grow approximately parallel to the surface as shown in Figure 13 [144]. Conventional specimen preparation aims to eliminate these lateral cracks, although this is not always successful.

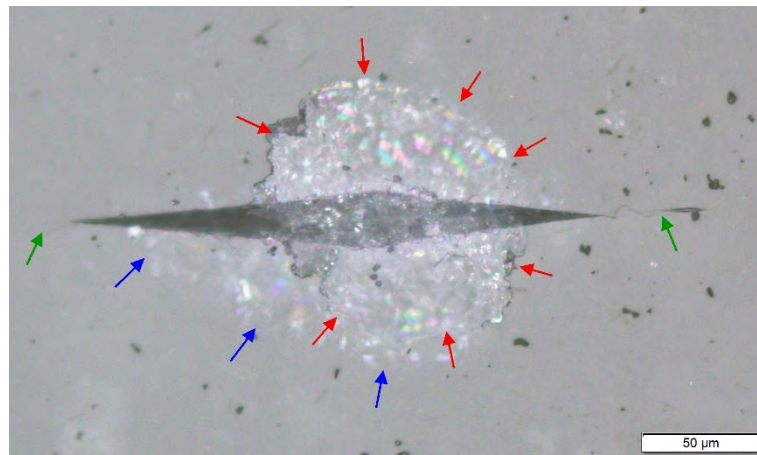


Figure 13: Knoop indentation crack with median crack propagating normal to the indented plane (tips indicated by green arrows) and two systems of subsurface lateral cracks (red and blue arrows) with their crack planes approximately parallel to the surface.

The aspects related to the use of Knoop indentation cracks for fracture toughness measurement on components or thin specimens which need investigation can be summed up:

- Investigation of the influence of the material's Poisson's ratio and the true geometry of such cracks on the geometry factor,
- clarification of the influence of lateral cracks on fracture toughness measurements,
- evaluation of the geometry factor for the specific multi-axial stress fields of component tests such as the NBT or the B3B-test for relevant crack and part geometries.

4 Improved Tests for Strength and Fracture Toughness

This chapter will present contributions which address the challenges outlined in chapter 3 based on the publications that are part of this thesis. The respective publications are summarised in each section to point out the new achievements. The methods used are briefly described and then the most important results are explained. In cases where the results involve complicated, long formulae, their complete presentation is omitted and reference is made to the original publication. Please note that the nomenclature used in this text may differ from that used in the original papers.

4.1 Extension of the Application Range of the Ball-on-Three-Balls Test

This section summarizes the results of publications A ,B and C. Following some preliminary investigations of rectangular plates of a very limited size range [79, 145], a systematic approach was taken to answer the questions related to the B3B test, which are presented in Chapter 3. To this end, numerical [146, 147], analytical [63] and experimental [148, 149] methods were used. To investigate the stress distribution and the maximum stress, the test was described with three different FE models, which have an increasing degree of realism, complexity and computational effort [146].

To determine a simple, new pre-factor $f_{B3B,new}$ and to treat square plates, a partial model was used that utilizes the symmetry of the setup. The support situation and the load application were modeled using point-like conditions. In contrast to the previous calculations, parametrization for different geometrical variations was carried out by relating the specimen geometry (R , t) to the support radius (R_S). To investigate a more realistic load application situation, a FE model was used which describes the load introduction using an ideal Hertzian contact pressure field [123, 125] acting on a circular region (the contact zone) in the center of the specimen. For a given load ball diameter, the size of the contact zone and the magnitude of the contact pressure depend on the applied load. This enables an evaluation of load dependent effects on the maximum stress. These analyses were conducted for various Youngs' moduli. This time efficient, simplified approach allowed the evaluation of a sufficient number of individual cases to cover a similar geometry range as the simple point-load model. In order to investigate the effects of large deformation, an existing analytical description of the deformation of point loaded plates was used [146]. To validate results obtained with the previously described models and the effects of large deformation, an even more elaborate FE-model was used which contains the specimen and the support and load balls and takes both friction and the contact situation into account. Experimental validation of the stress

calculation was carried out by comparing measurements with results that were obtained using the Ring-on-Ring test on the basis of the fracture statistical size effect [148].

The new factor $f_{B3B,new}$ is presented in eq. (22), the calculation of an effective diameter D_{eff} for square plates in eq. (23). Additionally, for the special case of hexagonal plates two possibilities for the strength evaluation were explored. On one hand, a dedicated factor $f_{B3B,hex}$ has been determined for a limited specimen geometry range, on the other hand different effective diameters were proposed and analyzed. It turned out that an equal-area circle is the most suitable effective geometry and can be used together with $f_{B3B,new}$ [150].

A corrected factor f_{corr} , eq. (24), could be obtained based on two individual factors k_1 and k_2 , which take the effects of the distributed contact load and the large deflection into account, respectively. They should be applied when the fracture load/specimen strength surpasses a certain value that can be obtained from eq. (25) or from look-up diagrams provided in [146]. The factors k_1 and k_2 are lengthy expressions which are not reproduced here but can be found in paper A [146]. The range of application of this evaluation of the B3B test is given in Table 1.

$$f_{B3B,new} = \exp \left[0.697(1+\nu) - 0.118 \cdot \ln \frac{t}{R_s} - 0.728 \sqrt[4]{\frac{R}{R_s} \left(\frac{t}{R_s} \right)^2} \right] \quad (22)$$

$$D_{eff} = 2R_{eff} = L \left(1.053 - 0.017 \frac{tL}{R_s^2} \right) \quad (23)$$

$$f_{corr} = f_{B3B,new} \cdot k_1(D_{SB}, t, P, \nu_{LB}, E_{LB}, \nu, E) \cdot k_2(D, t, D_{SB}, P, \nu, E) \quad (24)$$

$$\sigma_{lim} = -347 - 497 \sqrt{\frac{t}{R_s}} - 0.062 \sqrt{E} + 68 \sqrt[4]{E \frac{t}{R_s}} \quad (25)$$

Table 1: Range of application of eqs. (22) - (25), [146].

relative diameter D/D_s	1.05 ... 2.0
relative plate length L/D_s	1.085 ... 1.95
$f_{B3B,new}$	t/D_s of discs: 0.025 ... 0.3 t/D_s of plates: 0.05 ... 0.3
$f_{corr}(k_1, k_2), \sigma_{lim}$	t/D_s 0.05 ... 0.25
Poisson's ratio ν	0.1 ... 0.4
Young's modulus (GPa)	70 ... 400
$\sigma_{f,max}$ (MPa)	... 2000

Figure 14 shows the trend of f_{test} for the B3B test with load for specimens with various thicknesses. The load dependence is weak for thick specimens with a high Young's modulus. Coloured symbols indicate results obtained with the 3D-FE model including contact and friction, black lines are plots of eq. (24).

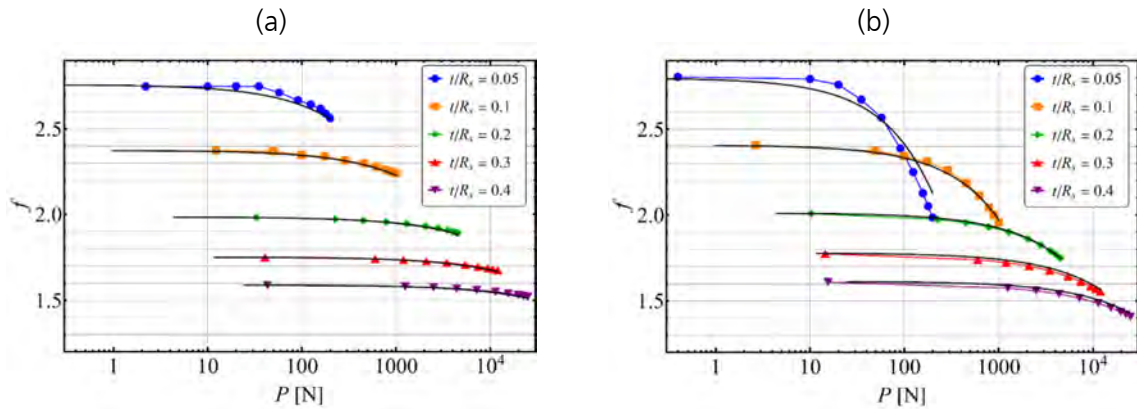


Figure 14: Load dependence of the factor $f_{B3B,new}$ for the B3B test for two different tested materials with typical material properties, cp. Figure 10. (a) Alumina with $E = 420\text{GPa}$ and (b) Glass with $E = 70\text{GPa}$ [146].

The application domains of this new solutions are illustrated in Figure 15: The plot shows f_{test} for the B3B-test depending on load for a specimen of a fixed diameter with given Young's modulus and Poisson's ratio on a fixed support radius but with various thicknesses. The red bullets indicate $f_{B3B,new}$ as in eq. (22). For all cases inside the green region the actual $f_{test} \geq 0.98 \cdot f_{B3B,new}$, i.e. the error in the evaluation of strength through eq. (22) is limited to 2%. The dashed green line is a representation of eq. (25). Specimens with a strength $\sigma_f > \sigma_{lim}$ have to be evaluated using f_{corr} as in eq. (24). This is possible for all conditions inside the pink region up to a maximum strength of $\sigma_{f,max} = 2000\text{MPa}$. For even stronger specimens individual FEA are recommended.

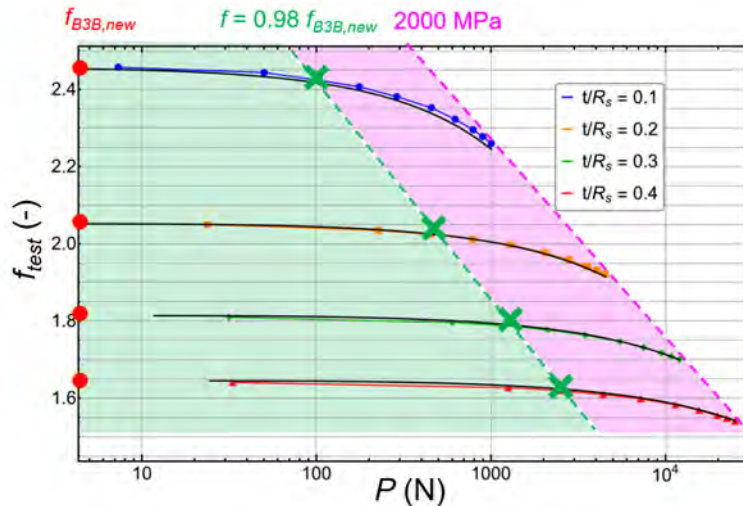


Figure 15: Application domains for eqs. (22) - (25) for one material and a single specimen and support diameter.

The description of effects of large deformation and load also allowed to analyze several variations of the test set-up aiming to answer the following questions: Does it make sense to use smaller support balls to minimized the effect of large deformation? At which loads can the formation of contact cracks at the load introduction location be expected, which may interfere with the regular

fracture process caused by the tensile stress? Is there any benefit in using other than bearing steel grade balls for the test?

Figure 16a indicates, that the correction factor k_2 , which addresses large deflection effects, approaches unity for smaller than ideal (touching) support balls. Yet this comes at much more complicated construction needs of the support. Figure 16b gives conditions for a specimen thickness for which no formation of ring cracks at the load ball can be expected according to Auerbach's law [151]. Combinations of strength and specimen thickness in the green shaded region below the curves are considered safe. The blue symbols indicate experiments where contact cracks appeared. Furthermore, experimental evidence exists, that even if such cracks are present, they do not interfere with the regular fracture process and do not influence the measured strength [152, 153]. Since a higher Young's modulus of the load ball shifts the limiting curve downwards, the use of hard metal or ceramic load balls is not recommended except for cases where plastic deformation of the load ball becomes an issue.

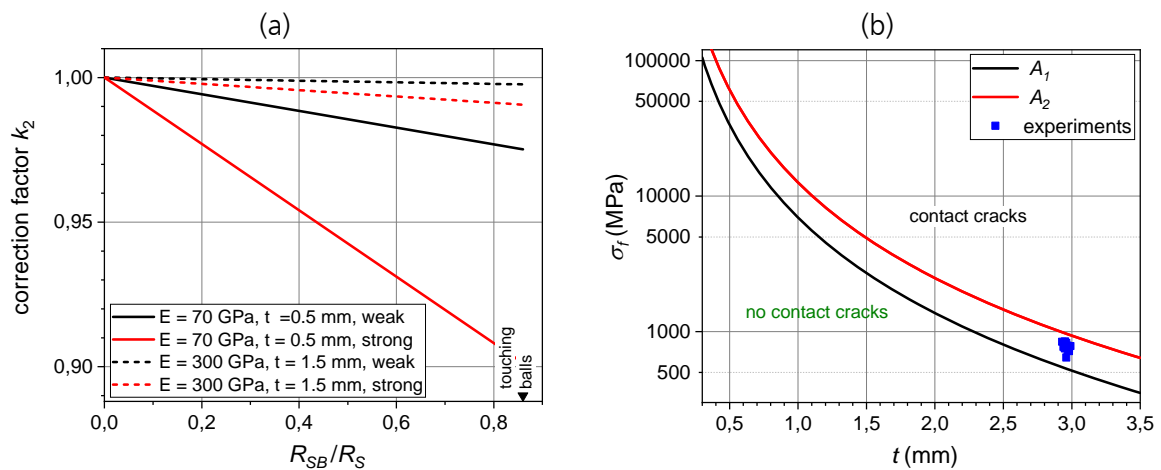


Figure 16: (a) Effect of using smaller than touching support balls on the stress in B3B tests. "Strong" refers to a fracture stress of $\sigma_f = 2000$ MPa, "weak" to $\sigma_f = 500$ MPa. (b) Boundary curves for contact crack formation at the load ball compared to experimental findings. The two curves refer to different choices A_1 and A_2 of Auerbach's constant for the investigated material [146].

Additionally, the Weibull effective volume V_{eff} and effective area S_{eff} of the B3B test were determined [147]. This allowed for an experimental comparison of the B3B test with the standardized and widely accepted RoR-test using disc specimens made from a commercial alumina. The experiments were conducted in the validity regime of $f_{B3B,new}$ for point-load conditions, i.e. below σ_{lim} [146]. Results are shown in Figure 17. According to eq. (9), characteristic strength values of samples of different S_{eff} should lie on a line with a slope of $1/m_{ex}$, where m_{ex} is similar to the Weibull moduli of the individual samples. This condition is fully satisfied for samples of the two different B3B specimen sizes (B-1, B1.7) and two Ring-on-Ring samples (R-1-BT, R-1-T). Additional tests show the influence of soft interlayers between the load ball and the specimen for B3B tests (B-1.7-BT) and the lack of such interlayers in RoR-tests (R-1). In the former case the contact area is increased by an unknown amount which leads to a decrease of stress as compared to the point load situation. As a consequence, the strength is overestimated. In the latter case, it was shown that no homogeneous support nor load application along circles was achieved which

led to stress concentrations below the load ring and thus an underestimation of strength. This was confirmed using fractography [148].

An experimental validation of the stress analysis for the case involving large deformations was done by in-situ measurement of the deflection of thin glass specimens by tomography and radiography. Even though the techniques have a limited resolution, the measurements show an excellent agreement with FEA [149].

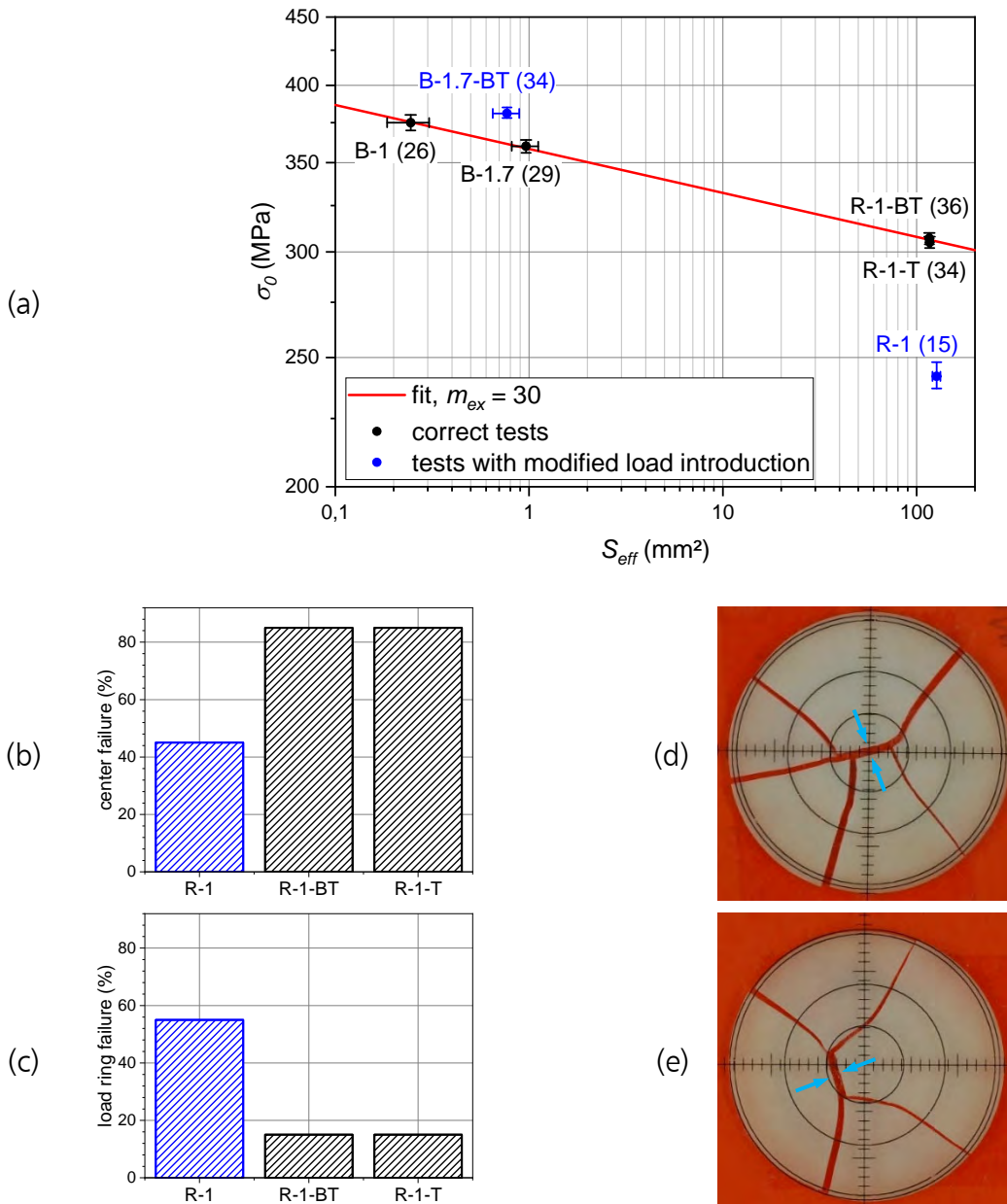


Figure 17: Experimental comparison of B3B and RoR-test results using the Weibull size effect. (a) Size extrapolation plot, cp. eq. (9). (b) and (c) Number of center and load ring failures respectively in RoR-tests. (d) and (e) Fractured RoR-specimens with center and load ring failure, respectively. Rings indicate the load ring, support ring and specimen contours, respectively, blue arrows indicate the failure origins [148].

4.2 A Strength Test Methodology for AM Ceramics

This section presents how initial work on the mechanical testing of LCM ceramics (publication D) and experience from the application of the AM method in material design as summarized in publication E have led to the development of a customized strength testing method. A failure analysis and initial measurement results with the method as presented in publication F complete this part.

Strength measurements on LCM ceramics were carried out using established methods such as uniaxial and biaxial flexure tests. The results are compiled in Figure 18. The influence of surface structures has been demonstrated by comparing measurements on machined specimens with smooth surfaces (diamonds) and those with wavy as-printed + sintered surfaces (circles). For as-printed + sintered specimens one testing direction (green) was significantly weaker than the other directions, while for the machined specimens, all orientations had the same strength. Furthermore, it was shown that the surface structures and their detrimental influence on strength can be avoided by selecting suitable process parameters like much thinner layers (down triangles). [133].

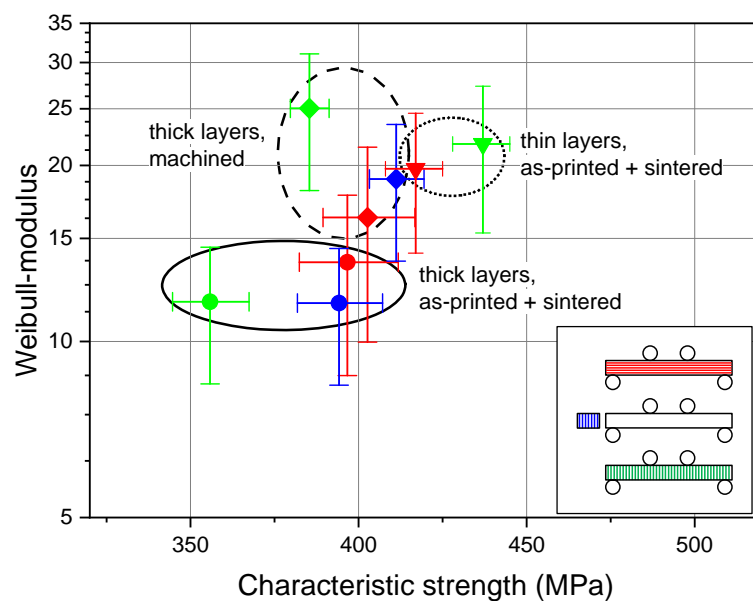


Figure 18: Characteristic strengths and Weibull moduli of various LCM ceramic samples. The inset shows the testing directions with respect to the layer orientation. Adapted from [133].

The experience gained during this investigation clearly showed that conventional strength tests deliver meaningful results but are too elaborate. The activities on materials design with the help of the LCM process, which are summarized in [129] motivated the quest for a AM specific efficient strength test methodology.

In a joint research project ("CharAM", FFG-IraSME 877684 & ZIM ZF4076461LT9), a specimen has been developed that is suitable for strength testing of additive manufactured ceramics [154-157]. The so-called CharAM-specimen consists of 48 pins in the form of carefully designed constant moment cantilever beams attached to a base plate. The base plate consists of two solid plates joined together at a specified angle. By varying this angle, different orientations of the cantilever

axis and the prospective tensile loaded face can be achieved with respect to the direction of material build up during the AM process, Figure 19. In order to reproduce typical dimensions of LCM components, the cantilevers are approximately 10mm long and 1mm thick. Strength testing is performed by loading each cantilever to failure at a predefined loading point. All specimens that fracture within the constant moment testing region, Figure 20a, are considered valid [156].

In commercial LCM printers, two such CharAM-specimens can be produced in one printing process. This means that a sufficient number of individual specimens to determine the strength distribution can be produced very quickly and easily. The surface of the CharAM-specimen, which was in contact with the build platform (i.e. the underside of the lower part of the base plate) and may have different properties than the rest of the material [135], is not important for the strength measurement. The individual samples are free-standing during the thermal post-treatment and are not in contact with kiln furniture. On one hand this simplifies handling and the need for documentation during sample production. On the other hand, contamination of the test surface can be avoided.

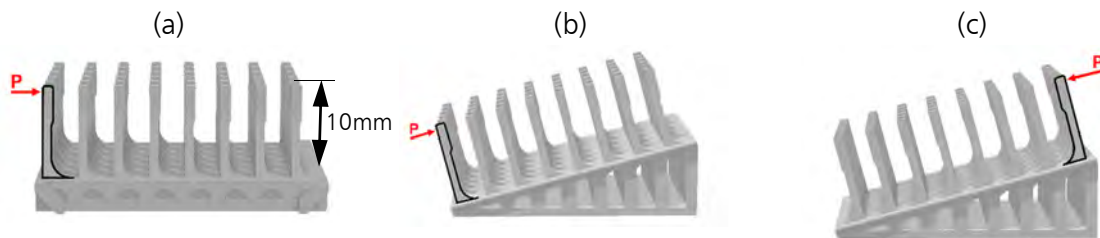


Figure 19: Variations of the CharAM specimen. The building direction z is vertical. (a) 0° , the cantilever axis (tensile face) is oriented parallel to the printing direction z . (b) The tensile face is oriented 15° down-skin and (c) 15° up-skin [156].

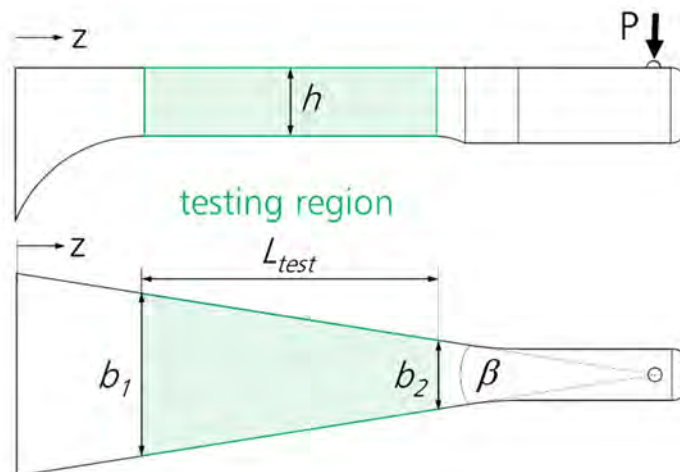


Figure 20: Schematic of a constant moment cantilever beam used in the CharAM-specimen [156].

The maximum stress in the testing region L_{test} is constant and can be calculated using

$$\sigma_f = \frac{3P}{h^2 \tan(\beta/2)} \quad (26)$$

The effective volume V_{eff} and effective area S_{eff} are given by

$$V_{eff} = \frac{h L_{test} (b_1 + b_2)}{4(m+1)} \quad \text{and} \quad (27)$$

$$S_{eff} = \frac{L_{test} (b_1 + b_2)}{2} \quad (28)$$

with the widths b_1 and b_2 and the length of the testing region L_{test} . Eq. (26) only applies if the test load is applied at the intersection point of the side edges of the specimen. In order to ensure this when carrying out the fracture tests, a small hemisphere is printed at this point, which makes it easy to apply the load at this position using a flat punch.

In first tests [157] and a round-robin test campaign involving three different laboratories [158], CharAM-specimens printed in three orientations were investigated. Individual Weibull strength distributions were evaluated for all CharAM-specimens.

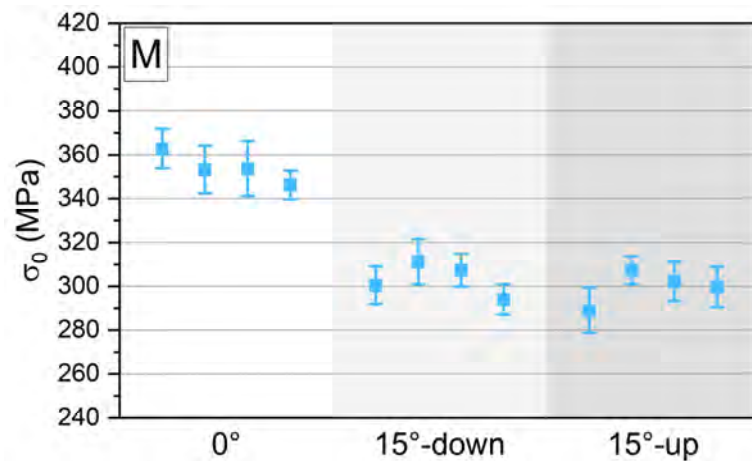


Figure 21: Characteristic strength of twelve CharAM-specimens of various orientations, results obtained on CharAM-specimens from one laboratory [158].

Figure 21 shows the strength of specimens printed in the three orientations as shown in Figure 19. The characteristic strength of the 0°-configuration is higher than that of both 15° configurations. It is also remarkable that for each orientation, four CharAM specimens printed in two different print jobs have the same strength.

In a first approach, the dimensions h and β were determined for all individual cantilevers by microscopic methods. This showed that i) the cross-sections of the beams deviate significantly from the planned target dimensions and are not rectangular, Figure 22a, and ii) the angle β does not have the ideal value either, Figure 22b. This leads to errors in the stress calculation. The non-rectangular cross-sections have too small a moment of inertia. The change in the opening angle means that the side edges of the specimen do not intersect at the printed load application point,

as shown in Figure 22b. This leads to an error in the stress evaluation. Its magnitude depends on the angle and the position of the fracture [156, 157].

As the manual measurement of the individual specimens is very time-consuming, Monte Carlo analysis was used to investigate whether it is appropriate to evaluate only with mean values for h and β , which are measured on a subset of the tested beams, and what influence this procedure has on the determination of the strength distribution parameters.

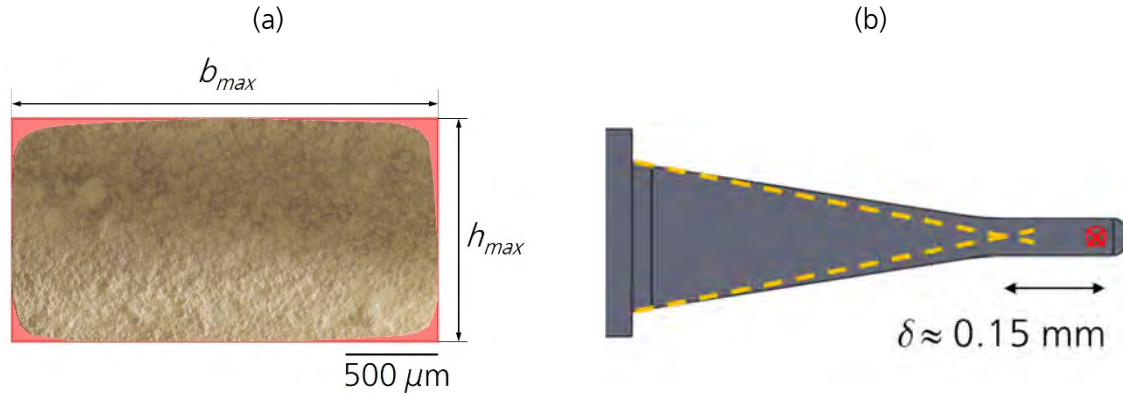


Figure 22: Specifics of CharAM cantilevers. (a) The actual cross section is far from a perfect rectangle. (b) The opening angle is different from $\beta = 18^\circ$, so that the load (if applied on the printed hemisphere \otimes) is no longer introduced in the intersection point of the side faces.

The results indicate that using mean values for the specimen dimensions will increase the uncertainty on every strength value to such an extent that a significant interaction with the scatter of strength will occur: most probably, a slight overestimation (approx. 1%) of characteristic strength will be determined and a significant underestimation of Weibull modulus by 10% - 20% [156].

These results show that a better and faster method must be used to determine the dimensions of the individual specimens. A method that uses 3D-scans of the base plates containing the remnants of the beams after fracture and automated detection of the required geometrical quantities was subsequently developed [159]. This procedure allows for determination of the shape of the actual cross sections (see Figure 22a) and evaluation of a correction factor k_{corr}

$$k_{corr} = \frac{I_{ideal}(b_{max}, h_{max})}{I} . \quad (29)$$

This factor quantifies the difference in moment of inertia of the irregular cross section I with respect to that of a perfect rectangular cross section I_{ideal} . It can be used to calculate a corrected strength $\sigma_{f,corr}$ according to

$$\sigma_{f,corr} = k_{corr} \sigma_f . \quad (30)$$

In addition, the factor k_{corr} allows an assessment how accurately the printed beams reproduce the desired rectangular cross-section: the better the rectangular shape is, the closer k_{corr} is to unity.

The experience gained so far with this method suggests that it is not only very suitable for measuring the strength of LCM components, but also for obtaining a wealth of information on the geometry of manufactured parts. This could be a very effective way of analyzing relationships between process details and geometry and/or strength – a potential which still has to be explored further.

4.3 Methods for Fracture Toughness Measurement on Components

This section recapitulates the work on fracture toughness measurement with surface cracks using the SCF-method and variations of it. First, the results of a detailed investigation of the geometry factor for realistic surface crack shapes (see Figure 7b) considering different Poisson's ratios are presented (publication G), followed by experimental investigations on the influence of lateral cracks as in publication H. Subsequently, the transfer of the SCF-method to spheres and discs is presented (publications I, J, K).

4.3.1 Improved Treatment of Two-Dimensional Surface Cracks

For surface cracks used in the SCF method, the influence of Poisson's ratio and realistic crack shape was analyzed parametrically using FE analysis and the J -integral method. The conversion from J -integral quantities to stress intensities according to $K = (E' \cdot J)^{1/2}$ was performed assuming plain strain conditions. The crack size, crack shape and the crack front – surface intersection angle were varied within a parameter range that is relevant for actual experiments on ceramics. The results were compared to the values obtained with the Newman & Raju solution Y_{NRF} [104] to identify cases of extreme differences. Additionally, a methodology was proposed to estimate how much material Δh has to be removed from specimens with as-indentured crack of a given size in order to arrive at a crack shape that has its highest stress intensity at point A. The geometry factor at point A (Figure 12b) is provided as empirical fitted function (eq. (31), for details see publication G) which is valid in the parameter range given in Table 2 [143]. It has an error less than 2.7% with respect to the FEA results.

$$Y_{s,A} \left(\frac{a}{c}, \frac{a}{t}, \frac{c}{b}, \nu, \chi, \phi = 0^\circ \right) = f \left(\frac{a}{c}, \frac{a}{t} \right) \cdot f_b \left(\frac{a}{c}, \frac{a}{t}, \frac{c}{b} \right) \cdot f_\nu \left(\frac{a}{c}, \frac{a}{t}, \nu \right) \cdot f_\chi \left(\frac{a}{c}, \frac{a}{t}, \chi \right) \quad (31)$$

Table 2: Range of application of eq. (31), [143, 160]

relative crack size a/h	0.01 ... 0.5
crack aspect ratio a/c	0.4 ... 1.2
relative crack width c/b	0.1 ... 0.5
crack-surface interaction angle χ	70° ... 110°
Poisson's ratio ν	0 ... 0.4

The results show, that when Y_{NRF} is applied to cracks in materials with $\nu \neq 0.3$ an error in Y of up to 16% can occur. Even for some cases with $\nu = 0.3$, that were studied previously, significant deviations in the range of 10% can occur. This may be due to using significantly finer meshes in the new, improved FE analyses. Examples for the influence of the parameters that have been additionally investigated, ν and χ , are shown in Figure 23. By comparison of the symbols (Y_{NRF})

with the red line (Y_S) in Figure 23a it is obvious, that even for a Poisson's ratio of $\nu = 0.3$ the crack front – surface interaction angle has an influence on the geometry factor which can reach 5% for common crack geometries with $\chi = 70^\circ$. For materials with smaller values of ν the effect becomes even more pronounced. Figure 23b shows that there is a small difference between Y_{NRF} (symbols) and the new results even for $\nu = 0.3$, which can be attributed to the details of the employed FE models. Overall, it turns out that for many cases of realistic (flat) crack shapes and especially for materials with $\nu \neq 0.3$ the use of Y_{NRF} can easily introduce an error of more than 5% -10% to the measurements.

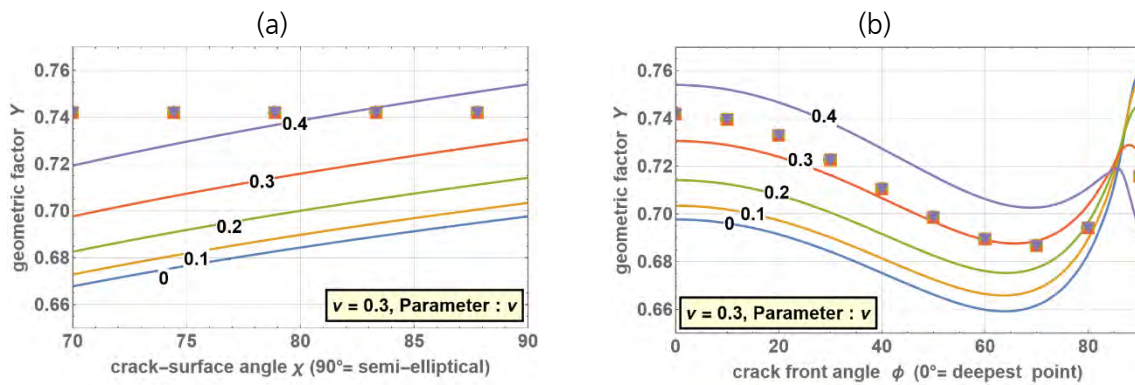


Figure 23: Comparison of the improved Y_S (lines) and Y_{NRF} (symbols) for typical cracks as used in the SCF Method ($a/t = 0.05$, $a/c = 0.7$) for different values of Poisson's ratio ν . (a) For ellipse segment cracks at point A as a function of surface interaction angle χ , cp. Figure 12. (b) For semi-elliptical cracks along the crack front (Point A at $\phi = 0$).

An additional aspect to be considered is the overall three-dimensional crack system formed during indentation. As-indented Knoop surface-cracks exhibit a nearly semi-elliptical configuration. At low indentation loads (<5kg) a single lateral crack system is additionally present, while at higher loads a secondary lateral crack system much further below the surface emerges, see Figure 13 and Figure 24 [144, 161]. Some sort of interaction of these crack systems during the fracture test may be conceivable.

The grinding procedure specified in the standards [97, 103] to obtain a residual-stress-free surface crack likely removes the lateral cracks, certainly the shallow ones if they are not too prominent, but probably not the deep secondary ones. This raises questions whether these are still appropriate pre-crack situations for valid SCF-tests and how the use of appropriate geometry factor solutions will influence results [162]. These issues were investigated experimntally by systematically grinding-off different Δh before the fracture tests. A large number of specimens of two ceramic materials with very different sub-surface Knoop crack systems was used to assess the effect of residual lateral cracks and different crack shapes. A secondary objective of this study was an assessment of the impact of the refined geometry factor Y_S on the measured results through comparison with independently determined fracture toughness values using alternative methods. It could be shown that, once a minimum Δh is removed, remnants of lateral cracks do not significantly interfere with the primary surface crack and correct K_{Ic} measurements are possible. In any case, cracks that have $Y_{S,A} = Y_{max}$ should be used, but this may require a higher grinding depth. Some of the resulting cracks exhibited shapes a/c and crack front – surface angles χ that were not covered by the existing parametric determination of Y_S . An extrapolation of the

existing parameter field was used in these cases and supported by verification of some exemplary cases through FEA [161, 163].

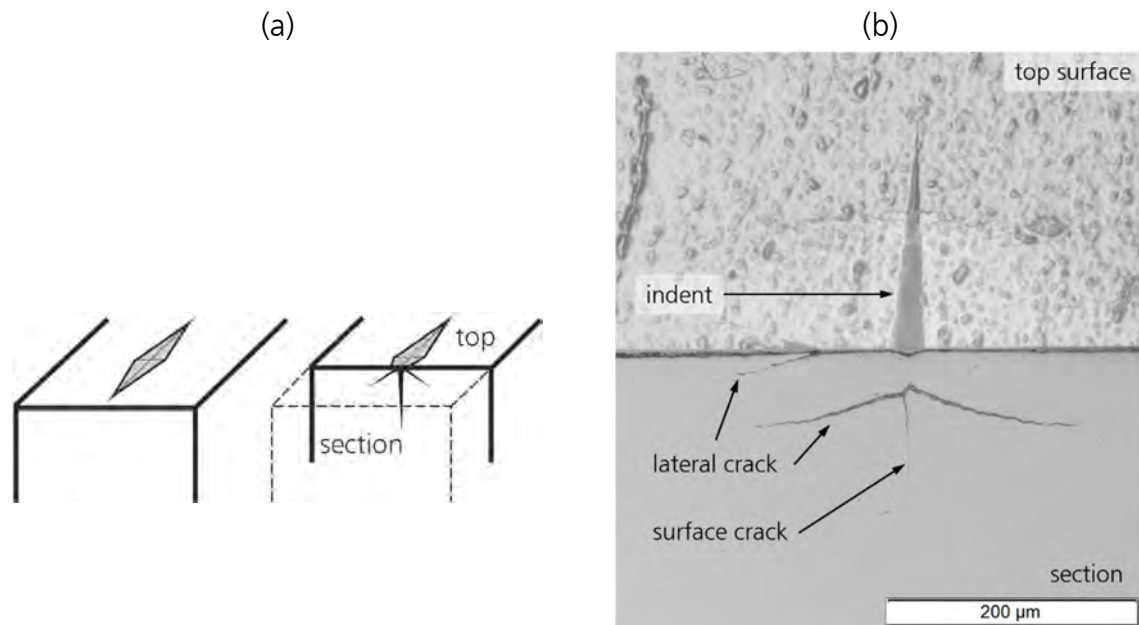


Figure 24: Knoop indentation crack system. (a) Serial sectioning procedure to obtain information on the crack system below the specimen surface. (b) Top surface and section of a Knoop indentation, surface crack and multiple lateral cracks in a dental ceramic [161].

The combined influence of Poisson's ratio and the termination angle χ may lead to a significant difference in K_{Ic} if calculated using the two proposed solutions Y_{NRF} or Y_S for the geometry factors. This is especially important for materials with low Poisson's ratio such as SiC, dental ceramics [161, 163] or glasses [164, 98]. The use of the Y_S for such cases is indicated.

4.3.2 Fracture Toughness of Balls, Discs and Plates

In order to measure the fracture toughness on the surface of spheres, the NBT can be used as basic test principle. Analogous to the procedure in the SCF method (section 2.4), small surface cracks can be introduced into the tensile-stressed region of the sphere surface using Knoop hardness indentations. In order to define a fracture toughness test in this way, two aspects must be evaluated: the change in the stress field in the notched ball due to the necessary removal of the plastic zone created by the indentation and the geometry factor Y for this configuration [165, 166].

Grinding off the hardness indentation and the plastically deformed zone underneath changes the shape of the ball and thus the stress field, Figure 25. These changes were evaluated for different grinding depths Δh and Poisson's ratios by FEA and considered by a correction factor $f_{\sigma}(\nu, L_N/D, \Delta h/R)$ in the stress calculation. Depending on the grinding depth Δh , the increase in the maximum stress can be up to 40%.

The determination of the geometry factor has been performed using two different approaches, a semi-analytical one and a FE analysis. As shown in Figure 25c, the stress in the ligament of the ground-off sphere (black line) remains very close to that of a rectangular bend specimen (red line). It was therefore assumed that the existing geometry factor for semi-elliptical surface cracks in rectangular cross sections derived by [104], Y_{NRF} , used in the standard for the SCF test is also valid in this case if an equivalent specimen thickness h_{eq} and width $b_{eq} = h_{eq}$ can be defined. Based on the stress distribution in the ground-off ball, h_{eq} has been evaluated so that the stress magnitude and gradient are similar in the notched ball and the equivalent bend bar and is provided for a range of relative crack sizes as fitted function. In a subsequent FE analysis, the geometry factor was additionally calculated for various values of Poisson's ratio and a considerable dependence on Poisson's ratio was found [165].

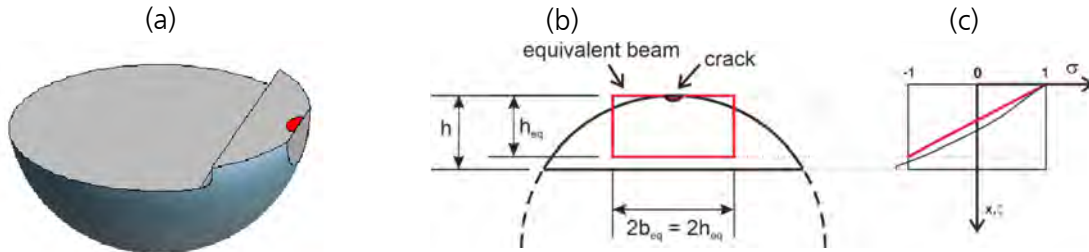


Figure 25: (a) Notched-Ball test with surface crack, (b) schematic of the ligament with crack and the equivalent rectangle, (c) stress in the equivalent rectangle (red line) compared to the actual stress in the ligament (black line) [165].

Summing these efforts up, the fracture toughness can be evaluated using eqs. (18) and (32) to (35), which are valid for the parameter range given in Table 3. The factor f_σ and the coefficients $m_0 - m_3$ and n_0 and n_1 can be found in publication I. There, an expression for a dedicated, alternative solution for the geometry factor for this load case can be found which avoids the calculation of h_{eq} and Y_{NRF} .

$$K_{Ic} = \sigma_{NBT} f_\sigma Y_{NRF,A} (h_{eq}) \sqrt{\pi a} \quad (32)$$

$$h_{eq} = f_h (h - \Delta h) \quad (33)$$

$$f_h = \frac{-2a/(h - \Delta h)}{\sigma_{z,Lig} \left(\xi = \frac{a}{h - \Delta h} \right) - 1} \quad (34)$$

$$\sigma_{z,Lig} = 1 + \left(m_0 \frac{L_N}{D} + m_1 \left(\frac{L_N}{D} \right)^2 \right) n_0 \xi + \left(m_2 \frac{L_N}{D} + m_3 \left(\frac{L_N}{D} \right)^2 \right) n_1 \xi^2 \quad (35)$$

Table 3: Range of application of eqs. (32) - (35), [165, 166].

relative notch length L_N/D	0.74 ... 0.82
relative notch width W_N/D	0.10 ... 0.15
relative notch width R_N/D	0.25 ... 0.40
Poisson's ratio ν	0.15 ... 0.35
crack aspect ratio a/c	0.4 ... 1.0
relative crack size a/R	0.005 – 0.065
relative grinding depth $\Delta h/R$	0.02 ... 0.05

An analysis of measurement uncertainties was conducted. The quantities σ_{NBT} and f_σ contribute with errors of $< \pm 1\% - 2\%$ each to the total error in K_{Ic} . The determination of the crack size has been identified as the most important source of uncertainty, but at the same time strategies how to minimize it were developed. It was found that an accurate determination of the crack depth a is essential and the least error ($< \pm 5\%$) occurs for shallow cracks that are critical at the deepest point. The cracks can be found much easier and measured more accurately on the fracture surfaces when fluorescent penetration dye is applied.

Finally, a method for the determination of the fracture toughness on balls with diameters of 2mm to 20mm has been established. Test on balls with diameters between 5mm – 5.55mm of various structural ceramics were performed. The results were in excellent agreement with values measured with the standardized SCF-method applied to bars and to literature values [166].

The SCF-method can also be applied to discs or plates which are biaxially loaded in the Ball-on-Three-Balls test [167, 168]. The surface crack is introduced centrally into the tensile face of the specimen opposite the load ball. In this case the removal of the plastic zone only changes the overall thickness of the specimen or component, what can be readily considered in the stress calculation. An especially challenging question in this case is the geometry factor of the crack. The stress field of the B3B test is not rotationally symmetric and has steep gradients. This implies that not only the relative size (with respect to the specimen size) of the crack plays a role for Y but also the exact position and its orientation with respect to the support positions.

Again, the geometry factor was evaluated using FE analyses. An ideal central position of the crack and an ideal orientation as shown in Figure 26 were used. For this configuration, empirical formulae were obtained that fit the FEA results for the geometry factors Y_A and Y_C for a range of geometrical configurations specified in Table 4. Similar to the standardized variant of the SCF-method, only cracks which are critical at point A should be considered for the evaluation of fracture toughness according to eq. (36). A detailed expression for Y_A can be found in publication K [167].

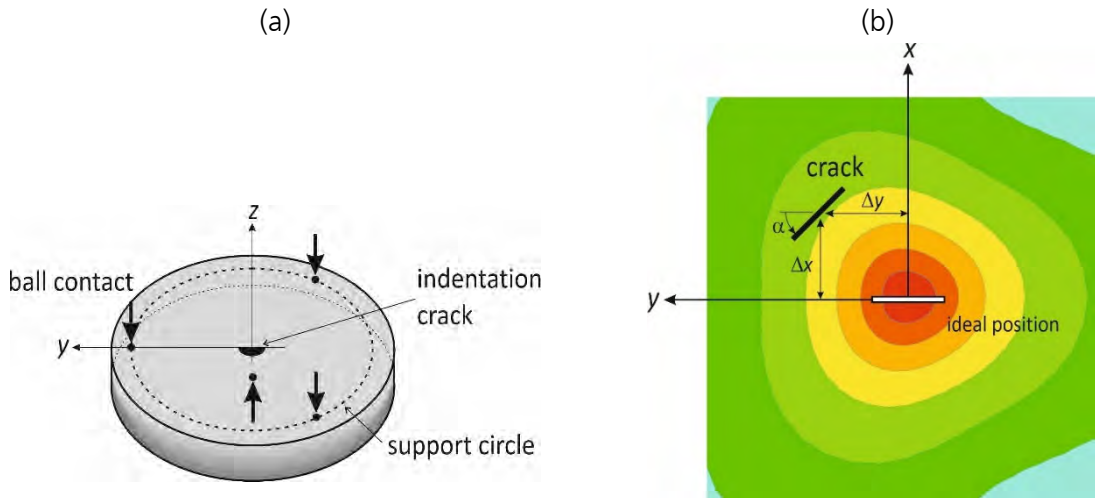


Figure 26: (a) Schematic of the Ball-on-Three-Balls fracture toughness test, view of tensile face of the disc. (b) Stress contours in the center of the disc, ideal and offset + rotated position of the crack [167].

$$K_{Ic} = \sigma_{f,B3B} Y_A \left(\frac{a}{c}, \frac{a}{t}, \frac{t}{R_s}, \nu \right) \sqrt{\pi a} \quad (36)$$

Table 4: Range of application of eq. (36), [167].

crack aspect ratio a/c	0.4 ... 0.8
relative pre-crack size a/t	0.05 ... 0.2
relative plate thickness t/R_s	0.1 ... 0.3
Poisson's ratio ν	0.1 ... 0.4

Non-ideal positions of the pre-crack, see Figure 26b, were investigated by FEA and experimentally. The experiments showed that a rotation of the surface crack with respect to the positions of the support balls has not influence on the results, which was confirmed by the numerical analysis. The effect of an offset of the crack away from the center of the support circle was investigated parametrically. Such offsets can therefore be corrected when experiments are evaluated.

Fracture toughness can be determined with an uncertainty of $\pm 5\% - \pm 10\%$ for specimens larger than 8mm in diameter and thicker than 0.5mm. For accurate measurements it is important to position the crack within $\pm 120\mu\text{m}$ of the stress maximum, to know the Poisson's ratio accurately, and to test cracks that have the maximum stress intensity factor at their deepest point. A method to achieve this (i.e. how to determine the necessary amount of material removal) has been additionally published [167].

The method has been validated by testing several structural and functional ceramics and comparing the results with literature data [169]. Since its introduction it has been frequently applied to fracture toughness measurements on dental ceramics [170-174].

5 Summary and Outlook

In this thesis, new developments for the characterisation of strength and fracture toughness of ceramic materials and components are presented. Important aspects of the work carried out were, on one hand, to reach accuracy, precision and analyse possible errors. On the other hand, if FE analyses were necessary to obtain stresses or other quantities, these analyses were carried out parametrically so that a large range of possible testing geometries was covered. To facilitate the use of the results by other members of the scientific community, such results were provided as empirical equations fitted to the FEA results.

The **Ball-on-Three-Balls test** is a robust **strength test** for discs and plates from ceramics and other brittle materials and has been used over the last twenty years. With the help of FE analyses, a simplified expression to evaluate the strength from the fracture loads has now been developed, together with an extension of the application range of the test beyond purely linear-elastic conditions with small deformations. Additionally, Weibull effective volumes and areas for many specimen geometries have been provided. The FE analyses were experimentally verified for some specific loading scenarios. With this information it is now possible to convert results obtained with this test to other load cases. Similar to standardized strength test for ceramics, the B3B-test is now empowered to serve as universal tool for material characterization and also for design purposes. Nevertheless, these developments have created the need for more work on this test:

- » A new class of ceramics with a huge potential in medical applications shows transformation plasticity [175-177], which makes the existing stress calculations invalid. Similar complications arise when single crystals with anisotropic elastic properties are tested. The incorporation of suitable material laws into the stress evaluation is therefore an urgent research topic.
- » A method to incorporate accurate measurement of deflection should be installed.
- » As preparation for a possible standardization of the test, a round robin test program in which several typical materials are tested by a range of laboratories in order to thoroughly investigate the robustness of the test is desirable.

In order to measure the **strength of AM ceramic components**, a test procedure has been designed that fully exploits the potential of LCM additive manufacturing. For this procedure, the feasibility was demonstrated, an analysis of possible errors revealed the need for a data-intensive but manageable evaluation procedure. A round robin exercise demonstrated the validity of the method not only in terms of strength measurement, but also for the assessment of geometric parameters as a function of processing details. Future work will concentrate on the following topics.

- » Investigation of multi-material parts and bi-material interfaces [178, 179].
- » Experience needs to be built up, if and how the test method can be used by more laboratories and with other DLP methods. This involves also the task of making the evaluation procedure easier and more widely accessible.
- » Finally, the applicability of the method to other ceramic AM methods such as binder jetting, material extrusion and material jetting has to be explored.

The Surface-Crack-in-Flexure method is an important **method** to determine the **fracture toughness of ceramics**. Since small surface crack are used as pre-cracks in this method it is especially suitable to be used on small components or thin specimens. This goal has been achieved by transferring the concept to different specimen geometries without compromising the essential principles of rigorous fracture toughness evaluation. As a result, fracture toughness tests for small balls and thin discs have been established. Together with these achievements it was recognized that the consideration of the exact geometry of the used surface cracks together with a correct value for Poisson's ratio can significantly improve existing evaluation procedures, even when severe secondary crack systems are present. The elaborate experimental investigation that led to this conclusion clearly revealed additional research needs:

- » The expression for a precise geometry factor for ellipse segment-shaped surface cracks need an extension for crack-surface interaction angle smaller than 70° [161, 163].
- » The indentation method is cheap and readily available to introduce pre-cracks but it turns out that they are difficult to find on fracture surfaces. Considering the progress in laser machining for ceramics, alternative methods for pre-crack generation should be investigated.

6 Literature

- [1] R. Danzer, T. Lube: "New Fracture Statistics for Brittle Materials", in: R. C. Bradt, D. P. H. Hasselmann, D. Munz, M. Sakai, V. Ya. Shevchenko (Eds.), *Fracture Mechanics of Ceramics*, 1996, Plenum Publishing Corp., 425-439
- [2] R. Danzer, P. Supancic, J. Pascual, T. Lube: "Fracture Statistics of Ceramics - Weibull Statistics and Deviations from Weibull Statistics", *Engineering Fracture Mechanics* **74** [18] (2007), 2919-2932
- [3] A.A. Wereszczak: "Custom Mechanical Strength Test Specimens for Brittle Materials and their Components", in: Tatsuki Ohji, Mrityunjay Singh (Eds.), *Engineered Ceramics - Current Status and Future Prospects*, The American Ceramics Society and Wiley & Sons Inc., Hoboken, 2016, 29-45
- [4] VDI 3405 Blatt 8.1: *Additive manufacturing processes - Design rules - Parts using ceramic materials*, 2021
- [5] VDI 3405 Blatt 8.2: *Additive manufacturing processes - Test specimens for ceramic parts*, 2021
- [6] H. Czichos, T. Saito, L. Smith: *Handbook on Materials Measurement Methods*, Springer, New York, 2006
- [7] W.E.C. Creyke, I.E.J. Sainsbury, R. Morrell: *Design with Non-ductile Materials*, Applied Science Publishers, London, 1982
- [8] D.W. Kingery, H.K. Bowen, D.R. Uhlmann: *Introduction to Ceramics*, John Wiley & Sons, New York, 1976
- [9] C.E. Inglis: "Stress in a Plate due to the Presence of Cracks and Sharp Corners", *Transactions of the Royal Institution of Naval Architects* **55** (1913), 219-230
- [10] A.A. Griffith: "The Phenomenon of Rupture and Flow in Solids", *Philosophical Transactions of the Royal Society of London* **A221** (1920), 163-198
- [11] G.R. Irwin: "Fracture", in: S. Flügge (Ed.), *Handbuch der Physik*, Springer-Verlag, Berlin, 1958, 551-589
- [12] R.W. Davidge: *Mechanical Behaviour of Ceramics*, Cambridge University Press, Cambridge, 1979
- [13] B.R. Lawn: *Fracture of Brittle Solids*, Cambridge Solid State Science Series, Cambridge University Press, Cambridge, 1993

- [14] D. Munz, T. Fett: *Ceramics*, Springer Series in Materials Science 36, Springer, Berlin, Heidelberg, 1999
- [15] D. Gross, T. Seelig: *Fracture Mechanics*, Mechanical Engineering Series, Springer, Berlin, 2006
- [16] H. Tada, P. Paris, G.R. Irwin: *The Stress Analysis Handbook*, Del Research Corporation, St. Louis, 1985
- [17] Y. Murakami: *The Stress Intensity Factor Handbook*, Pergamon Press, New York, 1986
- [18] W. Weibull: *A Statistical Theory of the Strength of Materials*, Ingeniörsvetenskapsakademiens Handlingar 151 151, Generalstabens Litografiska Anstalts Förlag, Stockholm, 1939
- [19] W. Weibull: "A Statistical Distribution Function of Wide Applicability", *Journal of Applied Mechanics* **18** (1951), 293-298
- [20] A.d.S. Jayatilaka, K. Trustrum: "Statistical Approach to Brittle Fracture", *Journal of Materials Science* **12** (1977), 1426-1430
- [21] R. Danzer: "A General Strength Distribution Function for Brittle Materials", *Journal of the European Ceramic Society* **10** (1992), 461-472
- [22] L.N. McCartney: "Extensions of a Statistical Approach to Fracture", *International Journal of Fracture* **15** (1979), 477-487
- [23] A.G. Evans: "A General Approach for the Statistical Analysis of Multiaxial Fracture", *Journal of the American Ceramic Society* **61** [7-8] (1978), 302-308
- [24] R. Danzer, T. Lube, P. Supancic, R. Damani: "Fracture of Ceramics", *Advanced Engineering Materials* **10** [4] (2008), 275-298
- [25] EN 843-5: *Advanced Technical Ceramics - Mechanical properties of monolithic ceramics at room temperature: Part 5 - Statistical Evaluation*, 2007
- [26] ASTM C1239: *Standard Practice for Reporting Uniaxial Strength Data and Estimating Weibull Distribution Parameters for Advanced Ceramics*, 1995
- [27] ISO 20501: *Fine ceramics (advanced ceramics, advanced technical ceramics) — Weibull statistics for strength data*, 2019
- [28] R. Danzer, T. Lube: "Fracture Statistics of Brittle Materials: It Does not always have to be Weibull Statistics", in: K. Niihara (Ed.), *Proc. of Ceramic Materials, Components for Engines*, Tokyo, 1998, Japan Fine Ceramics Association, 683-688
- [29] R. Danzer, T. Lube, P. Supancic: "Monte-Carlo Simulations of Strength Distributions of Brittle Materials - Type of Distribution, Specimen- and Sample Size", *Zeitschrift für Metallkunde* **92** [7] (2001), 773-783
- [30] C.A. Johnson, W.T. Tucker: "Advanced Statistical Concepts of Fracture in Brittle Materials, Ceramics and Glasses", *Engineered Materials Handbook* **4** (1991), 709-715
- [31] C.A. Johnson, W.T. Tucker: "Weibull Estimators for Pooled Fracture Data", in: C. R. Brinkman, S.F. Duffy (Eds.), *Life Prediction Methodologies and Data for Ceramic Materials, ASTM STP 1201*, American Society for Testing and Materials, 1994

- [32] R. Danzer, G. Reisner, H. Schubert: "Der Einfluß von Gradienten in der Defektdichte und Festigkeit auf die Bruchstatistik von spröden Werkstoffen", *Zeitschrift für Metallkunde* **83** (1992), 508-517
- [33] K. Duan, Y.-M. Mai, B. Cotterell: "R-Curve Effect on Strength and Reliability of Toughened Ceramic Materials", *Journal of Materials Science* **30** (1995), 1405-1408
- [34] T. Lube, J. Pascual, R. Danzer: "Influence of an Apparent R-curve on Strength and Fracture Statistics of Ceramic Laminates", *International Journal of Materials Research* **100** [8] (2009), 1137-1144
- [35] J. Pascual, T. Lube, R. Danzer: "Fracture Statistics of Ceramic Laminates Strengthened by Compressive Residual Stresses", *Journal of the European Ceramic Society* **28** [8] (2008), 1551-1556
- [36] J. Pascual Herrero, F. Chalvet, T. Lube, G. de Portu: "Strength Distributions in Ceramic Laminates", *Materials Science Forum* **492-493** (2005), 581-586
- [37] R. Danzer, P. Supancic, T. Lube: "Failure Statistics Beyond the Weibull Behavior", *Ceramic Engineering and Science Proceedings* **24** [4] (2003), 497-502
- [38] R. Morrell: *Flexural Strength Testing of Ceramics and Hardmetals*, Measurement Good Practice Guide 7, NPL, Teddington, 1997
- [39] R. Morrell: *Biaxial Flexure Strength Testing of Ceramic Materials*, Measurement Good Practice Guide 12, National Physical Laboratory, Teddington, 1998
- [40] D.C. Cranmer, D.W. Richerson: eds., *Mechanical Testing Methodology for Ceramic Design and Reliability*, Marcel Dekker, New York, 1998
- [41] F.I. Baratta, W.T. Matthews, G.D. Quinn: "Errors Associated with Flexure Testing of Brittle Materials", U.S. Army Materials Technology Laboratory, Watertown, 1987, 43 S.
- [42] ASTM C1499: *Standard Test Method for Monotonic Equibiaxial Flexural Strength of Advanced Ceramics at Ambient Temperature*, 2019
- [43] ISO 6872: *Dentistry - Ceramic Materials*, 2015
- [44] R. Bermejo, P. Supancic, R. Danzer: "Influence of measurement uncertainties on the determination of the Weibull distribution", *Journal of the European Ceramic Society* **32** [2] (2012), 251-255
- [45] ASTM C1683: *Standard Practice for Size Scaling of Tensile Strengths Using Weibull Statistics for Advanced Ceramics*, 2019
- [46] G.D. Quinn: "Weibull Effective Volumes and Surfaces for Cylindrical Rods Loaded in Flexure", *Journal of the American Ceramic Society* **86** [3] (2003), 475-479
- [47] G.D. Quinn: "Weibull Strength Scaling for Standardized Rectangular Flexure Specimens", *Journal of the American Ceramic Society* **86** [3] (2003), 508-510
- [48] T. Lube, I. Khader, A. Kailer, U. Degenhardt, K. Berroth: "Ermüdungsbruch in Siliziumnitrid", in: Svea Mayer, Michael Panzenböck, Helmut Clemens (Eds.), *Praktische Metallographie Sonderband*, 2014, INVENTUM GmbH, 353-357
- [49] T. Lube, S. Witschnig, P. Supancic, R. Danzer, O. Schöppel: "The Notched Ball Test - Characterisation of Surface Defects and Their Influence on Strength", in: James R. Varner,

- Marlene Wightman (Eds.), *Fractography of Glasses and Ceramics VI*, 2012, Wiley, 225-234
- [50] S. Béhar-Lafenêtre, T. Lube, S. Ait-Zaid: "Recent Advances on Fast Fracture Strength of Zerodur® for Space Applications", in: CNES Toulouse (Ed.), *Proc. of 14th European Conference on Spacecraft Structures, Materials and Environmental Testing*, Toulouse, 2016
- [51] T. Lube, S. Béhar-Lafenêtre: "Strength behaviour of etched Zerodur®", *Journal of the European Ceramic Society* **37** (2017), 4407-4413
- [52] T. Lube, I. Kraleva: "Defects and Fracture Statistics in Low-Pressure Injection Moulded Alumina Components", *Praktische Metallographie* **48** (2011), 442-453
- [53] T. Lube, R. Morrell, I. Kraleva: "The Effect of Defects and Materials Texture on the Fracture of Low-Pressure Injection Moulded Alumina Components", in: James R. Varner, Marlene Wightman (Eds.), *Fractography of Glasses and Ceramics VI*, 2012, Wiley, 57-64
- [54] G.D. Quinn: *Fractography of Ceramics and Glasses*, Special Publication 960-16, US Government Printing Office, Washington, 2020
- [55] ASTM C1322: *Standard Practice for Fractography and Characterization of Fracture Origins in Advanced Ceramics*, 2005
- [56] EN 843-1: *Advanced Technical Ceramics - Mechanical properties of monolithic ceramics at room temperature: Part 1 - Determination of Flexural Strength*, 2006
- [57] ASTM C1161: *Standard Test Methods for Flexural Strength of Advanced Ceramics at Ambient Temperature*, 2002
- [58] ISO 14704: *Fine ceramics (advanced ceramics, advanced technical ceramics) — Test method for flexural strength of monolithic ceramics at room temperature*, 2016
- [59] ASTM C1684: *Standard Test Methods for Flexural Strength of Advanced Ceramics at Room Temperature - Cylindrical Rod Strength*, 2008
- [60] J.B. Wachtman, W.R. Cannon, M.J. Matthewson: *Mechanical Properties of Ceramics*, Wiley-Interscience, New York, Chichester, 2009
- [61] G.D. Quinn, R. Morrell: "Design Data for Engineering Ceramics: A Review of the Flexure Test", *Journal of the American Ceramic Society* **74** [9] (1991), 2037-2066
- [62] T. Lube, M. Manner, R. Danzer: "The Miniaturisation of the 4-Point Bend-Test", *Fatigue and Fracture of Engineering Material Structures* **20** [11] (1997), 1605-1616
- [63] M. Staudacher, P. Supancic, T. Lube: "The Ball-on-Ring-test: Enhancing an analytical solution by numerical analysis for elastic deformation and small displacements", *Journal of the European Ceramic Society* **43** (2023), 7167-7177
- [64] A. Börger, P. Supancic, R. Danzer: "The ball on three balls test for strength testing of brittle discs - stress distribution in the disc", *Journal of the European Ceramic Society* **22** [8] (2002), 1425-1436
- [65] H. Fessler, D.C. Fricker: "A Theoretical Analysis of the Ring-On-Ring Loading Disk Test", *Journal of the American Ceramic Society* **67** [9] (1984), 582-588

- [66] A.F. Kirstein, R.M. Woolley: "Symmetrical Bending of Thin Circular Elastic Plates on Equally Spaced Point Supports", *Journal of Research of the National Institute of Standards* **71C** [1] (1967), 1-10
- [67] D. Shetty, A.R. Rosenfield, P. McGuire, G.K. Bansal, W.H. Duckworth: "Biaxial Flexure Test for Ceramics", *American Ceramic Society Bulletin* [59 (12)] (1980), 1193-1197
- [68] H.L. Frandsen: "The small displacement elastic solution to the ball-on-ring testing method", *Mechanics of Materials* **55** (2012), 33-40
- [69] H.L. Frandsen: "Weibull statistics effective area and volume in the ball-on-ring testing method", *Mechanics of Materials* **73** (2014), 28-37
- [70] R. Danzer, P. Supancic, W. Harrer: "Der 4-Kugerversuch zur Ermittlung der biaxialen Biegefestigkeit spröder Werkstoffe", in: Jochen Kriegesmann (Ed.), *Technische keramische Werkstoffe*, HvB Verlag GbR., Ellerau, 2009, 1-48
- [71] L.M. Powers, J.A. Salem, A.S. Weaver: "Stresses in Ceramic Plates Subjected to Loading Between Concentric Rings", in: Jonathan A. Salem (Ed.), *Fracture resistance testing of monolithic and composite brittle materials*, ASTM International, West Conshohocken, Pa., 2002, 30-45
- [72] J.A. Salem, L. Powers: "Guidelines for the Testing of Plates", in: Hua-Tay Lin, Waltraud M. Kriven (Eds.), *27th International Cocoa Beach Conference on Advanced Ceramics and Composites. January 26-31, 2003, Cocoa Beach, Florida*, American Ceramic Society, Westerville, Ohio, 2003, 357-364
- [73] A. Börger, P. Supancic, R. Danzer: "The ball on three balls test for strength testing of brittle discs - Part II: analysis of possible errors in the strength determination", *Journal of the European Ceramic Society* **24** [10-11] (2004), 2917-2928
- [74] R. Danzer, P. Supancic, W. Harrer, Z. Wang, A. Börger: "Biaxial Strength Testing on Mini Specimens", in: E. E. Gdoutos (Ed.), *Fracture of Nano- and Engineering Materials and Structures*, Springer, Dordrecht, 2006, 589-590
- [75] W. Harrer, R. Danzer, P. Supancic, T. Lube: "Influence of the Sample Size on the Results of B3B-Tests", *Key Engineering Materials* **409** (2009), 176-184
- [76] E. Özkol, A.M. Wätjen, R. Bermejo, M. Deluca, J. Ebert, R. Danzer, R. Telle: "Mechanical characterisation of miniaturised direct inkjet printed 3Y-TZP specimens for microelectronic applications", *Journal of the European Ceramic Society* **30** (2010), 3145-3152
- [77] Y. Torres, R. Bermejo, F.J. Gotor, E. Chicardi, L. Llanes: "Analysis on the mechanical strength of WC-Co cemented carbides under uniaxial and biaxial bending", *Materials & Design* **55** (2014), 851-856
- [78] F. Fleischhauer, M. Ternner, R. Bermejo, R. Danzer, T. Graule, A. Mai, J. Kübler: "Fracture Toughness and Strength Distribution at Room Temperature of Zirconia Tapes used for Electrolyte Supported Solid Oxide Fuel Cells", *Journal of Power Sources* **275** [2] (2015), 217-226
- [79] R. Belli, M. Wendler, A. Petschelt, D. Mevec, T. Lube, W. Harrer, R. Danzer, U. Lohbauer: "Chairside CAD/CAM materials. Part 2: flexural strength testing", *Dental Materials* **33** [1] (2017), 99-109
- [80] T. Klünsner, T. Lube, C. Gettinger, L. Walch, R. Pippa: "Influence of WC-Co hard metal microstructure on defect density, initiation and propagation kinetics of fatigue cracks

- starting at intrinsic and artificial defects under a negative stress ratio", *Acta Materialia* **188** (2020), 30-39
- [81] M. Gruber, A. Leitner, D. Kiener, P. Supancic, R. Bermejo: "Effect of crystal orientation on the hardness and strength of piezoelectric LiNbO₃ substrates for microelectronic applications", *Materials & Design* **213** (2022), 110306
- [82] B. Thomas, D.W. West, W. E. Jr, K. Wyckoff: "Effect of Machining Parameters on the Surface Finish and Strength of Hot Pressed Silicon Nitride", *Powder Metallurgy International* **20** [3] (1988), 39-44
- [83] H.H.K. Xu, S. Jahanmir, L.K. Ives, L.S. Job, K.T. Ritchie: "Short-Crack Toughness and Abrasive Machining of Silicon Nitride", *Journal of the American Ceramic Society* **79** [12] (1996), 3055-3064
- [84] G.D. Quinn, L.K. Ives, S. Jahanmir: "On the nature of machining cracks in ground ceramics. Part I: SRBSN strength and fractographic analysis.", *Machining Science and Technology* **9** (2005), 169-210
- [85] G.D. Quinn, L.K. Ives, S. Jahanmir: "On the nature of machining cracks in ground ceramics. Part II: Comparison to other silicon nitrides and damage maps", *Machining Science and Technology* **9** (2005), 211-237
- [86] A.A. Wereszczak, J.J. Swab, R.H. Kraft: "Effects of Machining on the Uniaxial and Equibiaxial Flexure Strength of CAP3 AD-995 Al₂O₃", Army Research Laboratory, 2005
- [87] P. Supancic, R. Danzer, S. Witschnig, E. Polaczek, R. Morrell: "A New Test to Determine the Tensile Strength of Brittle Balls - The Notched Ball Test", *Journal of the European Ceramic Society* **29** (2009), 2447-2459
- [88] S. Strobl, T. Lube, P. Supancic, O. Schöppl, R. Danzer: "Surface strength of balls made of five structural ceramic materials evaluated with the Notched Ball Test (NBT)", *Journal of the European Ceramic Society* **37** (2017), 5065-5070
- [89] O. Schöppl, T. Lube: "Testing Methods on Ceramic Rolling Elements for Hybrid Bearings", *Materials Performance and Characterization* **4** [1] (2015), 209-225
- [90] ISO 19843: *Rolling bearings — Ceramic bearing balls — Determination of strength by notched ball test*, 2018
- [91] ÖNORM M 6341: *Rolling Bearings — Ceramic bearing balls, Determination of the strength — Notched ball test*, 2013
- [92] A.A. Wereszczak, T.P. Kirkland, O.M. Jadaan: "Strength Measurement of Ceramic Spheres Using a Diametrically Compressed "C-Sphere" Specimen", *Journal of the American Ceramic Society* **90** [6] (2007), 1843–1849
- [93] R. Morrell: "Fracture toughness testing for advanced technical ceramics: internationally agreed good practice", *Advances in Applied Ceramics* **105** [2] (2006), 88-98
- [94] ASTM E399: *Standard Test Method for Linear-Elastic Plan-Strain Fracture Toughness K_{IC} of Metallic Materials*, 2017
- [95] D. Munz: "What Can We Learn from R-Curve Measurements?", *Journal of the American Ceramic Society* **90** [1] (2007), 1-15

- [96] ISO 15732: *Fine Ceramics (Advanced Ceramics, Advanced Technical Ceramics) – Test method for fracture toughness of monolithic ceramics at room temperature by single edge precracked beam (SEPB) method*, 2003
- [97] ASTM C1421: *Standard Test Methods for Determination of Fracture Toughness of Advanced Ceramics at Ambient Temperature*, 2018
- [98] G.D. Quinn, J.J. Swab: "Fracture toughness of glasses as measured by the SCF and SEPB methods", *Journal of the European Ceramic Society* **37** [14] (2017), 4243-4257
- [99] A. Schellenberger, R. Belli, J. Karsten, U. Lohbauer: "On the robustness of the Single-Edge-Precracked-Beam (SEPB) method for fracture toughness testing of ceramic materials", *Engineering Fracture Mechanics* **291** (2023), 109527
- [100] ISO 23146: *Fine Ceramics (Advanced Ceramics, Advanced Technical Ceramics) – Test method for fracture toughness of monolithic ceramics - single-edge V-notched beam (SEVNB) method*, 2012
- [101] R. Damani, R. Gstrein, R. Danzer: "Critical Notch Root Radius in SENB-S Fracture Toughness Testing", *Journal of the European Ceramic Society* **16** (1996), 695-702
- [102] R. Damani, C. Schuster, R. Danzer: "Polished notch modification of SENB-S fracture toughness testing", *Journal of the European Ceramic Society* **17** [14] (1997), 1685-1689
- [103] ISO 18756: *Fine ceramics (Advanced Ceramics, Advanced Technical Ceramics) – Determination of fracture toughness of monolithic ceramics at room temperature by the surface crack in flexure (SCF) method*, 2005
- [104] J.C. Newman, I.S. Raju: "An Empirical Stress-Intensity Factor Equation for the Surface Crack", *Engineering Fracture Mechanics* **15** [1-2] (1981), 185-192
- [105] R.M. McMeeking, A.G. Evans: "Mechanics of Transformation-Toughening in Brittle Materials", *Journal of the American Ceramic Society* **65** (1982), 242-246
- [106] A.H. Heuer, F.F. Lange, M.V. Swain, A.G. Evans: "Transformation Toughening - An Overview", *Journal of the American Ceramic Society* **69** [3] (1986), i-iv
- [107] M.V. Swain, R.H.J. Hannink: "Metastability of the Martensitic Transformation in a 12 mol% Ceria-Zirconia Alloy: II, Grinding Studies", *Journal of the American Ceramic Society* **72** [8] (1989), 1358-1364
- [108] P.F. Becher, M.V. Swain: "Grain-Size-Dependent Transformation Behaviour in Polycrystalline Tetragonal Zirconia", *Journal of the American Ceramic Society* **75** [3] (1992), 493-502
- [109] R.H.J. Hannink, P.M. Kelly, B.C. Muddle: "Transformation Toughening in Zirconia-Containing Ceramics", *Journal of the American Ceramic Society* **83** [3] (2000), 461-487
- [110] N. Ramachandran, D.K. Shetty: "Rising-Crack-Growth Resistance (R-Curve) Behaviour of Toughened Alumina and Silicon Nitride", *Journal of the American Ceramic Society* **74** [10] (1991), 2634-2641
- [111] Y.-M. Mai, B.R. Lawn: "Crack-Interface Grain Bridging as a Fracture Resistance Mechanism in Ceramics: II, Theoretical Fracture Mechanics Model", *Journal of the American Ceramic Society* **70** [4] (1987), 289-294

- [112] P.L. Swanson, C.J. Fairbanks, B.R. Lawn, Y.-M. Mai, B.J. Hockey: "Crack-Interface Grain Bridging as a Fracture Resistance Mechanism in Ceramics: I, Experimental Study on Alumina", *Journal of the American Ceramic Society* **70** (1987), 279-289
- [113] P. Chantikul, S.J. Bennison, B.R. Lawn: "Role of Grain Size in the Strength and R-Curve Properties of Alumina", *Journal of the American Ceramic Society* **73** [8] (1990), 2419-2427
- [114] R.W. Steinbrech, A. Reichl, A. Schaarwächter: "R-Curve Behavior of Long Cracks in Alumina", *Journal of the American Ceramic Society* **73** [7] (1990), 2009-2015
- [115] R.W. Steinbrech, O. Schenkel: "Crack-Resistance Curves of Surface Cracks in Alumina", *Journal of the American Ceramic Society* **71** [5] (1988), C271-C273
- [116] S. Fünfschilling, T. Fett, R. Oberacker, M.J. Hoffmann, H. Özcoban, H. Jelitto, G.A. Schneider, J.J. Kruzic: "R Curves from Compliance and Optical Crack-Length Measurements", *Journal of the American Ceramic Society* **93** [9] (2010), 2814-2821
- [117] T. Lube, R. Danzer: "Mechanical Properties and Reliability of Advanced Ceramics", in: James Zhijian Shen, Tomaž Kosmač (Eds.), *Advanced Ceramics for Dentistry*, Butterworth-Heinemann, Waltham, USA, 2014, 173-199
- [118] T. Lube: "Fracture Toughness Measurement", in: M. Pomeroy (Ed.), *Encyclopedia of Materials: Technical Ceramics and Glasses*, Elsevier, Oxford, 2021, 762-774
- [119] M. Minary-Jordan: "Formidable Challenges in Additive Manufacturing of Solid Oxide Electrolyzers (SOECs) and Solid Oxide Fuel Cells (SOFCs) for Electrolytic Hydrogen Economy toward Global Decarbonization", *Ceramics* **5** (2022), 761-779
- [120] D.W. Richerson: *The Magic of Ceramics*, John Wiley & Sons, Hoboken, 2012
- [121] T. Bauer, C. Eggs, K. Wagner, P. Hagn: "A Bright Outlook for Acoustic Filtering: A New Generation of Very Low-Profile SAW, TC SAW, and BAW Devices for Module Integration", *IEEE Microwave Magazine* **16** [7] (2015), 73-81
- [122] F. Baino, G. Magnaterra, E. Fiume, A. Schiavi, L.-P. Tofan, M. Schwentenwein, E. Verné: "Digital light processing stereolithography of hydroxyapatite scaffolds with bone-like architecture, permeability, and mechanical properties", *Journal of the American Ceramic Society* **105** [3] (2022), 1648-1657
- [123] H. Hertz: "Über die Berührung fester elastischer Körper", *Journal für die reine und angewandte Mathematik* **92** (1881), 156-171
- [124] K.L. Johnson: *Contact Mechanics*, Cambridge University Press, Cambridge, 1985
- [125] A.C. Fischer-Cripps: *Introduction to Contact Mechanics*, Mechanical Engineering Series, Springer, New York, 2007
- [126] A. Zocca, P. Colombo, C.M. Gomes, J. Günster: "Additive Manufacturing of Ceramics: Issues, Potentialities, and Opportunities", *Journal of the American Ceramic Society* **98** [7] (2015), 1983-2001
- [127] Z. Chen, Z. Li, J. Li, C. Liu, C. Lao, Y. Fu, C. Liu, Y. Li, P. Wang, Y. He: "3D printing of ceramics: A review", *Journal of the European Ceramic Society* **39** [4] (2019), 661-687
- [128] Y. Lakhdar, C. Tuck, J. Binner, A. Terry, R. Goodridge: "Additive manufacturing of advanced ceramic materials", *Progress in Materials Science* **116** (2021), 100736

- [129] T. Lube, M. Staudacher, A.-K. Hofer, J. Schlacher, R. Bermejo: "Stereolithographic 3D printing of ceramics: challenges and opportunities for structural integrity", *Advanced Engineering Materials* **25** (2022), 2200520
- [130] S. Cano, T. Lube, P. Huber, A. Gallego, J.A. Naranjo, C. Berges, S. Schuschnigg, G. Herranz, C. Kukla, C. Holzer, J. Gonzales-Guiterrez: "Influence of the infill orientation on the properties of zirconia parts produced by Fused Filament Fabrication", *Materials* **13** [14] (2020), 3158
- [131] Z. Chen, J. Li, C. Liu, Y. Liu, J. Zhu, C. Lao: "Preparation of high solid loading and low viscosity ceramic slurries for photopolymerization-based 3D printing", *Ceramics International* **45** [9] (2019), 11549-11557
- [132] ÖNORM EN ISO/ASTM 52921: *Normbegrifflichkeiten für die Additive Fertigung — Koordinatensysteme und Prüfmethodologien*, 2017
- [133] J. Schlacher, T. Lube, W. Harrer, G. Mitterramskogler, M. Schwentenwein, R. Danzer, R. Bermejo: "Strength of Additive Manufactured Alumina", *Journal of the European Ceramic Society* **40** [14] (2020), 4737-4745
- [134] G. Mitterramskogler, R. Gmeiner, R. Felzmann, S. Gruber, C. Hofstetter, J. Stampfl, J. Ebert, W. Wachter, J. Laubersheimer: "Light curing strategies for lithography-based additive manufacturing of customized ceramics", *Additive Manufacturing 1-4* (2014), 110-118
- [135] W. Harrer, M. Schwentenwein, T. Lube, R. Danzer: "Fractography of zirconia-specimens made using additive manufacturing (LCM) technology", *Journal of the European Ceramic Society* **37** (2017), 4331-4338
- [136] S. Strobl, T. Lube, P. Supancic, M. Stoiser, O. Schöppl, R. Danzer: "Mechanical properties of silicon nitride rolling elements in dependence of size and shape", *Journal of the European Ceramic Society* **34** (2014), 4167–4176
- [137] ISO 21113: *Fine Ceramics (Advanced Ceramics, Advanced Technical Ceramics) – Test method for fracture toughness of monolithic ceramics thin plates at room temperature*, 2018
- [138] A.-K. Hofer, R. Walton, O. Ševeček, G.L. Messing, R. Bermejo: "Design of damage tolerant and crack-free layered ceramics with textured microstructure", *Journal of the European Ceramic Society* **40** [2] (2020), 427-435
- [139] J. Schlacher, A. Jabr, A. Hofer, R. Bermejo: "Contact damage tolerance of alumina-based layered ceramics with tailored microstructures", *Journal of the American Ceramic Society* **105** (2022), 4387-4399
- [140] M. Tokita: "Progress of Spark Plasma Sintering (SPS) Method, Systems, Ceramics Applications and Industrialization", *Ceramics* **4** (2022), 160-198
- [141] A. Jabr, H.N. Jones, A.P. Arguelles, S. Trolrier-McKinstry, C. Randall, R. Bermejo: "Scaling up the cold sintering process of ceramics", *Journal of the European Ceramic Society* **43** (2023), 5319-5329
- [142] T. Fett: *Stress Intensity Factors, T-Stresses, Weight Functions - Supplementary Volume*, Schriftenreihe des Instituts für Keramik im Maschinenbau IKM 55, Karlsruher Institut für Technologie (KIT), Karlsruhe, 2009
- [143] S. Strobl, P. Supancic, T. Lube, R. Danzer: "Surface Crack in Tension or in Bending - A Reassessment of the Newman and Raju Formula in Respect to Fracture Toughness

- Measurements in Brittle Materials", *Journal of the European Ceramic Society* **32** (2012), 1491–1501
- [144] T. Lube: "Indentation Crack Profiles in Silicon Nitride", *Journal of the European Ceramic Society* **21** [2] (2001), 211-218
- [145] D. Mevec: "Auslegung einer Festigkeitsprüfung von Dentalkeramik mittels des B3B-Tests", Diplomarbeit, Institut für Struktur- und Funktionskeramik, Montanuniversität, Leoben, 2016
- [146] M. Staudacher, T. Lube, P. Supancic: "The Ball-on-Three-Balls strength test for discs and plates: Extending and simplifying stress evaluation", *Journal of the European Ceramic Society* **43** [2] (2023), 648-660
- [147] M. Staudacher, A. Eggel, P. Supancic, T. Lube: "The Ball-on-Three-Balls strength test: Effective volumes and surfaces for Weibull strength scaling", *Journal of the European Ceramic Society* **44** (2024), 173-183
- [148] M. Staudacher, T. Lube, J. Schlacher, P. Supancic: "Comparison of Biaxial Strength Measured with the Ball-on-Three-Balls- and the Ring-on-Ring-Test", *Open Ceramics* **6** (2021)
- [149] M. Staudacher, G. Pinzón, J. Adrien, J. Lachambre, E. Maire, J. Chevalier, T. Lube: "The ball-on-three-balls strength test: In-situ testing through X-ray radiography and tomography", *Open Ceramics* **17** (2024)
- [150] J. Essmeister, A.A. Altun, M. Staudacher, T. Lube, M. Schwentenwein, T. Konegger: "Stereolithography-based additive manufacturing of polymer-derived SiOC/SiC ceramic composites", *Journal of the European Ceramic Society* **42** (2022), 5343-5354
- [151] F. Auerbach: "Absolute Härtemessung", *Annalen der Physik* **279** [5] (1891), 61-100
- [152] W. Harrer, R. Danzer, P. Supancic, T. Lube: "Influence of Contact Stress on the Determination of Strength in the Ball-on-Three-Balls Test", *Praktische Metallographie* **45** (2008), 18-32
- [153] R. Danzer, W. Harrer, T. Lube, P. Supancic: "Influence of Contact Damage on Strength and Fractography of Ball on Three Balls Test Specimens", in: James R. Varner, George D. Quinn, Marlene Wightman (Eds.), *Fractography of Glasses and Ceramics V*, 2007, Wiley-Interscience, 203-214
- [154] U. Scheithauer, D. Brouczek, N. Lorenz, T. Lube, M. Reichel, H. Schmid, S. Scholz, E. Schwarzer-Fischer, M. Schwentenwein, M. Staudacher: "Methodik zur mechanischen Charakterisierung additiv gefertig-ter Bauteile als Funktion der Ausrichtung während des Bauprozesses und den daraus resultierenden Oberflächeneigenschaften (CharAM)", in: Martina Zimmermann (Ed.), *Proc. of Werkstoffe und Bauteile auf dem Prüfstand: Prüftechnik – Kennwertermittlung – Schadensvermeidung, 40. Vortrags- und Diskussionstagung Werkstoffprüfung 2022*, Dresden, 2022, 131-136
- [155] A.L. Gebhardt: "Prüfkörperauslegung und Ergebnisinterpretation für die Festigkeitsbewertung gedruckter filigraner Keramikstrukturen", Master's Thesis, TU Dresden & Fraunhofer-Institut für Keramische Technologien und Systeme IKTS, Dresden, 2020
- [156] M. Staudacher, T. Lube, J. Glettler, U. Scheithauer, M. Schwentenwein: "A novel test specimen for strength testing of ceramics for additive manufacturing", *Open Ceramics* **15** (2023), 100410

- [157] J. Gletter: "Entwicklung eines Prüfaufbaus für additiv gefertigte Prüfkörper -Entwicklung, Verifikation und Untersuchung der Festigkeit als Funktion der AM Druckrichtung", Masterarbeit, Lehrstuhl für Struktur- und Funktionskeramik, Montanuniversität, Leoben, 2023
- [158] M. Staudacher, U. Scheithauer, M. Reichel, N. Lorenz, M. Schwentenwein, T. Lube: "Strength testing of additive manufactured ceramics – A round robin using the CharAM-methodology", *Open Ceramics* (submitted 2023)
- [159] Z. Jiang: "Entwicklung und Umsetzung einer Methodik zur automatischen Kennwertermittlung aus Oberflächendaten eines 3D-Scanners für die mechanische Charakterisierung von keramischen AM-Bauteilen mittels CharAM-Verfahren", Master's Thesis, TU Dresden & Fraunhofer-Institut für Keramische Technologien und Systeme IKTS, Dresden, 2023
- [160] S. Strobl, P. Supancic, T. Lube, R. Danzer: "Corrigendum to "Surface Crack in Tension or in Bending - A Reassessment of the Newman and Raju Formula in Respect to Fracture Toughness Measurements in Brittle Materials" [J. Eur. Ceram. Soc. 32 (8) (2012) 1491–1501]", *Journal of the European Ceramic Society* **38** (2018), 355-358
- [161] J. Lühbauer, U. Lohbauer, M. Henrich, M. Munz, T. Lube, R. Belli: "Intricacies involving the evaluation of fracture toughness obtained by the surface-crack-in flexure method", *Journal of the American Ceramic Society* **105** (2022), 7582-7599
- [162] G.D. Quinn, J.A. Salem: "Effect of Lateral Cracks on Fracture Toughness Determined by the Surface-Crack-in-Flexure-Method", *Journal of the American Ceramic Society* **85** [4] (2003), 873-880
- [163] R. Belli, J. Lühbauer, U. Lohbauer, M. Henrich, M. Munz, T. Lube: "Reply to Quinn GD, Salem JA, Swab JJ. Comment On: Lühbauer J, Lohbauer U, Henrich M, Munz M, Lube T, Belli R. Intricacies involving the evaluation of fracture toughness obtained by the surface-crack-in-flexure method. J Am Ceram Soc., 2022;105(12):7582-7599.", *Journal of the American Ceramic Society* **106** (2023), 6371-6377
- [164] A.L. Fry, C. Krug, L. Ladinger, T. Lube, S.H. Kim, J.C. Mauro: "Fracture toughness of Ca-, Sr-, and Ba-aluminoborosilicate glasses", *Journal of the American Ceramic Society* **107** (2024), 830-843
- [165] S. Strobl, P. Supancic, T. Lube, R. Danzer: "Toughness Measurement on Ball Specimens, Part I: Theoretical Analysis", *Journal of the European Ceramic Society* **32** (2012), 1163-1173
- [166] S. Strobl, T. Lube, O. Schöppl: "Toughness measurement on ball specimens. Part II: Experimental procedure and measurement uncertainties", *Journal of the European Ceramic Society* **34** (2014), 1881-1892
- [167] T. Lube, S. Rasche, T.G.T. Nindhia: "B3B-K1c fracture toughness test – geometric function formulae for semi-elliptical surface cracks in bi-axial bending", *Journal of the American Ceramic Society* **99** [1] (2016), 249–256
- [168] S. Rasche, S. Strobl, M. Kuna, R. Bermejo, T. Lube: "Determination of strength and fracture toughness of small ceramic discs using the small punch test and the ball-on-three-balls test", *Procedia Materials Science* **3** (2014), 961-966
- [169] S. Strobl, S. Rasche, C. Krautgasser, E. Sharova, T. Lube: "Fracture toughness testing of small ceramic discs and plates", *Journal of the European Ceramic Society* **34** [6] (2014), 1637-1642

- [170] R. Belli, M. Wendler, D. de Ligny, M.R. Cicconi, A. Petschelt, H. Peterlik, U. Lohbauer: "Chairside CAD/CAM materials. Part 1: Measurement of elastic constants and microstructural characterization", *Dental Materials* **33** [1] (2017), 84-98
- [171] P.F. Cesar, A. Della Bona, S.S. Scherrer, M. Tholey, R. van Noort, A. Vichi, R. Kelly, U. Lohbauer: "ADM guidance—Ceramics: Fracture toughness testing and method selection", *Dental Materials* **33** [6] (2017), 575-584
- [172] T. Fromm, R. Borchardt, Y. Xuan, K. Durst, S.M. Rosiwal: "Realization of diamond/metal laminates through brazing of freestanding diamond foils", *Key Engineering Materials* **809** (2019), 309-313
- [173] R. Belli, M. Wendler, A. Petschelt, T. Lube, U. Lohbauer: "Fracture toughness testing of biomedical ceramic-based materials using beams, plates and discs", *Journal of the European Ceramic Society* **38** (2018), 5533-5544
- [174] L.F. Guilardi, A. Werner, N. De Jager, G.K.R. Pereira, C.J. Kleverlaan, M.P. Rippe, L.F. Valandro: "The influence of roughness on the resistance to impact of different CAD/CAM dental ceramics", *Brazilian Dental Journal* **32** [6] (2022), 54-65
- [175] P. Palmero, M. Fornabaio, L. Montanaro, H. Reveron, C. Esnouf, J. Chevalier: "Towards long lasting zirconia-based composites for dental implants. Part I: innovative synthesis, microstructural characterization and in vitro stability", *Biomaterials* **50** (2015), 38-46
- [176] H. Reveron, M. Fornabaio, P. Palmero, T. Fürderer, E. Adolfsson, V. Lughi, A. Bonifacio, V. Sergo, L. Montanaro, J. Chevalier: "Towards long lasting zirconia-based composites for dental implants: Transformation induced plasticity and its consequence on ceramic reliability", *Acta biomaterialia* **48** (2017), 423-432
- [177] J. Chevalier, A. Liens, H. Reveron, F. Zhang, P. Reynaud, T. Douillard, L. Preiss, V. Sergo, V. Lughi, M. Swain, N. Courtois: "Forty years after the promise of «ceramic steel?»: Zirconia-based composites with a metal-like mechanical behavior", *Journal of the American Ceramic Society* **103** [3] (2020), 1482-1513
- [178] J. Schlacher, A.-K. Hofer, S. Geier, I. Kraveva, R. Papšik, M. Schwentenwein, R. Bermejo: "Additive manufacturing of high-strength alumina through a multi-material approach", *Open Ceramics* **5** (2021)
- [179] J. Schlacher, S. Geier, M. Schwentenwein, R. Bermejo: "Towards 3D-printed alumina-based multi-material components with enhanced thermal shock resistance", *Journal of the European Ceramic Society* **44** (2024), 2294-2303

7 Selected Publications

- A **M. Staudacher, T. Lube, P. Supancic:** "The Ball-on-Three-Balls strength test for discs and plates: Extending and simplifying stress evaluation", *Journal of the European Ceramic Society* **43** [2] (2023), 648-660, <https://doi.org/10.1016/j.jeurceramsoc.2022.09.047>
- B **M. Staudacher, A. Eggel, P. Supancic, T. Lube:** "The Ball-on-Three-Balls strength test: Effective volumes and surfaces for Weibull strength scaling", *Journal of the European Ceramic Society* **44** (2024), 173-183, <https://doi.org/10.1016/j.jeurceramsoc.2023.09.018>
- C **M. Staudacher, T. Lube, J. Schlacher, P. Supancic:** "Comparison of Biaxial Strength Measured with the Ball-on-Three-Balls- and the Ring-on-Ring-Test", *Open Ceramics* **6** (2021), <https://doi.org/10.1016/j.oceram.2021.100101>
- D **J. Schlacher, T. Lube, W. Harrer, G. Mitteramskogler, M. Schwentenwein, R. Danzer, R. Bermejo:** "Strength of Additive Manufactured Alumina", *Journal of the European Ceramic Society* **40** [14] (2020), 4737-4745, <https://doi.org/10.1016/j.jeurceramsoc.2020.03.073>
- E **T. Lube, M. Staudacher, A.-K. Hofer, J. Schlacher, R. Bermejo:** "Stereolithographic 3D printing of ceramics: challenges and opportunities for structural integrity", *Advanced Engineering Materials* **25** (2022), 2200520, <https://doi.org/10.1002/adem.202200520>
- F **M. Staudacher, T. Lube, J. Glettler, U. Scheithauer, M. Schwentenwein:** "A novel test specimen for strength testing of ceramics for additive manufacturing", *Open Ceramics* **15** (2023), 100410, <https://doi.org/10.1016/j.oceram.2023.100410>
- G **S. Strobl, P. Supancic, T. Lube, R. Danzer:** "Surface Crack in Tension or in Bending - A Reassessment of the Newman and Raju Formula in Respect to Fracture Toughness Measurements in Brittle Materials", *Journal of the European Ceramic Society* **32** (2012), 1491–1501, <http://dx.doi.org/10.1016/j.jeurceramsoc.2012.01.011>
- H **J. Luhbauer, U. Lohbauer, M. Henrich, M. Munz, T. Lube, R. Belli:** "Intricacies involving the evaluation of fracture toughness obtained by the surface-crack-in flexure method", *Journal of the American Ceramic Society* **105** (2022), 7582-7599, <http://dx.doi.org/10.1111/jace.18667>

- I **S. Strobl, P. Supancic, T. Lube, R. Danzer:** "Toughness Measurement on Ball Specimens, Part I: Theoretical Analysis", *Journal of the European Ceramic Society* **32** (2012), 1163-1173, <http://dx.doi.org/10.1016/j.jeurceramsoc.2011.12.003>
- J **S. Strobl, T. Lube, O. Schöppel:** "Toughness measurement on ball specimens. Part II: Experimental procedure and measurement uncertainties", *Journal of the European Ceramic Society* **34** (2014), 1881-1892, <http://dx.doi.org/10.1016/j.jeurceramsoc.2013.12.052>
- K **T. Lube, S. Rasche, T.G.T. Nindhia:** "A fracture toughness test using the Ball-on-three-balls test", *Journal of the American Ceramic Society* **99** [1] (2016), 249–256, <http://www.dx.doi.org/10.1111/jace.13842>

T. Lube's contributions according to Credit[#]

	Paper										
	A	B	C	D	E	F	G	H	I	J	K
Conceptualization	✓	✓	✓	✓	✓	✓	✓		✓	✓	✓
Methodology	✓	✓	✓	✓	✓	✓	✓	✓	✓	✓	✓
Software		✓		n.a.	n.a.						
Validation	✓	✓	✓	✓	n.a.	✓	✓	✓	✓	✓	✓
Formal analysis	✓	✓	✓	✓	n.a.	✓		✓		✓	✓
Investigation					n.a.		✓		n.a.	✓	✓
Resources	✓	✓	✓	✓	✓	✓	✓	✓	✓	✓	✓
Data Curation	✓	✓	✓	✓	n.a.	✓	✓	✓	✓	✓	✓
Writing - Original Draft	✓		✓		✓			✓		✓	✓
Writing - Review & Editing	✓	✓	✓	✓	✓	✓	✓	✓	✓	✓	✓
Visualization	✓		✓		✓	✓	✓	✓		✓	✓

empty cells: no contribution by TL

n.a. ... not applicable

[#]<https://www.elsevier.com/authors/policies-and-guidelines/credit-author-statement>,
<https://doi.org/10.1002/leap.1210>

Paper A

M. Staudacher, T. Lube, P. Supancic: "The Ball-on-Three-Balls strength test for discs and plates: Extending and simplifying stress evaluation", *Journal of the European Ceramic Society* **43** [2] (2023), 648-660, <https://doi.org/10.1016/j.jeurceramsoc.2022.09.047>

Open access article distributed under the terms of the Creative Commons CC-BY license



The Ball-on-Three-Balls strength test for discs and plates: Extending and simplifying stress evaluation

Maximilian Staudacher^{*}, Tanja Lube, Peter Supancic

Department of Materials Science, Montanuniversität Leoben, Franz Josef-Strasse 18, A-8700 Leoben, Austria

ARTICLE INFO

Keywords:

Ball-on-Three-Balls testing
Finite Element Analysis
Biaxial testing
Strength testing
Brittle failure

ABSTRACT

The Ball-on-Three-Balls-test has proven to be an accurate and easy-to-use option for strength testing. However, the maximum stress must be calculated based on Finite-Element-Analysis results. For this purpose, a fitted function was already provided. This function is based on results which were generated under the assumption of punctiform load introduction. Deviations from these conditions occur through an increase in contact-area between the loading ball and the specimen, large specimen deformations, friction, or plastic deformation of the balls. These non-linear effects are investigated by Finite-Element-Analysis for a wide range of specimens. It is shown that the maximum stress is sensitive to the area of contact between the loading ball and the specimen. Furthermore, thin specimens are subject to large deformations, which significantly decrease the maximum stress. Therefore, a revised fitted function is derived. For specimens with exceptional geometries, non-linear effects are considered with correction factors added to the new fitted function.

1. Introduction

Strength testing is probably the most important tool for ceramic material characterization and material development. It allows the determination of both general mechanical strength and the scatter thereof, which then enables the prediction and reduction of component failure [1]. Today, a number of mechanical testing methods are widely available and well examined. They can be categorized by the type of stress field that the specimen is subjected to, which is usually either uniaxial or biaxial. The main uniaxial testing methods are 3-or 4-point-bending, tensile and compression tests [2,3]. Biaxial testing methods can be classified by the symmetry of their stress distribution, being either axisymmetric or not. Examples for common methods with axisymmetric stress distributions are the Ring-on-Ring-test (RoR), the Ball-on-Ring-test or the Ball-with-flat-on-Ring-test [4–6]. Common methods employing non-axisymmetric stress distributions are the Ball-on-Three-Balls-test (B3B), the Piston-on-Three-Balls-test (P3B), the Ball-on-Ring-of-Balls-test and the Three-Balls-on-Three-Balls-test [7–12]. A significant disadvantage of axisymmetric tests is that a high degree of flatness of the specimen is required in order to guarantee even contact throughout the ring. This results in either additional specimen preparation requirements or deviations from the ideal analytical stress field due to uneven load distribution [13,14]. Therefore, tests utilizing a support of three balls have been

developed since non-planar discs can still be stably supported. The Piston-on-Three-Balls-test shows a similar problem, since the surface beneath the punch has to be planar to ensure uniform load application – the condition that has been assumed to derive the equation for the stress calculation. Furthermore, with increasing deformation of the sample, the assumption of an extended area of uniform pressure is lost and load application shifts towards the outer edge of the piston. This leaves testing methods such as the Ball-on-Three-Balls-test as one of the most tolerant to non-planar specimens and most flexible in terms of specimen geometry. As a result, it is among the most common biaxial testing methods and is employed for a variety of materials [15–24]. An extensive study about the influence of the most important sources of error has been conducted by Börger et al. [25]. Furthermore, the strongly localized area of maximum stress allows testing of specific regions of a component to generate spatially resolved strength results [26]. A prerequisite for an accurate evaluation for all tests that use an analytical stress calculation is to perform them under conditions of small deflections and linear elastic material behavior, i.e. maintaining a linear stress-deflection relationship. This is assured by prescribing that the support radius is smaller than about 6–20 times the specimen thickness [4,13,20]. Taking into account that manufacturing tolerances make support rings smaller than 5 mm in radius impractical [13], the lower limit for the thickness of strong specimens is approximately 0.5 mm in the RoR-test. The B3B-test, however, can easily

^{*} Corresponding author.

E-mail address: maximilian.staudacher@unileoben.ac.at (M. Staudacher).

<https://doi.org/10.1016/j.jeurceramsoc.2022.09.047>

Received 6 July 2022; Received in revised form 23 September 2022; Accepted 24 September 2022

Available online 28 September 2022

0955-2219/© 2022 The Author(s). Published by Elsevier Ltd. This is an open access article under the CC BY license (<http://creativecommons.org/licenses/by/4.0/>).

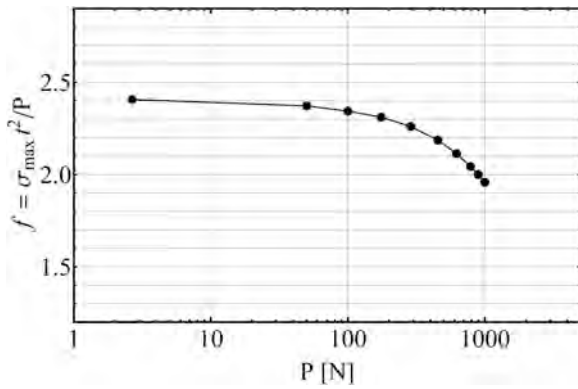


Fig. 1. FEA-results for the factor f in dependence of the applied load P for an exemplary specimen with a radius of 12 mm, a support radius of 10 mm and a thickness t of 1 mm. The specimen’s Young’s modulus and Poisson’s ratio are 70 GPa and 0.22, respectively.

be scaled down to much smaller support radii. With the use of standardized bearing balls, specimens as small as $2 \times 2 \times 0.13 \text{ mm}^3$ have been tested successfully [27–29]. However, the main disadvantage of the B3B-test is that no sufficiently accurate analytical description of the full stress field is available and numerical analysis has to be employed to determine the maximum stress and the effective volume or surface for each specimen [30,31]. This then entails new difficulties in making those results available. One possibility is to provide fitting functions for the factor f , which relates the applied load and the maximum tensile stress, as has been done by Börger et al. [30]. Yet, these functions are cumbersome to use and only provide a solution for the ideal case of punctiform load introduction and small deformations. Deviations from these ideal conditions lead to a load dependency of the factor f , as shown for an exemplary specimen in Fig. 1, which is not represented in [30]. This may lead to a significant overestimation of the specimen’s strength [32].

Within this work, a new expression for the ideal case of both discs and square plate specimens will be derived by utilizing FEA for linear elastic isotropic materials. By modifying the range and variables of the underlying data field, a new and simpler fit with similar accuracy to the one derived by Börger et al. [30] will be presented. Furthermore, the difference between the ideal case and real testing situations, such as an increase in contact-area between the loading ball and the specimen, large specimen deformations, friction, or plastic deformation of the loading ball will be discussed. The effect of large specimen deformations will be investigated by utilizing a combined analytical and numerical approach. The effect of an increasing contact-area at the loading ball will be examined by utilizing FEA. This will yield correction factors which describe the load-dependency of the factor f . The performance of

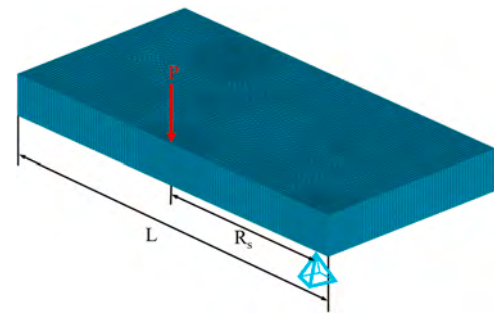


Fig. 3. Meshed Model 2 with a punctiform load P applied.

this new evaluation and its corrections will be assessed by comparison with an elaborate FEA model. The practical aspects given by the new evaluation and its valid domain of application will be discussed.

2. Methods

2.1. Finite-Element-Analysis

FEA was performed to generate grid points for fitting and to investigate specific effects. All simulations were conducted utilizing the commercial FEA-program ANSYS R21.1 (ANSYS Inc., PA 15317, Canonsburg, USA). Each of the following models was implemented as a script written in Ansys-Parametric-Design-Language (APDL). This allowed using them in automated parametric studies for a wide range of geometries and isotropic material properties, covering several thousand unique combinations.

2.1.1. Simplified models for discs

To investigate the dependence of the factor f on the testing geometry as well as the specimen’s elastic properties, the 3D-model shown in Fig. 2a) was utilized. Due to the symmetry of the system and loading conditions, the model could be reduced to one sixth of the full disc. In Model 1A, the loading ball was represented by a punctiform load applied in the center of the disc. The support ball was represented by a punctiform boundary condition at the support radius R_s . Consequently, this model represents the ideal case during testing. The specimen was meshed with 178958 SOLID95 elements (20-node brick elements) and 749574 nodes. The script further facilitates the implementation of various types of load application in the center of the specimen. To examine the influence of a finite area of contact, a Hertzian contact-pressure distribution with varying extent was utilized in Model 1B, as depicted in Fig. 2b).

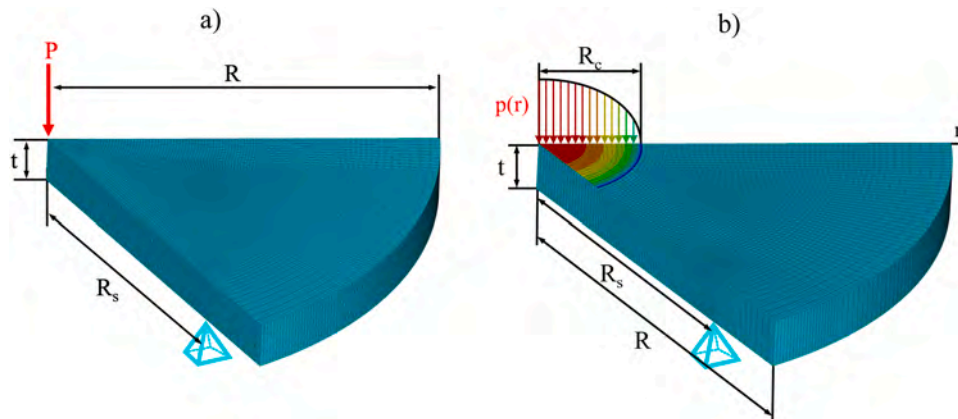


Fig. 2. a) displays the meshed Model 1A with a punctiform load P applied. b) shows Model 1B, but with a Hertzian contact-pressure distribution $p(r)$ applied.

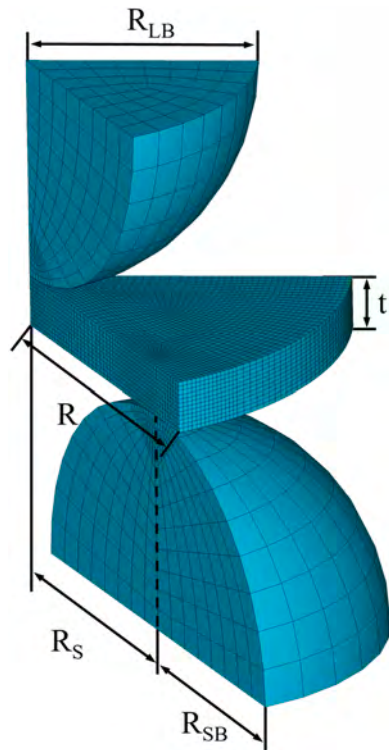


Fig. 4. Meshed model of the specimen and the loading/support balls, Model 3.

2.1.2. Simplified model for square plates

Model 2 serves the same purpose as Model 1A, but for square plates. Due to the reduced symmetry of the system, one half of the plate has to be simulated, as displayed in Fig. 3. Both the loading and the support balls were represented by a punctiform load (or boundary condition) applied in the center of the disc and at the support radius R_s , respectively. The specimen was meshed with a minimum of 162216 SOLID95 elements and 682140 nodes, depending on the specimen’s thickness and overhang.

2.1.3. Complete 3D-Model for discs

Model 3 serves as a validation for the simplified models. It represents a 3D-model of the testing assembly, based on a model first developed by Börger et al. [30]. Symmetry conditions allowed a reduction to one sixth of the full testing assembly, see Fig. 4. The specimen was meshed with a minimum of 40392 SOLID95 elements and 173061 nodes and a maximum of 70668 SOLID95 elements and 301375 nodes, depending on the specimen’s thickness and overhang. The loading ball was meshed with 1750 SOLID95 elements and 8196 nodes, the support ball using 3500 SOLID95 elements and 15582 nodes. The contact between the loading ball and the specimen was meshed with 375 CONTA174 (8-node surface elements) and 375 TARGET170 elements (8-node surface elements), the contact between the support ball and the specimen with 490 CONTA174 and 490 TARGET170 elements. The friction coefficient was set to $\mu = 0.5$ and symmetric contact calculations were employed. Since this model includes interactions between the specimen and the balls as well as load-dependent changes to the testing assembly and is solved under non-linear conditions, a better representation of real testing situations is given. A mesh convergence analysis for this and the other mentioned models can be found in Appendix A of this work.

2.2. Analytic solution for the deflection of plates

Kirstein et al. already developed an analytical solution for the deflection of thin centrally loaded plates on symmetric point supports in 1966 [33]. This solution is valid for a minimum of three supporting

points up to a theoretical maximum of an infinite number of support points, which would represent a ring supported situation. Within the context of this paper, their solution will be utilized for the special case of $m = 3$ support points and a central punctiform load. The deflection w at a position with radial distance r from the center of a disc with radius R and supported on points with distance D_s from the evaluated position is given by:

$$w = w_0 + \frac{3P(1 - \nu^2)}{2\pi Et^3} \left(r^2 \ln \rho - \frac{1}{m} \sum_{s=1}^m D_s^2 \ln \frac{D_s}{c} \right) \tag{1}$$

with

$$w_0 = \frac{P(1 - \nu^2)}{2\pi \kappa Et^3} \left[\sum_{s=1}^m D_s^2 \ln \frac{D_s'}{r_s'} + (\kappa^2 - 1)c^2 \operatorname{Re}\{L_m(\zeta)\} + \frac{m(1 - \rho^2)R_s^2}{\kappa + 1} \right] + \gamma_3 \tag{2}$$

and

$$\gamma_3 = \frac{3P(1 - \nu^2)R_s^2}{2\pi \kappa Et^3} \left[A_m(\beta) + (1 - \kappa^2)B_m(\beta) - \kappa \ln \beta - \frac{1 - \beta^2}{\kappa + 1} \right]. \tag{3}$$

Here, P denotes the applied load, E the specimen’s Young’s modulus, t the specimen’s thickness, R_s the support radius, β the ratio R_s/R , and ν the Poisson’s ratio of the specimen. Other parameters of the equation will not be discussed here, the authors refer to the original work by Kirstein et al. [33].

2.3. Fitting

Every fit in this work has been performed in Mathematica 13.1 (Wolfram Research, IL 61820, Champaign, USA) with the command *NonlinearModelFit*. This command performs a least sum of squared errors fit on any given type of ansatz function by adjusting user-specified constants within the function. The deviation between the value of the fit $x_{i,fit}$ and the fitted data $x_{i,ref}$ for data point i will be referred to as residual error and is determined by

$$\text{Residual error } [\%] = 100 \cdot \frac{x_{i,fit} - x_{i,ref}}{x_{i,ref}} \tag{4}$$

For each fit, the maximum positive and negative residual error for the complete data field will be given. Furthermore, the mean residual error for a fit based on n grid points is given by

$$\text{Mean residual error } [\%] = 100 \cdot \frac{\sum_{i=1}^n \operatorname{Abs}\left(\frac{x_{i,fit} - x_{i,ref}}{x_{i,ref}}\right)}{n} \tag{5}$$

3. Simplifying the stress calculation

3.1. Discs

Due to the lack of an accurate analytical solution for the stress field, it must be numerically evaluated instead. Börger et al. [30] performed Finite-Element-analysis for the special case of contacting support balls. If not stated otherwise, this assumption will be maintained throughout this work. For this case, the support radius R_s is given by the radius of the support balls R_{SB} by

$$R_s = R_{SB} \frac{2}{\sqrt{3}} \tag{6}$$

In general, the maximum tensile stress σ_{max} in the center of a bent plate scales with the applied load P and the inverse square of the thickness of the plate t :

$$\sigma_{max} = f \frac{P}{t^2} \tag{7}$$

The factor f is a dimensionless function which takes the material

Table 1
Constants m_1 - m_3 utilized in Eq. (9).

m_1	m_2	m_3
0.697	-0.118	-0.728

Table 2
Accuracy parameters describing the deviation of Eq. (9) to the data field for discs and Eq. (10) used in Eq. (9) to the data field for square plates.

Accuracy parameter	Discs	Square plates
Maximum residual error [%]	+ 1.4	+ 1.6
Minimum residual error [%]	-1.9	-1.6
Mean residual error [%]	+ 0.52	+ 0.63

properties and the involved geometry into account. Within their work, they reduced the factor f for the B3B-test to being dependent on the specimen's thickness t , the specimen's radius R , the support radius R_s and the Poisson's ratio ν . Furthermore, the results of a parametric study were made available by providing a fitted function for f :

$$f_{B\ddot{o}rger} \left(\frac{t}{R}, \frac{R_s}{R}, \nu \right) = c_0 + \frac{c_1 + c_2 \frac{t}{R} + c_3 \left(\frac{t}{R} \right)^2 + c_4 \left(\frac{t}{R} \right)^3}{1 + c_5 \frac{t}{R}} \left(1 + c_6 \frac{R_s}{R} \right) \quad (8)$$

This function covers the range of $0.55 \leq R_s/R \leq 0.9$, $0.05 \leq t/R \leq 0.6$ and $0.2 \leq \nu \leq 0.3$. This range was later extended to $0.1 \leq \nu \leq 0.4$ by Danzer et al. [32]. The value of $f_{B\ddot{o}rger}$ determined with this fit has an error $\leq \pm 1\%$ with respect to the numerical solution. This accuracy is made possible by providing a set of constants c_0 - c_6 for different Poisson's ratios in an increment of 0.05; a total of 49 constants. If the tested material has a Poisson's ratio not tabulated, linear interpolation must be performed. This makes implementation of this equation prone to errors and cumbersome. In order to simplify the calculation of the maximum stress, a new study on f has now been conducted. Up to now, f was always expressed and evaluated with its arguments relative to R . However, the influence of the support radius R_s on the value of f is significantly higher than that of the specimen's radius R . Therefore, a new data field for f based on the now modified parameters t/R_s , R/R_s and ν was generated by FEA utilizing Model 1, with a total of 1400 datapoints. The data field covers $1.05 \leq R/R_s \leq 2$, $0.05 \leq t/R_s \leq 0.6$ and $0.1 \leq \nu \leq 0.4$. Based on this data, a new empirical fit was developed. Now, the factor f can be determined by

$$f_{new} \left(\frac{t}{R_s}, \frac{R}{R_s}, \nu \right) = \exp \left[m_1(1 + \nu) + m_2 \ln \frac{t}{R_s} + m_3 \sqrt[4]{\frac{Rt^2}{R_s^3}} \right] \quad (9)$$

with m_1 - m_3 as listed in Table 1 and the limits of valid application as the range of the fitted data field.

An overview of the general deviation from Eq. (9) to the fitted data can be found in Table 2. Fig. 5a-e) provide a more comprehensive overview of the fit's accuracy. In terms of specimen geometry, the lowest accuracy/largest deviation is generally found in the peripheral regions. Similarly, a low accuracy for exceptionally low and high Poisson's ratios can be observed. However, most technical ceramics exhibit a Poisson's ratio in the range of 0.2 – 0.3 [31], a range well described by the fit. Furthermore, typical specimens for the Ball-on-Three-Balls-test exhibit geometries as marked in Fig. 5c). Here, a maximum and minimum deviation as low as + 0.15% and – 0.7%, respectively, are achieved. In principle, a small loss in (overall) accuracy as compared to the fit by B\ddot{o}rger et al. [30] is observed, though only in regions of minimal interest. Fig. 5 further gives the possibility to derive highly accurate strength results for individual geometries by utilizing the given deviation in combination with Eq. (9) to determine the applied stress as originally calculated with FEA.

3.2. Square plates

Another very common specimen geometry are square plates, which can be tested in similar testing fixtures as discs. The factor f for these specimens does not deviate much from similarly sized disc-shaped specimens, but the difference is large enough to necessitate a separate treatment. This is due to the fact that the overhang, i.e. the part of the specimen from the outer edge to the support radius, has a small but still pronounced effect on the maximum tensile stress. Therefore, instead of describing square plates with fit very similar to Eq. (9), the authors opted to provide a conversion from square plates to equivalent discs, as has been done for other methods [4,34]. An equivalent disc is defined by its diameter D_{eff} , which is chosen in a way so that the maximum stress is the same as in the square plate specimen. All other geometry parameters, such as the specimen's thickness and the support radius, remain unchanged. Therefore, only the conversion from the square plate's edge length L to the equivalent diameter is needed. In order to derive this conversion, Model 2 was utilized and 1035 datapoints were generated. The data field covers $2.165 \leq L/R_s \leq 3.899$, $0.0449 \leq t/R_s \leq 0.736$ and $0.05 \leq \nu \leq 0.45$. Based on this data, a conversion from square plates to discs was developed. The effective diameter D_{eff} is determined by

$$D_{eff} = L \left(1.053 - 0.017 \frac{tL}{R_s^2} \right). \quad (10)$$

An overview of the deviation for the factor f , derived with the conversion to equivalent discs and Eq. (9), to the FEA-data for square plates can be found in Table 2.

It should be noted that this conversion is only valid in the range $2.17 \leq L/R_s \leq 3.9$, $0.1 \leq t/R_s \leq 0.6$ and $0.1 \leq \nu \leq 0.4$.

4. Improving accuracy for high-load testing situations

So far, all simulations have been conducted with Models 1A and 2 described in Sections 2.1.1 and 2.1.2. As previously stated, this model represents the ideal case during testing with both punctiform load introduction and support conditions. It is evident that this will not represent reality in a number of practical cases and that some errors are to be expected. Errors due to geometric deviations of various aspects of the testing setup have already been discussed by B\ddot{o}rger et al. and deemed negligible [25]. Therefore, the aforementioned errors mostly arise because no interactions between the loading or support balls and the specimen are represented in the model. First, an increase in load results in deformation of the loading ball and the specimen in the area of contact, whereby the assumption of punctiform load introduction loses its validity. Instead, a finite area of contact and load introduction is established. Second, large deflection of the specimen may occur under certain conditions, causing it to roll off the support balls. This results in a shift of contact position towards the center of the support circle, altering the applied bending moment and with it the maximum tensile stress. Third, friction between the loading ball and the specimen can have a significant influence on the maximum tensile stress of the specimen. It induces shear stresses under the area of contact, which act through the specimen thickness and thus reduce the maximum tensile stress.

Due to these interactions being included, Model 3, as described in Section 2.1.3, is significantly better suited to provide an accurate representation of reality. This then provokes the idea of using this model in a similar way to the previous section and incorporate all the mentioned effects into the evaluation at once. The main drawback of this model is its high processing time due to its use of contact calculations despite a decrease in the overall number of elements. In general, the evaluation takes about 70–80 times longer than for Model 1A. In order to represent the mentioned effects in the calculation of maximum stress, a higher number of parameters would be needed. First, the load-dependence has to be considered, which is influenced by the elastic constants of both the specimen and the support or loading balls. This would result in the

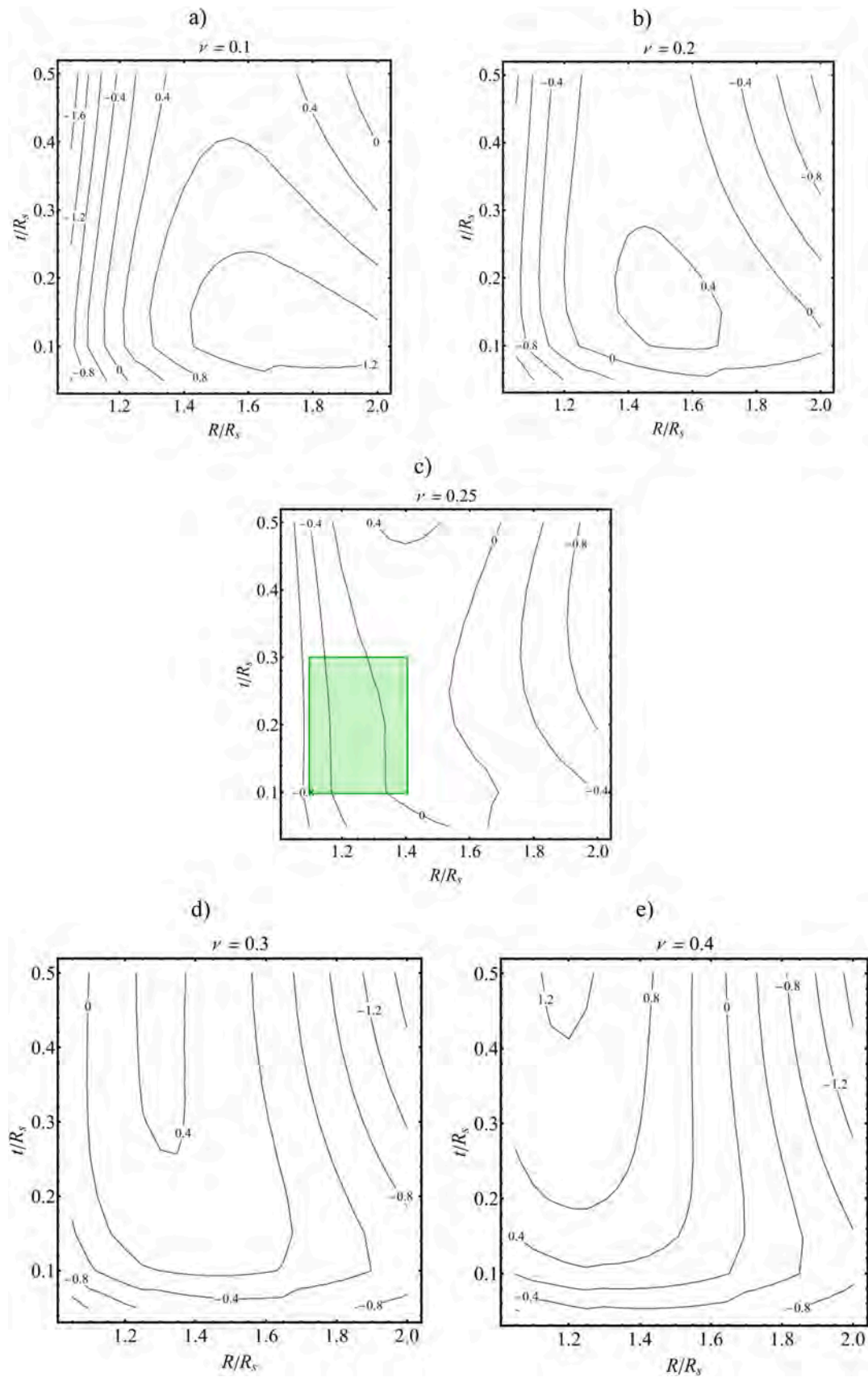


Fig. 5. Overview of the relative error of f_{new} to the fitted data points.

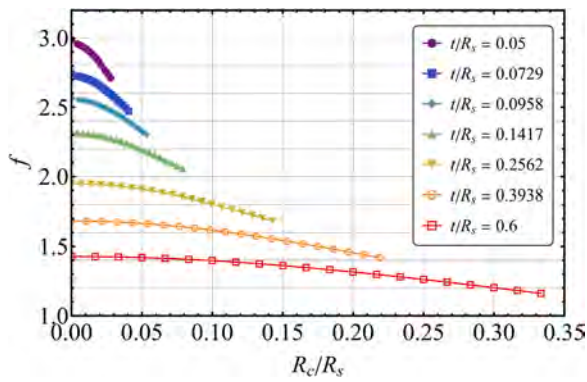


Fig. 6. The factor f in dependence of the relative contact radius and the specimen’s relative thickness as predicted by FEA. Values at $R_c/R_s = 0$ are those which correspond to the point-load situation, and which are described by Eq. (7).

addition of up to four new parameters. To properly capture each dependency, each relevant parameter would have to be varied within its relevant range in at least 10 steps. Putting all those considerations together, a new parameter field with a size well within millions of data points would be necessary. In combination with the high processing time, a study like this would require immense computing power. Developing an accurate fit for such a data field would be another challenge by itself.

Therefore, a different method has to be considered. Within this work, a separation approach will be utilized. By taking an individual look at each major effect, a better understanding of its consequences can be achieved. Ideally, the deviations from the ideal solution f_{new} caused by them can be described separately with correction factors k_i . Combining these expressions multiplicatively, as shown in Eq. (11), will yield a corrected factor f_{corr} . If each k_i is a somewhat manageable functional expression with sufficiently similar results to FEA, this method will provide a valuable alternative evaluation, but within a much shorter time.

$$f_{corr} = f_{new} \prod_i k_i \tag{11}$$

In the upcoming sections, a closer look at the change in load application and the specimen’s deflection will be taken and functional expressions to describe their influence on the factor f will be provided.

4.1. Contact at the loading ball

As mentioned in the previous section, an increase in load establishes a finite area of contact between the loading ball and the specimen. This causes a change in load introduction from the ideal punctiform load to a distributed load over a circular contact area at the center of the specimen. The size of this area will be quantified by its radius, which will be referred to as the contact radius R_c . In principle, an increase in contact radius reduces the bending moment and with it the stress applied on the specimen. This change in stress has been investigated by FEA with Model 1B described in Section 2.1.1. Instead of a punctiform load, a Hertzian pressure distribution for the contact between a sphere and a flat surface has been applied. With this model, a parametric study of approximately 6000 simulations on the influence of the contact radius R_c on the maximum stress (i.e. the factor f) has been conducted. More specifically, the contact radius R_c was varied for a wide range of specimen geometries, such as the specimen’s thickness t , the specimen’s radius R and the support radius R_s . Additionally, the influence of the applied load P , the specimen’s Young’s modulus E and Poisson’s ratio ν was investigated as well. In conclusion, only the contact radius, specimen’s thickness and support radius have a distinct influence on the maximum stress. The other parameters mentioned have an influence on the contact radius, but

Table 3
Constants h_1 - h_5 utilized in Eq. (12).

h_1	h_2	h_3	h_4	h_5
1.0052	0.00063	-0.5928	1.6756	1.3523

Table 4
Accuracy parameters describing the deviation of Eq. (12) and Eq. (15) to their respective fitted data fields.

Accuracy parameter	k_1	$s_{red} (k_2)$
Maximum residual error [%]	+ 1.0	+ 6.4
Minimum residual error [%]	-0.50	-13
Mean residual error [%]	0.16	3.7

not on the maximum stress directly. This allowed to reduce the number of relevant parameters to just three. By using dimensionless relative parameters, e.g. the relative contact radius R_c/R_s and relative thickness t/R_s , the number of parameters could be further reduced to two. Based on these findings, a reduced data field with 525 data points to describe the change in maximum stress, i.e. the factor f , was generated. The influence of these two parameters on f is shown in Fig. 6.

By fitting this data field, a functional expression for the change of f due to the change in contact area can be provided. The correction k_1 can be given as

$$k_1(a/R_s, t/R_s, \nu, E, E_{LB}, \nu_{LB}, P) = h_1 + h_2 \ln(R_c/R_s \cdot t/R_s) + h_3 \frac{(R_c/R_s)^{h_4}}{(t/R_s)^{h_5}} \tag{12}$$

where

$$R_c = \sqrt[3]{\frac{3PR_{LB}}{4} \left(\frac{1-\nu^2}{E} + \frac{1-\nu_{LB}^2}{E_{LB}} \right)} \tag{13}$$

with R_c describing the contact radius based on the Hertzian solution. E_{LB} and ν_{LB} are the Young’s modulus and Poisson’s ratio of the loading ball, respectively. R_{LB} denotes the radius of the loading ball. The fitting constants h_1 - h_5 are listed in Table 3. An overview of the deviation of Eq. (12) to the fitted data can be found in Table 4.

4.2. Deflection of the specimen

A different problem is raised through the interaction of the specimen and the support balls. With increasing specimen deflection, the point of contact progressively shifts inwards. This reduces the applied bending moment due to decreasing leverage. Since the bending moment is directly proportional to the maximum stress and therefore the factor f , a functional expression for the change in bending moment is equal to the searched correction k_2 . This effect is especially pronounced when materials with high strength (> 1000 MPa) and low Young’s modulus (< 100 GPa), such as high-strength glass, are tested. In order to predict the extent of this effect, the change in leverage, i.e. the shift in contact position at the support balls, has to be known. By considering the geometry of the problem, trigonometry can be utilized to express the shift in contact x_{shift} from the slope s_{con} of the specimen with

$$x_{shift} = R_{SB} \text{Sinarctans}_{s_{con}}, \tag{14}$$

where R_{SB} is the radius of the support ball. A schematic of the geometric relations is shown in Fig. 7.

Therefore, the problem can be reduced to the determination of the slope of the specimen’s deflection curve at the point of contact. Ideally, this information can be directly deduced from an analytical expression. Favorably, Kirstein et al. [33] derived an analytical description for the deflection of point-loaded plates on an arbitrary number of equally spaced point supports, as explained in Section 2.2. If we differentiate a

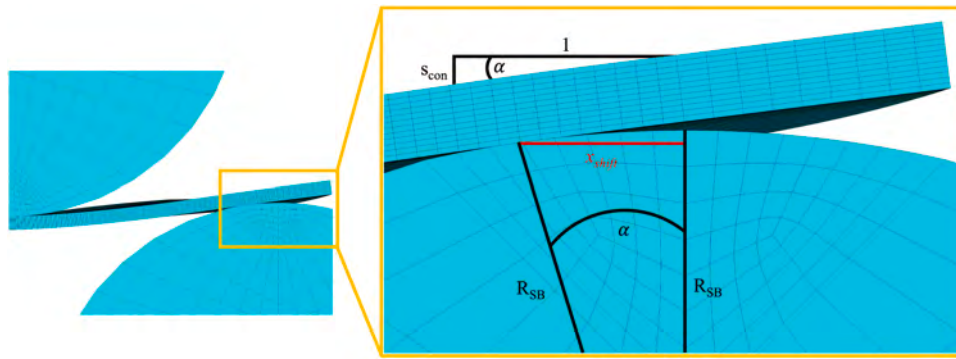


Fig. 7. Geometric relations for the contact point shift between the specimen and the support ball.

function describing the deflection of a specimen, a function describing its slope is obtained. However, due to its complexity, this cannot be done analytically for the solution by Kirstein et al. Therefore, a numerical approach had to be employed. First, the number of variables for the numerical evaluation had to be reduced. This was done by factoring out P/Et^2 , which leaves a reduced function for the deflection that is independent of the applied load and the specimen's Young's modulus. Therefore, the variables had been narrowed down to R , R_s , ν and t . By forming dimensionless relative parameters, i.e. the relative radius R/R_s and relative thickness t/R_s , the number of parameters could be further reduced to three. A parametric study on those three parameters for the reduced slope at the point of support was conducted and a data field comprising 1330 data points was generated. By fitting, an approximation for the analytical derivation of the equation by Kirstein et al. at this position can be given. The fit for the reduced slope s_{red} can therefore be expressed as

$$s_{red} = (1 - \nu^2) \frac{R/R_s}{t/R_s} \left(0.0015 - 1.13 \frac{1}{(R/R_s)^2} \right). \quad (15)$$

A summary of the deviation of Eq. (15) to the fitted data can be found in Table 4. The high relative deviation stems from the deviation for low absolute values of the reduced slope. Here, a small deviation in absolute value causes a large relative deviation due to the reference value being very small. This large error would therefore only come into play when very small deflections are involved, a case where an application of this fit or correction is neither necessary nor recommended. Combining the reduced slope with the load- and material-specific term previously factored out yields the actual slope s_{con} at the contact point between the specimen and the support ball

$$s_{con} = \frac{P}{Et^2} \left[(1 - \nu^2) \frac{R/R_s}{t/R_s} \left(0.0015 - 1.13 \frac{1}{(R/R_s)^2} \right) \right] \quad (16)$$

with the variables as denoted in previous equations. Since the slope at the point of contact is now known, Eq. (14) can be utilized to predict the shift in contact position x_{shift} with

$$x_{shift} = R_{SB} \text{sinarctan} \frac{P}{Et^2} \left[(1 - \nu^2) \frac{R/R_s}{t/R_s} \left(0.0015 - 1.13 \frac{1}{(R/R_s)^2} \right) \right] \quad (17)$$

Due to the small value of the argument of the trigonometric functions, s_{con} , a small angle approximation ($\text{sinarctan} x \approx x$) can be performed. This then gives

$$x_{shift} = R_{SB} \frac{P}{Et^2} \left[(1 - \nu^2) \frac{R/R_s}{t/R_s} \left(0.0015 - 1.13 \frac{1}{(R/R_s)^2} \right) \right] \quad (18)$$

for x_{shift} . In order to predict the change in bending moment, the relative change in leverage has to be calculated. This is done by subtracting x_{shift} from the original lever arm, i.e. the support radius R_s , and then dividing

the result by R_s . Since the slope determined with Eq. (16) is negative, x_{shift} is negative as well and has to be added to R_s instead in order to correctly portray the change in leverage. This then yields

$$k_2 = \frac{R_s + x_{shift}}{R_s} \quad (19)$$

for the change in bending moment k_2 . Inserting Eq. (17) into Eq. (19), utilizing the relationship from Eq. (6) and simplifying the resulting expression gives

$$k_2 = 1 + \frac{\sqrt{3}}{2} \frac{P}{Et^2} \left[(1 - \nu^2) \frac{R/R_s}{t/R_s} \left(0.0015 - 1.13 \frac{1}{(R/R_s)^2} \right) \right] \quad (20)$$

4.3. Friction & plastic deformation of the loading ball

The influence of friction and plastic deformation has been investigated through FEA with a model employing contact calculations. It was found that friction between the specimen and the loading ball starts to play an increasingly important role if the specimens are thin. For thin and highly flexible specimens, i.e. $t/R_s = 0.05$ and $E = 70$ GPa, a reduction in the maximum tensile stress of about 4% from the frictionless case to the same setup with $\mu = 0.5$ has been observed. This is due to the shear stresses caused by friction starting to affect the stress at the opposing face, resulting in a reduction of maximum tensile stress. For thicker and less flexible specimens, this effect is in the range of about 1–2%. As will be explained in the upcoming sections, thin and flexible specimens are difficult to describe with the models established in this work and will have to be treated separately. Since this effect is only significant for a small portion of possible specimen geometries, while having only a minor influence on the remaining ones, no functional expression for the influence of friction will be provided. Additionally, friction between the support balls and the specimen is not present if the balls are allowed to rotate freely [25].

Another possible source of error is plastic deformation of the loading ball. The expected effect would be similar to what has been covered in Section 4.1. A FE study using an ideal bilinear elastic-plastic material model for the loading ball [35], solely for the influence of plastic deformation on the contact situation, was conducted. It revealed a nearly linear relation between the increase in load and the increase in contact radius compared to the pure elastic case. If the material properties of the balls are known, this additional increase can be determined and added to the elastic deformation. This would provide a new contact radius R_c' for the usage in k_1 and no further changes to the calculation of the maximum tensile stress would have to be made.

4.4. The load-corrected stress evaluation

Combining the correction factors k_1 and k_2 with f_{new} ultimately yields the corrected factor f_{corr}

Table 5
Material parameters for "typical" specimens.

Specimen material	R/R_s [-]	E [GPa]	ν [-]
Glass	1.2	70	0.22
Zirconia		210	0.25
Alumina		420	0.2

$$f_{corr} \left(\frac{t}{R_s}, \frac{R}{R_s}, \nu, E, \nu_{LB}, E_{LB}, P \right) = f_{new} k_1 k_2 \quad (21)$$

which now takes additional load- and material-dependent effects into account. The following sections will provide an overview of the performance and accuracy of this functional expression for f_{corr} .

5. Validation and Comparison of f_{corr}

Before the comparison of f_{corr} to FEA results obtained with Model 3, some aspects of the behavior of the correction factors k_1 and k_2 have to be discussed. First, thin specimens exhibit the highest relative deflections and with it the strongest curvature. This especially affects the size of the zone of contact between the loading ball and the specimen, where the curvature is most pronounced. As discussed in Section 4.1, the size of the contact area has a strong effect on the maximum stress. However, the correction factor k_1 is based on the assumption of Hertzian contact between a sphere and a flat surface. This suggests a smaller area of contact compared to contact between a sphere and a concave surface. Therefore, k_1 underestimates the effect of contact for large deflections. Second, the geometric assumptions necessary for the equation given by Kirstein et al. [33] lose their validity for large deflections. Due to the correction factor k_2 being deducted from this equation, an error for

exceptionally thin specimens is expected. A comparison of the slope at the point of contact as obtained with FEA and the prediction by Eq. (1) for thin specimens with large deflections shows an overestimation by the analytical solution. Additionally, Kirstein et al. assume punctiform load introduction, while an extended load introduction is closer to real testing situations. This reduces the applied bending moment and with it the deflection, which is another reason for the overestimation of the slope at the point of contact. Therefore, the correction factor k_2 generally overestimates the effect of deflection for exceptionally thin specimens.

Model 3 mentioned in Section 2.1.3 was utilized as a base of comparison and a tool for the validation of Eq. (21). More specifically, the load dependency of the factor f was determined with both methods for a range of parameters. On one hand, this range includes "typical" specimens and testing setups, as one would encounter on a regular basis. On the other hand, the edge-cases of possible parameter combinations were also examined to work out the limits of Eq. (21)'s applicability. All comparisons in this chapter are based on a testing setup that utilizes steel balls with a Young's Modulus of 210 GPa and a Poisson's ratio of 0.33. For typical specimens, a relative radius R/R_s of 1.2 and a range of relative thicknesses t/R_s from 0.05 to 0.4 were chosen. The material-specific parameters are listed in Table 5. Fig. 8a-c) depict the change in f in dependence of the applied load P , predicted by both FEA and Eq. (21). The corresponding maximum stress for each curve is approximately 2 GPa. Except for specimens with a relative thickness of 0.05, exceptional agreement between the two methods is achieved. The maximum relative error for specimens with $t/R_s \geq 0.1$ is less than 1%. It should be noted that FEA was conducted with non-linear geometric behavior considered, which is represented accurately by the functional expressions.

Eight edge-cases were investigated to cover extreme specimen

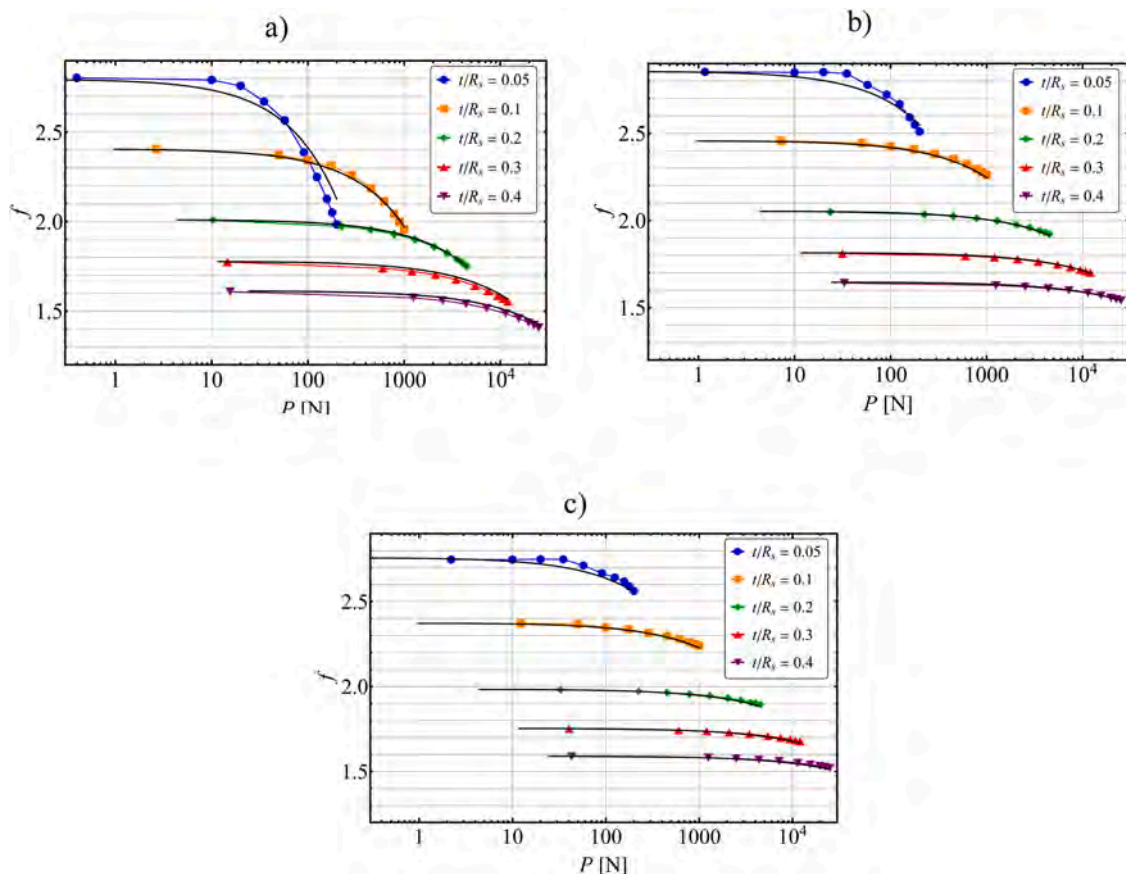


Fig. 8. Dependence of f on the applied load P as predicted by FEA and by Eq. (21). The colored markers represent the results of FEA, the continuous black line represents f_{corr} Eq. (21). The maximum tensile stress for each curve is approximately 2 GPa. The results for glass are shown in a), zirconia in b) and alumina in c).

Table 6

Geometry and material parameters as well as the maximum relative deviation from f_{corr} to FEA for a number of investigated edge cases.

Designation	R/R_s [-]	E [GPa]	ν [-]	Max. dev.
Case 1	1.05	70	0.1	< 2%
Case 2			0.4	< 2%
Case 3		420	0.1	2%
Case 4			0.4	< 2%
Case 5	1.525	70	0.1	6%
Case 6			0.4	< 2%
Case 7		420	0.1	< 2%
Case 8			0.4	< 2%

Table 7

Parameter range for the accurate application of Eq. (21).

t/R_s [-]	R/R_s [-]	E [GPa]	ν [-]	σ_{max} [MPa]
0.1 – 0.5	1.05 – 1.525	70–420	0.1 – 0.4	≤ 2000

Note that for the special case of specimens similar to case 5, i.e. highly flexible specimens ($E \leq 100$ GPa) with a high strength ($\sigma_F \geq 1$ GPa) and a Poisson’s ratio in the range of 0.1–0.15, deviations of up to 6% are expected.

geometries and extreme material properties. As before, the relative thickness was varied, but now in the range from 0.05 to 0.5. Two main cases were differentiated: An exceptionally small relative radius of 1.05 (i.e. a small overhang) and large relative radius of 1.525 (i.e. large overhang). Within each case, 4 combinations of material parameters were evaluated. The specific parameters are listed in Table 6. Fig. 1 of the supplementary material depicts the results for cases 1–4, while Fig. 2 of the supplementary material depicts the results for cases 5–8. Again, specimens with a relative thickness of 0.05 exhibit the highest deviation, with the exception of case 2 and 8, and will not be included in the following observations. For cases 1–4, i.e. specimens with very low relative radius, an overall good agreement is observed. The highest deviation is displayed in case 3 by the specimen with a relative thickness of 0.1. However, the maximum deviation for this specific combination of parameters is about 2%, which is well within the desired accuracy. For cases 5–8, i.e. specimens with a very high relative radius, a similar situation is found. Cases 6–8 exhibit good agreement, only the specimen with a relative thickness of 0.1 in case 7 displays a deviation of about 1.6%. Case 5 however indicates a problem for highly flexible specimens with a low Poisson’s ratio. Here, even the thickest specimen exhibits a constant deviation of about 4%. The specimen with a relative thickness of 0.1 exhibits an error of up to 5.9%, albeit only for a maximum stress of more than 1 GPa.

As discussed in the beginning of this chapter, both corrections either underestimate (k_1) or overestimate (k_2) their respective influences with increasing load. Due to the factors k_1 and k_2 being utilized in multiplicative combination, these errors cancel each other out and an accurate description can evidently be achieved for most specimens. However, they cannot sufficiently describe specimens with a relative thickness < 0.01 . Considering these aspects, the range of parameters for the application for f_{corr} , i.e. Eq. (21), is given in Table 7. Since f_{corr} has been compared to FEA only up to a maximum tensile stress of 2 GPa, the authors do not recommend application for specimens with a higher strength. Within the given range, Eq. (21) replaces individual FEA with an error typically $\leq \pm 2\%$.

6. Practical aspects

The test set-up of the B3B-test was originally designed using three contacting balls to provide the support of the specimen on a perfect circle and a ball of similar size as loading ball, as depicted in [25,30]. Due to the ability of the support balls to rotate at their position during

Table 8

Summary of the valid parameter ranges for the functional expressions of f .

	t/R_s	R/R_s or L/R_s	E [GPa]	ν	σ_{max} [MPa]
f_{new}	0.1 – 0.6	1.05 – 2	–	0.1 – 0.4	material specific, Eq. 23
$f_{new, square}$	0.1–0.6	2.17 - 3.9	–	0.1 – 0.4	material specific, Eq. 23
f_{corr}	0.1 – 0.5	1.05–1.525	70–420	0.1 – 0.4	≤ 2000

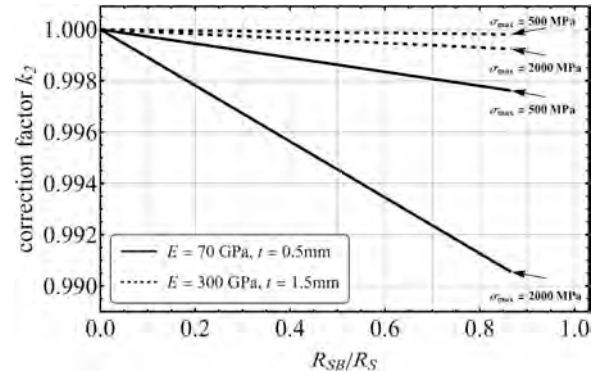


Fig. 9. Correction factor k_2 for exemplary specimens ($R = 6$ mm, $R_s = 5$ mm) in dependence of the radius of the support balls (in fractions of the support radius). Through lines represent thin, flexible (glass) specimens ($t = 0.5$ mm, $E = 70$ GPa), dashed lines represent thicker, more typical ceramic specimens ($t = 1.5$ mm, $E = 300$ GPa). Two cases are shown: $\sigma_{max} = 500$ MPa and $\sigma_{max} = 2000$ MPa.

the test, friction can be minimized, and an important source of error can be eliminated [25]. Furthermore, this set-up facilitates jig-designs with exceptionally easy handling. Preferably, ball bearing grade steel balls are used, since they are easy to obtain and available in a fine grading of radii over a wide range of sizes. The separate description of the influences of two important issues of the B3B test – the contact situation through k_1 and the deflection effects through k_2 – paves the way to an analysis of some practical aspects of the test. In the following sections, these aspects will be discussed within the validity range of Eq. (21), as given in Table 8, for exemplary specimens with radius of $R = 6$ mm on a support radius of $R_s = 5$ mm. The ideal ball radius for this set-up is $R_{SBI} = R_{LBI} = 4.33$ mm.

6.1. Support ball size

In Section 4.2 and in Eqs. (17) and (19), the influence of the specimen’s deflection on the maximum stress in the specimen is described and quantified. It is obvious that this effect is more pronounced if the specimen is supported on large balls. The influence of the shift of contact on the maximum stress can be reduced if smaller than ideal support balls are used. For any test geometry, the correction factor k_2 depends linearly on the ratio of the support ball radius over support radius, R_{SB}/R_S . For $R_{SB}/R_S = 0$, $k_2 = 1$, for larger ratios $k_2 < 1$. This trend is illustrated in Fig. 9 for thin specimens with a Young’s modulus of $E = 70$ GPa and more typical, thicker specimens with $E = 300$ GPa at two failure stresses. It can be seen that the effect of using smaller support balls is very small unless very flexible materials with extremely high strength are tested. Using smaller balls will also require a new design of the test fixture, which will certainly be more complicated than the one suggested earlier [25,30], especially regarding the exact positioning of the support balls and their ability to rotate.

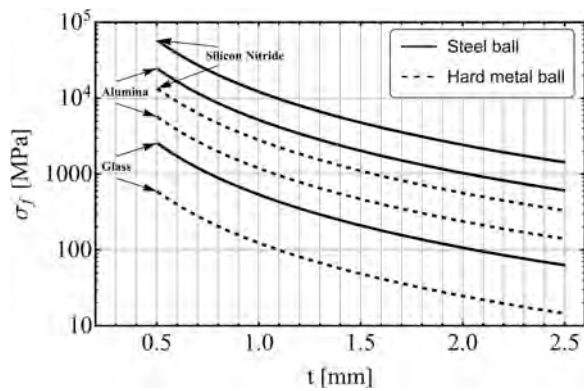


Fig. 10. Strength-thickness map for B3B-tests on exemplary specimens ($R = 6$ mm, $R_s = 5$ mm) of glass, alumina, and silicon nitride. If the measured strength of a specimen with a given thickness t is below its respective line, no contact cracks are expected. The through lines refer to loading with a steel loading ball with the ideal radius $R_{LBi} = 4.33$ mm, the dashed lines refer to loading with hard-metal ball with $R_{LB} = 1$ mm.

6.2. Contact of the specimen with the loading ball

The ideal loading situation in the B3B-test is a punctiform load introduction. Of course, this cannot be achieved using a ball to apply the load. It has been shown in Section 4.1 how an increase in the size of the area of load introduction influences the maximum stress. In practice, the desirable situation of keeping the size of this area as small as possible is favored by two means: by using a loading ball with a higher Young's modulus (see Eq. (13)) or by using a smaller loading ball (i.e. smaller than the ideal size which is equal to the contacting support balls). Eqs. (12) and (13) can be employed to evaluate the influence of using a hard metal loading ball of ideal size with a Young's modulus of $E_{LB} = 600$ GPa instead of steel balls. This only has a negligible influence of less than 1% on the correction factor k_1 . The effect of using a smaller loading ball is slightly more pronounced, with deviations up to 3% for very small balls. These numbers were obtained for the condition of a maximum tensile stress of 2000 MPa in the specimens. The effect will be even smaller at lower stresses.

Moreover, any contact of a ball with a surface, as at the site of load introduction in the B3B-test, bears the risk of the formation of contact cracks if a certain critical load P_c is exceeded [36]. Upon increase of the load beyond this critical value such cracks may grow, penetrate the thickness of the specimens and lead to failure [37]. This is an unwanted situation that can be avoided if the load at fracture due to bending, P_f , is less than the critical load P_c for the formation of contact cracks, i.e. $P_f < P_c$.

For common ball sizes used in the B3B test, this situation can be analyzed by using Auerbach's law for the contact between a flat surface and a ball. According to Auerbach's observations [38], the load required to produce contact cracks P_c is proportional to the radius of the loading ball: $P_c = A \cdot R_{LB}$. The constant A (Auerbach constant) has been related to the elastic constants of the involved materials and the surface energy γ of the cracked material [39,40], and has further been determined experimentally for various material (i.e. specimen and ball) combinations [41–45]:

$$P_c = \frac{3\pi^3}{16} \frac{\phi_a}{\phi_a} \left(\frac{1-\nu^2}{E} + \frac{1-\nu_{LB}^2}{E_{LB}} \right) \frac{2\gamma}{(1-\nu^2)} E R_{LB} \quad (22)$$

Eq. (22) or experimental values for A can be used to plot curves of $\sigma(P_c)$, using Eq. (7), for a given specimen geometry as a function of the specimen's thickness t . Such curves can be used to find limiting conditions for contact cracking during B3B-tests. An example for such curves for the exemplary specimen is given in Fig. 10 for various specimen materials (glass, alumina, silicon nitride) and a steel loading ball of ideal

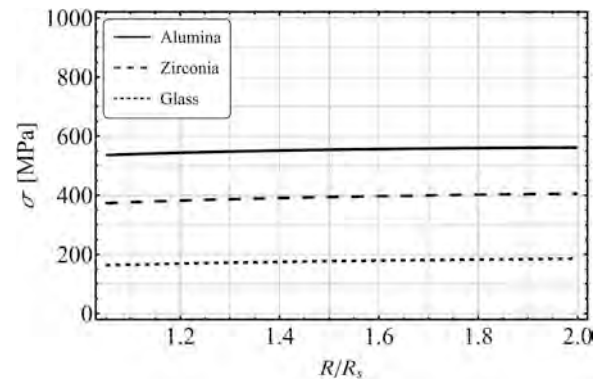


Fig. 11. 2%-Limit for selected specimens with varying Young's modulus in dependence of R/R_s .

size R_{LBi} . If the expected strength of the specimen is below the line at a given thickness, no contact cracks should be generated during the B3B-test. For glass, $A = 62$ N/mm was taken from [41], for alumina, $A = 590$ N/mm from [42] and for silicon nitride, a value of $A = 1360$ N/mm using materials properties given in [46], Eq. (22) $\phi_a = 0.0011$ [39] and the relation $K_{Ic}^2 = 2\gamma E / (1-\nu^2)$ was used. Additionally, Fig. 10 depicts the same limit curves for a loading ball made from hard-metal and with a radius $R_{LB} = 1$ mm.

It is obvious from Eq. (22) how the size and Young's modulus of the loading ball influence the limit curve: the smaller R_{LB} , the smaller is P_c and the higher E_{LB} , the smaller is A . Both trends shift the limit curve towards lower strength values. These findings discourage the use of smaller or stiffer loading balls. However, the use of balls with R_{LBi} and a high Young's modulus may be indicated for cases where high fracture loads prevail, and plastic deformation of the loading ball is an issue.

Several simplifications have been made for the construction of Fig. 10. The data for A are related to the contact between a ball and a thick, flat specimen that does not deform globally. In the case of the B3B-test, the contacted surface is concave and under a general compressive equi-biaxial stress. The curvature will increase the contact area in comparisons to the flat surface case and thus decrease the overall magnitude of the contact stress field. The overall compressive equi-biaxial stress state at the loaded surface of the specimen additionally hinders contact cracking, since tensile stresses are relevant for this phenomenon. The limit curves in the presented map can therefore be regarded as conservative estimates.

6.3. Domains of application

As is evident from the plots in Fig. 6, the factor f does not deviate a lot from f_{new} , i.e. the values of f on the ordinate axis, for certain conditions. These conditions are given by the specimen geometry (relative thickness and relative radius), its elastic properties and the applied load. Even though f_{corr} gives the more accurate result for f , it is not necessary to use this lengthy expression in all cases. In order to determine which expression to use, the impact of the correction factors k_1 and k_2 has been investigated for all valid parameter combinations. A combined correction of k_1 and k_2 of 2% has been set as the limit for the application of f_{new} . This means that if $f_{corr}/f_{new} < 0.98$, f_{new} does not sufficiently describe f anymore and f_{corr} has to be utilized instead. For the following graphs and statements, a testing fixture utilizing steel balls with a Young's modulus of 210 GPa and a Poisson's ratio of $\nu = 0.33$ is assumed. This then reduces the possible parameters to R/R_s , t/R_s , E and ν of the specimen as well as the applied load P . To display the limits in a way that is not dependent on the absolute geometry of the specimen, the applied load will be expressed by the maximum applied stress σ (or the measured strength) instead. Fig. 11 depicts the 2%-limit in dependence of R/R_s for exemplary specimens made from glass, zirconia, and alumina with t/R_s

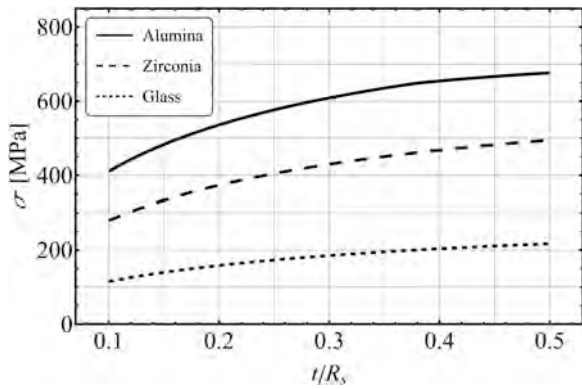


Fig. 12. 2%-Limit for selected specimens with various Young's moduli and Poisson's ratios in dependence of t/R_s .

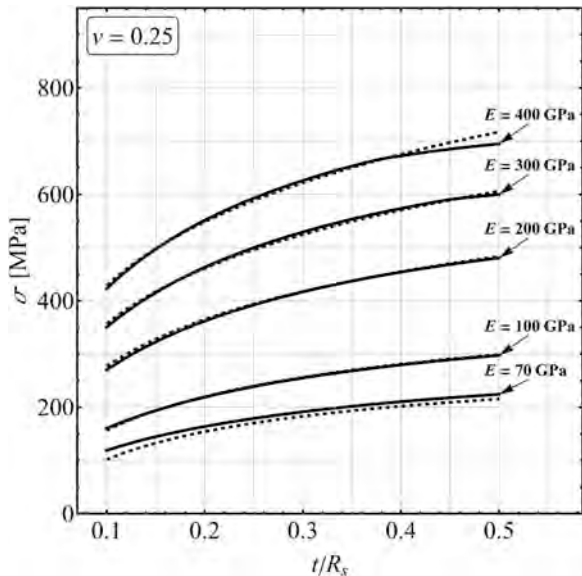


Fig. 13. Comparison of the 2% limit, expressed by the functional expression (dashed), and the curves derived by f_{corr} , for $\nu = 0.25$.

= 0.2. The lines in this Figure display the maximum stress that can be applied to the material before the deviation between f_{corr} and f_{new} is $\geq 2\%$. Therefore, if a specimen exhibits a strength below this line, the simplified evaluation, i.e. Eq. (9), can be utilized. If the strength is higher, then Eq. (21) has to be utilized to accurately determine f .

Fig. 11 shows that R/R_s does not strongly influence the limit. This was found to be true for all other possible configurations of t/R_s , E and ν . Therefore, the following graphs will depict the limits only in dependence of t/R_s , E and ν . Fig. 12 displays the application limits for typical materials such as glass, zirconia, and alumina.

In order to ensure that the parameter R/R_s can safely be omitted, each datapoint for a specific configuration (t/R_s , E , ν) actually represents the lowest value of all R/R_s in its valid range of 1.05–2 for that configuration. This means that the limits shown always assume the worst case in terms of R/R_s , so that no matter what value of R/R_s the tested specimen exhibits, the limit shown might actually be lower than 2%, but never higher. Fig. 3a)-c) of the supplementary material display the limits for more cases, including the special cases discussed in Section 5. An alternative route to convey these limits in a more general form is by providing a functional expression. By setting the Poisson's ratio of the

specimen to a fixed and common value, one function can describe a very broad range of materials and geometries. This has been done for $\nu = 0.25$, which gives

$$\sigma_{lim} \leq -347 - 497\sqrt{t/R_s} - 0.062\sqrt{E} + 68\sqrt[4]{E \cdot t/R_s} \quad (23)$$

to describe the limiting strength σ_{Flim} (in MPa) for the application of f_{new} in dependence of t/R_s and E (in MPa). An overview of the accuracy of this expression is shown in Fig. 13. Again, R/R_s was chosen in a way so that it represents the worst-case scenario. Regarding the Poisson's ratio, $\nu = 0.25$ was chosen since it represents a value close to that of many technical ceramics [31]. A change to a higher Poisson's ratio would shift the curves slightly upwards, while lowering the Poisson's ratio would shift them slightly downwards.

Eq. (23) provides a convenient tool to decide which factor, f_{new} (for $\sigma_F < \sigma_{lim}$) or f_{corr} (for $\sigma_F > \sigma_{lim}$), has to be used to obtain the most accurate result for σ_{max} for a given test geometry or which test geometry is suitable to allow for the use of the simple expression of f_{new} , Eq. (7).

Overall, 3 regimes for the evaluation of f can be defined. If the strength of the material is below the limits displayed in Fig. 13, then the simple functional expression f_{new} (Eq. (9)) can be utilized. If the strength of the material is higher, than the more complex functional expression f_{corr} (Eq. (21)) has to be used. Finally, if the geometry- or material parameters of a specimen are not covered by the given range for f_{new} or f_{corr} , as summarized in Table 8, then individual FEA has to be conducted to determine f . Note that this work has been performed for linear elastic isotropic materials. If the tested specimen exhibits anisotropic behavior or material nonlinearities (such as plastic deformation of the specimen), then neither f_{new} nor f_{corr} should be applied. Again, this would then be a typical case where individual FEA has to be performed.

7. Summary

- 1) A simplified model of the B3B-test has been utilized to analyze the factor f for a wide range of geometric and material parameters and a new fitted function f_{new} , for the evaluation of the B3B-test is presented.
- 2) A conversion from square plate specimens to discs with an equivalent diameter D_{eff} for the calculation of f is given. This allows stress evaluation for square plates with the new fitted function f_{new} from 1).
- 3) The influence of the applied load on the factor f was investigated. Two major effects have been considered separately. First, the increase of contact area between the loading ball and the specimen due to high loads and elastic deformation was investigated. Second, the shift in contact position between the specimen and the support balls due to deflection of the specimen was examined. For each effect, a correction factor that describes the deviation in f is presented.
- 4) By utilizing these corrections, a range of geometries and material properties can be defined, for which the ideal punctiform solution f_{new} gives an error $< 2\%$ for the calculated maximum stress. Within this range, the simplified evaluation from 1) is sufficient.
- 5) Cases, which are not included in 4) can be accurately represented by taking the corrections from 3) into account and using $f_{corr} = f_{new}k_1k_2$. Such, the load-dependence of f is given for most practical specimens with strengths up to 2 GPa.
- 6) Cases, which are not included in 5), have been identified. For these cases, the authors recommend referring to individual solutions by Finite-Element-Analysis.
- 7) Using the correction factors, the effect of modifications of the suggested test set-up were discussed. It was shown that the use of small support or loading balls or balls with a high Young's modulus has very limited beneficial effects while making the test less practicable. A simple estimation was proposed that showed that contact cracking

at the loading ball can be avoided by using sufficiently thin specimens.

Declaration of Competing Interest

The authors declare that they have no known competing financial interests or personal relationships that could have appeared to influence the work reported in this paper.

Acknowledgements

M. Staudacher gratefully acknowledges financial support by the Austrian BMVIT and BMWFW in the project "CharAM" (FFG 877684) of the COIN/IraSME program.

Appendix A. – Mesh convergence analysis

In order to obtain the optimum number of elements and mesh configuration for each model, a mesh convergence analysis has been performed. Fig. A1a) shows the absolute factor f for Model 1 in dependence of the total number of elements for three different thicknesses. Fig. A1b) shows the factor f normalized to the value obtained with the highest number of elements. The black markers indicate the mesh utilized in this work.

Since the results of the mesh configuration utilized in this work only display a maximum relative error of 0.5% to the result obtained by approximately tripling the number of elements, it was deemed sufficiently accurate. Model 2 utilizes a similar mesh-density in the central region of maximum stress and is loaded in the same way, hence why no additional mesh convergence analysis was performed for this model.

Due to the different type of loading, the analysis has also been performed for Model 3. As before, Fig. A2a) shows the absolute factor f for three different thicknesses, while Fig. A2b) shows the normalized factor f .

As before, the factor f calculated with the mesh utilized in this work shows a maximum relative error of about 0.6% to the factor f calculated with a model with double the number of elements. For this model, special care was taken to primarily increase the number of elements in the contacting regions of both the balls and the specimen as well as the central tensile loaded regions of the specimen. Due to the iterative nature of the contact analysis, larger deviations between different mesh densities are expected. As soon as the relevant abort criteria are met, the solver is stopped. Since the amount and step size of these iterations changes for each mesh density, final solutions may be just below the abort criteria or well below it. This allows changes of f in both directions, as observed for the thickest specimen in Fig. A2.

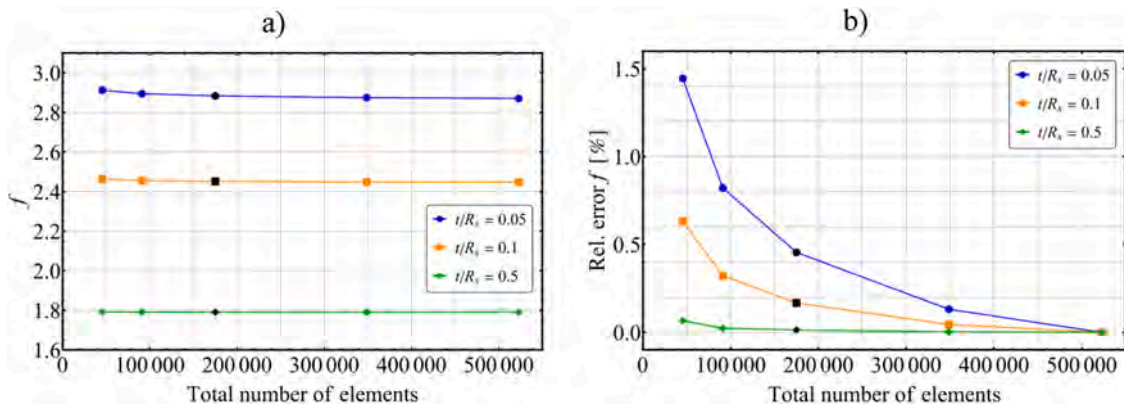


Fig. A1. Results for the factor f (a) absolute values, (b) normalized values) in the mesh convergence analysis for the model from Section 2.1.1 for a specimen with $R/R_s = 1.33$, $E = 210$ GPa, $\nu = 0.25$ and varying thickness. The black markers represent the mesh configuration that was either used directly or slightly modified (in dependence of the specimen's geometry) in this work.

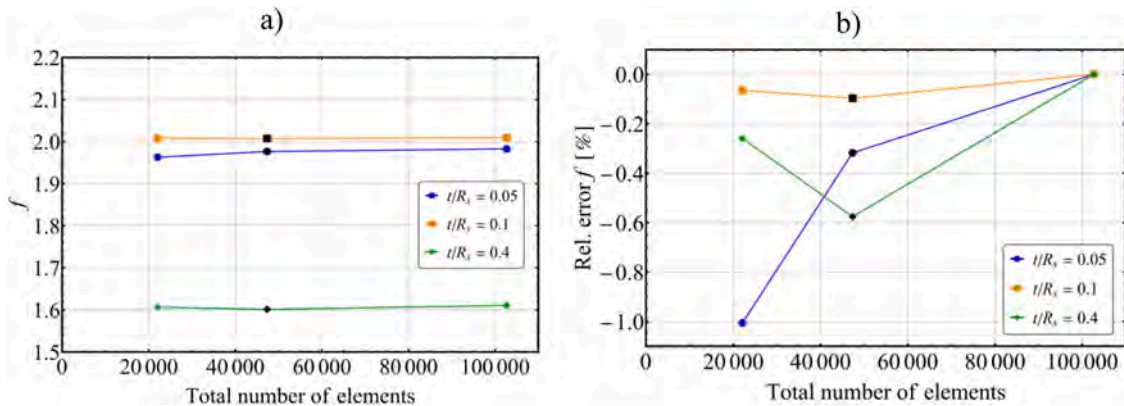


Fig. A2. Results for the factor f (a) absolute values, (b) normalized values) in the mesh convergence analysis for the model from Section 2.1.3 for a specimen with $R/R_s = 1.05$, $E = 70$ GPa, $\nu = 0.25$ and varying thickness. The black markers represent the mesh configuration that was either used directly or slightly modified (in dependence of the specimen's geometry) in this work.

Appendix B. Supporting information

Supplementary data associated with this article can be found in the online version at [doi:10.1016/j.jeurceramsoc.2022.09.047](https://doi.org/10.1016/j.jeurceramsoc.2022.09.047).

References

- [1] R. Danzer, Mechanical Performance and Lifetime Prediction, in: Encyclopedia of Advanced Ceramics, pp. 385–398.
- [2] DIN EN 843–1:2008–08: Advanced technical ceramics - Mechanical properties of monolithic ceramics at room temperature - Part 1: Determination of flexural strength; German version EN 843–1:2006, German Institute for Standardisation (Deutsches Institut für Normung), 2008.
- [3] D.C. Cranmer, D.W. Richerson (Eds.), Mechanical Testing Methodology for Ceramic Design and Reliability, CRC Press, Taylor & Francis Group, Boca Raton, London, New York, 2018.
- [4] ASTM C 1499–05: Test Method for Monotonic Equibiaxial Flexural Strength of Advanced Ceramics at Ambient Temperature, ASTM International, West Conshohocken, PA, 2005.
- [5] D. Shetty, A.R. Rosenfield, P. McGuire, G.K. Bansal, W.H. Duckworth, Biaxial flexure test for ceramics, *Am. Ceram. Soc. Bull.* (1980) 1193–1197.
- [6] T.R. Wilshaw, Measurement of tensile strength of ceramics, *J. Am. Ceram. Soc.* 1968 (1968) 111–112.
- [7] D.J. Godfrey, Fabrication, formulation, mechanical properties, and oxidation of sintered Si₃N₄ ceramics using disc specimens, *Mater. Sci. Technol.* 1 (1985) 510–515.
- [8] R.J. Roark. Roark's Formulas for Stress and Strain, 8th ed., McGraw-Hill, New York, 2012.
- [9] A.F. Kirstein, R.M. Woolley, Symmetrical bending of thin circular elastic plates on equally spaced point supports, *Journal of Research of the National Bureau of Standards, Sect. C Eng. Instrum.* 71C (1967).
- [10] J.R. Wachtmann Jr, W. Capps, J. Mandel, Biaxial flexure tests of ceramic substrates, *J. Mater.* (1972) 188–194.
- [11] D.J. Godfrey, S. John, Disc flexure tests for the evaluation of ceramic strength, Proceedings 2nd International Conference of Ceramic materials and Components for Engines, 1986, 657–665.
- [12] T. Fett, G. Rizzi, E. Ernst, R. Müller, R. Oberacker, A 3-balls-on-3-balls strength test for ceramic disks, *J. Eur. Ceram. Soc.* 27 (2007) 1–12.
- [13] R. Morell, Biaxial flexural strength testing of ceramic materials: a National measurement good practice guide no. 12, *Natl. Phys. Lab.* (2007).
- [14] M. Staudacher, T. Lube, J. Schlacher, P. Supancic, Comparison of biaxial strength measured with the Ball-on-Three-Balls- and the Ring-on-Ring-test, *Open Ceram.* 6 (2021), 100101.
- [15] E. Chicardi, R. Bermejo, F.J. Gotor, L. Llanes, Y. Torres, Influence of temperature on the biaxial strength of cemented carbides with different microstructures, *Int. J. Refract. Met. Hard Mater.* 71 (2018) 82–91.
- [16] H.P.R. Corado, P.H.P.M. Da Silveira, V.L. Ortega, G.G. Ramos, C.N. Elias, Flexural strength of vitreous ceramics based on lithium disilicate and lithium silicate reinforced with zirconia for CAD/CAM, *Int. J. Biomater.* 2022 (2022) 5896511.
- [17] E. Dashjav, M. Gellert, G. Yan, D. Grüner, N. Kaiser, S. Spannenberger, I. Kraveva, R. Bermejo, M.-T. Gerhards, Q. Ma, J. Malzbender, B. Roling, F. Tietz, O. Guillon, Microstructure, ionic conductivity and mechanical properties of tape-cast Li_{1.5}Al_{0.5}Ti_{1.5}P₃O₁₂ electrolyte sheets, *J. Eur. Ceram. Soc.* 40 (2020) 1975–1982.
- [18] F. Fleischhauer, R. Bermejo, R. Danzer, A. Mai, T. Graule, J. Kuebler, Strength of an electrolyte supported solid oxide fuel cell, *J. Power Sources* 297 (2015) 158–167.
- [19] L.M. González, E. Chicardi, F.J. Gotor, R. Bermejo, L. Llanes, Y. Torres, Influence of the test configuration and temperature on the mechanical behaviour of WC-Co, *Metals* 10 (2020) 322.
- [20] J.P. Gross, J. Malzbender, R. Schwaiger, Strength assessment of Al₂O₃ and MgAl₂O₄ using micro- and macro-scale biaxial tests, *J. Mater. Sci.* 57 (2022) 7481–7490.
- [21] M. Gruber, A. Leitner, I. Kraveva, D. Kiener, P. Supancic, R. Bermejo, Understanding the effect of surface flaws on the strength distribution of brittle single crystals, *J. Am. Ceram. Soc.* (2018) 5705–5716.
- [22] W. Harrer, R. Danzer, P. Supancic, Influence of surface quality on the biaxial strength of silicon nitride, *Prakt. Metallogr. Sonderband* 42 (2010) 141–146.
- [23] M.A. Lodes, F.S. Kachold, S.M. Rosiwal, Mechanical properties of micro- and nanocrystalline diamond foils, *Philosophical transactions. Series A, Mathematical, physical, and engineering sciences* 373, 2015.
- [24] N. Sheth, C. Greenly, R. Bermejo, J.C. Mauro, C.G. Pantano, S.H. Kim, Effects of acid leaching treatment of soda lime silicate glass on crack initiation and fracture, *J. Am. Ceram. Soc.* 104 (2021) 4550–4558.
- [25] A. Börger, P. Supancic, R. Danzer, The ball on three balls test for strength testing of brittle discs: Part II: analysis of possible errors in the strength determination, *J. Eur. Ceram. Soc.* 24 (2004) 2917–2928.
- [26] R. Bermejo, P. Supancic, I. Kraveva, R. Morrell, R. Danzer, Strength reliability of 3D low temperature co-fired multilayer ceramics under biaxial loading, *J. Eur. Ceram. Soc.* 31 (2011) 745–753.
- [27] M. Gruber, I. Kraveva, P. Supancic, J. Bielen, D. Kiener, R. Bermejo, Strength distribution and fracture analyses of LiNbO₃ and LiTaO₃ single crystals under biaxial loading, *J. Eur. Ceram. Soc.* 37 (2017) 4397–4406.
- [28] W. Harrer, R. Danzer, P. Supancic, T. Lube, Influence of the sample size on the results of B3B-Tests, *KEM* 409 (2009) 176–184.
- [29] E. Özkol, A.M. Wätjen, R. Bermejo, M. Deluca, J. Ebert, R. Danzer, R. Telle, Mechanical characterisation of miniaturised direct inkjet printed 3Y-TZP specimens for microelectronic applications, *J. Eur. Ceram. Soc.* 30 (2010) 3145–3152.
- [30] A. Börger, P. Supancic, R. Danzer, The ball on three balls test for strength testing of brittle discs: Stress distribution in the disc, *J. Eur. Ceram. Soc.* 22 (2002) 1425–1436.
- [31] D. Munz, T. Fett, Ceramics: Mechanical Properties, Failure Behaviour, Materials Selection, Springer, Berlin, Heidelberg, 1999.
- [32] R. Danzer, P. Supancic, W. Harrer, Der 4-Kugelversuch zur Ermittlung der biaxialen Biegefestigkeit spröder Werkstoffe, *Kriegsmann, J. Hrsg Tech. Keram. Werkst.* (2009) 1–48.
- [33] A.F. Kirstein, W.H. Pell, R.M. Woolley, L.J. Davis, Deflection of centrally loaded thin circular elastic plates on equally spaced point supports, *J. Res. Natl Bur. Std. Sect. C Eng. Instrum.* 70C (1966) 227–244.
- [34] J.D.S. Ramos, S. Fraga, G.F. Vogel, L.G. May, Influence of the geometry of ceramic specimens on biaxial flexural strength: Experimental testing and finite element analysis, *Cerámica* 64 (2018) 120–125.
- [35] B. Scholtes (Ed.), Forschungsberichte aus dem Institut für Werkstofftechnik Metallische Werkstoffe der Universität Kassel, Kassel, University Press, 2012.
- [36] H. Hertz, Ueber die Berührung fester elastischer Körper, *J. für die reine und Angew. Math.* 1882 (1882) 156–171.
- [37] T. Fett, E. Ernst, D. Munz, Contact strength measurements of bars under opposite sphere loading, *J. Mater. Sci. Lett.* 21 (2002) 1955–1957.
- [38] F. Auerbach, Absolute Härtemessung, *Annalen der Physik* 279 (1891) 61–100.
- [39] A.C. Fischer-Cripps, Introduction to contact mechanics, 2nd ed., Springer, New York, 2007.
- [40] P.D. Warren, Determining the fracture toughness of brittle materials by Hertzian indentation, *J. Eur. Ceram. Soc.* 15 (1995) 201–207.
- [41] J.P.A. Tillet, Fracture of Glass by Spherical Indenters, *Proc. Phys. Soc. B* 69 (1956) 47–54.
- [42] M.T. Laugier, Hertzian indentation of sintered alumina, *J. Mater. Sci.* 19 (1984) 254–258.
- [43] R. Mougnot, D. Maugis, Fracture indentation beneath flat and spherical punches, *J. Mater. Sci.* 20 (1985) 4354–4376.
- [44] S.K. Lee, S. Wuttiaphan, B.R. Lawn, Role of microstructure in hertzian contact damage in silicon nitride: I, mechanical characterization, *J. Am. Ceram. Soc.* 80 (1997) 2367–2381.
- [45] J. Wade, S. Ghosh, P. Claydon, H. Wu, Contact damage of silicon carbide ceramics with different grain structures measured by Hertzian and Vickers indentation, *J. Eur. Ceram. Soc.* 35 (2015) 1725–1736.
- [46] T. Lube, J. Dusza, A silicon nitride reference material - a testing program of ESIS TC6, *J. Eur. Ceram. Soc.* 27 (2007) 1203–1209.

Supplementary material

A) Special (extreme) cases for comparison to FEA

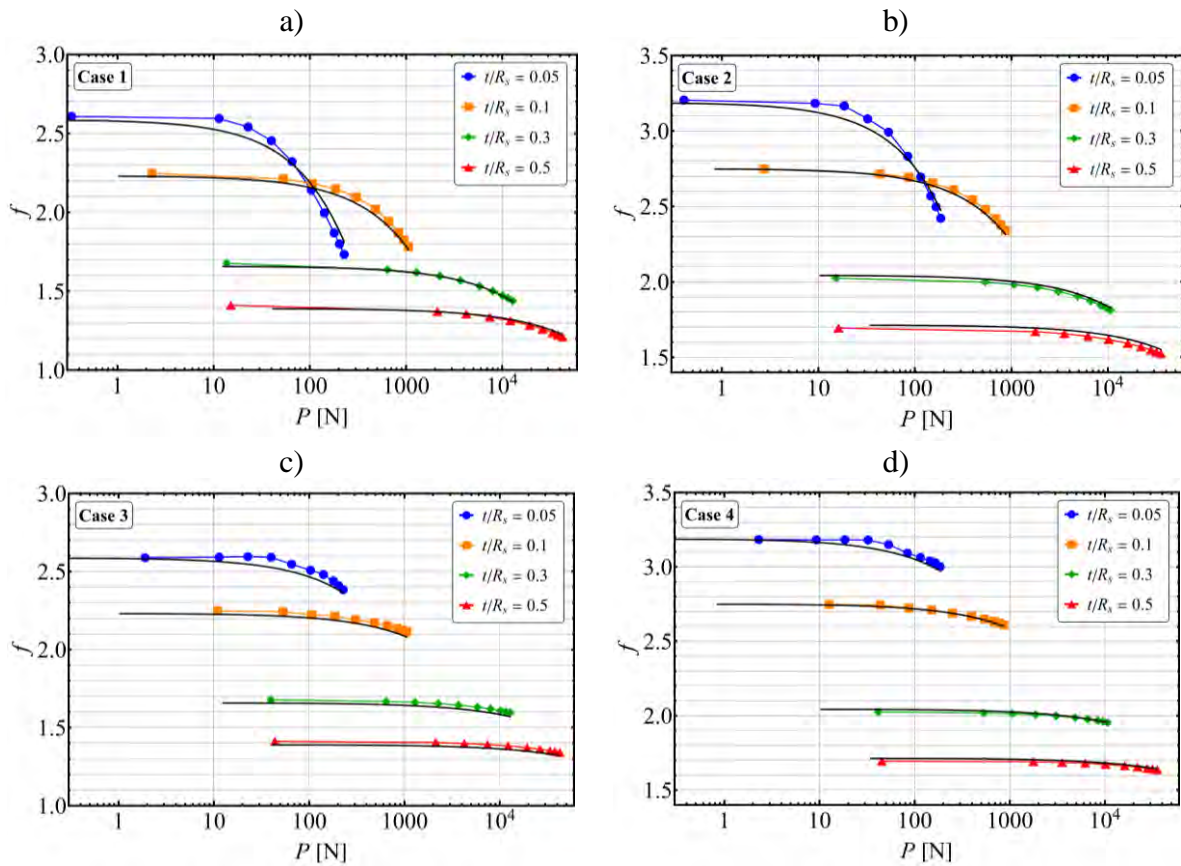
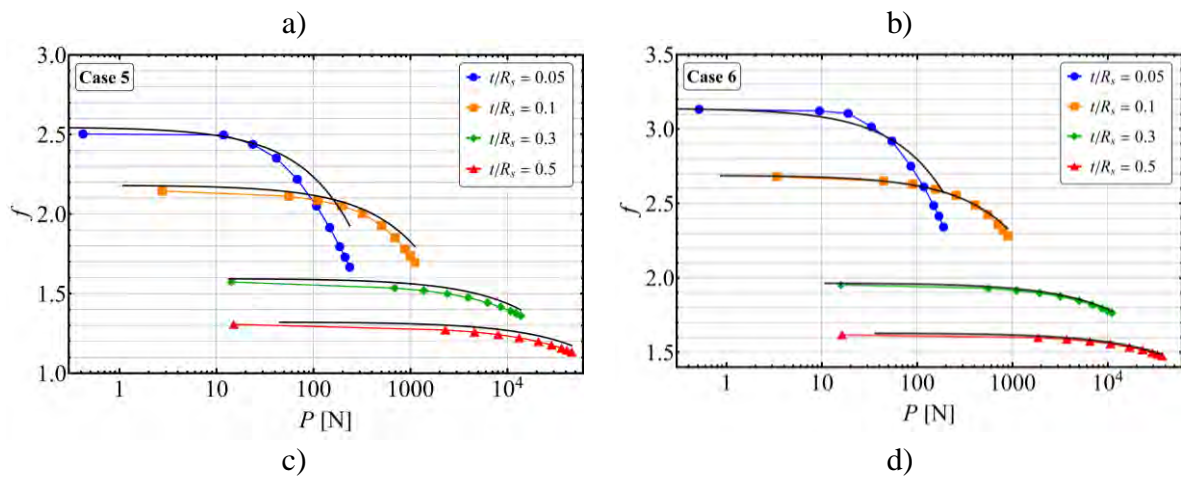


Figure 1: Dependence of f on the applied load as predicted by FEA and eq. Fehler! Verweisquelle konnte nicht gefunden werden.. Figures a), b), c) and d) show the results of specimen 1, 2, 3 and 4, respectively.



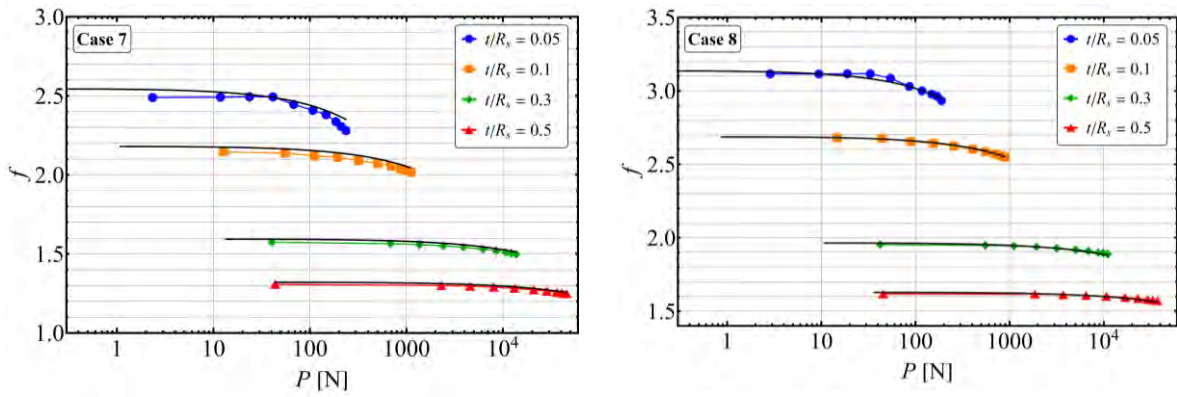
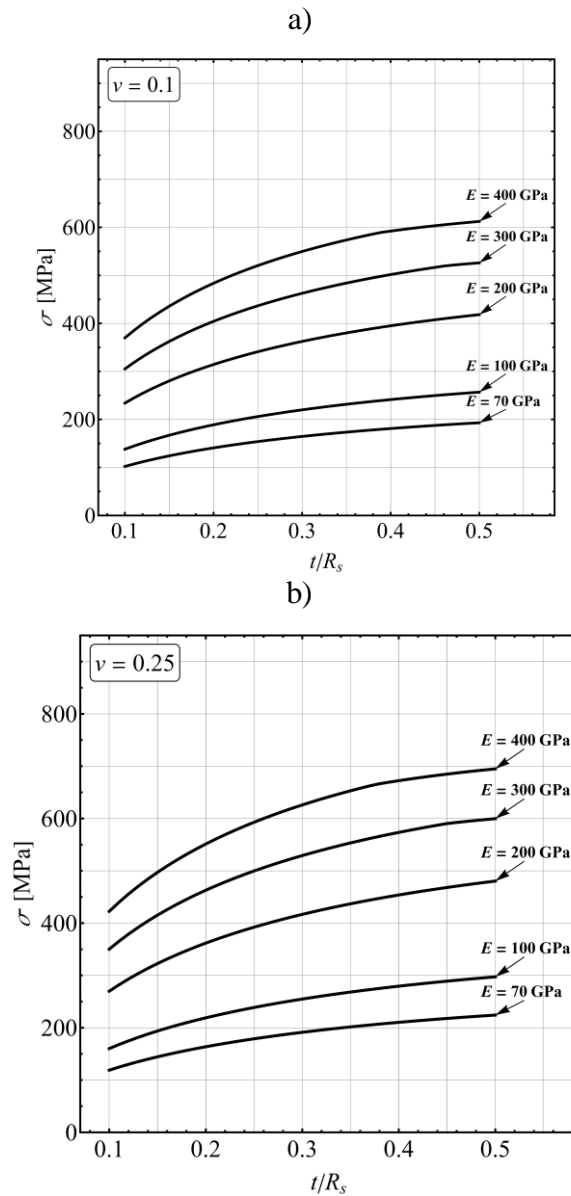


Figure 2: Dependence of f on the applied load predicted by FEA and eq. **Fehler! Verweisquelle konnte nicht gefunden werden.** Figures a), b), c) and d) show the results of specimen 5, 6, 7 and 8, respectively.

B) 2% limits for f_{corr} for various materials



c)

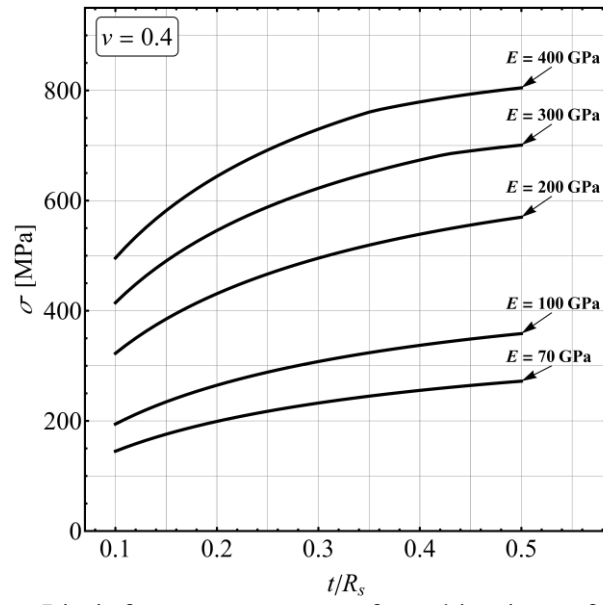


Figure 3: 2%-Limit for extreme cases of combinations of E , ν and t/R_s .

Paper B

M. Staudacher, A. Eggel, P. Supancic, T. Lube: "The Ball-on-Three-Balls strength test: Effective volumes and surfaces for Weibull strength scaling", *Journal of the European Ceramic Society* **44** (2024), 173-183, <https://doi.org/10.1016/j.jeurceramsoc.2023.09.018>

Open access article distributed under the terms of the Creative Commons CC-BY license



The Ball-on-Three-Balls strength test: Effective volumes and surfaces for Weibull strength scaling

Maximilian Staudacher, Anna Egel, Peter Supancic, Tanja Lube *

Department of Materials Science, Montanuniversität Leoben, Franz Josef-Strasse 18, A-8700 Leoben, Austria

ARTICLE INFO

Keywords:

Effective volume
Weibull theory
Strength testing
Biaxial testing
B3B-test

ABSTRACT

In order to compare the strength results of brittle materials from various testing methods or use the data for design purposes, it is essential to know the effective volume (V_{eff}) or surface (S_{eff}) for every loading scenario. For the Ball-on-Three-Balls-test (B3B), V_{eff} and S_{eff} have to be determined and investigated through Finite-Element-Analysis due to the lack of an accurate analytical description of the stress field. Through this work, the effective volume and surface of the B3B-test are made available as tabulated data for a wide range of specimen geometries and materials, along with the tools to utilize the data. A fitting model for the dependency of V_{eff} and S_{eff} on the Weibull-modulus for any given specimen geometry is provided. The influence of load-dependent non-linear effects on V_{eff} and S_{eff} is discussed. Finally, the necessity of V_{eff} and S_{eff} for statistical strength analysis is demonstrated through a practical example.

1. Introduction

Due to the brittle nature of ceramics and glasses, special care has to be taken during component design. Most notably, the scatter of strength has to be considered adequately. For this purpose, a multitude of uniaxial and biaxial strength testing methods have been developed over the past decades. Some of the most commonly used uniaxial testing methods are 3- and 4-point bending, while the Ring-on-Ring-test (RoR), Ball-on-Ring-test (BoR) or Ball-on-Three-Balls-test (B3B) make up some of the most common biaxial testing methods [1]. Each method differs in the general shape of the specimen, e.g. bars for uniaxial tests or plates for biaxial tests, and the general concept of the fixture to apply the respective bending moment on the specimen, e.g. with rollers, rings or balls. Therefore, each testing method applies a unique stress field on the respective specimen. In combination with the statistical nature of failure of ceramics, strength results for the same material may vary immensely between each of the mentioned methods. Through Weibull-theory and its underlying assumptions [2–4], it is possible to take the differing stress fields of each method into account and to compare the respective strength results [5]. This comparison is based on the concept of the effective volume, V_{eff} , or the effective surface, S_{eff} . For some testing methods, these quantities can be derived analytically if a closed form solution for the stress field is available [6–9]. However, this is not the case for the B3B-test, where Finite-Element-Analysis (FEA) has to be

employed for stress evaluation. In this work, FEA will be utilized to assess the influence of various testing geometries on V_{eff} and S_{eff} for the B3B-test. The influence of nonlinear effects on these values will be discussed and quantified in the context of strength comparison. Ultimately, an example for a pooled Weibull evaluation will be given, showcasing the application of the results and expressions provided in this work. The numerical values of V_{eff} and S_{eff} are made available for a wide range of testing geometries and materials. Additionally, the FEA-postprocessing routine to evaluate the effective volume and surface is outlined in the appendix of this work.

2. Theoretical Background

It is well accepted that the strength of brittle specimens tested in tension can be statistically described by the two-parameter Weibull distribution [3,4,10], which is typically represented by its cumulative form (CDF=Cumulative Distribution Function)

$$P(\sigma) = 1 - \exp \left[- \left(\frac{\sigma}{\sigma_0} \right)^m \right] \quad (1)$$

The scale and shape parameters of the Weibull distribution are σ_0 and m , which correspond to the characteristic strength and the Weibull modulus of the considered sample. The expression Eq. (1) represents the probability of failure at a given applied tensile stress level σ , i.e. the

* Corresponding author.

E-mail address: tanja.lube@unileoben.ac.at (T. Lube).

expectation value of the fraction of specimens which fail at stresses less or equal to σ . The choice of the stress σ in a general test configuration is not definite. Usually, it is defined as the maximum value in a given stress field, e.g. the applied stress in a homogeneous tensile test or the edge fiber tension in a uniaxial bending test, or a meaningful equivalent stress in a complicated, multiaxial stress field. Therefore, the resulting Weibull parameters depend on the details of strength test interpretation. Due to its flexibility, the Weibull distribution can be used as an empirical strength distribution to describe the measured strength of brittle samples for many cases.

If specimens of a single material with varying geometry or varying loading configurations are tested, systematic shifts of the expectation value of the Weibull parameters, predominately the characteristic strength, are observed. This effect is attributed to the size effect of strength and can be described by the Weibull-theory of the strength of brittle materials. This concept is linked to the material's behavior under several assumptions (e.g. defect-controlled failure; randomly distributed and independent defects from a unimodal size distribution, weakest link hypothesis, etc. [2,4,11,12]) and leads to material specific strength parameters, namely the Weibull modulus m and the Weibull material scale parameter Σ_0 . While the Weibull modulus is a pure number, the unit of the scale parameter is given by $\text{stress} \cdot (\text{volume})^{1/m}$, i.e. $\text{Pa} \cdot \sqrt[m]{\text{m}^3}$. The knowledge of these parameters allows the calculation of the characteristic strength σ_0 of a homogeneously tensile loaded specimen with volume V , namely by:

$$\sigma_0 = \Sigma_0 \cdot (V)^{-1/m} \quad (2)$$

Consequently, the size effect of the characteristic strength is inherently implemented by the scaling law, Eq. (2), so that the empirical ansatz Eq. (1) can be rewritten as:

$$P(\sigma, V) = 1 - \exp\left[-V \left(\frac{\sigma}{\Sigma_0}\right)^m\right] = 1 - \exp\left[-\frac{V}{V_0} \left(\frac{\sigma}{\sigma_0}\right)^m\right] \quad (3)$$

For practical (dimensional) reasons, the Weibull material scale parameter Σ_0 is often replaced by an arbitrary reference volume V_0 (in m^3 or mm^3) and its related characteristic strength σ_0 (in Pa or MPa, respectively). The failure probability for specimens loaded in inhomogeneous tensile stress fields can be determined by taking the scaling law Eq. (2) into account. For a given stress distribution $\sigma(x, y, z)$, the corresponding probability of failure can be expressed by:

$$P(\sigma, V) = 1 - \exp\left[-\int_V \left(\frac{\sigma(x, y, z)}{\Sigma_0}\right)^m dV\right] \\ = 1 - \exp\left[-\frac{V}{V_0} \int_V \left(\frac{\sigma(x, y, z)}{\sigma_0}\right)^m dV\right] \quad (4)$$

The integration has to be performed over the entire specimen's tensile loaded regions. For stress fields with a spatial distribution that is independent of the applied load, $\sigma(x, y, z)$ can be expressed as

$$\sigma(x, y, z) = \sigma_{\text{ref}} \cdot g(x, y, z) \quad (5)$$

with a load-dependent amplitude factor σ_{ref} and a dimensionless, load-independent and spatially varying shape function $g(x, y, z)$. Note that if the spatial distribution of the stress field, i.e. $g(x, y, z)$, changes during the loading history, this has to be considered appropriately [13]. A recommended choice for σ_{ref} is the maximum first principal stress, so that g is normalized and restricted to a numerical range between 0 and +1 in the case of uniaxial stress fields. Many important loading configurations (e.g. uniaxial 3- or 4-point bending test, the RoR-test, etc.) sufficiently fulfill the assumption for Eq. (5). It should be noted that the accuracy of Eq. (5) depends on the extent of any non-linearities in the test setup, which will be discussed in Section 4.3 of this work. To simplify Eq. (4), Eq. (5) is utilized to define the effective volume V_{eff} by

$$V_{\text{eff}} = \int_V \left(\frac{\sigma(x, y, z)}{\sigma_{\text{ref}}}\right)^m dV = \int_V g(x, y, z)^m dV \quad (6)$$

which can be considered as the equivalent, homogeneously loaded volume of the tested specimen. The advantage of introducing the effective volume is that it can be calculated only once for a given type of test-setup or loading case. The expression for the probability of failure for inhomogeneous stress distributions can therefore be generalized to

$$P(\sigma, V) = 1 - \exp\left[-V_{\text{eff}} \left(\frac{\sigma}{\Sigma_0}\right)^m\right] = 1 - \exp\left[-\frac{V_{\text{eff}}}{V_0} \left(\frac{\sigma}{\sigma_0}\right)^m\right] \quad (7)$$

where $\sigma = \sigma_{\text{ref}}$. To relate the effective volume to the specimen's volume in a given setup or load-configuration, a ratio k

$$k = \frac{V_{\text{eff}}}{V} \quad (8)$$

can be defined [4,14]. In the case of uniaxial stress fields and with the recommended choice of σ_{ref} to normalize $g(x, y, z)$, the resulting effective volume is always less or equal to the specimen's volume and therefore $k \leq 1$. In the limiting case of a homogeneous tensile stress field, k equals 1. For multiaxial stress states, an equivalent uniaxial stress σ_{eq} must be defined through a failure criterion in order to replace $\sigma(x, y, z)$ with $\sigma_{\text{eq}}(x, y, z)$ in Eq. (6). For some failure criteria (e.g. the PIA-criterion), k can exceed 1, which would represent a more critical test compared to uniaxial loading. Within the field of technical ceramics, two of the most prominent and widely employed failure criteria are the First-Principal-Stress criterion (FPS) [15] and the Principle-of-Independent-Action (PIA) [16–18]. As implied by the name, the FPS-criterion assumes that only the first principal stress contributes to failure, and therefore $\sigma_{\text{eq,FPS}}$ is given through

$$\sigma_{\text{eq,FPS}} = \sigma_1 \quad (9)$$

with σ_1 as the first principal stress. On the other hand, the PIA-criterion includes the contribution of all principal stresses, which is especially relevant when they are of similar magnitude. The equivalent stress $\sigma_{\text{eq,PIA}}$ is determined by

$$\sigma_{\text{eq,PIA}} = \sqrt[m]{\langle \sigma_1 \rangle^m + \langle \sigma_{\text{II}} \rangle^m + \langle \sigma_{\text{III}} \rangle^m} \quad (10)$$

With σ_{II} and σ_{III} as the second and third principal stress, respectively, and m as the Weibull-modulus of the investigated material. If any of the principal stresses is compressive, they will be discarded from this evaluation, which is indicated by the “Macaulay-Brackets” $\langle \rangle$.

If defects on tensile loaded surfaces or edges dominate the strength behavior, an effective surface or effective edge length can be defined analogously to Eq. (6). Through calculating a surface or path integral with respect to the normalized stress field, a corresponding expression to Eq. (7) for the probability of failure is given by

$$P(\sigma, V) = 1 - \exp\left[-S_{\text{eff}} \left(\frac{\sigma}{\Sigma_0}\right)^m\right] = 1 - \exp\left[-\frac{S_{\text{eff}}}{S_0} \left(\frac{\sigma}{\sigma_0}\right)^m\right] \quad (11)$$

(Note, that in this case the Weibull material scale parameter Σ_0 is different from Eq. (2) and has the units $\text{Pa} \cdot \sqrt[m]{\text{m}^2}$). For many uniaxial stress states, closed form solutions for V_{eff} or S_{eff} can be derived analytically according to Eq. (6), and are widely used due to their simplicity and accuracy. As an example, the effective volume of a rectangular beam with width b , height h tested in flexure on a support span l subjected to 4-point bending (4PB) in a $1/4$ -point-setup is given as [7].

$$V_{\text{eff,4PB}} = \frac{lbh(m+2)}{4(m+1)^2} = V \cdot \frac{(m+2)}{4(m+1)^2} \quad (12)$$

Note that the effective volume depends on the Weibull modulus, which is always the case for inhomogeneous stress fields. For more complicated stress fields, approximate expressions can be found in literature. One example is the effective volume for the Ring-on-Ring-test under the PIA-criterion developed by Salem et al. [9,19] which was incorporated into the corresponding standard. Another example is the

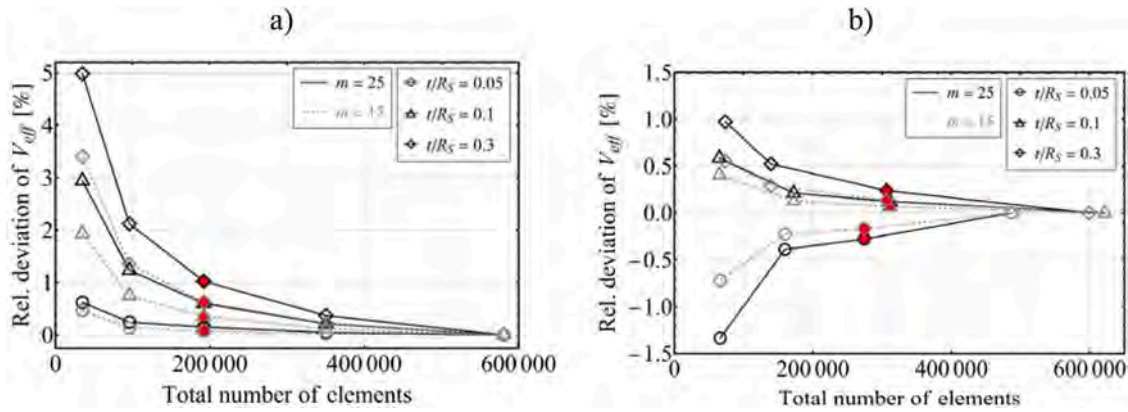


Fig. 1. Mesh convergence analysis for each model. a) shows the relative error to the result with the highest number of elements for *Model 1*, b) for *Model 2*. The red markers represent the approximate number of elements used in this work.

Table 1

Minimum and maximum number of elements and nodes used in each model.

Model	<i>Model 1</i>	<i>Model 2</i>	<i>Model 3</i>
Min/Max num. of elements	155936 / 202734	225472 / 422730	47373 / 78009
Min/Max. num. of nodes	652265 / 847223	933429 / 1775043	197379 / 325153

analytically derived expression for the Ball-on-Ring-test under the PIA-criterion, which is restricted to values of m from the range of natural numbers [20]. Note that for both cases, the stress field is well described through analytical expressions. Unfortunately, a simple analytical expression for the stress field of the Ball-on-Three-Balls-test is not available and consequently no analytical expression for the effective volume can be found. Instead, numerical analysis through FEA must be performed in order to determine the effective volume or effective surface for any given specimen.

3. Methods

3.1. FEA-Models

All simulations conducted in this work utilized ANSYS Mechanical Release 2022R1 by ANSYS Inc. (Southpointe 2600 Ansys Drive, PA 15317, Canonsburg, USA). Each model is implemented in APDL (Ansys Parametric Design Language) to allow detailed, script-based access to the model and documentation with varying input parameters. The Finite-Element-Analysis models utilized in this work are based on the ones already discussed in previous work [21], and the same designation will be utilized. Furthermore, a more detailed description of the models and their boundary conditions is given in that work. *Model 1* is a 3D-model of a disc-specimen with punctiform displacement constraints, i.e. a punctiform load applied at the central node of the specimen and punctiform boundary conditions representing the support balls. Due to symmetry, it is sufficient to evaluate just one sixth of the total disc. This results in constraining the out-of-plane displacements of the nodes on the mirror-symmetry faces. *Model 2* is a 3D-model of a square-plate-specimen. Again, the load is applied at a single node in the center of the specimen, and the support balls are represented by punctiform boundary conditions. Due to the symmetry of this problem, it is sufficient to model one half of the full specimen and the constraints of nodes in the symmetry plane are set as described for *Model 1*. The difference to previous iterations of both *Model 1* and *Model 2* is a complete overhaul of the mesh, to achieve a significantly finer mesh in the center and a coarser mesh at the edge of the disc or square plate. This overhaul was necessary since the effective volume is much more sensitive to the

mesh size, especially in the high-stress regions. Finally, *Model 3* represents a 3D-model of the full testing assembly, including the load- and support balls. The main difference to the other models is the way that the load is applied on the specimen. By displacing the load ball and utilizing contact simulations under the assumption of a friction coefficient $\mu = 0.5$ for the contact pairs, a closer representation of a real-world load application is given. The same applies for the support balls. With this model, load-dependent effects, such as specimen deformation and increasing contact areas between the balls and the specimen, can be considered. Since disc-specimens are analyzed, the problem can be reduced to one sixth of the full testing assembly. It should be mentioned that the results generated with *Model 3* are only valid for a testing setup as described in [22,23] where supporting balls are large and in contact with each other.

The effective volume and surface were determined as outlined in Appendix A and 5th order Gauss-Legendre-Quadrature was utilized for numerical integration. Preliminary studies were conducted to determine the error of 5th order Gauss-Legendre-Quadrature compared to the exact analytical result for a linear stress distribution within a single element. If an error $\leq 2\%$ has to be achieved for all $m \leq 50$, the difference between the maximum and minimum stress within a single element must be smaller than 40% of the maximum stress. Therefore, for each model, special care was taken to avoid large stress gradients by adjusting the number of elements in both radial and vertical direction, depending on the respective specimen geometry. A mesh convergence analysis for the effective volume was performed for *Model 1* and *Model 2*, and the results are shown in Fig. 1a) and b). A mesh convergence analysis for the maximum stress for *Model 3* was already performed in [21]. Due to the large computational demand of *Model 3*, it was not feasible to significantly increase the number of elements. Therefore, this model is not fully converged for the accurate determination of the effective volume and surface and will only be utilized for qualitative analyses instead. The minimum and maximum number of elements utilized for each model are given in Table 1. For the specimen and loading or support balls, 20-node brick elements (SOLID186) were utilized. The contacting regions were modelled with CONTA174 and TARGE170 elements. To determine the effective surface, only the tensile loaded face of the model was evaluated. To avoid any influence of the tensile stress field around the contact regions between the balls and the specimen on both the effective volume and surface, a small part of the specimen was removed at the respective regions for each model. The removed region is determined by a circle around the contact region and a depth of about one third of the specimen's thickness. In the case of *Model 1* and *Model 2*, this removal was especially important due to the punctiform load introduction and boundary conditions, which caused numerical artifacts.

Model 1 and *Model 2* were each used to calculate the effective volume and surface for a wide range of specimen geometries. The relevant

Table 2
Range of parameters.

Parameter	t/R_S	$R/R_S (L/D_S)$	ν	m
Range	0.05–0.5	1.05–2	0.1–0.4	0–50
Step size	0.05	0.05	0.05	1

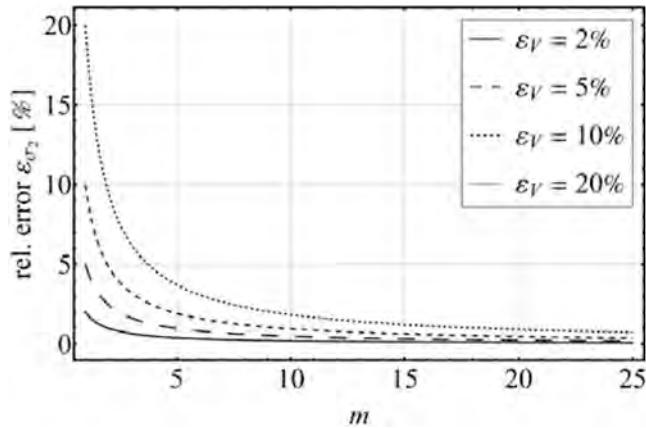


Fig. 2. Relative error in σ_2 through strength extrapolation, i.e. ϵ_{σ_2} , in dependence of the Weibull modulus m . Each line represents ϵ_{σ_2} for a different value of the error in $V_{eff,1}$.

specimen geometries for discs are the specimen’s thickness t , the specimen’s radius R and the support radius R_S , which is determined from the support ball radius R_{SB} through

$$R_S = R_{SB} \frac{2}{\sqrt{3}} \quad (13)$$

if the support balls are in contact with each other. For square plates, the same parameters are used, with the plate’s edge length L instead of R , and the support diameter D_S instead of R_S . For each specimen geometry, the effective volume and surface were determined for different Poisson’s ratios ν and a range of m from $m=0$ to $m=50$. The full range of investigated parameters is given in Table 2. To reduce the total number of variables, the geometric parameters were combined to the relative thickness t/R_S and the relative specimen radius R/R_S for discs or L/D_S for square plates.

For each of the 71400 combinations of these parameters (10 steps for $t/R_S \times 20$ steps for $R/R_S \times 7$ steps for $\nu \times 51$ steps for m), Model 1 and Model 2 were utilized to determine the values of the effective volume and the effective surface with both the FPS-criterion and the PIA-

criterion. If not stated otherwise, all data evaluation for this work has been conducted with Mathematica 13.1 from Wolfram Research, Inc. (100 Trade Center Drive, Champaign IL 61820–7237, USA).

3.2. The necessary accuracy of V_{eff} and S_{eff}

One aspect to consider is the accuracy of V_{eff} that is needed to convert the characteristic strength from one testing method or specimen geometry to a different one. Through equating Eq. (7) for the same probability of failure, but two characteristic strengths $\sigma_{0,1}$ and $\sigma_{0,2}$ with their respective effective volume $V_{eff,1}$ and $V_{eff,2}$, Eq. (14) can be derived:

$$\sigma_{0,2} = \sigma_{0,1} \left(\frac{V_{eff,1}}{V_{eff,2}} \right)^{1/m} \quad (14)$$

Note that this relationship can also be derived through Eq. (2). The Weibull modulus m plays a very important role when relating the strength levels, and for typical technical ceramics, m is often found to be in the range of 10–25. Therefore, assuming that m is high enough, even a large error in one of the effective volumes does not influence the error in characteristic strength $\sigma_{0,2}$ significantly. To better understand this influence, we assume that a Weibull-analysis was performed on specimens tested with the B3B-test, and the characteristic strength $\sigma_{0,1}$ was determined. If this characteristic strength shall be extrapolated to that of a different specimen size or testing method, i.e. $\sigma_{0,2}$, the effective volume of the B3B-test, $V_{eff,1}$, and the effective volume of the other specimen’s or method, $V_{eff,2}$, is necessary. If the effective volume of the B3B-test, $V_{eff,1}$ is not well known and affected by an error ϵ_V , an erroneous converted characteristic strength $\sigma_{0,2,err}$ is obtained. The relative error ϵ_{σ_2} between $\sigma_{0,2,err}$ and $\sigma_{0,2}$ can be defined through

$$\epsilon_{\sigma_2} = \frac{\sigma_{0,2,err} - \sigma_{0,2}}{\sigma_{0,2}} = \frac{\sigma_{0,1} \left(\frac{V_{eff,1}(1+\epsilon_V)}{V_{eff,2}} \right)^{1/m} - \sigma_{0,1} \left(\frac{V_{eff,1}}{V_{eff,2}} \right)^{1/m}}{\sigma_{0,1} \left(\frac{V_{eff,1}}{V_{eff,2}} \right)^{1/m}} = (1 + \epsilon_V)^{1/m} - 1 \quad (15)$$

with the variables as defined before. Fig. 2 depicts ϵ_{σ_2} in dependence of the Weibull modulus m for several fixed errors ϵ_V of $V_{eff,1}$.

For $m \geq 10$, even with ϵ_V as large as 20%, a relative error of less than 2% for $\sigma_{0,2}$ is obtained. While the effective volume still has to be determined accurately for materials with a low Weibull modulus ($m \leq 5$), this is not the case for materials with a medium to high Weibull modulus ($m > 10$). Note that this consideration is only relevant for strength extrapolation and is not generally true for all applications of V_{eff} .

4. Results

The following results will only be shown and discussed for disc-

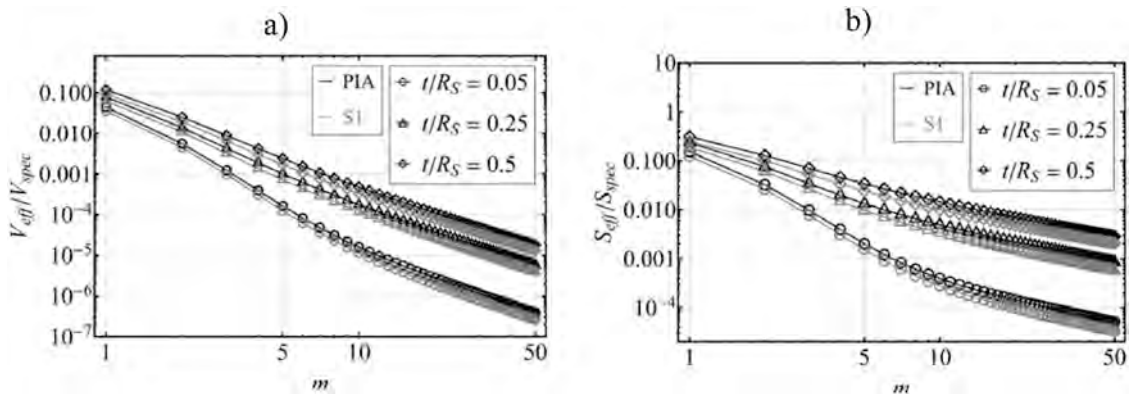


Fig. 3. Dependence of the relative effective volume (a)) and relative effective surface (b)) for the PIA criterion on the Weibull modulus m for different relative specimen thicknesses t/R_S and $\nu = 0.25$. The effective volume and surface were divided by the specimen’s volume V_{spec} or tensile loaded face S_{spec} , respectively, and are plotted on a double-logarithmic scale.

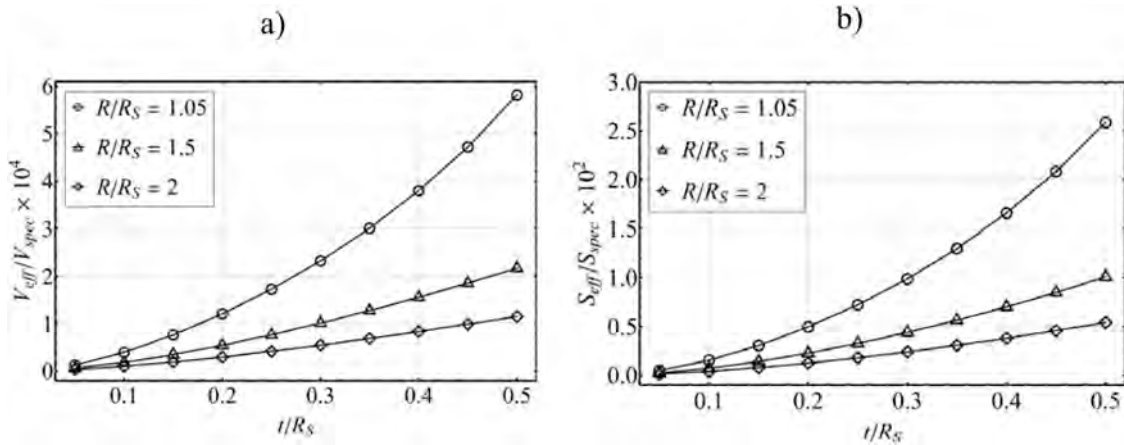


Fig. 4. Dependence of the relative effective volume (a) and effective surface (b) for the PIA criterion on the specimen's thickness t for different relative specimen radii R/R_S for $\nu=0.25$ and $m=15$. The effective volume and surface were divided by the specimen's volume V_{spec} or tensile loaded face S_{spec} , respectively.

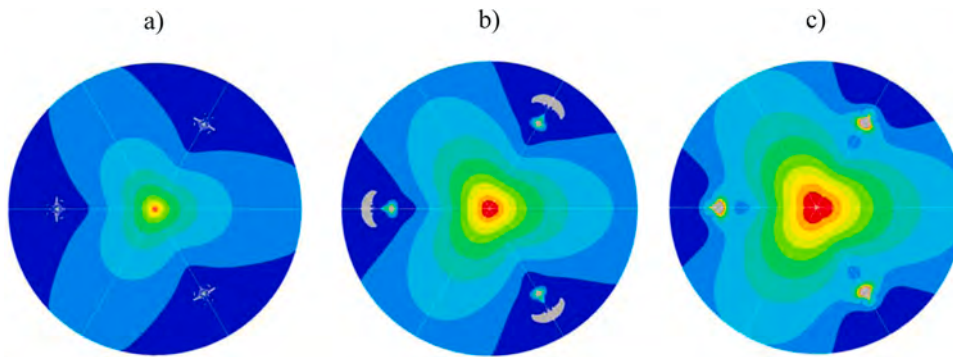


Fig. 5. Variation of the tensile stress field (first principal stress) for different relative thicknesses of a specimen with $R/R_S=1.5$ and $\nu=0.25$. a) displays the result for a specimen with $t/R_S=0.05$, b) for $t/R_S=0.25$ and c) for $t/R_S=0.5$. Each contour gives a 10%-percentile of the maximum stress from 0 (blue) to the maximum stress (red). Gray represents compressive stresses.

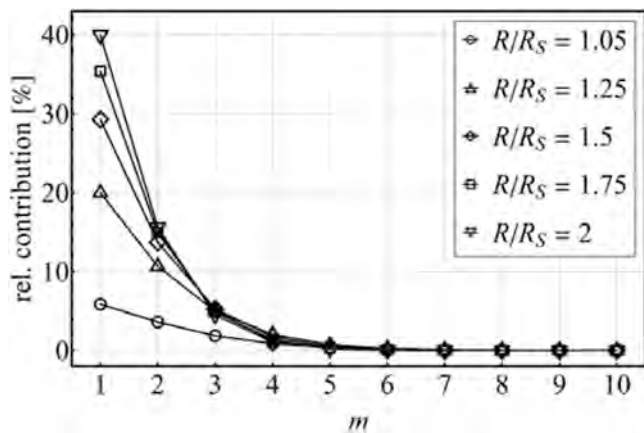


Fig. 6. Contribution of the overhang to the effective volume (PIA criterion). The results were obtained with Model 1 for discs with $t=0.2$ mm, $R_S=10$ mm and $\nu=0.25$.

shaped specimens, but almost identical tendencies are found for square plates. The maximum first principal stress in the center of the specimen was utilized for σ_{ref} .

4.1. Geometrical dependencies of V_{eff} and S_{eff}

The effective volume in dependence of the Weibull modulus m is

given in Fig. 3. Note the strong decrease of V_{eff} (more than six orders of a magnitude) with an increase in m and the change of slope at approximately $m=2$ and $m=10$.

The influence of the specimen's thickness on the effective volume and effective surface is shown in Fig. 4a) and b) for an exemplary geometry. Contrary to initial assumptions based on the behavior of S_{eff} for the Ring-on-Ring-test, the effective surface for the B3B-test is strongly dependent on the specimen's thickness, similar to the effective volume, where this effect was expected. This is due to a change in the general shape of the stress field, i.e. a widening of the region of maximum stress with an increase in thickness, as shown in Fig. 5a)-c).

To assess the influence of the relative specimen radius R/R_S , V_{eff} was evaluated for either the full specimen, $V_{eff,full}$, or just the regions included within R_S , $V_{eff,support}$. Fig. 6 displays the relative contribution of the overhang

$$rel.contr. = \frac{V_{eff,full} - V_{eff,support}}{V_{eff,full}} \tag{16}$$

in dependence of the Weibull modulus for several geometries. It is evident that the overhang significantly influences V_{eff} for very low Weibull moduli ($m<5$) but has a vanishing influence as soon as m increases.

4.2. The relation of V_{eff} to S_{eff}

For many bending-based testing methods, it is possible to analytically derive a relationship between the effective surface and the effective

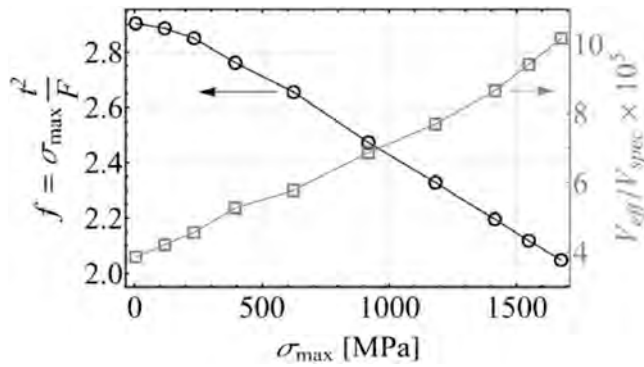


Fig. 7. Normalized maximum tensile stress and normalized effective volume (PIA criterion) in dependence of the maximum tensile stress σ_{max} for $m=10$. The results were obtained with *Model 3* for a disc with $t = 0.5$ mm, $R = 10.5$ mm, $R_s = 10$ mm, a Young’s modulus of 70 GPa and $\nu = 0.25$.

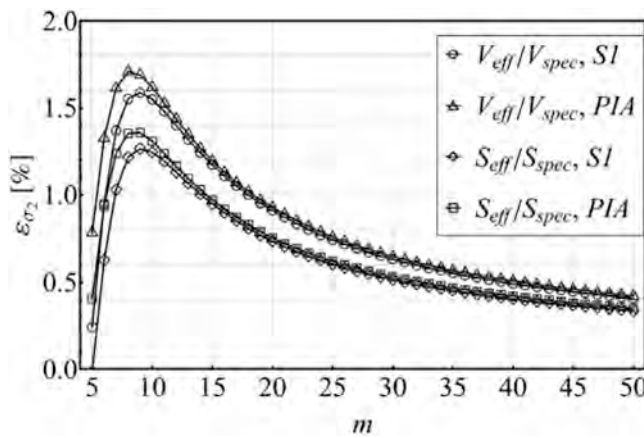


Fig. 8. Relative error in strength extrapolation, ϵ_{σ_2} , in dependence of the Weibull modulus m for the same parameters as in Fig. 7. The maximum tensile stress is 233 MPa.

Table 3

Geometry and testing parameters. N gives the number of tested specimens, t_{mean} the average specimen thickness and the related standard deviation (STD), t_{min} and t_{max} the minimum and maximum specimen thickness, respectively, and s gives the crosshead-speed.

Designation	N	$t_{mean} \pm STD$ [mm]	t_{min} [mm]	t_{max} [mm]	s [mm/min]
Sample A	37	0.246 ± 0.013	0.222	0.281	0.6
Sample B	53	1.548 ± 0.024	1.460	1.608	1.5

volume for the same multiaxial stress criteria. In the ideal bending case, a linear decrease of the magnitude of stress within a specimen from the tensile surface to the neutral plane (a path perpendicular to the bending axis/plane, parallel to the loading direction) is observed, independent of the position on the specimen. Considering this behavior and disregarding the lateral surfaces, Eq. (6) can be utilized to derive the relationship

Table 4

Results of strength testing, with \hat{m}_b as the biased and \hat{m}_{ub} as the unbiased Weibull modulus, and all other variables as defined before. The subscripts *lower* and *upper* indicate the extent of the 90% confidence intervals for the respective variable.

Designation	\hat{m}_b [-]	\hat{m}_{ub} [-]	\hat{m}_{lower} [-]	\hat{m}_{upper} [-]	$\hat{\sigma}_0$ [MPa]	$\hat{\sigma}_{0,lower}$ [MPa]	$\hat{\sigma}_{0,upper}$ [MPa]	S_{eff} [mm ²]	$S_{eff,lower}$ [mm ²]	$S_{eff,upper}$ [mm ²]
Sample A	12.1	11.7	9.4	14.5	1134	1106	1162	0.048	0.037	0.075
Sample B	17.5	17.1	14.3	20.4	906	894	919	0.639	0.540	0.802

$$V_{eff} = S_{eff} \frac{t}{2(m+1)} \tag{17}$$

to relate V_{eff} and S_{eff} , with the other variables as defined before [9,24]. Through analyzing the B3B-test with FEA, it was found that an ideal linear decrease of stress is not given for the centermost region of the specimen. Since the central region determines the majority of V_{eff} , this deviation from the ideal case is too severe ($\pm 50\%$) to utilize the conversion given in Eq. (17). Therefore, separate results for V_{eff} and S_{eff} have to be utilized to accurately determine both quantities.

4.3. The impact of non-linear effects

Previous work of the authors has shown that the maximum tensile stress may strongly depend on the applied load, especially for thin and flexible specimens. This is due to non-linear effects, e.g. specimen deformation and deviations from the ideal punctiform load introduction [21]. However, not just the maximum tensile stress, but the general shape of the tensile stress field changes due to these effects. Consequently, this impacts the results for V_{eff} and S_{eff} , in particular for high values of the Weibull-modulus m . To assess the influence of non-linear effects on the effective volume and surface, *Model 3* was utilized. Due to the increase in computational complexity by the use of contact simulations, the number of total elements had to be lower than that of the other models. Therefore, the absolute values for V_{eff} and S_{eff} differ slightly from the values generated through *Model 1* and *Model 2*, but the general tendencies can still be analyzed. Through previous investigations [21], it has been determined that thin glass specimens, e.g. with a relative thickness $t/R_s = 0.05$ and a Young’s modulus = 70 GPa, exhibit the strongest load-dependency within the valid range of parameters (see Table 2). For the following analysis, these parameters along with $R/R_s = 1.05$ and $\nu = 0.25$ were utilized. Fig. 7 displays the results for the normalized stress f

$$f = \sigma_{max} \frac{t^2}{F} \tag{18}$$

with F as the applied load and t as the specimen’s thickness. On the secondary vertical axis, the normalized effective volume V_{eff}/V_{spec} in dependence of the maximum tensile stress for $m=10$ is shown. The effective volume has been calculated with the respective maximum tensile stress σ_{max} as the reference stress σ_{ref} and by utilizing the PIA-criterion. While f decreases by about 30% through a decrease in bending moment, the normalized effective volume increases nearly threefold at a maximum stress of about 1600 MPa. The increase is caused by a widening of the central region of maximum tensile stress.

However, this strong dependency of V_{eff} on the applied load is not as

Table 5

Results of the pooled evaluation based on the maximum-likelihood method.

Parameter	Result
Reference surface S_0 [mm ²]	0.041
$\hat{\sigma}_0$ [MPa]	1132
\hat{m} [-]	13.5
$\hat{\Sigma}_0$ [MPa $\sqrt[13.5]{mm^2}$]	894

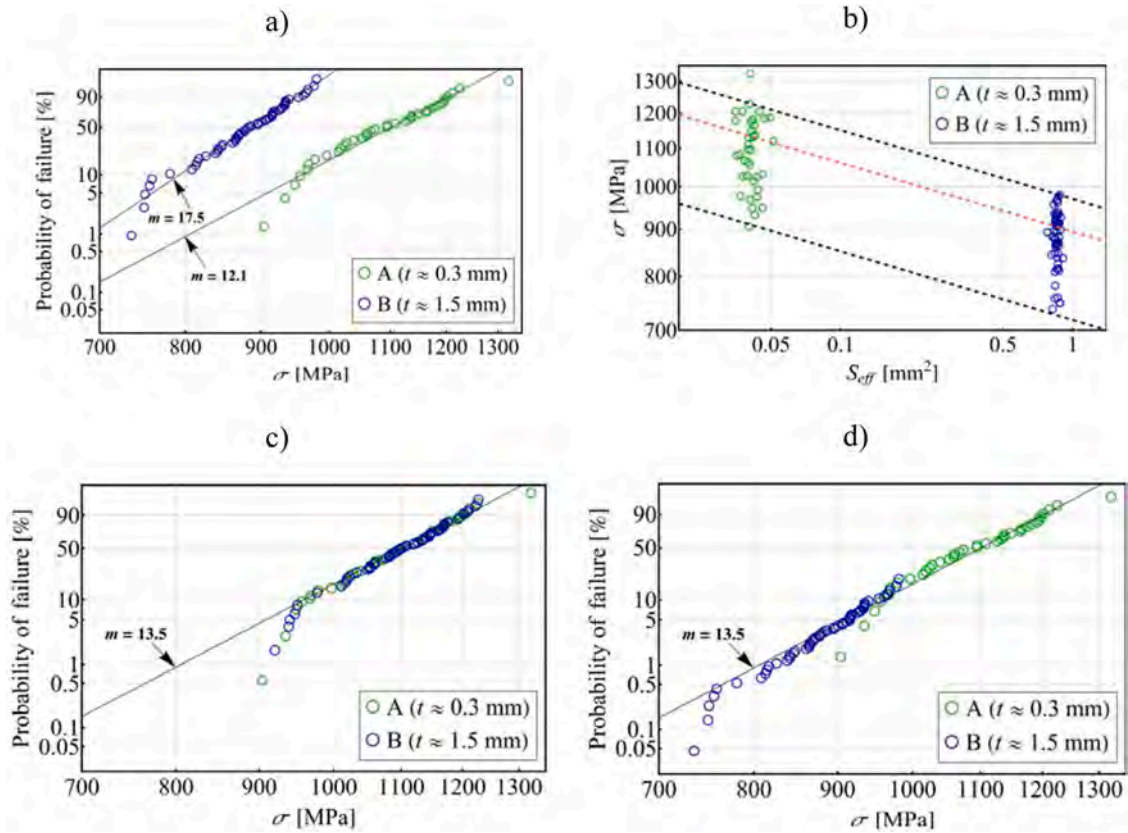


Fig. 9. a) depicts a Weibull plot of each sample individually. b) displays individual specimen strength plotted with their respective effective surface. The red line displays the 63% quantile. The negative inverse slope of the line corresponds to $\hat{m}_{pooled} = 13.5$. The upper and lower black lines represent the 95% and 5% quantiles, respectively. c) shows both samples in a traditional format, with each specimen's strength extrapolated to $S_0 = 0.041 \text{ mm}^2$. d) shows both samples in a traditional format as well, but with the probability of failure of each specimen extrapolated to $S_0 = 0.041 \text{ mm}^2$. The slope of the black line in c) and d) is the Weibull modulus obtained through the pooled evaluation.

Table 6

Natural coordinates of the corner nodes of an element in three-dimensional space.

i	1	2	3	4	5	6	7	8
ξ_i	-1	1	1	-1	-1	1	1	-1
η_i	1	1	-1	-1	1	1	-1	-1
ζ_i	-1	-1	-1	-1	1	1	1	1

Table 7

Integration points r_i and associated weights w_i for 5th order Gauss-Legendre-Quadrature.

Index i	Integration points r_i	Weights w_i
1	0	0.568889...
2 & 3	$\pm 0.538469...$	0.478629...
4 & 5	$\pm 0.90618...$	0.236927...

relevant as it might first appear. This is due to two reasons: First, the results shown represent the worst-case scenario within the investigated parameter range. Second, V_{eff} and S_{eff} are most commonly used to convert or extrapolate strength results, as given through Eq. (14). As shown in Section 3.2, the influence of an error in V_{eff} or S_{eff} on the error in strength extrapolation using Eq. (14) is strongly dependent on the material's Weibull-modulus m . For the results shown in Fig. 7, the observed relative error in V_{eff} , ϵ_V , has been translated to an error in strength extrapolation, i.e. $\epsilon_{\sigma 2}$, according to Eq. (15). Fig. 8 gives the result for $\epsilon_{\sigma 2}$ in dependence of m for V_{eff} and S_{eff} , each calculated with

both the PIA and S1 multiaxial stress criterion. In various previous work on the B3B-test, a general error of 2% on the obtained results was often utilized as an accuracy limit [21–23,25]. Therefore, these findings are discussed in the context of this accuracy limit and the displayed results correspond to a reduction of f by about 2%, which occurs at 233 MPa.

A maximum for $\epsilon_{\sigma 2}$ is reached between $m=8$ and $m=9$, depending on the effective size and stress criterion. This behavior is caused by two contrasting effects. On one hand, the error of the effective volume ϵ_V increases with an increase in m , see Fig. 7. On the other hand, the effect of this error on the stress extrapolation $\epsilon_{\sigma 2}$ decreases rapidly with an increase in m , as shown in Fig. 2. Most notably, $\epsilon_{\sigma 2}$ is always smaller than the error in f , i.e. 2%. If the maximum stress is increased further, the maximum of $\epsilon_{\sigma 2}$ increases and shifts to slightly higher Weibull-moduli. For the highest loaded case in Fig. 7, with a maximum tensile stress of about 1600 MPa, the maximum of $\epsilon_{\sigma 2}$ reaches nearly 10% and is found between $m=9$ and $m=10$. Note that this analysis has been performed on the “worst-case scenario”. For thicker and stiffer specimens, the influence of non-linear effects will decrease drastically, as will the value of $\epsilon_{\sigma 2}$. Therefore, for the range of parameters given in Table 2, $\epsilon_{\sigma 2}$ will always be smaller than the error of f . To determine an accurate result for the effective size, $\epsilon_{\sigma 2}$ should be smaller than 2%. This is guaranteed if the error of f is less than or equal to 2%. Through an equation and figures given in [21], a limit for the maximum applied load (in the form of a maximum specimen strength) to achieve an error of less than 2% in f can easily be predicted. These tools are valid for any combination of testing and material parameters as given in Table 2. If the tested specimens are within or close to these limits, non-linear effects don't need to be considered and the results given in this work are sufficiently accurate. If the tested specimens surpass these limits significantly, the authors

recommend individual FEA to determine the most accurate results for the effective volume and surface.

4.4. Data availability

Any attempt to provide a functional expression describing the effective volume and surface were deemed either insufficiently accurate or too unwieldy to provide any meaningful benefit. The most accurate way to evaluate V_{eff} or S_{eff} for a specific geometry is to rely on interpolation of the generated data field. Therefore, all datapoints for discs and square plates, i.e. each effective size for both multi-axial stress criteria, are provided in the [supplementary material](#) of this work. These files are available in the comma-separated value format (.csv), the tab-separated format (.tsv) and as Excel-files (.xlsx). Each line contains the respective geometry- or material parameters (t/R_S , R/R_S , v and m) as well as the associated value for the effective size. To aid data evaluation, scripts for the interpolation of these data-files are provided in several coding languages (Mathematica & Python) as well as integrated in an Excel-file. Note that data evaluation through the Excel-file is limited to linear interpolation, while the other scripts allow higher order interpolation and are defaulted to third-order interpolation. For $m \geq 2$, the difference between linear and third-order interpolation is in the range of -8.2% to $+8.0\%$, with the highest differences obtained for specimens with a small relative thickness ($t/R_S < 0.2$). Due to the aforementioned effect of the Weibull-modulus on the size-scaling of strength data, this difference will only be relevant for small Weibull-moduli such as $m < 5$.

For some applications, such as a pooled evaluation of several sets of data, it is necessary to describe the dependence of the effective volume on the Weibull-modulus m . For common strength tests such as 3- or 4-point-bending, this dependency is given through their closed form solutions for the effective volume and effective surface. Since no closed form solution is available for the B3B-Test, a different method must be employed. For each fixed combination of geometric and material parameters, the effective volume V_{eff} or surface S_{eff} can be described through the expression

$$V_{eff}(m)_{t/R_S, R/R_S, v} = V_{spec} \times \exp \left[v_0 + v_1 \frac{m-1}{m+1} + v_2 \ln m + v_3 m^4 + v_4 \frac{1}{m} \right] \quad (19)$$

$$S_{eff}(m)_{t/R_S, R/R_S, v} = S_{spec} \times \exp \left[s_0 + s_1 \frac{m-1}{m+1} + s_2 \ln m + s_3 m^4 \right] \quad (20)$$

with v_0 - v_4 (or s_0 - s_3) as constants determined through fitting of the respective datapoints and the other variables as defined before. V_{spec} and S_{spec} are the total volume of the specimen or the area of the tensile loaded face, respectively. This expression can be utilized to fit both discs and square plates and both multi-axial stress criteria. The determination of v_0 - v_4 (or s_0 - s_3) is included in the Python and Mathematica scripts in the [supplementary material](#). The authors recommend to fit Eqs. (19) & (20) to the results from $m=2$ to $m=50$ to achieve an error of less than 5% (which is the default range within the provided scripts). If this range in m is narrowed, the error of the fits will decrease.

5. Employing V_{eff} and S_{eff} for pooled Weibull evaluation

To give an example for the need and application of the data and expressions provided above, strength results from B3B-testing of Si_3N_4 will be utilized. Due to the high variability in geometry in some of the tested specimens, the standard procedure according to EN-843-5 provides erroneous results. Instead, a pooled data evaluation through taking the effective volume or surface of each specimen into account is performed and the results are discussed.

The specimen material SL200 B ($v=0.27$, Young's modulus=305 GPa) was produced by CeramTec (CeramTec-Platz 1–9, 73207 Plochingen, Germany) and provided as rectangular billets [26]. From these, square plates with an edge length $L=11$ mm and an approximate

thickness $t=0.25$ mm or $t=1.5$ mm were cut. The tension-loaded side of each specimen was ground with a D46-diamond grit grinding wheel to purposely introduce surface defects. The testing fixture is built according to the design outlined in [23,27,28] and support balls with a diameter of $2R_{SB}=7.5$ mm were utilized, resulting in a support radius $R_S=4.33$ mm. All specimens were tested with the universal testing machine Z010 (ZwickRoell GmbH & Co. KG, August-Nagel-Strasse 11, 89079 Ulm, Germany) at a constant crosshead-speed s and failure occurred within 5–15 s. The dimensions of the tested specimens and their testing parameters are given in Table 3.

The strength was calculated according to [21]. The results of the statistical strength evaluation according to EN-843-5 are given in Table 4 [29]. Note that this procedure assumes the same geometry for each specimen in each sample. To differentiate from the true, unknown parameters σ_0 and m , the results obtained from an “estimator”, e.g. maximum likelihood, will be denoted as $\hat{\sigma}_0$ and \hat{m} . Fractography has shown that failure is caused by surface flaws, hence why the effective surface S_{eff} will be utilized for any further analyses. For these results, the average geometry of each sample was utilized to determine S_{eff} through interpolation of the data provided in the [supplementary material](#) of this work. Note the difference in S_{eff} of more than one order of magnitude between the samples.

To determine the material's Weibull-modulus from the information gained from both samples, the characteristic strength of each set of strength data is plotted in dependence of the effective surface or volume on a logarithmic scale. This is a graphical representation of Eq. (14). Then, the slope of a linear regression k_{reg} through all pairs of data is determined. From k_{reg} , the “regression modulus” \hat{m}_{reg} is determined through $\hat{m}_{reg} = -1/k_{reg}$. From the results given in Table 4, a “regression modulus” \hat{m}_{reg} of 11.5 is determined.

However, the specimens of Sample A show a significant variation in thickness, with a relative difference of approximately 26% from the thinnest to the thickest specimen. As shown in previous chapters, the specimen's thickness has a pronounced effect on the effective surface and effective volume of B3B-specimens. Therefore, statistical strength evaluation according to EN-843-5 for this set of data is flawed, since a nearly constant specimen geometry, i.e. similar effective surface for each individual specimen, is assumed. Instead, strength evaluation for multiple specimen geometries should be performed through a pooled Weibull evaluation, as first outlined by Johnson & Tucker in 1992 [4,11,30]. The method will be presented utilizing the effective volume, but it can equally be applied using the effective surface. Similar to data evaluation in EN-843-5, this procedure is based on the maximum-likelihood method to obtain point estimates of the parameters of the distribution that describes the scatter of strength data. In the context of measuring the strength σ_i of n specimens, the likelihood function L is defined through

$$L = \prod_{i=1}^n p_i \quad (21)$$

with p_i as the probability density to obtain σ_i . Consequently, the likelihood L is a measure for the probability to obtain the measured sample. The estimates for the searched parameters are defined to be those for which L becomes maximal. To simplify the numerical evaluation, the likelihood can be expressed as the log-likelihood function

$$\ln L = \sum_{i=1}^n \ln p_i \quad (22)$$

instead, since it has been shown that the maximum of L corresponds to the maximum of $\ln L$. In the case of the Weibull distribution, the distribution parameters are m and σ_0 for a chosen reference volume V_0 , with p_i as the probability density function (PDF) of the Weibull distribution. The PDF is obtained by differentiating the cumulative distribution function, i.e. Eq. (7), with respect to σ_i , which gives

$$p_i = \left(\frac{dP}{d\sigma} \right)_{\sigma=\sigma_i} = m \frac{V_{eff,i}}{V_0} \frac{\sigma_i^{m-1}}{\sigma_0^m} \exp \left[- \frac{V_{eff,i}}{V_0} \left(\frac{\sigma_i}{\sigma_0} \right)^m \right] \quad (23)$$

with the variables as defined before. Inserting Eq. (23) into Eq. (22) yields an expression for the log likelihood function $\ln L$

$$\ln L = n \ln(m) - n m \ln(\sigma_0) + \sum_{i=1}^n \ln \left(\frac{V_{eff,i}}{V_0} \right) + (m-1) \sum_{i=1}^n \ln(\sigma_i) - \sum_{i=1}^n \frac{V_{eff,i}}{V_0} \left(\frac{\sigma_i}{\sigma_0} \right)^m \quad (24)$$

for a set of n strength measurements. To maximize $\ln L$, partial derivatives with respect to either m or σ_0 are taken and set equal to zero, respectively. By combining the two resulting equations, a function solely depending on m is obtained. Solving this equation gives a maximum-likelihood estimate \hat{m} for m :

$$0 = \frac{n}{\hat{m}} + \sum_{i=1}^n \frac{1}{V_{eff,i}} \frac{dV_{eff,i}}{dm} + \sum_{i=1}^n \ln \sigma_i - n \frac{\sum_{i=1}^n \left(V_{eff,i} \sigma_i^{\hat{m}} \ln \sigma_i + \sigma_i^{\hat{m}} \frac{dV_{eff,i}}{dm} \right)}{\sum_{i=1}^n V_{eff,i} \sigma_i^{\hat{m}}} \quad (25)$$

Since the term $dV_{eff,i}/dm$ occurs, it is necessary to know the functional dependence of the effective volume for each specimen on the Weibull-modulus m (see Eq. (20)). With \hat{m} determined, the maximum-likelihood estimate $\hat{\sigma}_0$ for σ_0 is obtained through

$$\hat{\sigma}_0 = \sqrt[n]{\frac{1}{n} \sum_{i=1}^n \frac{V_{eff,i}}{V_{0,i}} \sigma_i^{\hat{m}}} \quad (26)$$

Following this procedure for the experimental data and utilizing S_{eff} instead of V_{eff} , new and consistent results for $\hat{\sigma}_0$ and \hat{m} were determined, as given in Table 5. Similarly, the method can be applied using average specimen geometries for each sample instead of individual specimen geometries. This vastly reduces the necessary number of functional expressions for S_{eff} to just one per sample. It should be mentioned that \hat{m} can also be determined from Eq. (24) by utilizing a maximizing algorithm and avoiding the usage of derivatives (as has been done in this work) instead of finding the root of Eq. (25). The benefit of utilizing Eq. (25) over Eq. (24) is a more reliable convergence towards \hat{m} due to the reduction of two variables to one.

Fig. 9a) shows a traditional Weibull plot for each sample, with the data as measured from strength testing. As expected, smaller specimens exhibit a higher strength due to the size effect [3,4]. Fig. 9b) shows the strength of each sample, but now in dependence of the effective surface for each individual specimen. Through this presentation, the large scatter of the effective surface of specimens of sample A is clearly visible. In Fig. 9c), a traditional Weibull plot is depicted again, but with the strength of both samples extrapolated to the same reference surface, i.e. $S_0 = 0.041 \text{ mm}^2$, through strength scaling according to Eq. (14). This results in a horizontal shift of the individual datapoints, especially those of Sample B, as the reference surface is the average effective surface of Sample A. If the material behaves according to Weibull theory, a mixing of both distributions should be observed, as shown in this case. Finally, Fig. 9d) shows a Weibull plot with the probability of failure of each specimen extrapolated to the reference surface $S_0 = 0.041 \text{ mm}^2$. The extrapolated probability of failure $P_{0,i}$ for each specimen i is obtained through

$$\ln \ln \left(\frac{1}{1 - P_{0,i}} \right) = \ln \ln \left(\frac{1}{1 - P_i} \right) + \ln \left(\frac{S_0}{S_{eff,i}} \right) \quad (27)$$

with P_i as the probability of failure for each specimen, and $S_{eff,i}$ as the

respective effective surface of that specimen [4]. This approach gives insight into the material's behavior at low strengths and if an extrapolation based on Weibull-Theory is reasonable. If the material behaves according to Weibull theory, a single linear trend with a clear distinction between the individual samples should be observed, as shown in Fig. 9d).

In conclusion, through testing several different specimen geometries and a subsequent pooled data evaluation, more information about the tested material can be acquired. First, testing at several different V_{eff} or S_{eff} (through varying the specimen geometry or the testing method) gives a better understanding whether the investigated material can be considered a "Weibull-material" or not [31]. Furthermore, due to the increased number of individual specimens for statistical analysis, the confidence intervals will be reduced [32]. Finally, testing larger specimens results in testing larger defects, through which lower probabilities of failure are measured, instead of extrapolated, as depicted in Fig. 9d) [33,34].

6. Summary

In this work, the effective volume V_{eff} and the effective surface S_{eff} have been investigated for the Ball-on-Three-Balls-test (B3B). While the B3B-test is a commonly used biaxial strength testing method, these quantities have only been available for a small range of specimen geometries and materials so far. This is due to the lack of an accurate analytical description for the stress field of the B3B-test. Consequently, V_{eff} and S_{eff} must be numerically determined through Finite-Element-Analysis (FEA).

Therefore, a thorough analysis of the effective volume and surface for the B3B-test for a wide range of specimen geometries and materials has been conducted. Two models were implemented in ANSYS to determine the effective volume and surface for both discs and square plates. In the supplementary material of this work, the effective volume and surface is provided as tabulated data in various formats together with the tools to utilize them for specific specimens. Furthermore, the influence of non-linear effects on the accuracy of the provided data is discussed and quantified through a separate FEA-model. Additionally, the necessary accuracy of the provided results for Weibull strength scaling is investigated.

For any given choice of geometry parameters within the range of this work, a fitting model that describes V_{eff} and S_{eff} as a function of the Weibull modulus is given. Finally, the application of the results and functions provided in this work for the statistical analysis of experimental strength data is demonstrated through an example of pooled Weibull evaluation. In the appendix of this work, the determination of the effective volume and surface through a FEA-post-processing routine is outlined in detail.

Declaration of Competing Interest

The authors declare that they have no known competing financial interests or personal relationships that could have appeared to influence the work reported in this paper.

Acknowledgements

M. Staudacher gratefully acknowledges financial support by the Austrian BMVIT and BMWFW in the project "CharAM" (FFG 877684) of the COIN/IraSME program. The authors would like to thank Johannes Neumüller for his work on the scripts provided in the supplementary material of this work.

Appendix A. Numerical evaluation of V_{eff} and S_{eff}

This section will demonstrate the determination of V_{eff} and S_{eff} from the results of FEA, based on the procedure given in [35]. It will be outlined for the determination of V_{eff} and the use of linear elements, but it can equally be applied to the determination of S_{eff} or the use of higher order elements.

Generally speaking, the procedure aims to determine $V_{eff}^{(e)}$ in each element individually through

$$V_{eff}^{(e)} = \iiint_{V^{(e)}} \left[\frac{\sigma^{(e)}(x, y, z)}{\sigma_{ref}} \right]^m dV \quad (28)$$

with the superscript (e) referring to quantities of the individual elements and the other variables as defined before. The maximum first principal stress in the center of the specimen was utilized for σ_{ref} . Through numerical integration of Eq. (28) and subsequent summation of the results of all individual elements, V_{eff} for the full model is obtained. To simplify the integration limits for an element in an arbitrary position in three-dimensional space, its position in cartesian coordinates (x, y, z) is transformed to a natural coordinate system (ξ, η, ζ), in which each element is represented as a cube within the space $(-1, 1)$.

Within natural coordinates, each element is described through $i = 8$ shape functions $h_i(\xi, \eta, \zeta)$, which give the value 1 at each respective node with position (ξ_i, η_i, ζ_i) and 0 at all other nodes:

$$h_i(\xi, \eta, \zeta) = \frac{1}{8} (1 + \xi_i \xi) (1 + \eta_i \eta) (1 + \zeta_i \zeta) \quad (29)$$

The coordinates (ξ_i, η_i, ζ_i) of each node within an element are given in Table 6. Superimposing these functions gives a linear interpolation within the element for any value at each node. If this is performed for the cartesian coordinates x_i, y_i and z_i of each node, the following transformation functions are derived:

$$x^{(e)}(\xi, \eta, \zeta) = \sum_{i=1}^8 x_i^{(e)} h_i(\xi, \eta, \zeta) \quad (30)$$

$$y^{(e)}(\xi, \eta, \zeta) = \sum_{i=1}^8 y_i^{(e)} h_i(\xi, \eta, \zeta) \quad (31)$$

$$z^{(e)}(\xi, \eta, \zeta) = \sum_{i=1}^8 z_i^{(e)} h_i(\xi, \eta, \zeta) \quad (32)$$

In order to use this transformation in the following calculations, the determinant of the Jacobian-Matrix $J^{(e)}(\xi, \eta, \zeta)$ for the three-dimensional case will be necessary, which is given through

$$J^{(e)}(\xi, \eta, \zeta) = Det \begin{bmatrix} \frac{\partial x}{\partial \xi} & \frac{\partial y}{\partial \xi} & \frac{\partial z}{\partial \xi} \\ \frac{\partial x}{\partial \eta} & \frac{\partial y}{\partial \eta} & \frac{\partial z}{\partial \eta} \\ \frac{\partial x}{\partial \zeta} & \frac{\partial y}{\partial \zeta} & \frac{\partial z}{\partial \zeta} \end{bmatrix} \quad (33)$$

Similarly, superimposing the shape functions for the results of stress evaluation, i.e. the equivalent stress $\sigma_{eq,i}^{(e)}$ at each node, gives a function $f^{(e)}(\xi, \eta, \zeta)$ that allows stress interpolation within each element:

$$f^{(e)}(\xi, \eta, \zeta) = \sum_{i=1}^8 \sigma_{eq,i}^{(e)} h_i(\xi, \eta, \zeta) \quad (34)$$

This finally allows stress integration with natural coordinates within a single element to determine its effective volume $V_{eff}^{(e)}$ according to

$$V_{eff}^{(e)} = \iiint_{V^{(e)}} \left[\frac{f^{(e)}(\xi, \eta, \zeta)}{\sigma_{ref}} \right]^m dV = \int_{-1}^1 \int_{-1}^1 \int_{-1}^1 \left[\frac{f^{(e)}(\xi, \eta, \zeta)}{\sigma_{ref}} \right]^m J^{(e)}(\xi, \eta, \zeta) d\xi d\eta d\zeta \quad (35)$$

with the variables as defined before. The next step is a numerical integration of Eq. (35). In this work, Gauss-Legendre-Quadrature is utilized, which gives accurate estimates for the definite integral of a function in the space $(-1, 1)$ through

$$\int_{-1}^1 f(x) dx \approx \sum_{i=1}^n w_i f(r_i) \quad (36)$$

for the one-dimensional case. The points of integration r_i are given by the order n of the Gauss-Legendre-Quadrature as the roots of the n^{th} Legendre polynomial, and w_i are the respective quadrature weights. The integration points and associated weights for 5th-order quadrature are given in Table 7. For multiple dimensions, the integration points are iterated in every dimension and the associated weights are the product of their respective one-dimensional weights.

Applying this procedure to Eq. (35) with a n^{th} order quadrature converts the integral to

$$V_{eff}^{(e)} = \sum_{i=1}^n \sum_{j=1}^n \sum_{k=1}^n \left[\frac{f^{(e)}(r_i, r_j, r_k)}{\sigma_{ref}} \right]^m w_i w_j w_k J^{(e)}(r_i, r_j, r_k) \quad (37)$$

for the effective surface of a single element. By conducting this evaluation for every tensile loaded element and adding them up, the effective volume V_{eff} for the full model is determined. In the same way, the effective surface can be determined for two-dimensional elements. For higher-order-elements, the procedure doesn't have to be changed as long as the results of stress evaluation are saved on the nodes at the corners of elements.

However, a problem arises for two-dimensional elements or element-faces in a three-dimensional model (e.g. when S_{eff} shall be determined for a three-dimensional model). While these faces are defined by two dimensions in natural coordinates, their position is determined by three dimensions in the cartesian space. Therefore, the transformation functions yield a non-square Jacobi-Matrix, for which the determinant can't be formed. In that case, the determinant of the Gram-Matrix $J^{(e)T}(\xi, \eta) \times J^{(e)}(\xi, \eta)$ is formed instead and its square root $G^{(e)}(\xi, \eta)$ replaces $J^{(e)}(\xi, \eta)$ in Eq. (35).

$$G^{(e)}(\xi, \eta) = \sqrt{Det[J^{(e)T}(\xi, \eta)J^{(e)}(\xi, \eta)]} \quad (38)$$

Appendix B. Supporting information

Supplementary data associated with this article can be found in the online version at [doi:10.1016/j.jeurceramsoc.2023.09.018](https://doi.org/10.1016/j.jeurceramsoc.2023.09.018).

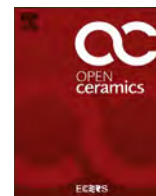
References

- [1] R. Morrell, Biaxial flexural strength testing of ceramic materials: A National Measurement Good Practice Guide No. 12, National Physical Laboratory, 2007.
- [2] Weibull W., A Statistical Theory of the Strength of Materials, Generalstabens Litografiska Anstalts Förlag, Stockholm, 1939.
- [3] D. Munz, T. Fett, Ceramics: mechanical properties, failure behaviour. Materials Selection, Springer, Berlin, Heidelberg, 1999.
- [4] J.B. Wachtman, M.J. Matthewson, W.R. Cannon, Mechanical Properties of Ceramics, Wiley, Hoboken, New Jersey, 2009.
- [5] G.K. Bansal, W.H. Duckworth, D.E. Nieszt, Strength-size relations in ceramic materials: investigation of an alumina ceramic, J. Am. Ceram. Soc. 59 (1976) 472–478.
- [6] R. Jain J. Lock S.F. Duffy Effective area and effective volume calculations for ceramic test SPEcimens, in: ASME Turbo Expo Orlando (Ed.) ASME Turbo Expo. 2009 231 239.
- [7] G.D. Quinn, Weibull strength scaling for standardized rectangular flexure specimens, J. Am. Ceram. Soc. 86 (2003) 508–510.
- [8] G.D. Quinn, Weibull effective volumes and surfaces for cylindrical rods loaded in flexure, J. Am. Ceram. Soc. 86 (2003) 475–479.
- [9] ASTM C 1499–05: Test Method for Monotonic Equibiaxial Flexural Strength of Advanced Ceramics at Ambient Temperature, ASTM International, West Conshohocken, PA, 2005.
- [10] H. Rinne, The Weibull Distribution: A Handbook, CRC Press, Boca Raton, 2009.
- [11] C.A. Johnson, W.T. Tucker, Advanced Statistical Concepts of Fracture in Brittle Materials, Ceramics and Glasses, Eng. Mater. Handb. 4 (1991) 709–715.
- [12] R. Danzer, A general strength distribution function for brittle materials, J. Eur. Ceram. Soc. 10 (1992) 461–472.
- [13] I.E. Reimanis, R.A. Schaut, Hertzian testing to obtain flaw distributions in high strength glasses and glass-ceramics, J. Am. Ceram. Soc. 99 (2016) 3712–3718.
- [14] ASTM C 1683 - 10: Practice for Size Scaling of Tensile Strengths Using Weibull Statistics for Advanced Ceramics, ASTM International, West Conshohocken, PA, 2019.
- [15] D. Gross, T. Seelig. Bruchmechanik: Mit einer Einführung in die Mikromechanik, 6th ed., Heidelberg Springer Vieweg, Berlin, 2016.
- [16] P. Stanley, H. Fessler, A.D. Sivill, An engineer's approach to the prediction of failure probability of brittle components, Proc. Brit. Ceram. Soc. 22 (1973) 453–487.
- [17] A.M. Freudenthal, Statistical approach to brittle fracture, Fracture 2 (1968) 591–619.
- [18] R.L. Barnett, P.C. Hermann, J.R. Wingfield, C.L. Connors, Fracture of Brittle Materials Under Transient Mechanical and Thermal Loading, 1967.
- [19] J.A. Salem, L. Powers, Guidelines for the testing of plates, in: H.-T. Lin, W. M. Kriven (Eds.), 27th International Cocoa Beach Conference on Advanced Ceramics and Composites: January 26-31, 2003, Cocoa Beach, Florida, American Ceramic Society, Westerville, Ohio, 2003, pp. 357–364.
- [20] D.J. Godfrey, S. John, Disc flexure tests for the evaluation of ceramic strength, Proc. 2nd Int. Conf. Ceram. Mater. Compon. Engines 14–17 (1986) 657–665.
- [21] M. Staudacher, T. Lube, P. Supancic, The Ball-on-Three-Balls strength test for discs and plates: Extending and simplifying stress evaluation, J. Eur. Ceram. Soc. 43 (2023) 648–660.
- [22] A. Börger, P. Supancic, R. Danzer, The ball on three balls test for strength testing of brittle discs: Stress distribution in the disc, J. Eur. Ceram. Soc. 22 (2002) 1425–1436.
- [23] R. Danzer, P. Supancic, W. Harrer, Der 4-Kugerversuch zur Ermittlung der biaxialen Biegefestigkeit spröder Werkstoffe, Kriegsman, J. (Hrsg): Tech. Keram. Werkst. (2009) 1–48.
- [24] H.L. Frandsen, Weibull statistics effective area and volume in the ball-on-ring testing method, Mech. Mater. 73 (2014) 28–37.
- [25] A. Börger, P. Supancic, R. Danzer, The ball on three balls test for strength testing of brittle discs: Part II: analysis of possible errors in the strength determination, J. Eur. Ceram. Soc. 24 (2004) 2917–2928.
- [26] T. Lube, J. Dusza, A silicon nitride reference material—A testing program of ESIS TC6, J. Eur. Ceram. Soc. 27 (2007) 1203–1209.
- [27] W. Harrer, R. Danzer, P. Supancic, T. Lube, The Ball on Three Balls Test: Strength Testing of Specimens of Different Sizes and Geometries, Proc. 10th ECeS Conf. 2008 (2008) 1271–1275.
- [28] R. Danzer, A. Börger, P. Supancic, M.A. Ruiz, Villanueva, Ein einfacher Festigkeitsversuch für Scheiben aus spröden Werkstoffen, Mat. -Wiss. U. Werkst. 34 (2003) 490–498.
- [29] DIN EN 843–5: 2007: Advanced technical ceramics - Mechanical properties of monolithic ceramics at room temperature - Part 5: Statistical analysis, German Institute for Standardisation (Deutsches Institut für Normung), 2007.
- [30] C.A. Johnson, W.T. Tucker, Weibull estimators for pooled fracture data life prediction methodologies and data for ceramic materials, ASTM STP 1201 (1994).
- [31] R. Danzer, T. Lube, P. Supancic, R. Damani, Fracture of ceramics, Adv. Eng. Mater. 10 (2008) 275–298.
- [32] R. Danzer, T. Lube, P. Supancic, Monte Carlo simulations of strength distributions of brittle materials – type of distribution, specimen and sample size, Int. J. Mater. Res. 92 (2001) 773–783.
- [33] R. Danzer, P. Supancic, J. Pascual, T. Lube, Fracture statistics of ceramics – Weibull statistics and deviations from Weibull statistics, Eng. Fract. Mech. 74 (2007) 2919–2932.
- [34] R. Danzer, T. Lube, New fracture statistics for brittle materials, Fract. Mech. Ceram. 11 (1996) 425–439.
- [35] D. Mevec, Auslegung einer Festigkeitsprüfung von Dentalkeramik mittels des B3B-Tests, Chair of Structural and Functional Ceramics, Montanuniversität Leoben, 2016, (<https://pureadmin.unileoben.ac.at/ws/portalfiles/portal/1861498/ACI3285197n01vt.pdf>).

Paper C

M. Staudacher, T. Lube, J. Schlacher, P. Supancic: "Comparison of Biaxial Strength Measured with the Ball-on-Three-Balls- and the Ring-on-Ring-Test", *Open Ceramics* **6** (2021), <https://doi.org/10.1016/j.oceram.2021.100101>

This article is available under the Creative Commons CC-BY-NC-ND license



Comparison of biaxial strength measured with the Ball-on-Three-Balls- and the Ring-on-Ring-test



Maximilian Staudacher^{*}, Tanja Lube, Josef Schlacher, Peter Supancic

Department of Materials Science, Montanuniversität Leoben, Franz Josef-Strasse 18, A-8700, Leoben, Austria

ARTICLE INFO

Keywords:

Ball-on-Three-Balls testing
Ring-on-Ring testing
Finite element analysis
Alumina
Weibull size effect
Biaxial testing

ABSTRACT

The Ball-on-Three-Balls-test (B3B) and the Ring-on-Ring-test (RoR) were conducted on alumina discs and compared based on Weibull-Theory. The influence of various intermediate layers was evaluated. To support these findings, Finite-Element-Analysis was conducted to analyze the effects of deviations from ideal loading conditions. The influence of friction between sample and fixture and the effects of an inhomogeneous load distribution on the maximum stress were investigated. The experiments demonstrated that measuring corresponding strength values with both testing methods is possible. To properly assess the strength using the RoR-test, intermediate layers must be used. Teflon-foils or adhesive tapes are considered suitable. If no intermediate layer is used, the materials strength will be underestimated. Finite-Element-calculations show that this effect cannot be explained by the influence of friction and is rather caused by a non-homogeneous load distribution along the load-ring. Fractography supports these findings.

1. Introduction

Ceramic components have found their way into a multitude of highly technological and specific fields of application due to their unique thermal, electrical, chemical and mechanical properties [1]. However, some of their most notable downsides are the lack of ductility and a large scattering of mechanical strength [2]. On the upside, if the mechanisms behind these problems are understood well, component failure can be predicted and minimized [3]. Mechanical strength testing is well known as one of the key methods in order to understand failure behavior and a wide number of tests have been developed. The most common testing methods are some types of uniaxial tensile or compressive tests, uniaxial bending tests and biaxial bending tests [4]. The latter two are established as the main methods for strength testing of ceramic materials [4].

One of the main benefits of biaxial testing compared to uniaxial testing is the reduced influence of specimen preparation on its edges and the consequential possibility to omit edge preparation at all. Machining of ceramic materials is usually very time- and cost-intensive due to their inherent hardness and wear resistance. Additionally, any preparation method may introduce defects or flaws at already failure sensitive locations such as edges and surfaces. During uniaxial bending, edges and surfaces are subjected to the maximum stress as well and therefore influence failure significantly. On the other hand, biaxial tests like the

Ring-on-Ring-test are less dependent on specimen preparation at the edges since the maximum stresses occur at or in the area close to the specimen's center. Thus, the quality of the edge preparation is in most cases negligible with respect to the strength measurement in the specimen's center. If the specimens are manufactured in compatible size and shape, even testing in as-fabricated condition is possible [5]. Furthermore, biaxial loading provides a better representation of real-world loading scenarios of typical ceramic parts than uniaxial loading.

To ensure an independence of specimen orientation and uniform load distribution, equi-biaxial stress states are preferred. Several different tests with widely varying stress fields have been developed. The most common ones are the Ring-on-Ring-test [6,7], the Ball-on-Ring-test [8], the Piston-on-Balls-test [9], the Ball-on-Three-Balls-test [10,11] and the Three-Balls-on-Three-Balls-test [12]. In this work, the focus will be on the Ring-on-Ring-test (RoR) and the Ball-on-Three-Balls-test (B3B).

The Ring-on-Ring test is standardized in ASTM C1499 [6]. This establishes a good understanding of its capabilities and limitations. Alongside that, the loading condition exhibits a cylindrical symmetry which leads, in the case of isotropic materials, to a cylindrical symmetrical stress field that can be expressed in an analytical closed form. This allows an easy calculation of results and "effective" specimen sizes. Due to the comparatively large portion of maximum stress in the specimen's center, a good representation of the materials general strength can be

^{*} Corresponding author.

E-mail address: maximilian.staudacher@unileoben.ac.at (M. Staudacher).

measured. The major drawback of the Ring-on-Ring method is the need for some sort of lubricant or intermediate layer to reduce friction between the specimen and the loading fixture [6,13]. Especially intermediate layers might change load application depending on their material and thickness. Miniaturization of testing rigs is impeded by manufacturing tolerances of loading and support rings, resulting in a minimum support ring diameter of about 10 mm [13]. Moreover, concentric alignment of loading and support ring has to be ensured since small deviations of about 1% cause a difference in measured strength of about 2% [14]. No definitive numbers concerning the accuracy are available. However, an indication of precision (i.e. the coefficient of variation) of about 5–14% is mentioned in ASTM C1499 [6]. If intermediate layers are used, testing proves to be rather time consuming and cumbersome compared to other biaxial testing methods.

In contrast to the RoR-test, the Ball-on-Three-Balls-test does not require any intermediate layers. This major upside is achieved through elimination of all sources of friction by using freely movable balls as a support structure instead of a fixed ring [10]. The use of large balls (diameter typically approx. 70% of the specimens diameter) inhibits contact failure associated with the loading ball [15]. Furthermore, the combination of an easy testing procedure and the general benefits of biaxial testing (little to no specimen preparation) allow a comparatively high testing output. Typically, standardized bearing balls are used as support and load members, which allows test miniaturization with specimens as small as 2.0 mm × 2.0 mm due to the balls tight manufacturing tolerances [16–19]. This can prove to be very useful if only small batches of material, like in the dental ceramic field, are available [20,21]. The stress field exhibits a characteristic three-fold symmetry with the maximum tensile stress in the center between the three supporting balls. Since the region of maximum stress is comparatively small, localized strength testing of specific features or regions of interest within a specimen is possible [22]. However, if the general strength of a specimen has to be determined, the small region of maximum stress proves to be a significant drawback in terms of effective volume or area [23]. Another drawback is the absence of any analytical description of the stress field. Therefore, Finite-Element-Analysis results obtained for a large variety of possible test geometries have to be interpolated in order to determine the maximum stress in the center of the disc [24], or approximated using a fitted expression [10,25]. So far, the B3B-test has not been standardized. All in all, the B3B-test is robust against inaccurate specimen shapes and alignment errors and can be performed with a typical error of less than 2% [11].

According to ASTM C1499, and in order for the analytical stress expression to be valid, the possible specimen geometries for the RoR-test are limited by plate theory (and contact pressure) and the maximum amount of deflection [6,14,26]. As a result, typical values (for materials tested in this work) for the ratio of thickness to support ring diameter range between 0.1 and 0.023 in order to limit the error to ±2% [27]. As for the B3B-test, the authors refer to work published by Danzer et al. [25]. It describes suitable combinations of the parameters of relative strength (fracture strength divided by Young's modulus) and relative thickness (thickness divided by specimen radius), to guarantee a sufficiently small area of contact between the balls and the specimen. Ceramics generally show a low relative strength, which allows testing with $0.1 < t/R < 0.5$, with t being the specimen's thickness and R the specimen's radius.

So far, not many comparisons of strength results obtained with the B3B-test and with other test methods, especially standardized biaxial ones are available [28,29]. The main emphasis of the present work was to investigate whether the strength results measured with the Ball-on-Three-Balls-test and the Ring-on-Ring-test are comparable to each other in the framework of the statistical theory of fracture, i.e. in a similar way to 4- and 3-point bend tests [30]. Another topic of investigations was the role of intermediate layers on the strength. Furthermore, the influence of friction on the stress field was analyzed. To complement a series of performed fracture tests, Finite-Element-Analysis was conducted for the Ring-on-Ring-test.

2. Methods and material

2.1. Weibull fracture statistics and size effect

In order to compare the strength values and Weibull distributions determined with different test configurations, we presume that we investigate a “Weibull material” [31], i.e. a material which shows a size effect on strength as described by the Weibull theory [32–34]. In the following this idea is outlined for cases where specimens fail due to a defect located within the bulk of the material, but the concept can analogously be applied to failure due to surface located defects [16]. According to Weibull-Theory, the probability of failure P at a certain (equivalent) stress σ_r is given by:

$$F(\sigma, V) = 1 - \exp\left[-\frac{V_{eff}}{V_0} \left(\frac{\sigma_r}{\sigma_0}\right)^m\right] \quad (1)$$

with m being the “Weibull-modulus”, which describes the scatter of measured strengths, and the characteristic strength σ_0 , which is related to the reference volume V_0 . Characteristic strength is defined as the stress necessary to achieve a 63.2% probability of failure at $V_{eff}/V_0 = 1$. The effective Volume V_{eff} is defined by the integral over the positive values of the stress field $\sigma(\vec{r})$:

$$V_{eff} = \int_{\sigma>0} \left(\frac{\sigma(\vec{r})}{\sigma_r}\right)^m dV \quad (2)$$

with σ_r as an arbitrary reference stress, usually representing the maximum stress in the specimen [30]. V_{eff} describes the theoretical volume of a tensile specimen with the same probability of failure at σ_r as the non-homogeneously loaded specimen. In the case of biaxial loading, some form of equivalent stress has to be defined to properly quantify the complex stress state. Several methods such as the S1 criteria or PIA are proposed [30,35]. For this work, the “Principle of Independent Action”, or PIA, was used [36]. If σ_I , σ_{II} and σ_{III} are the (positive, tensile) principle stresses and m is the Weibull modulus, the equivalent stress σ_e is calculated as:

$$\sigma_e = (\sigma_I^m + \sigma_{II}^m + \sigma_{III}^m)^{1/m} \quad (3)$$

and can be used in the same way as in an uniaxial scenario in all equations previously mentioned (note: in case of compressive stress components, these contributions are clipped to zero). Utilizing eq. (1) to compare different volumes at the same probability of failure, the following relationship can be derived:

$$\frac{\sigma_1}{\sigma_2} = \left(\frac{V_{eff,2}}{V_{eff,1}}\right)^{1/m} \quad (4)$$

with σ_i and $V_{eff,i}$ describing strength and effective volume of specimen type 1 or 2. Elaborating on eq. (4), larger effective volumes result in a lower strength and vice versa. This behavior can be utilized to compare different specimen sizes or testing methods for the same material. If characteristic strength of different specimen types is plotted as a function of effective volume on logarithmic scales, all data pairs should yield a straight line with slope $-1/m_{reg}$ [30]. If that condition is satisfied and the Weibull modulus m_{reg} derived from the slope is similar to that of each dataset, the tested material is a “Weibull material” [31]. This principle will be the basis for the comparison of samples tested with different testing methods in this work.

2.2. Investigated material

The investigated material Frialit F99.7 contains 99.5% alumina [37]. Its grain size is about 10 μm , and its microstructure contains about 2% pores as well as 1%–2% Mg-spinel. The microstructure of Frialit is shown

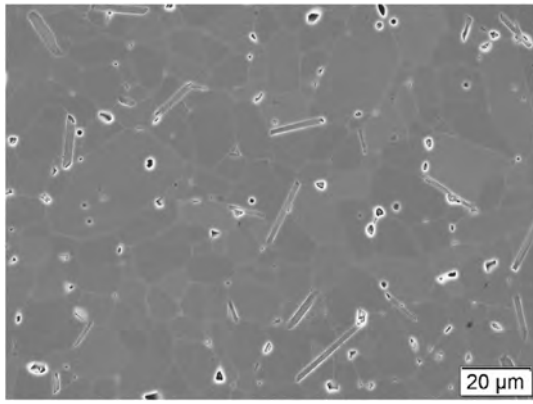


Fig. 1. Microstructure of KYOCERA Frialit, SEM, with clearly visible pores and elongated spinel grains.

in Fig. 1. The basic material properties can be found in Table 1. It was sourced from KYOCERA Fineceramics Solutions GmbH (68229, Mannheim, Germany) [37]. The material was provided as a rod of 28 mm diameter, which was cut and diamond ground into 1 mm and 1.7 mm thick discs. The prospective tension-loaded side of each specimen received a final grinding step using a D15 diamond grit wheel.

2.3. Experimental

The first developments on the Ball-on-Three-Balls method started in the 80s and were later further developed by Börger et al. [10,11,38,39]. It allows testing of discs and plates with minimal specimen preparation or even in as-sintered condition. It utilizes a single steel or carbide ball to apply the load and three moveable balls (which are in contact with each other) as a support structure [25]. The basic design is shown in Fig. 2(a) and a typical specimen after testing is shown in Fig. 3(a). The result is a localized maximum of stress in the center of the disc on the opposite side of the loading ball [40]. The maximum stress at failure σ_f of the specimen is calculated by the following formula [10,25]:

$$\sigma_f = f \left(\frac{2t}{D}, \frac{D_S}{D}, \nu \right) \cdot \frac{F}{t^2} \quad \text{with } D_S = \frac{2D_B}{\sqrt{3}} \quad (5)$$

with F as the applied force, ν as the Poisson's ratio, D as the specimen's diameter, t as the specimen's thickness, D_S as the diameter of the circle on which the three support points lie (i.e. support diameter) and D_B as the support ball diameter. The factor f is determined by interpolation of Finite-Element-Analysis results which assume load introduction by a point load [24] or by using a fitted polynomial on these FEA-results depending on the specimen's geometry and Poisson's ratio [10,25]. For this work, the maximum stress at failure was evaluated by using a third order interpolation function calculated with Mathematica 12.0 (Wolfram Research, IL 61820, Champaign, USA). The effective volumes and areas were determined by interpolation of FEA results as well.

The principle of the RoR-test can be seen in Fig. 2(b) and a specimen after testing in is shown in Fig. 3(b). Coaxial steel-rings are used to apply the load evenly along a certain radius and to provide support for the specimen. The result is a stress field with nearly equal and constant radial and tangential stresses within the diameter of the loading-ring and a drop-off towards the edge of the specimen. The stress field is ideally symmetric with respect to the central axis. An analytical solution of the stress field can be derived. The maximum stress at failure σ_f for discs is determined by Ref. [6]:

$$\sigma_f = \frac{3F}{2\pi t^2} \left[(1-\nu) \frac{D_S^2 - D_L^2}{2D^2} + (1+\nu) \ln \frac{D_S}{D_L} \right] \quad (6)$$

where F is the applied force, ν the Poisson's ratio, t the specimen's

Table 1
Mechanical properties of KYOCERA Frialit [37].

Property	Unit	KYOCERA Frialit
Density	[g/cm ³]	≥3.90
Purity	[weight-%]	>99.5
Open porosity	[Vol.-%]	0
Average grainsize	[μm]	10
Flexural strength DIN-EN 843-1	[MPa]	350
Weibull modulus	[–]	>10
Fracture toughness K_{Ic} (SEVNB)	[MPa m ^{1/2}]	3.5
Compressive strength	[MPa]	3500
Young's modulus	[GPa]	380
Poisson's ratio	[–]	0.22
Vickers Hardness HV1	[–]	1760

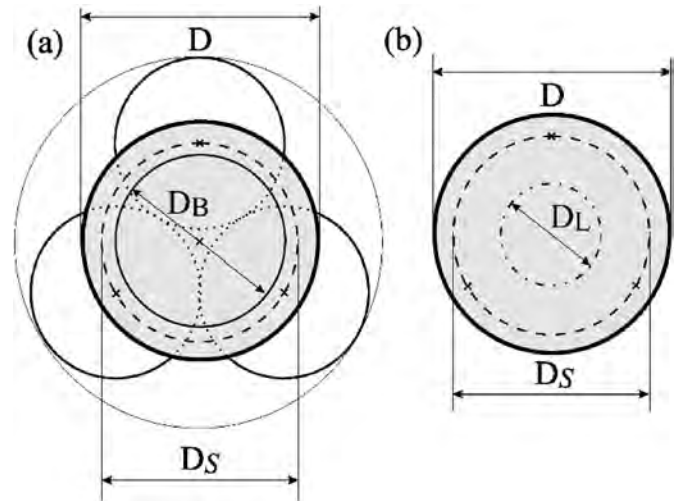


Fig. 2. Schematic of the B3B (a) and the RoR (b) loading layout [ref 36,43].

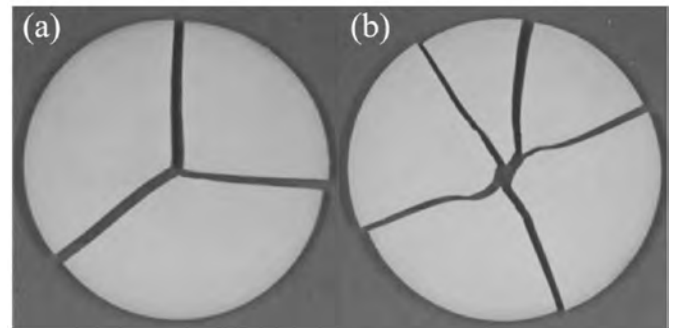


Fig. 3. Typical crack-patterns of fractured specimens for the B3B- (a) and RoR- (b) test.

thickness, D the specimen's diameter, D_L the load ring diameter and D_S the support ring diameter. The RoR-method has been proven to allow testing of discs and plates as well [6,41]. However, some limitations related to the specimen's thickness apply. If the specimen is too thin, large deformations restrict the use of linear geometric relations. If specimens are too thick, plate theory does not apply anymore and contact stress increase to a level where localized contact failure occurs [14,26,42].

An important task during testing is to reduce friction between specimen and support and loading rings in order to avoid additional stresses which are not taken into account in eq. (6). The common approach is to either use intermediate layers or lubricants. Lubricants allow testing without any influence on the stress field, but greatly impede

fractographic analysis, whereas intermediate layers might change load application and distribution. In this work, several different loose and adhesive materials were employed as intermediate layers. Their names, manufacturers, materials and properties are found in Table 2. Adhesive tape was used because of two reasons: i) to eliminate friction and - a beneficial side effect - ii) to keep the fracture pieces together to facilitate fractographic analysis. If adhesive tape was used, it was always applied to the compression-loaded side to ensure the smallest possible impact on strength results. Care was taken to use intermediate layers only for tests with expected fracture loads below loads that lead to failure of the layer itself. Loose layers were solely utilized between the support ring and the specimen (tension-loaded side). Sample strength was evaluated using eq. (6). The effective volumes and areas were calculated in the same manner as done for the Ball-on-Ring test by Frandsen [43]. The occurring integrals were solved numerically in Mathematica 12.0.

All experiments were conducted using a Zwick Z010 test frame (ZwickRoell GmbH & Co. KG, 89079, Ulm, Germany) equipped with a Doli control system (Doli, 72525, Münsingen, Germany). B3B tests were conducted using 15.08 mm diameter balls (resulting in a support diameter of 17.42 mm). RoR testing rigs were manufactured from 42CrMo4 (1.7225) and hardened to HRC > 40 and has a surface -finish of about 1.2 μm . The discs were tested using a support-ring diameter of 17.24 mm and a loading-ring diameter of 8.31 mm, both with a cross-section diameter of 1.2 mm. In order to compare both testing methods, different thicknesses and intermediate layers were used. Table 3 shows all tested samples and gives details on the testing conditions. F_p describes the pre-load, v the constant cross-head speed, RH relative humidity, T the ambient temperature and N the number of tested specimens. Each sample, with the exception of R-28-1 and B-28-1.7-BT, was in alignment with standards [6] or with previously published guidelines [47,48]. R-28-1 was tested without any layers or lubricants and was therefore not tested according to standards. In contrast, the B3B-method does not call for any compliant layers, hence why B-28-1.7-BT was not tested correctly.

The Weibull parameters m (unbiased) and σ_0 were estimated from the strength of the individual specimens for each dataset using the Maximum-Likelihood-Method [2,4]. Confidence-intervals for m and σ_0 provide additional information about the statistical uncertainty which is essential when comparing multiple datasets [49]. In this work, 90% confidence intervals will be used.

2.4. Finite-Element-Analysis

Finite-Element-Analysis was conducted to complement the experiments. More specifically, the influence of friction during Ring-on-Ring testing for 28 mm diameter discs with a thickness of 1 mm, was evaluated. In order to ensure consistent model properties throughout different scenarios, the commercial FEA-program ANSYS R19.1 (ANSYS Inc., PA 15317, Canonsburg, USA) was chosen for its ability to implement Ansys-Parametric-Design-Language (APDL) scripts. To investigate the influence of friction within a geometrically perfect test situation, a simple 2D-

Table 2

Names, manufacturers, materials and properties of utilized intermediate layers [44–46].

Trade name	Manufacturer	Material	Layer thickness	Adhesive thickness
PTFE virginal foil 0.05–600	High-tech-flon (78467, Konstanz, Germany)	Teflon	50 μm	–
PTFE tape 0.08 V SW	High-tech-flon (78467, Konstanz, Germany)	Teflon	51 μm	38 μm
Flashbreaker® 1	Airtech International, Inc. (CA 91708, Chino, USA)	Polyester	25 μm	30 μm

Table 3

Summary of tested sets. The prefix indicates the testing method: B3B-method (B-) or the RoR-method (R-). The first number is the specimen diameter; the second number the specimen thickness, both in mm. The suffix indicates the intermediate layers: BT (Flashbreaker® 1 compression side, loose Teflon tension side) or T (Teflon-tape compression side, loose Teflon foil tension side). F_p describes the pre-load, v the constant cross-head speed, RH relative humidity, T the ambient temperature and N the number of tested specimens.

Designation	F_p [N]	v [mm/min]	RH [%]	T [°C]	N [–]
B-28-1	10	0.5	24	23.2	30
B-28-1.7	20	2	52	22.6	30
B-28-1.7-BT	20	2	51	22.4	32
R-28-1	20	1.5	50	24.5	28
R-28-1-T	20	1.5	21	22.6	30
R-28-1-BT	20	8.5	49	21.5	29

contact-model was sufficient to assess the full problem due to rotational symmetry. This model allows quantitative statements and comparison with existing analytical solutions [40]. More specifically, the specimen (Young's Modulus = 380 GPa, $\nu = 0.22$) was meshed with 3145 PLANE183 (8-node quad elements) elements and 9948 nodes. The loading and supporting rings (Young's Modulus = 210 GPa, $\nu = 0.3$) were meshed with 490 PLANE183 elements and 1516 nodes. Surfaces, which will come into contact during testing, were meshed with 338 CONTA172 and 338 TARGET169 elements. Symmetric contact calculation was utilized and the friction coefficient μ between specimen and both rings was varied between 0 and 0.5 in steps of 0.1. The model was loaded by a force of 600 N. The model is shown in Fig. 4(a).

Additionally, the influence of uneven surfaces of the loading ring and thus uneven load application was examined using FEA. For this investigation, a simplified 3D-model had to be used (no contact calculations). Therefore, only qualitative statements can be deduced. This model was meshed with 35266 SOLID 95 elements (20-node brick elements) and 140759 nodes. Due to symmetry, the model could be reduced to one half. The uneven load application was realized by applying an oscillating force with equally spaced maxima and minima along the load-ring contour. The script allowed for changes in both frequency and number of load maxima (Z) and amplitude (A) in percentage of the applied total force. An example of the model with an uneven force applied is shown in Fig. 4(b).

To verify the simplified model as described above, a single contact scenario of the full testing assembly was modeled with a 3D-contact-model (material properties as mentioned above). The surface of the loading ring was modified so that it follows a sine with an amplitude of 5 μm and 3 full periods along its circumference, similar to the load in Fig. 4(b). The model is shown in Fig. 4(c).

3. Results & discussion

As previously explained, the size effect will be used to compare different testing methods. Since fractography did not show volume flaws to be responsible for failure, the effective area will be used instead of effective volume as the basis for future comparison [16,35]. A comparison is valid, when two requirements are met. First, RoR samples have to exhibit a lower strength than B3B samples due to the larger effective area. Second, if a fit of eq. (4) through all data pairs (which appears as straight line in the plot of characteristic strength versus effective area), results in a fitted Weibull modulus m_{reg} (the inverse slope of the straight line) which is close to the Weibull moduli of the individual sets.

The number of specimens N , Weibull parameters m and σ_0 as well as their 90% confidence intervals and effective area S_{eff} for each dataset are found in Table 4. Fig. 5(a) allows for a better overview of these results. R-28-1 specimens stand out due to their low Weibull modulus ($m = 15$) and poor characteristic strength. All other samples have a comparable Weibull modulus of $25 \leq m \leq 35$. Other findings are the slightly increased Weibull moduli for samples tested with intermediate layers, as all of them exhibit $m > 34$. Furthermore, the datasets R-28-1-T and R-28-1-BT are

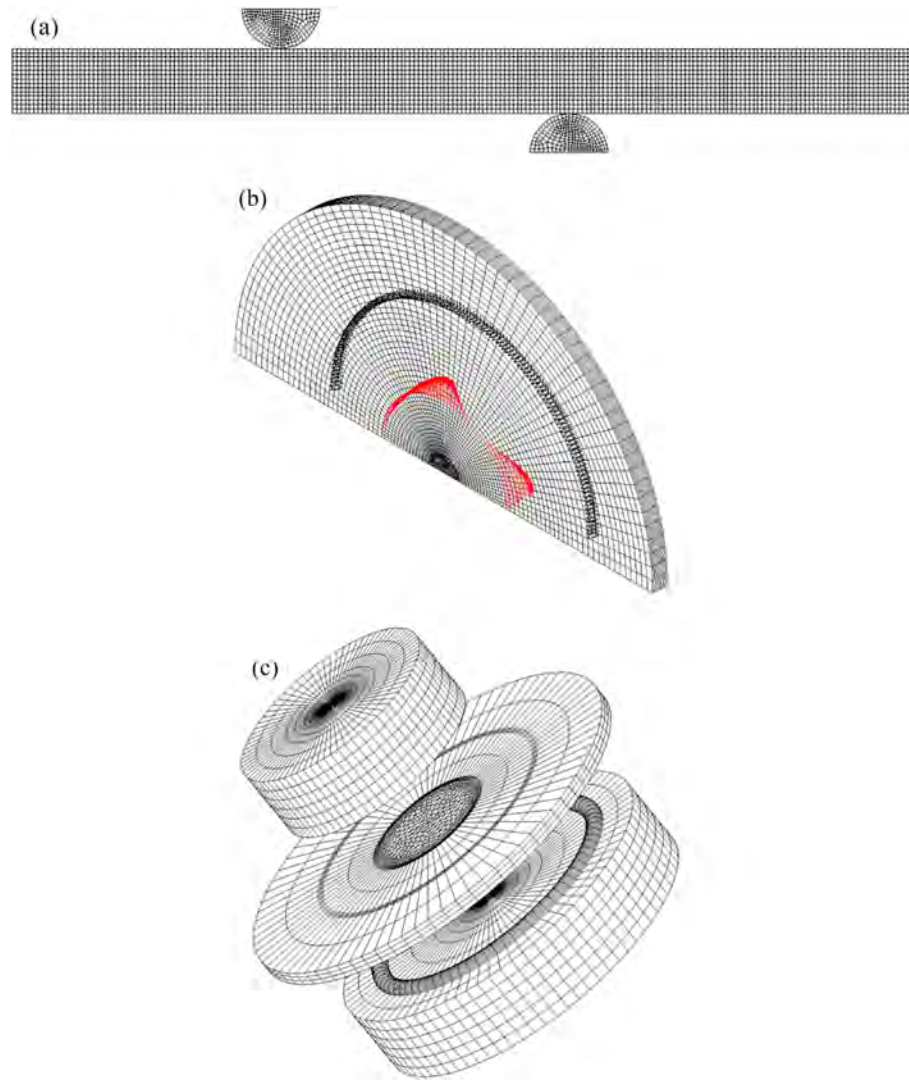


Fig. 4. Models and mesh for the FEA analysis. (a) Shows the model to investigate the influence of friction, (b) shows the model to test the influence of uneven loading with parameters $A = 100\%$ and $Z = 3$. The bottom plane in (b) marks the symmetry plane employed to reduce processing time. (c) Shows the model of the full testing assembly for more precise calculations of uneven surfaces.

nearly identical. A significant difference in strength and effective area between B3B and RoR samples is evident. When the effective area is considered, RoR specimens show a lower strength and higher effective area than B3B samples, as seen in Fig. 5(b). The regression fits all but two datasets (R-28-1 and B-28-1.7-BT), which were not considered since their testing details deviated from the standard procedure. The fit according to eq. (4) implies $m_{reg} = 30$, which is in excellent agreement with all datasets except R-28-1. Note the high difference in strength between all RoR sample sets and R-28-1. Furthermore, B-28-1.7-BT samples deviate by exhibiting significantly higher strength than other B3B sample sets.

Two samples were not tested in accordance with standards or

established guidelines: B-28-1.7-BT and R-28-1. B-28-1.7-BT was tested with Flashbreaker® 1 on its compressive side to observe the influence of intermediate layers on force application and strength measurement for the B3B test. The R-28-1 RoR-specimens were tested without any intermediate layers. It is evident that a significant deviation from other samples ensued.

In the B3B test, as compared to B-28-1.7, specimens tested with an interlayer on the compressive side (B-28-1.7-BT) show a significantly increased strength (i.e. +5%). This can be explained by a change in load application.

The factor f was determined assuming a point load, i.e. with a contact

Table 4

Results of strength testing of various specimens. m and σ_0 as described beforehand, with indices “lower” and “upper” referring to the borders of their 90% confidence interval. S_{eff} refers to the average effective area of specimens tested.

Designation	N [-]	m [-]	m_{lower} [-]	m_{upper} [-]	σ_0 [MPa]	$\sigma_{0, lower}$ [MPa]	$\sigma_{0, upper}$ [MPa]	S_{eff} [mm ²]
B-28-1	30	26	19	31	375	370	380	0.245
B-28-1.7	30	29	22	36	360	356	364	0.965
B-28-1.7-BT	32	34	26	41	381	378	385	0.770
R-28-1	28	15	11	19	242	237	248	126.8
R-28-1-T	30	34	26	42	305	302	308	116.8
R-28-1-BT	29	36	27	44	307	304	310	116.4

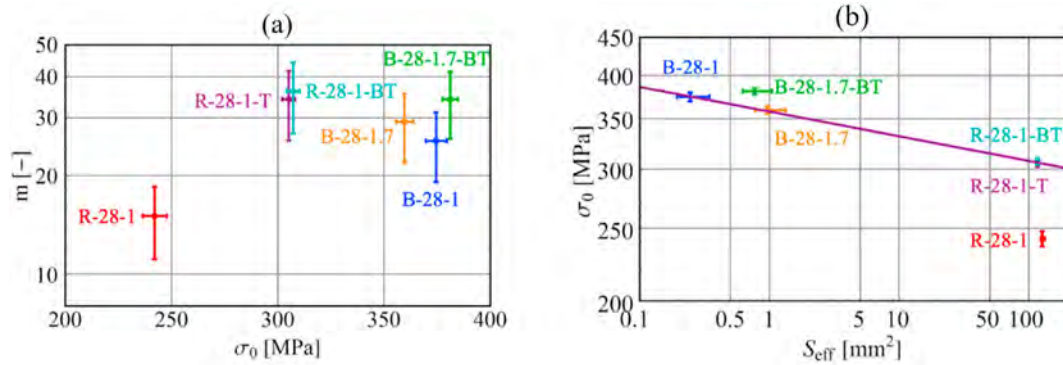


Fig. 5. Results of strength testing. (a) Depicts the Weibull modulus m and the characteristic strength σ_0 as well as their confidence intervals, (b) depicts the characteristic strength for each sample depending on their effective area S_{eff} .

radius $R_c = 0 \text{ mm}$. For load introduction over an actual contact area under the ball with a Hertzian contact pressure [50] $f(R_c > 0 \text{ mm})$ depends on the contact radius (which increases with applied load), as can be seen in Fig. 6. Note that the circles in Fig. 6 indicate the values of $f(R_c = 0 \text{ mm})$. For most testing situations covered with available FEA results [10,11] the specimens will fracture at loads which are low enough to give small contact areas. For such small contact areas, the actual f is not much different from $f(R_c = 0 \text{ mm})$. For example, the dashed areas in Fig. 6 refer to a decrease of maximal 2% in f , which is an experimental error that is acceptable.

Using the information from Fig. 6 the effect of a compliant interlayer on B3B strength results can be explained qualitatively. A soft interlayer will lead to an increased contact area between the loading ball and the specimens as compared to the situation without any layer, resulting in a lower value of $f(R_c)$ and a lower maximum stress. An increased load will be necessary to break the specimen. If $f(R_c = 0 \text{ mm})$ which is greater than $f(R_c > 0 \text{ mm})$ is used for the evaluation of strength from the fracture load, the strength of each specimen will be overestimated. This statement relies on the assumption that the effective area is not changed substantially. Using compliant layers for the Ball-on-Three-Balls-test creates a load

introduction situation which deviates from the assumptions that were made for theoretical stress evaluation. Consequently, incorrect stress results will be obtained.

For the RoR set-up, tests without interlayers (R-28-1) which are influenced by friction, lead to an approximately 20% lower strength as compared to tests with applied interlayers (R-28-1-T and R-28-1-BT).

To investigate the influence of friction on the stress in the disc, the stress on the tensile surface along a radial path from the disc center to its edge was evaluated for varying friction coefficients and compared with the analytical solution found by Fessler & Fricker [40]. The numbers presented were evaluated for a typical fracture load for our specimens, i.e. 600 N. Only radial stresses are shown since tangential stress exhibit the same behavior with a lower stress concentration near the loading ring position. Fig. 7(a) shows the FEA results of radial (σ_r) stress in absolute values, Fig. 7(b) displays the radial stress results σ_r normalized by the central stress $\sigma_i = \sigma_r(r = 0)$. Fig. 7(c) shows the results as predicted by equation 14–16 in Fessler & Fricker in absolute values, and the normalized curves are found in Fig. 7(d). The dashed line represents the position of the loading ring. The exact results of σ_i and $\sigma_{r,max}$ and their comparison to Fessler & Fricker can be found in Table 5.

As indicated by the FEA results, an increase in friction results in a decrease in radial stress at the loading ring radius (up to ~8% with $\mu = 0.5$) and a decrease in radial and tangential stress in the central region (up to ~10% with $\mu = 0.5$). The position of maximum stress moves towards the loading ring radius but not outside the central region. These findings for the central region are in good accordance with Fessler & Fricker [40]. As indicated by the FEA results, an increase in friction results in a decrease of stress throughout the specimen. The relative stress concentration near the load ring position ($\sigma_{r,max}/\sigma_i$) increases as friction increases. According to FEA this effect is not very strong (1.6% for $\mu = 0-3.4\%$ for $\mu = 0.5$, cp. Table 5). This is much lower than predicted by the Fessler & Fricker solution which results in up to 13% for $\mu = 0.5$. However, it is stated in Ref. [40] that the analytical model overestimates the stress at the loading ring radius due to a discontinuity in the equations, which explains the difference with respect to the FEA results. Thus, only a very small influence on the effective area can be expected from this effect, but an increased probability of failure from locations near the load ring radius. If friction is not eliminated, higher loads are necessary for specimens to fail and thus the strength would be overestimated. For the given geometry, and from the data in Table 5 this effect is estimated to be in the order of 5%–10%. With our RoR-tests without any intermediate layers a significant decrease in apparent strength was observed. We conclude that the action of friction alone cannot explain the observed result.

Another approach to explain the low strength is a change in load application due to the omission of any intermediate layers. More precisely, instead of a perfect line contact along both the load and support ring, an uneven load application through several contact points is suspected. If layers were used, the slight differences of height along the rings

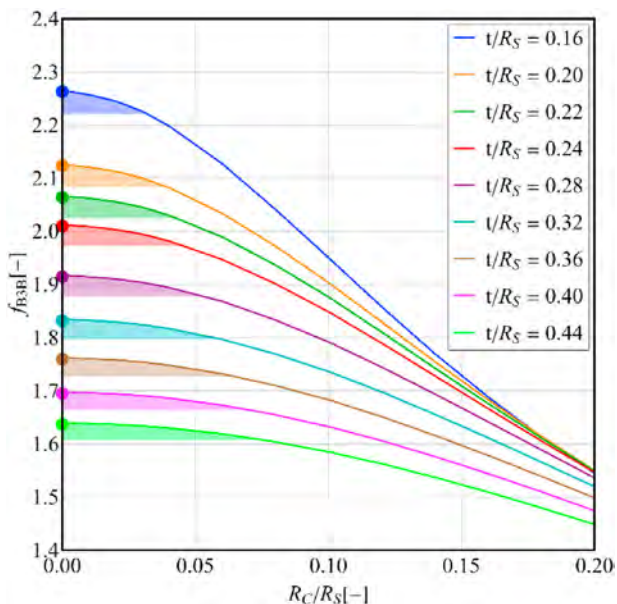


Fig. 6. Factor f depending on the Hertzian contact zone under the central loading ball for different values of thickness t to support radius R_s and the geometry $D = 12 \text{ mm}$, $D_s = 10 \text{ mm}$ and $\nu = 0.3$. The circles represent the values of f_{B3B} which are used for the evaluation of strength from fracture load. The shaded areas indicate an error $<2\%$ [50].

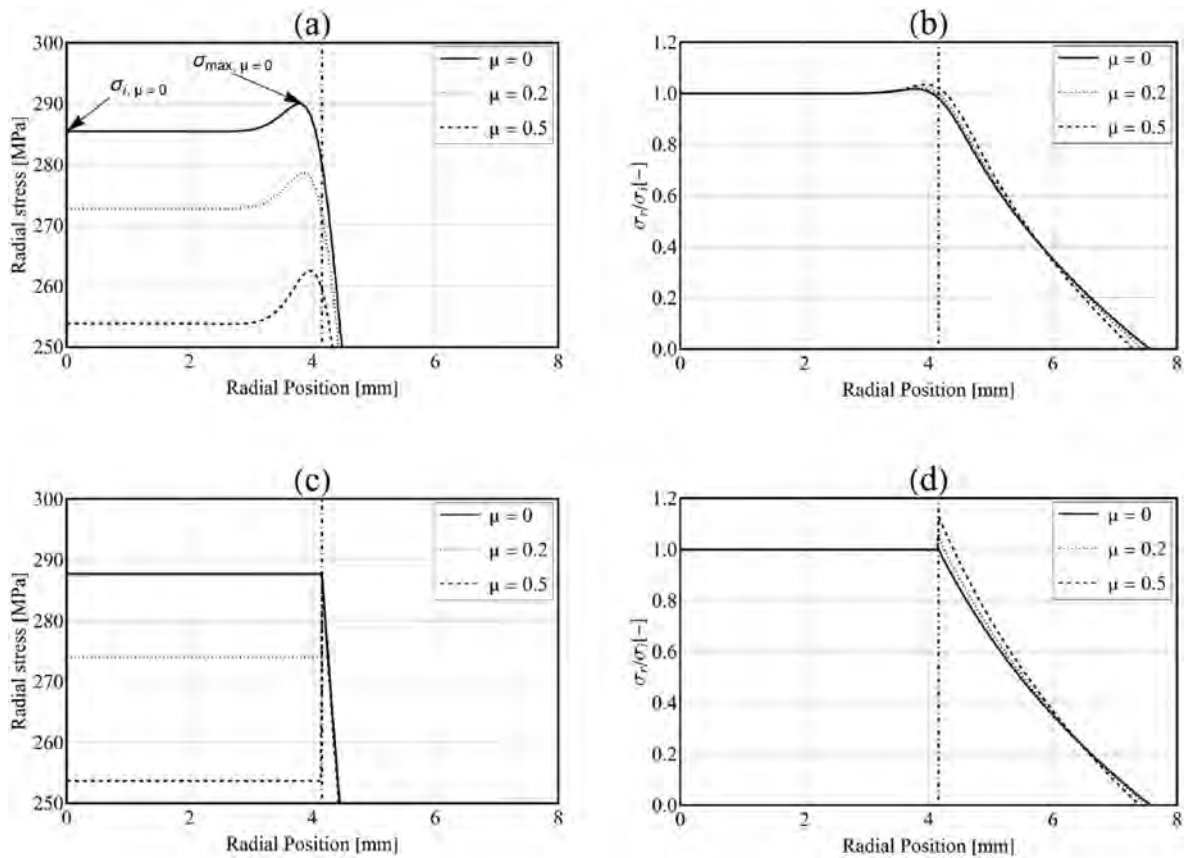


Fig. 7. Radial stress for different friction coefficients: (a) shows the absolute FEA results, (b) the normalized FEA results, (c) the absolute results of Fessler & Fricker and (d) the normalized results of Fessler & Fricker [40]. The dash-dotted line marks the position of the loading ring.

Table 5
Detailed results of FEA and Fessler & Fricker’s analytical solution for radial stress.

Friction Coefficient	$\sigma_i/\sigma_{i,\mu=0}$ FEA	$\sigma_i/\sigma_{i,\mu=0}$ Fessler	$\sigma_{r,max}/\sigma_i$ FEA	$\sigma_{r,max}/\sigma_i$ Fessler	$\sigma_{max,FEA}/\sigma_{max,Fessler}$
$\mu = 0$	1	1	1.016	1	1.008
$\mu = 0.1$	0.978	0.976	1.018	1.024	0.988
$\mu = 0.2$	0.956	0.953	1.021	1.048	0.969
$\mu = 0.3$	0.934	0.929	1.025	1.075	0.951
$\mu = 0.4$	0.911	0.905	1.029	1.102	0.933
$\mu = 0.5$	0.890	0.882	1.034	1.131	0.915

and specimens would be mitigated out, but without any layers they might influence load introduction in a way that would underestimate the samples strength. The FEA results in the case of ideal conditions (i.e. a constant line load) and 5 load maxima are shown in Fig. 8. The parameter A was set to 100%, meaning that the force along the loading ring diameter oscillates between 0% and 200% of the constant line load. Alongside that, the maximum stress at the tensile face is displayed in Table 6 and selected stress trends are shown in Fig. 9. Localized stress concentration along the loading ring circumference occur, while the stress level in the center of the disc remains unchanged. With an increasing amount of load maxima, the maximum stress decreases. Note that these results were obtained without considering friction. As previous results have shown, friction would result in a small general decrease of stress, similar to the trend shown in Fig. 7(a). However, the large stress concentrations at the loading ring radius would still be present.

It can be expected that this leads to an increased number of fractures from these locations of stress concentration. Additionally, these specimens will also fracture at a lower load compared to specimens that fail from the central region and consequently their strength will be

underestimated. It can also be expected, that this results in an increased scatter in strength, i.e. a lower Weibull modulus.

Note the difference in maximum stress for the case of three load maxima compared to ideal conditions, which is equal to an increase of nearly 20%. The difference in strength between the datasets R-28-1-T and R-28-1 is approximately 20% as well.

For a more accurate representation of the real loading scenario, the full model with a modified surface on the loading ring was evaluated. The results for the contact model shown in Fig. 4(c) with a maximum difference of 10 μm between the highest and lowest points of the loading ring surface are shown in Fig. 10(a). Even at a load similar to the fracture load during our experiments, full contact along the load ring cannot be achieved. Alternating regions of contact and no contact ensue. As can be seen in Fig. 10(b), a 3D-scan of the loading ring used in this work shows that even by machining with care a variation of about 20 μm between the highest and lowest points of such a ring can be present. Even smaller differences than what we found on a turned ring can result in a partial loss of contact along the circumference and an increase in stress at the remaining contact areas.

To verify the predicted results, the fractures of specimens from sets R-28-1, R-28-1-T and R-28-1-BT were investigated on a macroscopic scale. According to the positions of fracture origins, specimens were allocated to one of three groups:

- Fracture origin at or very close to the loading ring
- Fracture origin in the central region
- Location of fracture origin not identifiable, unknown

Since the number of unknown fracture origins were about 30% independent of the investigated sample, only the differences in clearly assignable fractures are discussed. In Fig. 11, it is evident that dataset R-

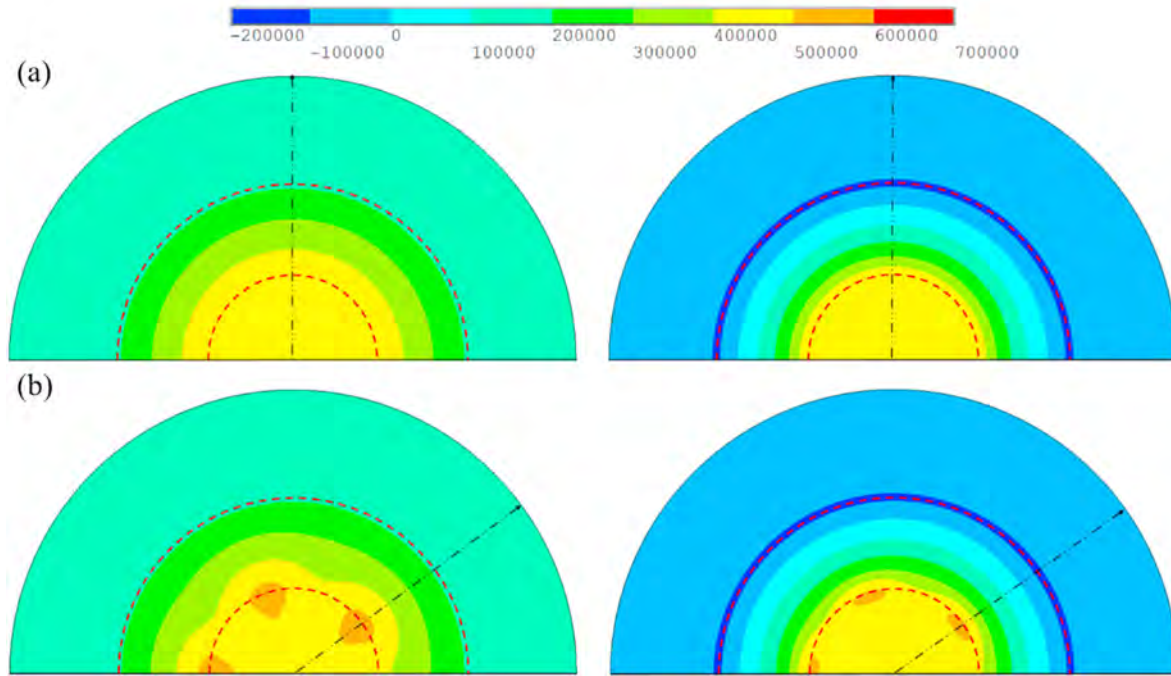


Fig. 8. Tangential (left) and radial (right) stress field (in Pa/N) for two cases of load introduction: ideal load introduction (a) and 5 load maxima (b). The dashed lines mark the load- and support-ring positions. The paths along which the stress trends in Fig. 9 are evaluated are marked by the dashed-dotted arrow.

Table 6

Maximum radial ($\sigma_{r,max}$) and tangential ($\sigma_{t,max}$) tensile stress for different load introduction cases as well as their ratios to the central stress (σ_i).

No. of Osz. [-]	$\sigma_{r,max}$ [MPa]	$\sigma_{r,max}/\sigma_i$ [-]	$\sigma_{t,max}$ [MPa]	$\sigma_{t,max}/\sigma_i$ [-]
Z = 0	290	1.016	287	1.005
Z = 3	337	1.181	338	1.184
Z = 5	312	1.093	320	1.121
Z = 10	296	1.037	301	1.054

28-1 (without interlayers) exhibits a significantly higher fraction of fractures from the loading ring, while the specimens with interlayers (R-28-1-T and R-28-1-BT) have a higher number of fractures from the center. No major distinction between dataset R-28-1-T and R-28-1-BT were found. Contrary to the Ball-on-Three-Balls-test, using no compliant layers for the Ring-on-Ring-test creates a load introduction situation which deviates from the assumptions that were made for analytical stress evaluation. Consequently, incorrect stress results will be obtained.

4. Summary

Biaxial strength tests were conducted on a commercial alumina ceramic (Frialit 99.7, Kyocera) using the Ball-on-Three-Balls-test and the Ring-on-Ring-test. Two different specimen thicknesses were investigated and details of the test procedure, namely the use of compliant layers, were varied. The results were compared based on the size effect predicted by Weibull fracture statistics. Additionally, the influence of friction and uneven loading was investigated using Finite-Element-Analysis.

Generally, it could be shown experimentally that both tests deliver comparable results within a Weibull approach. The B3B test can thus be used to evaluate the strength of specimen that may be too small or too thin to be tested with the RoR-test. This holds true as long as the tests are performed in a way where the real loading situation is as close as possible to the one assumed for the theoretical description of the test.

For the numerical evaluation of the B3B-test, load application by a point load is assumed, which is realized in most testing situations. If compliant interlayers are used between the loading ball and the specimen, the assumption is corrupted and a significant strength

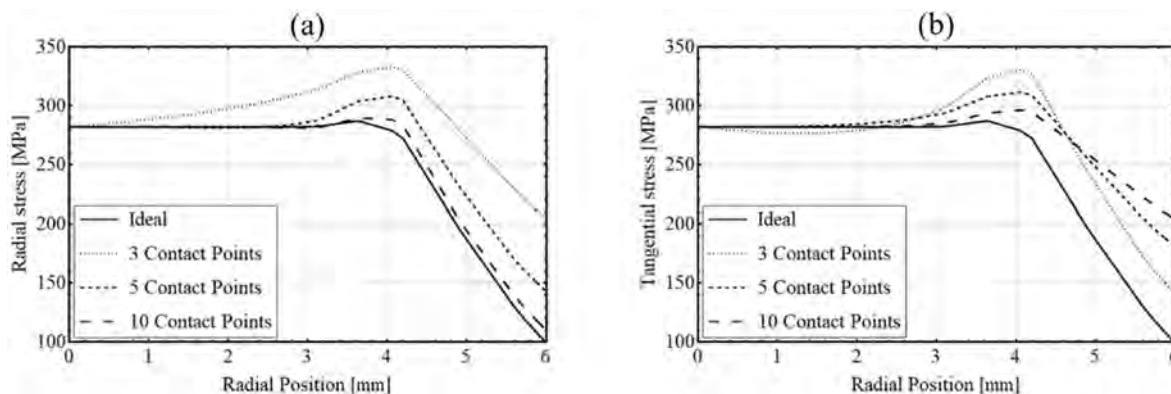


Fig. 9. Comparison of radial (a) and tangential (b) stress trends for various pointwise and ideal load introduction cases.

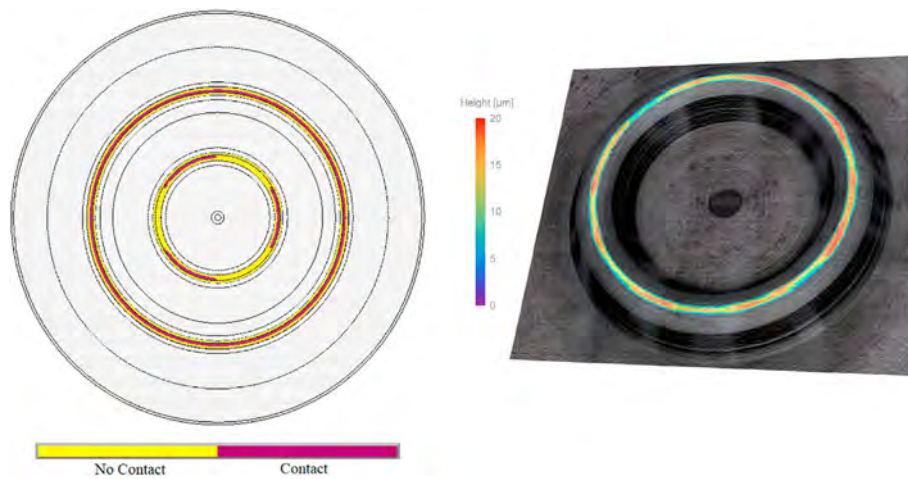


Fig. 10. (a) shows the contact status of the FEA model with a wavy loading ring surface, (b) shows a scan of the used loading ring.

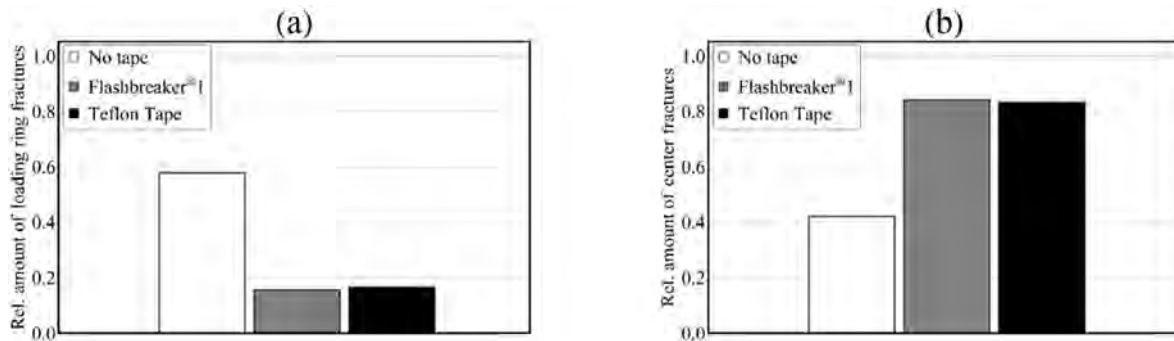


Fig. 11. Positions of fracture origins for the datasets R-28-1 (white), R-28-1-BT (gray) and R-28-1-T (black). (a) Shows the amount of fracture origins at or very close to the loading ring, (b) the amount of fracture origins at the center.

overestimation may result.

For the analytical description of the RoR-test, frictionless testing and uniform load introduction is assumed. If friction is not avoided, the specimen strength will be overestimated. If deviations from uniform ring-load introduction are present, the specimen strength will be underestimated due to the formation of regions of increased stress at the loading ring circumference. Even for deviations as small as a waviness of the loading ring surface of $\pm 5 \mu\text{m}$, regions without any contact of the loading ring and the specimen form and an increase in stress in the remaining regions ensues. Compliant interlayers help to achieve uniform load introduction with the additional benefit of a reduction of friction in the RoR-test.

Finite Element Analysis findings are supported by experimental results and fractography.

Declaration of competing interest

The authors declare that they have no known competing financial interests or personal relationships that could have appeared to influence the work reported in this paper.

Acknowledgements

M. Staudacher gratefully acknowledges financial support by the Austrian BMVIT and BMWFV in the project “CharAM” (FFG 877684) of the COIN/IraSME program. J. Schlacher gratefully acknowledges financial support by the ERC Consolidator Grant 817615 – “CeraText”. Furthermore, the authors want to thank the reviewers for their valuable input during revision.

References

- [1] R.N. Katz, Overview of ceramic materials, design, and application, in: M. Kutz (Ed.), *Mechanical Engineers' Handbook 1: Materials and Mechanical Design*, third ed., Wiley, Hoboken, N.J., 2006, pp. 433–449.
- [2] D. Munz, T. Fett, *Ceramics: Mechanical Properties, Failure Behaviour, Materials Selection*, Springer, Berlin, Heidelberg, 1999.
- [3] C.R. Brinkman, S.F. Duffy, *Life Prediction Methodologies and Data for Ceramic Materials*, ASTM International, 100 Barr Harbor Drive, PO Box C700, West Conshohocken, PA, 1994, 19428-2959.
- [4] J.B. Wachtman, M.J. Matthewson, W.R. Cannon, *Mechanical Properties of Ceramics*, Wiley, Hoboken, New Jersey, 2009.
- [5] D. Shetty, A.R. Rosenfield, P. McGuire, G.K. Bansal, W.H. Duckworth, *Biaxial Flexure Test for Ceramics*, American Ceramic Society Bulletin, 1980, pp. 1193–1197.
- [6] C. ASTM, *Test Method for Monotonic Equibiaxial Flexural Strength of Advanced Ceramics at Ambient Temperature*, ASTM International, West Conshohocken, PA, 2005, 1499-05.
- [7] ISO 17167:2018, *Fine Ceramics (Advanced Ceramics, Advanced Technical Ceramics) — Mechanical Properties of Monolithic Ceramics at Room Temperature — Determination of Flexural Strength by the Ring-On-Ring Test*, International Organization for Standardization, Geneva, Switzerland, 2018.
- [8] G. Isgrò, P. Pallav, J.M. van der Zel, A.J. Feilzer, The influence of the veneering porcelain and different surface treatments on the biaxial flexural strength of a heat-pressed ceramic, *J. Prosthet. Dent* 90 (2003) 465–473.
- [9] EN ISO 6872:2015: *Zahnheilkunde - Keramische Werkstoffe*, Europäisches Komitee für Normung, 2015.
- [10] A. Börger, P. Supancic, R. Danzer, The ball on three balls test for strength testing of brittle discs: stress distribution in the disc, *J. Eur. Ceram. Soc.* 22 (2002) 1425–1436.
- [11] A. Börger, P. Supancic, R. Danzer, The ball on three balls test for strength testing of brittle discs: Part II: analysis of possible errors in the strength determination, *J. Eur. Ceram. Soc.* 24 (2004) 2917–2928.
- [12] T. Fett, G. Rizzi, E. Ernst, R. Müller, R. Oberacker, A 3-balls-on-3-balls strength test for ceramic disks, *J. Eur. Ceram. Soc.* 27 (2007) 1–12.
- [13] R. Morell, *Biaxial Flexural Strength Testing of Ceramic Materials: A National Measurement Good Practice Guide No. 12*, National Physical Laboratory, 2007.

- [14] L.M. Powers, J.A. Salem, A.S. Weaver, Stresses in ceramic plates subjected to loading between concentric rings, in: J.A. Salem (Ed.), *Fracture Resistance Testing of Monolithic and Composite Brittle Materials*, ASTM International, West Conshohocken, Pa., 2002, pp. 30–45.
- [15] W. Harrer, R. Danzer, P. Supancic, T. Lube, Einfluss von Kontaktspannungen auf die Festigkeit im 4-Kugelversuch, *Pharm. Manag. PM* 45 (2008) 18–32.
- [16] R. Danzer, P. Supancic, W. Harrer, T. Lube, A. Börger, Biaxial strength testing on mini specimens, in: Gdoutos E.E. (eds) *Fracture of Nano and Engineering Materials and Structures*. Springer, Dordrecht, pp. 589–590.
- [17] M. Deluca, R. Bermejo, M. Pletz, P. Supancic, R. Danzer, Strength and fracture analysis of silicon-based components for embedding, *J. Eur. Ceram. Soc.* 31 (2011) 549–558.
- [18] M. Gruber, I. Kraveva, P. Supancic, J. Bielen, D. Kiener, R. Bermejo, Strength distribution and fracture analyses of LiNbO₃ and LiTaO₃ single crystals under biaxial loading, *J. Eur. Ceram. Soc.* 37 (2017) 4397–4406.
- [19] E. Özkol, A.M. Wätjen, R. Bermejo, M. Deluca, J. Ebert, R. Danzer, R. Telle, Mechanical characterisation of miniaturised direct inkjet printed 3Y-TZP specimens for microelectronic applications, *J. Eur. Ceram. Soc.* 30 (2010) 3145–3152.
- [20] M. Wendler, R. Belli, A. Petschelt, D. Mevec, W. Harrer, T. Lube, R. Danzer, U. Lohbauer, Chairside CAD/CAM materials. Part 2: flexural strength testing, *Dent. Mater.* 33 (2017) 99–109.
- [21] J.R. Wachtmann, Jr, W. Capps, J. Mandel, Biaxial flexure tests of ceramic substrates, *J. Mater.* (1972) 188–194.
- [22] R. Bermejo, P. Supancic, I. Kraveva, R. Morrell, R. Danzer, Strength reliability of 3D low temperature co-fired multilayer ceramics under biaxial loading, *J. Eur. Ceram. Soc.* 31 (2011) 745–753.
- [23] W. Harrer, R. Danzer, P. Supancic, T. Lube, Influence of the sample size on the results of B3B-tests, *KEM* 409 (2009) 176–184.
- [24] Chair of structural and functional ceramics, ball-on-3-balls test (B3B) – strength testing, <https://www.isfk.at/interaktive-berechnungstools/b3b-strength-test>, accessed 14 December 2020.
- [25] R. Danzer, P. Supancic, W. Harrer, (Hrsg), in: J. Kriegsmann (Ed.), *Der 4-Kugelversuch zur Ermittlung der biaxialen Biegefestigkeit spröder Werkstoffe*, Technische keramische Werkstoffe, 2009, pp. 1–48.
- [26] J.A. Salem, L. Powers, Guidelines for the testing of plates, in: H.-T. Lin, W.M. Kriven (Eds.), *27th International Cocoa Beach Conference on Advanced Ceramics and Composites*: January 26–31, 2003, Cocoa Beach, Florida, American Ceramic Society, Westerville, Ohio, 2003, pp. 357–364.
- [27] ASTM F394-78: Test Method for Biaxial Flexure Strength (Modulus of Rupture) of Ceramic Substrates (Discontinued 2001), ASTM International, West Conshohocken, PA, 1996.
- [28] C. Quintana, C. Rodríguez, F.J. Belzunce, A.C. Caballero, C. Baudín, Ceramic materials characterization using miniature mechanical tests: comparison between B3B and SPT tests, *J. Eur. Ceram. Soc.* 39 (2019) 4113–4121.
- [29] Y. Torres, R. Bermejo, F.J. Gotor, E. Chicardi, L. Llanes, Analysis on the mechanical strength of WC-Co cemented carbides under uniaxial and biaxial bending, *Mater. Des.* 55 (2014) 851–856.
- [30] C. ASTM, Practice for Size Scaling of Tensile Strengths Using Weibull Statistics for Advanced Ceramics, ASTM International, West Conshohocken, PA, 2019, 1683 - 10.
- [31] R. Danzer, T. Lube, P. Supancic, R. Damani, Fracture of ceramics, *Adv. Eng. Mater.* 10 (2008) 275–298.
- [32] W. Weibull, *A Statistical Theory of the Strength of Materials*, Generalstabens Litografiska Anstalts Förlag, Stockholm, 1939.
- [33] R. Danzer, A general strength distribution function for brittle materials, *J. Eur. Ceram. Soc.* 10 (1992) 461–472.
- [34] W. Weibull, A statistical distribution function of wide applicability, *J. Appl. Mech.* 18 (1951) 293–297.
- [35] S. Nohut, A general formulation for strength prediction of advanced ceramics by ball-on-three-balls (B3B)-test with different multiaxial failure criteria, *Ceram. Int.* 38 (2012) 2411–2420.
- [36] R.L. Barnett, P.C. Hermann, J.R. Wingfield, C.L. Connors, *Fracture of Brittle Materials under Transient Mechanical and Thermal Loading*, IIT Research Inst, Chicago IL, 1967.
- [37] FRIATEC GmbH, Division Keramik (Mannheim, DE), Werkstoffdatenblatt FRIALIT F99,7.
- [38] D.J. Godfrey, S. John, Disc flexure tests for the evaluation of ceramic strength, *Proceedings 2nd International Conference of Ceramic materials and Components for Engines* (1986) 657–665.
- [39] R. Danzer, A. Börger, P. Supancic, M.A. Ruiz Villanueva, Ein einfacher Festigkeitsversuch für Scheiben aus spröden Werkstoffen, *Mat.-wiss. u. Werkstofftech.* 34 (2003) 490–498.
- [40] H. Fessler, D.C. Fricker, A theoretical analysis of the ring-on-ring loading disk test, *J. Am. Ceram. Soc.* 67 (1984) 582–588.
- [41] W. Adler, D. Mihora, Biaxial flexure testing: analysis and experimental results, in: *Fracture Mechanics of Ceramics*, pp. 227–245.
- [42] A. Wereszczak, T.P. Kirkland, K. Breder, H. Lin, M. Andrews, Biaxial strength, strength-size-scaling, and fatigue resistance of alumina and aluminum nitride substrates, *Int. J. Microcircuits Electron. Packag.* 22 (1999) 446–458.
- [43] H.L. Frandsen, Weibull statistics effective area and volume in the ball-on-ring testing method, *Mech. Mater.* 73 (2014) 28–37.
- [44] High-tech-flon® films and fabrics (konstanz, DE), produktinformation PTFE virginale folie 0.05 - 600. <https://shop.hightechflon.com/ptfe-folie-teflon-folie-virginale-0.05mm-wei%3%9f/Page-16-1-126-176.aspx>, 2020. (Accessed 18 February 2020).
- [45] High-tech-flon® films and fabrics (konstanz, DE), produktinformation PTFE klebeband 0.08 V SW. <https://shop.hightechflon.com/P/TFE-Teflon-virginale-Klebeband-0,08-V-SW-0,08mm/Page-16-1-97-71.aspx>, 2020. (Accessed 18 February 2020).
- [46] AIRTECH europe sarl (differdange, LU), datenblatt Flashbreaker®, https://catalog.airtechintl.com/product_estore.php?product_id=1145&lang=EN, 2019. (Accessed 18 February 2020), 1.
- [47] T. Lube, W. Harrer, P. Supancic, Practical Guide to Ball-on-three-Balls (B3B-) Testing. Ber-2010-066-Tlu,wha,phs, ISFK, 2019.
- [48] R. Danzer, W. Harrer, P. Supancic, T. Lube, Z. Wang, A. Börger, The ball on three balls test—strength and failure analysis of different materials, *J. Eur. Ceram. Soc.* 27 (2007) 1481–1485.
- [49] R. Danzer, T. Lube, P. Supancic, Monte-carlo simulations of strength distributions of brittle materials - type of distribution, specimen- and sample size, *Z. Metallkd.* 92 (2001) 773–783.
- [50] T. Lube, P. Supancic, T. Albrecht, H. Bürke, *Strength Tests with Biaxial Loading - a Comparison of Methods*, Messe München, 2018.

Paper D

J. Schlacher, T. Lube, W. Harrer, G. Mitteramskogler, M. Schwentenwein, R. Danzer, R. Bermejo: "Strength of Additive Manufactured Alumina", *Journal of the European Ceramic Society* **40** [14] (2020), 4737-4745, <https://doi.org/10.1016/j.jeurceramsoc.2020.03.073>

Open access article distributed under the terms of the Creative Commons CC-BY license



Original Article

Strength of additive manufactured alumina

J. Schlacher^{a,*}, T. Lube^a, W. Harrer^a, G. Mitteramskogler^b, M. Schwentenwein^b, R. Danzer^a, R. Bermejo^a

^a Department of Materials Science, Montanuniversitaet Leoben, Franz Josef-Strasse 18, A-8700, Leoben, Austria

^b Lithoz GmbH, Mollardgasse 85a/2/64-69, A-1060, Wien, Austria



ARTICLE INFO

Keywords:

Additive manufacturing
Alumina
LCM
Strength
Fractography

ABSTRACT

The strength of 3D-printed alumina parts fabricated using the Lithography-based Ceramic Manufacturing (LCM) technology is investigated. The influence of the sintering parameters, printing direction, surface condition (i.e. machined or as-printed), and/or geometry on the strength distribution is studied under uniaxial and biaxial bending tests. Weibull parameters, i.e. characteristic strength and Weibull modulus, are determined and compared between the different samples. Experimental findings show that samples sintered at higher temperatures yield higher Weibull modulus, associated with a more homogeneous microstructure. Fractographic analyses reveal the influence of surface finish (as-printed or machined) on strength and show the importance of reporting testing configuration along with printing direction to assess the mechanical response of 3D-printed parts. Based on these results, manufacturing recommendations are given which shall advance the progress in optimization of alumina ceramics fabricated using the LCM technology.

1. Introduction

Due to their outstanding properties, e.g. biocompatibility, wear resistance, resistance to corrosion, among others, advanced ceramics have established as materials for exceptional usage in the technical applications [1]. A critical aspect in the fabrication of ceramic materials is associated with the relatively expensive and time consuming step of machining the sintered material in order to shape the final ceramic component. This poses a limitation in the design of complex parts [2]. In recent years, the developments in the sector of additive manufacturing, especially in the area of metals and polymers, have provided with optimal solutions for designing complex materials systems [3,4]. An overview of the current methods and capabilities of additive manufacturing in the field of ceramics can be found in [5]. Among the different techniques, the Lithography-based Ceramic Manufacturing (LCM) technology has consolidated as a promising route to fabricate highly complex ceramic structures based on a *layer-by-layer* photopolymerisation process [6–9]. This method belongs to the stereolithographic printing techniques, and has been developed in the last years by the company Lithoz GmbH. In general, the LCM-process takes advantage of the photo-curable of the slurry, which consists of a homogeneously dispersed ceramic powder within a polymer matrix and enables thus the layer-by-layer fabrication of ceramic green-bodies. The polymer has to be removed after fabrication of the ceramic green body

in a debinding step. After a subsequent standard sintering process, ceramics with high density as compared to those fabricated with traditional processing routes can be manufactured [7]. More details on the manufacturing process can be found in [6–10]. There is a need to determine the mechanical properties of LCM-alumina in comparison to conventional alumina ceramics utilized in technical applications. In general, additive manufactured samples or parts are assembled layer-by-layer and hence a dependence of the mechanical properties on the printing direction as well as on the surface quality of the part may be expected, as shown in a preliminary study on uniaxial bend bars [11].

The aim of this work is to explore the microstructure-strength relationship of additive manufactured alumina, with special focus on the sintering conditions, surface quality and printing direction and their influence on strength. Different samples containing the same alumina slurry but with different printing directions, sintering parameters, surface condition (i.e. machined or as-printed), and/or geometry (i.e. prismatic bar or disc) are investigated. Uniaxial and biaxial bending tests in different configurations are performed to assess the effect of printing direction on the strength distribution of 3D-printed alumina parts. Results are analysed in the framework of Weibull statistics. Microstructural and fractographical analyses are carried out to interpret the strength results.

* Corresponding author.

E-mail address: josef.schlacher@unileoben.ac.at (J. Schlacher).

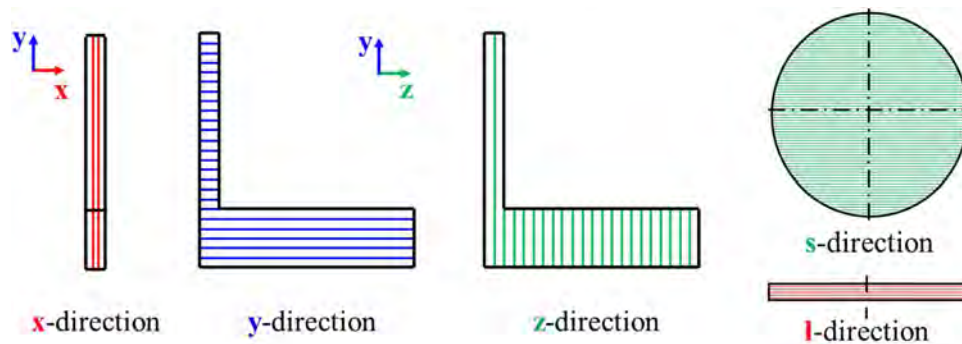


Fig. 1. Schematic illustration of layered L-shaped parts and discs showing the layer assembly with respect to the printing direction (i.e. x, y and z for L-shaped parts, and s and l for discs).

2. Experimental

2.1. Samples and tested geometries

All samples were produced by Lithoz GmbH, Vienna, Austria, via the LCM-technology using a CeraFab 7500 3D-printer. The ceramic material of study was alumina. The feedstock employed was LithaLox 350, an alumina-based, photocurable suspension. The characteristics of the alumina material are listed in the datasheets of the company [12]. Different samples containing the same alumina slurry but with different printing directions, sintering parameters, surface condition (i.e. machined or as-printed), and/or geometry (i.e. prismatic bar or disc) were investigated, referred to as A, B1, B2, and C hereof. Sample A was sintered at 1500 °C for 20 h and exhibited a relative density of approximately 96 %, whereas samples B1, B2, and C were sintered at 1650 °C for 2 h, with a relative density of 98 %. The individual printed layer thickness in samples A, B1 and B2 was ~50 µm before sintering, which corresponds to approximately 40 µm after sintering. In sample C the thickness was ~25 µm before sintering, i.e. ~20 µm after sintering. Fig. 1 shows schematically the printed “L-shaped” parts as well as “Disc-shaped” parts, indicating the corresponding layer assembly with respect to the three different printing directions, i.e. x, y and z for the L-shaped parts, and s and l for the discs.

In order to test samples A, B1 and B2 under uniaxial bending, standard bend bars of dimension $b = 2.5 \text{ mm}$, $h = 2 \text{ mm}$, $l \approx 25 \text{ mm}$ were cut out of the printed L-shaped parts, as shown schematically in Fig. 2 (bottom left). Three testing configurations were selected (Fig. 2, up and right) to account for the effect of the printed directions of the layers on the mechanical response of the parts. For testing sample C under biaxial bending, nominal sintered dimensions (i.e. diameter $D \approx 7.5 \text{ mm}$, and thickness $t \approx 1.3 \text{ mm}$) were taken without further machining, with the printed layers arranged as shown in Fig. 1 (right). The

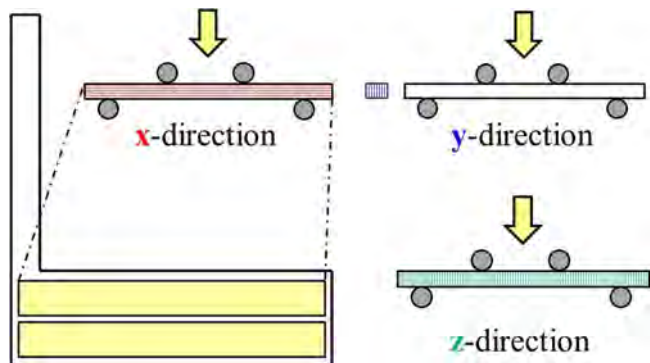


Fig. 2. (bottom left) Schematic of two bend bars cut out of the L-shaped part. (up and right) Schematic illustration of the bend bars in the three different testing directions (x, y and z).

Table 1

Samples of study classified according to the sintering condition, geometry, surface conditioning and testing configuration.

Sample	Sintering conditions	Geometry	Surface condition	Test configuration
A	1500 °C, 20h	Prismatic bar	Machined	x
	1500 °C, 20h	Prismatic bar	Machined	y
	1500 °C, 20h	Prismatic bar	Machined	z
B1	1650 °C, 2h	Prismatic bar	Machined	x
	1650 °C, 2h	Prismatic bar	Machined	y
	1650 °C, 2h	Prismatic bar	Machined	z
B2	1650 °C, 2h	Prismatic bar	As-printed	x
	1650 °C, 2h	Prismatic bar	As-printed	y
	1650 °C, 2h	Prismatic bar	As-printed	z
C	1650 °C, 2h	Disc	As-printed	s
	1650 °C, 2h	Disc	As-printed	l

testing surface (tensile side) in samples A and B1 was machined with a diamond wheel (grinding finish with a D15 grit), whereas samples B2 and C were tested as-printed.

Table 1 shows the different samples, according to the sintering condition, geometry, surface conditioning and testing configuration.

2.2. Surface characterization and microstructural analysis

In order to study the surface quality of the as-printed and diamond-ground samples, images of the tensile sides were taken using a scanning electron microscope (JEOL JCM-6000Plus Neoscope™, JEOL Ltd., Tokyo, Japan). To investigate the microstructures of the different samples A, B and C, cross-sections taken perpendicular and parallel to the printing direction were prepared. Four to six specimens were polished to a 1 µm mirror finish using a Struers Pedemax-2 equipment. Subsequently, thermal etching was carried out at 1400 °C for 20 min to reveal the grain boundaries. The grain size distributions were determined for each sample on SEM microstructures using the line-intersection method according to [13].

2.3. Mechanical testing and evaluation of strength

Uniaxial and biaxial bending tests were performed with respect to the printing direction as shown in Fig. 2, and specified in Table 1. The uniaxial bending strength was measured under four-point bending (4PB) in samples A, B1 and B2 (prismatic bars), following the standard EN 843-1 [14]. The biaxial strength was measured using the Ball-on-three-Balls (B3B) test in sample C (discs) [15,16]. In this loading configuration, the specimens are symmetrically supported by three balls on one face and loaded by a fourth ball in the centre of the opposite face; this guarantees well-defined three-point contacts. The four balls had a diameter of 5.5 mm. One of the main advantages of this method is that the maximal stress developed during the test is located far from the

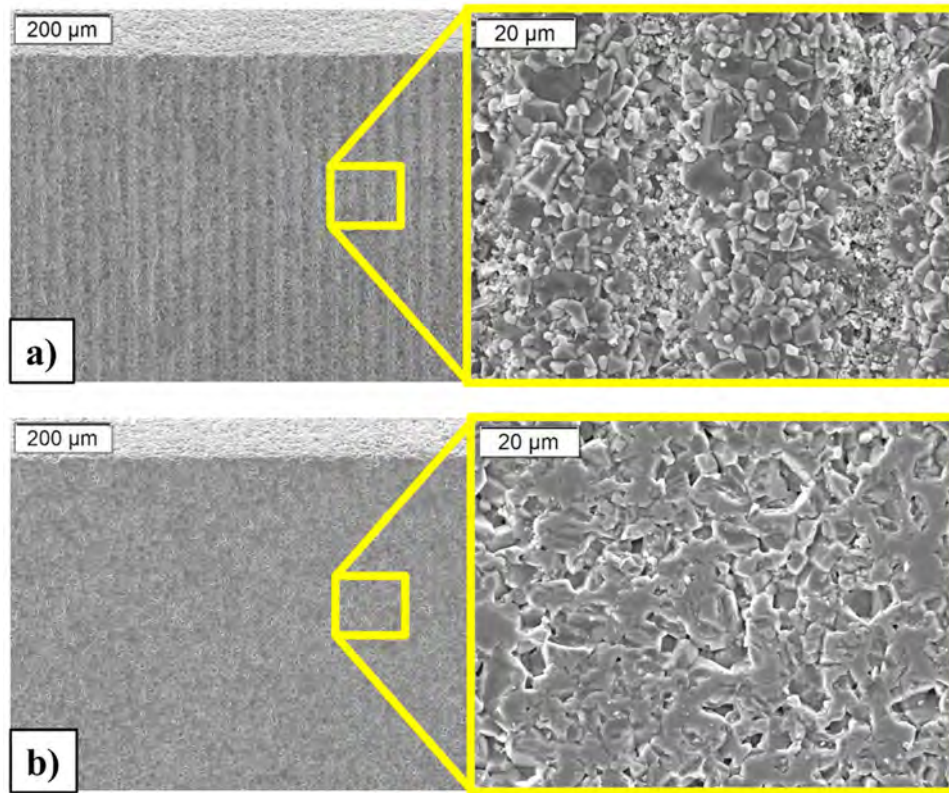


Fig. 3. Surface characteristics of the tensile sides: a) as-printed and b) machined condition.

edges (corners) of the sample, avoiding influence of edge defects [17]. Between 13 and 28 specimens were tested per sample for statistical significance. All bending tests were performed in ambient conditions, i.e. room temperature (~23 °C) and ~40 % relative humidity. A universal testing machine (Zwick 010, Zwick/Roell Ulm, Germany) with a load cell of 10 kN was employed for the uniaxial tests. The B3B-tests were carried out using a universal testing machine (Microstrain,

Messphysik, Fürstenfeld, Austria) with a load cell of 1 kN. A pre-load between 10 N and 20 N was applied to all specimens, which were loaded until fracture with a cross-head speed of 1 mm/min. The maximum load at fracture, F , of each specimen was recorded. The 4PB flexural strength σ_f was calculated as [14]:

$$\sigma_f = \frac{3 F (S_1 - S_2)}{2 b h^2}, \tag{1}$$

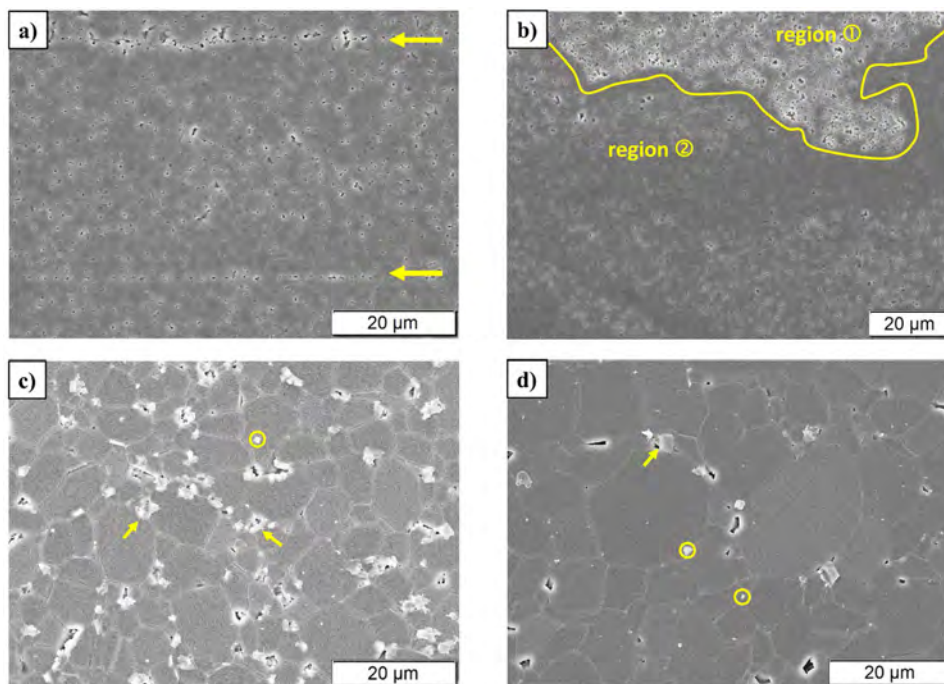


Fig. 4. Microstructures of LCM-alumina: a) sample A (cross-section perpendicular to the layers). The arrows indicate the layer boundaries, b) sample A (cross-section parallel to the layers). The yellow line separates the regions with different porosity, c) sample B, d) sample C. The arrows and the circles in (c) and (d) indicate the second phases [25].

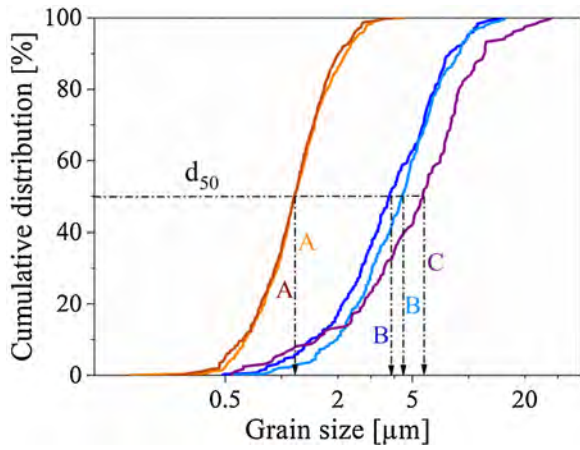


Fig. 5. Grain size distributions of the different samples A, B and C, with samples A and B measured both perpendicular and parallel to the printing layer direction, and sample C only in parallel direction.

where b is the specimen width, h is the specimen height, S_1 and S_2 are the outer and inner spans (i.e. 20 mm and 10 mm), respectively. In the B3B-test the strength is defined as the maximum tensile stress in the midpoint of the tensile side of the specimen, σ_{max} , and can be calculated according to [15]:

$$\sigma_{max} = f \frac{F}{t^2} \tag{2}$$

where F is maximum load at fracture, t is the specimen thickness, and f is a dimensionless factor, depending on the Poisson's ratio, specimen size and support geometry [15]. For alumina specimens, with a Poisson's ratio of 0.23, and thickness $t = 1.3$ mm, a factor $f \approx 1.6$ was calculated through an interactive tool at www.isfk.at [18].

The strength data were evaluated according to Weibull statistics [19], following the standard EN-843-5 [20]. The strength distributions were obtained and the characteristic strength, σ_0 , and Weibull modulus, m , were determined and compared for all samples [21,22].

2.4. Fractography

Fractographic analyses were carried out to investigate the failure origin, size, type and location of the critical flaws, following the recommendations as in [23,24]. Selected fracture surfaces of the tested specimens were gold coated using an Agar Sputter Coater, and subsequently investigated using a SEM (JEOL JCM-6000Plus Neoscope™, JEOL Ltd., Tokyo, Japan).

3. Results and discussion

3.1. Surface and microstructure

Fig. 3a and b shows SEM images in two different magnifications

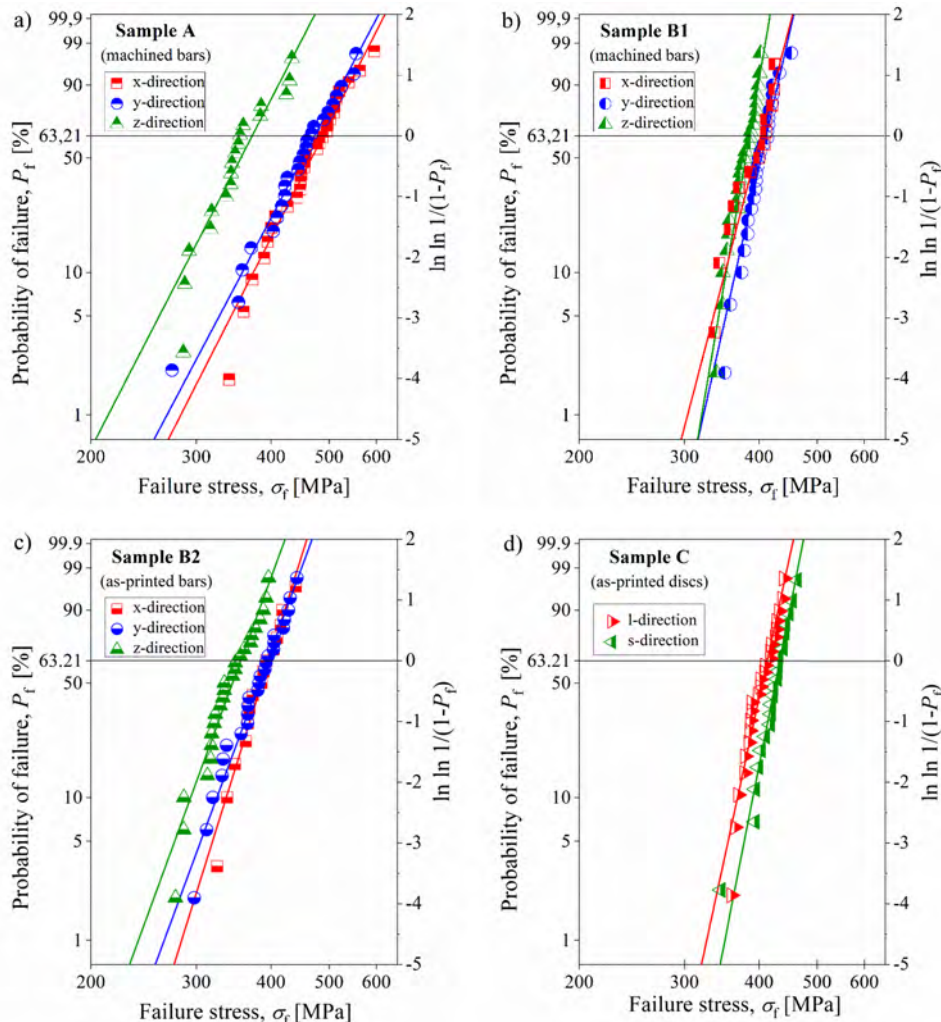


Fig. 6. Strength distributions of (a) sample A (bars, machined), (b) sample B1 (bars, machined), (c) sample B2 (bars, as-printed), and (d) sample C (discs, as-printed).

Table 2

Characteristic strength, σ_0 , and the Weibull modulus, m , with the corresponding 90 % confidence intervals for samples A, B1, B2 and C, for the different test configurations.

Sample	Test configuration	Number of specimens	Characteristic strength, σ_0 [MPa]	Weibull modulus, m [-]
A	x	28	488 [469–509]	8.4 [6.2–10.3]
	y	24	473 [451–496]	8.1 [5.8–10.1]
	z	18	372 [352–393]	8.3 [5.6–10.7]
B1	x	13	403 [389–417]	16.3 [10.0–21.5]
	y	25	411 [403–419]	18.9 [13.7–23.5]
	z	25	385 [380–391]	25.0 [18.1–30.9]
B2	x	15	397 [382–412]	13.7 [8.8–17.8]
	y	25	394 [382–407]	11.6 [8.4–14.4]
	z	25	356 [345–367]	11.7 [8.5–14.5]
C	s	22	433 [425–441]	21.8 [15.3–27.3]
	l	24	413 [405–421]	19.7 [14.2–24.6]

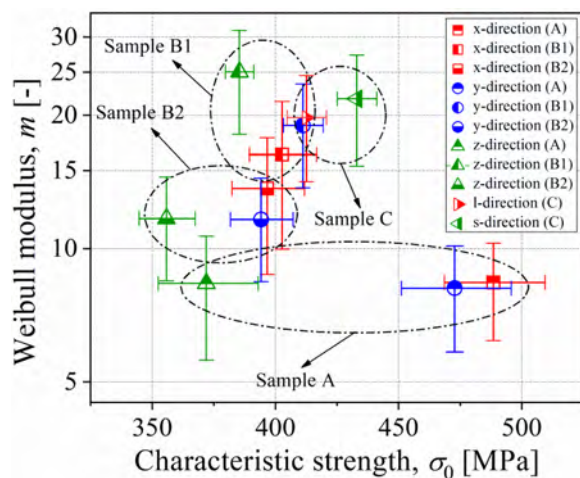


Fig. 7. Weibull modulus plotted versus the characteristic strength of samples A, B1, B2 and C for the different printing directions (x, y, z, l and s).

Table 3

Estimation of defect sizes for surface defects $a_{c,s}$ as well as volume flaws $a_{c,v}$ according to the Griffith criterion.

Sample	Test configuration	σ_0 [MPa]	$a_{c,s}$ [μm]	$a_{c,v}$ [μm]
A	x	488	10	30
	y	473	10	32
	z	372	17	50
B1	x	403	14	44
	y	411	14	42
	z	385	15	48
B2	x	397	15	45
	y	394	15	45
	z	356	20	56
C	s	433	12	38
	l	413	13	42

corresponding to the as-printed and machined tensile surface of bending bars (sample B), respectively. The wave-like structure of the as-printed surface in Fig. 3a is associated with the printing process. The "wave length" observed is of the order of the printing layer thickness. It is likely that this kind of structure is formed due to an overexposure of the polymer at the free edges of the part, which occurs when rather thick layers are printed. The surface of the bending bar specimens with machined surface appears relatively smooth, as can be seen in Fig. 3b.

Fig. 4a and b shows SEM microstructural images of cross-sections of sample A prepared perpendicular and parallel to the printing direction, respectively. It can be seen that this material has a relatively fine-grained microstructure; however, it exhibits a level of high porosity at the interfaces between the layers. This may be related to the lower

sintering temperature (i.e. 1500 °C). As a result, the layer boundaries are clearly distinguished in the SEM image (indicated by arrows in Fig. 4a). Nevertheless, regions immediately above or below the boundaries are rather pore-free. This is evidenced in Fig. 4b, which shows a polished section not perfectly parallel to the layers: the upper region on the micrograph (referred to as region ①) shows the layer boundary with higher porosity, the lower region (named as region ②) reveals a rather dense microstructure adjacent to the boundary. This finding agrees with the lower relative density (ca. 96 %) measured in sample A.

Fig. 4c and d shows SEM images of the microstructure of samples B and C, respectively. The microstructure is more homogenous than in sample A, with rather larger grains but a lower amount of porosity, associated with the higher sintering temperature (i.e. 1650 °C). The layer boundaries were not visible in samples B and C. Thermal etching lead to the formation of new phases at the triple points (most likely MgAl_2O_4 from alumina and sintering aids [25]), as indicated by the arrows and circles in Fig. 4c and d.

The lower sintering temperature of 1500 °C, as in sample A, yields a relatively fine grained microstructure with almost negligible grain growth, despite the relatively long dwelling time of 20 h. However, this sintering condition is not ideal for the formation of a homogeneous microstructure with high density, and high porosity (especially at the interlayer boundaries) was found. A higher sintering temperature of 1650 °C with only 2 h dwelling time, as chosen for samples B and C, leads to an enhanced densification and therefore to a more homogeneous microstructure and less porosity.

Fig. 5 plots the grain size distributions of samples A, B and C, with samples A and B measured both perpendicular and parallel to the printing layer direction. The mean grain size of sample A is $d_{50} \approx 1.2 \mu\text{m}$ in both printing directions. Sample B has a mean grain size $d_{50} \approx 3.8 \mu\text{m}$ perpendicular to the layers and $d_{50} \approx 4.4 \mu\text{m}$ parallel to the layers, and sample C shows a wider grain size distribution (parallel to the layers) and a larger grain size, with $d_{50} \approx 5.7 \mu\text{m}$.

3.2. Strength distributions

Fig. 6a–d shows the strength distributions of the different samples A, B1, B2 and C, for the different testing configurations (x, y, z, s and l), respectively. The probability of failure, P_f , is represented versus the failure stress, σ_f , in a Weibull diagram. The full lines correspond to the best fit of the strength data according to the maximum likelihood method [20].

The characteristic strength, σ_0 , and the Weibull modulus, m , with the corresponding 90 % confidence intervals are given in Table 2.

For sample A (machined surface), there is a clear effect of the printing direction on the strength distribution (Fig. 6a). The characteristic strength of the specimens tested in z-configuration (372 MPa) is significantly lower than that of specimens tested in x- and y-configuration (488 MPa and 473 MPa, respectively), the x- and y-

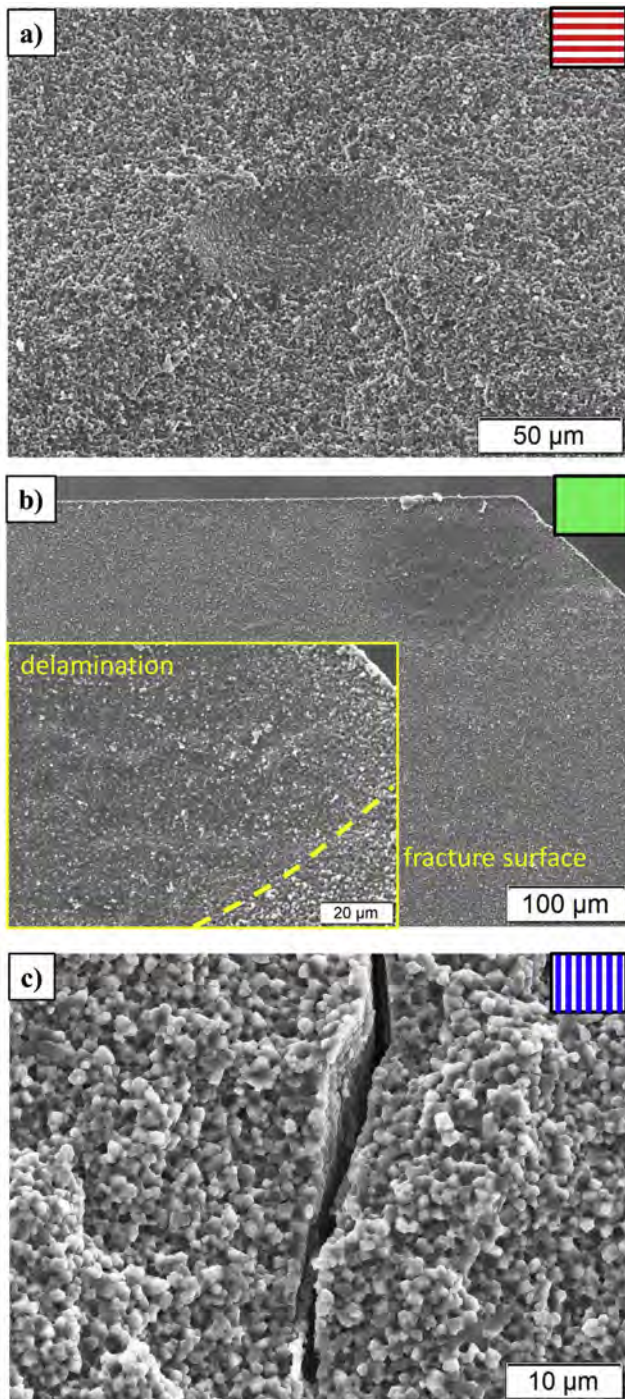


Fig. 8. Representative volume defects in specimens from sample A (machined): (a) trapped pore between two layers (x-configuration), (b) delaminated area (z-configuration) and (c) delamination (y-configuration).

configuration being statistically identical with a 90 % confidence. The Weibull modulus in all three configurations is rather low ($m \approx 8$).

For sample B1 (machined surface), the difference in the strength distributions between the x-, y-, and z-configuration is almost negligible (Fig. 6b), with slightly lower strength for the latter. The Weibull modulus is rather high, ranging between $m = 16$ and $m = 25$.

For sample B2 (as-printed surface), the difference in the strength distributions between the x- and y-configuration is negligible (Fig. 6c), with a stronger decrease in strength for the z-configuration as compared to sample B1. The Weibull modulus in sample B2 ($m \approx 12$) is slightly higher than that of sample A, but significantly lower than that of sample

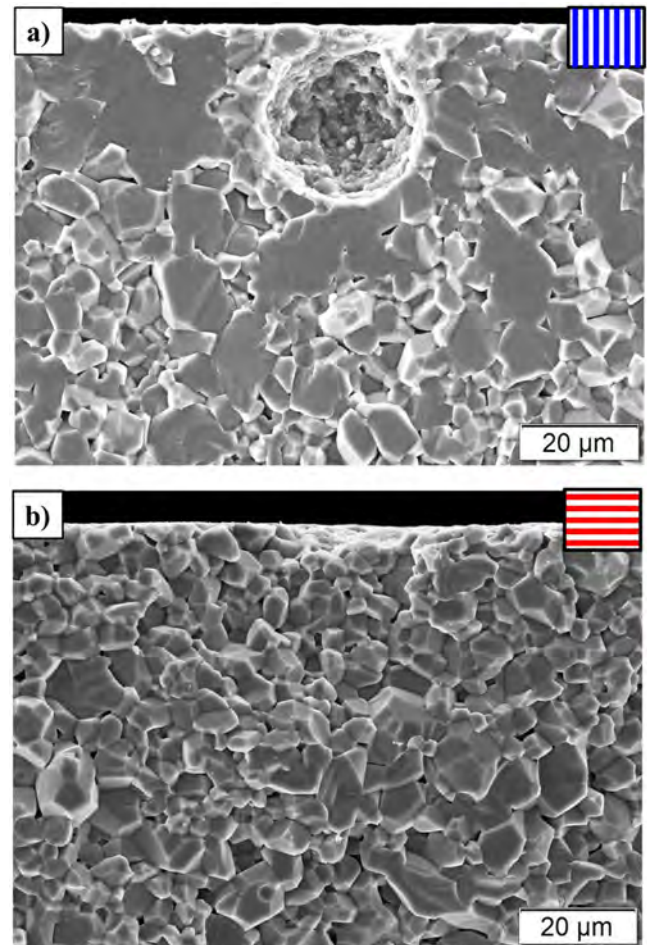


Fig. 9. Sub-surface or surface defects in specimens from sample B1 (machined): (a) pore in y-configuration, and (b) machining defect in x-configuration.

B1.

For sample C (as-printed surface), there is a slightly difference in the strength distributions between s- and l-configuration (Fig. 6d), with ~ 5 % higher characteristic strength in the former (433 MPa versus 413 MPa). The Weibull modulus is rather high and similar for both configurations ($m \approx 21$).

For the sake of comparison, Fig. 7 plots the Weibull modulus versus the characteristic strength for all tested samples, with the corresponding 90 % confidence intervals. In general, the characteristic strengths in x- and y-configuration in sample A, B1 and B2 are identical with a 90 % confidence, within each individual sample. The strength in z-configuration in sample A is significantly lower (~ 30 %), whereas in samples B1 and B2 only a slightly decrease is observed. In this regard, a positive effect of the surface machining on the strength parameters can be seen. The low Weibull moduli of sample A (machined) and sample B2 (as-printed) indicate a large scatter in the strength among tested specimens, which may be related to a relatively large difference in the size, type and/or location of critical defects in the specimen. In the case of sample A, the low Weibull modulus may be also related to the lower sintering temperature (1500 °C) and higher porosity. The increase in Weibull modulus in B1 may be associated with the surface machining, which may have eliminated some surface defects of a different size compared to inherent microstructural flaws. The high Weibull modulus in sample C may be related to the testing conditions (biaxial bending), where edge effects are neglected, and/or to the smaller size of the printing layers (i.e. 20 µm) thus limiting the natural defect size.

3.3. Estimation of critical flaw sizes

According to Linear Elastic Fracture Mechanics, the Griffith criterion can be used to estimate the critical defect size, a_c , causing the failure in brittle materials, as follows [26]:

$$a_c = \frac{1}{\pi} \left(\frac{K_{Ic}}{Y\sigma_f} \right)^2 \quad (3)$$

where K_{Ic} is fracture toughness, σ_f is the fracture strength, and Y is a geometry factor taking into account the defect shape and loading configuration [27]. Table 3 shows the estimated critical defect sizes calculated with the characteristic strength, σ_0 , of the different samples A, B1, B2 and C, considering a value of $Y = 1.12$ for semi-elliptical surface flaws or $Y = 2/\pi$ for the penny-shaped volume defects, respectively [24,28]. The fracture toughness of $\sim 3 \text{ MPa m}^{1/2}$ determined for this material using the SEVNB method in [29], was employed in the calculations.

3.4. Failure analysis

Fig. 8 shows SEM images of typical defects that caused the failure of the LCM-alumina specimens from sample A. In many cases, the reasons for failure in x- and y-configuration were relatively large pores, which were trapped between two adjacent layers. Their size is rather uniform, extending approximately one layer thickness, i.e. $40 \mu\text{m}$ (Fig. 8a). The failure stress of the specimen shown in Fig. 8a was 550 MPa. The defect size observed correlates with the estimated size for volume defects as given in Table 3. The scatter in strength (low Weibull modulus) measured in sample A may be related to the different positions of the volume pores in the specimens and to the non-uniform stress field as for flexural bending tests, decreasing towards the neutral axis with respect to the distance from the tensile surface. Fig. 8b shows a typical defect found in specimens from sample A tested in z-configuration: a delaminated area between two printed layers. Since this type of defect is often larger than the trapped pores, the strength in z-configuration is smaller than in x- and y-configuration. Pronounced delaminations were also found on x- and y-specimens (Fig. 8c). However, the failure stress of the specimen shown in Fig. 8c was as high as 467 MPa, within the strength interval for specimens tested in x- or y-configuration. In these specimens the load was applied parallel to the layer boundaries and thus possible interlaminar inhomogeneities were not responsible for failure. This finding indicates that, depending on the direction of the applied stress field with respect to the layer direction, specific defects can limit the strength of a specimen (as in z-direction) or remain uncritical (as in x- or y-direction).

Fig. 9 shows typical fracture surfaces of sample B1 (machined tensile surfaces). Failure origins were in a few cases small sub-surface pores (Fig. 9a) or – more frequently – grinding defects at the surface associated with the machining process (Fig. 9b). The defect size correlates with the size of the diamond grit used by the grinding wheel. In this regard, machining defects are rather uniform in size, which can explain the relatively low scatter in strength and thus higher Weibull modulus of sample B1.

Fig. 10 shows typical fracture surfaces of sample B2 (as-printed). The already mentioned “wave-like” surfaces were responsible for failure, especially under y- and z-configuration. They were caused by the over-exposure at the free edges of the printed part. Fig. 10a shows the fracture surface of a specimen, where such a wavy structure can be seen. When tested in y-configuration, the load is applied parallel to the “waves” and the grooves between the waves do not necessarily compromise the strength. However, when tested in z-configuration, the applied stress is perpendicular to the grooves. Consequently, they may

act as stress concentrators and reduce strength, especially if additional damage (artifacts) as shown in Fig. 10b and c is present in the grooves. Such artifacts may be a result of removal of excess slurry from the surface of the printed parts. Since these features are relatively uniform in size, they yield a low scatter in strength. The slightly lower strength in z-configuration is a consequence of the damage inside the grooves. Finally, the size of such wavy structure is of the order of the estimated

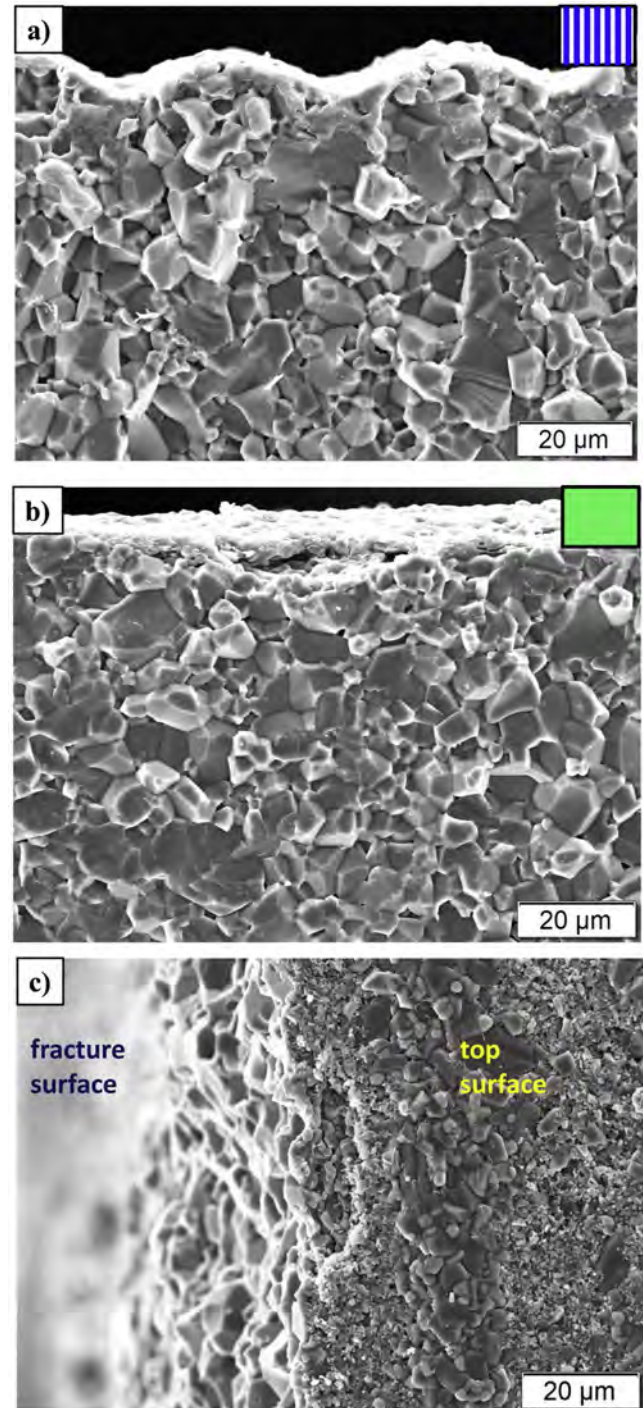


Fig. 10. Surface or surface near defects in specimens from sample B2 (as-printed): (a) wavy surface in y-configuration, (b) artefact in z-configuration, and (c) artefact similar to the one shown in (b) visible on the top surface in z-configuration.

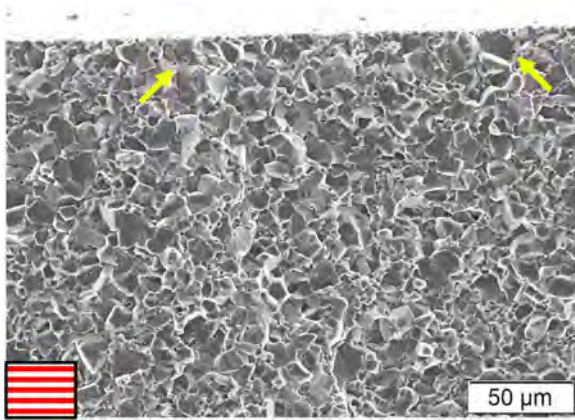


Fig. 11. Typical fracture surface of the discs in sample C (as-printed). Two large grains near the tensile side are indicated by arrows [25].

defect size for sample B2, as listed in Table 3.

Fig. 11 shows a typical fracture surface of a broken disc from sample C tested with the B3B method. Although the strength of sample C was measured on “as-printed” discs, no wavy structures were observed on the surface. No obvious defects could be identified either as failure causing entities. Comparing estimated defect sizes from Table 3 and the grain size distribution in sample C (Fig. 5), it can be concluded that the estimated critical defect size is in the range of the size of the larger grains in sample C, as indicated in Fig. 11 (see arrows). It may be hypothesized that exceptionally weak grain boundaries along big grains may act as failure origins in this sample.

4. Summary and conclusions

The effect of the sintering parameters, printing direction, surface condition (i.e. machined or as-printed), and/or geometry (i.e. prismatic bar or disc) on strength was investigated in alumina samples 3D-printed using LCM technology.

The uniaxial strength results obtained in sample A (sintered at 1500 °C and machined) show how process-typical defects like delaminations or large pores may – or may not – influence strength, depending on the relation between printing and loading direction. Planar defects with fixed orientation to the printing direction, such as weak layer boundaries or interlaminar inhomogeneities, are only strength limiting when the load is applied along the printing direction, but do not affect the strength in other loading directions. However, 3-dimensional defects such as pores trapped inside the printed layers compromise the strength in all loading configurations.

The comparison of uniaxial strength between samples B1 (machined) and B2 (as-printed), both sintered at 1650 °C, reveals an effect of the surface structure on the strength distribution, influenced by the printed direction. Nevertheless, the strength of as-printed surfaces obtained with parameters for rather fast printing may yield similar strength as the one obtained with machined surfaces, especially in the case that the post-printing cleaning be performed with care to avoid additional surface damage.

The biaxial bending results on system C (sintered at 1650 °C and as-printed) show that a choice of process parameters which result in a smooth surface can produce a material with a high, orientation-independent strength and a low scatter (high Weibull modulus).

This study demonstrates that additive manufacturing of ceramics does need consideration of more parameters than conventional ceramic processing. Not only the successful and costly efficient design of LCM alumina components has to consider aspects such as printing direction

in relation to loading direction, but also testing protocols for the parts must be able to characterize these aspects.

Declaration of Competing Interest

The authors declare that they have no known competing financial interests or personal relationships that could have appeared to influence the work reported in this paper.

Acknowledgements

The authors highly acknowledge the financial support of the Austrian BMVIT through the program “Produktion der Zukunft” within the project addmanu (FFG 849297). J. Schlacher and R. Bermejo gratefully acknowledge financial support by the ERC Consolidator Grant 817615 – “CeraText”.

References

- [1] D. Munz, T. Fett, *Ceramics. Mechanical Properties, Failure Behaviour, Materials Selection*, Springer, Berlin, 1999.
- [2] F. Klocke, Modern approaches for the production of ceramic components, *J. Eur. Ceram. Soc.* 17 (2) (1997) 457–465.
- [3] M. Hofmann, 3D printing gets a boost and opportunities with polymer materials, *ACS Macro Lett.* 3 (4) (2014) 382–386.
- [4] M. Attaran, The rise of 3-D printing: the advantages of additive manufacturing over traditional manufacturing, *Bus. Horiz.* 60 (5) (2017) 677–688.
- [5] T. Chartier, C. Dupas, M. Lasgorceix, J. Brie, N. Delhote, C. Chaput, Additive manufacturing to produce complex 3D ceramic parts, *J. Ceram. Sci. Technol.* 6 (2) (2014) 95–104.
- [6] N. Travitzky, A. Bonet, B. Dermeik, T. Fey, I. Filbert-Demut, L. Schlier, T. Schlordt, P. Greil, Additive manufacturing of ceramic-based materials, *Adv. Eng. Mater.* 16 (6) (2014) 729–754.
- [7] M. Schwentenwein, J. Homa, Additive manufacturing of dense alumina ceramics, *Int. J. Appl. Ceram. Technol.* 12 (1) (2015) 1–7.
- [8] A.D. Lantada, Ad. Blas Romero, M. Schwentenwein, C. Jellinek, J. Homa, Lithography-based ceramic manufacture (LCM) of auxetic structures: present capabilities and challenges, *Smart Mater. Struct.* 25 (5) (2016) 054015.
- [9] Ad. Blas Romero, M. Pfäffinger, G. Mitterramskogler, M. Schwentenwein, C. Jellinek, J. Homa, A. Diaz Lantada, J. Stampfl, Lithography-based additive manufacture of ceramic biodevices with design-controlled surface topographies, *Int. J. Adv. Manuf. Technol.* 88 (5–8) (2017) 1547–1555.
- [10] S. Nachum, J. Vogt, F. Raether, Additive Manufacturing of Ceramics: Stereolithography Versus Binder Jetting, *Ceramic Forum International/Berichte (DKG 93)*, (2016), pp. E27–E33.
- [11] T. Lube, J. Schlacher, W. Harrer, R. Danzer, G. Mitterramskogler, M. Schwentenwein, *Mechanische Eigenschaften von gedruckten Keramiken, Praktische Metallographie Sonderband 52* (2018) 229–234.
- [12] <https://www.lithoz.com/produkte/material>, 2018 (Accessed on 20 January 2020).
- [13] EN 623-3, *Advanced Technical Ceramics – Monolithic Ceramics – General and Textural Properties-part 3: Determination of Grain Size*, (1993).
- [14] EN 843-1, *Advanced Technical Ceramics – Monolithic Ceramics- Mechanical Properties at Room Temperature – Part 1: Determination of Flexural Strength*, (1995).
- [15] A. Börger, P. Supancic, R. Danzer, The ball on three balls test for strength testing of brittle discs: stress distribution in the disc, *J. Eur. Ceram. Soc.* 22 (9–10) (2002) 1425–1436.
- [16] A. Börger, P. Supancic, R. Danzer, The ball on three balls test for strength testing of brittle discs: part II: analysis of possible errors in the strength determination, *J. Eur. Ceram. Soc.* 24 (10–11) (2004) 2917–2928.
- [17] W. Harrer, R. Danzer, P. Supancic, T. Lube, Influence of the sample size on the results of B3B-tests, *Key Eng. Mater.* 409 (409) (2009) 176–184.
- [18] <https://www.isfk.at/de/960/>, 2013 (Accessed on 20 October 2019).
- [19] W. Weibull, A statistical distribution function of wide applicability, *J. Appl. Mech.* 18 (1951) 253.
- [20] EN 843-5, *Advanced Technical Ceramics – Mechanical Properties of Monolithic Ceramics at Room Temperature – Part 5: Statistical Analysis*, (1996).
- [21] R. Danzer, A general strength distribution function for brittle materials, *J. Eur. Ceram. Soc.* 10 (1992) 461–472.
- [22] R. Danzer, T. Lube, New fracture statistics for brittle materials, *Fract. Mech. Ceram.* 11 (1996) 425–439.
- [23] R. Morrell, *Fractography of Brittle Materials. NPL Good Practice Guide No. 15*, National Physical Laboratory, Teddington, UK, 1999.
- [24] G.D. Quinn, *Fractography of Ceramics and Glasses*, NIST Special Publication SP 960-16e2, US Government Printing Office, Washington, 2016.
- [25] J. Schlacher, *Charakterisierung von additiv gefertigtem Aluminiumoxid*, Master

- Thesis, Lehrstuhl fuer Struktur- und Funktionskeramik, Montanuniversitaet Leoben, 2019.
- [26] A.A. Griffith, The phenomenon of rupture and flow in solids, *Philos. Trans. R. Soc. London A221* (1920) 163–198.
- [27] R. Danzer, T. Lube, P. Supancic, R. Damani, Fracture of advanced ceramics, *Adv. Eng. Mater.* 10 (4) (2008) 275–298.
- [28] R. Danzer, On the relationship between ceramic strength and the requirements for mechanical design, *J. Eur. Ceram. Soc.* 34 (2014) 3435–3460.
- [29] T.G.T. Nindhia, J. Schlacher, T. Lube, Fracture toughness (K_{Ic}) of lithography based manufactured alumina ceramic, *IOP Conference Series: Materials Science and Engineering* 348 (2018) 012022.

Paper E

T. Lube, M. Staudacher, A.-K. Hofer, J. Schlacher, R. Bermejo: "Stereolithographic 3D printing of ceramics: challenges and opportunities for structural integrity", *Advanced Engineering Materials* 25 (2022), 2200520, <https://doi.org/10.1002/adem.202200520>

Open access article distributed under the terms of the Creative Commons CC BY license

Stereolithographic 3D Printing of Ceramics: Challenges and Opportunities for Structural Integrity

Tanja Lube, Maximilian Staudacher, Anna-Katharina Hofer, Josef Schlacher, and Raul Bermejo*

This article reviews the current activities at the Montanuniversität Leoben on the design, processing, and characterization of 3D printed advanced ceramics using the lithography-based manufacturing technology. An overview of the challenges and the opportunities offered to improve the mechanical properties of printing ceramics is given. Their brittle failure is analyzed within the framework of linear elastic fracture mechanics, considering specific aspects of additive manufacturing. Several issues associated with the printing process are addressed, such as surface quality, geometry control, influence of printing directions, as well as the need to establish testing protocols for 3D printed parts. Based on the layer-by-layer capabilities of the stereolithographic process, bio-inspired material design concepts are discussed aiming to enhance the mechanical resistance of 3D-printed ceramics. By tailoring the layer architecture and microstructure of the parts, high strength and fracture resistance may be achieved.

key elements in materials selection. Contrary to metals, ceramics show a relatively large scatter in strength, associated with the size, location, and type of processing flaws (intrinsic) or surface defects (extrinsic) in the component. Elimination of (large) intrinsic flaws and/or inhomogeneities has been achieved through colloidal processing,^[2] leading to higher strengths and less scatter. However, extrinsic flaws such as surface defects or cracks, associated with the hard machining of the ceramic components are still a challenge. Costly post-processing protocols involving fine polishing or lapping are often needed, thus narrowing the applications to planar and simple structures, fabricated by conventional routes such as uniaxial pressing, tape, or slip casting.


1. Introduction

The progress of advanced technologies in various fields, such as telecommunication, e-mobility and medicine, is followed by the need for high-performance materials. Requirements for structural and functional applications can often be fulfilled by the outstanding properties of ceramic materials. Regarding structural properties, ceramics exhibit low specific density, high wear resistance as well as chemical and thermal stability. Furthermore, ceramics are often the materials of choice for their functional properties, such as electrical or thermal conductivity/resistance, piezo-electricity, or optical characteristics.^[1]

Despite the outstanding structural properties of ceramics, such as high hardness and strength, their brittle character limits the market for high demanding applications, where reliability and safety are

Additive manufacturing (AM) technologies are now paving the path to fabricating ceramic components of high complexity without the need for post-processing, avoiding the high risk of introducing surface defects, which may lead to catastrophic failure under loading. AM technologies emerging in the field of ceramics can be categorized according to the preprocessing of the ceramic powder prior to 3D printing, in: 1) powder-based; 2) solid-based; and 3) slurry-based.^[3,4] The former employs powder beds, where the powder particles are compacted through droplets of resin in the case of binder-jetting or are directly sintered through the energetic input of a laser (powder bed fusion). The latter technologies utilize feedstocks based on solids or slurries using polymeric matrices with embedded ceramic powder particles as fillers. An example of a solid-based technology is material extrusion, where, adapted from polymeric 3D printing, a filament, filled with ceramic particles, is deposited on a building platform due to the melting and cooling of the filament. In contrast, for most slurry-based technologies, light is the energy source that leads to the solidification of photosensitive polymeric suspensions, so-called vat-based photopolymerization (VPP). Variants of this technology are stereolithography (SLA), which is a point-by-point process, and digital light processing (DLP). The latter uses a frame of multiple mirrors to project layers of consolidated pixels, resulting in a layer-by-layer build-up of a ceramic component. DLP processes, such as lithography-based ceramic manufacturing (LCM), can print with high resolutions, making it possible to fabricate geometries with a precision of $\approx 100 \mu\text{m}$. Although the development of solids or slurries containing ceramic powder particles as fillers remains a great challenge, materials intended for structural

T. Lube, M. Staudacher, A.-K. Hofer, J. Schlacher, R. Bermejo
Department of Materials Science
Structural and Functional Ceramics
Montanuniversität Leoben
Franz Josef Strasse 18, Leoben 27268, Austria
E-mail: raul.bermejo@unileoben.ac.at

 The ORCID identification number(s) for the author(s) of this article can be found under <https://doi.org/10.1002/adem.202200520>.

© 2022 The Authors. Advanced Engineering Materials published by Wiley-VCH GmbH. This is an open access article under the terms of the Creative Commons Attribution License, which permits use, distribution and reproduction in any medium, provided the original work is properly cited.

DOI: 10.1002/adem.202200520

application, such as alumina (Al₂O₃), zirconia (ZrO₂), or silicon nitride (Si₃N₄), have already been successfully printed.^[3,5]

Additive manufacturing enables new opportunities to fabricate ceramic components with “intricate” geometries for particular applications, such as dental ceramics, scaffolds, catalysts, or nozzles. Even though hard machining can be avoided, the wavelike structure of printed surfaces, due to the layer-by-layer build-up, entails new challenges for the mechanical performance of printed components. Therefore, new testing protocols must be developed to characterize the mechanical performance of 3D printed components. Not only for the assessment of properties in material development, but also for process monitoring and quality control. Strength may depend on relations between printing and loading direction, which has to be considered in the design of components. In contrast, opportunities are also offered through 3D technology thanks to the layer-by-layer and multimaterial approach. One possible approach is the development of a tailored (bioinspired) microstructure and architecture to enhance mechanical strength and/or “damage tolerance.” These aspects will be addressed in this article.

2. Aspects of the strength of stereolithographic 3D-printed ceramics

Ceramic components that are subjected to mechanical stress exceeding their strength eventually fail by brittle fracture. Brittle fracture is caused by the extension of the most critical small imperfection which is present. Such flaws can stem from the production process, machining, handling, and service.^[6–9] For convenience, they can be described as small cracks distributed on the surface or in the volume of a component. Through the application of the principles of linear elastic fracture mechanics, the strength σ_f of material with fracture toughness K_{Ic} then depends on the size a_c of the largest (or critical) flaw present.

$$\sigma_f = \frac{K_{Ic}}{Y\sqrt{\pi a_c}} \quad (1)$$

Naturally, this size varies from component to component.^[6–9] Therefore, the strength of a ceramic material cannot be given by a single number and is described by a strength distribution function instead. Usually, the Weibull distribution, Equation (2), is used to this end.

$$F(\sigma, V) = 1 - \exp \left[-\frac{V}{V_0} \left(\frac{\sigma}{\sigma_0} \right)^m \right] \quad (2)$$

The strength of ceramics is thus reported as characteristic strength σ_0 (the stress at which the failure probability is $F = 63\%$, for specimens of volume V_0) and Weibull modulus m (describing the scatter of strength). Note that Equation (2) implies that the strength depends on the loaded volume, i.e., it is size-dependent. Knowledge of these parameters allows for a statistical design procedure to assess the reliability of a component at a given stress. A large number of specimens is required to obtain the parameters of this distribution function.^[10] The strength distribution is graphically represented as a “Weibull-Plot,” which is a linearized representation of Equation (2).^[11]

Equation (2) combined with Equation (1) implies that the strength distribution is actually a mapping of the size distribution of critical defects. To analyze the strength behavior of AM ceramics, it is thus convenient to look at Equation (1). For a given material, the fracture toughness is a material property and it can be assumed that it is quite similar for AM ceramics and conventionally manufactured ceramics. It is worth mentioning that AM offers the possibility of tailoring the fracture toughness of a material through architectural and/or microstructural design, as will be described in Section 3. In any case, the critical defect size is related to the existing defect population, which is strongly influenced by the specific processing route.^[6–9]

Additive manufacturing of components differs in several aspects from traditional methods. The former requires feedstocks that contain a very high amount of polymer binder.^[12–14] For instance, stereolithographic manufacturing uses slurries with a typical ceramic content of $\approx 50\%$. Homogenization and stabilization of such slurries is a challenge: agglomeration of either the ceramic particles or the polymer phase would inevitably lead to defects in the final product. The optimization according to rheological behavior and particle dispersion in the photopolymeric suspension is crucial for sintered ceramic properties.^[15–18] The debinding of such green bodies must be performed in an especially cautious way to avoid either cracking or the formation of large defects generated by evaporating gaseous reaction products.^[12–14]

Another AM-specific origin for defects is the layer-wise building process. It may lead to defects at different locations of a component, i.e., in the volume or at the surface. Such defects have a preferred orientation with respect to the building direction and lead to a strength that depends on the relation between building direction and stress direction, i.e., an orientation-dependent strength.^[19–21] Sufficient bonding of two subsequent layers has to be ensured to avoid delamination defects and systematically weak layer interfaces. An example of the influence of insufficiently bonded layers on strength can be found in the literature^[22] and is exemplified in **Figure 1**.

The layered structure of the material is clearly visible on polished sections normal to the layer planes and large, highly porous regions can be found at the layer boundaries. The strength of machined specimens stressed in the z -direction and in the (x - or) y -direction is significantly different. Delaminated regions act as defects causing a low strength in the first specimen series (z -loaded), while the same type of defect is present but not failure causing for the other two loading directions (x - and y -loaded).^[22]

One of the benefits of using additive manufacturing technologies for the production of ceramic components is the possibility to avoid hard machining to obtain the final shape. It can be assumed that most AM components will be used with the as-fired surfaces without any modification. As a consequence, surface defects which are characteristic of each printing process, require special attention. In LCM, two effects contribute to the occurrence of unique surface structures. Light scattering caused by the ceramic particles within the polymeric system may lead to over-polymerization, causing its theoretically straight edges to bulge out. This generates a wavy surface of each exposed cross-sectional layer, being neither strictly straight nor normal to the building platform, but bulged outwards instead, as seen

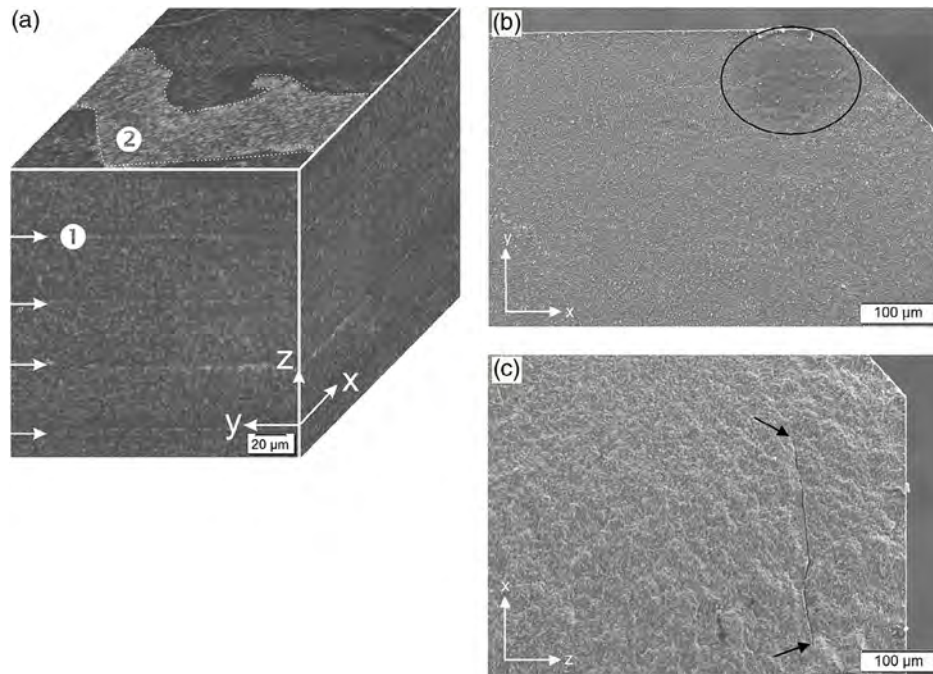


Figure 1. a) 3D visualization of a sintered vat-based photopolymerization (VPP) body with insufficient layer bonding. Porous seams are visible at the layer boundaries ① + white arrows and extended planar porous regions are present at the boundaries ②. b) fracture surface showing a delaminated region causing a low failure stress (250 MPa) in a specimen stressed in the z-direction, c) fracture surface showing a similar delamination-type defect in a specimen stressed in the y-direction. In this case failure was caused by a pore close to the tensile surface, resulting in a strength of 440 MPa. Adapted under the terms of the CC-BY license.^[22] Copyright 2021, The Authors. Published by Elsevier.

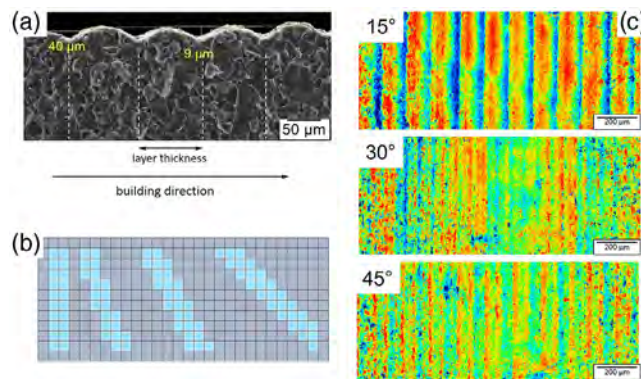


Figure 2. a) Bulged-out edge due to over-polymerization. Adapted under the terms of the CC-BY license.^[22] Copyright 2021, The Authors. Published by Elsevier. b) schematic representation of the staircase effect, c) scans of surfaces with different orientations with respect to the building direction. Each specimen has been manufactured with the same processing parameters, only the building direction has been altered. The height scale spans 15 μm from blue to red.

in **Figure 2a**. This effect is more pronounced when thick layers are printed with high exposure energy.^[3,23] Second, smooth inclined contours must be replicated with pixels that are limited to about $40\ \mu\text{m} \times 40\ \mu\text{m}$ in size, resulting in what is commonly known as aliasing or the staircase effect.^[24] Therefore, each angled surface is made up of a stepped sequence of squares with different sequences for each minor change in incline (Figure 2b). In summary, each combination of process parameters (e.g., exposure energy and time) and geometry parameters (e.g., surface incline) yields a specific surface structure. Examples of this

variety are shown in Figure 2c, which depicts scans of surfaces differently orientated with respect to the building direction.

Figure 3a shows strength distributions of two sets of specimens from the same material but with different surfaces, due to over-polymerization. In both sets specimens are stressed in the z-direction, one set has smooth machined surfaces, and the other set has as-sintered surfaces with a surface structure as depicted in Figure 3b. A reduction of strength and an increase in scatter can be observed, which may be due to the stress concentration effect of the grooves, cp. also Figure 5. If the grooves

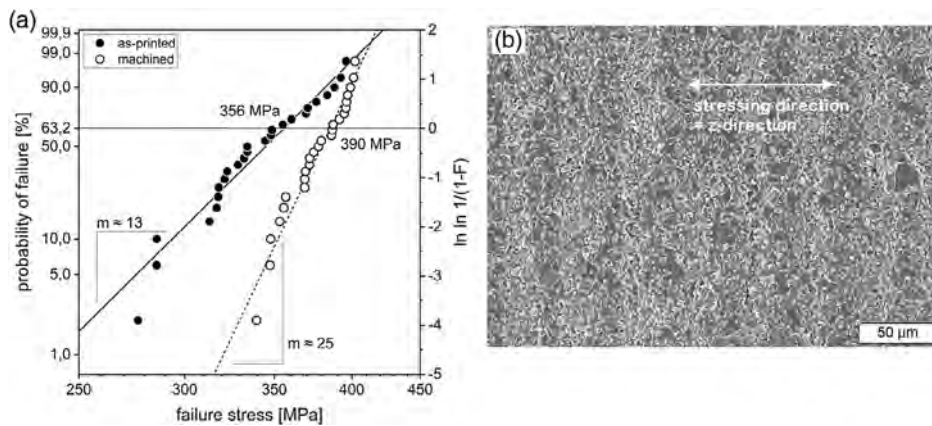


Figure 3. a) Strength distributions for specimens with as-printed and smooth, machined surfaces. The stress direction was normal to the layer planes (z-direction). b) as-printed surface with stressing direction indicated. Adapted under the terms of the CC-BY license.^[22] Copyright 2021, The Authors. Published by Elsevier.

are stressed in the longitudinal direction, no reduction of strength can be found.^[22]

The effect of aliasing on the strength is shown in **Figure 4**. Square plates (10 mm × 10 mm × 1 mm) were printed at five different inclines (0°, 15°, 30°, 45°, 90°) to the vertical building direction using parameters that do not lead to over-polymerization. Strength values for the plates were obtained with the biaxial Ball-on-Three-Balls-Test.^[25,26] A clear dependence of the characteristic strength on the printing orientation was observed. 90° specimens exhibit the highest strength, followed by 0° specimens. The low strength of 15° and 30° samples is in good agreement with the expected influence of surface structures for this incline, cp. Figure 2c. Ensuing fractography indicates that fracture follows the grooves on the surface, further pointing out the importance of these structures on the failure behavior.

While the effect of over-polymerization can be avoided by choosing suitable processing parameters that lead to smooth surfaces,^[22] the aliasing effect is intrinsic to the method and thus is the orientation-dependent strength. Both effects however are due to structures that are in the same order of magnitude as typical failure causing defects. They lead to high local stress gradients, which are

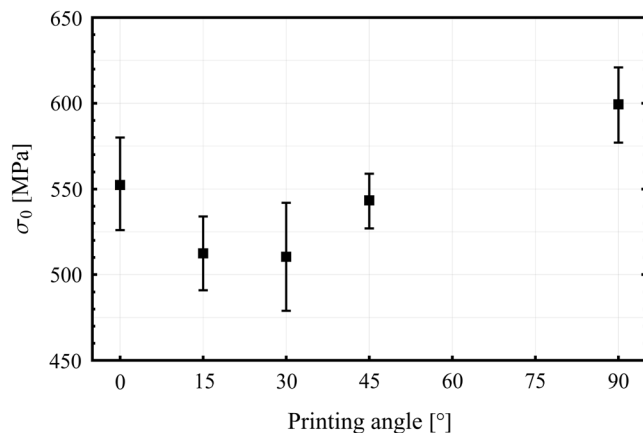


Figure 4. Biaxial strength as a function of inclination of the tensile surface towards the building direction. Each point represents 30 measurements.

superposed on a general stress field. Such stress situations are not generally covered by the theory of brittle fracture and may lead to new fracture statistical effects. Thus, a better understanding of the underlying mechanisms for the influence of building directions on strength has to be performed. Stress calculations by the authors using the Finite-Element submodel technique show that a typical over-polymerization structure of the surface of a flexed specimen causes an increase in the maximum surface stress of about 50%, compared to that of an ideally flat surface, **Figure 5**. However, the effect vanishes within several ten µm depths. As indicated in the literature,^[27] such stress concentrations may significantly change the dangerously loaded volume (effective volume^[9]) of a component, which in turn affects the probabilistic design concept.

The reliable design of LCM components has to take this effect into account in a proper way. For instance, structures that contain struts in various orientations (**Figure 6**) should be designed in a way to account for the orientation-dependent strength. Such a change in design could be that struts printed in “weak directions” are either avoided or realized with larger cross-sections.

Standardized testing methods that are typically used to assess the strength of ceramics, like 4-point bend tests^[28] or biaxial flexure tests,^[29] do not account for such phenomena. Furthermore, typical standardized test specimens like slender bending bars or thin discs or plates are unfavorable for AM. The need for testing methods that can both capture AM process-specific influences

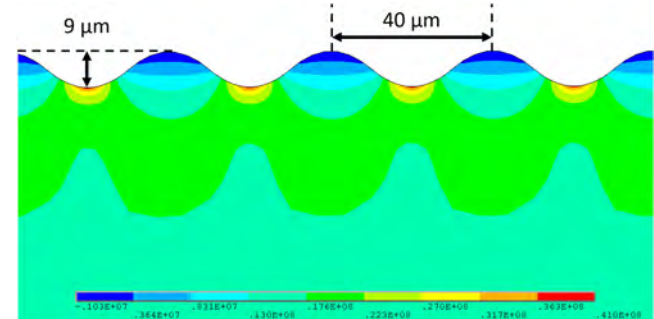


Figure 5. Stress concentrations superposing the bending stress due to the wavy structure generated by over-polymerization, cp. Figure 2a.

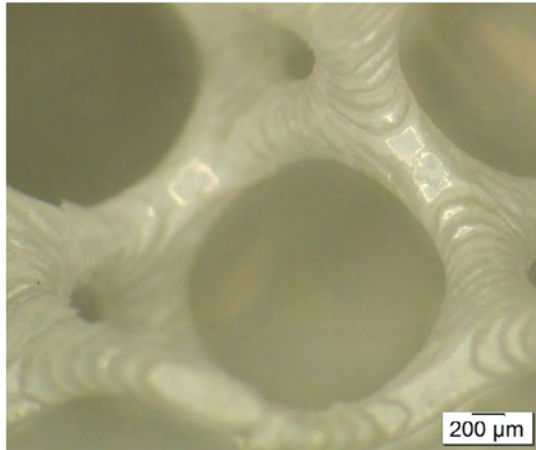


Figure 6. Scaffold structure manufactured using the lithography-based ceramic manufacturing (LCM) method consisting of struts with various orientations.

and utilize a specimen geometry that can be conveniently manufactured by AM is obvious.

In recent research project (CharAM - Charakterisierung der realen mechanischen Eigenschaften von keramischen AM-Bauteilen, FFG of BMDW and BMK, Austria and ZIM of BMWK, Germany) a new type of specimen, as shown in **Figure 7**, is investigated to this end. It consists of an assembly of 48 cantilevers on a common baseplate which is designed to exhibit an extensive region of constant stress. The baseplate can be inclined at any desired slope between 0° and the maximum possible incline without the need for supporting structures. Together with an automated test procedure that loads and fractures these cantilevers sequentially, an economic methodology is developed to capture the process-specific strength as well as its scatter. Such results can be used for material characterization to provide essential data for design but also for periodic quality control.

3. Opportunities for the Design of Damage Tolerant 3D-Printed Components

3.1. Architectural Design

In the past decades, much effort has been directed to designing ceramic-based multilayer architectures with improved

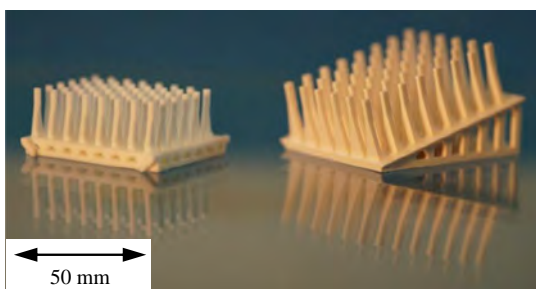


Figure 7. LCM manufactured test bodies to evaluate the orientation-dependent strength. Left: surfaces with 0° incline to the building direction, sintered, right: 15° incline, green body.

strength and/or toughness. Multilayer designs have been studied in many ways aiming to improve both the resistance to crack propagation and the mechanical reliability of ceramic materials and components.^[30–32] For instance, composite materials using symmetric multilayer architectures (e.g., mullite–alumina or alumina–zirconia among others) can exhibit enhanced fracture toughness, higher fracture energy, and in some cases non-catastrophic behavior compared to their constituent brittle (monolithic) materials. An important aspect of their design is the role of layer interfaces. Two main approaches regarding the interface fracture energy between layers concern the use of “weak” or “strong” interfaces. 1) Layered ceramics designed with weak interfaces can yield significantly enhanced fracture energy (failure resistance) favored through interface (or inter-layer) delamination. In this type of behavior, referred to as “graceful failure”,^[30] the fracture of the first layer is followed by crack propagation along the weak interface or within the weaker interlayer without undergoing catastrophic failure. The reinforcement mechanisms during fracture resemble those found in natural systems such as mollusk shells, and are mainly related to the low fracture energy of the interfaces and/or the large difference in elastic properties between their constituents^[33]; 2) Layered ceramics with strong interfaces have proven to be effective by introducing compressive residual stresses in the layers. The location of the compressive stress layers, either at the surface layer or embedded in the architecture, can either increase the mechanical strength^[34,35] or enhance the resistance to fracture and/or crack propagation (so-called damage tolerance),^[32,36–38] respectively. The idea of compressive stresses in the outer layers is based on the observations in “strengthened glasses,” the concept first studied by Nordberg et al.,^[39] and technically exploited, for instance, in Gorilla glass.^[40] It has been also demonstrated the feasibility of this approach to improve the mechanical strength and the insensitivity to subcritical crack growth in ceramics.^[41] The second approach, where compressive layers are embedded in the architecture, may lead to the arrest of the propagation of surface defects, thus increasing significantly the fracture energy of the material and guaranteeing a minimum strength (also called “threshold strength”), below which no failure can occur (see **Figure 8**). Recently, novel concepts have been pursued to design ceramics using a non-periodic disposition of “embedded” compressive layers (i.e., architectures with nonregular spacing between layers) to result in reliable components with unprecedented damage tolerance.^[42] In either case, residual compressive stresses have been utilized to reinforce conventional (planar) multilayer structures based on simple processing approaches (e.g., tape casting of symmetric and periodic layered

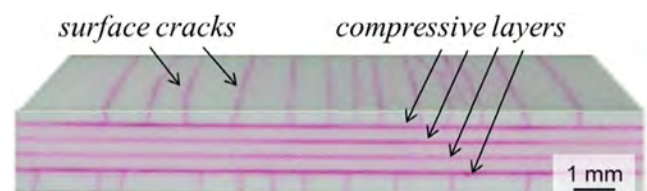


Figure 8. Thermal-shock-induced surface cracks stopped at the embedded compressive layers.^[36,44] Adapted with permission.^[36] Copyright 2017, Elsevier.

ceramics, where each layer is composed of only one material).^[32,43]

3.2. Microstructural Design

Progress in processing and manufacturing techniques has enabled tailoring of the microstructure of ceramic materials to achieve outstanding functional properties.^[45,46] “Textured” ceramics are an example of success, where the crystallographic orientation and morphology of individual grains can be tailored during the sintering process.^[47] Among the several techniques to fabricate textured ceramics, templated grain growth (TGG) has shown great potential applied to inorganic systems.^[48,49] In TGG, a subset of template particles is uniformly distributed in a fine (matrix) powder and the templates are aligned during forming (e.g., using tape casting^[50]). After densification, the oriented template grains grow preferentially with further heating by consuming the non-oriented matrix grains and, as a result, the final microstructure consists of elongated grains with a preferred orientation distribution (see **Figure 9**),^[51] which resembles the organized microstructure as found in nacre.^[52] A novel approach to increase the toughness in layered ceramics, while keeping the crack arrest capability, is to introduce textured layers as embedded features.^[37,51,53] This concept has been recently demonstrated, both under bending and contact loading, in tape-casted alumina-based layered ceramics designed with “textured” layers embedded between “equiaxed” layers.^[54,55]

In this regard, there is a great potential for employing additive manufacturing techniques, based on layer-by-layer deposition methods, to fabricate 3D-printed multilayer architectures (of different complexity) with improved fracture resistance and guaranteed minimum strength. The “multimaterial” approach aiming to tailor the microstructure of the parts by combining materials during the printing work has already been successfully employed in recent years; some examples will be presented in the next section.

3.3. Advances in Stereolithography-Based Additive Manufacturing

The concepts of alternating ceramic layers in a multilayer architecture have been attempted using stereographic 3D printing in

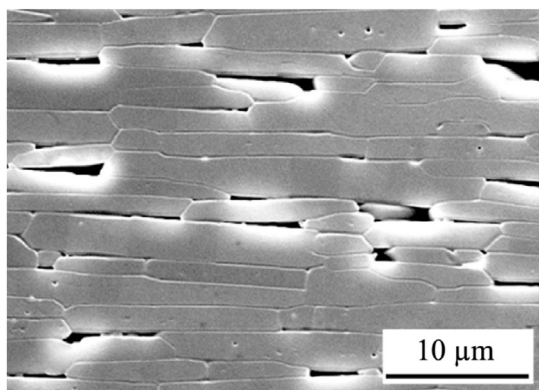


Figure 9. Textured microstructure of an alumina ceramic after Templated Grain Growth. Adapted with permission.^[51] Copyright 2010, Elsevier.

alumina–zirconia-based composites. In the work of Schlacher et al.^[56] a multimaterial approach was employed by embedding alumina–zirconia layers between outer pure alumina layers, aiming to tailor internal stresses in the layers. The in-plane compressive residual stresses in outer alumina layers were generated owed to the different thermal expansion coefficients of the combined material layers. **Figure 10a** shows the multilayer design with outer alumina layers. **Figure 10b** illustrates the “strong” interface between both alumina and alumina-zirconia materials. Biaxial bending performed both on the 3D-printed multimaterial and monolithic alumina parts revealed the effect of compressive stresses in the outer layers. A characteristic strength higher than 1 GPa was measured on the alumina multimaterial system, compared to ≈ 650 MPa in monolithic alumina, taken as a reference (**Figure 10c**). This is the first report on employing additive manufacturing to tailor the strength of alumina ceramics, taking advantage of the layer-by-layer printing process, and maybe extended to other ceramic systems.^[56]

Another strategy involves the use of the stereolithographic process to tailor the microstructure of ceramics after the method of templated grain growth (TGG). Recent work by Hofer et al.^[57] has demonstrated the feasibility of fabricating textured alumina by employing a lithography-based ceramic manufacturing process. **Figure 11a** summarizes the process as follows: 1) A photo-curable ceramic slurry (1) containing “platelets” (large aspect ratio alumina particles) is filled into a transparent rotatable vat (2) where a new film of slurry is distributed by a blade and the vat rotation (3). The slurry height is set and the building platform (4) is immersed into the slurry bed, leaving a gap, of a few microns (e.g., ≈ 25 μm), between the vat bottom and the building platform (or last printed layer (5)). The corresponding layer is then polymerized by the light source (6) from beneath the vat. This process is repeated for each layer until the final height of the part (total number of layers) is reached. The alignment of the platelets can be enhanced through the shear stresses generated in the gap between the vat bottom (2) and the doctor blade (3), during the rotation of the vat. The 3D-printed samples can then be thermally treated up to 430 °C to burn out the polymer, and finally sintered at 1600 °C (heating rate of 5 °C min^{-1} and dwell time of 6 h). The schematic in **Figure 11b** illustrates the TGG process and the corresponding microstructure after sintering. This study opens new possibilities in the fabrication of complex 3D ceramic geometries with horizontally aligned textured microstructure, aiming to tailor structural and/or functional properties.^[57]

Although much progress has been achieved in improving the resistance to crack propagation in two-dimensional multilayer composites, the potential of complex architectural design has not been sufficiently exploited or explored. Combining the multimaterial approach with the microstructural design capabilities of the stereolithographic 3D-printing technique may offer a new pathway to designing complex parts with outstanding mechanical strength and reliability. This is very important because spatial control and composite “connectivity” (i.e., number of dimensions in which each feature is self-connected) of the individual layers of a composite may ultimately be the key to developing and controlling useful and unique properties. As a matter of fact, the layer-wise architecture of many hybrid planar devices offers unique opportunities for tailoring the internal stress fields

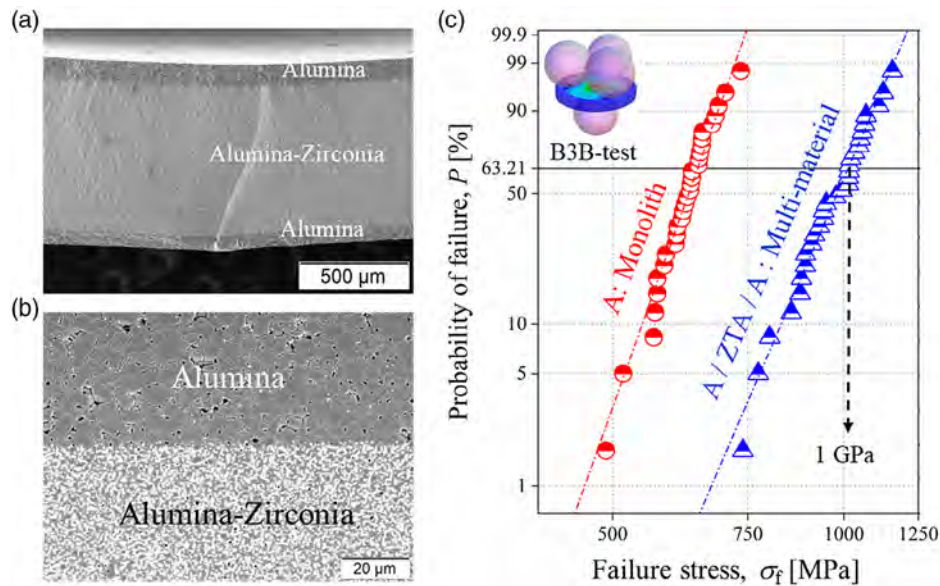


Figure 10. a) Multilayer design combining outer alumina layers with embedded alumina–zirconia layers; b) Detail of the “strong” interface between both alumina and alumina–zirconia materials; c) Multimaterial biaxial strength distribution compared to monolithic material. Adapted under the terms of the CC-BY license.^[56] Copyright 2021, The Authors. Published by Elsevier.

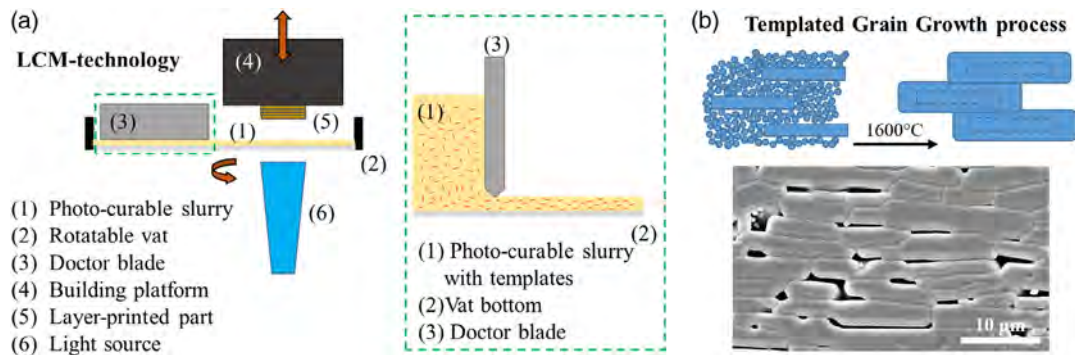


Figure 11. a) Schematic of the LCM technique and b) the template grain growth process. Adapted under the terms of the CC-BY license.^[57] Copyright 2021, The Authors. Published by Elsevier.

and microstructure to enhance “damage tolerance” in the ceramic parts. For instance, by arranging layers using different connectivity, more complex systems can be designed.^[58] Both structural and functional properties may be tailored within the 3D architecture, as a function of materials combination, microstructure orientation, etc. Distribution of embedded features in particular locations in the structure (as in **Figure 12**) could help to “trap” the propagation of cracks in distinct directions, thus increasing the structural reliability of ceramic devices. The stacking sequence of different layers within a plane would allow tailoring the spatial distribution of internal embedded features in a 3D architecture. The fabrication of ceramics combining microstructure and architecture significantly extends the state of the art in ceramic science and technology, and thus shall open new possibilities for the design of novel ceramic devices with significantly improved reliability.

4. Summary

The advent of additive manufacturing may open new paths to designing ceramic components with more complex geometry and enhanced structural performance. Tailored microstructures with controlled grain boundaries engineered in a hierarchical architecture hold the key to a new generation of “damage tolerant” ceramics. For instance, microstructural features (e.g., texture degree, tailored internal stresses, second phases, interfaces) manufactured in a 3D-printed architecture may provide outstanding lifetime and reliability to both structural and functional ceramic devices. However, it is still necessary to develop accurate and adjustable testing methods to evaluate the mechanical properties of 3D printed ceramic components. Especially challenging is the assessment of failure on multimaterials with intricate geometries, which may contain spatially

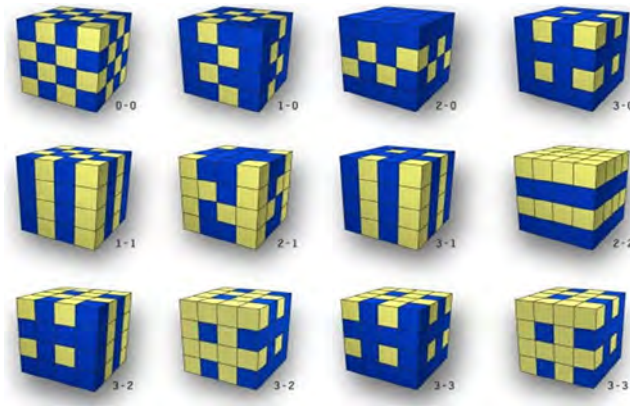


Figure 12. Schematic of 3D complex architectures with different connectivities.^[36,58] Reproduced with permission.^[36] Copyright 2017, Elsevier.

resolved distinct microstructures. The standardization of testing protocols for 3D printed ceramics is still in its infancy.

Acknowledgements

The funding for this research was provided by the European Research Council (ERC) excellent science grant “CERATEXT” through Horizon 2020 program under contract 817615 and by the Austrian ministries BMDW and BMK through the FFG-project “CharAM” of the COIN/IraSME program under contract 877684.

Conflict of Interest

The authors declare no conflict of interest.

Keywords

architectural design, ceramics, mechanical testing, multimaterials, stereolithography

Received: April 13, 2022

Revised: May 20, 2022

Published online: June 8, 2022

- [1] C. B. Carter, M. G. Norton, *Ceramic Materials: Science and Engineering* Springer, New York **2013**.
- [2] F. F. Lange, *J. Am. Ceram. Soc.* **1989**, *72*, 3.
- [3] Z. Chen, Z. Li, J. Li, C. Liu, C. Lao, Y. Fu, C. Liu, Y. Li, P. Wang, Y. He, *J. Eur. Ceram. Soc.* **2019**, *39*, 661.
- [4] ISO/ASTM 52900, *Additive Manufacturing — General Principles — Fundamentals and Vocabulary* **2021**.
- [5] <https://www.lithoz.com/> (accessed: February 2022)
- [6] W. D. Kingery, H. K. Bowen, D. R. Uhlmann, *Introduction to Ceramics*, John Wiley & Sons, New York **1976**.
- [7] R. W. Davidge, *Mechanical Behaviour of Ceramics*, Cambridge University Press, Cambridge **1979**.
- [8] J. B. Wachtman, M. J. Matthewson, W. R. Cannon, *Mechanical Properties of Ceramics*, Wiley, Hoboken, NJ, **2009**.
- [9] D. Munz, T. Fett, *Ceramics: Mechanical Properties, Failure Behaviour, Materials Selection*, Springer, Berlin, **2001**.

- [10] EN 843-5, *Advanced Technical Ceramics – Monolithic Ceramics – Mechanical Properties at Room Temperature – Part 5: Statistical Analysis* **1996**.
- [11] R. Danzer, T. Lube, P. Supancic, R. Damani, *Adv. Eng. Mater.* **2008**, *10*, 275.
- [12] M. Schwentenwein, J. Homa, *Int. J. Appl. Ceram. Technol.* **2015**, *12*, 1.
- [13] A. de Blas Romero, M. Pfaffinger, G. Mitterramskogler, M. Schwentenwein, C. Jellinek, J. Homa, A. Díaz Lantada, J. Stampfl, *Int. J. Adv. Manuf. Technol.* **2017**, *88*, 1547.
- [14] A. D. Lantada, A. de Blas Romero, M. Schwentenwein, C. Jellinek, J. Homa, *Smart Mater. Struct.* **2016**, *25*, 54015.
- [15] M. Borlaf, A. Serra-Capdevila, C. Colominas, T. Graule, *J. Eur. Ceram. Soc.* **2019**, *39*, 3797.
- [16] M. Borlaf, N. Szubra, A. Serra-Capdevila, W. W. Kubiak, T. Graule, *J. Eur. Ceram. Soc.* **2020**, *40*, 1574.
- [17] B. Oezkan, F. Sameni, S. Karmel, D. S. Engstrøm, E. Sabet, *Addit. Manuf.* **2021**, *47*, 102225.
- [18] A.-K. Hofer, J. Rabitsch, D. Jutrzenka-Trzebiatowska, C. Hofstetter, I. Gavaldá-Velasco, J. Schlacher, M. Schwentenwein, R. Bermejo, *Int. J. Appl. Ceram. Technol.* **2022**, *19*, 174.
- [19] R. B. Osman, A. J. van der Veen, D. Huiberts, D. Wismeijer, N. Alharbi, *J. Mech. Behav. Biomed. Mater.* **2017**, *75*, 521.
- [20] W. Harrer, M. Schwentenwein, T. Lube, R. Danzer, *J. Eur. Ceram. Soc.* **2017**, *37*, 4331.
- [21] C. Marsico, M. Øilo, J. Kutsch, M. Kauf, D. Arola, *Addit. Manuf.* **2020**, *36*, 101450.
- [22] J. Schlacher, T. Lube, W. Harrer, G. Mitterramskogler, M. Schwentenwein, R. Danzer, R. Bermejo, *J. Eur. Ceram. Soc.* **2020**, *40*, 4737.
- [23] G. Mitterramskogler, R. Gmeiner, R. Felzmann, S. Gruber, C. Hofstetter, J. Stampfl, J. Ebert, W. Wachter, J. Laubersheimer, *Addit. Manuf.* **2014**, *1–4*, 110.
- [24] S. A. Rasaki, D. Xiong, S. Xiong, F. Su, M. Idrees, Z. Chen, *J. Adv. Ceram.* **2021**, *10*, 442.
- [25] A. Börger, P. Supancic, R. Danzer, *J. Eur. Ceram. Soc.* **2002**, *22*, 1425.
- [26] A. Börger, P. Supancic, R. Danzer, *J. Eur. Ceram. Soc.* **2004**, *24*, 2917.
- [27] C. Liu, S. Aengenheister, S. Herzog, Y. Deng, A. Kaletsch, K. Schmitz, C. Broeckmann, *J. Eur. Ceram. Soc.* **2021**, *41*, 1415.
- [28] EN 843-1, *Advanced Technical Ceramics - Monolithic Ceramics - Mechanical Properties at Room Temperature - Part 1: Determination of Flexural Strength* **1995**.
- [29] ISO 6872, *Dentistry – Ceramic Materials* **2015**.
- [30] W. J. Clegg, K. Kendall, N. M. Alford, T. W. Button, J. D. Birchall, *Nature* **1990**, *347*, 455.

- [31] D. B. Marshall, J. J. Ratto, F. F. Lange, *J. Am. Ceram. Soc.* **1991**, 74, 2979.
- [32] M. Rao, J. Sanchez-Herencia, G. Beltz, R. M. McMeeking, F. Lange, *Science* **1999**, 286, 102.
- [33] E. Munch, M. E. Launey, D. H. Alsem, E. Saiz, A. P. Tomsia, R. O. Ritchie, *Science* **2008**, 322, 1516.
- [34] J. Pascual, T. Lube, R. Danzer, *J. Eur. Ceram. Soc.* **2008**, 28, 1551.
- [35] D. J. Green, R. Tandon, V. M. Sglavo, *Science* **1999**, 283, 1295.
- [36] R. Bermejo, *J. Eur. Ceram. Soc.* **2017**, 37, 3823.
- [37] Y. Chang, R. Bermejo, G. L. Messing, *J. Am. Ceram. Soc.* **2014**, 97, 3643.
- [38] V. M. Sglavo, M. Paternoster, M. Bertoldi, *J. Am. Ceram. Soc.* **2005**, 88, 2826.
- [39] M. E. Nordberg, E. L. Mochel, H. M. Garfinkel, J. S. Olcott, *J. Am. Ceram. Soc.* **1964**, 47, 215.
- [40] <https://www.corning.com/worldwide/en.html> (accessed: February 2022).
- [41] C. Krautgasser, R. Danzer, M. Deluca, P. Supancic, F. Aldrian, R. Bermejo, *J. Eur. Ceram. Soc.* **2016**, 36, 4095.
- [42] L. Sestakova, R. Bermejo, Z. Chlup, R. Danzer, *Int. J. Mater. Res.* **2011**, 102, 613.
- [43] V. M. Sglavo, M. Bertoldi, *Acta Mater.* **2006**, 54, 4929.
- [44] R. Bermejo Moratinos, L. Ceseracciu, L. Llanes, M. Anglada, *Key Eng. Mater.* **2009**, 409, 94.
- [45] Y. Yan, J. E. Zhou, D. Maurya, Y. U. Wang, S. Priya, *Nat. Commun.* **2016**, 7, 13089.
- [46] S. F. Poterala, S. Trolrier-McKinstry, R. J. Meyer, G. L. Messing, *J. Appl. Phys.* **2011**, 110, 14105.
- [47] G. L. Messing, S. Poterala, Y. Chang, T. Frueh, E. R. Kupp, B. H. Watson, R. L. Walton, M. J. Brova, A.-K. Hofer, R. Bermejo, R. J. Meyer, *J. Mater. Res.* **2017**, 32, 3219.
- [48] M. M. Seabaugh, I. H. Kerscht, G. L. Messing, *J. Am. Ceram. Soc.* **1997**, 80, 1181.
- [49] G. L. Messing, S. Trolrier-McKinstry, E. M. Sabolsky, C. Duran, S. Kwon, B. Brahmaroutu, P. Park, H. Yilmaz, P. W. Rehrig, K. B. Eitel, E. Suvaci, M. Seabaugh, K. S. Oh, *Crit. Rev. Solid State Mater. Sci.* **2004**, 29, 45.
- [50] R. E. Mistler, E. R. Twiname, *Tape Casting: Theory and Practice* American Ceramic Society, Westerville, OH **2000**.
- [51] R. J. Pavlacka, G. L. Messing, *J. Eur. Ceram. Soc.* **2010**, 30, 2917.
- [52] S. Deville, E. Saiz, R. K. Nalla, A. P. Tomsia, *Science* **2006**, 311, 515.
- [53] R. Pavlacka, R. Bermejo, Y. Chang, D. Green, G. L. Messing, *J. Am. Ceram. Soc.* **2013**, 96, 1577.
- [54] A.-K. Hofer, R. Walton, O. Ševeček, G. L. Messing, R. Bermejo, *J. Eur. Ceram. Soc.* **2020**, 40, 427.
- [55] J. Schlacher, A. Jabr, A.-K. Hofer, R. Bermejo, *J. Am. Ceram. Soc.* **2022**, 105, 4387.
- [56] J. Schlacher, A.-K. Hofer, S. Geier, I. Kraveva, R. Papšík, M. Schwentenwein, R. Bermejo, *Open Ceramics* **2021**, 5, 100082.
- [57] A.-K. Hofer, I. Kraveva, R. Bermejo, *Open Ceram.* **2021**, 5, 100085.
- [58] R. E. Newnham, D. P. Skinner, L. E. Cross, *Mater. Res. Bull.* **1978**, 13, 525.



Tanja Lube is an assistant professor at the Chair of Structural and Functional Ceramics of Montanuniversität Leoben (MUL). Her research activities focus on mechanical behavior and testing of ceramics, fracture mechanics, fracture statistics, fractography, and failure analysis of ceramic components. She has published over 75 peer-reviewed papers and 3 book chapters.



Maximilian Staudacher is a Ph.D. candidate at the Chair of Structural and Functional Ceramics of Montanuniversität Leoben (MUL). He investigates the mechanical behavior of brittle materials through modeling and simulation, with a focus on mechanical testing and fracture statistics. His area of research covers both conventionally fabricated as well as additive manufactured materials.



Anna-Katharina Hofer is a Ph.D. candidate at the Chair of Structural and Functional Ceramics at the Montanuniversität Leoben (MUL). The focus of her research is on processing, with the main emphasis on the sintering of multimaterial architectures and tailored microstructures of 3D-printed ceramics.



Josef Schlacher is a Ph.D. candidate at the Chair of Structural and Functional Ceramics at the Montanuniversität Leoben (MUL). His research work focuses on the mechanical characterization and fracture behavior of 3D-printed ceramic composites with tailored microstructures.



Raul Bermejo is Professor of Materials Science at the Montanuniversität Leoben (MUL), where he holds the Chair of Structural and Functional Ceramics at MUL. He is adjunct faculty at the Penn State University and is the recipient of an ERC-Grant “CeraText,” on bioinspired ceramic materials for engineering applications. He is the associate editor of the Journal of the American Ceramic Society, and has published over 120 peer-reviewed papers and 3 book chapters.

Paper F

M. Staudacher, T. Lube, J. Glettler, U. Scheithauer, M. Schwentenwein: "A novel test specimen for strength testing of ceramics for additive manufacturing", *Open Ceramics* **15** (2023), 100410, <https://doi.org/10.1016/j.oceram.2023.100410>

Open access article distributed under the terms of the Creative Commons CC-BY



A novel test specimen for strength testing of ceramics for additive manufacturing

Maximilian Staudacher, Tanja Lube^{*}, Jürgen Glettler, Uwe Scheithauer, Martin Schwentenwein

Department of Materials Science, Montanuniversität Leoben, Franz Josef-Strasse 18, A-8700, Leoben, Austria

ARTICLE INFO

Handling Editor: Dr P Colombo

Keywords:
Strength testing
Vat photopolymerization
Orientation dependency

ABSTRACT

This paper introduces a new method for strength testing of additively manufactured ceramics, which was designed to take the characteristics of the manufacturing process into account. It was developed for time- and material efficient specimen fabrication and its design allows adjustment so that different surface orientations can be investigated. This gives insight into the influence of surface structures on the measured strength, which vary significantly depending on the surface orientation.

Functional expressions for strength evaluation and the determination of effective volume are given and validated through Finite Element Analysis (FEA). The influence of surface structures on the measured strength is analyzed based on Weibull theory and FEA. Other influences on the accuracy of this testing method are discussed and quantified based on practical observations. The manufacturing process, testing setup and statistical evaluation for specimens of three different configurations is outlined and the results and applicability of this method are discussed.

1. Introduction

In the past decades, ceramic materials have taken an increasingly prominent position in many technical fields, which can frequently be traced back to their unique combination of mechanical and functional properties. Some of their most relevant characteristics are a high hardness, strength, and wear resistance. Whilst these properties are sought after in many applications, they severely limit the geometric complexity of ceramic components due to time- and cost intensive machining. Therefore, new shaping and manufacturing methods have been developed, aiming to increase component complexity while simultaneously reducing machining effort. Amongst the most promising methods to achieve this goal are the different additive manufacturing (AM) technologies. Through layered material deposition, AM has opened the path to near-net-shaped ceramic components with similar properties to conventionally manufactured ones. It should be noted that many different AM technologies exist, and all have their merits and limitations [1,2].

In order to optimize the manufacturing process, it is of utmost importance to accurately determine the component's functional and mechanical properties. However, AM introduces a number of additional challenges that have to be considered for the determination of the

component's mechanical properties. Notable differences to regular bulk ceramics are the layered structure, the layers' orientation in relation to the applied load or the influence of periodically structured surfaces. As an example, digital-light-processing (DLP) based vat photopolymerization enables the fabrication of a ceramic green body with high spatial resolutions. The starting point for the green body is a slurry consisting of ceramic-powder dispersed in a photo curable polymer. The light source is directed at the slurry with a plethora of small mirrors, whose size determine the maximum resolution of the process, as each of them represent a curable pixel [3–7]. As a consequence, aliasing effects occur if a structure of any incline is manufactured, as depicted in Fig. 1a). This effect causes the surface to exhibit unique wave patterns for each inclination, i.e. surface orientation, as shown in Fig. 1b). It is well known that surface defects can have a severe effect on the measured strength due to the higher geometry-factor compared to defects found within the bulk material [8]. Due to the orientation dependent surface structures, stress concentrations may form and amplify this effect. This results in changes of the measured strength in dependence of the surface orientation [9]. Moreover, recent work has shown that the strength of specimens manufactured with AM is significantly dependent on whether the specimen is loaded perpendicular or parallel to the building direction. It has to be noted that this difference can be eliminated if the

^{*} Corresponding author.

E-mail address: tanja.lube@unileoben.ac.at (T. Lube).

surface of both specimen types is machined [10,11]. However, machining of the final component is not always possible and would reduce the benefit gained through additive manufacturing and should therefore be avoided altogether. Apart from these two extreme orientations, the mechanical properties of the intermittent orientations are of high interest as well.

Ideally, all of this information can be gathered through a single testing method for a wide range of surface orientations. Then, it could be directly implemented into the design process of an additively manufactured component to increase material efficiency and component reliability.

Testing methods such as four-point bending or biaxial testing methods have the upside of already being established and standardized [12,13]. One of their major downsides is the time- and material intensive process of manufacturing each specimen. Especially with high resolution methods, such as DLP-based vat photopolymerization, the number of specimens that can be manufactured simultaneously is severely limited. Additionally, the high number of layers causes long manufacturing times. Furthermore, if specimens are not oriented parallel or perpendicular to the building direction, support structures are necessary, which further increases material consumption and decreases surface quality. Therefore, new testing methods have to be developed to accurately assess the mechanical properties with respect to the specifics of AM.

Within this work, a new strength testing method for DLP-based vat photopolymerization based on a novel specimen geometry, as displayed in Fig. 2, is presented. An introduction to the test specimen itself, its stand-out characteristics, and the reasoning behind them is given. Based on practical observations, a thorough analysis of possible sources of error and their influence on the measured results is carried out. The possible sources of error are quantified by theoretical considerations, Monte-Carlo analysis, and Finite-Element-Analysis (FEA). Limits for the influence of surface structures on the measured strength are given through a numerical analysis based on Weibull-theory. The implementation of the new testing method with the use of widely available testing equipment is shown. Empirical results obtained with the new testing method are given and discussed in relation to AM-specific features. Although this testing method was developed for DLP-based vat photopolymerization, its applicability to other manufacturing methods is conceivable.

2. Theoretical considerations

2.1. Specimen characteristics

The development of this test specimen was performed at IKTS

Dresden and is given in Refs. [14,15]. The basic elements of the test specimen are a baseplate and 48 cantilevers attached to the baseplate's upper surface. Through increasing the thickness of the cantilevers towards the baseplate, a strong support for loading is formed. The other end of the cantilevers will be loaded perpendicular to their longitudinal axis (see Fig. 3), resulting in a bending load. The specimen's baseplate is formed by two solid plates with an arched structure in between, as shown in Fig. 3.

In combination with the anchoring points at each end of the longitudinal edge, a rigid base for clamping or mounting of the test specimen is formed. The angle of the upper solid plate can be adjusted to subsequently yield any desired surface orientation for the cantilevers attached to it. Within this work, three configurations of the test specimen have been investigated, as shown in Fig. 4. Fig. 4a) displays the reference specimen, which will be referred to as "Type A". The inclination of the longitudinal axis of the cantilevers to the z-axis (see Fig. 3) is 0°. The cantilevers in specimen "Type B1", as shown in Fig. 4b), are angled at 15° to the z-axis. The same angle is chosen for specimen "Type B2", as shown in Fig. 4c), but with the cantilevers rotated along their longitudinal axis by 180°. Therefore, the tension loaded side is downskin for cantilevers of configuration B1 and upskin for configuration B2.

The design of the cantilever is the same for each configuration of the test specimen. A detailed overview of its geometry is given in Fig. 5. A small bulge at the front of the cantilever ensures load introduction at the correct position. Due to the linear increase of the cross section in the marked region, a constant bending moment acts within this part of the cantilever. This section serves as the intended region of failure and the maximum tensile stress σ_{max} at the specimen's surface is given through

$$\sigma_{max} = \frac{6P}{kh^2} \quad (1)$$

with P as the applied load and h as the thickness of the specimen within this region. The variable k describes the slope of the inclined flanks and is determined by

$$k = \frac{b_2 - b_1}{L} = 2 \tan\left(\frac{\alpha}{2}\right) \quad (2)$$

with L as the length and b_1 & b_2 as the width at the beginning and end of the region of constant bending moment. Another way to determine k is by the opening angle α of the cantilever's flanks.

In order to trace the broken cantilevers to their respective counterparts on the baseplate after testing, each cantilever is marked by two binary codes which indicate the row and the column of the cantilever on the baseplate [15]. This allows testing of all cantilevers on the specimen in one session without the need to demount the specimen or collect each broken cantilever directly after failure.

To get a better understanding of the accuracy of the new testing

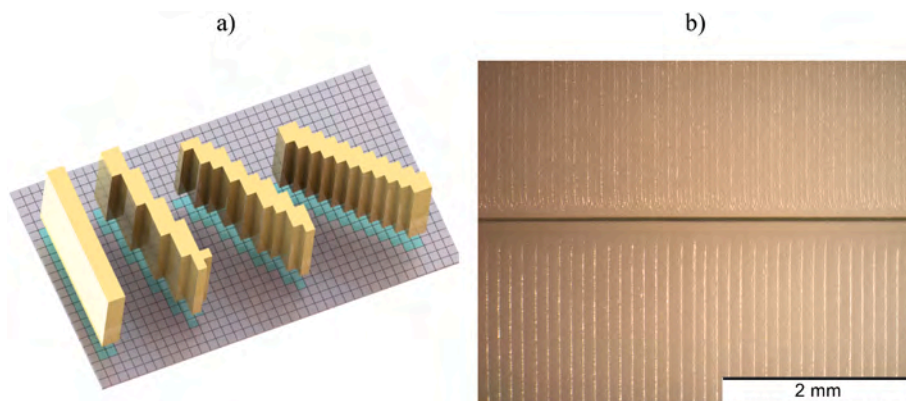


Fig. 1. a) shows a schematic of the aliasing effect due to the pixel-based nature of the DLP-based vat photopolymerization process (incline from left to right: 0°; 15°; 30° and 45°). The same effect occurs in building direction as well due to the layerd manufacturing process. A side-by-side comparison of the surface structures due to differing surface orientations is given in b). The upper surface was manufactured at an incline of 45°, the lower one at 15°.

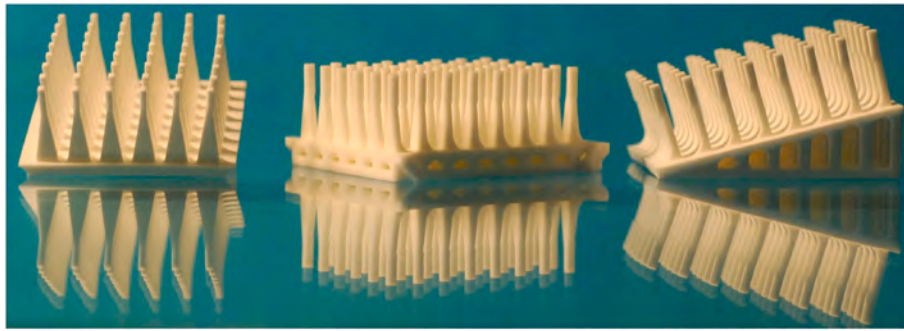


Fig. 2. Sintered test specimen in three different configurations. For size indication refer to Fig. 3.

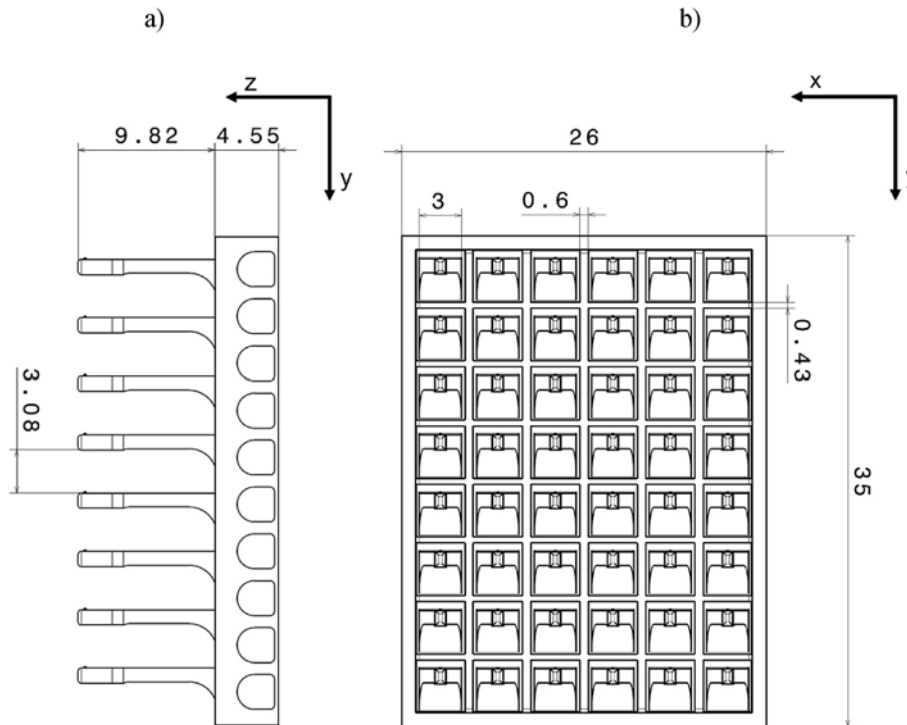


Fig. 3. Overview of the test specimen in side-view in a) and top-view in b), with its most significant dimensions given and the load direction along the y-axis.

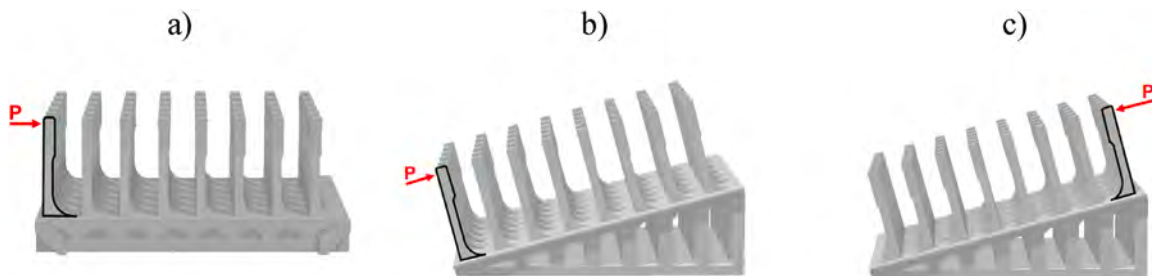


Fig. 4. Schematic for each variation of the test specimen, with the orientation of the cantilever highlighted by the black lines and the direction of the applied load P given in red. The 0° configuration is shown in a), the 15° configuration in b) and the rotated 15° configuration, i.e. $15^\circ-180$, is shown in c). (For interpretation of the references to colour in this figure legend, the reader is referred to the Web version of this article.)

method, some aspects have been investigated with FEA. A model of the cantilever attached to a part of the baseplate was implemented in ANSYS Mechanical R.22.1 by ANSYS Inc. (Southpointe 2600 Ansys Drive, PA 15317, Canonsburg, USA) through APDL (Ansys Parametric Design Language) by importing a CAD-file of the model. The model was meshed with 224868 SOLID186 elements (20-node elements), and 316950

nodes and is shown in Fig. 6. A mesh convergence analysis was performed to ensure the use of sufficiently small elements.

2.2. Stress field validation

Since eq. (1) was derived by utilizing Euler-Bernoulli beam theory,

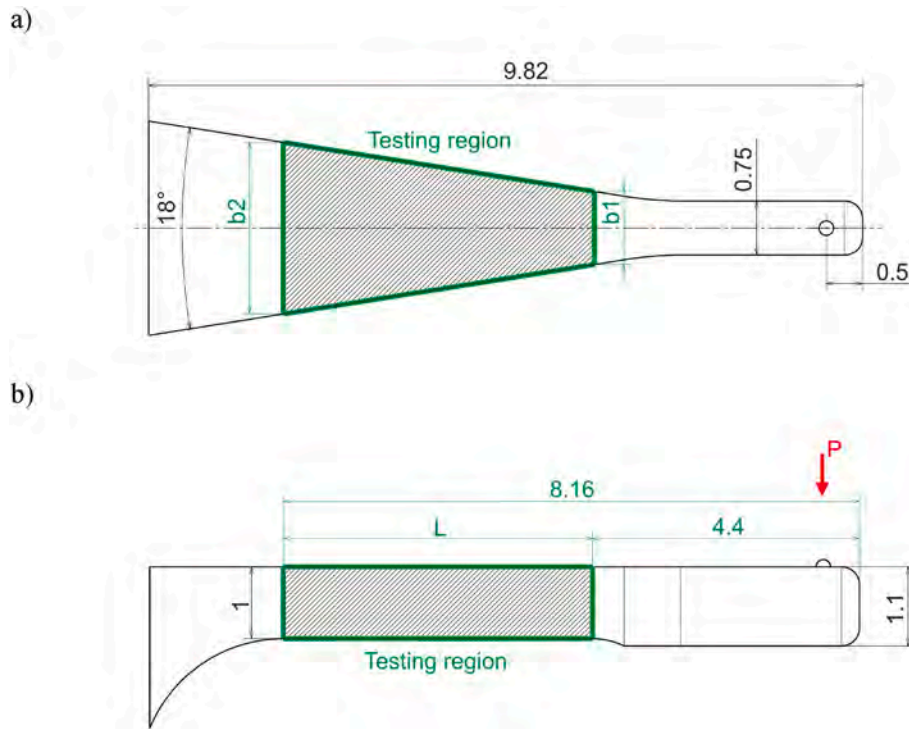


Fig. 5. Geometry of the cantilever, shown in top view in a) and side view in b). All measurements are given in mm. The region of constant bending moment is marked in green and the applied load P is marked in red. (For interpretation of the references to colour in this figure legend, the reader is referred to the Web version of this article.)

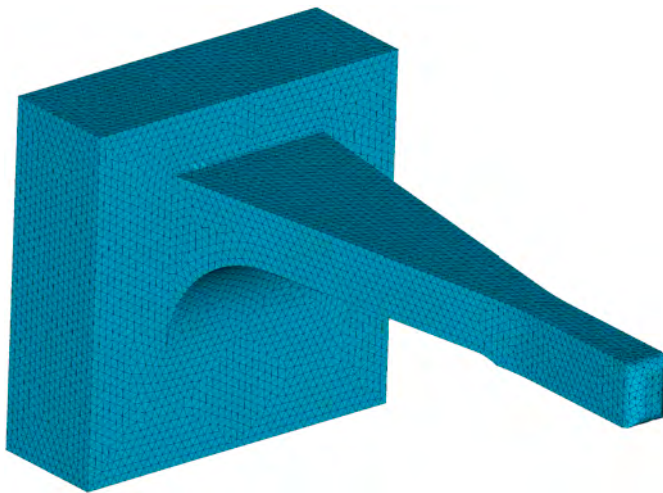


Fig. 6. Meshed model of the cantilever with a small portion of the baseplate.

some effects such as transverse shear strains are not considered [16]. Even though these effects are minor for thin beams and small displacements, a comparison between the FEA-derived stress field and the ideal stress field given by eq. (1) for the tensile surface was conducted. The results are shown in Fig. 7. Eq. (1) underestimates the stress in the central region by about 1.6% and overestimates the stress in the edge-regions by about 0.5%. Overall, excellent agreement between eq. (1) and FEA-results is achieved, validating the use of Euler-Bernoulli beam theory to calculate the maximum stress.

2.3. Effective volume and surface

An important consideration during design was material efficiency. More specifically, as much as possible of the manufactured volume

should be stressed at or close to the maximum tensile stress. This efficiency can be quantified by calculating the effective volume V_{eff} or effective surface S_{eff} in relation to the overall stressed volume V or surface S of the specimen. For the region of constant bending moment, an analytical solution for V_{eff} can be derived by solving the integral

$$V_{eff} = \iiint_{\sigma > 0} \left[\frac{\sigma(x, y, z)}{\sigma^*} \right]^m dx dy dz \quad (3)$$

for the tensile regions of the stress field $\sigma(x, y, z)$ normalized by an arbitrary tensile stress σ^* with m as the Weibull-modulus [8,17]. If the maximum tensile stress in the specimen is used for σ^* , this then yields

$$V_{eff} = \frac{hL(b_1 + b_2)}{4(m + 1)} \quad (4)$$

for the effective volume, with h as the thickness of the region of maximum stress of the cantilever. The other symbols are as defined previously. If the small contribution of the side faces of the beam are neglected, the effective surface S_{eff} is derived by the general relationship between S_{eff} and V_{eff} for a stress distribution induced through bending:

$$S_{eff} = V_{eff} \frac{2(m + 1)}{h} = \frac{L(b_1 + b_2)}{2} \quad (5)$$

Fig. 8 shows the relative effective volume of the testing region, i.e. the ratio of V_{eff} to the total stressed volume V , of one cantilever of the novel test specimen in comparison to traditional flexural strength tests [18]. Note that the volume of the supporting structures, i.e. the base plate, is not taken into account, as this material would also be needed to a similar extent for the overhang or support structures for the other tests. Due to the large region of constant maximum stress at the surface of the cantilever, a high material-efficiency compared to traditional bend-testing methods is achieved. If the total volume V_{tot} of the specimen, i.e. including all supporting structures, is considered, the new specimen exhibits slightly higher efficiency than 3-point-bending bars.

Similar to before, the functional expressions for the effective volume

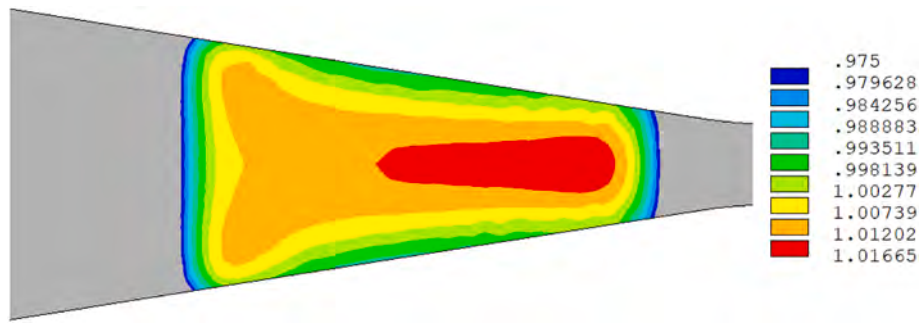


Fig. 7. Result of the stress field determined by FEA, σ_{FEA} , in relation to the constant stress at the surface σ_{max} as given by eq. (1). The contours give the ratio $\sigma_{FEA}/\sigma_{max}$.

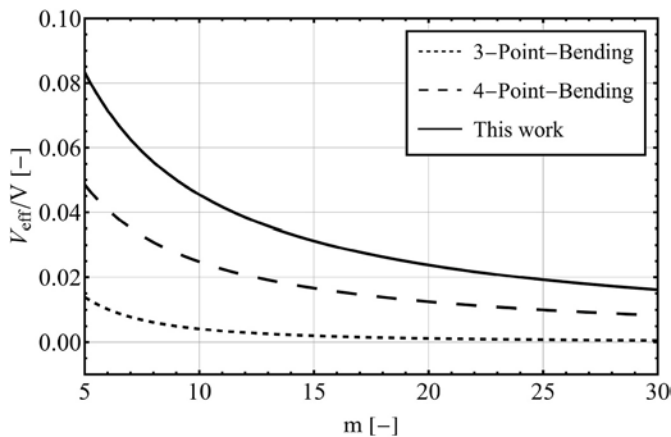


Fig. 8. Comparison of the relative effective volume for the novel test specimen, 3-point-bending bars and 4-point bending bars.

and surface (eq. (4) and (5)) were derived under the assumption of ideal conditions, i.e. a constant bending moment. In order to validate these expressions, the FEA-model from the previous section was utilized. The analytical and the numerical results in dependence of the Weibull modulus m are shown in Fig. 9. For $m \geq 10$, good agreement between eq. (4) and FEA is achieved. Note that the numerical results were generated for the full cantilever (excluding the region in immediate proximity of load introduction) while the analytical solution describes only the region of constant bending moment. This explains the increasing error for low Weibull moduli ($m < 5$) due to the increasing contribution of low-stress regions to the effective volume.

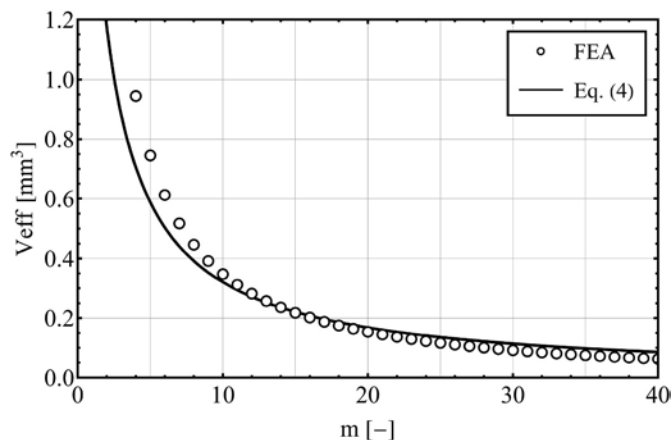


Fig. 9. Effective volume for the cantilever in dependence of the Weibull modulus calculated with either eq. (4) or FEA.

2.4. Influence of surface orientation

To assess the influence of surface structures, an approach based on Weibull theory was considered [19]. Since these surface structures modify the tensile stress field, the effective sizes (V_{eff} and S_{eff}) will change as well. Based on the size-effect, a change in measured strength is to be expected [8]. To accurately represent these surface structures, which are on a sub-millimeter scale, the mesh of the FEA-model has to be several times smaller than in the previous model. By utilizing sub-modelling, the region of constant bending moment can be modelled and meshed individually. Due to the simpler geometry of the sub-model, a mapped mesh with element sizes on a sub-micrometer scale can be implemented [20,21]. The sub-model is meshed with 52404 SOLID186 elements and 244031 nodes. With this sub-model, the observed periodic surface structures of the manufactured specimens are directly implemented in FEA. A sinusoidal wave was deemed as the best representation of the measured data, with the amplitude and wavelength for each specimen type determined through surface characterization (see chapter 4.3). These structures were subsequently implemented in the sub-model and compared to the case of an ideal flat surface structure, i.e. specimens of type A. The investigated results were the change in maximum tensile stress and the influence of the surface structures on the effective volume and surface. The maximum tensile stress of the flat specimen was chosen as the reference stress σ^* for the calculation of V_{eff} and S_{eff} for the other specimen types. Utilizing the size effect described by Weibull theory [8], the expected measured strength of a specimen σ_B of an effective volume $V_{eff,B}$ is given by

$$\frac{\sigma_B}{\sigma_A} = \left(\frac{V_{eff,A}}{V_{eff,B}} \right)^{1/m} \quad (6)$$

with $V_{eff,A}$ and σ_A as the known effective volume and strength, respectively. In the case presented here, the subscript B corresponds to the specimen with a structured surface and A corresponds to the flat specimen. The very same principle can be applied utilizing the effective surface instead of the effective volume. The ratio σ_B/σ_A for each specimen type, based on either V_{eff} or S_{eff} , will be used to quantify this effect.

3. Practical aspects

All equations and investigations presented in the last section were derived or conducted under the assumption of ideal specimen geometries, i.e. as given in Fig. 5. A comprehensive analysis of the first prototypes revealed a number of deviations from the ideal geometry. On one hand, the general dimensions of the sintered cantilever did not correspond to those given in Fig. 5, even though a state-of-the-art printer (see chapter 4) was utilized. On the other hand, these dimensions fluctuated for each cantilever, even within one test specimen. Therefore, the initial concept of measuring a single cantilever, which is representative for the whole specimen, had to be investigated and reworked. In the upcoming section, the observed deviations from the ideal specimen

geometry and ideal loading situation will be discussed.

3.1. Non-ideal geometry of the cantilevers

The most relevant dimensions for stress evaluation are the thickness h and the opening angle α of the cantilevers, as given in eq. (1). Contrary to initial assumptions, these dimensions are different for each cantilever within each test specimen. Therefore, measuring the dimensions of just a single cantilever is not adequate to accurately determine the fracture stress for each cantilever. Other options are to either determine mean values from the measurements of several cantilevers or to use individual measurements from every cantilever. In order to determine a suitable number of measurements for the average values, a Monte-Carlo (MC) analysis was conducted with Mathematica 12.0 by Wolfram Research, Inc. (100 Trade Center Drive, Champaign IL 61820-7237, USA) [22,23]. More specifically, the characteristic strength σ_0 and Weibull modulus m were determined with dimensions from either individual or average measurements. An overview of the principle of this analysis is given in Fig. 10. The dimensions for each specimen were randomly generated based on normal distributions, which are determined from measurements of manufactured specimens. The final result of the MC analysis is the relative difference between the Weibull parameters determined with either individual or average dimensional measurements.

3.2. Position of load introduction

Another problem caused by the deviation from intended cantilever dimensions is a shift of the point of load introduction away from the ideal loading position. The cantilever is designed so that the extensions of the inclined flanks intersect at the point of load introduction. At this location, a small bulge is added to facilitate a well-defined load application. This condition is needed so that the maximum stress in the intended region of failure can be determined by eq. (1). If the slope k of the edges, i.e. the opening angle α , changes, the intersection point does no longer coincide with the position of the bulge, as shown by the blue lines in Fig. 11. Instead, the intersection of the edges is shifted by a distance a , depending on α , while the load will still be applied at the bulge. A schematic of this effect is given in Fig. 11.

The influence of a on the maximum stress $\sigma_{\max,shifted}$ can be considered analytically and is given through

$$\sigma_{\max,shifted}(x, a) = \frac{3F(x-a)}{h^2 x \tan\left(\frac{\alpha}{2}\right)} \quad (7)$$

with x as the distance from the ideal loading point for $\alpha = 18^\circ$ and the other symbols as defined before. The relative error in maximum stress in dependence of x and a is defined by

$$Rel. error[\%] = \frac{\sigma_{\max,shifted} - \sigma_{\max}}{\sigma_{\max}} \quad (8)$$

with σ_{\max} as defined in eq. (1).

3.3. Shape of the cantilever cross-section

Further deviations from the ideal specimen geometry are related to the cross-section of the cantilevers. Even directly after specimen fabrication, the desired rectangular cross-section is not achieved by DLP-based vat photopolymerization, resulting in a barrel shaped cross-section instead. This effect is still evident after sintering, as shown in Fig. 12. Another reason for geometric deviations might be the subsequent thermal crosslinking of suspension that is still adhering because it has not been cleaned off.

For the derivation of eq. (1), a rectangular cross-section with height h was assumed to derive a simple functional expression for the section modulus. If the maximum thickness of the cantilever in the center, h_{\max} , is utilized as h , the section modulus will be overestimated. This will result in an underestimation of the measured strength of the cantilever.

4. Experimental

4.1. Specimen fabrication

The test specimens were manufactured in-house from the alumina-based slurry LithaLox350 with the DLP-based vat photopolymerization printer CeraFab 7500, both produced by Lithoz GmbH (Mollardgasse 85A, 1060 Vienna, Austria). The most relevant printing parameters are given in Table 1.

All specimens were manufactured from the same slurry batch and excess slurry was removed with the solvent LithaSol20 produced by Lithoz GmbH. A total of 18 test specimens were manufactured, with 6 specimens per specimen type. The size of the building platform allows manufacturing of two specimens side by side as a single batch. All specimens of the same type, i.e. A, B1 or B2, were treated simultaneously during thermal postprocessing and according to the procedure recommended by Lithoz GmbH. Debinding was performed in a KU15/06/A furnace and sintering in a HTL10/17 furnace, both manufactured by ThermConcept (Friedrich-List-Strasse 17, 28309 Bremen, Germany). The maximum temperature during debinding was 430°C , then the specimens were transferred into the sintering furnace. Sintering of the specimens was conducted at 1650°C for 2 h. For the sintering process, special care was taken to guarantee an upright position of the cantilevers by tilting the angled specimens by 15° . Thus, the deformation of cantilevers due to their own weight was kept to a minimum.

4.2. Strength testing

The specimens were tested with the universal testing machine Z010 by ZwickRoell GmbH & Co. KG (August-Nagel-Strasse 11, 89079 Ulm,

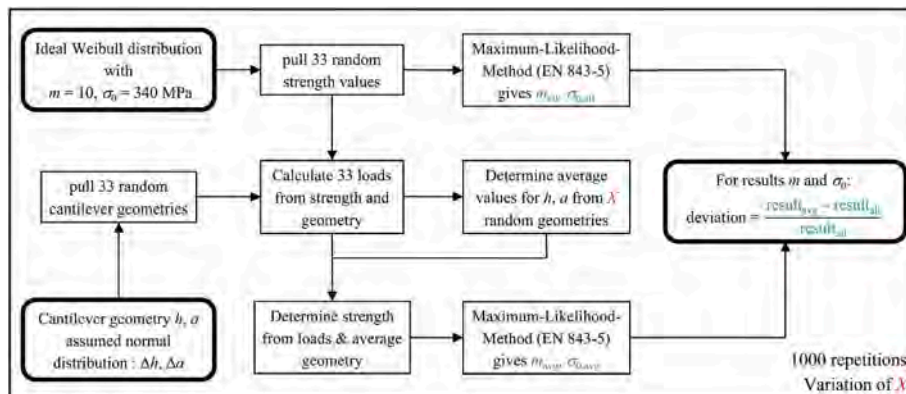


Fig. 10. General Principle of the Monte-Carlo analysis.

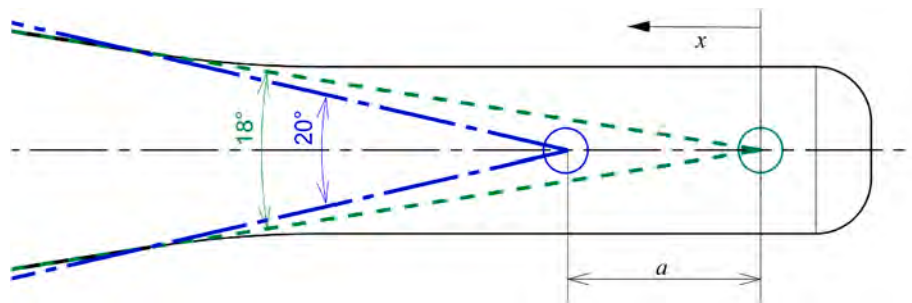


Fig. 11. Positional change of the ideal point of load introduction due to the change in opening angle α . Green: ideal situation, blue: situation for a cantilever with a larger than ideal flank opening angle. The load will always be applied at the green circle due to the bulge at this position. (For interpretation of the references to colour in this figure legend, the reader is referred to the Web version of this article.)

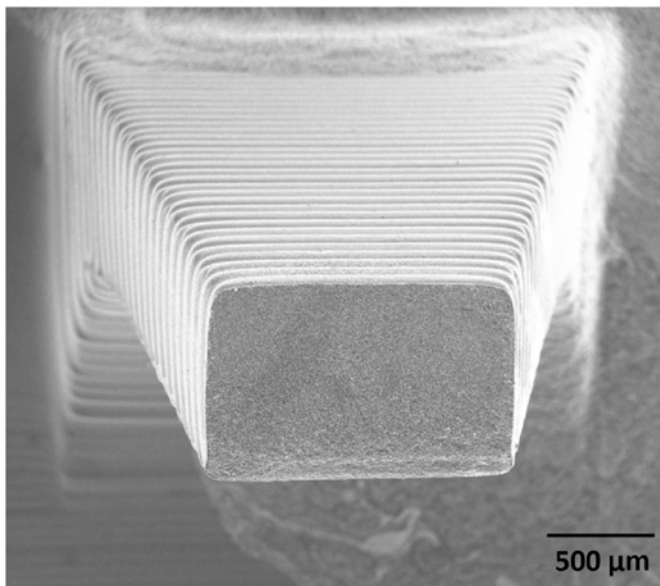


Fig. 12. Fracture surface of a sintered cantilever of specimen type B1. Note that the observed cross-section deviates significantly from the assumed rectangular cross-section.

Table 1
Printing parameters utilized for specimen manufacturing.

Layer thickness [μm]	Lateral resolution [μm]	DLP-Intensity [mW/cm ²]	DLP-Energy [mJ/cm ²]
25	40	100	150

Germany) equipped with a KAP-S load cell (maximum load = 200 N) by AST GmbH (Marschnerstrasse 26, 01307 Dresden, Germany) and operated through a control system by Doli Elektronik GmbH (Rudolf-Diesel-Strasse 3, 72525 Münsingen, Germany). Each specimen was mounted on an X–Y table by clamping two sides of the baseplate, as shown in Fig. 13. The cantilevers of each specimen were tested successively through a slim metal probe. The X–Y table enabled an adjustment of the specimen’s position in the X–Y plane (see Fig. 13), so that each cantilever was loaded perpendicular to its longitudinal axis at the intended point of load introduction (bulge). The cantilevers were loaded at a constant crosshead speed of 1 mm/min.

Prior to strength analysis, the validity of each individual bending test was verified. This involves checking for unsteady loading curves, large geometric imperfections, and failures outside the region of constant bending moment. The relevant dimensions of each cantilever, i.e. the thickness h_{max} and the opening angle α , were determined on the

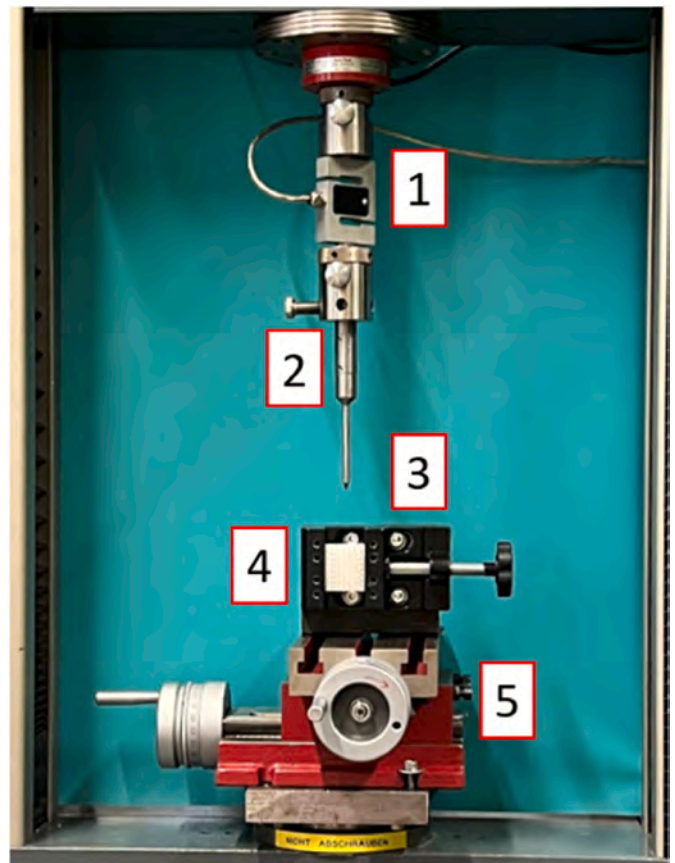


Fig. 13. Testing setup for a specimen of Type A (4), which is held in place by a clamping fixture (3) that is mounted on a X–Y table (5). The metal probe (2) is fixed to the load cell (1). This setup can be used for each specimen type without modification.

remainders of the cantilevers on the baseplate (h_{max}) and on the fractured cantilevers (α), respectively, with a SZH10 stereomicroscope by Olympus K.K. (2-3-1 Nishi-Shinjuku, 163-0914 Tokyo, Japan) within the Olympus Stream Motion Software 2.2. Strength results were obtained utilizing eq. (1). Statistical Weibull analysis was performed with the Maximum-Likelihood method in accordance with the standard EN-843-5 [24].

4.3. Surface characterization and fractography

The surface structures of the cantilevers were characterized with a VK-X1000 Laser-Confocal-Microscope by Keyence Corporation (1-3-14 Higashi-Nakajima, 533-8555 Osaka, Japan). 6 cantilevers of each type

were examined, and an average surface structure was determined from 60 line-measurements on each cantilever. Fracture surfaces were investigated using a JEOL K.K. (3-1-2 Musashino Akishima-Shi, 196-8558 Tokyo, Japan) NeoScope JCM-6000Plus. Prior to imaging, the cantilevers were coated with gold sputtering.

5. Results

5.1. Errors affecting single strength values

To quantify the influence of the shift in loading position a on the measured strength, typical values of a were determined for five cantilevers of each type of specimen. For specimens of type A, the average shift was $a = -158\mu\text{m}$, with $a = -161\mu\text{m}$ and $a = -133\mu\text{m}$ for type B1 and B2, respectively. With these values, an average relative error in maximum stress between +1.6% and +3.7% is expected, depending on the position of failure, as displayed in Fig. 14. Combining the largest single value for the shift in load introduction $a = -281\mu\text{m}$ (measured on a specimen of type B1) with the shortest possible failure length $x = 4.4$ mm would yield a maximum error of about +6.4%.

Similarly, the influence of non-rectangular cross-sections is quantified by evaluating the shapes of ten cross-sections of each specimen type in detail. The section moment of the barrel shaped cross section W_{barrel} was determined numerically with CATIA Version 5.19 (Dassault Systèmes, 78140 Vélizy-Villacoublay, France) and compared to the ideal section moment W_{ideal} given through

$$W_{ideal} = \frac{b_{max} h_{max}^2}{6} \quad (9)$$

with b_{max} as the cross-section's maximum width and h_{max} as defined before. The relative error between W_{barrel} and W_{ideal} is calculated with

$$Rel. error[\%] = \frac{W_{ideal} - W_{barrel}}{W_{barrel}} \quad (10)$$

and the results are shown in Fig. 15. On average, the section moment will be overestimated by about 3.5%–5.7% if h_{max} and b_{max} are used for the calculation. This leads to the same underestimation for the maximum strength.

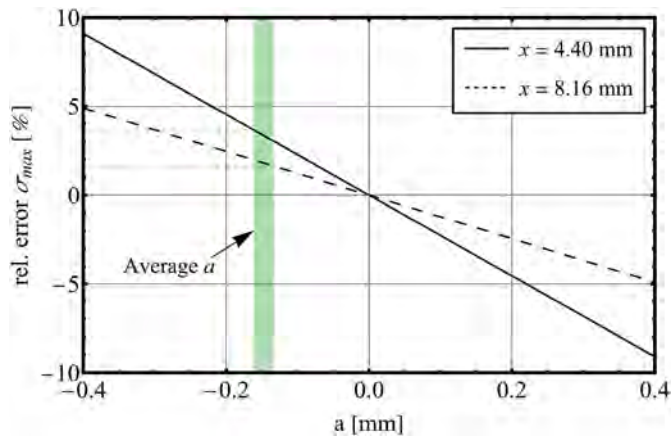


Fig. 14. Influence of the shift a in loading position on the maximum stress. The black through line represents the solution of eq. (8) for the upper limit (failures at the very beginning of the region of constant bending moment) of this effect, whereas the dashed black line indicates the solution for the lower limit (failures at the end of the region of constant bending moment). The green bar represents the range of typical average values of a for all three specimen types. (For interpretation of the references to colour in this figure legend, the reader is referred to the Web version of this article.)

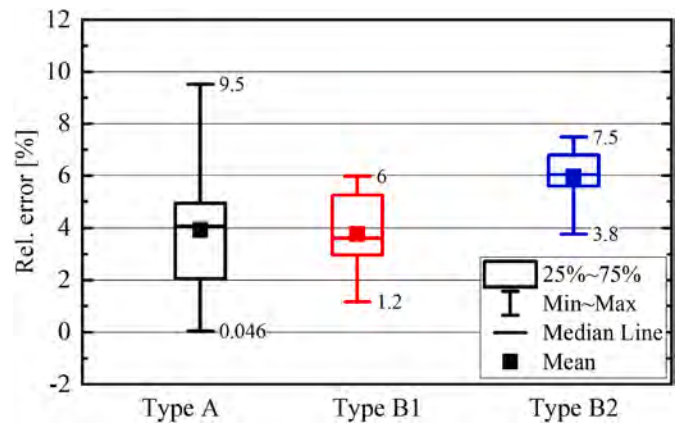


Fig. 15. Relative error between the barrel shaped cross-section and the ideal rectangular cross-section for each specimen type.

5.2. Errors affecting the Weibull distribution

The influence of utilizing average dimensions instead of individual dimensions on the Weibull evaluation is assessed through MC-analysis. The parameters of the underlying distributions for the dimensions h_{max} and α are given Table 2. They were determined with measurements taken from four specimens of the 0° configuration, with a minimum of 47 cantilevers per specimen. The final result of the MC analysis is the relative difference between the Weibull parameters determined with individual or average dimensional measurements. 1000 randomized runs were conducted, and the results are displayed as distribution densities in Fig. 16a)-c).

Note that the extent of the deviation in σ_0 does decrease with an increased number of measurements for the average dimensions, while the extent of the deviation in m does not change substantially. In general, the center of the density distribution is at about +1% deviation in σ_0 and -12% deviation in m . Further investigations based on MC analysis have shown that the influence of Δh on the deviation of σ_0 and m is significantly higher than that of $\Delta\alpha$.

5.3. Strength and orientation dependency

The number of valid bending tests N , the characteristic strength σ_0 , and the Weibull modulus m as well as their respective 90% confidence intervals are given in Table 3 for each specimen. Table 4 gives the same parameters for a combined evaluation of multiple test specimens. This has only been performed if the confidence intervals of all test specimens included overlap. Fig. 17 displays the individual results of strength testing and for the combined evaluations sorted by each specimen type.

It is evident that the characteristic strength of both 15° configurations (Type B1 & B2) is lower than that of the 0° -configuration (Type A). The difference in characteristic strength between specimens of Type B1 and B2 is not statistically relevant as most of their confidence intervals overlap. The same is true for the Weibull modulus of each specimen type. Furthermore, significant differences between batches can be observed, e. g. specimens of batch two and three of Type A. An exemplary fracture surface for a specimen of Type B2 is given in Fig. 18. It is evident that the origin of failure is within the groove of the surface. This was found in the majority of observed cases. In the displayed case, the

Table 2

Parameters used for the normal distributed values of the height h_{max} and the opening angle α for the Monte-Carlo analysis.

Parameter	Mean μ	Standard deviation Δ
Height h_{max} [mm]	1.13	0.017
Opening angle α [-]	17.76	0.72

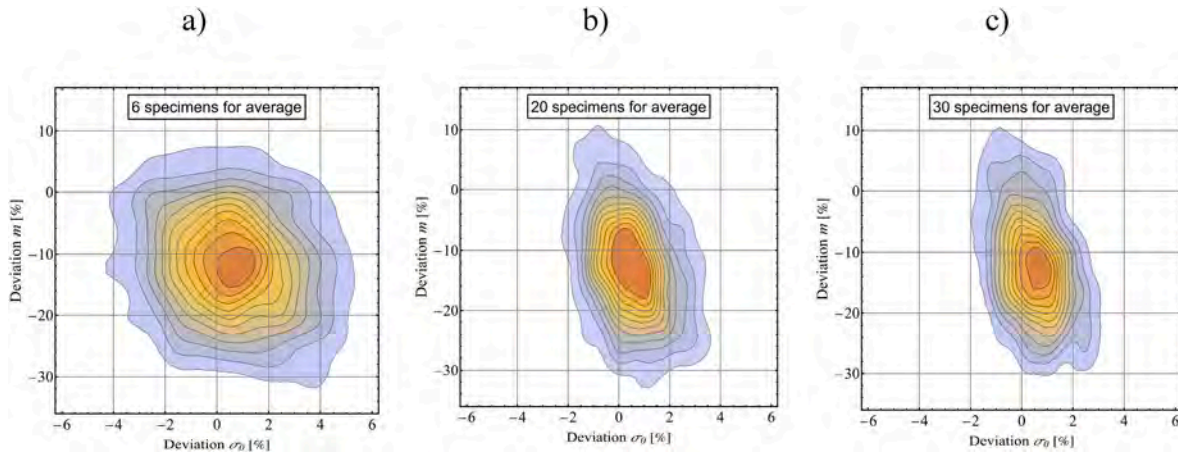


Fig. 16. Results of the MC analysis. Each figure shows the density distribution of the relative difference in m and σ_0 between individual and average dimension measurements for 1000 simulations. In a), 6 random dimensions are used to determine the average dimensions, 20 in b) and 30 in c).

Table 3

Results of strength testing for each specimen. N gives the number of valid bending tests, m and m_{ub} the biased and unbiased Weibull modulus, and σ_0 the characteristic strength with *lower* and *upper* indicating the respective 90% confidence intervals. The designation starts with the specimen type, followed by the batch number and finally the specimen number within that batch.

Type	Designation	N [-]	m [-]	m_{ub} [-]	m_{lower} [-]	m_{upper} [-]	σ_0 [-]	$\sigma_{0,lower}$ [-]	$\sigma_{0,upper}$ [-]
A	A.1.1	25	12.3	11.7	8.9	15.2	342	332	352
	A.1.2	19	12.4	11.5	8.5	15.8	352	340	365
	A.2.1	33	9.1	8.8	7.0	11.1	335	323	346
	A.2.2	29	10.7	10.2	8	13.1	336	326	348
	A.3.1	18	8.8	8.1	5.9	11.2	376	357	396
	A.3.2	32	11.5	11.0	8.7	13.9	364	354	375
B1	B1.1.1	44	16.3	15.8	13.0	19.2	301	296	306
	B1.1.2	41	13.7	13.3	10.8	16.3	287	281	293
	B1.2.1	27	9.9	9.4	7.3	12.2	320	309	332
	B1.3.2	32	8	7.7	6.1	9.8	281	270	292
	B2	B2.1.1	47	13.6	13.2	10.9	15.9	323	317
B2.1.2	47	12.3	11.9	9.9	14.5	296	290	302	
B2.2.2	29	15.9	15.2	11.8	19.5	317	311	324	
B2.3.1	44	11.5	11.2	9.2	13.6	333	325	341	

Table 4

Results of the combined evaluation of strength testing results for specimens of type A.

Designation	N [-]	m [-]	m_{ub} [-]	m_{lower} [-]	m_{upper} [-]	σ_0 [-]	$\sigma_{0,lower}$ [-]	$\sigma_{0,upper}$ [-]
A.1.1 + A.1.2	44	12.2	11.8	9.7	14.4	347	339	354
A.2.1 + A.2.2	62	9.8	9.5	8.1	11.3	336	328	343
A.3 (A.3.1 + A.3.2)	50	10.0	9.8	8.1	11.7	369	360	378
A.1 & A.2 (A.1.1 + A.1.2 + A.2.1 + A.2.2)	106	10.6	10.4	9.2	11.9	340	335	346

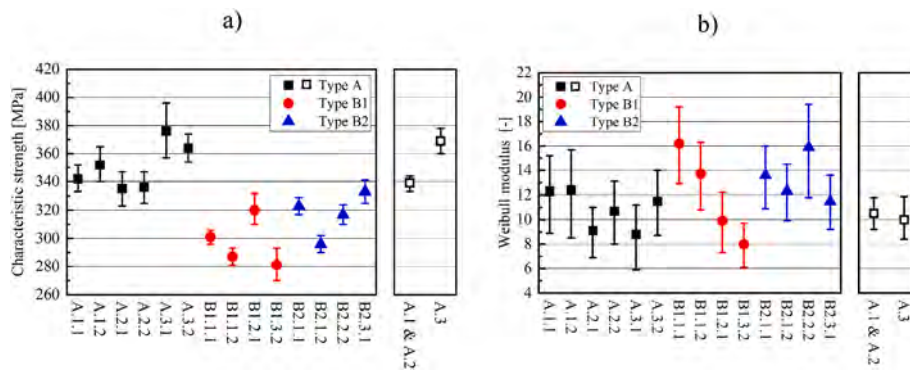


Fig. 17. a) shows the characteristic strength and b) shows the (unbiased) Weibull modulus of each tested specimen. The combined evaluation of multiple test specimens is displayed separately through the black open markers. The 90%-confidence intervals are given by the error bars.

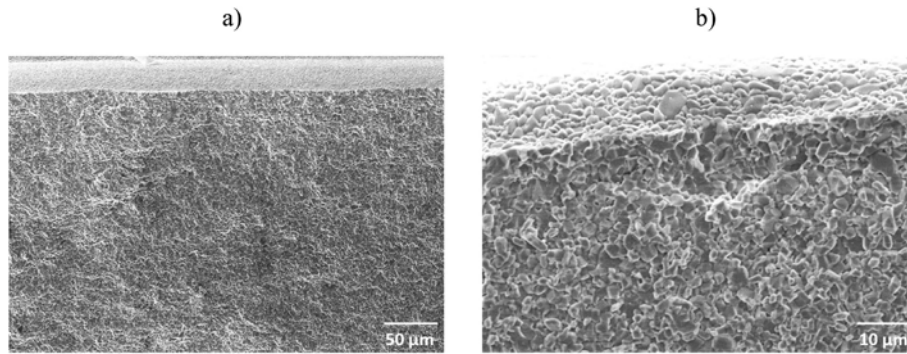


Fig. 18. SEM-image of a typical fracture surface of a 15°–180° specimen in a) with the failure-causing defect depicted in b).

failure is caused by a pore as shown in Fig. 18b).

To assess the influence of surface orientation on the measured strength, the surface structures are investigated in detail. Surface characterization has shown that specimens of Type A did not exhibit any surface structures except the regular surface roughness after sintering, which appeared on all specimen types. Therefore, this configuration will be considered as ideally flat for further comparison and discussions. Characterization of the surface structures of the other configurations revealed a periodical wave-like structure. This structure can be quantified with two parameters, the wavelength and the wave’s amplitude. The average values for both 15° configurations are given in Table 5.

These structures were subsequently implemented in the sub-model and compared to the case of an ideal flat surface structure, i.e. specimens of Type A. As shown in Fig. 19, the maximum stress at the surface increases significantly. The stress increase for each type of specimen is given in Table 6. The maximum stress increases by about 54% for Type B1 and 45% for Type B2, with the maximum stress located in the valleys of the grooves. These are thus preferred locations for fracture.

Further results from FEA are the effective volume V_{eff} and effective surface S_{eff} . Each value was determined by utilizing the same normalization stress σ^* , that is the maximum tensile stress of specimen Type A. Note that for specimens of Type B1, the structured surface increases the effective surface by more than a factor of ten, while the effective volume increases by approximately 60%. The ratio σ_B/σ_A gives the influence of the increase in effective sizes on the measured strength based on either V_{eff} or S_{eff} . These results are also shown in Table 6.

6. Discussion

Regarding each individual strength result, the shift in ideal loading position a causes an average overestimation of the applied stress from 1.6% to 3.7%, which results in an underestimation of the materials’ strength by the same amount. The further the cantilevers fail from the point of load introduction, the smaller this effect becomes. In this work, the majority of cantilevers failed at a distance of 6mm–7mm from the point of load introduction, meaning that the deviation in stress is likely to be smaller than 2.7%. Therefore, this effect is rather small and a does not have to be evaluated for each specimen, but the authors recommend to check this issue on several random cantilevers. In a similar way, the deviating shape of the cross section causes a general underestimation of the materials strength by 8%–10% through an overestimation of the section modulus. In combination with the problem of the shift in loading

Table 5

Average quantification parameters of the surface structures for each specimen type.

Parameter	Type A (0°)	Type B1 (15°)	Type B2 (15°–180°)
Amplitude [μm]	–	12.8	10.7
Wavelength [μm]	–	122.6	123.3

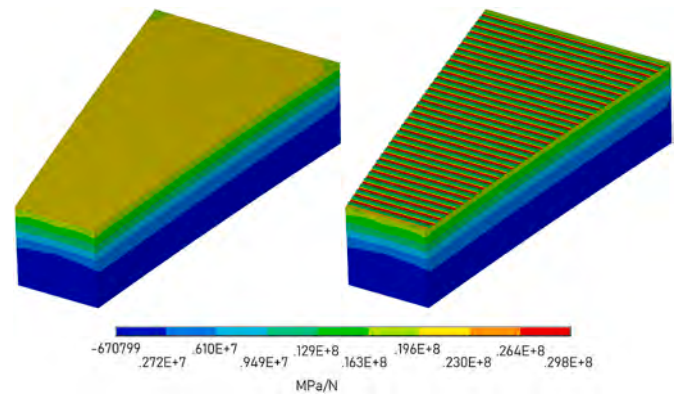


Fig. 19. Distribution of the first principal stress for an ideal specimen without surface structures (Type A, left) and with surface structures (Type B2, right). Both simulations were conducted for specimens with the same length and width. The height of the wavy specimen was chosen so that the zero line of the sinusoidal wave is the same as the height of the ideal specimen, which gives the same specimen volume.

Table 6

Relative increase of the maximum tensile stress σ_{max} , effective volume V_{eff} and effective surface S_{eff} for each specimen type as well as the expected change in the measured strength σ_B/σ_A due to the change in either V_{eff} or S_{eff} for $m = 10$.

Parameter	Flat surface Type A (0°)	Type B1 (15°)	Type B2 (15°–180°)
σ_{max}	1	1.54	1.45
V_{eff}	1	1.62	1.39
S_{eff}	1	12.82	8.45
σ_B/σ_A (V_{eff})	1	0.95	0.97
σ_B/σ_A (S_{eff})	1	0.78	0.8

position, an average underestimation of the material’s strength of about 12% with an uncertainty of about $\pm 4\%$ remains, which is similar for all specimen types. This means that a direct comparison between different specimen types, i.e. different surface orientations, of the same material is feasible. If the absolute strength of the tested material is of high importance, both effects have to be checked and considered for strength evaluation.

Due to the dimensional inconsistency, the influence of utilizing average values for the cantilever’s dimensions on the results of Weibull evaluation was investigated. Monte-Carlo analysis has shown that utilizing average values will slightly shift both the average characteristic strength (+1%) and the average Weibull modulus (–12%). While these values would still be acceptable, the possible deviation in m ranges from +10% to –30%, which is too much to allow Weibull evaluation with average dimensions. Increasing the number of measurements to

determine the average dimensions does not decrease the possible variation in Weibull modulus. Therefore, individual measurements of both the specimen's thickness and the opening angle for each cantilever are recommended to neglect this effect. However, the aforementioned uncertainty of $\pm 4\%$ for each individual strength result limits the maximum detectable scatter of the material's strength. With this uncertainty, a precise determination of the material's Weibull modulus m is possible for $m \leq 20$ [23].

The analysis of the influence of surface structures on the measured strength shows that the increase in effective surface from a flat to a structured specimen is notably larger than in effective volume. This is due to the surface structures mainly affecting the stress distribution at the surface and the first 10 μm of the bulk material. A long-range influence on the stress distribution in the bulk material was not detected. This forms a strong initial stress gradient from the increased surface stress towards the neutral plane. S_{eff} is only dependent on the stress in the edge fiber, where the stress increases the most. Additionally, the regions of increased stress make up a significant portion of the total surface, hence why a stress increase of 54% (to the power of $m = 10$) results in an extreme increase in S_{eff} . For V_{eff} , the regions of increased stress only make up a very small part of the total volume, which is why its increase is much smaller compared to that of S_{eff} . Usually, the defects found at the origin of failure are either surface defects (for which S_{eff} is relevant) or volume defects (for which V_{eff} is relevant). Therefore, these results give the upper and lower limits for the influence of the observed surface structures, with σ_B/σ_A as an estimation of the change in measured strength. The actual decrease in measured strength depends on whether the defects are more akin to surface- or volume defects.

The strength results obtained in this work show a significant drop-off in strength from the 0° configuration to the other configurations. This decrease is in good agreement with the expected results based on the concept of effective volume or surface and previous work [11,19]. It is evident that the influence of surface structures on the measured strength should not be neglected. This observation is further supported by the results of fractographic analysis, which shows that a high number of fractures originated in the grooves of the surface structures.

Despite these uncertainties, this novel testing method provides a number of promising advantages over common testing methods such as uniaxial and biaxial bending. First and foremost, it allows the fabrication of 96 test specimens, i.e. cantilevers, with a single manufacturing batch. This is well enough to perform a well-founded Weibull analysis on each specimen. Therefore, two different configurations could be manufactured within one batch, which further increases the time- and material efficiency of this method. Additionally, since all cantilevers are manufactured within one batch, it is possible to make out differences between individual batches and thermal treatments. Other methods often require a number of batches to fabricate the necessary number of specimens for statistical evaluation, which adds an additional layer of variation to those methods. This variation may stem from differences in specimen handling and cleaning or, if not handled properly, from modification of the slurry. The observed deviations from the ideal specimen geometry are the most important sources of error. If the non-rectangular cross-section of the cantilevers is not taken into account, a direct comparison of specimens manufactured from the same material is still possible. However, this error is too large to accurately determine the absolute characteristic strength and Weibull modulus of the utilized material. The other errors, which also affect the individual strength results, can be minimized by increasing the reproducibility during manufacturing. As an example, the specimens tested in this work were individually cleaned by hand, with low variations in the amount of solvent used. The solvent interacts with the specimen's surface and could therefore easily influence the measured results. Similarly, specimens were successively manufactured throughout three to five days without a complete exchange of slurry. During this time, interaction with the environment or contamination of the slurry might have occurred, changing the properties of the source material.

Taking these manufacturing-related effects into account, the next step in the development of this testing method would be a higher degree of automation. This includes procedures such as 3D-scanning the whole specimen, from which the cantilevers dimensions are evaluated automatically. Furthermore, a round robin with individual manufacturing and controlled testing could aid in determining the most important areas of improvement.

7. Summary

In this work, a new method for strength testing of additively manufactured materials is presented. The testing method is based on a novel specimen, which was designed to take the characteristics of additive manufacturing into account. On one hand, it was developed for time- and material efficient fabrication. Each specimen consists of a base plate and 48 cantilevers attached to it, thus generating enough data to perform statistical analysis. A large effective volume in comparison to well-known strength testing methods further contributes to the specimen's efficiency. On the other hand, the specimen can easily be adjusted so that different surface orientations can be investigated. This gives insight into the influence of surface structures on the measured strength, which vary significantly depending on the surface orientation.

Functional expressions for strength evaluation and the determination of effective volume and surface are given and validated with Finite Element Analysis (FEA). The influence of surface structures on the measured strength is analyzed based on Weibull theory and FEA. Other possible influences on the accuracy of this testing method are discussed through analytical considerations, Monte-Carlo analysis, and FEA. These effects are quantified based on practical observations and their impact is discussed. An example for a possible testing fixture is shown and demonstrated for multiple specimen configurations. More specifically, a minimum of four specimens for three different configurations were fabricated and tested. The results are evaluated statistically through Weibull theory. The observed influence of surface structures on the measured strength is in good agreement with the predictions based on FEA.

Overall, the deviation of the dimensions of the manufactured specimens from the ideal geometry limits the achievable accuracy of this testing method for strength determination. This effect can be minimized if the dimensions for each tested cantilever are individually recorded and if the fabrication process is streamlined and reproducibility is increased. However, the testing method can depict differences between different surface orientations and between specimens from each manufacturing batch. The latter is especially important for additive manufacturing, as regular testing methods such as uniaxial four-point bending and biaxial bending often require multiple batches to produce the necessary number of specimens for statistical analysis.

Data availability

Data will be made available on request.

Declaration of competing interest

The authors declare that they have no known competing financial interests or personal relationships that could have appeared to influence the work reported in this paper.

Acknowledgements

M. Staudacher gratefully acknowledges financial support by the Austrian BMVIT and BMWFW in the project "CharAM" (FFG 877684) of the COIN/IraSME program.

References

- [1] Z. Chen, Z. Li, J. Li, C. Liu, C. Lao, Y. Fu, C. Liu, Y. Li, P. Wang, Y. He, 3D printing of ceramics: a review, *J. Eur. Ceram. Soc.* 39 (2019) 661–687.
- [2] A. Zocca, P. Colombo, C.M. Gomes, J. Günster, Additive manufacturing of ceramics: issues, potentialities, and opportunities, *J. Am. Ceram. Soc.* 98 (2015) 1983–2001.
- [3] A. de Blas Romero, M. Pfaffinger, G. Mitteramskogler, M. Schwentenwein, C. Jellinek, J. Homa, A. Díaz Lantada, J. Stampfl, Lithography-based additive manufacture of ceramic biodevices with design-controlled surface topographies, *Int. J. Adv. Manuf. Technol.* 88 (2017) 1547–1555.
- [4] A.D. Lantada, A. de Blas Romero, M. Schwentenwein, C. Jellinek, J. Homa, Lithography-based ceramic manufacture (LCM) of auxetic structures: present capabilities and challenges, *Smart Mater. Struct.* 25 (2016), 54015.
- [5] S. Nachum, J. Vogt, F. Raether, Additive manufacturing of ceramics: stereolithography versus binder jetting, *Ceram. Forum Int.* 93 (2016).
- [6] N. Travitzky, A. Bonet, B. Dermeik, T. Fey, I. Filbert-Demut, L. Schlier, T. Schlördt, P. Greil, Additive manufacturing of ceramic-based materials, *Adv. Eng. Mater.* 16 (2014) 729–754.
- [7] M. Schwentenwein, J. Homa, Additive manufacturing of dense alumina ceramics, *Int. J. Appl. Ceram. Technol.* 12 (2015) 1–7.
- [8] D. Munz, T. Fett, *Ceramics: Mechanical Properties, Failure Behaviour, Materials Selection*, Springer, Berlin, Heidelberg, 1999.
- [9] T. Lube, M. Staudacher, A.-K. Hofer, J. Schlacher, R. Bermejo, Stereolithographic 3D printing of ceramics: challenges and opportunities for structural integrity, *Adv. Eng. Mater.* 25 (2023), 2200520.
- [10] T. Lube, J. Schlacher, W. Harrer, R. Danzer, G. Mitteramskogler, M. Schwentenwein, *Mechanische Eigenschaften von gedruckten Keramiken, Praktische Metallographie Sonderband*, 2018, pp. 229–234.
- [11] J. Schlacher, T. Lube, W. Harrer, G. Mitteramskogler, M. Schwentenwein, R. Danzer, R. Bermejo, Strength of additive manufactured alumina, *J. Eur. Ceram. Soc.* 40 (2020) 4737–4745.
- [12] ASTM C1161 - 18, Test Method for Flexural Strength of Advanced Ceramics at Ambient Temperature, ASTM International, West Conshohocken, PA, 2018.
- [13] DIN EN 843-1:2008-08, Advanced Technical Ceramics - Mechanical Properties of Monolithic Ceramics at Room Temperature - Part 1: Determination of Flexural Strength, German Institute for Standardisation (Deutsches Institut für Normung), 2008. German version EN 843-1:2006.
- [14] Werkstoffe und Bauteile auf dem Prüfstand. Prüftechnik - Kennwertermittlung - Schadensvermeidung, Tagung Werkstoffprüfung 2022, DGM, 2022.
- [15] A.L. Gebhardt, Prüfkörperauslegung und Ergebnisinterpretation für die Festigkeitsbewertung gedruckter filigraner Keramikstrukturen, Master's Thesis, Dresden, 2020.
- [16] S. Timoshenko, *History of Strength of Materials: with a Brief Account of the History of Theory of Elasticity and Theory of Structures*, Dover Publications, New York, 1983.
- [17] J.B. Wachtman, M.J. Matthewson, W.R. Cannon, *Mechanical Properties of Ceramics*, Wiley, Hoboken, N.J., 2009.
- [18] G.D. Quinn, Weibull strength scaling for standardized rectangular flexure specimens, *J. Am. Ceram. Soc.* 86 (2003) 508–510.
- [19] C. Liu, S. Aengenheister, S. Herzog, Y. Deng, A. Kaletsch, K. Schmitz, C. Broeckmann, Application of Weibull theory to laser surface textured Al2O3, *J. Eur. Ceram. Soc.* 41 (2021) 1415–1426.
- [20] E. Narvydas, N. Puodziuniene, A.K. Thorappa, Application of finite element sub-modeling techniques in structural mechanics, *Mechanika* 27 (2021) 459–465.
- [21] N.G. Cormier, B.S. Smallwood, G.B. Sinclair, G. Meda, Aggressive submodelling of stress concentrations, *Int. J. Numer. Methods Eng.* 46 (1999) 889–909.
- [22] R. Danzer, T. Lube, P. Supancic, Monte Carlo simulations of strength distributions of brittle materials – type of distribution, specimen and sample size, *Int. J. Mater. Res.* 92 (2001) 773–783.
- [23] R. Bermejo, P. Supancic, R. Danzer, Influence of measurement uncertainties on the determination of the Weibull distribution, *J. Eur. Ceram. Soc.* 32 (2012) 251–255.
- [24] DIN EN 843-5 2007, Advanced Technical Ceramics - Mechanical Properties of Monolithic Ceramics at Room Temperature - Part 5: Statistical Analysis, German Institute for Standardisation (Deutsches Institut für Normung), 2007.

Paper G

S. Strobl, P. Supancic, T. Lube, R. Danzer: "Surface Crack in Tension or in Bending - A Reassessment of the Newman and Raju Formula in Respect to Fracture Toughness Measurements in Brittle Materials", *Journal of the European Ceramic Society* **32** (2012), 1491–1501, <http://dx.doi.org/10.1016/j.jeurceramsoc.2012.01.011>

Re-used as author according to Elsevier's copyright agreement.

Surface crack in tension or in bending – A reassessment of the Newman and Raju formula in respect to fracture toughness measurements in brittle materials

Stefan Strobl^{a,b,*}, Peter Supancic^{a,b}, Tanja Lube^a, Robert Danzer^a

^a Institut für Struktur- und Funktionskeramik, Montanuniversität Leoben, Peter-, Tunner-Straße 5, A-8700 Leoben, Austria¹

^b Materials Center Leoben Forschung GmbH, Roseggerstraße 12, A-8700 Leoben, Austria^d

Received 30 September 2011; received in revised form 14 December 2011; accepted 7 January 2012

Available online 6 February 2012

Abstract

The Newman and Raju formula for the stress intensity factor of a semi-elliptical surface crack loaded in uniaxial tension or in bending has been developed about 30 years ago using an FE-analysis for several geometric parameters and fitting an empirical equation to the data points. The Poisson's ratio analyzed was 0.3.

In this paper a reassessment of the Newman and Raju formula is made, where all relevant geometric parameters of crack and specimen and the Poisson's ratio are considered. The deviations of the old formula from the new results are up to 21%, if the full range of Poisson's ratio is taken into account. Furthermore the influence of the crack-surface intersection angle is discussed.

The results of this work are important for more precise fracture toughness measurements in brittle materials and give a practical guidance for appropriate specimen preparation for fracture toughness measurements, which is also considered here.

© 2012 Elsevier Ltd. All rights reserved.

Keywords: Semi elliptical surface crack; Stress intensity factor; SCF method; Fracture toughness; Poisson's ratio

1. Introduction

The majority of standardized fracture toughness testing methods for ceramics use bending beams, containing a crack as sharp as possible and a well-defined geometry. The fracture toughness K_{Ic} is determined by application of the Griffith/Irwin failure criterion:

$$K_{Ic} \geq K = \sigma Y \sqrt{a\pi} \quad (1)$$

K_{Ic} is the mode I fracture toughness, K is the stress intensity factor (SIF), σ is a representative stress in the uncracked specimen (e.g. stress at the outer fibre at fracture), a the size of the crack and Y is a geometric factor, which is determined by the

geometry of the specimen, the crack shape and the course of the stress field. For details see standard text books on fracture mechanics or on mechanical properties of ceramics.^{1–3} Information on geometric factors for typical loading cases and standard specimen geometries can be found in literature.⁴

The Newman and Raju formula (NRF) is commonly used in the “Surface Crack in Flexure” (SCF)-method to determine fracture toughness in brittle materials. For materials with the Poisson's ratio $\nu = 0.3$, Newman and Raju (NR)⁵ have developed a parameterized and generalized solution (i.e. fitting function) of the geometric factor $Y = Y(a, c, t, b, \phi)$ of a semi-elliptical surface crack in the stress field of a uniaxial tensile loaded or bended bar (thickness t and width $2b$). Therefore, Y depends on the geometry of the crack (crack width $2c$, crack depth a), the bar's cross-section and on the position at the crack front given by the crack angle ϕ , see Fig. 1.

Of course, fracture is initiated at the position the largest SIF along the crack front. But there exists some shortcomings which may conflict the exact determination of SIF and fracture toughness: Thirty years ago computer capacity was very limited which made a relatively coarse mesh necessary. Therefore the

* Corresponding author at: Institut für Struktur- und Funktionskeramik, Montanuniversität Leoben, Peter-Tunner-Straße 5, A-8700 Leoben, Austria. Tel.: +43 3842 402 4113; fax: +43 3842 402 4102.

E-mail address: stefan.strobl@mcl.at (S. Strobl).

^c www.isfk.at.

^d www.mcl.at.

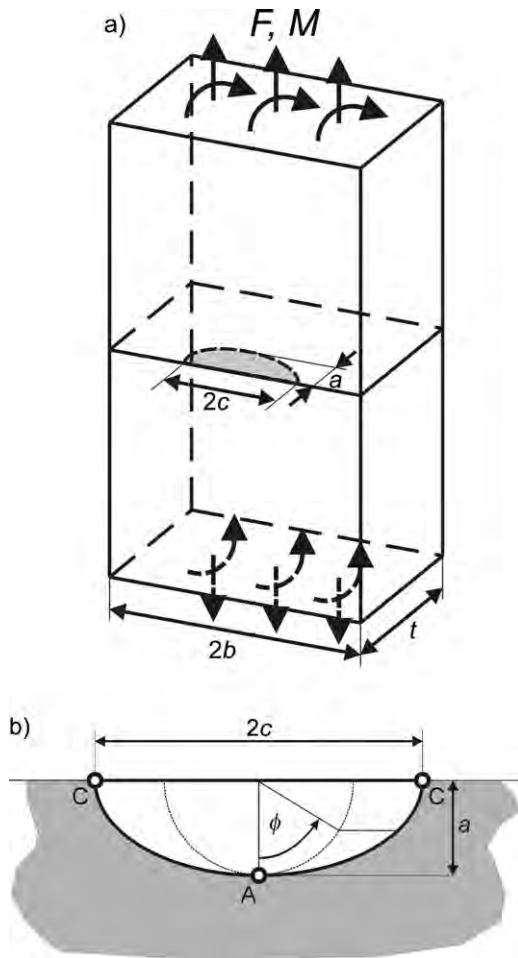


Fig. 1. (a) Schematic of a pre-cracked beam (loaded by normal force F or moment M) and (b) detail of the semi-elliptical crack assumed for the NRF. The crack width $2c$ at the surface and the crack depth a are indicated as well as the points A ($\phi = 0^\circ$) and C ($\phi = 90^\circ$), where the geometric factor Y can reach a maximum in the NRF.

precision of the analysis was not very high. (NR) specified their FE accuracy with $\pm 3\%$ compared to the analytical solution in terms of a completely embedded circular crack.^{6,7}

In addition, to keep the fitting function simple, it cannot be very precise for all possible values of geometric parameters. NR claim that their provided fitting function has a maximum error of $\pm 5\%$ (related to the maximum of Y along the crack front) according to their FE results.⁵

Secondly, the analysis was only made for materials having the Poisson's ratio $\nu = 0.3$ which is the typical value of steels. This is also a good approximation for many engineering material classes. However, there are also many other materials – e.g. ceramics for structural applications or hard coatings – with a significant deviation regarding this value.^{2,8–10}: Diamond (0.07), titanium diboride (0.1), zirconium diboride (0.14), glass and silicon carbide (0.16), hard metal and alumina (0.2), titan (0.36) or PMMA (0.4). Because even structural ceramics can deviate substantially, the Poisson's ratio should be considered in the data evaluation. In the literature, some calculations for an individual set of parameters can be found, e.g. by Isida et al.^{4,11} in 1983, where for a special crack geometry data for several different

Poisson's ratios are tabulated. But there is no general solution available.

Finally, the geometry of surface cracks used for fracture toughness measurements is – in general – not semi elliptical (the crack-surface intersection angle differs from 90°) which may result in additional uncertainties. This topic is treated in^{12–15} in detail and addressed in.^{16,17} A specific example has been studied by Fett.¹⁸ For a crack, with the shape of circle segment, the differences to the semi-elliptical crack in the geometric factors are less than: $\pm 7\%$ in point A and less than $\pm 2\%$ in point C (see Fig. 1) for cracks having the same aspect ratio a/c . These results also are made for a specific case and their accuracy is unknown. The influence of crack-surface intersection angle will be investigated in detail in this work.

For these reasons, a reassessment of the NRF and a new fitting equation for the SIF is made in this paper. Semi elliptical cracks and cracks having a geometry, which is more relevant for fracture toughness testing of brittle materials, are considered. All results and the new fitting equation for the SIF are given at our home page (www.isfk.at/de/1006/) as an interactive WebMathematica tool. It is shown that – for realistic testing geometries – the NRF may result in huge deviations of the correct value in point A (up to 40% for $\nu = 0.3$).

Another aspect in SCF testing arises from the fact that – depending on the crack geometry and the Poisson's ratio – fracture can start at the deepest position of the crack (point A) or at its intersection with the specimen's surface (point C). The SCF analysis is valid for experiments with fracture origins at point A, while experiments with origins at point C are invalid for several reasons. In the last part of this paper parameter regimes are defined, where valid SCF-tests with origins at point A can be guaranteed.

2. Methodology – FE model and parameters

The geometric factor Y for a surface crack having the geometry of an ellipse segment was determined in a parametric study for tension and bending loading (each 3125 FE runs). The results were used to define an interpolation function for Y . The considered parameter intervals are given in Table 1.

Characteristic parameters in our model are the crack depth a and its length at the surface c . Note that the crack intersects the surface with the angle χ (see Fig. 2), since the crack has the shape of a segment. The midpoint of the (truncated) ellipse is Δt ahead of the surface. It holds:

$$a_0 = \frac{a(a \cos(-\chi) + c \sin(-\chi))}{2a \cos(-\chi) + c \sin(-\chi)} \quad (2)$$

and

$$\Delta t = a_0 - a \quad (3)$$

The other semi-axis c_0 can be derived using the ellipse equation. Eq. (2) shows that for the crack shape ratio with the highest analyzed axis ratio ($a/c = 1.2$) the intersection angle of the semi-ellipse segment is $\chi \geq 70^\circ$. This determines the lower limit for the parametric FE-study. Lower angles, which were possibly

Table 1

Parameter and considered parameter intervals for the realized FE study. For each parameter five equidistant design points have been used. For a/t the values 0.01, 0.05, 0.1, 0.3 and 0.5 have been chosen.

Dimensionless parameter name	Symbol	Lower limit	Upper limit
Rel. crack depth	a/t	0.01	0.5
Crack aspect ratio	a/c	0.4	1.2
Rel. crack width	c/b	0.1	0.5
Poisson's ratio	ν	0	0.4
Crack-surface intersection angle	χ	70°	110°

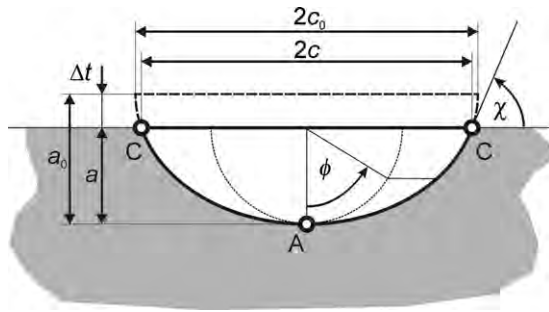


Fig. 2. Geometry of a surface crack (depth a , width $2c$) having the shape of an ellipse segment. Also the intersection angle χ is defined. The semi axes of the ellipse are: a_0 , c_0 .

needed, have been extrapolated and checked by some specific FE runs.

The computation of stress distribution in the specimen was performed in ANSYS Mechanical APDL Version 13.0. The quarter-model of the bar includes about 16,000 to 60,000 brick-elements (i.e. SOLID186).

The J -Integral method^{19,20} – with quarter node collapsed crack tip elements (CTE) – was used to calculate the SIF. This well-implemented state-of-the-art method provides accurate results (the error is less than 0.01% compared to the analytical solution in the case of a fully embedded circular crack in pure tension).¹⁹ Due to the CTE and the resulting ansatz functions, the crack tip singularity exponent is given with -0.5 . Generally, this exponent deviates from this value if there is some influence of boundaries (e.g. at the free surface or near interfaces). So the SIF results are the “best fit” of the actual stress field with K as (FE internal) fit coefficient.

For all crack sizes, 30 elements along the crack front have been used and their alignment around the crack tip was equal. This was realized with an all hexahedron-meshed parallelepiped. Crack mesh details for different crack geometries are pointed out in Fig. 3, where three special cases are given exemplarily. The SIF was evaluated at all 61 nodes (including mid nodes) along the crack front.

In every case, singularity elements (CTE) along the crack front and a plain strain assumption (effective Young's modulus $E^* = E/(1 - \nu^2)$) were deployed for the determination of the stress intensity, more precisely with the formulation $K = \sqrt{E^* \cdot J}$.

This approach is commonly accepted (e.g. see^{19,21}), although generally plain stress state should occur at the surface. However, Zúñiga et al.²² claim that the stress distribution at the surface can

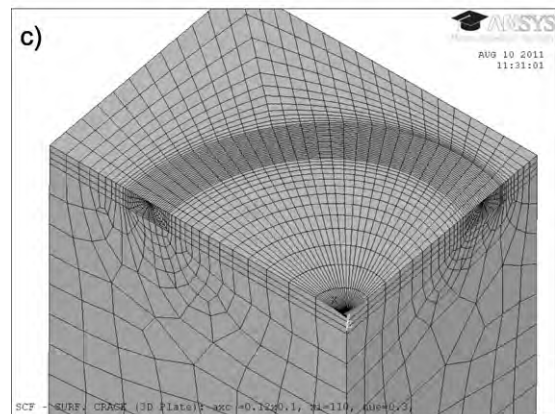
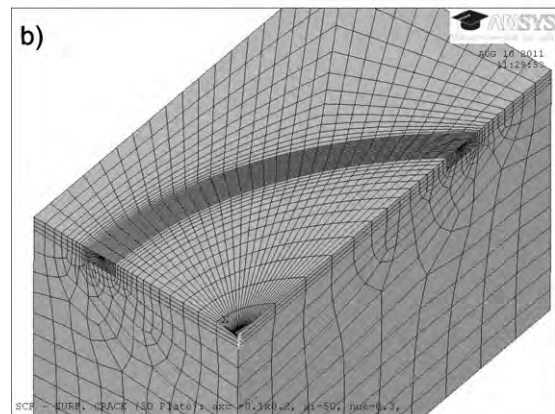
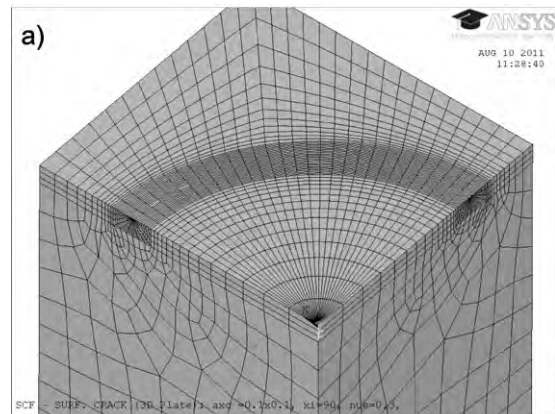


Fig. 3. Three examples of crack geometries and meshing details near the crack front. (a) $a/c = 1$ and $\chi = 90^\circ$, (b) $a/c = 0.5$ and $\chi = 50^\circ$, (c) $a/c = 1.2$ and $\chi = 110^\circ$.

significantly deviate from the plain stress assumption in a 3D-geometry with crack. In addition, since the resulting K -values are always higher for plain strain, the calculation of the SIF at the region very close to the surface is a good approximation regarding safety aspects (e.g. for fatigue or proof of safety calculations).

Correlated to Eq. (1) the geometric factor along the crack front can be expressed with the related K , the nominal crack opening stress σ (i.e. 1 MPa) and the crack depth a (Note: Y always refers to the crack depth a , what means that a is taken as the typical defect size).

3. Results

The FE results and their tendencies behave, of course, similar to the generalized solution of NR.⁵ For this reason this work has a focus on the main differences to the NRF and on the influence of the Poisson's ratio and the crack-surface interaction angle on the geometric factor. Since these effects are more pronounced for bending than for uniaxial tension loading all further results are plotted for $\chi = 90^\circ$, $c/b=0.1$ and the bending case, if not specified else wise.

In Fig. 4 the current FE results (lines) are shown as a function of ϕ (the ratio a/t is parameter of the curves) for a semi-circular crack and are compared with the fitting solution of NR (plotted as points). The values of $a/t=0$ are extrapolated (the last design point is at 0.01) and represent an infinitesimal small crack. This also eases the comparison with other publications, e.g. NR.

As expected, both results are nearly identical for $\nu=0.3$ (Fig. 4a). Obvious deviations just occur for higher relative crack sizes as well as around $\phi \simeq 85^\circ$. The last observation results from the facts, that the free surface influences the SIF (see also Section 4.3) and that there was no design point (i.e. node) in the calculation of NR. In other words their mesh was too coarse for such a detailed analysis.^{6,7} For $\phi=90^\circ$ the agreement is good, since a design point for NR is there.

For $\nu=0$ (see Fig. 4b) the results consequently shift compared to the NRF. This indicates that the Poisson's ratio has a significant influence on SIF. On the other hand there is no change in course of Y in the vicinity of $\phi=90^\circ$. The effect of the free surface is reduced since the Poisson's ratio decreases to zero.

In Fig. 4 two "exact" reference data points of Y for $\nu=0$ and 0.3 published by Isida et al.¹¹ are marked. They showed that their method has an error less than 0.1%, which can also be shown with the method by Fett²³. The results are tabled for an infinite plate (pure tension loading). Their obtained values of 0.659 and 0.036, respectively, are in excellent agreement with the present work: for $\nu=0.3$ (see Fig. 4a) the extrapolated values of the interpolation function are 0.660 (tension) and 0.659 (bending). For $\nu=0$ (see Fig. 4b) they are 0.635 (tension) and 0.636 (bending). Of course both loading cases should be equal in an infinite plate.

For shallow cracks ($a/c=0.4$) an analogue comparison is illustrated in Fig. 5. The results in point A and C match the NRF quite good for $\nu=0.3$ (Fig. 5a). Large deviations arise just in between these points, especially for small relative crack sizes (max. 12% at $\phi \approx 60^\circ$). The results obtained for $\nu=0$

(Fig. 5b) confirm the same down-shifting trend as for semi-circular cracks. This results in high average deviations.

In the following, the influence of the Poisson's ratio is investigated in more detail. As anticipated, the curves respecting semi-circles and $\nu=0.3$ correlate well with the fit of NR (Fig. 6a). Inside the specimen the geometric factor increases (much stronger than linear) with increasing Poisson's ratio, but near the surface the effect is contrary; Y declines for higher Poisson's ratios. The same non linear trends can be observed for small crack shape ratios a/c , see Fig. 6b.

The influence of the crack-surface intersection angle χ on the SIF is very pronounced (along the whole crack front; see Fig. 7). In both cases, semi-circular and shallow crack, χ influences the SIF even at the deepest point of the crack (A), although the characteristic crack parameters a and c (only these both are normally used to characterise the crack) are kept constant and the crack front has almost the same curvature in point A. Here the SIF and Y , respectively, decline with decreasing χ . In point C the influence of χ is very strong compared with point A. The magnitude of this effect has to be observed skeptically. For instance, the J -Integral evaluation is valid for such a vertex point with an acute angle if there is no material perpendicular to the crack front. This will not be discussed in detail here.

In the case of $a/c=1$ (Fig. 7a), the value for $Y(\chi=90^\circ)$ differs from $Y(\chi=70^\circ)$ in point A by about 10%, which is a noticeable effect and has also a direct impact on fracture toughness measurements. For $a/c=0.4$ (see Fig. 7b), this influence is significantly lower with deviations of about 1.5% than for narrow crack (the same trend can be found in the uncertainty analysis in¹⁷).

4. Data fitting and discussion

To determine a generalized solution for $Y = Y(a/c, a/t, c/b, \phi, \nu, \chi)$ all its six parameters have to be regarded. Additionally, a fitting function derived from the data interpolation has to be accurate and easy to handle at the same time. NR fitted their results by a mainly engineering ansatz function and an empirical approach and the fitting formula is "easy to apply in practice". To begin with, the NRF is analyzed in terms of accuracy and expandability for the new parameters ν and χ .

4.1. Comparison of the results with the NRF

NR claim that their provided fitting function has a maximum error of $\pm 5\%$ ⁵ according to their FE results and their indicated fitting error always is related to the maximum along the crack front. In addition they specified their FE accuracy with $\pm 3\%$ compared to the analytical solution in terms of a completely embedded circular crack.^{6,7} Because they used a relative coarse mesh, especially along the crack front, some detail got lost near the free surface. Due to this point and considering the error by data fitting – it is clear why their solution deviates from the results in this work. The maximum fitting error with respect to the current position along the crack front probably increases up to 10%. By adding other terms to fit two more parameters

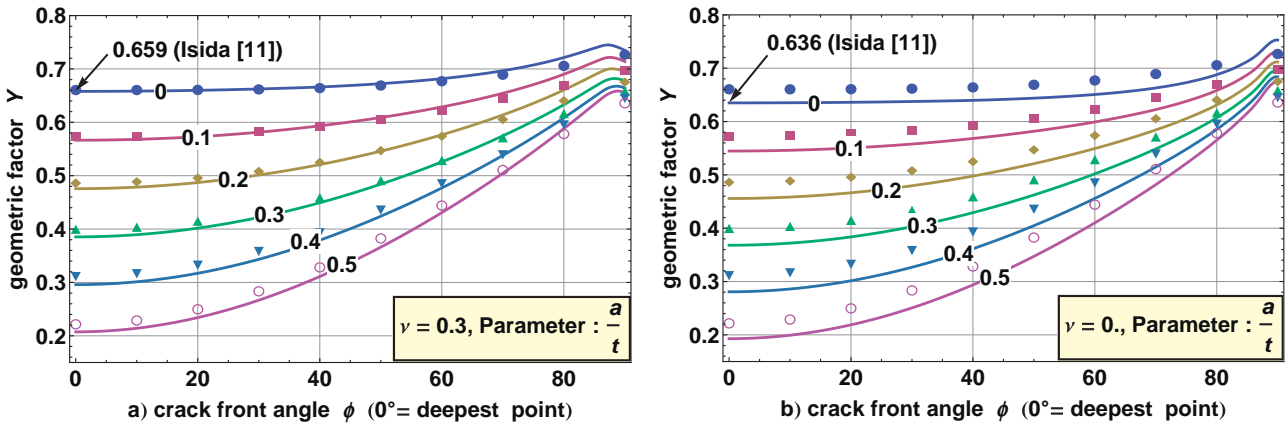


Fig. 4. Our FE results (lines) compared with the NRF (points) in the case of a semi-circular crack ($a/c=1$) along the crack front. Parameter in the curves is the relative crack depth a/t . (a) $\nu=0.3$ and (b) $\nu=0$.

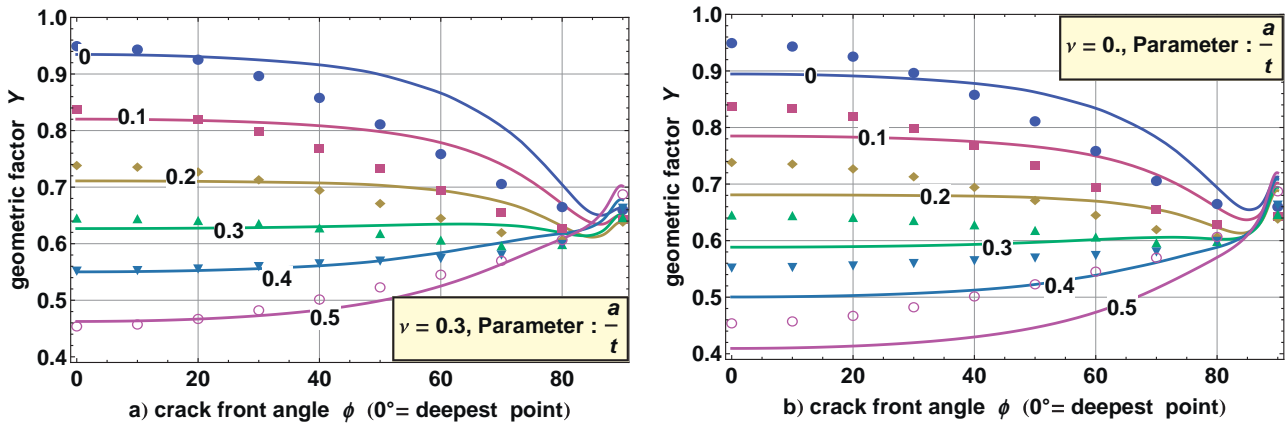


Fig. 5. Our FE results (lines) compared with the NRF (points) in the case of a shallow semi-elliptical crack ($a/c=0.4$) along the crack front. Parameter in the curves is the relative crack depth a/t . (a) $\nu=0.3$ and (b) $\nu=0$.

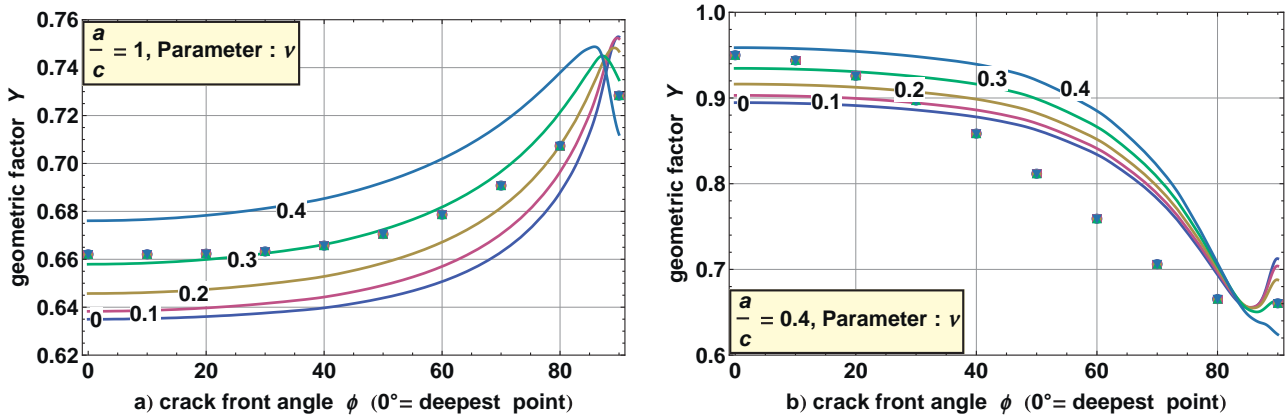


Fig. 6. Influence on Y of the Poisson's ratio ν plotted as parameter against ϕ ($a/t=0$). The lines represent the actual FE study; the solution of NR (points) is independent from ν . (a) $a/c=1$ and (b) $a/c=0.4$.

would further increase the error and let the dimension of the fitting function blow up.

To determine the accuracy of the given NRF two examples for bending with $\nu=0.3$, $c/b=0.1$ and $\chi=90^\circ$ are illustrated in Fig. 8. The NR solution within the intersecting parameter intervals fits the actual FE results quite good in point A

(deviation maximum: 7.7%, average: 1.5%) and in point C (deviation maximum: 8.2%, average: 2.4%). But between those points, the maximum deviation rises up to about 13% (mean: 2.6%) – this worst (and relevant) case is given in Fig. 8a. Assuming other relative crack depths (see Fig. 8b) the general agreement is better, but the deviation is also for point A about

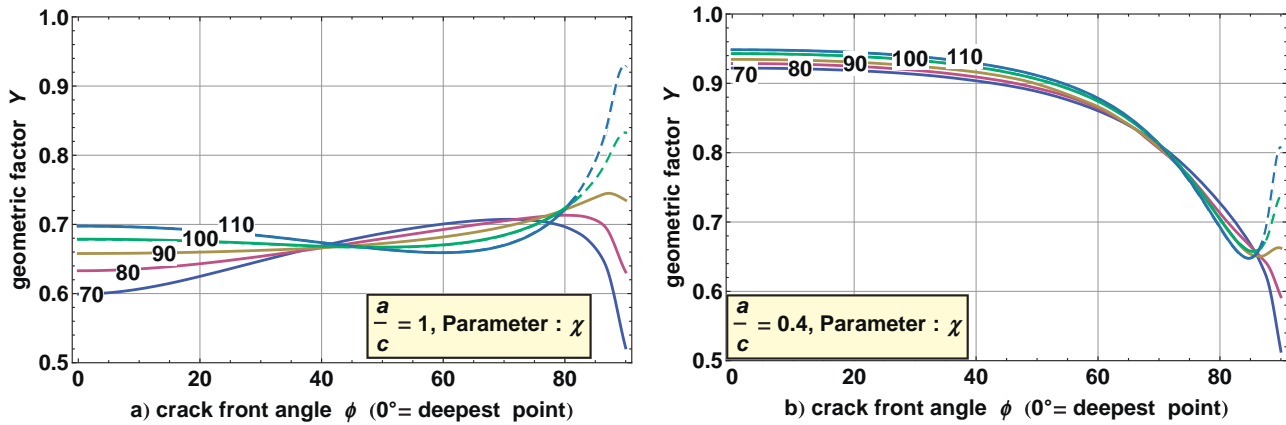


Fig. 7. Influence of the crack-surface interaction angle χ plotted as parameter against ϕ with $a/t=0$ and $\nu=0$. Subfigure (a) shows $a/c=1$ and (b) $a/c=0.4$.

10% ($a/c=1.2$ and $\phi=0^\circ$). For tension the deviations are about the half of the bending case.

Because of these differences in Y , a new fitting function was created instead of additional (correction) term for NRF for $\nu \neq 0.3$ and $\chi \neq 90^\circ$.

4.2. Practical aspects in terms of fracture toughness evaluation with the SCF-method

The surface crack in flexure (SCF) method is frequently used to determine the fracture toughness of ceramics.^{5,24,25} A Knoop hardness indent is made on the tensile loaded side of a rectangular bending bar. The indent causes some plastic deformation around the intended zone, which also causes unknown internal stresses. They are relaxed by removing the plastic deformed material by grinding-off the surface layer of the specimen's surface which contains the plastically deformed zone. Thus, a crack with the shape of an ellipse section is introduced in the surface (Fig. 2). Size and geometry of the surface crack has to be determined by fractographic means (which may need some fractographic experience).

A representative example of a crack after grinding – used for the SCF-method – is illustrated in Fig. 9 for a silicon carbide ceramic. The crack is made visible using fluorescent penetration

dye. All needed parameters (a , c and χ) can easily be determined with a commercial light microscope. Note that – in the actual case – the crack surface interaction angle χ is about 70° .

All assumed parameter intervals for this analysis (see Table 1) are realistic in terms of the practical feasibility of the SCF-method. The limits of the crack geometry parameter are mainly designated through a qualified indentation load (i.e. HK10) and concerning commercial structural ceramics.

The intersection angle χ was chosen as an input parameter (instead of the grinding depth Δt) because it is much easier to determine than Δt . Concerning that the SCF-method will be an important application area of the SIF of such type of surface cracks the approaches for fitting are focusing on pure bending as the main loading case.

4.3. Simplified approach for data fitting

In general, the stress singularity at the free surface (at point C) is not proportional to $r^{-1/2}$ (with r as the distance from the crack tip) according to Fett,¹⁸ Hutar^{26–28} and deMatos.²¹ Strictly spoken, the K -concept is therefore not valid at point C and it can only be used as a rough approximation at the vertex point. This is even more important including the effect of the Poisson's ratio and the results also depend on the crack-surface intersection angle χ .

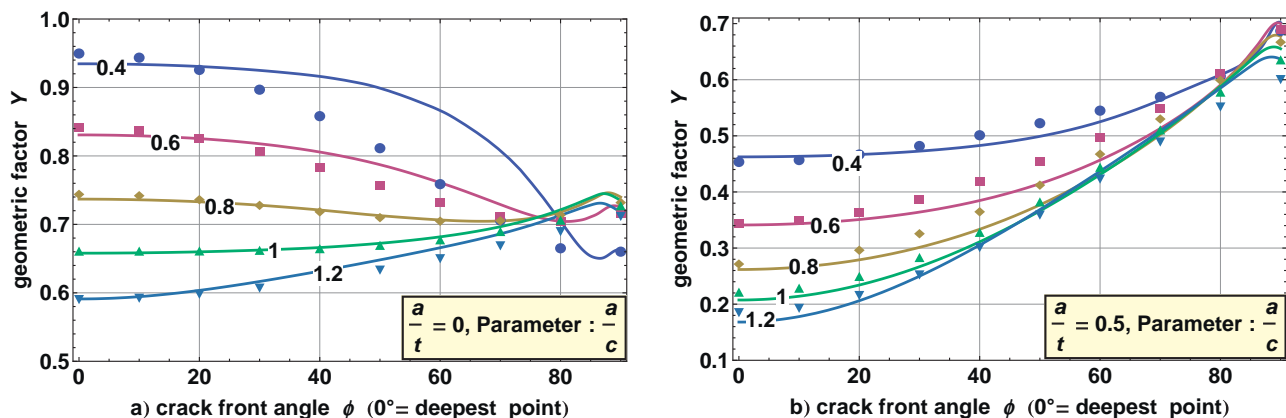


Fig. 8. Comparison of the solution for Y in bending of NR (points) and the actual FE results (lines) plotted against the crack front angle ϕ Parameter in the curves is the crack shape a/c . a) $a/t=0$ and b) $a/t=0.5$.

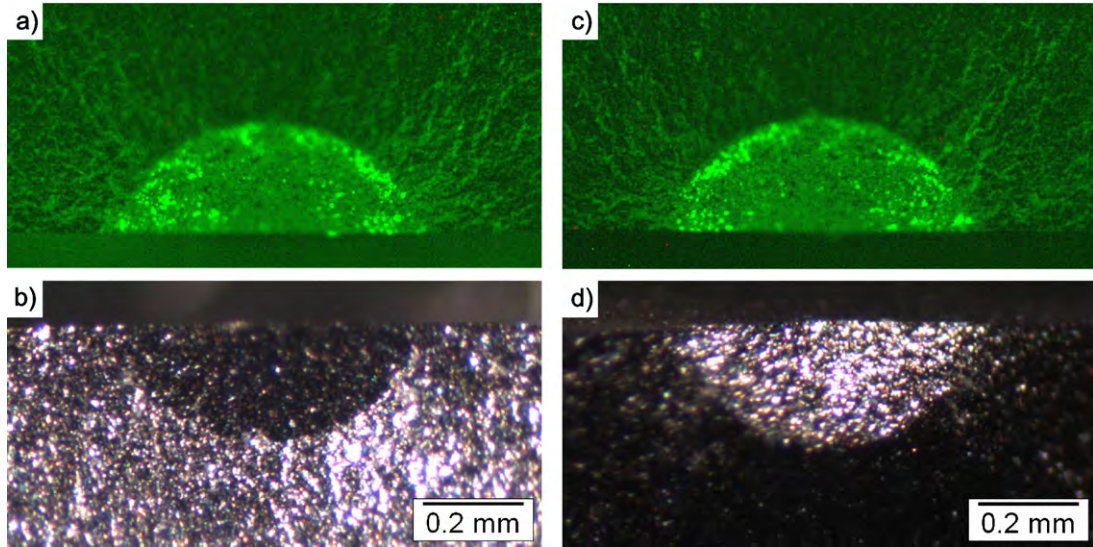


Fig. 9. Typical example of a Knoop crack in silicon carbide after removal of the plastic zone by grinding and after fracture. (a) and (c): visualisation of the crack by fluorescent penetration dye and UV-light. (b) and (d): conventional stereo microscopy. The crack-surface interaction angle χ is about 70° .

This twilight zone can be avoided by generating crack geometries, where $Y_A(\phi = 0^\circ)$ reaches its maximum value along the crack front. This guaranties the validity of fracture toughness evaluation for each specimen.

The value of the geometric function Y_A in the case of bending can be approximated by the fitting function in Eq. (4). The maximum fitting error is less than 2.7% and the average fitting error is about 0.4% (standard deviation: 0.3%). The geometric factor is:

$$Y\left(\frac{a}{c}, \frac{a}{t}, \frac{c}{b}, \nu, \chi, \phi = 0^\circ\right)_{\text{Bending}} = f \cdot f_b \cdot f_\nu \cdot f_\chi \quad (4)$$

with

$$\begin{aligned} f\left(\frac{a}{c}, \frac{a}{t}\right) &= \left(1.11 + 1.71 \left(\frac{a}{c}\right)^{1.42}\right)^{(-1/2)} \left(1.16 - 0.094 \frac{a}{c}\right. \\ &+ \left(-1.67 + \frac{0.174}{0.256 + (a/c)}\right) \frac{a}{t} + \left(-0.09\right. \\ &- 0.045 \left(1 - \frac{a}{c}\right) - \frac{-0.316}{0.14 + (a/c)}\right) \left(\frac{a}{t}\right)^2 \\ &\left. - 0.186 \left(\frac{a}{t}\right)^3\right) \end{aligned} \quad (5)$$

and

$$\begin{aligned} f_b\left(\frac{a}{c}, \frac{a}{t}, \frac{c}{b}\right) &= \cos\left(1.04 \left(\frac{c}{b} - 0.1\right) \left(2 \frac{a}{t}\right)^{0.5} 90^\circ\right)^{(-1/2)} \\ &\times \left(1 + \left(\frac{a}{c} - 0.41\right) \left(\frac{c}{b} - 0.1\right)\right) \\ &\times \left(-0.38 \left(\frac{a}{c}\right)^2 + 1.4\right) \\ &\times \left(0.074 + 1.26 \left(\frac{a}{t}\right)^3\right) \end{aligned} \quad (6)$$

and

$$\begin{aligned} f_\nu\left(\frac{a}{c}, \frac{a}{t}, \nu\right) &= \left(1 + 0.97\nu \left(-0.15 \left(\frac{a}{c}\right) + 0.13 \left(\frac{a}{c}\right)^2\right)\right. \\ &\times \left(6.43 \frac{a}{t} - 6.15 \left(\frac{a}{t}\right)^{0.5}\right) \\ &\times \left.+ 0.68\nu^2 \left(0.68 - 0.09 \left(\frac{a}{c}\right)^2\right)\right. \\ &\left.\left(1 - 1.8 \frac{a}{t} + 9.12 \left(\frac{a}{t}\right)^2\right)\right) \end{aligned} \quad (7)$$

and

$$\begin{aligned} f_\chi\left(\frac{a}{c}, \frac{a}{t}, \chi\right) &= \left(1 - 0.31 \left(\frac{a}{c}\right)^{1.7} \left(-1.46 - 4.25 \left(\frac{a}{t}\right)^2\right)\right. \\ &\times \left.\left(1 - \left(\frac{90}{\chi}\right)^{0.72}\right)\right) \end{aligned} \quad (8)$$

Additional terms to approximate the geometric factor along the whole crack front are given in Appendix A. The solution for the case of pure tension is treated in Appendix B.

To quantify the importance of consideration of the new parameters, the NRF ($\nu = 0.3$ and $\chi = 90^\circ$) and the new fit according to Eq. (4) is compared with the results of the actual FE study (interpolation) within the parameter range ($0 \leq \nu \leq 0.4$ and $70^\circ \leq \chi = 90^\circ$) in the case of pure bending, see Table 2. For all other parameters the intersecting intervals have been chosen.

At this point it should clearly be said that the NRF was made for $\chi = 90^\circ$ and $\nu = 0.3$. But even for $\nu = 0.3$ and $\chi = 90^\circ$ the deviation rises up to 11% for both points A and C. In the worst case the deviations are about 50% which occur at $\nu = 0$ and $\chi = 70^\circ$ in both points. These extremely high deviations regarding the actual FE results are minor relevant for the SCF-method because they occur in point A only for almost semi-circular cracks for which Y_A is the minimum along the whole crack front.

Table 2

Maximum fitting error of the NRF and the fit according to Eq. (4) regarding the FE results (interpolation).

		Point A		Point C		Complete crack front	
		max.	mean	max.	mean	max.	mean
NRF							
$70^\circ \leq \chi \leq 90^\circ$	$0 \leq \nu \leq 0.4$	47.8%	7.7%	50.5%	14.8%	50.5%	5.0%
$70^\circ \leq \chi \leq 90^\circ$	$\nu = 0.3$	39.5%	5.4%	41.2%	15.8%	41.2%	4.4%
$\chi = 90^\circ$	$0 \leq \nu \leq 0.4$	18.9%	4.2%	11.7%	4.4%	20.7%	4.0%
$\chi = 90^\circ$	$\nu = 0.3$	11.4%	1.6%	10.9%	2.8%	13.8%	2.7%
Actual fit Eq. (4)							
$70^\circ \leq \chi \leq 90^\circ$	$0 \leq \nu \leq 0.4$	2.7%	0.4%	38.6%	11.1%	38.6%	4.0%
$70^\circ \leq \chi \leq 90^\circ$	$\nu = 0.3$	1.9%	0.4%	28.2%	11.4%	30.1%	4.0%
$\chi = 90^\circ$	$0 \leq \nu \leq 0.4$	2.3%	0.3%	6.9%	2.3%	6.9%	1.0%
$\chi = 90^\circ$	$\nu = 0.3$	1.8%	0.4%	5.8%	2.4%	6.7%	1.0%

The actual formula, given in Eq. (4), has a good agreement (max. 2.7% and 0.4% averaged) in point A in the complete field of the parameters which was the main purpose of this fit. With the assumption of $\chi = 90^\circ$ the geometric factor can be calculated with a maximum deviation of 6.9% (mean: 1%) that is a tolerable fitting error. It is about the half compared to the NRF.

Considering Table 2 makes obvious that the new fitting function provides in every case a higher accuracy than the NRF even our equation is of similar length.

4.4. Evaluation of the minimum grinding depth

To get a valid K_{Ic} value also the ASTM standard for the SCF-method²⁴ instructs to use shallow crack shapes with $Y_A > Y_C$, i.e. the maximum of Y should be positioned at point A. In practice, the easiest way to realize this, is to increase the grinding depth Δt . But where is the critical grinding depth? It is not satisfying and a waste of time to see after testing and data evaluation that this sample has to be rejected. So what do one know about the specimen after indentation (before grinding): the original crack width $2c_0$ at the surface, the original thickness t_0 of the bar and an idea of the original crack shape a_0/c_0 (maybe approximated with $a_0/c_0 = 1$, from literature or determined in a pretest for the given material).

As can be seen from the results, Y_A as well as the maximum along the crack front Y_{Max} depend on the χ and ν . The Poisson's ratio is given for a specific material and χ is predetermined by the grinding depth, if you do serial sectioning to find the equilibrium

depth, since $Y_A = Y_{Max}$. With this in mind one can calculate the critical grinding depth Δt related to c_0 with the FE results under tension and bending, that is illustrated in Fig. 10.

For ease of use, the relative grinding depth $\Delta t/c_0$ can be approximated for bending Eq. (9) and tension Eq. (10). The maximum fitting error for both solutions is less than 1.35% of c_0 . This approximation takes also the Poisson's ratio as well as the initial crack shapes in the range $0.8 \leq a_0/c_0 \leq 1.2$ into account:

$$\begin{aligned} \frac{\Delta t}{c_0} \left(\frac{a_0}{c_0}, \frac{c_0}{t_0}, \nu \right)_{\text{Bending}} &= 0.493 + 1.28 \left(\frac{a_0}{c_0} - 1 \right) \\ &+ 1.15 \frac{c_0}{t_0} - 1.84 \left(\frac{c_0}{t_0} \right)^2 + 3.43 \left(\frac{a_0}{c_0} \right)^{0.4} \left(\frac{c_0}{t_0} \right)^4 \\ &+ \left(1 - 0.88 \frac{c_0}{t_0} \right) (-0.15\nu - 1.3\nu^2 + 1.73\nu^4) \end{aligned} \quad (9)$$

and

$$\begin{aligned} \frac{\Delta t}{c_0} \left(\frac{a_0}{c_0}, \frac{c_0}{t_0}, \nu \right)_{\text{Tension}} &= 0.518 + 1.4 \left(\frac{a_0}{c_0} - 1 \right) \\ &- 0.152 \frac{c_0}{t_0} + 0.84 \left(\frac{c_0}{t_0} \right)^2 - 0.55 \left(\frac{c_0}{t_0} \right)^3 \\ &+ \left(-2.1 + \frac{c_0}{t_0} \right) (0.045\nu + 1.1\nu^2 - \nu^3) \end{aligned} \quad (10)$$

To illustrate the significance of these findings a short example is presented. As material with a very low Poisson's ratio a

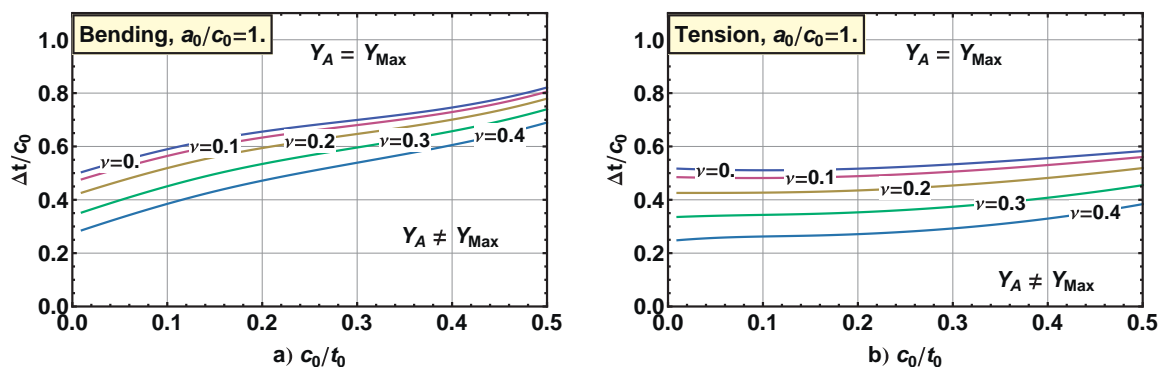


Fig. 10. Rel. grinding depth Δt plotted vs. the initial rel. crack width c_0 for an initial crack shape of $a_0/c_0 = 1$. Above the lines the maximum SIF occurs at the deepest point of the crack. Parameter is the Poisson's ratio. (a) bending and (b) tension case.

commercial silicon carbide was chosen with $\nu = 0.16$. A standard 4-point bending beam ($3 \times 4 \times 50 \text{ mm}^3$) was produced to carry out a fracture toughness test with the SCF-method with an indenter load of 4 kg (Knoop). After indentation, a surface layer of about $75 \mu\text{m}$ was removed ($60 \mu\text{m}$ are suggested by Eq. (9) for $a_0/c_0 = 1$) to initiate the fracture at the deepest point of the crack. The specimen used for testing had the following geometry: $t = 2.853 \text{ mm}$, $b = 2.001 \text{ mm}$, $a = 57 \mu\text{m}$, $c = 91 \mu\text{m}$ and $\chi = 65^\circ$. For this specimen the NRF results in geometric factors of $Y_A = 0.808$ and $Y_C = 0.716$. The actual interpolation function provides the values $Y_A = 0.737$ and $Y_C = 0.526$, respectively. In both cases point A has the highest value of Y along the whole crack front; however, the results of the formulas differ significantly. Considering the influence of the Poisson's ratio and the crack-surface intersection angle allows a difference of Y_A of about 8.8% to be obtained. Furthermore, the supported fitting formula provides in point A $Y_A = 0.730$ instead of 0.737 which encompasses a fitting error of about 1%.

5. Concluding remarks

The geometry factor Y was calculated within a practical range of crack and specimen geometries by FEA. These results are compared with the Newman and Raju formula.

The developed interpolation function of the new results takes also the Poisson's ratio and the crack-surface interaction angle into account, which has a significant influence on the geometric factor. If the crack aspect ratio a/c is low enough, the deepest point of the crack gets critical; this is a well-defined situation in fracture mechanics. Hence, fitting functions for the geometric factor Y in tension and bending have been developed for this specific case considering the new parameters.

The influence of the surface-crack interaction angle on Y_A is high for almost semi-circular cracks but decrease with decreasing crack shape ratios a/c .

The implications for fracture toughness measurements using SCF-methods are discussed. The above argument indicates to aim shallow cracks for fracture toughness measurement with the SCF-method. Also the critical grinding depth Δt was calculated to guarantee that Y_A becomes the maximum. An approximate formula for the grinding depth is given regarding pre-known quantities. This simplifies, among other things, the practical usage of the standardized SCF-method for a (scientific) determination of the fracture toughness.

Acknowledgements

Financial support by the Austrian Federal Government (in particular from the Bundesministerium für Verkehr, Innovation und Technologie and the Bundesministerium für Wirtschaft, Familie und Jugend) and the Styrian Provincial Government, represented by Österreichische Forschungsförderungsgesellschaft mbH and by Steirische Wirtschaftsförderungsgesellschaft mbH, within the research activities of the K2 Competence Centre on "Integrated Research in Materials, Processing and Product Engineering", operated by the Material Center Leoben Forschung GmbH in the framework of the Austrian COMET Competence Centre Programme, is gratefully acknowledged.

Appendix A. Fit function for Y along the crack front under bending load

The results of the FEM-calculations for Y along the complete crack front in the case of bending can be approximated by Eq. (A.1) with a maximum fitting error of 6.7% and an average fitting error of 0.9% (standard deviation: 1%). The only restriction for this fit along the crack front is $\chi=90^\circ$. Note that f_ϕ reduces to 1 in the case $\phi=0^\circ$ (i.e. in point A).

$$Y\left(\frac{a}{c}, \frac{a}{t}, \frac{c}{b}, \nu, \chi = 90^\circ, \phi\right)_{\text{Bending}} = f \cdot f_b \cdot f_\nu \cdot f_\chi \cdot f_\phi \quad (\text{A.1})$$

$$\begin{aligned} f_\phi\left(\frac{a}{c}, \frac{a}{t}, \frac{c}{b}, \nu, \phi\right) &= \left(\left(\frac{a}{c}\right)^2 \sin(\phi)^2 + \cos(\phi)^2\right)^{1/4} \\ &\left(1 + \left(0.11 \left(1.9 - \frac{a}{c}\right) \left(1 + \frac{a}{t}\right) - 0.02 / \left(\frac{a}{c}\right) \sin\left(\frac{a}{t} 360\right)\right) \left(1 + 11\nu \left(\frac{a}{t}\right)^6 \left(0.11 - \left(0.13 - \frac{a}{t}\right)^2\right)\right)\right) \\ &\left(\frac{\phi}{90}\right)^3 + 0.05(1 - 3.7\nu) \left(\frac{\phi}{90}\right)^{10} + 0.085 / \left(\frac{a}{c}\right) (1 - 2.3\nu) \left(\frac{\phi}{90}\right)^{20} - 0.05 / \left(\frac{a}{c}\right) \left(\frac{\phi}{90}\right)^{50} \\ &\left(1 + \left(0.28 \left(2\frac{a}{t}\right)^{0.9} + 0.72 \left(2\frac{a}{t}\right)^{\left(1+2.3\frac{a}{c}\right)}\right) \left(0.69 \left(\frac{a}{t} + 0.25\right)\right)\right) \\ &\left(\left(2.15 - 0.28\frac{c}{b}\right) \left(\left(\frac{\phi}{90}\right)^{\left(3.9-1.99\frac{a}{t}\right)} + \left(\frac{\phi}{90}\right)^3 \left(1 - \frac{\phi}{90}\right)\right)\right) \\ &\left(1 + 1.8 \left(1 - \frac{\phi}{90}\right) \left(\left(-0.54\nu + 0.07\frac{c}{b}\right) \left(\frac{\phi}{90}\right)^6 + \left(1 - 2\frac{a}{t}\right)\right)\right) \\ &\left(\left(\left(1.2 - \frac{a}{t}\right) / 0.8\right)^4 0.7 \left(\frac{\phi}{90}\right)^{2.5} - 3 \left(\left(1.2 - \frac{a}{t}\right) / 0.8\right) \exp\left[-19.5 \left(1 - \frac{\phi}{90}\right)\right]\right) \end{aligned} \quad (\text{A.2})$$

Appendix B. Fit function for Y along the crack front in pure tension

The numerical values of the geometric factor Y in the case of tension can be approximated by Eq. (B.1). This equation fits the FE results within a maximum error of 1% (average: 0.21%) for point A. Along the whole crack front – with the restriction $\chi=90^\circ$ – the maximum fitting error is 2.6% (average: 0.36%). Note that $f_{\phi,T}$ reduces to 1 in the case $\phi=0^\circ$ (i.e. in point A).

$$Y\left(\frac{a}{c}, \frac{a}{t}, \frac{c}{b}, \nu, \chi, \phi\right)_{\text{Tension}} = f_T \cdot f_{b,T} \cdot f_{\nu,T} \cdot f_{\chi,T} \cdot f_{\phi,T} \quad (\text{B.1})$$

$$f_T\left(\frac{a}{c}, \frac{a}{t}\right) = \left(0.864 + 1.626\left(\frac{a}{c}\right)^{1.57}\right)^{-1/2} \times \left(1 + \left(0.027 + 0.01/\left(\frac{a}{c}\right)\right)\frac{a}{t} + (-0.3 - 0.116\left(1 - \frac{a}{c}\right) + 0.415/\left(\frac{a}{c}\right))\left(\frac{a}{t}\right)^{2.3}\right) \quad (\text{B.2})$$

$$f_{b,T}\left(\frac{a}{c}, \frac{a}{t}, \frac{c}{b}\right) = 1 + 0.0105\frac{a}{c}\left(\frac{c}{b} + 25.7\left(\frac{c}{b}\right)^4\right) \times \left(1 + 118\left(0.08 - \left(\frac{c}{b} - 0.36\right)^2\right)\right) \times \left(\frac{a}{t} - 0.14\left(2\frac{a}{t}\right)^{10}\right) / \left(\frac{a}{c}\right) \quad (\text{B.3})$$

$$f_{\nu,T}\left(\frac{a}{c}, \frac{a}{t}, \nu\right) = \left(1 + 0.77\nu\left(\left(\frac{a}{c}\right)^{0.5} - 1\right)\right) \times \left(-0.16 - \left(\frac{a}{t}\right)^2\right) + \nu^2\left(-0.1 - 0.225\frac{a}{c} + 0.39\left(\frac{a}{c}\right)^{0.5}\right)\left(6.31 + 3.4\frac{a}{t} - 1.2\left(\frac{a}{t}\right)^{0.5}\right) \quad (\text{B.4})$$

$$f_{\chi,T}\left(\frac{a}{c}, \frac{a}{t}, \frac{c}{b}, \chi\right) = \left(1 + 0.44\left(1 + 0.33\left(\frac{c}{b}\right)^2\right)\left(\frac{a}{c}\right)^{1.9}\right) \times \left(1 - \left(\frac{90}{\chi}\right)^{0.7}\right) - 0.004(90 - \chi)\left(\frac{a}{t}\left(\frac{c}{b}\right)^3 + 0.22\frac{a}{t}\right) \quad (\text{B.5})$$

$$f_{\phi,T}\left(\frac{a}{c}, \frac{a}{t}, \frac{c}{b}, \nu, \phi\right) = \left(\left(\frac{a}{c}\right)^2 \sin(\phi)^2 + \cos(\phi)^2\right)^{1/4} \times \left(1 + 0.056\left(\frac{\phi}{90}\right)^2 + 0.12\left(\frac{a}{c}\right)^{-0.9}\left(1 - 3\left(1 - \frac{a}{c}\right)^5\right)\left(\frac{\phi}{90}\right)^{(5+4(a/c))}\right) \times \left(1 + 0.24\left(\frac{a}{t}\right)^3 / \left(\frac{a}{c}\right)\left(\frac{\phi}{90}\right)^3 + 0.96\left(\frac{a}{t}\right)^2\left(\frac{c}{b} - 0.1\right)\left(\frac{a}{c}\right)^{0.5}\left(\frac{\phi}{90}\right)^2\right) \times \left(1 + 0.32\nu\left(\left(\frac{a}{c} - 0.8\right) + 0.45\frac{a}{t}\left(1 - 1.6\frac{c}{b}\right)\right)\left(\frac{\phi}{90}\right)^{2.5} - 0.136\left(\frac{\nu}{0.4}\right)^2\left(\frac{\phi}{90}\right)^{(25(a/c))}\right) \quad (\text{B.6})$$

References

1. Lawn BR. *Fracture of brittle solids*. 2nd ed. Cambridge: Cambridge University Press; 1993.
2. Munz D, Fett T. *Ceramics – mechanical properties, failure behaviour, materials selection*. Berlin: Springer; 2001.
3. Fett T, Munz D. *Stress intensity factors and weight functions*. Southampton UK and Boston USA: Computational Mechanics Publications; 1997.
4. Murakami Y. *Stress intensity factors handbook*. Oxford: Pergamon Press; 1987-2001.
5. Newman JC, Raju IS. An empirical stress-intensity factor equation for the surface crack. *Engineering Fracture Mechanics* 1981;**15**:185–92.
6. Raju IS, Newman JC. Improved stress-intensity factors for semi-elliptical surface cracks in finite-thickness plates. NASA Report TM-X-72825; 1977.
7. Newman JC, Raju IS. Analysis of surface cracks in finite plates under tension or bending loads. NASA. Report TP-1578; 1979.
8. Shackelford JF. *CRC materials science and engineering handbook*. Boca Raton, FL: CRC Press; 1994.
9. Field JE. *Properties of natural and synthetic diamond*. London: Academic Press; 1992.
10. Czichos H, Hennecke M. *Hütte – Das Ingenieurwissen*. Berlin Heidelberg: Springer; 2008.
11. Isida M, Noguchi H, Yoshida T. Tension and bending of finite thickness plates with a semi-elliptical surface crack. *International Journal of Fracture* 1984;**26**:157–88.
12. McGowan JJ. *A critical evaluation of numerical solutions to the benchmark surface flaw problem*. Westport: Society for Experimental Stress Analysis; 1980.
13. Newman JC. A review and assessment of the stress intensity factor for surface cracks. Chang JB, editor. *Part-through crack fatigue life prediction, ASTM STP 687*. American Society for Testing and Materials; 1979.
14. Smith FW. The elastic analysis of part-circular surface flaw problems by the alternation method. Chang JB, editor. *The surface crack: physical problems and computational solutions*. New York: American Society of Mechanical Engineers; 1972.
15. Smith FW, Alavi MJ. Stress intensity factors for a part-circular surface flaw. In: *1st international pressure vessel conference*. 1969. p. 793–800.
16. Quinn GD, Gettings RJ, Kübler J. Fracture toughness by the surface crack in flexure (SCF) method: results of the VAMAS Round Robin. *Ceramic Engineering and Science Proceedings* 1994;**15**:846–55.
17. Quinn GD, Kübler J, Gettings RJ. Fracture toughness of advanced ceramics by the surface crack in flexure (SCF) method: a VAMAS Round Robin. VAMAS Report No. 17. Report 1994.
18. Fett T. *Stress intensity factors – T-stresses – weight functions. Supplement volume (IKM 55)*. Karlsruhe: KIT Scientific Publishing; 2009.
19. Anderson TL. *Fracture mechanics – fundamentals and applications*. Boca Raton FL: CRC Press; 2005.
20. Courtin S, Gardin C, Bézine G, Ben Hadj Hamouda H. Advantages of the J-integral approach for calculating stress intensity factors when using the commercial finite element software ABAQUS. *Engineering Fracture Mechanics* 2005;**72**:2174–85.
21. de Matos PFP, Nowell D. The influence of the Poisson's ratio and corner point singularities in three-dimensional plasticity-induced fatigue crack closure: a numerical study. *International Journal of Fatigue* 2008;**30**:1930–43.

22. Zúñiga DF, Kalthoff JF, Canteli AF, Grasa J, Doblaré M. Three dimensional effects along the crack front influencing the validity criteria for determining fracture toughnesses. 11th International Conference on Fracture, Turin (Italy): 2005.
23. Fett T. Stress intensity factors for semi-elliptical surface cracks in a plate under tension based on the Isida's solution. *International Journal of Fracture* 1991;**48**:139–51.
24. ASTM C 1421-01b. *Standard test methods for determination of fracture toughness of advanced ceramics at ambient temperature*. American Society for Testing and Materials; 2001.
25. ISO 18756. *Fine ceramics (advanced ceramics, advanced technical ceramics) – determination of fracture toughness of monolithic ceramics at room temperature by the surface crack in flexure (SCF) method*; 2003.
26. Hutar P, Náhlík L, Knésl Z. Quantification of the influence of vertex singularities on fatigue crack behavior. *Computational Materials Science* 2009;**45**:653–7.
27. Hutar P, Náhlík L, Knésl Z. The effect of a free surface on fatigue crack behaviour. *International Journal of Fatigue* 2010;**32**:1265–9.
28. Hutar P, Sevcík M, Náhlík L, Zouhar M, Seitl S, Knésl Z, et al. Fracture mechanics of the three-dimensional crack front: vertex singularity versus out of plain constraint descriptions. *Procedia Engineering* 2010;**2**:2095–102.

Paper H

J. Luhbauer, U. Lohbauer, M. Henrich, M. Munz, T. Lube, R. Belli: "Intricacies involving the evaluation of fracture toughness obtained by the surface-crack-in flexure method", *Journal of the American Ceramic Society* **105** (2022), 7582-7599, <http://dx.doi.org/10.1111/jace.18667>

This article is available under the Creative Commons CC-BY-NC-ND license.

RESEARCH ARTICLE

Intricacies involving the evaluation of fracture toughness obtained by the surface-crack-in-flexure method

Julia Lubauer¹ | Ulrich Lohbauer¹ | Martina Henrich¹ | Maximilian Munz² |
Tanja Lube²  | Renan Belli¹ 

¹Friedrich-Alexander-Universität
Erlangen-Nürnberg (FAU),
Forschungslabor für dentale
Biomaterialien, Zahnklinik 1 –
Zahnerhaltung und Parodontologie,
Erlangen, Germany

²Department of Materials Science,
Montanuniversität Leoben, Leoben,
Austria

Correspondence

Renan Belli,
FAU–Friedrich-Alexander-Universität
Erlangen-Nürnberg, Zahnklinik
1–Zahnerhaltung und Parodontologie,
Forschungslabor für dentale
Biomaterialien, Glueckstraße 11, 91054
Erlangen, Germany.
Email: renan.belli@fau.de

Abstract

Among the several methods available for the measurement of the fracture toughness (K_{IC}), the surface-crack-in-flexure (SCF) has the advantages of being based on an easy-to-produce short (application relevant) crack size of defined geometry with a naturally sharp crack tip. The production of ready-to-test cracked specimens is fast and uncomplicated, rendering accurate results with low scatter. However efficient and reliable, the procedural steps for the obtainment of a valid crack need revisions, especially on aspects concerning the polishing depth, the removal of lateral cracks, the obtainment of an appropriate crack geometry, and the use of adequate solutions for the geometry factor. In this study we attend to these issues by systematically polishing a large number of specimens of two ceramic materials having very distinct subsurface Knoop crack systems to assess the effect of remnants of lateral cracks. By evaluating the geometry factor of the median precrack along the entire crack front, we provide valid ranges for the crack geometry regarding the crack-surface intersection angle as resulting from the polishing depth, extending the applicability of the Strobl et al. solution to shallow cracks in detriment of the Newman and Raju formula that is poised to overestimations of K_{IC} of up to 10%. Our results debunk the belief that lateral cracks affect the obtained K_{IC} , but demonstrate the necessity of a minimum polishing depth for the attainment of valid crack geometries.

KEYWORDS

fracture toughness, Knoop indentation, lateral cracks, lithium disilicate, silicon nitride, stress intensity factor, surface-crack-in-flexure

This is an open access article under the terms of the [Creative Commons Attribution-NonCommercial-NoDerivs](https://creativecommons.org/licenses/by-nc-nd/4.0/) License, which permits use and distribution in any medium, provided the original work is properly cited, the use is non-commercial and no modifications or adaptations are made.

© 2022 The Authors. *Journal of the American Ceramic Society* published by Wiley Periodicals LLC on behalf of American Ceramic Society.

1 | INTRODUCTION

In a paper from 2002, Quinn and Salem^{1*} attended to the problem of testing inaccuracies when using the surface-crack-in-flexure (SCF) method (standardized at the time in ASTM C1421-99) for measuring the mode-I fracture toughness (K_{Ic}) of ceramic materials at room temperature. In that occasion, their focus was directed to the effects of remnants of lateral cracks (LCs) resulting from Knoop indentation on the obtained K_{Ic} -values using the Newman and Raju formula (NRF) for the crack geometry factor Y ,² as detailed in the standard. The need for the removal of the damage zone under the indentation imprint had been recognized in studies prior to that: if not done, it would lead to some underestimation of K_{Ic} from crack-opening residual tensile stresses,^{3,4} along with reports^{5–8} that the persistence of LCs due to conservative polishing might induce an overestimation of K_{Ic} -values and high scatter of the data. This led Quinn and Salem¹ to reevaluate their substantial archive of broken SCF specimens and test new sets of an alpha silicon carbide material at increasing polishing depths X , with $X = nh$, using the indentation depth as the unit of measure (h is defined as $2d_1/30$, being d_1 the half-long diagonal of the indentation imprint). The 1999 version of ASTM C1421 recommended a minimum polishing depth X of $3h$ to remove the damage zone and $4.5–5h$ for LCs. Figure 1 shows the profile of the Knoop crack system, adapted from references 1 and 9.

Quinn and Salem¹ made some observations: (i) of their stock of hundreds of broken SCF specimens, only those measured to have a K_{Ic} -value $<3 \text{ MPa}\sqrt{\text{m}}$ were found to contain significant remnants of LCs; (ii) small traces of LCs in materials having K_{Ic} -values $>3 \text{ MPa}\sqrt{\text{m}}$ were within the scatter of the data; (iii) their SCF dataset of 17 specimens from NIST's silicon nitride reference material SRM 2100 polished to $4.5–5h$ showed no LC remnants and a K_{Ic} -value matching those obtained using the chevron-notched-beam (CNB) and single-edge-precracked-beam (SEPB) methods, seen thus as a testament of test precision. Their new tests on two different batches of silicon carbide yielded a plot of K_{Ic} versus X showing mostly low K_{Ic} -values at $X = 0h$ as origin of a steep increase up to a peak at $X \sim 5h$, followed by a slight decrease up to about $X \sim 11h$ (vestiges of LCs were ascertained for $X \leq 7.5h$). They concluded that the presence of LC remnants can be responsible for an artificial increase of the calculated K_{Ic} -value up to 12%; the leveling off at the K_{Ic} -values measured using SEPB and CNB methods

was used as the yardstick for correctness. Emphasis was given to the necessity of polishing Knoop indented surfaces of low- K_{Ic} materials up to $7–10h$ in depth, to guarantee the complete elimination of LCs. The recommendation to extend the polishing depth beyond $4.5–5h$ appeared in the 2003 version of ISO 18756 and in the 2009 version of ASTM C1421, along with the instruction to take the measure of certifying the disappearance of LCs by monitoring the polishing procedure under the microscope.

Since Quinn's and Salem's paper,¹ the case of LCs was considered as good as closed. However diligent and commendable their contribution had been, new developments on the front of the SCF method indicate that some aspects went unregarded. Specifically, an improved solution for the geometry shape factor Y for the semi-elliptical surface crack has been made available in 2012 by Strobl et al.,^{10,11} revealing that diverging cases from the limitation of NRF to materials having a Poisson's ratio ν of 0.3 and crack-surface intersection angles χ of 90° cannot avert substantial overestimations of Y (up to 50%). In exploring the SCF method using the refined solution from Strobl et al.^{10,11} in LC-free specimens since then, we obtained values of K_{Ic} on average 10%–15% lower than when calculated with NRF.^{12–18} Quinn's and Salem's SCF results showing a mere offset of 9%–12% over SEPB and CNB must now be considered under a new light. Their relatively low number of specimens and high data scatter may benefit from a new, more comprehensive evaluation. It is thus our opinion that a revision of aspects pertaining to the influence of LC remnants, recommended polishing depth, and valid crack geometries on the basis of the SCF method is due.

2 | MATERIALS AND METHODS

2.1 | Materials

In order to evaluate the effect that remnants of LCs induce on the obtained K_{Ic} -values, and therefore the depth of polishing necessary to achieve a median crack that is undisturbed but also has a geometry in which Y is maximum at the deepest point, we selected two familiar materials with known different subsurface cracks systems. Commercial materials with a track record of service reliability disposing of a repository on characterization data on chemistry, microstructure, and mechanical behavior were preferred. Additionally, from the observations of Quinn and Salem,¹ materials having a K_{Ic} -value of less than $3 \text{ MPa}\sqrt{\text{m}}$ are especially susceptible to the nucleation of deep LCs; one of the materials should therefore have a K_{Ic} -value that lies below that threshold, and the other significantly above.

* One finds therein some background on the development of the standard and a somewhat retrospective account of the literature on descriptions of the anatomy of the Knoop and Vickers crack systems with respect to the origins and dimension of lateral cracks. We intend thus not to repeat those here.

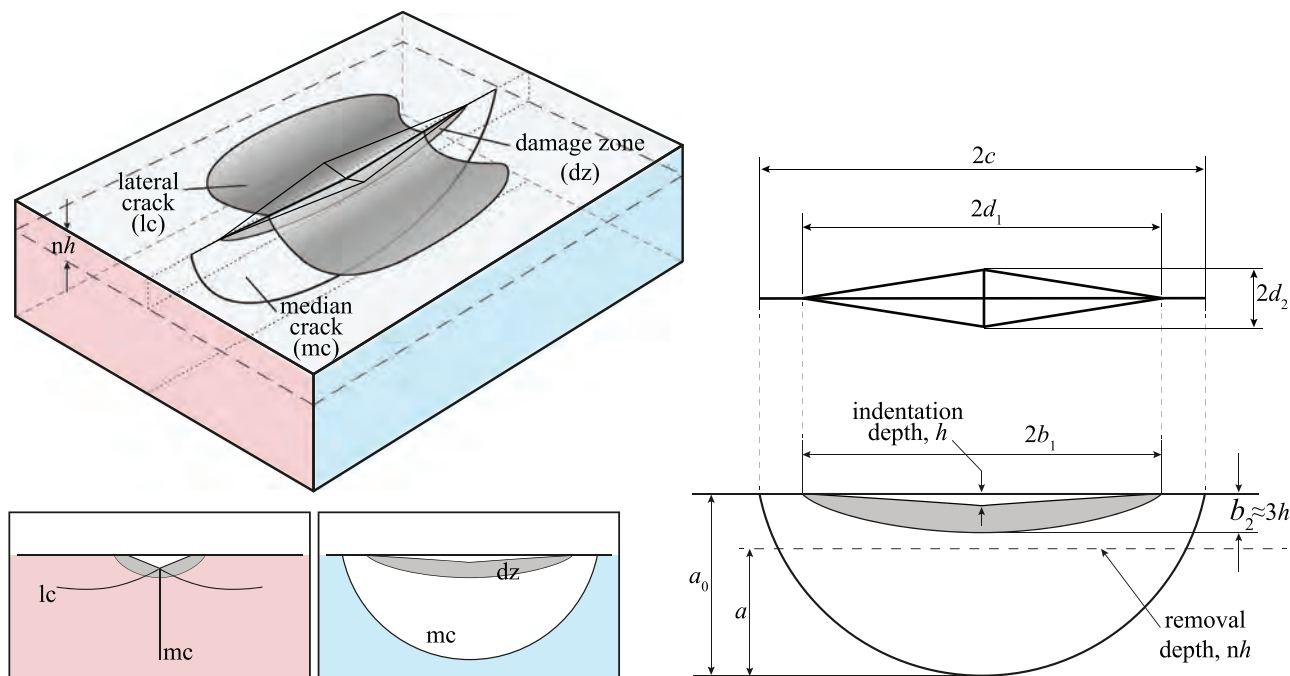


FIGURE 1 Schematic of the Knoop indentation-crack system adapted from reference 1 (left-hand side), showing a 3D view from above through the material and the profiles of the lateral planes in 2D projections. On the right-hand side the dimensions of the indentation and median crack are given (adapted from reference 9)

The first material is a gas pressure sintered silicon nitride produced by CeramTec (Plochingen, Germany) under the name of SL200B, subjected to the reference material testing program led by the Technical Committee 6 “Ceramics” of the European Structural Integrity Society (ESIS), introduced in reference 19 and characterized in references 20–23. The SL200B material contains ~3wt% Al_2O_3 and ~3wt% Y_2O_3 as additives giving rise to a microstructure containing β - Si_3N_4 grains of 1–5 μm in length with aspect ratio of about 3–5, and a 12.4 vol% amorphous silicate glass interphase. It is delivered in plates of 47 mm \times 11 mm \times 102 mm that show a lighter “skin” layer of ~1.5 mm and a darker “core” region; the core contains a larger volume fraction of α -Fe (0.08 vol%) than the skin (0.01 vol%), with the latter showing slightly higher values of Young’s modulus (skin = 307.0 GPa, core = 302.8 GPa), shear modulus (121.2 GPa vs. 119.9 GPa), and Poisson’s ratio (0.266 vs. 0.262).²² The K_{IC} -value of the core material has been measured previously using the SEVNB method rendering $4.9 \pm 0.1 \text{ MPa}\sqrt{\text{m}}$ ²⁴ and the CNB method rendering $5.2 \pm 0.1 \text{ MPa}\sqrt{\text{m}}$.

The second material is a partially crystallized lithium disilicate (hereafter LS2) glass ceramic used for dental prosthetic applications commercialized under the brand IPS e.max[®] CAD by Ivoclar Vivadent AG (Schaan, Liechtenstein), currently taken as gold-standard dental glass-ceramic for single- and multi-unit replacement regarding clinical performance²⁵ and mechanical properties.^{13,15,26}

The material is delivered as partly crystallized cuboid blocks of different sizes containing 32.6 vol% Li_2SiO_3 , 3.9 vol% Li_3PO_4 , and 0.7 vol% $\text{Li}_2\text{Si}_2\text{O}_5$ as an intermediate state to be machined and subsequently annealed to achieve the final microstructure composed of 62.2 vol% 1–2 μm $\text{Li}_2\text{Si}_2\text{O}_5$, 7.2 vol% submicrometric Li_3PO_4 , and 0.6 vol% cristobalite embedded in a SiO_2 -rich (79.2 mol%) residual glass.¹⁵ It has a Young’s modulus of 102.5 GPa, a shear modulus of 42.2 GPa, and a Poisson’s ratio of 0.216²⁷ after annealing. The K_{IC} -value of this LS2 material has been published in 2019 by Quinn et al.²⁸ using the SCF method, reporting values measured under N_2 atmosphere to amount to $2.34 \pm 0.17 \text{ MPa}\sqrt{\text{m}}$ and $2.09 \pm 0.13 \text{ MPa}\sqrt{\text{m}}$ in air (both $n = 10$ specimens), calculated using the NR formula. In the same set of experiments, their results using the SEPB method rendered $2.10 \pm 0.06 \text{ MPa}\sqrt{\text{m}}$ in N_2 gas ($n = 10$).²⁸ In references 29 and 30, we presented indirect evidences of a modest R-curve behavior.

The microstructure of both materials is shown in Figure 2.

2.2 | Specimen shaping

Beam-shaped specimens for the SCF method were produced following the dimensions recommended in ASTM C1421 to be tested in four-point bending (4PB) with support span S_s of 20 mm and loading span S_l of 10 mm.

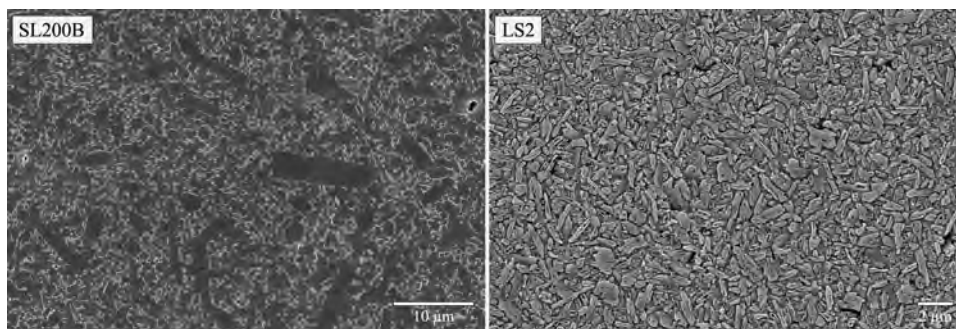


FIGURE 2 Microstructure of the evaluated materials. (A) SL200B, polished and etched with CF_4/O_2 -plasma, (B) LS2, etched with 5% hydrofluoric acid for 10 s

The LS2 material was sawed in the as-supplied pre-crystallized state (B32 cuboid blocks $15 \text{ mm} \times 15 \text{ mm} \times 32 \text{ mm}$) using a water-cooled diamond-embedded copper disc in an automatic sawing machine (Buehler 5000) in beams of 25 mm in length L , each block rendering six specimens. A grinding wheel D15 was used to wet grind two non-opposing sides to obtain the final cross-section height $W \times$ width B of 3.0×4.0 ($\pm 0.1 \text{ mm}$ tolerance). The annealing heat treatment recommended by the manufacturer aimed to induce the Li_2SiO_3 to $\text{Li}_2\text{Si}_2\text{O}_5$ transformation and achieve final microstructure and properties was conducted in a Programat EP 3010 (Ivoclar Vivadent AG) at ramp rate of $90^\circ\text{C}/\text{min}$ to 830°C , 10 s dwell time, and subsequent heating at $30^\circ\text{C}/\text{min}$ to 850°C and dwell time of 10 min; slow cooling was conducted at $10^\circ\text{C}/\text{min}$ down to 710°C , after which the specimens were exposed to ambient convective air. This annealing treatment has shown to heal crack-type defects induced by sawing and/or grinding and not induce warping or bending of the specimen.

The SL200B material was serially sawed under water-cooling from the as-supplied geometry in beams of 47 mm in length L , each plate rendering ~ 40 specimens. The “skin” region was maintained to ease the obtainment of more specimens per block, resulting in bicolor specimens containing a $\sim 1.5 \text{ mm}$ thick light-gray on one of the 3 mm width sides (see Figure 3). Grinding was performed on all sides with a D46 resin-bonded diamond grinding disc according to the procedures in Test Method C1161 to a final cross-section height $W \times$ width B of 4.0×3.0 ($\pm 0.1 \text{ mm}$ tolerance).

2.3 | Measurements using the SCF method according to ASTM C1421

A Knoop indentation was placed at the center of the lower (tensile) side of each specimen at $L/2$ and $B/2$. For the LS2 material the indented surface was the wider side ($B = 4 \text{ mm}$), whereas for the SL 200B material the narrow

surface ($B = 3 \text{ mm}$) was the indented one so as to avoid the “skin” region. From the start of this series of experiments, the recommendation of ASTM C1421 to tilt the beams upon indentation at 0.5° along the long axis L was followed, aimed to facilitate posterior fractographic pre-crack measurement; a second series of 11 specimens of the LS2 material was indented without this tilt. Care was taken to align the main axis of the indenter perpendicular to the length (L) of the beam, using an indentation force of 98 N (10 kg weight) with a full-load dwell time of 15 s. The length of the indentation diagonal d was measured under $10\times$ magnification under a stereomicroscope and used to calculate the impression depth h , taking $h = 2d_1/30$. Sequential polishing of the indented surface was performed within 5 min of indentation using P600 (for LS2) or P240 (for SL200B) SiC papers in dry conditions in alternating directions, with periodical checking of the surface under the microscope and measuring the beam thickness with a ball caliper having a resolution of 0.002 mm and an accuracy of $\pm 0.004 \text{ mm}$ as certified by the manufacturer (Mitutoyo, Japan) (see Figure 3). The



FIGURE 3 Ball caliper used to measure the polished depth of SCF specimens during the polishing procedures. Note the “skin” and the “core” in the specimen of the SL200B material

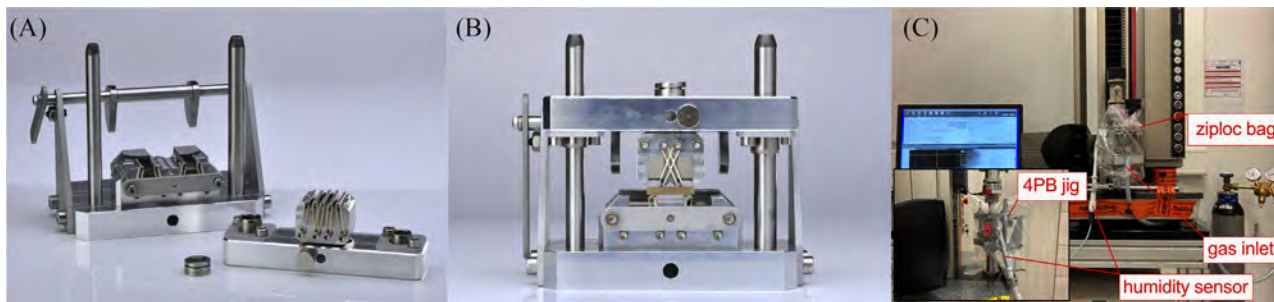


FIGURE 4 (A) Custom 4PB jig used to guarantee alignment and articulation; (B) CNB specimen positioned in a 10–20 mm spans; (C) jig mounted on the universal testing machine for tests under N_2 atmosphere

thickness was constantly measured at $L/2$ and $B/2$ after wiping the specimens from the grinding dust, with the polishing interrupted at different X in order to cover the range of $0 < X/h \leq 12$. The caliper was checked periodically with gage blocks to ascertain reproducibility of measurements. During polishing, the intersection of the LCs at the surface plane became visible in the LS2 material; for each specimen at the final interrupted X , the distance between the two LCs was measured under the microscope when still present. LCs in the SL200B material were not visible on the surface during sequential polishing. Ten specimens of SL200B and 16 of LS2 were kept unpolished ($X = 0h$). The lower edges of the specimens from LS2 were chamfered and their strength later corrected by a factor 1.002. All specimens were kept stored in a desiccator under vacuum until 2 h prior to testing, dried in an oven at 150°C for 1 h and later exposed to ambient air.

Specimens were tested in a universal testing machine at a cross-head speed of 1.5 mm/min using a custom-built 4PB fixture (see Figure 4A,B and reference 31) with the precrack in tension and aligned at the middle of the inner loading rollers. The 4PB entire jig was involved in a Ziploc-type bag with two sealed entries, one for a humidity sensor and the other for N_2 gas infusion (See Figure 4C). Once the atmosphere inside the bag was moisture-free as seen in the sensor dialog, the bag was completely sealed, additional 1–2 min were given for ascertaining constant 0% humidity, the bag was further inflated and the jig was loaded until fracture of the specimen.

The displacement of the specimen during the test was tracked by the speckle-correlation method registered by a video camera recording the speckle pattern on the surface of the specimen created by a laser beam through the plastic bag. The fracture stress was calculated using the maximum force at fracture and specimen dimensions:

$$\sigma_f = \frac{3F_{\max}(S_s - S_l)}{2BW^2} \quad (1)$$

The fractographic analysis was conducted on gold-sputtered fractured surfaces to increase the reflectivity of precracks, recorded on a stereomicroscope coupled with a video camera and a calibrated image software (ZenCore, Zeiss). The images were imported in a freeware (ImageJ) for the measurement of the precrack dimensions $2c$ and a . The shape of the crack boundaries was fit to a segment of a circle and the angle χ determined from a visually determined tangent line with the circle at point C using software tools. The stress intensity factor at fracture was calculated using:

$$K_{Ic,SCF} = Y\sigma_f\sqrt{\pi a_c}. \quad (2)$$

Two Y solutions for semi-elliptical surface cracks were used: the new solution for truncated semi-elliptical surface cracks revisited by Strobl et al.,^{10,11} and the NRF,² the latter still recommended in ASTM C1421 version 2018. The NRF, which already contains embedded the term $\sqrt{\pi}$ from Equation (2), is given in two forms, that is, for point C (Y_C) and for point A (Y_A). The maximum value of Y should determine whether the crack initiated from the deepest point A or at the intersection with the surface at point C; the latter case should make the test invalid and is recommended in the standard to be rejected. In Figure 5A the geometry of the median Knoop crack is illustrated referring to the dimensions used for the calculation of the Y solutions of Strobl et al. and NRF.

2.4 | Comparison methods using the CNB method

To offer a comparison to the obtained values from the SCF method, we prepared additional specimens to be tested using another of the three fracture toughness tests standardized in ASTM C1421, namely the CNB. The procedures followed strictly the guidelines from the standard, respecting the criteria for validity, and consisted of sawing a V-notch using a diamond disc for the CNB specimens. The

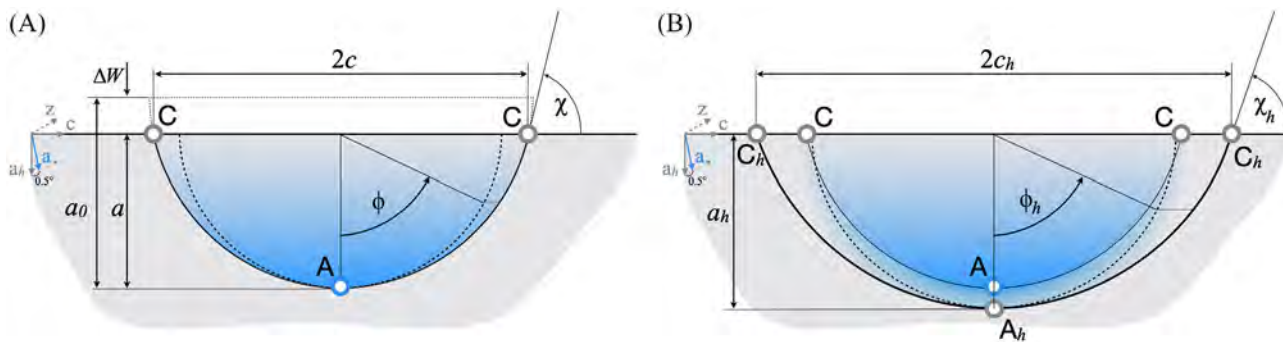


FIGURE 5 (A) Geometry of the Knoop median crack (blue) after polishing a thickness of ΔW , thus reducing the initial crack size from a_0 to a , and the width $2c_0$ to $2c$, defining points A and C, the latter intersecting the surface at an angle χ . ϕ is the projection to the crack front in degrees. Plane $a_h c$ -plane is the plane-of-view (grey), while the ac -plane (blue-grey) is 0.5° out-of-plane (in the z -direction), with the tip of the median crack (point A) at the farthest point. (B) Geometry of the halo boundary with dimensions denoted with a subscript letter h . The area circumscribed by the points $C-C_h-A_h-C_h-C-A-C$ is the halo. The points C, C_h , and A_h are located on the $a_h c$ -plane. ϕ_h is the projection to the crack front of the halo in degrees

dimensions W and B were, respectively, 4 mm and 3 mm for both materials and tested in 4PB in 10–20 mm spans in the same jig in N_2 atmosphere (loading rate of 0.05 mm/min).

2.5 | Visualization of the geometry of the subsurface Knoop crack system

In order to provide a description of the geometry of the subsurface crack system in terms of dimensions of the damage zone, median crack, and LCs, fractured half-specimens were indented (98 N, 15 s) at $\sim 100 \mu\text{m}$ from one long edge, flipped 90° , and diamond polished using an automatic polishing machine. Polishing was interrupted at different depths and the polished surface was photographed under a light microscope to reveal the evolution of the features of the Knoop subsurface system at different distances d_1 from the edge to the center of the indentation imprint.

3 | RESULTS AND DISCUSSION

3.1 | Subsurface crack profiles

The SL200B and LS2 materials showed very distinct subsurface crack systems when Knoop-indented with 98 N force, as revealed by sequential polishing of the sides of samples to create transverse cross-sections, as seen in Figures 6 and 7, respectively (the plane of view is that in red in Figure 1).

In SL200B, the damage zone depth b_2 extended around the imprint up to about $30\text{--}40 \mu\text{m}$ close to the center of the imprint, from which a median crack nucleated and grew to reach $a_0 = 162 \pm 5 \mu\text{m}$, as measured from the fracture surfaces of the unpolished specimens ($X = 0h$). The deeper

parts of the median crack were not very clear from the transverse sections, presumably because too tightly closed, so that they appeared shorter than a_0 values measured from the unpolished fractured specimens. LCs could only be seen as the transverse sections approached the center of the imprint at $d_1 < 50 \mu\text{m}$, departing from the center and bottom of the damage zone at very low angles to the surface, almost parallel to it, reaching no more than $40\text{--}50 \mu\text{m}$ in length. Here one cannot say for certain if the LCs are displayed in their full extent or likewise closed near the tip. During the polishing of the SCF specimens, LCs could not be distinguished on the polished surface, perhaps due to their low-angle orientation in respect to the surface. The long diagonal $2d_1$ measured $355 \pm 15 \mu\text{m}$, giving $h \approx 12 \mu\text{m}$. On the basis of the sections seen in Figure 6, both the damage zone and the LCs in SL200B might as well be completely removed by polishing the surface to about $50 \mu\text{m}$, $\sim 4h$.

The morphology of LCs in LS2 are depicted in Figure 7. The transverse sections revealed very clear LCs, even at distances d away from the extremity of the imprint (i.e., $d > d_1$), indicating that the elastic damage was not confined to the area under the imprint, as was the case for SL200B. As the transverse sections got closer to the center of the imprint, a wide crack is seen running down from the center of the imprint connecting both LCs. A damage zone under the imprint is not clearly distinguishable; a median crack is often not fully visible, presumably due to the two crack faces being too tightly closed. The LCs ran straight in the region near the extremities of the imprint and began to bow at the tip at sections closer to the center of the imprint; sectioning passed the center of the imprint led LCs frequently to grow laterally to ultimately chip off (not shown). With polishing passed the center of the indenter, LCs were observed to grow due to the polishing procedure. In LS2,

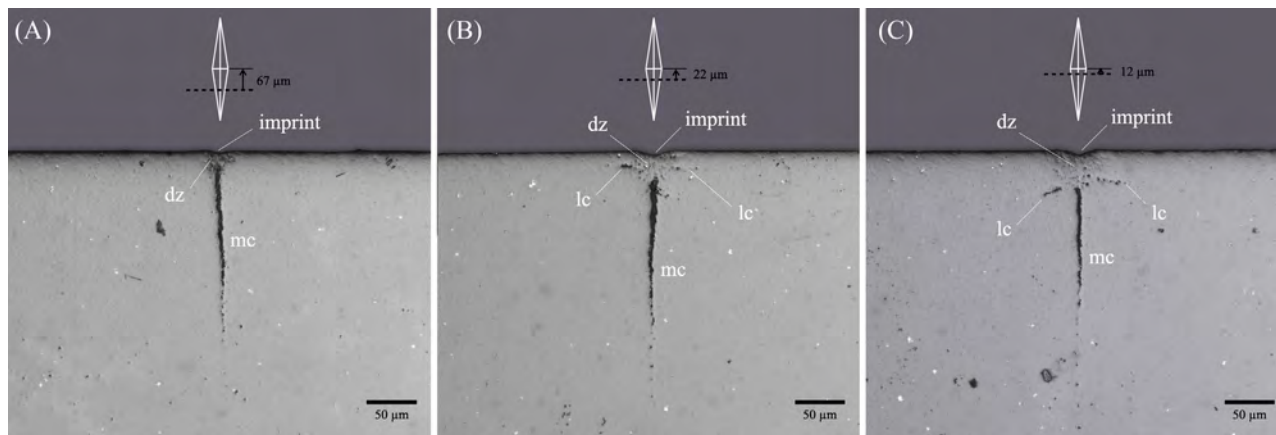


FIGURE 6 SL200B. Polished transverse cross-sections of the subsurface Knoop crack system at different distances from the center of the indentation imprint. (A) At about half-way from the extremity to the imprint toward its center, a small damage zone (dz) of about $20\ \mu\text{m}$ in depth is seen under the imprint, from which a wide median crack (mc) extends orthogonal to the surface into the depth; no lateral cracks (LCs) can be seen. The dz appears rough and heterogeneous. (B) At $22\ \mu\text{m}$ from the center, the dz becomes wider and deeper, from which two short LC nucleate in its center running parallel to the surface. (C) Nearing the center of the imprint, the dz extends about $50\ \mu\text{m}$ deep and the LCs reach the bottom of the dz, running now at a steeper angle to the surface, up to $40\text{--}50\ \mu\text{m}$ in length. The tip of the mc appears to get narrow and difficult to define

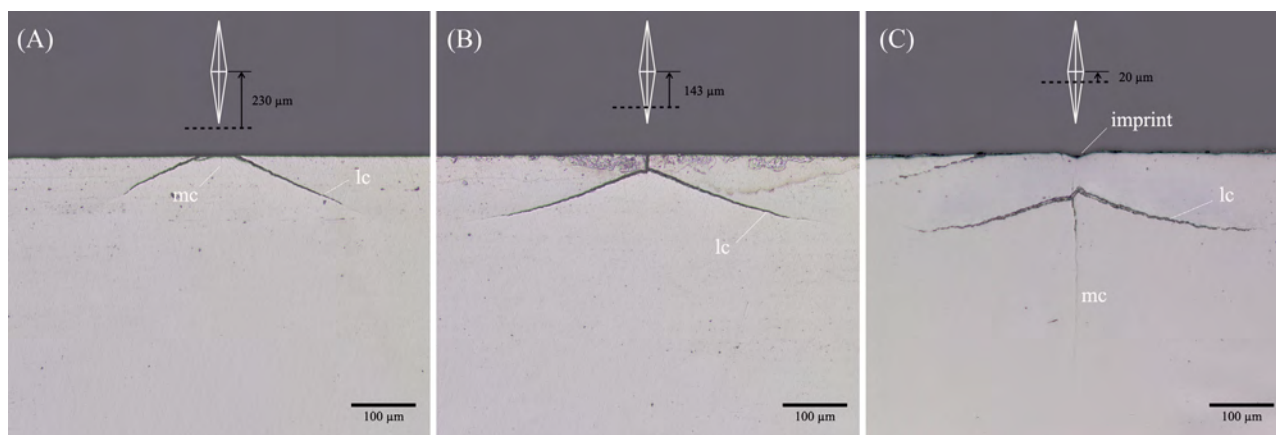


FIGURE 7 LS2. Polished transverse cross-sections of the subsurface Knoop crack system at different distances from the center of the indentation imprint. (A) Before the cross-section plane reaches the extremity of the imprint, lateral cracks (LC) can already be seen extending in a sharp angle to the surface, meaning that they bow to the sides and surpass the limits of the indentation. A shallow and narrow median crack (mc) can be seen. (B) As the cross-section enters the imprint, a wide crack is seen connecting the surface to the root of the LCs, from where they extend in to the depth in a sharp angle to the surface and begin to curve at the tip. The median crack is too narrow to be seen. (C) At $20\ \mu\text{m}$ from the center of the imprint, the root of the LCs reaches a depth of about $50\ \mu\text{m}$. The tips of the LCs curve toward the surface. An mc runs down from the bottom of the imprint, but its tip is too narrow to be distinguished. No clear damage zone can be distinguished as per alteration of morphology under the imprint

LCs could be easily distinguished on the surface during the polishing of the SCF specimens; measurements on the surface resulted in the half-2D profile plot in Figure 8. LCs started to be visible first around $25\text{--}40\ \mu\text{m}$ in depth, and their last remnants disappeared at polished depths $>90\text{--}120\ \mu\text{m}$. The shape of the LC profile in Figure 8 matches the images of the transverse sections very well, with LCs

developing at angles $\sim 55^\circ$ with respect to the surface plane and extending as much as $220\ \mu\text{m}$ laterally, provided that the cracks did not grow much during the polishing. Complete removal of LCs could be thus accomplished in the LS2 material by polishing about $6h$, with the long diagonal of the imprint $2d_1$ measuring $526 \pm 12\ \mu\text{m}$, giving $h \approx 17\ \mu\text{m}$. The mean median crack depth and width as measured at

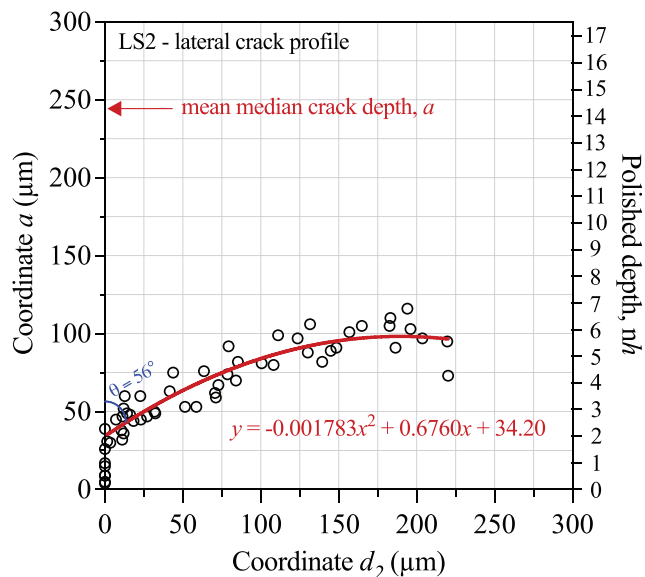


FIGURE 8 Half 2D profile of the subsurface lateral crack in the LS2 materials as measured at the surface of SCF specimens after the polishing protocol was finished

the surface of unpolished fracture specimens amounted to $a_0 = 244 \pm 42 \mu\text{m}$, and $2c = 515 \pm 45 \mu\text{m}$, respectively.

Having two distinct Knoop subsurface crack systems at our disposal, namely, SL200B showing an extensive damage zone developing under the indentation imprint and shy of LCs, and LS2 showing extensive LCs, allows us to better assign causal associations between these morphological alterations and any effect on the obtained K_{Ic} -values. This will be addressed in the following text.

3.2 | SCF experiments

It is important to note here that the fit function provided by Strobl et al. computes the value of Y at point A without distinguishing if the value of Y at $\phi = 0^\circ$ is actually the maximum occurring along the entire crack front or at any other value of ϕ . In turn, NRF provides the possibility of calculating Y at both points A and C, so that the evaluator can dismiss the condition $Y_A < Y_C$ as invalid, regardless of if the maximum of Y is located at one of those points or at neither of them. Whether one uses the solution of Strobl et al. or NRF to evaluate the value of Y , one gets no answer to the requisite $Y_A = Y_{\text{max}}$, or how both values diverge otherwise. To offer clarity in this regard, we evaluated our data using the original FEM-database of Strobl et al.^{10,11} and calculated for each data-point the value of Y at points A, C and at the point ϕ where it reaches a maximum. Those three values of Y were used to calculate K_{Ic} to build a series of plots of K_{Ic} versus X in Figures 9 and 10 with SL200B and LS2 side by side for comparison. Included are the evaluations

using NRF, and in all cases we give the distinction between data-points showing $Y_A > Y_C$ or $Y_A < Y_C$. In all K_{Ic} versus X plots, our CNB results of 10 valid specimens (mean and S.D., purple stripe) serve for comparison, together with previous data from the literature for the same material. An arbitrary third-order polynomial function was fitted to the SCF data to emulate Quinn's and Salem's¹ handling of their data; such a function would reveal an eventual "peaking" resulting from any artificial overestimation coming from an effect of LCs remnants beyond the removal of the damage zone, followed by a decrease at higher X when LCs were to be fully eliminated, provided that Y_{max} is used.

3.2.1 | SL200B material

A total of 146 SCF specimens were prepared for the SL200B material, from which 57 could not be evaluated, most of those at polishing depths $X > 8h$, whether because the crack could not be clearly identified and measured, or because the fracture originated from a defect other than the Knoop median crack (the latter more frequently at $X > 10h$). Overall, the limits of the median cracks in the SL200B material were not always very sharp, inducing some uncertainty in the measurements of a and $2c$ in some specimens; the lower the X , the clearer they appeared. Let us first evaluate the data using the solution of Strobl et al., with discussion on the differences to NRF set aside for later (see Section 3.2.4).

As seen in Figure 9A,B, the shape of the trend is similar in both cases, consisting of an increase in K_{Ic} with decreasing rates up to a plateau at a certain value of X . At values of $X < 5.5h$, the shape of the curve is most affected by using Y_{max} instead of Y_A ; the use of the latter underestimates K_{Ic} the lower the X . The curve using Y_A departs from a $K_{Ic,A}$ -value of $3.48 \text{ MPa}\sqrt{\text{m}}$ at $X = 0h$, increasing thereafter to reach a plateau of $5.02 \text{ MPa}\sqrt{\text{m}}$ at $X \sim 6.5h$, staying constant up to $X = 10h$. When Y_{max} is used, $K_{Ic,\text{max}}$ is $3.97 \text{ MPa}\sqrt{\text{m}}$ at $X = 0h$ and the curve reaches a near-constant plateau at $X \sim 4h$. Interestingly for the last case, the 95% confidence band of the SCF curve overlaps with the standard deviation of our CNB results ($K_{Ic,\text{CNB}} = 5.09 \pm 0.13 \text{ MPa}\sqrt{\text{m}}$) already at $X = 2.5h$, significantly earlier than the depth of $X \sim 4h$ identified in Figure 6 to be sufficient for the removal of both the damage zone and LCs. Here it is difficult to state if the LCs have relieved any of the tensile residual stress at $X < 4h$, as reported by Quinn and Salem¹ for their specimens, since LCs in SL200B were not much longer than the width of the damage zone; most of the residual tensile stress might have been kept stored in the damage zone acting to open the crack. The mean and S.D. values of $K_{Ic,\text{max}}$ at $X = 2.5h$ is $5.08 \pm 0.22 \text{ MPa}\sqrt{\text{m}}$, at $X = 4h$ $K_{Ic,\text{max}} = 5.07 \pm 0.22 \text{ MPa}\sqrt{\text{m}}$. The full removal of the

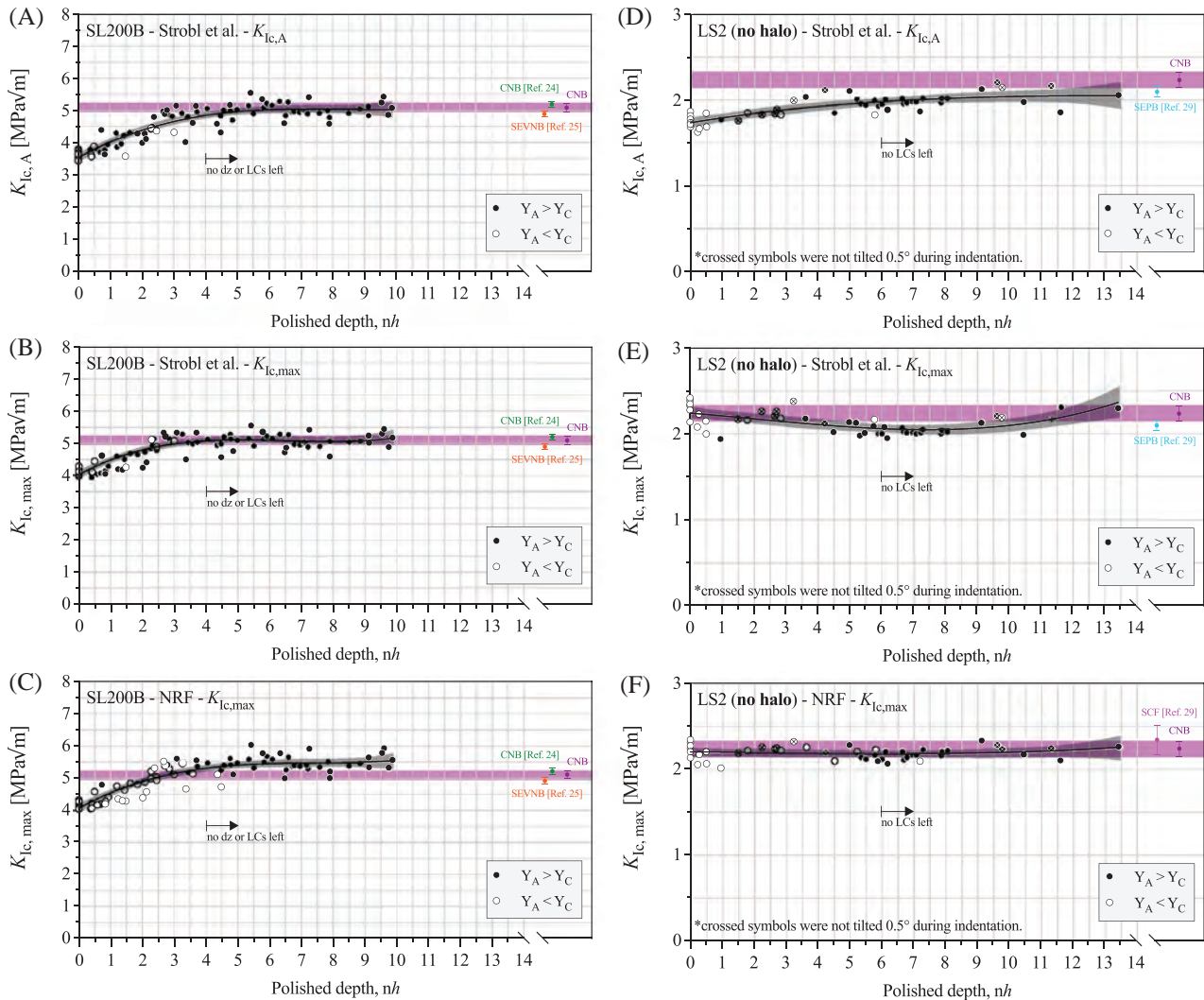


FIGURE 9 (Left column SL200B, right column LS2 specimens showing no halo). (A,B,D,E) K_{Ic} versus X (as multiple of h) plots using the Strobl et al. solution at point A or at the maximum value of Y , rendering $K_{Ic,A}$ and $K_{Ic,max}$, respectively. Our CNB results are added (purple circle) with S.D. as the purple band for reference, along with additional literature values. The fits to the data are third-order polynomial functions through all the data-points, with 95% confidence band. (C,F) Calculations using the NRF

damage zone—even the removal of the LCs at all—seem thus not to be necessary for achieving stable K_{Ic} -values with SL200B, provided that Y_{max} is used; for full-accuracy (on the basis of crack geometry), matching values of $K_{Ic,A}$ and $K_{Ic,max}$ were reached at $X \geq 4.5h$ (see close overlapping of blue and green data-points in Figure 10A). For $X > 0h$, values of $K_{Ic,C}$ are only slightly lower than $K_{Ic,A}$ up to $X = 2.5h$, decreasing heavily thereafter, when the polished depth induces χ to drop below $\sim 75^\circ$ (see Figure 10A,C,D).

3.2.2 | LS2 material

From the 127 specimens prepared for LS2, 119 could be evaluated; median crack boundaries were visible and sharp,

assuring a high certainty in measurements. However, in contrast to the precracks in SL200B, the great majority of the precracks in LS2 presented a double-boundary, the so-called “precrack halo.” Still, 39 specimens did not show any halo, and were evaluated separately using the crack dimensions a and $2c$ from the Knoop median crack, making the dataset in the K_{Ic} versus X plots in Figure 9D–F. To fill some of the gaps within the full range of X , new specimens were produced—this time foregoing the hitherto applied 0.5° tilt—to minimize the occurrence of halos and verify if they were indeed being caused by the tilting. From the 11 new “no 0.5° tilt” specimens, nine showed no halo, composing the dataset represented by the crossed symbols. Here too, a third-order polynomial function was used for fitting to both datasets together (tilted and not tilted), representing

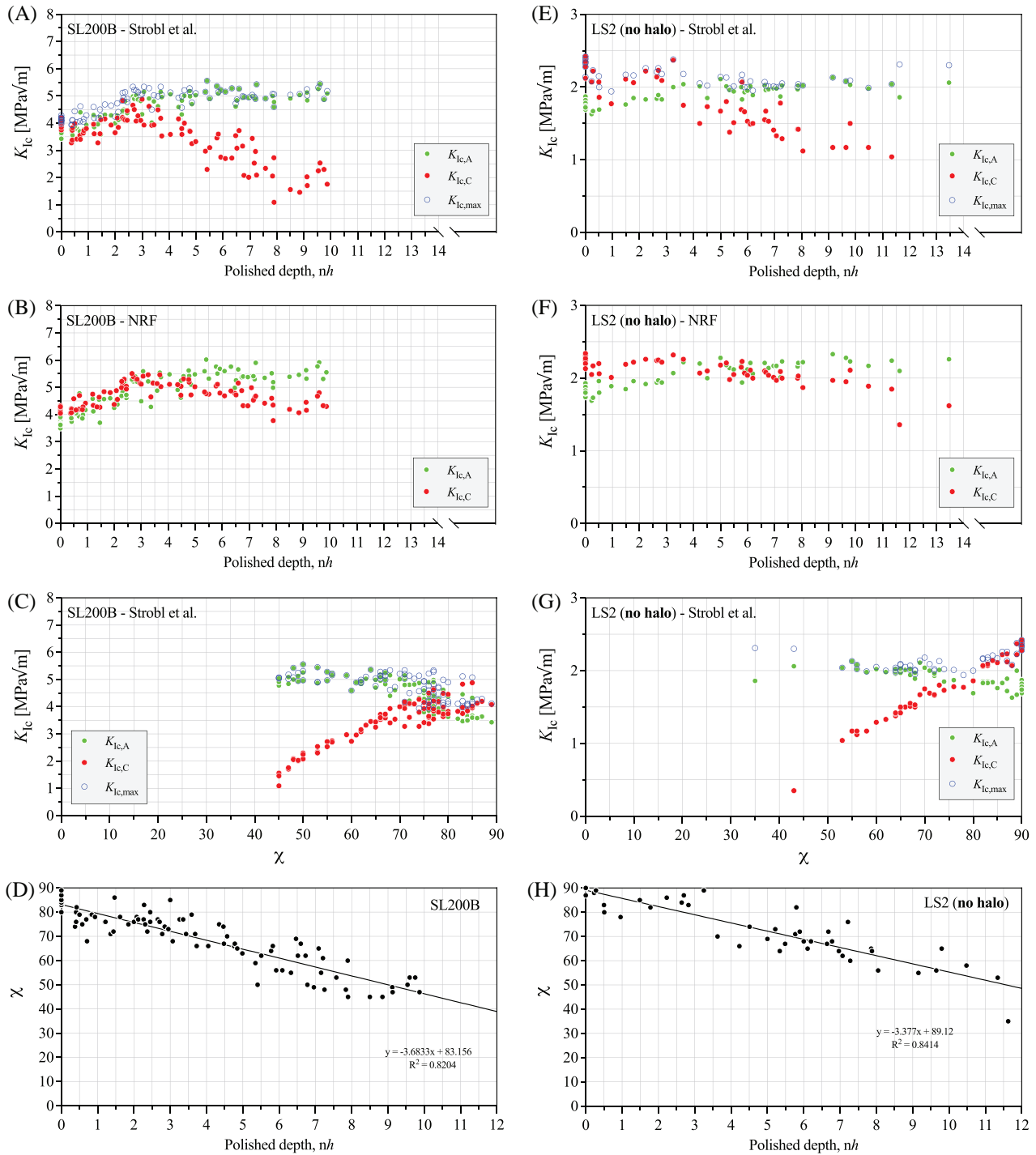


FIGURE 10 (Left column SL200B, right column LS2 specimens showing no halo). (A,E) K_{Ic} versus X (as multiple of h) plots using the Strobl et al. solution using Y_A , Y_C or Y_{max} . (B,F) Calculations using the NRF. (C,G) K_{Ic} versus χ for different values of Y . (D,H) Relationships between χ and X

the behavior of measurements undisturbed by the formation of a pre crack halo. The effect of halos will be closely addressed in Section 3.2.3.

Let us again address the use of the solution of Strobl et al. The curves in Figure 9D,E show distinct shapes, influenced mainly by the data-points at $X < 6.5h$. When using

Y_A , the curve departs from $K_{Ic,A} = 1.73 \text{ MPa}\sqrt{\text{m}}$ at $X = 0h$, increasing up to $X \sim 10h$. However, the 95% confidence bands overlap the plateau line of $K_{Ic,A} = 2.05 \text{ MPa}\sqrt{\text{m}}$ already at $X = 7.5h$. Based on that trend, one is led to believe that the damage zone and the presence of LCs would have the effect of decreasing the measured K_{Ic} . The shape of

the curve changes drastically when using Y_{\max} , which is substantially higher than Y_A for $X < 5h$, and equaling Y_C at $X = 0h$ (see Figure 10E). As opposed to SL200B, Y_C in LS2 becomes higher than Y_A for X values below $\sim 3h$, when χ is higher than about 75° . This difference between the two materials in terms of Y_{\max} (Y_{\max} moving away from Y_A in LS2) at low values of X is due in part to their difference in Poisson's ratio, but mainly due to the parameter a/W , which for LS2 is more than double than that for SL200B, once a for unpolished specimens was larger for LS2, and W was the long side of the specimen (4 mm) for SL200B and the short side (3 mm) for LS2. This has also the effect of increasing Y on point A for lower a/t ratios, accounting for the flatter curve in LS2 at lower X . For LS2, Y_{\max} matches Y_A sufficiently well within the range $5h \leq X \leq 11.5h$. For the two data-points at $X > 11.5h$, Y_{\max} was much higher than Y_A , inducing the curve to bow upward. The lower the χ (the deeper the polishing), the higher is the variation between Y_A and Y_{\max} for cracks with $a/c \sim 1$, as shown in Figure 7 in reference 10 (shown only for χ between 70° and 110°).

In LS2, LCs are completely removed at $X = 6h$ (see Figure 7), and the damage zone presumably at $X \sim 3h$. When using the solution of Strobl et al. with Y_A , truncating the data at $X < 3h$ gives a $K_{Ic,A} = 2.00 \pm 0.09$ MPa \sqrt{m} , which closely approaches the $K_{Ic,max}$ between $5h \leq X \leq 11.5h$ (2.06 ± 0.07 MPa \sqrt{m}), the range in which Y_{\max} matches Y_A very well (when blue and green symbols overlap, see Figure 10E,G). At $X = 3h$, only ~ 50 μm of material is removed, leaving a substantial part of the LCs still in place, which intersect the surface about 25 μm away from the median crack plane. Thus, those remnants of LCs between $3h$ and $6h$ seem not to affect the obtained K_{Ic} -values significantly, regardless of using Y_A or Y_{\max} , in disagreement with the conclusions from Quinn and Salem¹ (this will be shown later also for the case of specimens showing a halo).

The lower K_{Ic} -values obtained by the SCF method in comparison to the K_{Ic} -values obtained by CNB and SEPB methods is a consequence of the effect that crack extension Δa ($\Delta a = a_c - a$) and initial crack size a have on the resulting K_{Ic} -value in materials showing an R-curve behavior. Once initial cracks in SEPB and CNB grow longer before instability than in SCF, their tangent points between the applied stress intensity factor $K_{I,appl}(a)$ curve and the R-curve $K_{I,R}(\Delta a)$ (i.e., $K_{I,appl}(a) = K_{I,R}(\Delta a)$) is located farther along the R-curve, with the K_{Ic} -value being the $K_{I,R}$ -value at failure in a quasi-static test. In flat-R-curve materials, short-crack and long-crack fracture toughness methods should yield equivalent K_{Ic} -values.³² This behavior agrees with indications from the literature of the existence of an R-curve for this specific LS2 material.^{29,30}

3.2.3 | The effect of halos

Pre-crack halos have been described in earlier studies using the SCF method and analyzed in detail in a 1998 paper from Swab and Quinn,³³ using different ceramic materials. They classified the different reasons for halos appearing whether by evaluating the morphological appearance of the microstructure in the different crack regions, or by comparing pre-cracks in specimens tested in air or in N_2 atmosphere, eventually foregoing the polishing procedure. When environmentally assisted slow crack growth (SCG) was confirmed in tests in air, the inclusion of the halo in the pre-crack size led the K_{Ic} -value to match those tested in N_2 showing no halo, for instance in 99.9% alumina and in a glass-ceramic. Halos were also shown to develop when Knoop-indented specimens were not polished to remove the damage zone in a MgF_2 ceramic, thus indicating some influence of residual stress. In hot-pressed AlN, halos were found in test performed in air and in dry atmosphere, leading the authors to conclude that the halos formed due to the reorientation of the pre-crack prior to instability,³⁴ in view of the fact that all their specimens were tilted 0.5° off perpendicular to the long axis of the indenter. Because such halos due to crack kinking are rough topographic disturbances on the fracture plane, they can be manipulated to change appearance during fractographic analysis by altering the angle of light incidence, as opposed to sources of halo such as SCG. A description of the geometry and different planes involved in the formation of the pre-crack halo is illustrated in Figure 4B.

A pre-crack-kink halo looks like an uneven shadow surrounding the Knoop median pre-crack. The halos found in our LS2 specimens have the appearance of shadows, as shown in Figure 11 for different crack sizes, and although the LS2 material has been shown to be susceptible to SCG,^{29,35} our protocol of drying and testing in N_2 atmosphere at a high loading rate (1.5 mm/min) was meant to eliminate any relevant SCG effect. The extent of the observed halos thus cannot be reconciled with severe SCG events.

Halos appeared in polished as well as in unpolished specimens, and showed to be independent of the size of the remnant median pre-crack (thus negating any influence of the polishing procedure). Interestingly, Knoop median cracks that developed no halo were significantly larger than those that did ($a = 289 \pm 25$ μm , $2c = 563 \pm 28$ μm vs. $a_h = 214.8 \pm 13$ μm , $2c_h = 483 \pm 15$ μm as measured from unpolished specimens—compare Figure 9A,B with Figure 9C,D). In unpolished specimens, those that showed no halo were half-circle shaped ($\chi = 89.5^\circ \pm 1.2^\circ$), while those showing a halo were nearly half-circle shaped ($\chi_h = 81.1^\circ \pm 1.7^\circ$). This suggests that despite being tilted 0.5° , specimens

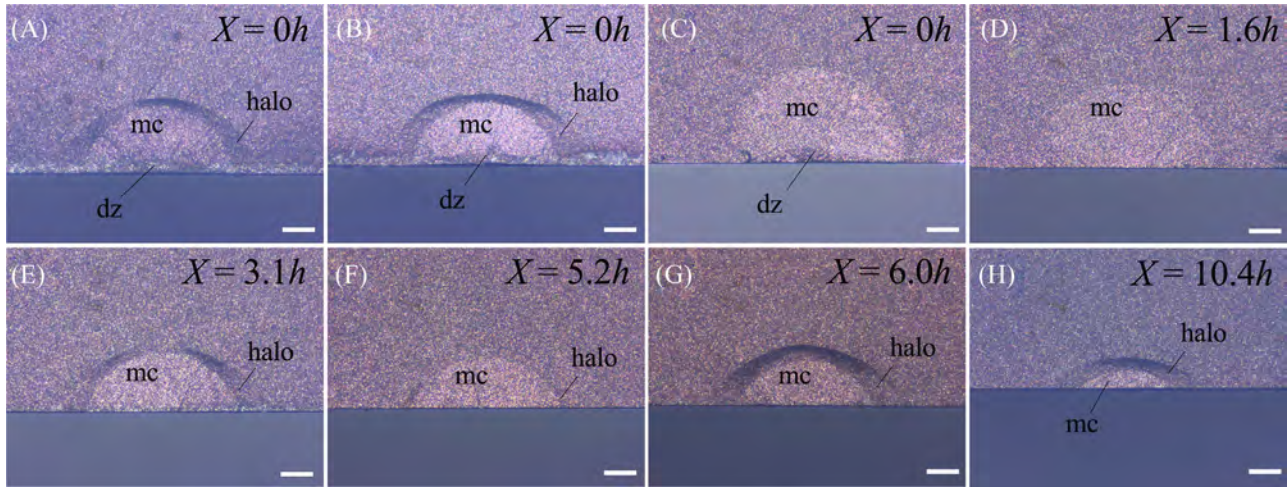


FIGURE 11 Examples of the appearance of median cracks in the LS2 material at different polishing depths. All these specimens were indented with a 0.5° tilt. Some show no halos (C,D), other small halos at the crack front near the surface (F), while large halos represent an increase of the entire critical crack front (A,B,E,G,H). Specimens in (A), (B), and (C) were not polished. Note how the median cracks in (C) and (D) are larger compared to those that presented a halo (A,B). Scale bar is $100\ \mu\text{m}$ (actual $5.6\times$ magnification). Plane of view is orthogonal to the long axis of the beam. dz, damage zone; mc, median crack

showing no halo developed their median cracks actually perpendicular to the surface, while those median cracks that developed a halo grew in an angle (on the ac-plane, see Figure 4) and seem to have suffered some resistance against crack growth, probably due to the contribution of a mode II stress condition.

As a rule, halos were wider at the surface (distance C-C_h) than at the deepest point (distance A-A_h) when seen from the plane-of-view, with the kink angle being steeper along points A-A_h (see Figure 4B) and becoming smoothed out toward points C_h (along points C-C_h). Actually, points C and C_h are on the same plane, and because of that, point C_h is not very distinguishable on the fracture surface since the shadow at this point vanishes (see Figure 9E,G,H). The shape of the halos was generally the same regardless of the initial median precrack ratio a/c (that is, not only in deeply polished specimens but also in unpolished and low- X precracks). Such a shape could be suggestive of the median precrack becoming critical first at the deepest part of the crack (i.e., $\phi = 0^\circ$) where the vectors of growth are bi-directional (along coordinates a and z , see Figure 4; z is parallel to the uniaxial bending stress and perpendicular to the plane-of-view), with the crack extending stably along the crack front ($\phi \rightarrow 90^\circ$) with the contribution of three vectors (along coordinates a , z , and c) within $0^\circ < \phi < 90^\circ$, with diminishing a and z contributions during crack extension, and ultimately $a = 0$ and $z = 0$ at point C_h. Meaning that the plane of the new critical crack front ϕ_h at instability is now perpendicular to the uniaxial stress direction; the crack reoriented to 0° (onto the a_hc -plane, see Figure 4B). In the hypothetical case of a crack extending first from point C

toward the deepest point ($\phi \rightarrow 0^\circ$) simultaneously from both sides meeting up at $\phi = 0^\circ$, chances would be that some misalignment of the fracture plane would take place, resulting in a fractographic feature akin to a wake hackle appearing along points A-A_h. By originating from one of the two points C, an asymmetric halo should be expected. These features were not seen in any of the specimens.

The distinction between taking the Knoop median crack dimensions ($a, 2c, \chi$) or the halo dimensions ($a_h, 2c_h, \chi_h$) to compute Y or Y_h for the evaluation of the K_{Ic} is demonstrated in Figures 12 and 13 (the dataset of specimens showing no halo is not included). Expectedly, by considering the original Knoop median precrack as the critical crack, lower values of K_{Ic} are obtained, once the extra external load necessary to extend the crack (and kink it) is computed for a shorter crack. That, assuming that the halo is formed before instability, and that crack extension (i.e., $\phi \rightarrow \phi_h$, C-A-C \rightarrow C_h-A_h-C_h) is stable concomitant to an increase in $K_{I,appl}$ taking place during the crack extension and crack kink. In that (most probable) scenario, the halo is formed during the development of the R-curve. Thus, it is not surprising that taking the halo as the critical crack size results in higher values of K_{Ic} . Even if the LS2 material had no R-curve, the reorientation from a mixed-mode condition to a pure-mode I plane would require the addition of an extra K -term. The data-points using the halo boundary as the critical crack size fall now within the S.D. range for our CNB tests or slightly below the lower bound, a strong suggestion that the crack extension during the formation of the halo involved some gain in $K_{I,appl}$ comparable to that developing during crack extension in the CNB specimen. Suggestively, the K_{Ic} -value of SCF is shifted farther

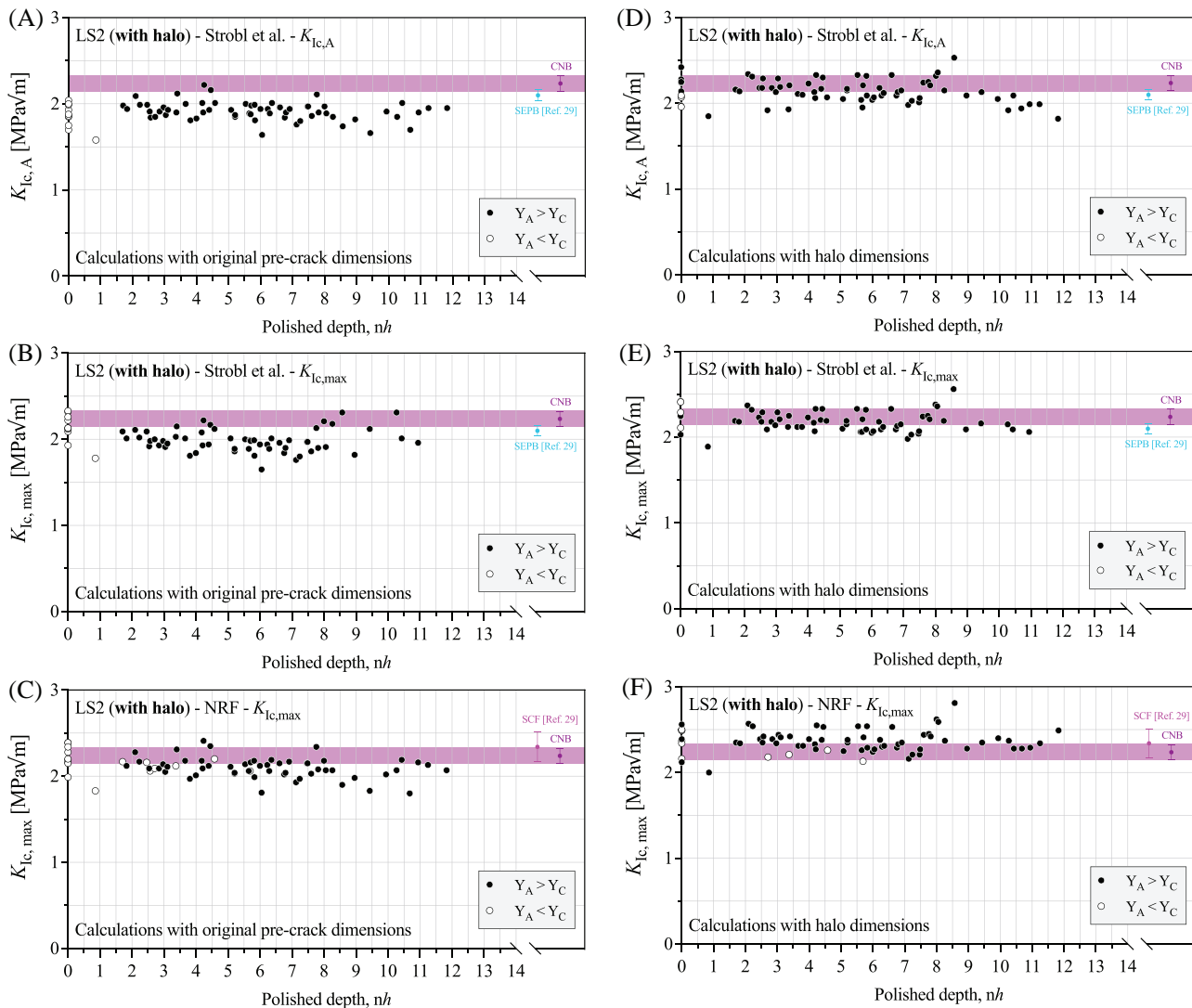


FIGURE 12 LS2 specimens showing a halo. (Left column calculations using original precrack dimensions, right column calculations using halo dimensions). (A,B,D,E) K_{Ic} versus X (as multiple of h) plots using the Strobl et al. solution at point A or at the maximum value of Y , rendering $K_{Ic,A}$ and $K_{Ic,max}$, respectively. Our CNB results are added (purple circle) with S.D. as the purple band for reference, along with SEPB values from reference 28. (C,F) Calculations using the NRF, along with SCF values from reference 28, which also used NRF

along the R-curve approaching the location of the K_{Ic} -value obtained in the CNB tests. Interestingly, that happened for specimens over the range $0h \leq X \leq 10h$, thus apparently compensating for the effect of residual stresses at $X < 3h$ and providing further support for the argument against the effect of LCs. Thus, in the situation in Figure 12D, the relationship of K_{Ic} versus X established in Figure 9D for the specimens developing no halo vanishes, and K_{Ic} seems to become constant over most of the entire range of X ($K_{Ic,max} = 2.30 \pm 0.48 \text{ MPa}\sqrt{\text{m}}$); for $X > 10h$, χ falls under 35° and Y_{max} diverges hugely from Y_A (Figure 13G,H). From this, it appears that, should R-curve materials show a halo consistent to those seen here, polishing can be shallow, if necessary, at all.

The scatter is however higher than for those specimens that showed no halo (dataset in Figure 9D–F). In the evaluations from Swab and Quinn,³³ the incorporation of the halo into the critical crack size was also shown to eliminate the R-curve behavior as concluded from tests with different initial crack sizes and leveled the values of K_{Ic} to those obtained using long-crack methods in alumina.

At high a/c ratios and high χ , as is the case for unpolished and low- X specimens, the value of Y tends to reach a maximum at the crack front near the surface (Point C, $\phi \sim 90^\circ$) and not at the deepest point (Point A, $\phi = 0^\circ$). This comes out of the solution from Strobl et al. as well as NRF (see Figure 13A,B), with the caveat that these two solutions

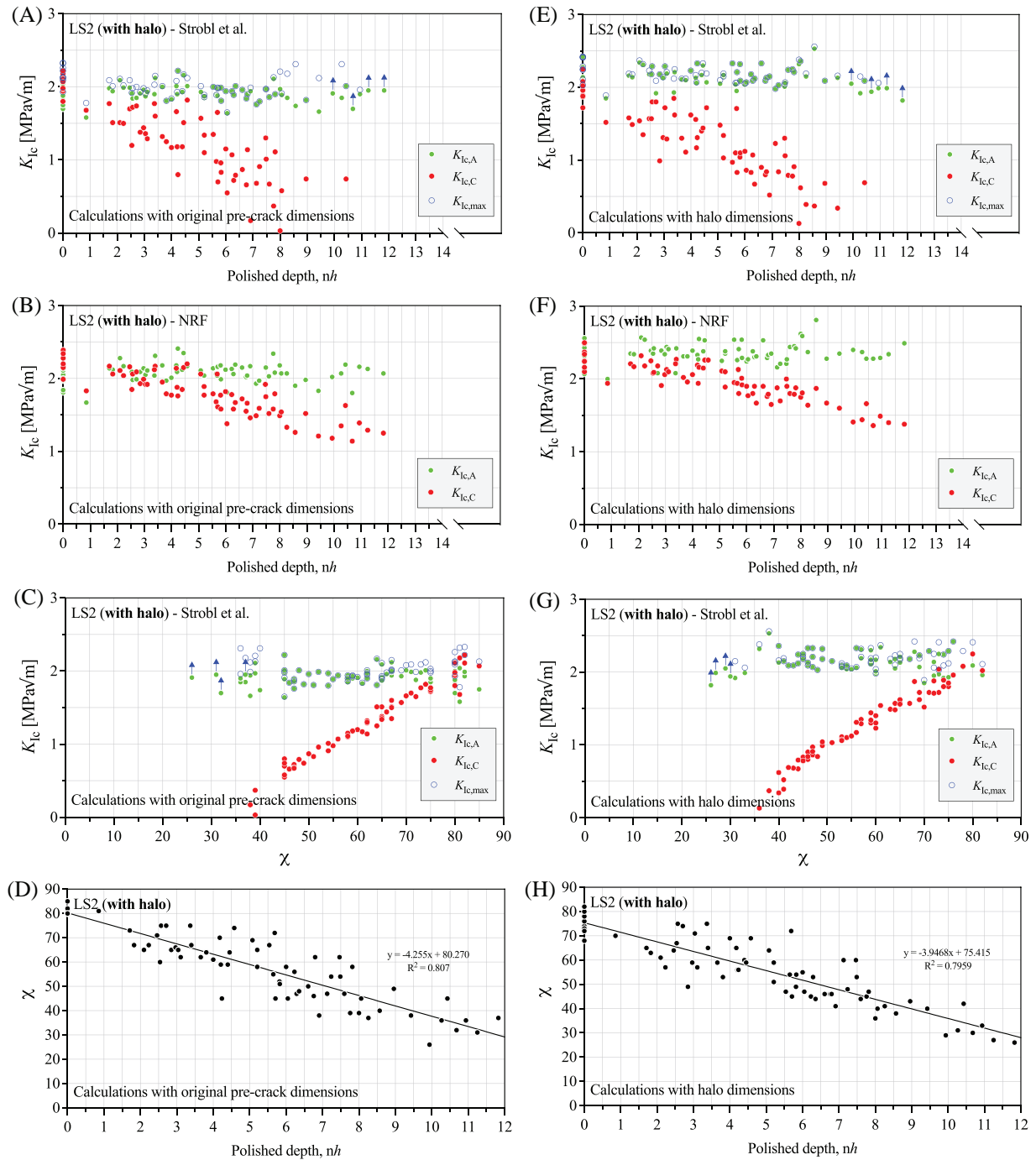


FIGURE 13 LS2 specimens showing a halo. (Left column calculations using original precrack dimensions, right column calculations using halo dimensions). (A,E) K_{Ic} versus X (as multiple of h) plots using the Strobl et al. solution using Y_A , Y_C , or Y_{max} . (B,F) Calculations using the NRF. (C,G) K_{Ic} versus χ for different values of Y . (D,H) Relationships between χ and X

assume the crack tip is oriented in-plane with the fracture plane (crack tip is in pure mode I loading); whether values of Y are favored to attain a maximum at point A under mixed-mode conditions even in high a/c ratios is currently not known since such solutions for Y are not available. Notwithstanding, the precrack growth during the formation of the halo (i.e., $\phi \rightarrow \phi_h$) led to the geometry of the halo boundary ($C_h-A_h-C_h$) to result in Y_h -values calculated

by both the Strobl et al. solution and NRF to become maximum now at the deepest part (see Figure 13E,F), due to lower a/c ratios and lower χ angles (Figure 13G) attained compared to the original precrack shape. That is, the development of halos widened the crack front, forcing Y to become maximum at point A, and that over almost the entire range of X (including at low- X and $X = 0h$) up to about $10h$ (corresponding to $\chi \sim 35^\circ$, see Figure 13H). Using

the geometry of the original precrack (which were smaller than those which developed no halo), good matching of Y_A and Y_{\max} occurred between the range of $70^\circ \geq \chi \geq 46^\circ$ (corresponding to a polishing depth between $2h \leq X \leq 8h$, see Figure 13C).

The precracks in the SL200B material exhibited no halos, even though SL200B has been shown by Fünfschilling et al.³⁶ to develop a steep R-curve departing from an intrinsic crack-tip toughness of $2.0 \text{ MPa}\sqrt{\text{m}}$ ³⁷ that flattens after 10–20 μm of crack extension (Δa) followed by a shallow rising plateau. The near-saturation of the R-curve after such short crack extensions is argued to lie on sharp transitions of toughening mechanisms dominated initially by high-energy expenditure elastic bridging, followed by partially debonded elastic bridges, and reaching a steady-state bridging zone consisting of frictional bridges of fully debonded $\beta\text{-Si}_3\text{N}_4$ grains.³⁸ Our Knoop median precracks of size 100–150 μm grew during indentation and are expected to have developed some condition of small-scale bridging³⁹ along the entire crack front (tip), akin to that observed for SL200B in reference 36—even before being monotonically loaded—and consist not of a pristine (bridging-zone free) crack. With the shape of the R-curve measured in reference 36 in mind, our cracks must show some stable crack extension during loading and become critical tangent to the R-curve passed its steeper incline thus sitting on the shallow rising plateau. Much further shielding of the crack tip is not gained at this point, and the development of a halo is undue. The obtained K_{Ic} -value obtained in a monotonic test is the tangent point extended toward the y-axis, even though computed for a shorter crack size defined by the border of the indentation median crack (the Δa is not readily visible at the crack surface). K -values are yet poised to vary between experiments, with shorter cracks and semi-circular cracks having the effect of slightly decreasing the magnitude (along the K_{appl} axis) of the R-curve, while unaffected its shape nor the earlier stages of its steep rise, as shown by Fett et al.⁴⁰ Our values of $K_{I,\max}$ for SCF were $5.07 \text{ MPa}\sqrt{\text{m}}$ and $5.09 \text{ MPa}\sqrt{\text{m}}$ for CNB, with a/W of ~ 0.04 and 0.37 , respectively, while the edge-to-edge notch in Fünfschilling et al.,³⁶ were in the order of $a/W \sim 0.63$ (all having $W = 4 \text{ mm}$), resulting in a $K_{R,\max} = 5.62 \text{ MPa}\sqrt{\text{m}}$.

3.2.4 | Strobl et al. solution versus NRF

For each of the datasets calculated using the solution of Strobl et al. for Y , a second dataset was created using the NRF for Y , shown for SL200B in Figures 9C and 10B, and for LS2 in Figures 9F,10F,12C,F, and 13B,F. In all cases, the $K_{Ic,\max}$ -values computed using the NRF resulted in significantly higher values, with an average increase of 7.6% for

SL200B and 5.3% for LS2—no halo (both for $X \geq 5h$). For $K_{Ic,A}$ these values increase to 8.5% and 9.0%, respectively.

For SL200B evaluated with NRF, the plateau values for SCF were shifted vertically above the range measured for the CNB specimens, a behavior that is not befitting the initial crack size dependency of K_{Ic} , as discussed above. The same anomaly was seen by Quinn and Salem¹ for their silicon carbide material in the region $4.5h < X < 7.5h$, for which remnants of LCs were ascribed (even though data-points located above their CNB and SEPB ranges were present up to $X \sim 10h$). K_{Ic} -values obtained by short-crack methods such as SCF rising above those based on large cracks (such as CNB) was seen as a sign of an artificial overestimation due to LCs. Correcting their values by about -8.5% would level off most their SCF values with $X > 4.5h$ to their CNB and SEPB results. In a comprehensive 2017 paper on the fracture toughness of glasses using the SCF and SEPB methods, Quinn and Swab⁴¹ reported that their SCF results using NRF were about 10% higher than when using the solution of Strobl et al., with the latter being more consistent and at the same level of their SEPB values; glasses are flat R-curve materials and K_{Ic} -values should match irrespective of testing method (provided they use an atomically sharp precrack).

For LS2, the dataset of precracks presenting no halo (Figures 9F and 10F), when treated with NRF gets flattened and shifted vertically to fall within the range defined by our CNB specimens; that situation would imply that LS2 has no R-curve behavior. When the precracks with halo are evaluated with NRF (Figures 12F and 13F), the dataset using the halo boundary as the critical crack size falls within the CNB range but mostly above it, and more interestingly, fitting perfectly within the range of the SCF results in N_2 gas ($2.34 \pm 0.17 \text{ MPa}\sqrt{\text{m}}$) obtained by Quinn et al.²⁷ for this LS2 computed with NRF, which was higher than their SEPB ($2.10 \pm 0.05 \text{ MPa}\sqrt{\text{m}}$) in the same study. Although they usually use the recommendation of ASTM C1421 to tilt the specimens 0.5° during indentation, this was not strictly stated, along with the missing information if the precracks showed or not showed halos, and how they were evaluated.

The problems associated with the NRF stem from the rough mesh that NR used in their FE-simulations, especially near the surface, and the parameter constraints employed, that is, for materials with a Poisson's ratio $\nu = 0.3$ and semi-elliptical precracks presenting crack-surface intersection angles of 90° . The reassessment of Strobl et al. of the NRF resulted in a parameterized fitting function expanded for cases including $0.4 \leq a/c \leq 1.2$, $0.01 \leq a/W \leq 0.5$, $0.1 \leq c/B \leq 0.5$, $0 \leq \nu \leq 0.4$, and $100^\circ \geq \chi \geq 70^\circ$. In their analysis, Strobl et al.^{10,11} found fitting errors using NRF of up to 7.7% at point A for $\chi = 90^\circ$ and $\nu = 0.3$, and up to 34.2% for $90^\circ \geq \chi \geq 70^\circ$ and $0 \leq \nu \leq 0.4$.

The NRF provides the possibility of calculating the Y -factor at point C (Y_C) and at point A (Y_A), with the crack to be regarded as invalid if $Y_A < Y_C$. It is worth noting that precracks in both SL200B and LS2 (no halo) showing $\chi > 68^\circ$ generally led to the forbidden condition of $Y_C > Y_A$ using NRF, while this was the case only for $\chi > 80^\circ$ using Strobl et al. Precracks showing χ above those values should thus in principle not be allowed for the evaluation of K_{Ic} —precisely the range where the effects of the damage zone and LCs are considered. The data-points of Quinn and Salem¹ with low- X are thus also deemed to have shown a crack geometry leading to invalid Y -values.

Obviously, the solution of Strobl et al. cannot fix the problem of crack geometries showing high a/c and high χ in resulting in the maximum Y -value being located at point C instead of point A. Unfortunately, Strobl et al. provide only a generalized geometric fitting function for Y_A , and not for Y_C . Instead, they provide an equation (with parameters a_0 , c_0 , W_0 , and ν) for the calculation of the minimum polishing depth (ΔW_{\min}) necessary to obtain a crack geometry resulting in the condition $Y_A = Y_{\max}$. For LS2, we obtain $\Delta W_{\min} = 153 \mu\text{m}$, which is equivalent to $\sim 8.7h$, invalidating all the data-points below that threshold. However, one really sees in Figure 10E,G that the blue and green symbols match well already at $X \geq 5h$ for LS2, corresponding to χ of about 72° , but overlap perfectly at first between $6.5h \leq X \leq 11.5h$, corresponding, respectively, to $67^\circ \geq \chi \geq 50^\circ$ (see Figure 10E,G,H). For SL200B, we obtain $\Delta W_{\min} = 63 \mu\text{m}$ (equivalent to $X \sim 5.3h$); values of Y_A equating those of Y_{\max} are shown in Figure 10A,C at $X \geq 4.5h$ (corresponding to $67^\circ \geq \chi \geq 45^\circ$, see Figure 10D). The calculation of ΔW_{\min} by Strobl et al. thus matches very well to our data; although slightly excessive, it safely places χ within those ranges. Additionally, the Y_A solution of Strobl et al. was simulated for the condition $110^\circ \geq \chi \geq 70^\circ$; specimens polished beyond $\sim 5h$ for LS2 and $\sim 2.5h$ for SL200B resulted invariably in $\chi < 70^\circ$. Despite that, the solution from Strobl et al. seems to be robust enough to yield extrapolated Y_A -values giving accurate K_{Ic} -values also for lower χ -values (i.e., shorter cracks), at least down to 40° – 45° (see Figures 10C,G and 13C,G).

4 | CONCLUSIONS

Our evaluation of SCF specimens at varying polishing depths, originally devised to assess the effect of LCs on the measured K_{Ic} , revealed the following facts:

1. The damage zone in SL200B showed the effect of reducing the measured K_{Ic} substantially; its removal needed not be complete (thus leaving the short LCs in their entirety) in order to reach a $K_{Ic,\max}$ -value

at $2.5h$ that is comparable to an accurate $K_{Ic,A}$ -value (when $Y_A = Y_{\max}$) at deeper polishing depths $X \geq 4.5h$.

2. The LS2 material developed deep and long LCs, but they showed not to influence the measured K_{Ic} -value. Although a polishing depth of $3h$ was shown to reach consistent K_{Ic} -values, high accuracy in K_{Ic} determination (when $Y_A = Y_{\max}$) could only be achieved for polishing depths in the range $6.5h \leq X \leq 11.5h$.
3. The values of Y_A given by Strobl et al., even when higher than Y_C , do not always correspond to the maximum value of Y along the entire crack front, especially at low polishing depths. For both materials, a very good match between Y_A and Y_{\max} took place at deeper polishing depths, where the crack-surface angle of encounter was smaller than 67° . Therefore, the rationale of polishing SCF specimens in order to obtain reliable K_{Ic} should be based more heavily on grounds pertaining to attaining an appropriate crack geometry, rather than due to LCs effects.
4. For low polishing depths, the Y_A solution from Strobl et al. yields values that are lower than the true Y_{\max} , underestimating K_{Ic} . For extended polishing depths, the Strobl et al. solution for Y_A yields accurate values for a wider range than it was evaluated for, for example, for shallow cracks showing crack-surface angles χ as low as $\sim 40^\circ$.
5. At low polishing depths, the NRF underestimates Y_A , making it (erroneously) invalid. When $Y_A > Y_C$, the NRF yields K_{Ic} -values of up to about 10% higher than the solution from Strobl et al.
6. When using the halo dimensions as the critical crack size, any effect of polishing vanishes, and the K_{Ic} levels off to that obtained for methods which yield K_{Ic} -values farther along the R-curve. In R-curve materials, such halos seem to develop during the rising of the R-curve if the obtained K_{Ic} with SCF still lie on the steeper incline of the R-curve with remaining potential for stable crack extension (the case of LS2). For SL200B, halos did not develop, as the K_{Ic} -value obtained by SCF apparently lies on the later near-plateau stage of the R-curve. The use of the formula for Y_A from Strobl et al. becomes valid when using the halo boundaries as crack dimensions due to their low χ to the surface, making any polishing superfluous.
7. Precrack halos seem to occur more frequently when the specimen is tilted at 0.5° during indentation; performing indentations at 90° with the surface reduces the frequency of halos.

Established the fact that damage zones, the morphology of LCs, and even the a/c ratios of pristine Knoop median cracks differ from material to material, and that

the most consistent parameter determining a valid Y_A -solution (i.e., $Y_A = Y_{\max}$ at Point A, where $\phi = 0^\circ$) seems to be the crack-surface termination angle χ , it appears to us that the recommendation of standards to make use of the parameter h to define the polishing depth can lead to unwanted uncertainties. From a practical standpoint, procedural preparation and testing of SCF specimens would profit from aiming for a polishing depth that assures that a minimum crack-surface termination angle χ of 67° and maximum of 40° is always achieved. This can be done in one of the two ways: by using the ΔW_{\min} formula given in Strobl. et al,^{10,11} or by performing a couple of pre-tests in unpolished specimens in order to measure the dimensions of the pristine Knoop median crack and subsequently calculating ΔW_{\min} geometrically. Not that the purpose of polishing should be the removal of LCs, we saw here that the requisite ΔW_{\min} for $67^\circ \geq \chi \geq 40^\circ$ will consequently remove LCs entirely for probably most materials.

ACKNOWLEDGMENT

The authors declare that they have no known competing financial interests or personal relationships that could have appeared to influence the work reported in this paper.

Open access funding enabled and organized by Projekt DEAL.

CONFLICT OF INTEREST

The authors declare no conflict of interest.

ORCID

Tanja Lube  <https://orcid.org/0000-0002-8808-2973>

Renan Belli  <https://orcid.org/0000-0003-0913-3996>

REFERENCES

1. Quinn GD, Salem JA. Effect of lateral cracks on fracture toughness determined by the surface-crack-in-flexure method. *J Am Ceram Soc.* 2002;85(4):873–80.
2. Newman JC, Raju IS. An empirical stress-intensity factor equation for the surface crack. *Eng Fract Mech.* 1981;15(1–2):185–92.
3. Wills RR, Mendiratta MG, Petrovic JJ. Controlled surface flaw initiated fracture in reaction-bonded Si₃N₄. *J Mater Sci.* 1976;11(7):1330–4.
4. Petrovic JJ, Dirks RA, Jacobson LA, Mendiratta MG. Effects of residual-stresses on fracture from controlled surface flaws. *J Am Ceram Soc.* 1976;59(3–4):177–8.
5. Quinn GD, Swab JJ, Hill MD. Fracture toughness by the surface crack in flexure (SCF) method. *Ceram Eng Sci Proc.* 1997;18(4):846–55.
6. Stech M, Rodel J. Method for measuring short-crack R-curves without calibration parameters: case studies on alumina and alumina aluminum composites. *J Am Ceram Soc.* 1996;79(2):291–7.
7. Quinn JB, Lloyd IK. Comparison of methods to determine the fracture toughness of three glass-ceramics at elevated temperatures. *J Am Ceram Soc.* 2000;83(12):3070–6.
8. Glaesemann GS, Ritter JE, Jakus K. Mixed-mode fracture in soda-lime glass using indentation flaws. *J Am Ceram Soc.* 1987;70(9):630–6.
9. Lube T. Indentation crack profiles in silicon nitride. *J Eur Ceram Soc.* 2001;21(2):211–8.
10. Strobl S, Supancic P, Lube T, Danzer R. Corrigendum to “surface crack in tension or in bending - a reassessment of the Newman and Raju formula in respect to fracture toughness measurements in brittle materials (vol 32, pg 1491, 2012)”. *J Eur Ceram Soc.* 2018;38(1):355–8.
11. Strobl S, Supancic P, Lube T, Danzer R. Surface crack in tension or in bending - a reassessment of the Newman and Raju formula in respect to fracture toughness measurements in brittle materials. *J Eur Ceram Soc.* 2012;32(8):1491–501.
12. Cicconi MR, Belli R, Brehl M, Lubauer J, Hayakawa T, Kimura K, et al. Nucleation mechanisms in a SiO₂-Li₂O-P₂O₅-ZrO₂ biomedical glass-ceramic: insights on crystallisation, residual glasses and Zr⁴⁺ structural environment. *J Eur Ceram Soc.* 2022;42(4):1762–75.
13. Lubauer J, Belli R, Peterlik H, Hurle K, Lohbauer U. Grasping the lithium hype: insights into modern dental lithium silicate glass-ceramics. *Dent Mater.* 2021;38(2):318–32.
14. Lubauer J, Belli R, Petschelt A, Cicconi MR, Hurle K, Lohbauer U. Concurrent kinetics of crystallization and toughening in multicomponent biomedical SiO₂-Li₂O-P₂O₅-ZrO₂ glass-ceramics. *J Non-Cryst Solids.* 2021;554:120607.
15. Belli R, Lohbauer U, Goetz-Neunhoffer F, Hurle K. Crack-healing during two-stage crystallization of biomedical lithium (di)silicate glass-ceramics. *Dent Mater.* 2019;35(8):1130–45.
16. Lubauer J, Hurle K, Cicconi MR, Petschelt A, Peterlik H, Lohbauer U, et al. Toughening by revitrification of Li(2)SiO₃ crystals in Obsidian (R) dental glass-ceramic. *J Mech Behav Biomed Mater.* 2021;124:104739.
17. Belli R, Wendler M, Cicconi MR, de Ligny D, Petschelt A, Werbach K, et al. Fracture anisotropy in texturized lithium disilicate glass-ceramics. *J Non-Cryst Solids.* 2018;481:457–69.
18. Belli R, Wendler M, Petschelt A, Lube T, Lohbauer U. Fracture toughness testing of biomedical ceramic-based materials using beams, plates and discs. *J Eur Ceram Soc.* 2018;38(16):5533–44.
19. Lube T, Duszka J. A silicon nitride reference material - a testing program of ESIS TC6. *J Eur Ceram Soc.* 2007;27(2–3):1203–09.
20. Lube T, Danzer R, Steen M. A testing program for a silicon nitride reference material. In: M. Matsui, S. Jahanmir, H. Mostgaci, M. Naito, K. Uematsu, R. Woesche, R. Morell, editors. *Improved ceramics through new measurements, processing and standards.* Westerville: The American Ceramic Society; 2003. p. 259–268.
21. Lube T, Danzer R. The ESIS silicon nitride reference material testing program. *Ceram Eng Sci Proc.* 2003;24(4):337–42.
22. Roebben G, Sarbu C, Lube T, Van der Biest O. Quantitative determination of the volume fraction of intergranular amorphous phase in sintered silicon nitride. *Mater Sci Eng., A.* 2004;370(1–2):453–58.
23. Kübler J. Procedure for determining the fracture toughness of ceramics using the single-edge-V-notched beam (SEVNB) method. GKSS-Forschungszentrum on behalf of the European Structural Integrity Society; 2000.
24. Lube T, Danzer R, Duszka J, Kübler J, Erauw J-P, Klemm H, Sglavo VM. ESIS reference material testing program

- strength and fracture toughness. Proceedings of the Conference Fractography 2003, IMR SAS Kosice, Stará Lesná, November 9–12, 2003, Slovak Republik. S86–93. IMR SAS Kosice; 2003.
25. Belli R, Petschelt A, Hofner B, Hajto J, Scherrer SS, Lohbauer U. Fracture rates and lifetime estimations of CAD/CAM all-ceramic restorations. *J Dent Res*. 2016;95(1):67–73.
 26. Wendler M, Belli R, Petschelt A, Mevec D, Harrer W, Lube T, et al. Chairside CAD/CAM materials. Part 2: flexural strength testing. *Dent Mater*. 2017;33(1):99–109.
 27. Belli R, Wendler M, de Ligny D, Cicconi MR, Petschelt A, Peterlik H, et al. Chairside CAD/CAM materials. Part 1: measurement of elastic constants and microstructural characterization. *Dent Mater*. 2017;33(1):84–98.
 28. Quinn GD, Swab JJ, Patel P. Fracture toughness of modern and ancient glasses and glass ceramics as measured by the SEPB method. *Ceram Eng Sci Proc*. 2018;39(2):1–13.
 29. Kirsten J, Belli R, Wendler M, Petschelt A, Hurle K, Lohbauer U. Crack growth rates in lithium disilicates with bulk (mis)alignment of the $\text{Li}_2\text{Si}_2\text{O}_5$ phase in the [001]direction. *J Non-Cryst Solids*. 2020;532:119877.
 30. Lubauer J, Ast J, Göken M, Merle B, Lohbauer U, Belli R. Resistance-curve envelopes for dental lithium disilicate glass-ceramics. *J Eur Ceram Soc*. 2022;42(5):2516–22.
 31. Belli R, Wendler M, Zorzini JJ, Lohbauer U. Practical and theoretical considerations on the fracture toughness testing of dental restorative materials. *Dent Mater*. 2018;34(1):97–119.
 32. Fett T. New contributions to R-curves and bridging stresses - Applications of weight functions. Karlsruhe: KIT Scientific Publishing; 2012.
 33. Swab JJ, Quinn GD. Effect of precrack “halos” on fracture toughness determined by the surface crack in flexure method. *J Am Ceram Soc*. 1998;81(9):2261–68.
 34. Marshall DB. Mechanisms of failure from surface flaws in mixed-mode loading. *J Am Ceram Soc*. 1984;67(2):110–16.
 35. Wendler M, Belli R, Valladares D, Petschelt A, Lohbauer U. Chairside CAD/CAM materials. Part 3: cyclic fatigue parameters and lifetime predictions. *Dent Mater*. 2018;34(6):910–21.
 36. Fünfschilling S, Fett T, Oberacker R, Hoffmann M, Özcoban H, Jellito H, et al. R curves from compliance and optical crack-length measurements. *J Am Ceram Soc*. 2010;93(9):2814–21.
 37. Fünfschilling S, Fett T, Hoffmann MJ, Oberacker R, Jellito H, Schneider GA. Determination of the crack-tip toughness in silicon nitride ceramics. *J Mater Sci Lett*. 2009;44(1):335–8.
 38. Fünfschilling S, Fett T, Hoffmann MJ, Oberacker R, Schwind T, Wippler J, et al. Mechanisms of toughening in silicon nitrides: the roles of crack bridging and microstructure. *Acta Mater*. 2011;59(10):3978–89.
 39. Kruzic JJ, Satet RL, Hoffmann MJ, Cannon RM, Ritchie RO. The utility of R-curves for understanding fracture toughness-strength relations in bridging ceramics. *J Am Ceram Soc*. 2008;91(6):1986–94.
 40. Fett T, Fünfschilling S, Hoffmann MJ, Oberacker R. Different R-curves for two- and three-dimensional cracks. *Int J Fract*. 2008;153(2):153–59.
 41. Quinn GD, Swab JJ. Fracture toughness of glasses as measured by the SCF and SEPB methods. *J Eur Ceram Soc*. 2017;37(14):4243–57.

How to cite this article: Lubauer J, Lohbauer U, Henrich M, Munz M, Lube T, Belli R. Intricacies involving the evaluation of fracture toughness obtained by the surface-crack-in-flexure method. *J Am Ceram Soc*. 2022;105:7582–7599.
<https://doi.org/10.1111/jace.18667>

Paper I

S. Strobl, P. Supancic, T. Lube, R. Danzer: "Toughness Measurement on Ball Specimens, Part I: Theoretical Analysis", *Journal of the European Ceramic Society* **32** (2012), 1163-1173, <http://dx.doi.org/10.1016/j.jeurceramsoc.2011.12.003>

Re-used as author according to Elsevier's copyright agreement.

Toughness measurement on ball specimens. Part I: Theoretical analysis

Stefan Strobl^{a,b,*}, Peter Supancic^{a,b}, Tanja Lube^a, Robert Danzer^a

^a Institut für Struktur- und Funktionskeramik, Montanuniversität Leoben, Peter-Tunner-Straße 5, A-8700 Leoben, Austria^c

^b Materials Center Leoben Forschung GmbH, Roseggerstraße 12, A-8700 Leoben, Austria^d

Received 26 August 2011; received in revised form 23 November 2011; accepted 5 December 2011

Available online 5 January 2012

Abstract

A new toughness test for ball-shaped specimens is presented. In analogy to the “Surface Crack in Flexure”-method the fracture toughness is determined by making a semi-elliptical surface crack with a Knoop indenter into the surface of the specimen. In our case the specimen is a notched ball with an indent opposite to the notch. The recently developed “Notched Ball Test” produces a well defined and almost uniaxial stress field.

The stress intensity factor of the crack in the notched ball is determined with FE methods in a parametric study in the practical range of the notch geometries, crack shapes and other parameters. The results correlate well with established calculations based on the Newman–Raju model.

The new test is regarded as a component test for bearing balls and offers new possibilities for material selection and characterisation. An experimental evaluation on several ceramic materials will be presented in a consecutive paper.

© 2011 Elsevier Ltd. All rights reserved.

Keywords: Fracture; Mechanical properties; Toughness and toughening; Si₃N₄; Notched Ball Test

1. Introduction

Structural ceramics, especially silicon nitride (Si₃N₄), are distinguished due to their special properties: low wear rates, high stiffness, low density, electrical insulation and high corrosion resistance. For this reason they are advantageous for highly loaded structural applications or when special properties (due to additional requirements) are needed. An important application with a rapidly growing market are hybrid bearings (ceramic rolling elements and metal races), which are used for high operation speeds (e.g. racing), current generators (e.g. in wind turbines) or in the chemical industry.^{1,2} Key elements of the bearings are the ceramic rolling elements, which should have to comply with highest requirements. But relevant standards for the proper determination of the mechanical properties of roller elements are missing.

Mechanical properties of ceramics depend to a large fraction on their microstructure, which is strongly influenced by

processing conditions. Therefore proper mechanical tests should be made on specimens cut out of the components, or – even better – on components themselves. The strength depends on the flaw populations occurring in the component which are – in general – different in the volume and at the surface. In roller bearing applications the highest tensile stresses occur at (and near) the surface of the rolling elements and surface flaws are of utmost significance for the strength of rolling elements. Therefore the highest loaded area in mechanical testing of bearing balls should be situated at the surface of the balls.

These conditions are fulfilled in the case of the Notched Ball Test (NBT)^{3–6} for the strength measurement of balls, which has recently been developed by several of the authors. A slim notch is cut into the equatorial plane of a sphere and the testing force is applied on the poles perpendicular to the notch. In that way an almost uniaxial tensile stress field is generated in the surface near area opposite the notch, which is used for the determination of the strength of the Notched Ball (NB) specimen. Therefore the NBT is very sensitive to surface flaws and relevant for determining the strength of ceramic balls. Note that a similar test, the C-Sphere Test,⁷ was proposed earlier, where the notch is not slim but wide and must have a precise shape. The quality of bearing balls is strongly related to a high toughness, which should also be measured at specimens cut out of the balls or on the balls themselves. In industry toughness measurements on

* Corresponding author at: Institut für Struktur- und Funktionskeramik, Montanuniversität Leoben, Peter-Tunner-Straße 5, A-8700 Leoben, Austria. Tel.: +43 3842 402 4113; fax: +43 3842 402 4102.

E-mail address: stefan.strobl@mcl.at (S. Strobl).

^c isfk@unileoben.ac.at, <http://www.isfk.at>.

^d mclburo@mcl.at, <http://www.mcl.at>.

bearing balls are commonly made with indentation methods (i.e. “Indentation Fracture”-method^{8–12} due to their ease of use. It has been recognised in the last years that the toughness values measured with indentation methods depend on the size and shape of the plastic deformation zone around the indent, which may vary from material to material. Therefore the resulting “Indentation Fracture Resistance” (IFR) is only a rough estimate of fracture toughness and has to be calibrated for each material and indentation load.

Standardised fracture toughness testing methods normally use standard beams, which contain a well defined crack and which are loaded and broken in 4-point bending. The fracture toughness K_C is determined by application of the Irwin failure criterion: $K = K_C$, where K is the stress intensity factor (SIF). Note that K and K_C mean pure Mode I configuration (i.e. crack opening). In the following the authors disclaim to use indices because the other loading Modes are not discussed. The critical stress intensity factor can be determined using the fracture load and with information on beam and crack geometry.

A prominent example is the “Single Edge V-Notched Beam” (SEVNB) method,¹³ in which, a slim notch is introduced in a bending beam using a razor blade. In that way straight notches with a tip radius of at least $3 \mu\text{m}$ can be produced. For materials having a mean grain size of several micrometers or greater, this is an accurate approximation of a crack^{14,15} but for fine grained materials sharper cracks would be beneficial for a precise toughness measurement.

Very sharp cracks are used in the “Surface Crack in Flexure” (SCF) method.^{16,17} A Knoop hardness indent is made on the tensile loaded side of a rectangular bending bar. Thus, an almost semi-elliptical and very sharp crack is introduced in the surface. The size of the remaining Knoop crack is determined by fractographic means, which may need some fractographic experience.

In comparison the SEVNB method is easier to apply and less time consuming but the SCF-method is more appropriate for materials with a very fine grain structure.

To measure the fracture toughness of ceramic balls, bending bars can machined out of balls, if the balls have minimum diameter, say 20–25 mm, but most of the produced rolling elements are smaller. So a simple toughness test for ball shaped components is needed. In this work we will focus on an extension of the SCF method on NB specimens.

2. The SCF-method applied to notched ball specimens

2.1. The Notched Ball Test for strength measurement

Recently, the “Notched Ball Test” (NBT) was established at the Institut für Struktur- und Funktionskeramik at Montanuniversität Leoben to measure the strength of ceramic balls, see Fig. 1. With a commercial diamond disc, a notch is cut into the equatorial plane of the ball (depth ca. 80% of the diameter) and the load F is applied at the poles (point 3) using a conventional testing machine. Then the notch is squeezed together and high tensile stresses occur in the surface region of the ball opposite to

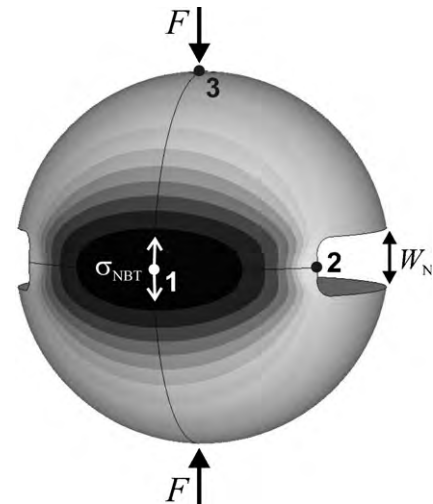


Fig. 1. Stress distribution of a notched ball (NB) specimen. The ball is loaded in compression with the force F perpendicular to the notch. This causes tensile stresses in the outer surface region of the ball opposite to the notch with a maximum stress σ_{NBT} at position 1. W_N is the notch width. Adapted from [6].

the notch root (the maximum stress σ_{NBT} is located at position 1, furthermore called peak stress).

The stress field in the NB only depends on the ball diameter D (ball radius R), the notch length L_N , the notch width W_N , the fillet radius R_N of the notch at the notch base, and on the Poisson’s ratio ν of the tested material. The geometric parameters are defined in Figs. 1 and 2.

To generalize the results the definition of the following dimensionless geometric parameters is convenient: the relative notch length $\lambda = L_N/D$, the relative width of the notch $\omega = W_N/D$, the relative radius of the fillet of the notch base $\rho = R_N/W_N$.

The peak stress σ_{NBT} can be calculated using Eq. (1), with h as the ligament thickness and f_N as dimensionless factor, which depends on the relative notch geometry (λ , ω , ρ) and the Poisson’s ratio ν , and which, in the parameter range used for tests,

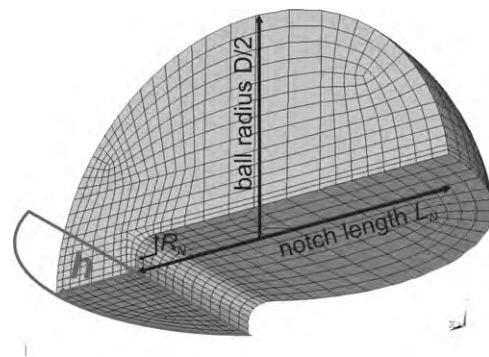


Fig. 2. The stress field in the specimen depends on the ball diameter D , the notch length L_N , the notch width W_N and the fillet radius R_N of the notch. The dimensionless geometric parameters are the relative notch length $\lambda = L_N/D$, the relative width of the notch $\omega = W_N/D$, the relative radius of the fillet of the notch base $\rho = R_N/W_N$. In the equatorial plane remains a ligament having the shape of a segment of a circle with the thickness $h = D - L_N$.

is $0.4 \leq f_N \leq 1.5$. A detailed analysis of f_N for a wide range of relative parameters can be found in.⁶

$$\sigma_{\text{NBT}} = f_N \times \frac{6F}{h^2} \quad \text{with} \quad f_N = f_N(\lambda, \omega, \rho, \nu) \quad (1)$$

The sample preparation is clearly specified and the geometry measurement of the NB specimen is precisely feasible. The simple testing setup minimizes measurement errors caused by inaccurate alignment. Because the loading point is far away from the area, where the maximum tensile stress occurs (and which is used for strength testing), the result is only very little influenced by the local contact situation (contact stresses). Furthermore friction is extremely reduced (in comparison to bending testing; here friction may have a very strong impact on stress determination) and can be neglected for data evaluation.

In summary the NBT is a very precise and simple testing method, which makes the characterisation of original ball surfaces possible. Up to now almost 1000 NB-tests on specimens having different diameters and relative notch geometries, and are made from different materials have been successfully tested in the laboratory of the authors.^{3–6,18}

2.2. Basic principles and fracture toughness determination

The common approach in fracture toughness testing for ceramic materials is based on the Griffith/Irwin fracture criterion:

$$K_C \geq K = \sigma Y \sqrt{a\pi}. \quad (2)$$

K_C is the Mode I fracture toughness, K is the stress intensity factor, σ is a reference stress in the uncracked specimen (e.g. outer fibre stress for bending), a is the size of the crack and Y is a geometric factor, which is determined by the geometry of the specimen, the crack shape and the course of the stress field. For details see standard text books on fracture mechanics or on mechanical properties of ceramics.^{19,20} Information on geometric factors for typical loading cases and standard specimen geometries can be found in literature.²¹

To apply this equation for fracture toughness determination, a well defined stress field, which contains a crack of well-known geometry and size, is needed. In the case of the standardized SCF-method^{16,17,22,23} a surface crack is produced with a Knoop indent in a bending bar specimen. The indent causes plastic deformation around the indented zone, which also causes unknown internal stresses. They are relaxed by removing the plastic deformed material by grinding-off a thin surface layer of the specimen's surface, in which the hardness impression was made. Then the specimen is loaded in four point bending, i.e. a well defined (known) stress field is applied. The load is increased until fracture occurs.

After fracture the crack size is determined on the fracture surface by fractographic means. It has a semi-elliptical shape. For a material with the Poisson's ratio $\nu = 0.3$ Newman and Raju^{24–26} have developed a parameterized and generalized solution of the geometric factor Y of a semi-elliptic crack in the stress field of a bent bar (thickness t and width $2b$). It depends on the geometry of the crack (crack width $2c$, crack depth a), the bar's cross-section

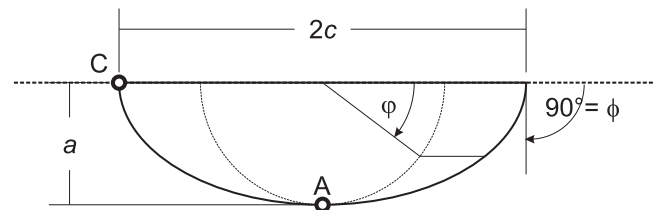


Fig. 3. Schematic of a semi elliptical crack. The crack width $2c$ at the surface and the crack depth a are indicated as well as the points A ($\varphi = 90^\circ$) and C ($\varphi = 0^\circ$), where the geometry factor Y can reach a maximum.

and on the position at the crack front given by the angle φ , see Fig. 3. The geometric factor $Y(a, t, b, c, \varphi)$ shows a maximum either in point A (deepest point of the crack) or in point C (crack front intersection with the specimen surface). In the following these special values of the geometric factor are called Y_A and Y_C . Tentatively $Y_A > Y_C$ for shallow cracks ($c > a$) and vice versa. Of course fracture is initiated at the position the largest stress intensity factor.

The SCF-method can be adopted for the loading situation in a NB specimen. The stress distribution in the NB specimen is well-known and similar to that in a conventional four point bending bar, i.e. almost uniaxial. The Knoop indent is introduced opposite to the notch, where the maximum stress occurs (position 1), see Fig. 4. In the following, the plastically deformed surface layer is ground off and the NB specimen is broken. For the evaluation of fracture toughness, the stress field of the NB specimen after grinding-off the plastically deformed surface layer has to be determined. Then the geometric factor of a semi-elliptical crack in that stress field has to be determined. Again the crack size and geometry will be measured by fractographic means.

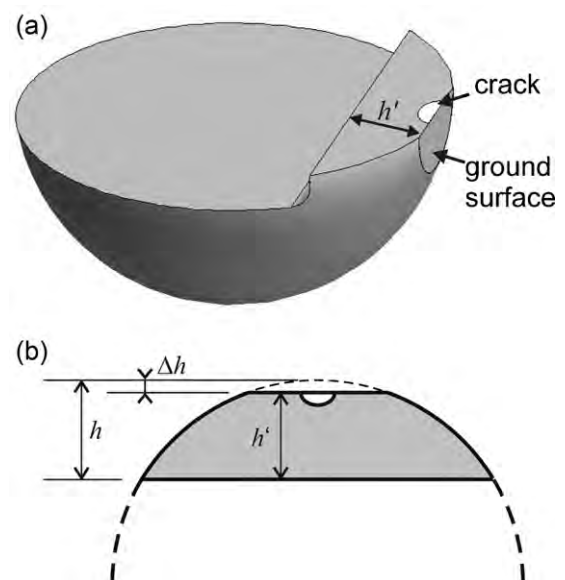


Fig. 4. Illustration of notched ball (half model) with a semi-elliptical crack (white) and ground down to remove the plastic zone around the indent. The remaining ligament thickness is ($h' = h - \Delta h$).

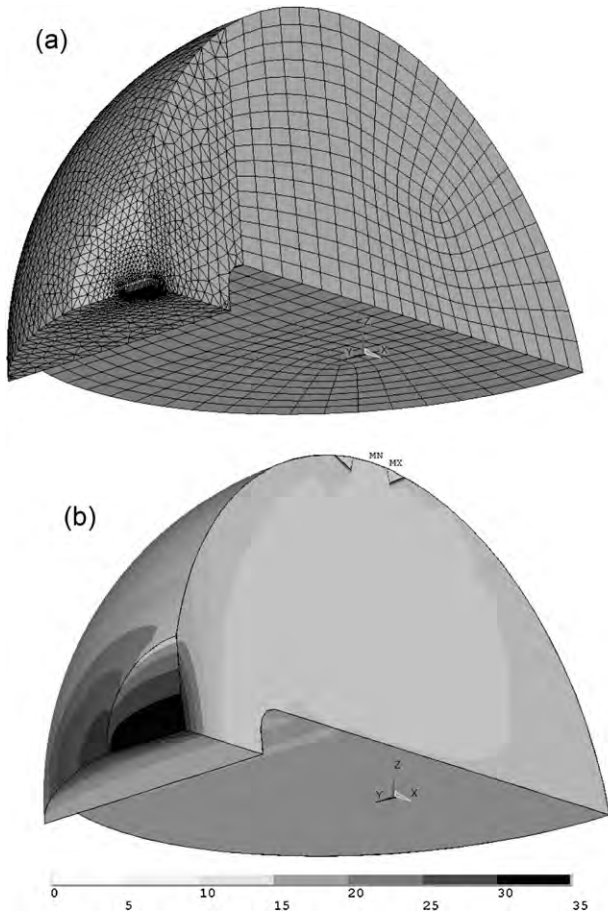


Fig. 5. Reference model of a ground-off notched ball specimen used for the parametric study: (a) mesh overview and (b) stress distribution (σ_z) without crack (compare with Fig. 1). Stress values given in MPa for an applied load of $F = 1$ N.

2.3. Stress distribution in the NB specimen due to material removal

As in the case of SCF measurements on bending bars, the plastically deformed material in the surface of the ball around the indent has to be removed. The thickness of the removed surface layer (removal depth) is called Δh , or in relative units $\alpha = \Delta h/R$, see Fig. 4.

The stress distribution in the ground-off NB specimen has been determined by a FE analysis which was performed in ANSYS 12.1/13.0. The quarter-model is shown in Fig. 5a and it includes about 35,000–50,000 elements (hexahedral- and tetrahedron-shaped). In the region, where the crack will be located (position 1'), the mesh is refined. A convergence study with an overall refinement of the mesh (i.e. half element size) showed no significant change of the peak stress. The uncertainties in the determination of the maximum tensile stress in the NB specimens are assumed to be less than 0.1% of its value.

If not specified elsewhere a reference model with the following standard parameters is used for all further investigations: $\lambda = 0.8$, $\omega = 0.15$, $\rho = 0.25$, $\nu = 0.3$, $\alpha = 0.04$, $\beta = 0.05$ and $\gamma = 0.5$, where β is the relative crack size ($\beta = a/R$) and γ represents the crack shape ($\gamma = a/c$). In Fig. 5b the stress field perpendicular

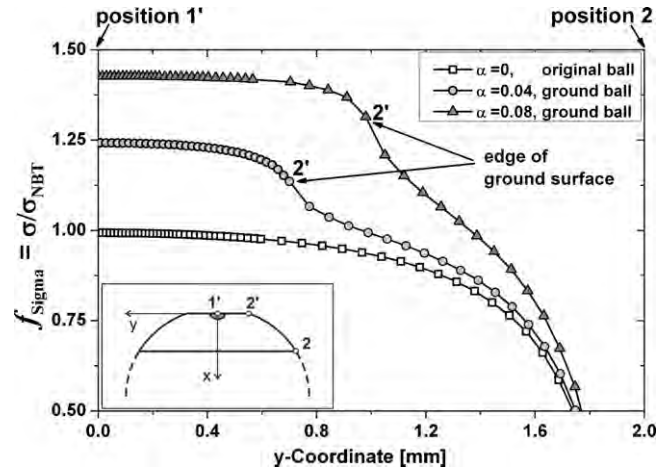


Fig. 6. Stress profile along a path at the surface of the notched ball specimen for the original ball and two different grinding depths α (calculated with FE analysis for the reference model) in relative units. The ratio σ/σ_{NBT} is called f_{Sigma} . The edge of the ground surface for each case is indicated with arrows (position 2'). The maximum stress value in position 1 (position 1', respectively) increases significantly with α .

to the notch plane (σ_z) at the surface of the reference specimen without crack and after grinding-off a surface layer is illustrated. The stress distribution and its maximum changes due to material removal (compare with Fig. 1).

It is interesting to note, that by modest geometric changes caused by the grinding-off material at the ball apex, the peak stress at the ground surface (position 1') increases significantly, see Fig. 6. For $\alpha = 0.04$ (the grinding depth is 4% of the ball radius), the peak stress increases almost 25% and for $\alpha = 0.08$ the stress rises strongly again.

In the following, stresses will be described in dimensionless (relative) units, i.e. they will be related to the maximum stress in a perfect NB specimen: $f_{Sigma} = (\sigma/\sigma_{NBT})$. Consider that σ_{NBT} is the first principal stress at position 1, see also Fig. 1. The relative stress at position 1' depends on the amount of removed material, the Poisson's ratio and the notch geometry.

Apart from the notch length, the notch geometry has a marginal effect on f_{Sigma} , so that the influence of ρ and ω is negligible. The relative stress at position 1' as a function of α and ν is plotted in Fig. 7. An interpolation function of f_{Sigma} based on 320 calculation points was used for data evaluation.

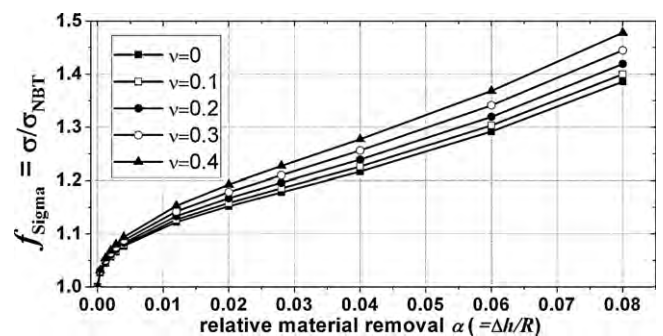


Fig. 7. Relative first principal stress f_{Sigma} at the specimen's surface opposite the notch (position 1') versus the relative removal α (main influence). Parameter is the Poisson's ratio ν .

Table 1
Overview and considered parameter intervals for the realised parametric FE study.

Dimensionless parameter name	Symbol	Lower limit	Upper limit	Number of design points
Notch length	$\lambda = L_N/D$	0.74	0.82	5
Notch width	$\omega = W_N/D$	0.10	0.15	2
Notch fillet radius	$\rho = R_N/W_N$	0.25	0.40	2
Poisson's ratio	ν	0.15	0.35	5
Grinding depth	$\alpha = \Delta h/R$	0.02	0.05	4
Crack depth	$\beta = a/R$	0.005	0.065	7
Crack aspect ratio	$\gamma = a/c$	0.4	1	7

An interactive applet of the interpolation (regarding λ , ω , ρ , ν and α) can be found in²⁷ and a fitting function is given in Appendix A. The fitting error is less than 0.25%.

In the experimental practice, to avoid a strong influence of measurement uncertainties, the grinding depth should be deep enough to be outside the parameter range, where the influence of grinding depth in stress is very pronounced. This is the case for $\alpha \geq 0.02$ (see Fig. 7), which used to be the lower limit of our parameter range. Furthermore α should be smaller than 0.05 to ensure an approximate linear course of f_{Sigma} (with respect to the variation of all other notch parameters). Both bounds fit the practical feasibility for commercial bearing ball diameters.

2.4. Numerical determination of the geometric factor Y

In Fig. 8 the stress field (σ_z) at the surface of the reference specimen, including a crack and after grinding-off, is illustrated. For all crack sizes, the amount of the elements along the crack front and their alignment around the crack tip was equal. This was performed with an all hexahedron-meshed cuboid (for mesh details see Fig. 8c).

In every case, the J -Integral method, singularity elements along the crack front and a plain strain assumption (effective Young's modulus $E^* = E/(1 - \nu^2)$) were deployed for the determination of the stress intensity, more precisely with the formulation $K = \sqrt{E^* \cdot J}$. Correlated to Eq. (2) the geometric factor along the crack front can be expressed with the related K , the crack opening stress (σ_z ; calculated in the first loading step) at position 1' and the crack depth a (Note: Y always refers to the crack depth a , see Eq. (2). This means that a not the crack width c is taken as the typical defect size).

The geometric factor Y (see Eq. (2)) was determined in a parameter study (about 20,000 FE runs). The results are used to define two interpolation functions for the geometric factor Y_A and Y_C , respectively. The parameter intervals given in Table 1 for the parametric study have been considered in equidistant steps.

All assumed intervals are realistic in terms of the practical feasibility, if the range of ball diameters is considered to be between 5 and 20 mm. The parameter intervals for the notch geometry are explained in⁶ (strength testing). The limits of the Poisson's ratio were chosen concerning typical structural ceramics (silicon carbide: 0.16 and zirconia: 0.34). The limits of the crack geometry parameter, β and γ , are mainly designated through a qualified indentation load (i.e. HK10).

To show the significance of each of the seven varied parameters for the value of the geometric factor Y , the trends are shown in Fig. 9. Only one of the seven parameters is varied in each subfigure, for the other six parameters, the values of the reference model were used. The standard crack shape is $\gamma = 0.5$ (ellipse with half axis ratio of 1/2) but for comparison also the curves for a semicircular crack ($\gamma = 1$) are also shown. In subfigure (a) the change of the geometric factor (Y_A and Y_C respectively) with the notch length is illustrated. Y_A decreases much more than Y_C with the notch length, which is reasonable: As a first approximation the ligament is loaded in pure bending. If the ligament h gets thinner (i.e. due to a deeper notch) and the crack size is constant the relative stress value at the crack tip at the surface (point C), so Y_C is not influenced. The relative stress value at the deepest point of the crack (point A) decreases for bended specimens, hence, Y_A is affected.

The notch parameters ρ and ω have almost no effect on Y (see subfigures (b) and (c)). Plot (d) shows the influence of the Poisson's ratio ν . Y_A and Y_C shift clearly with ν but in the opposite directions.

The tendency of Y_A is decreasing (see plot (e)) for an increasing amount of ground-off material (α).

The relative depth of the crack β has a stronger influence on the geometric factors Y_A and Y_C compared with the relative notch length λ , but both parameters have the same tendencies; see plot (a) and (f). Note that the influence of the analysed parameters on Y_C is weak. Plot (g) shows the course of Y in both points with respect to the crack shape (γ). For $\gamma \rightarrow 0$, Y_A tends to the analytical value of 1.12 and Y_C tends to become zero. Both facts reflect the analytical solutions for an edge through crack.²⁸ In summary, the main influences on the geometric factor Y are (i) the crack shape (γ) and size (β) and (ii) the ligament geometry (α and λ) with respect to the observed parameter intervals.

An interactive applet for the geometric factors Y_A and Y_C in a NB-specimen can be found in²⁷ and a fitting function is given in Appendix B. The fits provide an error of less than 1.5%.

Additionally, a semi-analytical approximation for the geometric factor of a semi-elliptical surface crack in the ground NB-specimen based on the Newman–Raju formula is pointed out in Appendix C.

2.5. Data evaluation

Summing it up, the fracture toughness K_C is determined by the stress value in the ground NB-specimen ($\sigma_{\text{NBT}} \times f_{\text{Sigma}}$) at fracture, the typical crack size a and the maximum of the geometric factor Y along the crack front, which is influenced by the geometry of the crack and the ligament:

$$K_C = \sigma_{\text{NBT}} f_{\text{Sigma}} Y_{\text{MAX}} \sqrt{a\pi} \quad (3)$$

For data evaluation, the established interpolation functions should always be used to avoid errors due to fitting of the FE results.

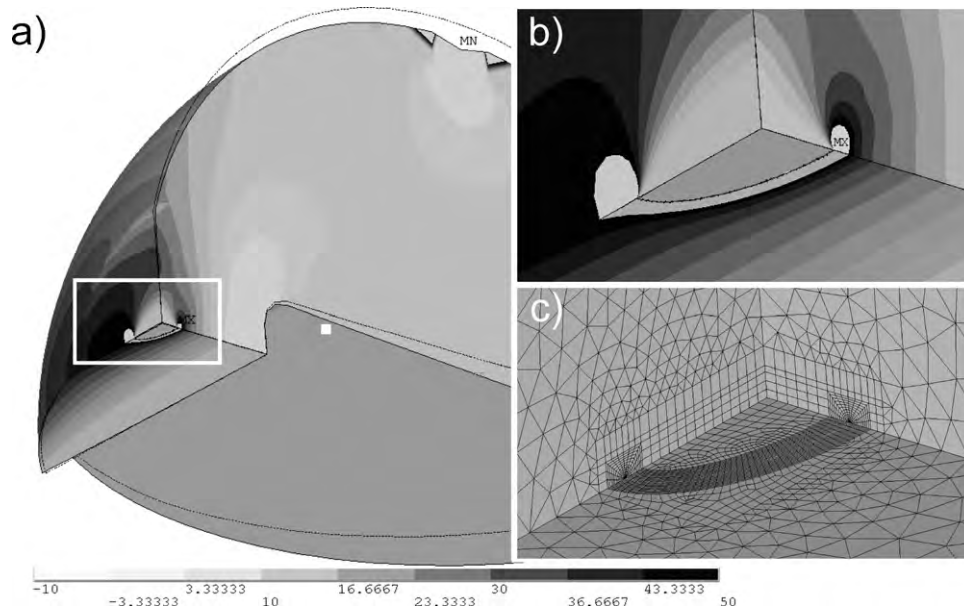


Fig. 8. Stress distribution (σ_z) of a ground-off notched ball specimen with crack: (a) overview and (b) detail of the crack. (c) FE mesh around the crack. For this calculation the reference parameters have been used.

3. Discussion

3.1. The precision of the FE model and the mesh quality

Due to the rising importance of fracture mechanics for proof of safety in structural applications, many different approaches for stress intensity factor (SIF) calculation have been developed. Next to the direct method,^{29–32} fitting the stress distribution near the crack tip, three implemented methods are available in the used FE tool ANSYS 13.0 for the linear elastic material behaviour: the “*J*-Integral”,^{29,33,34} “Virtual Crack Closure Technique” (VCCT)^{35–37} and “Crack Opening Displacement” (COD).²⁹

To estimate the principle error of these methods the resulting geometric factor Y can be compared to the analytical solution for a fully embedded circular crack in an infinite body ($Y = 2/\pi$). A quarter model of a finite block (full edge length 40 mm \times 40 mm \times 40 mm) with about 80,000 elements (all hexahedral) and with an embedded crack loaded in Mode I (crack radius $a = 1$ mm) was used. The *J*-Integral method with quarter node collapsed crack tip elements (CTE) provides the best accuracy out of all tested methods (the error is less than 0.01%). This statement can also be found in literature,²⁹ so this method was chosen for all investigation regarding the NB specimen.

Also a convergence study considering the level of mesh refinement in the NB was carried out for three resulting values: peak stress (position 1') and the SIF's K_A and K_C . The influences of local mesh refinements of the crack front and the rest of the NB specimen have been observed and compared to the reference model (see Table 1).

There is almost no effect of the crack front mesh refinement on peak stress (first principle stress at position 1'). A global refinement increases the peak stress slightly more (<0.05%).

The influence of mesh refinement on the SIF's is more delicate. The SIF value at the centre of the crack (point A) is not sensitive to crack front refinement. The value at the free surface (point C) is mesh dependent and is continuously decreasing with refinement at the crack front, which is an artifact due to *J*-value determination.²⁹

According to this situation the crack front meshing of the reference model seems to be qualified to provide accurate results within an estimated error of 0.5% (note that the principles of stress singularity near the crack tip was always presumed according to Eq. (2), details are discussed below). The mesh refinement apart from the crack front has a negligible effect ($\sim 0.05\%$) on SIF's.

3.2. Influence of the Poisson's ratio ν on the geometric factor

The dependence of the geometric factors Y on the Poisson's ratio ν for small ($\beta = 0.005$) and large ($\beta = 0.05$) cracks respectively (as determined in our FE analysis) is shown in Fig. 10. Also shown are the solution of Newman and Raju which is only carried out for $\nu \sim 0.3$. But for a precise determination of the geometric factor, the influence of the Poisson's ratio has also to be considered. (Note: own FE analysis of a rectangular beam under tension with a semi-elliptical surface crack showed that the variation of ν indicates the same tendencies as plotted in Fig. 10 for the NB-specimen.)

3.3. Deviations of the crack shape from the semi-elliptical shape

In our calculations (and also in the calculations of Newman and Raju) it is assumed that the crack is “perfectly”

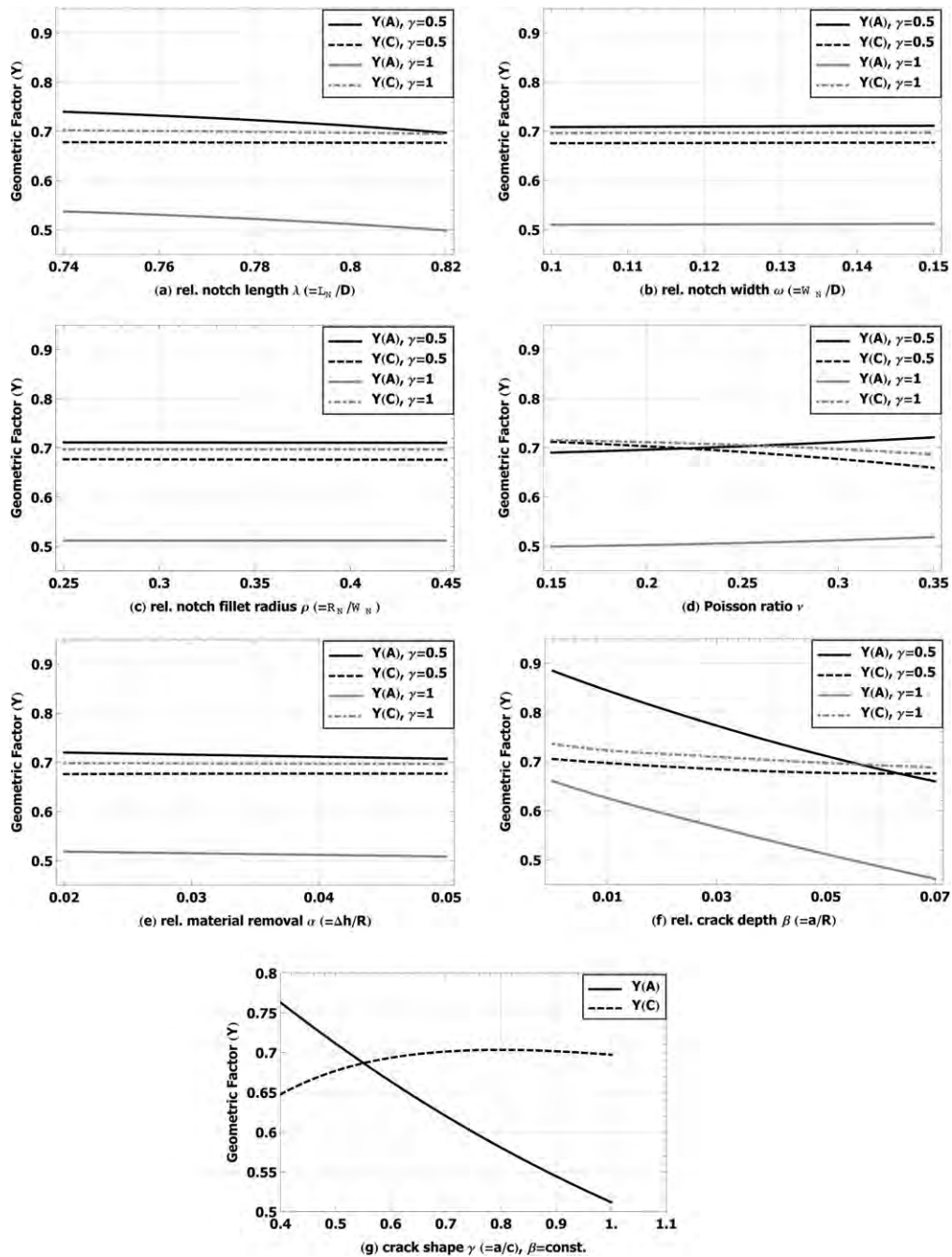


Fig. 9. Parametric study of the influence of model parameters on the geometric factor Y (in each case for point A and point C) in the dimensionless reference model. (a–c) Variation of the notch geometry (λ , ω , and ρ), (d) variation of the Poisson's ratio ν , (e) variation of the removed material α and (f–g) variation of the crack geometry β and γ .

semi-elliptically shaped. This assumption is also made in the standards for SCF toughness measurements. In reality, this is normally not the case. Even if the initial Knoop crack was perfectly semi-elliptical, grinding the surface layer of the crack will leave another contour. This case has been studied in,²⁸ where – for worst case assumption – the differences in the geometric factors are less than: $\pm 4\%$ in point A and less than $\pm 2\%$ in point C for cracks having the same aspect ratio a/c .

3.4. Stress singularity at the free surface

The maximum of the Y -values along the crack front is always located either at point A or at point C (see Fig. 3) and never between them,^{22,23,25} so just those two distinguished points have to be observed.

Generally at the free surface (at point C) the stress singularity is not proportional to $r^{-1/2}$ (with r as the distance from the crack tip) according to Fett,³⁸ Hutar^{30,32} and de Matos.³⁹

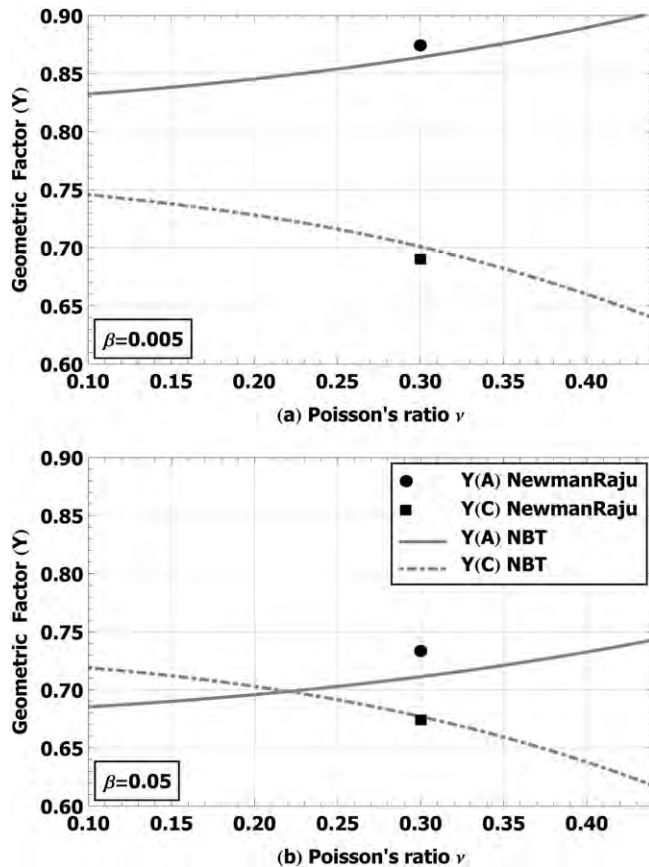


Fig. 10. Comparison of the Y -solutions of the own FE analysis (NBT) and the Newman–Raju formula plotted versus the Poisson's ratio ν for (a) small cracks ($\alpha = 0.5\%$) and (b) big cracks ($\alpha = 5\%$).

More precisely, the K -concept is therefore not valid at point C and it can only be used as an approximate approach. This effect is pronounced, if the crack intersects the surface perpendicular ($\phi \approx 90^\circ$) and the Poisson's ratio is unequal to zero (the Poisson's ratio also influences the thickness of this boundary layer).

Therefore the ASTM standard for the SCF-method¹⁶ instructs to use flat crack shapes with $Y_A > Y_C$, i.e. the maximum of Y should be positioned at point A. In practice, the easiest way to realise this is to increase the grinding depth Δh . This has several useful effects: the intersection angle ϕ gets smaller and the crack shape becomes flatter. The condition $Y_A > Y_C$ is fulfilled for flat crack shapes (the limit is at $\nu = 0.6 \div 0.8$, which depends on the crack size β).

On the other hand the ISO-standard for the SCF-method¹⁷ determines that the greater one out of both Y -value should be used for fracture toughness calculation. For this, two conditions have to be considered: (1) the crack has to be nearly semi-elliptical and (2) the datum has to be rejected, if $Y_A < Y_C$ and the fracture could be caused by preparation damage or corner pop-ins at the surface-point C.

4. Concluding remarks

The standardized SCF-method for fracture toughness measurements on ceramics is modified and applied to a new

specimen type, the notched ball. Compared to the NBT strength testing procedure, a modification of the geometry of the notched ball is necessary. Grinding-off the plastic zone produced by the Knoop indentation changes the peak stress at the ball apex. A dimensionless stress correction factor was evaluated by numerical analysis.

The geometry factor Y was calculated for a wide range of notch and crack geometries by FEA. These results are compared with the Newman–Raju formula (generalized solution used in the standard SCF-method). An interpolation function of the new results takes the Poisson's ratio into account, which is necessary for the characterisation of other structural ceramics.

If the crack aspect ratio is $a/c < 0.6$, the notched ball specimen also favours crack instability at the deepest point (point A), which is a well defined situation in fracture mechanics, therefore flat surface cracks should be aimed. With typical indentation crack sizes (that can be achieved for advanced ceramics) the new method may be applied to balls with diameters between 2 mm and 20 mm.

In the second part of the paper, which will be published soon, the experimental procedure of the new fracture toughness test are described in detail, measurement uncertainties are discussed and experimental results on silicon nitride balls are presented. The results fit well to measurement results determined using other standard testing procedures on bending test specimens.

Acknowledgements

Financial support by the Austrian Federal Government (in particular from the Bundesministerium für Verkehr, Innovation und Technologie and the Bundesministerium für Wirtschaft, Familie und Jugend) and the Styrian Provincial Government, represented by Österreichische Forschungsförderungsgesellschaft mbH and by Steirische Wirtschaftsförderungsgesellschaft mbH, within the research activities of the K2 Competence Centre on "Integrated Research in Materials, Processing and Product Engineering", operated by the Materials Center Leoben Forschung GmbH in the framework of the Austrian COMET Competence Centre Programme, is gratefully acknowledged.

Appendix A. Fit function for the maximum tensile stress in the NB specimen (at position 1') after material removal (an interactive applet with the original interpolation can be found in [27])

The results of the FEM-calculations were fitted to a polynomial. It is intended to keep the fit function simple and that the deviation of the fit function from the FE results should be less than 1%. The stress is given in relative units (normalised with the maximum tensile stress in a NB specimen without surface material removal). The relative stress significantly depends on the relative amount of material removed ($\alpha = \Delta h/R$), the relative notch length ($\lambda = 1 - h/(2R)$) and on the Poisson's ratio (ν). R is

Table A1
Coefficients for the fitting function for the stress factor (see Eq. (A.1)).

Indices	Fit coefficients (with $z_0 = 1.07844$)			
	a	b	c	d
10	-0.591634	2.37305	2.8519	2.74222
11	2.6177	4.54232	2.65985	1.65029
12	-2.06407	-19.5959	-3.41503	4.938
20	-1.39017	3.50268	-8.0687	9.59176
21	4.62443	6.77471	-9.46501	6.54502
22	-3.41374	-44.9503	11.1753	24.7514
30	3.08148	8.73812	20.9244	10.3407
31	-7.41486	17.1121	23.2816	3.63325
32	4.803	-164.037	-24.6965	18.151

the radius of the ball. The influences of the relative notch width and of the relative notch fillet radius are weak.

The general fit function for f_{Sigma} is given in Eq. (A.1) and the needed coefficients in Table A1. The fitting error is less than 0.25%.

$$\begin{aligned}
 f_{\text{Sigma}}(\lambda, \omega, \rho, \nu, \alpha) = & z_0 + \alpha(a_{10} + a_{11}\lambda + a_{12}\lambda^2) \\
 & \times (b_{10} + b_{11}\omega + b_{12}\omega^2)(c_{10} + c_{11}\rho + c_{12}\rho^2) \\
 & \times (d_{10} + d_{11}\nu + d_{12}\nu^2) + \alpha^2(a_{20} + a_{21}\lambda + a_{22}\lambda^2) \\
 & \times (b_{20} + b_{21}\omega + b_{22}\omega^2)(c_{20} + c_{21}\rho + c_{22}\rho^2) \\
 & \times (d_{20} + d_{21}\nu + d_{22}\nu^2) + \alpha^3(a_{30} + a_{31}\lambda + a_{32}\lambda^2) \\
 & \times (b_{30} + b_{31}\omega + b_{32}\omega^2)(c_{30} + c_{31}\rho + c_{32}\rho^2) \\
 & \times (d_{30} + d_{31}\nu + d_{32}\nu^2) \quad (\text{A.1})
 \end{aligned}$$

Appendix B. Fit function of the geometric factor Y in the ground NB-specimen (an interactive applet with the original interpolation can be found in [27])

The numerical values of the geometric factor Y_A and Y_C can be fitted in terms of the parameters λ , ν , α , β and γ . The influence of the notch parameters ω and ρ is negligible (consider Fig. 9); the reference values were used. The general fitting function – for Y_A and Y_C – is shown in Eq. (B.1). The needed coefficients are given in Table B1. The fitting error is less than 1.5% in point

C and less than 1% in point A.

$$\begin{aligned}
 Y(\lambda, \omega = 0.12, \rho = 0.25, \nu, \alpha, \beta, \gamma) \\
 = & z_0 + \gamma^{0.2}(a_{10} + a_{11}\lambda + a_{12}\lambda^2)(b_{10} + b_{11}\nu + b_{12}\nu^2) \\
 & \times (c_{10} + c_{11}\beta + c_{12}\beta^2)(d_{10} + d_{11}\alpha + d_{12}\alpha^2) \\
 & + \gamma(a_{20} + a_{21}\lambda + a_{22}\lambda^2)(b_{20} + b_{21}\nu + b_{22}\nu^2) \\
 & \times (c_{20} + c_{21}\beta + c_{22}\beta^2)(d_{20} + d_{21}\alpha + d_{22}\alpha^2) \\
 & + \gamma^2(a_{30} + a_{31}\lambda + a_{32}\lambda^2)(b_{30} + b_{31}\nu + b_{32}\nu^2) \\
 & \times (c_{30} + c_{31}\beta + c_{32}\beta^2)(d_{30} + d_{31}\alpha + d_{32}\alpha^2) \quad (\text{B.1})
 \end{aligned}$$

Appendix C. A semi-analytical approximation for the geometric factor of a semi-elliptical surface crack in the ground NB-specimen

More than 30 years ago Newman and Raju have derived an approximation for the geometric factor of a semi-elliptical surface crack in a bended rectangular bar. This solution is used for data evaluation in the standard SCF-method. The geometric factor of a semi-elliptical surface crack in the NB specimen having a ground surface can also be found – in a semi-analytical approximation – using the Newman and Raju solution. In the ligament of the ground NB specimen the course of the first principal stress – perpendicular to the surface – is almost linear decreasing (see Fig. C1). In other words the stress field is very similar to that of a bended rectangular bar. Therefore it is possible to define a bending bar, which has the same slope of the stress field as the ground NB specimen. The thickness of the bar is h_{eq} and, for simplicity, the half width b is defined to be $b = h_{\text{eq}}$ (see Fig. C1).

The equivalent beam thickness h_{eq} depends on the ligament geometry (mainly on α and λ) and the crack depth a . The stress distribution is nearly linear in the relevant region, i.e. over typical ranges of the crack depth a (for $0 \leq a \leq 0.25h'$).

A fitting function of the equivalent thickness h_{eq} – based at our FE results – is given in Eq. (C.1)–(C.3).

The relations have been derived by computing the stresses in the ligament of the actual (ground) notched ball specimen in

Table B1
Coefficients for the fitting function for the geometric factor (see Eq. (B.1)).

Indices	Point A (with $z_0 = 1.259$)				Point C (with $z_0 = -1.46387$)			
	a	b	c	d	a	b	c	d
10	-1.16634	0.84972	0.482606	1.23491	1.30137	1.3381	0.785785	2.27784
11	0.0191434	1.97075	28.3316	-3.02365	-0.0735881	0.315134	-0.0836458	-0.0569606
12	0.208143	-7.32415	-113.135	2.21254	-0.364722	-3.18661	1.64754	0.0292848
20	0.128234	1.33431	1.77848	1.18249	0.632871	0.983236	-0.247442	5.72478
21	-0.0209168	-1.41052	-11.5363	-10.7237	-0.259051	1.25891	-0.511638	2.34767
22	-0.153399	8.01953	64.7578	7.67749	-0.161234	-12.3825	1.13783	-1.71875
30	0.355241	3.16874	-1.3068	0.0796565	3.05859	-0.0162337	-1.20701	-1.53108
31	-0.217446	-2.99067	5.18989	-0.66641	-3.10434	-0.0538943	-14.9341	11.5755
32	-0.94953	17.7899	-29.3815	0.454138	2.0719	0.577001	84.2279	-8.59851

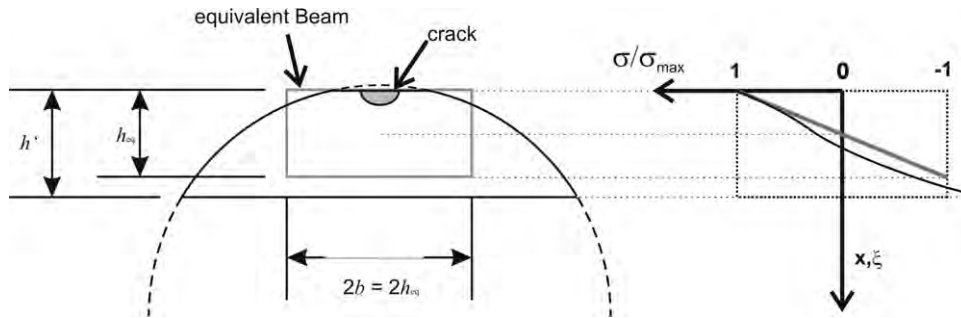


Fig. C1. The stress field in a bended beam of thickness h_{eq} and of width $2h_{eq}$ is almost equal to that of the stress field in a ground NB specimen (at least at the surface, where high stresses occur).

crack depth direction x (or $\xi = x/h'$) for several ball-notch configurations. For further information see.^{18,40}

$$h_{eq} = f_h h' \quad (C.1)$$

with

$$f_h = \frac{-2a/h'}{\sigma_{z,Lig}(\xi = a/h') - 1} \quad (C.2)$$

and

$$\sigma_{z,Lig} = 1 + (m_0\lambda + m_1\lambda^2)n_0\xi + (m_2\lambda + m_3\lambda^2)n_1\xi^2 \quad (C.3a)$$

with

$$\begin{aligned} m_0 &= -2.54721 & m_1 &= 2.17406 & m_2 &= 5.63419 & m_3 &= -6.07159 \\ n_0 &= 3.93603 & n_1 &= 3.00221 \end{aligned} \quad (C.3b)$$

Due to the modification discussed above and the approximations of the Newman and Raju, the determination of the geometric factor of a semi-elliptical crack in a ground NB specimen has an unknown uncertainty. Newman and Raju claim that their fitting function provided has a maximum error of $\pm 5\%$ according to their FE results.²⁵ In addition, they specified their FE accuracy with $\pm 3\%$ compared to the analytical solution in terms of a completely embedded circular crack.^{24,26} All their calculations have been made for a Poisson's ratio of $\nu = 0.3$. A direct comparison of the Newman and Raju formula and with own FE analysis for a semi-elliptical surface crack in a rectangular beam under pure tension showed an error of less than $\pm 3\%$ for $\nu = 0.3$.

For the NB model, a comparison of the Y-courses of our (very accurate) NBT-FE analysis with the approximations based on the Newman and Raju formula is shown in Fig. C2 (Note: all of our FEM values outside of $0.4 \leq \gamma \leq 1$ are extrapolated). For relative small crack sizes ($\beta = 0.005$, see Fig. C2a) both solutions agree surprisingly well; the maximum deviation is less than $\pm 1.2\%$. For bigger cracks ($\beta = 0.05$, see Fig. C2b) the maximum error for Y_A rises up to 2.9%, but for Y_C the difference between both solutions is still less than 1% for all analysed crack sizes. Generally, the agreement of the FE-results with the approximations based on the Newman and Raju formula and their tendencies is good but the agreement decreases with bigger relative crack sizes.

In general the semi-analytical calculations of Newman and Raju give the same trend with the crack shape as our FE calculations but they are only valid for $\nu = 0.3$. Our FE-solution can be used in the range of Poisson's ratio of interest (see Table 1).

References

- Kötttritsch H. *Science report: development centre steyr*. Steyr: SKF Österreich AG; 2007.
- Wang L, Snidle RW, Gu L. Rolling contact silicon nitride bearing technology: a review of recent research. *Wear* 2000;**246**:159–73.
- Supancic P, Danzer R, Harrer W, Wang Z, Witschnig S, Schöppel O. Strength tests on silicon nitride balls. *Key Engineering Materials* 2009;**409**:193–200.
- Supancic P, Danzer R, Wang Z, Witschnig S, Schöppel O. The Notched Ball Test – a new strength test for ceramic spheres. In: *9th international*

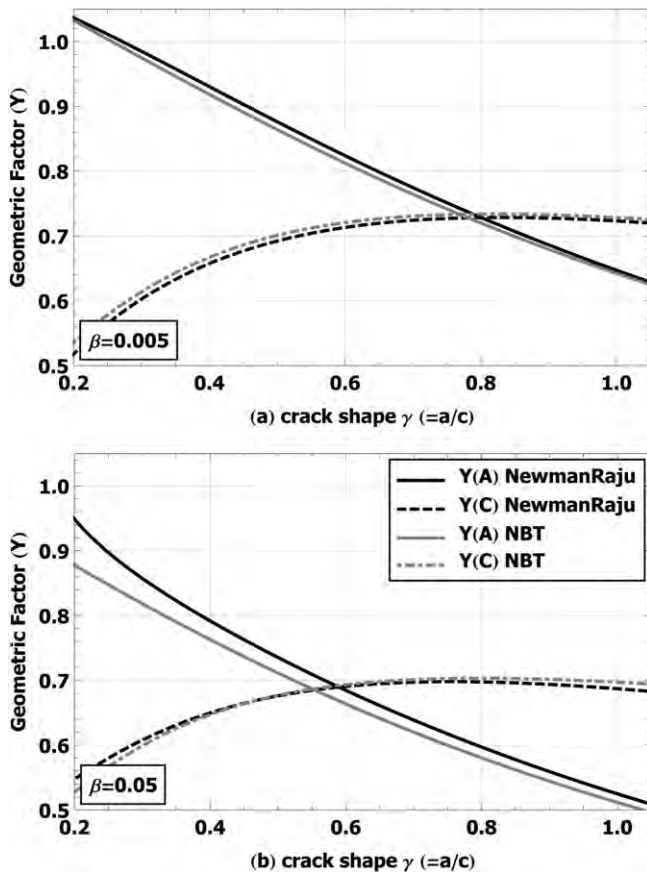


Fig. C2. Comparison of the geometric factors determined by FE-calculations and by a semi-analytical approach based on the Newman–Raju formula, plotted are values of the factor versus the crack shape γ for (a) small cracks ($\beta = 0.5\%$) and (b) big cracks ($\beta = 5\%$).

- symposium on ceramic materials and components for energy and environmental applications. Shanghai: The American Ceramic Society; 2009. p. 67–75.
5. Supancic P, Danzer R, Witschnig S, Polaczek E. The strength of ceramic balls – the Notched Ball Test. In: *18th European conference on fracture*. 2010.
 6. Supancic P, Danzer R, Witschnig S, Polaczek E, Morrell R. A new test to determine the tensile strength of brittle balls – the Notched Ball Test. *Journal of the European Ceramic Society* 2009;**29**:2447–59.
 7. Wereszczak AA, Kirkland TP, Jadaon OM. Strength measurement of ceramic spheres using a diametrically compressed “C-Sphere” specimen. *Journal of the American Ceramic Society* 2007;**90**:1843–9.
 8. ASTM 2094-08. *Standard specification for silicon nitride bearing Balls*. American Society for Testing and Materials; 2008.
 9. Lube T. Indentation crack profiles in silicon nitride. *Journal of the European Ceramic Society* 2001;**21**:211–8.
 10. Miyazaki H, Hyuga H, Yishizawa Y-I, Hiraio K, Ohji T. Relationship between fracture toughness determined by surface crack in flexure and fracture resistance measured by indentation fracture for silicon nitride ceramics with various microstructures. *Ceramics International* 2009;**35**:493–501.
 11. Niihara K, Morena R, Hasselman DPH. Further reply to “comments on elastic/plastic indentation damage in ceramics: the median/radial crack system”. *Journal of the American Ceramic Society* 1982;**65**:C-116.
 12. Anstis GR, Chantikul P, Lawn BR, Marshall DB. A critical evaluation of indentation techniques for measuring fracture toughness. I. Direct crack measurements. *Journal of the American Ceramic Society* 1981;**64**:533–8.
 13. CEN EN 14425-5. *Fine ceramics (advanced ceramics, advanced technical ceramics) – determination of fracture toughness of monolithic ceramics at room temperature by the single-edge vee-notched beam (SEVNB) method*; 2005.
 14. Damani R, Gstrein R, Danzer R. Critical notch root radius in SENB-S fracture toughness testing. *Journal of the European Ceramic Society* 1996;**16**:695–702.
 15. Damani R, Schuster C, Danzer R. Polished notch modification of SENB-S fracture toughness testing. *Journal of the European Ceramic Society* 1997;**17**:1685–9.
 16. ASTM C 1421-01b. *Standard test methods for determination of fracture toughness of advanced ceramics at ambient temperature*. American Society for Testing and Materials; 2001.
 17. ISO 18756. *Fine ceramics (advanced ceramics, advanced technical ceramics) – determination of fracture toughness of monolithic ceramics at room temperature by the Surface Crack in Flexure (SCF) method*; 2003.
 18. Witschnig S. *Zähigkeitsmessung an keramischen Kugeln*. Institut für Struktur- und Funktionskeramik. Diploma Thesis. Leoben: Montanuniversität Leoben; 2010.
 19. Munz D, Fett T. *Ceramics – mechanical properties, failure behaviour, materials selection*. Berlin: Springer; 2001.
 20. Lawn BR. *Fracture of brittle solids*. second ed. Cambridge: Cambridge University Press; 1993.
 21. Murakami Y. *Stress intensity factors handbook*. Oxford: Pergamon Press; 1987–2001.
 22. Quinn GD, Gettings RJ, Kübler J. Fracture toughness by the surface crack in flexure (SCF) method: results of the VAMAS round robin. *Ceramic Engineering and Science Proceedings* 1994;**15**:846–55.
 23. Quinn GD, Kübler J, Gettings RJ. Fracture toughness of advanced ceramics by the surface crack in flexure (SCF) method: a VAMAS round robin. VAMAS Report No. 17. Report 1994.
 24. Newman JC, Raju IS. Analysis of surface cracks in finite plates under tension or bending loads NASA. Report TP-1578; 1979.
 25. Newman JC, Raju IS. An empirical stress-intensity factor equation for the surface crack. *Engineering Fracture Mechanics* 1981;**15**:185–92.
 26. Raju IS, Newman JC. Improved stress-intensity factors for semi-elliptical surface cracks in finite-thickness plates NASA. Report TM-X-72825; 1977.
 27. <http://www.isfk.at>.
 28. Fett T, Munz D. *Stress intensity factors and weight functions*. Southampton UK and Boston USA: Computational Mechanics Publications; 1997.
 29. Anderson TL. *Fracture mechanics – fundamentals and applications*. Boca Raton, FL: CRC Press; 2005.
 30. Hutar P, Náhlík L, Knésl Z. Quantification of the influence of vertex singularities on fatigue crack behavior. *Computational Materials Science* 2009;**45**:653–7.
 31. Hutar P, Náhlík L, Knésl Z. The effect of a free surface on fatigue crack behaviour. *International Journal of Fatigue* 2010;**32**:1265–9.
 32. Hutar P, Sevcík M, Náhlík L, Zouhar M, Seitl S, Knésl Z, et al. Fracture mechanics of the three-dimensional crack front: vertex singularity versus out of plain constraint descriptions. *Procedia Engineering* 2010;**2**:2095–102.
 33. Banks-Sills L. Application of the finite element method to linear elastic fracture mechanics. *Applied Mechanics Reviews* 1991;**44**:447–61.
 34. Courtin S, Gardin C, Bézine G, Ben Hadj Hamouda H. Advantages of the J-integral approach for calculating stress intensity factors when using the commercial finite element software ABAQUS. *Engineering Fracture Mechanics* 2005;**72**:2174–85.
 35. Krueger R. Virtual crack closure technique: history, approach, and applications. *Applied Mechanics Reviews* 2004;**57**:109–43.
 36. Leski A. Implementation of the virtual crack closure technique in engineering FE calculations. *Finite Elements in Analysis and Design* 2007;**43**:261–8.
 37. Okada H, Kawai H, Araki K. A virtual crack closure-integral method (VCCM) to compute the energy release rates and stress intensity factors based on quadratic tetrahedral finite elements. *Engineering Fracture Mechanics* 2008;**75**:4466–85.
 38. Fett T. *Stress intensity factors – T-stresses – weight functions*. Supplement volume (IKM 55). Karlsruhe: KIT Scientific Publishing; 2009.
 39. de Matos PFP, Nowell D. The influence of the Poisson’s ratio and corner point singularities in three-dimensional plasticity-induced fatigue crack closure: a numerical study. *International Journal of Fatigue* 2008;**30**:1930–43.
 40. Lube T, Witschnig S, Supancic P. Fracture toughness of ceramic balls. In: *18th European conference on fracture*. 2010.

Paper J

S. Strobl, T. Lube, O. Schöpl: "Toughness measurement on ball specimens. Part II: Experimental procedure and measurement uncertainties", *Journal of the European Ceramic Society* **34** (2014), 1881-1892, <http://dx.doi.org/10.1016/j.jeurceramsoc.2013.12.052>

Re-used as author according to Elsevier's copyright agreement.



Toughness measurement on ball specimens. Part II: Experimental procedure and measurement uncertainties

Stefan Strobl^{a,b,*}, Tanja Lube^b, Oskar Schöppl^c

^a Materials Center Leoben Forschung GmbH, Roseggerstraße 12, 8700 Leoben, Austria¹

^b Institut für Struktur- und Funktionskeramik, Montanuniversität Leoben, Peter-Tunner-Straße 5, 8700 Leoben, Austria²

^c Research & Development Office, SKF Österreich AG, Seitenstettner Straße 15, 4401 Steyr, Austria³

Received 30 October 2013; received in revised form 3 December 2013; accepted 13 December 2013

Available online 25 January 2014

Abstract

The “Surface Crack in Flexure” method is widely used for fracture toughness (K_{Ic}) determination of ceramics. In part I of the paper we developed the theoretical fundamentals to apply this procedure to ceramic balls by using the stress application as developed for the so-called “Notched ball test”. The new test (SCF-NB) can be used to test spherical components without the need to cut out special specimens such as bending bars. In this work the practical part is presented including suggestions for crack introduction and specimen preparation and possible measurement errors are discussed. It is concluded that a measurement error less than $\pm 5\%$ is possible.

Experiments on balls and bars made from the same silicon nitride ceramic indicate that SCF-NB delivers the same K_{Ic} -values as standardised measurements on bars. Additionally, K_{Ic} -values obtained for silicon carbide, alumina and zirconia ceramics are presented. They coincide with K_{Ic} -data from the literature.

© 2014 Elsevier Ltd. All rights reserved.

Keywords: Rolling elements; Notched ball test; Fracture toughness; Hybrid bearings; Silicon nitride

1. Introduction

For most of all established methods for fracture toughness determination, the specimen geometry is standardised. Prismatic flexural beams with a cross section of 3 mm × 4 mm and >40 mm in length are used in the Single Edge V-Notch Beam (SEVNB),¹ the Chevron Notch (CN)² or the Surface Crack in Flexure (SCF)³ method.

The task in the present work is to measure the toughness of balls without cutting special specimens out of the balls. For that we follow the basic ideas of the SCF method,³ where a well-defined crack is made by an indent (Knoop) into surface of a

prismatic beam. Then the beam is loaded in flexure until failure occurs. From the crack geometry and the failure stress the critical stress intensity factor (fracture toughness) can be determined. One of the most important advantages of SCF method is that the start defect is a real crack and not a relatively sharp notch, which is required for the validity of linear elastic fracture mechanics (LEFM).⁴ A difficulty of the SCF method is that the indentation causes a plastically deformed zone, which provokes internal stresses. This can adulterate the testing results. Therefore the plastically deformed material has to be removed – e.g. by grinding – in order to avoid a preloading of the crack tip by residual stresses and to receive a fully closed and unloaded crack in order to follow the assumptions made for the evaluation of the experiments. Standards recommend to grind-off a layer having the thickness of 1/6 of the long indentation diagonal. An alternative suggestion for the grinding depth is given in,⁵ which additionally ensures that the critical point (where the stress intensity factor becomes a maximum) is not at the surface but at the deepest point of the crack where the determination of the stress intensity factor is more precise. Therefore this situation (critical point at the deepest position) is preferred. This grinding depth is approximately 1/3 of the long indentation diagonal

DOI of original article: <http://dx.doi.org/10.1016/j.jeurceramsoc.2011.12.003>.

* Corresponding author at: Institut für Struktur- und Funktionskeramik, Montanuniversität Leoben, Peter-Tunner-Straße 5, 8700 Leoben, Austria.
Tel.: +43 3842 402 4113; fax: +43 3842 402 4102.

E-mail addresses: stefan.strobl@mcl.at, stefan.strobl85@gmail.com (S. Strobl).

¹ mclburo@mcl.at, <http://www.mcl.at>.

² isfk@unileoben.ac.at, <http://www.isfk.at>.

³ oskar.schoeppl@skf.com, <http://www.skf.at>.

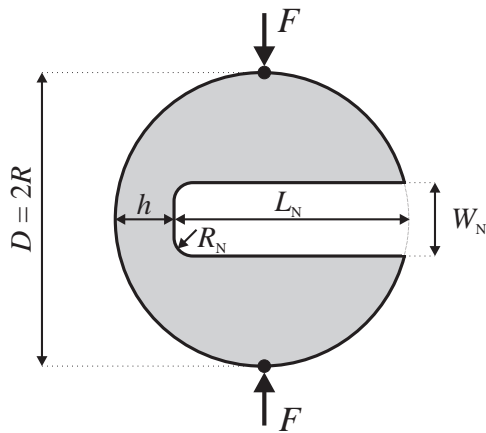


Fig. 1. Specimen in the notched ball test. The notch is defined by the length L_N , the width W_N and the fillet radius R_N of the notch. In the equatorial plane remains a ligament having the shape of a segment of a circle with the thickness $h = D - L_N$.

(more precisely it depends on the crack length before grinding and other additional parameters, see in Ref. 5).

The measurement of the crack shape is not straight forward since the crack's visibility may dependent on the material itself. The measured quantities are influenced by the operator⁶ as well as by the available devices (such as optical microscopy or SEM).⁷ The SCF standard³ contains some advices to facilitate the crack size measurement on the fracture surface. From them only fluorescent penetration dye (FPD) was used in this work. There are further methods to enhance the visibility of the crack and its detection, such as tilted indentation,³ non-fluorescent penetration dyes⁸ or decoration with lead acetate^{9,10} which are not discussed in the framework of this paper.

In the literature on the SCF testing, the geometric factor defined by Newman and Raju in the late seventies of the last century is used.^{11,12} In these papers an FE-analysis of the stress field is made. But in that time, the computers were relatively slow and a coarse FE mesh had to be used to keep the calculation time manageable. In a recent paper it has been shown, that – in extreme cases – this can cause errors up to 40% of the determined value⁵ (remark: the formula in the SCF-standard based on the work of Newman and Raju^{11,12} is fixed to a Poisson's ratio of 0.3 and a perfect semi-ellipse). Therefore a more precise solution for the geometric factor of the surface crack has been proposed, which is used for the data evaluation in this paper (see part I¹³).

In the new test a crack is introduced into the surface of a ball with an indenter. Then the plastically deformed material is ground-off and traction forces are applied to the crack using the principles of the notched ball test (NBT).^{14–18} In the NBT a notch is cut in the equatorial plane of the ball and afterwards the notch is squeezed together by introducing point loads at the poles perpendicular to the notch (see Fig. 1). This produces a very well defined stress field (note: the NBT has been standardised recently¹⁴). Tensile stresses occur at the surface opposite the notch root. This stress field (maximum tensile stress σ_{NBT}) is almost uniaxial, simple to calculate and almost insensitive regarding

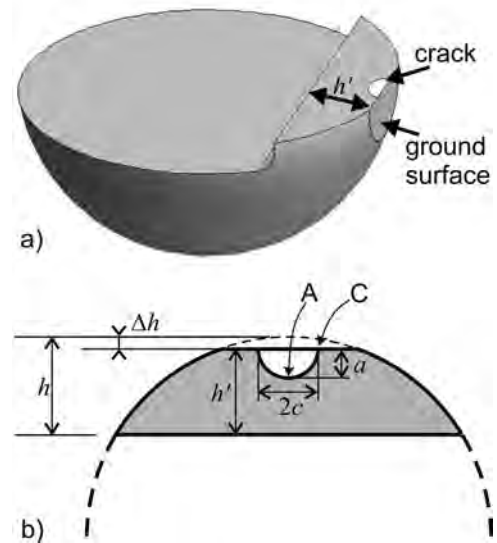


Fig. 2. Geometric situation in the fracture toughness test for balls. Shown is a half model of a notched ball with a semi-elliptical crack (white). The plastically deformed material is still removed (e.g. by grinding). The remaining ligament thickness is $h' = h - \Delta h$. Also shown are the positions A and C, where the crack may start growing.

measurement uncertainties caused by small geometry deviation and the testing setup. Furthermore, the specimen preparation is highly flexible. The needed parameters to describe the geometry of the notched ball specimen are illustrated in Fig. 1. All together, these are good preconditions for toughness testing. For the SCF test applied to balls we use the notation SCF-NB.

The theoretical background and the equations necessary to evaluate the experiments in this work are described in detail in the first part of this paper,¹³ but are shortly summarised in the following: for the creation of the start defect a Knoop hardness impression is used in analogy to the standardised SCF method to introduce an approximately semi-elliptical crack into the specimen surface, where the maximum tensile stress occurs (i.e. apex of the notched ball specimen).

The removal of residual stresses by grinding-off the deformed material applied to the notched ball specimen causes a change in the specimen geometry and thus an altered stress field at the position of the crack (see Fig. 2). This has to be taken into account in the data evaluation: the maximum tensile stress in the NBT, σ_{NBT} , has to be multiplied with a correction factor, f_{Sigma} , to get the stress in the specimen after removing the plastic deformed zone: $\sigma \rightarrow f_{\text{Sigma}} \cdot \sigma_{\text{NBT}}$.

The fracture toughness, K_{Ic} , is determined by the fracture stress, $f_{\text{Sigma}} \cdot \sigma_{\text{NBT}}$, the typical crack size, a , and the geometric factor, Y . The maximum of the geometric factor Y_{MAX} along the crack front is used for K_{Ic} calculation. Note that the value and position of the maximum depends on the geometry of the notch and of the crack and can either be at the deepest point of the crack (position A, see Fig. 2) or at the intersection of the crack with the surface (position C, see Fig. 2).

$$K_{Ic} = \sigma Y \sqrt{a\pi} = (\sigma_{\text{NBT}} f_{\text{Sigma}}) Y_{\text{MAX}} \sqrt{a\pi} \quad (1)$$

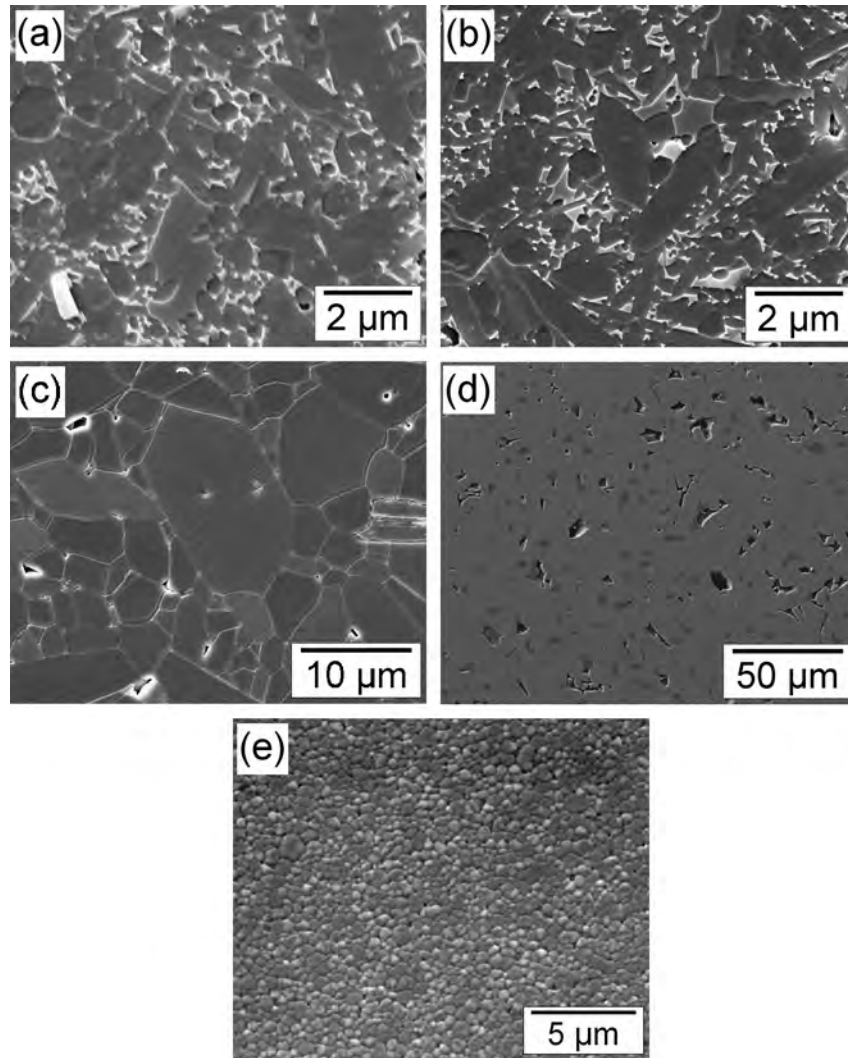


Fig. 3. SEM micrographs of all investigated materials: (a) SNRef – silicon nitride, (b) SN – silicon nitride, (c) AO – alumina, (d) SC – silicon carbide and (e) ZO – zirconia.

The geometry of the notch (see Fig. 1) is defined via the notch width W_N , the notch root radius R_N and notch length L_N . The ligament thickness h is obtained by the ball diameter D minus the notch length: $h = D - L_N$. The resulting parameters f_{Sigma} and Y were already investigated in detail in part I of this paper¹³ – for a better usability they were approximated by a fitting function. The remaining parameter in Eq. (1) is the crack depth a . Generally, the crack depth a and the crack shape a/c (see Fig. 2) are measured after the test on the fracture surfaces as proposed for the SCF method. The insertion of the crack as well as its measurement is the key topic of this part of the paper. The effect of measurement errors of the most important quantities such as crack dimensions on the resulting K_{Ic} -values will also be discussed.

To demonstrate the applicability of the method, tests were performed on balls with a diameter of about 5 mm on four different structural ceramic materials. The results were compared with test results gained with other testing methods and with literature data.

2. Materials of study

First, the new method was verified by applying it to a state of the art commercial silicon nitride ceramic (HIPed, overall ~10 wt% content of Al_2O_3 and Y_2O_3 additives). From this reference material (further called as SNRef) balls with a nominal diameter of 5 mm and standard bending bars were available. Fracture toughness was measured by the SEVNB method,¹ by the SCF method³ and with the SCF-NB. For both SCF methods (on bars and balls) Knoop indentation loads of 7 kg and 10 kg were used. A micrograph of SNRef can be found in Fig. 3a.

Polished balls made of four other structural ceramics were supplied by the company SKF, Austria, for a feasibility study. The balls had a diameter of ~5.55 mm and were polished to a mean surface roughness of approximately 10–15 nm, which is desired for adequate rolling contact performance. The materials are: HIPed silicon nitride with overall ~6 wt% Al_2O_3 and Y_2O_3 additives (SN), 99.7% alumina with MgO– SiO_2 additives (AO), sintered silicon carbide with B and C additives (SC) and

Table 1
Properties of the investigated ball materials.

Short name	SNRef	SN	AO	SC	ZO
Material	Silicon nitride	Silicon nitride	Alumina	Silicon carbide	Zirconia
Ball diameter [mm]	4.999 ± 0.001	5.550 ± 0.001	5.555 ± 0.001	5.554 ± 0.001	5.555 ± 0.001
Hardness (HV5)	1585 ± 29	1627 ± 44	1611 ± 66	2274 ± 128	1283 ± 13
Young's modulus [GPa]	306 ± 4	306.4 ± 0.1	386.6 ± 0.1	389.9 ± 0.1	217.5 ± 0.1
Poisson's ratio	0.268 ± 0.005	0.269 ± 0.001	0.234 ± 0.001	0.160 ± 0.001	0.332 ± 0.001

Table 2
Characteristic dimensions of notched balls specimen for fracture toughness tests. The data are mean values of sets of 5–6 specimens.

	SNRef	SN	AO	SC	ZO
Notch root radius R_N [μm]	155	234	285	256	250
Notch width W_N [μm]	628	609	691	641	628
Notch length L_N [μm]	3910 ± 2	4234 ± 2	4206 ± 4	4214 ± 8	4250 ± 3
z-Offset [μm]	15 ± 7	14 ± 2	2 ± 1	5 ± 4	24 ± 2

Y-TZP zirconia (ZO). Micrographs of these materials are shown in Fig. 3b–e.

The mean values and standard deviations of ball diameters, hardness and the elastic properties are given in Table 1. Note that the Poisson's ratio, ν , is important for an exact data evaluation (since the stress state in the SCF-NB is slightly biaxial). It influences σ_{NBT} , f_{Sigma} and Y , which enter into the calculation of K_{Ic} in Eq. (1). Furthermore, for certain crack shapes, the Poisson's ratio affects the position along the crack front, where the geometric factor Y becomes a maximum ($Y \rightarrow Y_{\text{MAX}}$). This topic is discussed in detail in Ref. 5.

The elastic constants (e.g. Young's modulus E , Poisson's ratio ν) were measured by resonant ultrasonic spectroscopy (RUS).^{19–21} Balls in the as-polished condition (= as received) were probed. Because of the almost perfect ball geometry (i.e. the balls are manufactured within very narrow tolerances),

the measurement error in the elastic constants was very small (<0.5%).

3. Sample preparation

3.1. Silicon nitride, alumina and silicon carbide

For the conventional SCF method, standard bending beams (3 mm × 4 mm × 50 mm) were diamond ground from larger plates. For SEVNB tests notches were manufactured into the 4 mm × 50 mm sides of the beam according to Ref. 1.

For the notch preparation of the NBT specimens one batch of balls (up to 30 specimens) was glued in a special guide rail and the notch with the desired depth was cut through all specimens with a diamond cutting wheel. This approach guarantees that the relevant surface area will not be damaged or pre-stressed

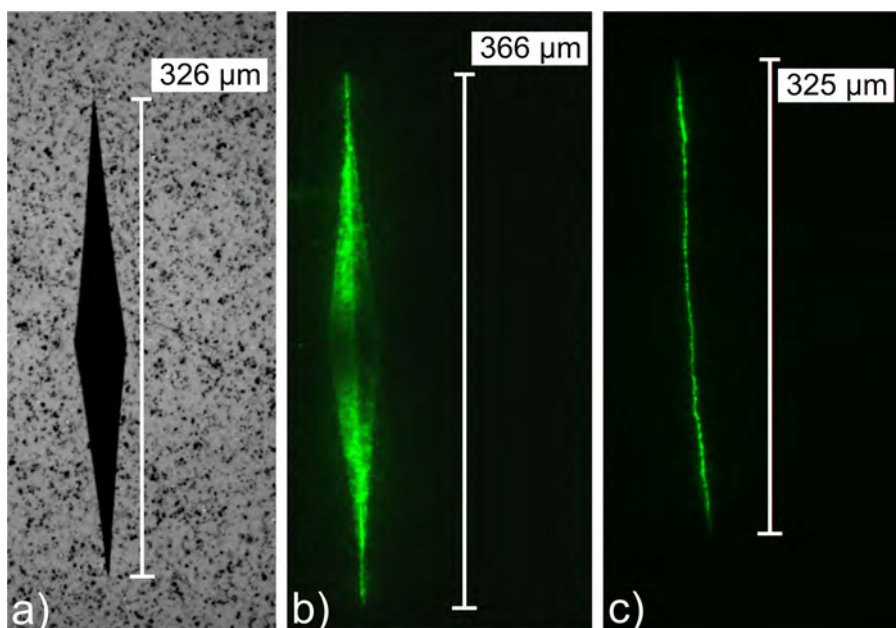


Fig. 4. HK15 Knoop indent in SNRef. (a) before grinding, (b) before grinding with fluorescent penetration dye (FPD) and under UV-light and (c) after grinding-off of the plastically deformed zone with FPD and under UV-light.

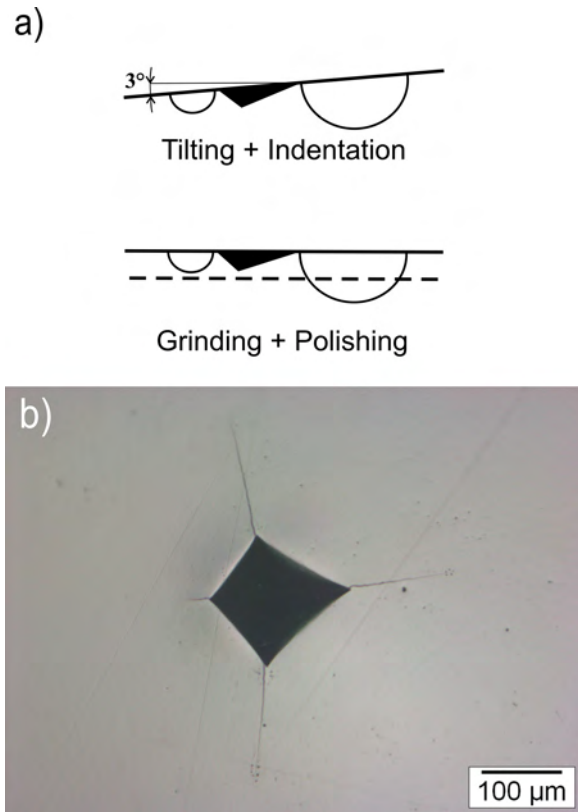


Fig. 5. Preparation method according to Ref. 22 for introduction of a surface crack in zirconia. (a) Schematic procedure and (b) example for ZO (HV20).

due to sample preparation and all samples have approximately the same notch depth.

All relevant specimen dimensions (see Table 2) including the deviation of the mid-cut plane versus the equatorial plane (i.e. z -offset) were measured according to the NBT standard¹⁴ and satisfied the requirements. One exception was the notch length with 75–78% of the ball diameter. The stresses for these specimens could be evaluated using the formulas in Ref. 18 (the NBT standard is designed for a notch length of $80 \pm 1\%$).

After the machining of the notch a crack was produced using a Knoop indenter. For this purpose the notched ball was glued on a chamfered blade which is marginally thinner than the notch. This assembly guarantees that the plane of the semi-elliptical crack is parallel to the notch mid-plane and permits an easy and reproducible Knoop indentation. Furthermore, the successful infiltration with FPD, the indentation size measurement and the grinding-off of the plastically deformed material is simplified.

In indentation pre-studies, which will not be discussed in detail in this work, the ideal indentation load (between 0.5 kg and 30 kg) for each material regarding crack formation and crack visibility was deduced. For all indentations the same hardness tester (Zwick 3212B) and a tilt angle of 3° was used. An example for an indentation load of 15 kg in silicon nitride is given in Fig. 4. Remark that the radius of the ball surface may significantly influence the resulting indentation size, as well as the resulting cracks next to the indent.

According to Refs. 3, 7 the long diagonal d of the Knoop indent (see Fig. 4a) should be used to calculate the necessary

depth of material removal $\Delta h = d/6$. In Fig. 4b, a photograph of the same indent under UV-light is illustrated, where the crack length $2c_0$ before grinding is easy to determine using the FPD (cf. Fig. 4a). This initial crack length was used for the calculation of Δh (according to Ref. 5), which in addition ensures that the critical point is not at the surface (point C, see Fig. 2) but at the deepest point of the crack (point A, see Fig. 2).

After grinding (see Fig. 4c) the crack remains clearly visible with FPD, and this crack length $2c$ can be used for verification of the crack shape, which is needed as input for the determination of the geometric factor.

The grinding process can be controlled very precisely by comparison of the levels of blade edge and the ball apex (highest point of the ball, if the notch is aligned downwards). Δh for data evaluation is obtained by the difference of ligament thickness h before grinding and of ligament thickness h' after grinding, i.e. $\Delta h = h - h'$.

In part I of this paper,¹³ the numerical calculations were performed for a crack depth a in the range of 0.5–6.5% of the ball radius and the grinding depth is restricted to 2% up to 5% of the ball radius. If no past experience exists, the indenter load that produces suitable cracks has to be determined, for each material in pre-studies. The same material dependent problems occur with the standard SCF method in bending bars. For the present investigation, a good trade-off was HK10, which was used for the silicon nitrides, alumina and silicon carbide ceramics.

3.2. Zirconia

In the case of zirconia it was not possible to create penny-shaped cracks with a Knoop indenter, even with indentation loads up to 500 N. For this reason, a special procedure was applied according to the suggestions in the VAMAS report⁷ for the SCF method and the work of Torres et al.²² With a Vickers indenter a hardness indent with a tilt angle of about 3° was produced in the apex of the notched ball specimen. One crack at the indentation corner was so small, that it was completely removed by the subsequent grinding procedure (see Fig. 5a). In pre-studies the indentation load of 196 N (HV20) showed the best result. A typical appearance of such a tilted Vickers indentation can be found in Fig. 5b. The left crack is significantly smaller than all others. As a minimum for the material removal Δh the half of the Vickers indent diagonal was chosen.

4. Testing procedure

4.1. General aspects

The testing procedure is similar to the procedure used for the conventional NBT for strength testing.^{14,18} A universal testing machine (Zwick GmbH & Co. KG, Ulm, Germany) with two parallel anvils made of silicon nitride plates was used. The tests were performed using displacement control so that fracture occurs within 5–10 s. The maximum load (i.e. at fracture) was used to determine the fracture stress σ_{NBT} .^{14,18}

After testing, the shape of the pre-crack was investigated at the fracture surfaces. The determination of the crack geometry

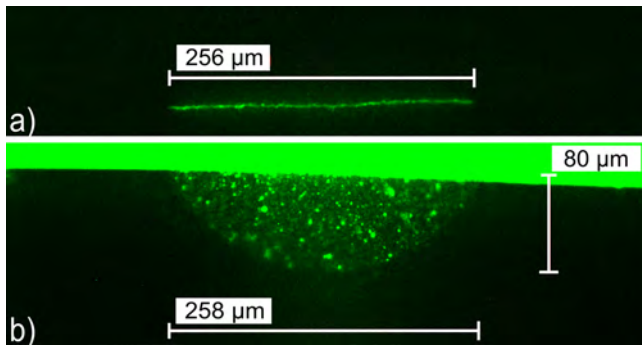


Fig. 6. Crack shape determination in SNRef (HK7) with FPD and UV light. (a) Full crack width $2c$ measured at the original surface (before fracture) and (b) crack depth a and full crack width $2c$ measured at the fracture surface.

at the fracture surface can be performed using a conventional stereo microscope with or without FPD. In the majority of cases the geometry of the crack (a and c) is easily to determine by fractographic analysis (and the use of FPD).^{3,7} In the present work all specimens were infiltrated with FPD (WB200, RIL-Chemie) before grinding to decorate the pre-crack. We suggest to measure the crack shape directly after testing, otherwise the dye may spread further onto the rest of the fracture surface and the pre-crack dimensions are overestimated.

4.2. Silicon nitride, alumina and silicon carbide

The ideal case is illustrated in Fig. 6 for SNRef. By comparison of the $2c$ measured at the ground surface before testing (Fig. 6a) with the $2c$ measured at the fracture surface (Fig. 6b), one can estimate the reliability of the crack shape determination. Generally the FPD method works quite well for silicon nitride, silicon carbide and alumina. Swab and Quinn²³ reported so-called “precrack halos” and possibly an influence of slow crack growth in alumina, but no halos were observed at all in our studies.

4.3. Zirconia

As mentioned in a previous section in zirconia the pre-crack was created via a tilted Vickers indent. Ideally three cracks remained in the sample after material removal – an example is illustrated in Fig. 7a. The direction of the stress in the NBT (indicated with arrows) was nearly perpendicular regarding the horizontally aligned crack. After testing this crack was clearly visible at the fracture surface (see Fig. 7b): it has a kidney shape. For data evaluation it was approximated as a semi-elliptical crack.

4.4. Indentation fracture resistance

The significance of indentation fracture resistance^{6,8,22,24–32} (IFR) test results is still somewhat unclear and therefore controversially discussed. But the method is often used – especially in industry – to get a rough estimate of the fracture toughness. Thereby a Vickers indent is introduced in the material and the lengths of the cracks originating from the corners of the indent

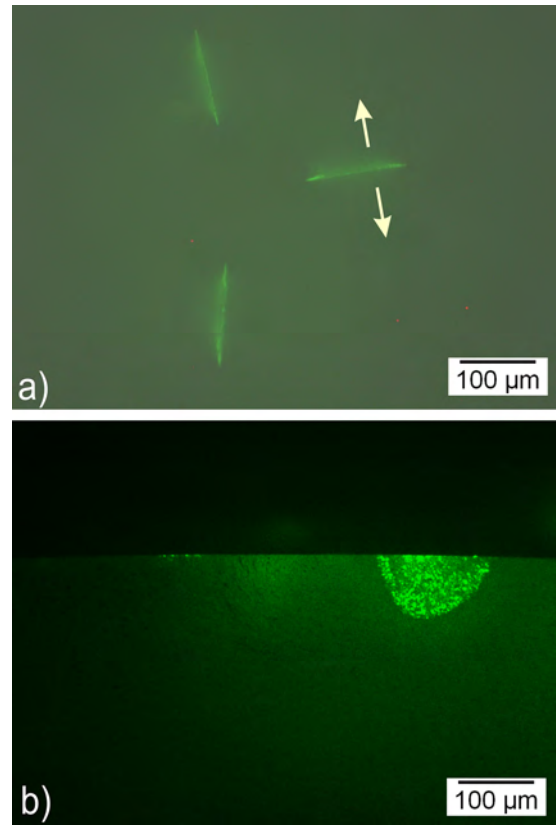


Fig. 7. Insertion of a crack via tilted Vickers indent in the material ZO (HV20). (a) After grinding at the surface with FPD, the arrows indicate the direction of the first principal stress in the NBT and (b) Crack shape determination at the fracture surface with FPD.

are measured. The IFR can be determined from the length of the cracks, the indentation load, the Young’s modulus and the hardness of the material. Many different equations for the evaluation of IFR tests exist, which have been calibrated to measurements in various materials. These equations may give quite different values for the IFR; K_{IFR} .

We will compare IFR test results (evaluated with two of these equations) with SCF and SEVNB test results. One is the equation of Niihara^{30,31} for penny-shaped cracks, which is also a criterion in the specification standard³³ for silicon nitride materials designated for ball bearing applications. The second equation has been proposed by Miyoshi.²⁸ It was developed considering a wide range of different ceramic materials and indentation loads.

We made the indents into the polished cross sections of the balls in the equatorial plane. At least 10 indents were measured for each material and each indentation load (1, 2, 5, 10, 20 and 30 kg).

5. Experimental results

5.1. Evaluation of the SCF-NB method: fracture toughness of the reference material

The results of fracture toughness tests on SNRef are summarised in Table 3. For the SCF tests the location of the maximum value for the geometry factor Y is indicated in the case of

Table 3

Results of fracture toughness measurements for SNRef on prismatic bars and balls.

Specimen type/SCF indentation load	Location of Y_{MAX}	No. of samples	a [μm]	c [μm]	a/c	K_{Ic} [$\text{MPa m}^{1/2}$]
Bar (SEVNB)		6				5.4 ± 0.1
Bar (SCF)/7 kg	A	5	71 ± 8	125 ± 5	0.57	5.7 ± 0.1
Bar (SCF)/10 kg	A	6	108 ± 13	158 ± 7	0.68	6.0 ± 0.2
Ball (SCF)/7 kg	A	6	87 ± 11	131 ± 5	0.66	6.1 ± 0.2
Ball (SCF)/10 kg	C	6	138 ± 3	177 ± 1	0.78	6.5 ± 0.1

semi-elliptical cracks. For most measurements the critical location was at the deepest point of the crack (point A, see Fig. 2). For the indentation load 10 kg on ball specimens, the maximum of the stress intensity factor occurred at the intersection of the crack with the specimen surface (point C).

The SEVNB method – evaluated according to the SEVNB standard¹ – provides a fracture toughness K_{Ic} of $5.4 \pm 0.1 \text{ MPa m}^{1/2}$ that is a little lower than all other K_{Ic} -results obtained for this material.

For the SCF method the results for K_{Ic} are given in Table 3. For tests on bars the indentation loads of 7 kg and 10 kg provided a $K_{Ic} = 5.7 \pm 0.1$ and $6.0 \pm 0.2 \text{ MPa m}^{1/2}$, respectively. The standard deviations of the fracture toughness data determined at different indentation loads do not overlap. As predicted for these crack shapes in Ref. 5 the fracture starts in point A.

For the SCF-NB (performed on balls), K_{Ic} was obtained according to part I.¹³ In the case of the balls indented with 7 kg the maximum of the stress intensity factor was at point A and the fracture toughness was $K_{Ic} = 6.1 \pm 0.2 \text{ MPa m}^{1/2}$. In the case of the balls indented with 10 kg the maximum of the stress intensity factor was at point C and the fracture toughness was $6.5 \pm 0.1 \text{ MPa m}^{1/2}$.

It should be noted that whether point A or C becomes critical depends on the Poisson's ratio and on geometrical details of the starter crack. In the actual case – as analysed in Refs. 5, 13 – the critical point is C if $a/c < 0.7$. This perfectly fits to the test results described in Section 5.1.

5.2. SCF-NB fracture toughness of four structural ceramics

Of each of the materials SN, AO, SC and ZO, six balls were used for SCF-NB testing, see Table 4. According to the theoretical prediction^{5,13} all specimens had the critical point at the surface (point C) due to the crack shape ratios of $a/c < 0.7$ (remember, the condition was $a/c < 0.7$).

All notched ball specimens made of SN were indented with 10 kg. The mean crack shape ratio is $a/c < 0.71$. Accordingly to this the stress intensity factors of point C ($6.2 \pm 0.1 \text{ MPa m}^{1/2}$) and point at A ($5.6 \pm 0.2 \text{ MPa m}^{1/2}$) were close together in the tests. The AO sample was split in two batches with 3 specimens each. One batch was indented with 5 kg and one with 10 kg that resulted in clearly different crack sizes (factor ~ 2). The K_{Ic} mean value for HK5 is slightly smaller than the value for HK10 but statistically indistinguishable. For all six SC notched balls an indentation load of 10 kg was used. This resulted in relatively big cracks, which showed extremely good overall measurability of the crack shape with FPD but also in a stereo microscope.

Therefore, the scattering in K_{Ic} with $3.0 \pm 0.3 \text{ MPa m}^{1/2}$ does not result from the measurement uncertainties of the crack depth or crack width. The K_{Ic} measurements of zirconia (ZO) resulted in $4.4 \pm 0.3 \text{ MPa m}^{1/2}$.

6. Discussion

6.1. Fracture toughness results

The K_{Ic} -values of the reference material (a silicon nitride ceramic) generally tends to increase with higher indentation loads (this observation is statistically significant). A plot for SNRef of the K_{Ic} -values versus the crack length Δa is shown in Fig. 8.

Δa denotes the crack length, where crack bridging effects may occur (e.g. due to grain interlocking). For a “Surface Crack in Flexure” it holds $\Delta a = a$. In the case of the SEVNB-test fracture is most likely caused by very small ($\Delta a < 10 \mu\text{m}$) cracks in front of the V-notch.^{36,37} Hence, the results of the SEVNB-tests are plotted at a crack length of $10 \mu\text{m}$. The result of SEVNB together with the SCF values implies the existence of a rising crack resistance curve, i.e. R -curve. This behaviour is typical for commercial silicon nitrides and has already extensively studied for some special materials. The data shown in Fig. 8 are consistent with the R -curves published in Ref. 38.

Another explanation for the high K_{Ic} -value of the HK10 indented balls could be the position of the critical point at the

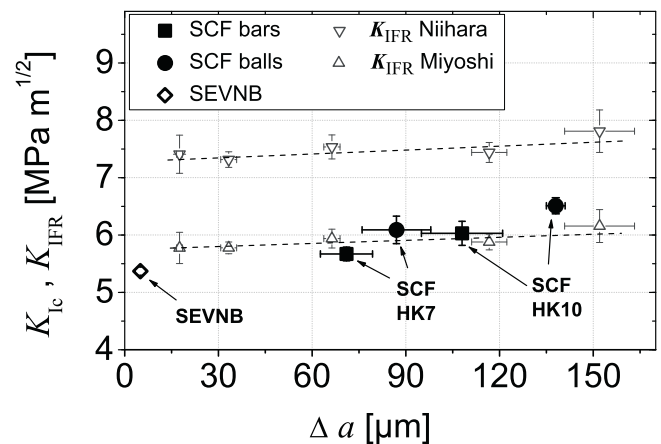


Fig. 8. Measurements of the fracture toughness K_{Ic} of SNRef using different testing methods: measurements with the SCF method on bars (squares) and balls (circles) and results determined with the SEVNB method (open diamond). Also shown are fracture resistance measurements, K_{IFR} , evaluated according to the equations of Niihara (downwards triangles) and Miyoshi (upwards triangles).

Table 4

Results of fracture toughness measurements with the modified SCF method on balls for SN, AO, SC and ZO materials.

Material/SCF indentation load	Location of Y_{MAX}	No. of specimens	a [μm]	c [μm]	a/c	K_{Ic} [$\text{MPa m}^{1/2}$]	K_{Ic} literature [$\text{MPa m}^{1/2}$]
SN/HK10	C	6	118 ± 7	165 ± 2	0.71	6.2 ± 0.1	6.2 ± 0.2 ²⁸
AO/HK5	C	3	125 ± 34	155 ± 40	0.81	4.3 ± 0.3	4.0 ± 0.2 ³⁴
AO/HK10	C	3	241 ± 25	274 ± 33	0.88	4.5 ± 0.1	–
SC/HK10	C	6	216 ± 32	268 ± 29	0.81	3.0 ± 0.3	$2.6\text{--}3.0$ ³⁵
ZO/HV20	C	6	69 ± 17	69 ± 10	1.00	4.4 ± 0.3	4.4 ± 0.4 ⁷

surface (at point C) in contrast to all other tests. In fact the correct description of a crack intersecting the surface (at point C) is still an open question. At point C the stress singularity does not exactly follow an inverse square root law³⁹ (as it is supposed in LEFM) and T-stresses may become relevant.^{39–41} In addition, pop-in-events – as mentioned in Appendix B of the SCF standard³ – are an unsolved uncertainty.

In order to force point A to become critical, it would be necessary to produce shallower cracks with a smaller a/c -ratio, i.e. to grind-off (a little) more material from the indented ball surface. An estimation for the minimum grinding depth for the conventional SCF method in flexure bars is given in Ref. 5, which can be analogously used for the NBT, by approximating bar's thickness with the thickness of the ligament of the notched ball specimen. For details see Ref. 42.

In the last column of Table 4 K_{Ic} values from literature are given for all materials (SN, AO, SC and ZO) for comparison. All these results have been measured with the SCF method on bars under similar indentation loads as used in this work. Also the microstructures are comparable – only the alumina ceramic has a smaller mean grain size than the AO ceramic. All K_{Ic} references fit well to the results in this work considering standard deviation.

6.2. Measurement error

For each new testing method the error analysis is a key element to understand how reliable, reproducible and sensitive the obtained result is regarding errors of the input data. In the discussed case the measurement of the crack shape is a crucial topic for the fracture toughness evaluation with surface cracks in the SCF method. Therefore, not only the reproducibility of surface cracks but also the measurement error in the crack length and the crack width is an important issue to be discussed.

In Fig. 9a, a comparison of crack dimensions measured with (i) grazing incident light and (ii) with FPD is shown. The cracks in alumina and zirconia were not measurable on the fracture surface without penetration dye, so no reference values are available for these materials. Hence, only the SN, SC and SNRef are discussed. The dashed lines in Fig. 9 indicate the $\pm 10\%$ confidence intervals. As one can see, most of the data points are within $\pm 10\%$ deviation. Large cracks seem to be measured longer without FPD. This means that the crack dimensions are not overestimated using FPD. The FPD measurements were repeated one day later and the same results were obtained.

As mentioned before, the full crack width $2c$ can be determined directly before fracture at the polished surface, preferably with FPD. This procedure is supposed to be more precise and reproducible than measurement of the crack width on the fracture surface. The results are illustrated in Fig. 9b – all measurements are within a deviation of $\pm 10\%$ for the investigated materials

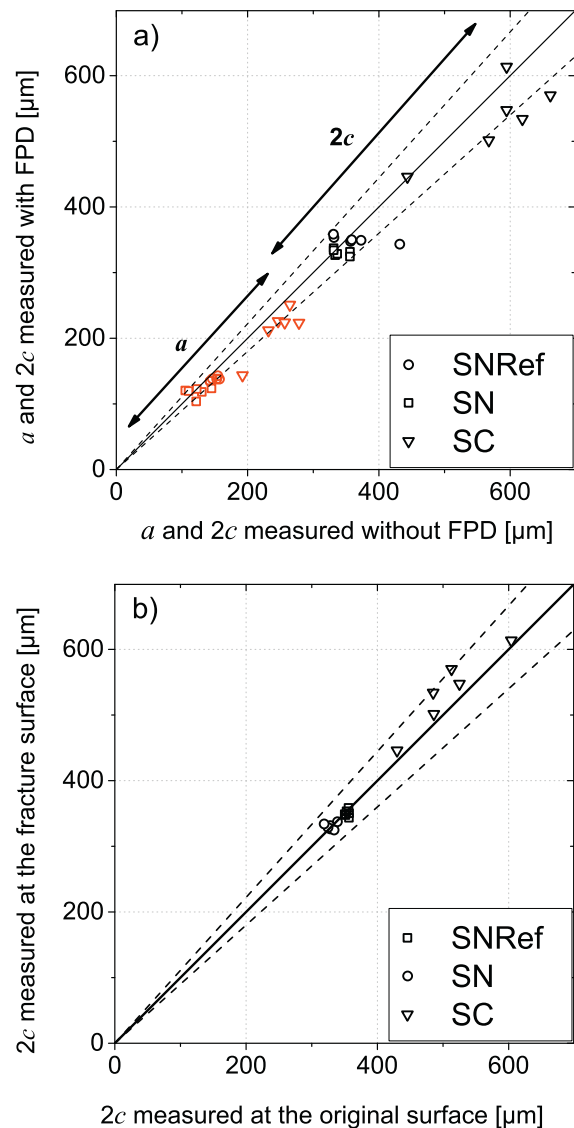


Fig. 9. (a) Comparison of the crack shape parameter a and c measured at the fracture surface with FPD vs. stereo microscope measurements without FPD and (b) comparison of full crack width $2c$ measured at the fracture surface vs. specimens surface (before fracture).

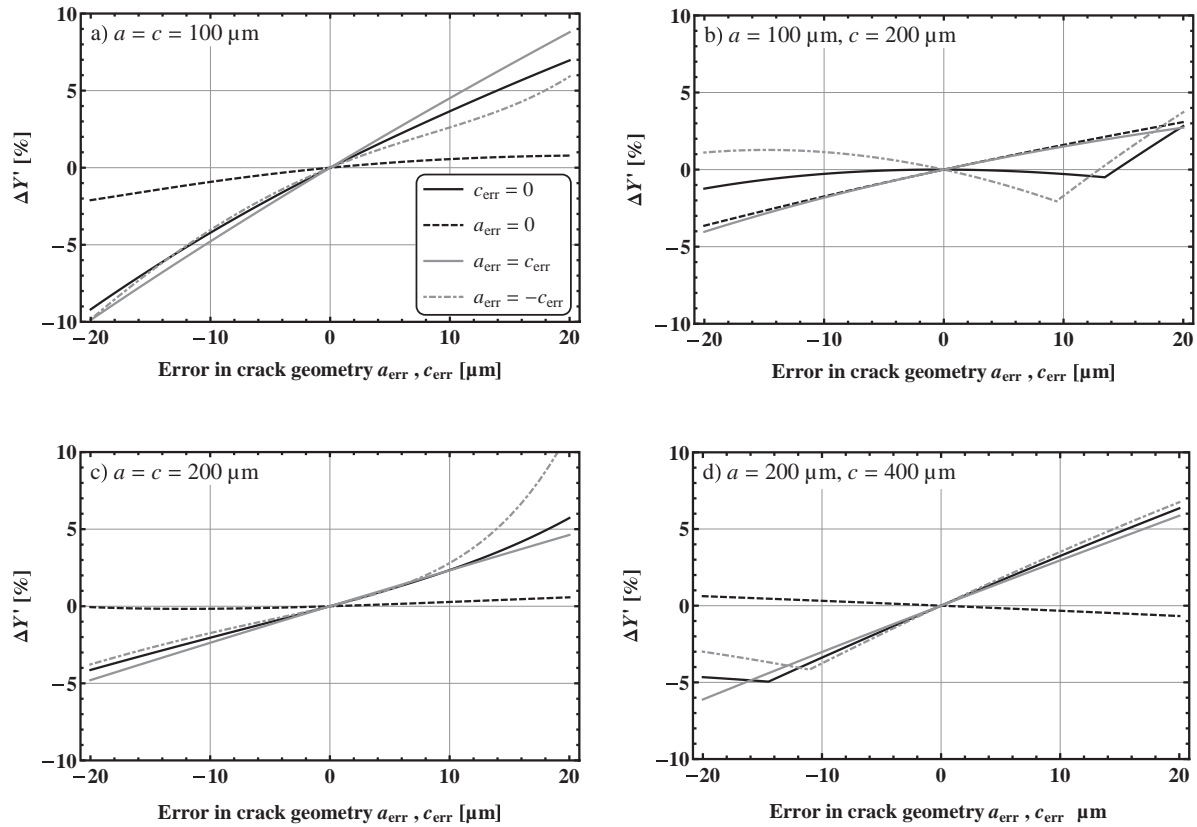


Fig. 10. Influence of crack shape measurement errors a_{err} and c_{err} on the accuracy of the (modified) geometric factor Y' . (a) Small crack and $a/c = 1$, (b) small crack and $a/c = 0.5$, (c) large crack and $a/c = 1$, (d) large crack and $a/c = 0.5$.

but the measurements at the fracture surface give tentatively (slightly) larger crack length values than the measurements at the specimens surface. Conclusions for the crack shape measurements with the used penetration dye are:

- (i) For fine grained materials the use of FPD is very useful, especially considering the ease of use, experience of the operator and time consumption. Ideally, the measurement precision does not suffer.
- (ii) In materials such as alumina the crack shape is very difficult to measure without FPD.
- (iii) The measurement of the crack at the polished surface is only possible with FPD and helps to keep the measurement uncertainties low (<5%).
- (iv) No scanning electron microscope analysis is necessary to obtain accurate crack shape geometries.

According to Eq. (1), K_{IC} depends on three factors. The errors in σ_{NBT} and f_{Sigma} were already discussed in the first part of this paper¹³ – both are typically less than 1–2%. The remaining factors are mainly affected by the crack size and shape. In addition, the critical point for the start of crack propagation may change abruptly (depending whether Y_{MAX} is in point A or in point C). As a consequence, we introduce a new variable $Y' = Y_{\text{MAX}}\sqrt{a\pi}$ for the error analysis. This approach enables us to investigate the influence of errors in the crack geometry, i.e. the error in the crack depth a_{err} and in the crack width c_{err} simultaneously. The

influence of other geometrical parameters and of the Poisson's ratio as well as their interaction with the crack shape deviation on the determination of the stress intensity factor is small (much lower than 1%) and can be neglected.

The geometrical factor Y is unit independent and was calculated in part I for all specimen geometries, which are relevant in practice. With Y' , the overall effect of crack dimension measurement errors on error in K_{IC} for a characteristic specimen can be investigated. Furthermore, the relative influence of a given a_{err} is stronger for small cracks than for big cracks. As reference geometry of the notched ball specimen, the following parameters were chosen for the error analysis: $D = 5$ mm, $L_{\text{N}} = 4$ mm, ($\rightarrow h = 1$ mm), $W_{\text{N}} = 0.5$ mm, $R_{\text{N}} = 0.125$ mm, $\Delta h = 100$ μm and $\nu = 0.3$. To cover all measured crack geometries in the investigated materials (see Tables 3 and 4), two representative crack depths ($a = 100$ μm and $a = 200$ μm) and two extrema in the crack shapes ($a/c = 0.5$ and $a/c = 1$) were investigated.

An error in the measurement can occur in four different kinds: only in a , only in c or in both (in the same direction or in the opposite direction, respectively). These four cases are plotted in Fig. 10a for $a/c = 1$ with $a = 100$ μm . If $a_{\text{err}} = 0$ and only c is incorrect, $\Delta Y'$ is nearly zero (which is equivalent to zero error in K_{IC}). For a measurement error of ± 20 μm in the crack dimensions a or c , $\Delta Y'$ rises up to 10%.

For a shallow crack ($a/c = 0.5$) with $a = 100$ μm (Fig. 10b) the error for ± 20 μm (in either a or c) is below 4% for the geometric factor in all cases, that are representative for the SN

and SNRef specimens. One reason for this low error could be that the geometric factor is critical in point A for most of the plotted data points. The curves are discontinuous and Y_{MAX} switches to point C on the right hand side of the graph.

For deeper cracks ($a = 200 \mu\text{m}$) point C always remains the critical one, as one can see in Fig. 10c and d. Again a measurement error exclusively in c has almost no effect on K_{IC} . When a_{err} is about $\pm 20 \mu\text{m}$ and c_{err} is about $-20 \mu\text{m}$, $\Delta Y'$ increases above 10% for $a/c = 1$. In all other configurations the resulting error stays below 5–6%. This can be quantified as the typical error in alumina and silicon carbide with 10 kg indents resulting from errors in the crack shape determination.

Three points can be concluded from this error analysis:

- The error in K_{IC} due to errors in crack geometry measurements is typically smaller than 10%. For shallow cracks the resulting error is smaller than 5%, which is an additional argument to create shallow cracks.
- The accurate determination of a is significantly more important than that of c (see dashed lines in Fig. 10).

6.3. Comparison IFR with fracture toughness test results

Tests on the SNRef material: For all used indentation loads cracks at the corners of the indents occurred, which could be used for the determination of the indentation fracture resistance, K_{IC} . Following the suggestion of Ref. 27 the test results are plotted in Fig. 8 versus the effective crack length $\Delta a = c_v - d_v/2$. c_v is the distance between indent centre and crack tip, and d_v the indent diagonal. K_{IFR} -results for all evaluated loads are illustrated as lines showing a slightly increase with the crack length. If the K_{IFR} -values are evaluated using the equation of Miyoshi, the values are about $6 \text{ MPa m}^{1/2}$. They are in good agreement with the SCF results. If the evaluation is made using the equation of Niihara (and therewith following the evaluation recommended in ASTM F 2094-08), the values are about $7.5 \text{ MPa m}^{1/2}$ and do not fit the measured fracture toughness values.

Tests on four structural ceramic materials (SN, AO, SC and ZO): The K_{IFR} test results shown in Table 4 and are plotted in Fig. 11. The K_{IC} -values are shown on the left hand side of the diagram without information about the crack length (see Table 4).

In the case of SN the K_{IFR} values were determined on indents made with a load of 1–30 kg. The indents in the AO and SC materials were only evaluable, if loads between 2 kg and 5 kg were applied. The other tests were rejected due to the influence of big pores, material break-outs and lateral cracks around the indents.

For ZO the scatter of the data was very large. As shown in Fig. 7b at an indentation load of 20 kg Palmqvist cracks were produced on each corner of the indent. This is in accordance with the work of Kaliszewski et al.²⁶ They found that half-penny cracks are created in zirconia (Y-TZP) with loads above 50 kg. The used IFR-formulas are only applicable for half-penny cracks and deliver erroneous values for other crack geometries. In our case the cracks had a kidney shape and the K_{IFR} data evaluation may become meaningless.

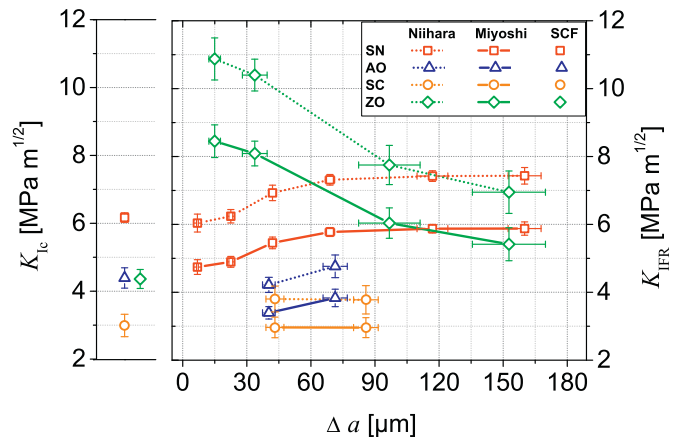


Fig. 11. Indentation fracture resistance versus effective crack length for four structural materials (SN, AO, SC and ZO). On the left hand side the K_{IC} results (measured with the modified SCF method on balls) is plotted. The indentation fracture resistance, K_{IFR} , was evaluated using the equations of Niihara³¹ and Miyoshi²⁸ respectively.

If the tests were evaluated with the Miyoshi equation the SN data nicely correlate with our fracture toughness values for higher indentation loads, but data evaluated with the Niihara equation do not. In the case of AO the K_{IFR} do not correlate with fracture toughness values irrespective which evaluation equation is used (neither Niihara nor Miyoshi). K_{IFR} -values of SC do not depend on indentation load. The Miyoshi formula gives K_{IFR} values which correlate with our K_{IC} test results.

The results of the IFR method can be summarised as following: (i) the commonly used IFR Niihara evaluation does not match the fracture toughness of all investigated materials, even of silicon nitride. (ii) In two materials (silicon carbide and silicon nitride) the Miyoshi formula fits the fracture toughness within the experimental standard deviation. (iii) The IFR method generally depends on the indentation load. An overestimation by the factor of 2.5 (in zirconia) is possible. (iv) Due to the formation of different crack patterns (Penny-shaped cracks, lateral cracks, Palmqvist cracks, etc.) the evaluation procedure for IFR may become meaningless. In summary IFR-measurements should not be used for the estimation of fracture toughness.

7. Conclusions

In part I of this paper¹³ the theoretical analysis of the SCF method applied to notched ball specimen (SCF-NB) was conducted. In this second part the method is applied to several structural ceramics to demonstrate the experimental applicability. The following conclusion can be drawn:

- The SCF method delivers the same testing results whether it is applied to beams (as described in standards) or to balls (SCF-NB).
- The data determined with the SCF-NB test also coincide with results measured with other methods and with literature data.
- The developed evaluation procedure proved to be suitable. For example it could be shown that it can be predicted whether

the highest stress intensity factor is at the position A or C of the crack front.

- It is recommended to prepare the specimens in such a way that point A will become critical. This can simply be made by grinding a little more of the indented volume away, so that the ratio a/c becomes less than 0.7 (shallower cracks). In point A the measurement uncertainties are much smaller than in C.
- The use of fluorescent penetration dye (FPD) is useful to measure the crack size.
- The measurements of the indentation fracture resistance showed, that the gained data strongly depend on the used evaluation method and are not reliable. It is recommended not to use indentation fracture resistance measurement for fracture toughness estimations.

The practical effort and time consumption should also be considered. The production of notched balls specimen directly from the balls for strength testing is generally faster than the production of a (standard) bending beam from a ball. The effort for the crack introduction, measurement, grinding procedure and testing is very similar to the effort in conventional SCF-testing and both methods have generally the same advantages and disadvantages. With the SCF-NB test also small spherical components can be tested, which seems not to be feasible with other reliable measurement techniques. A lower limit for the ball diameter for the preparation of a notched ball specimen is around 3 mm. Below that size the alignment of the crack and the cutting of the notch may cause considerable geometrical deviations; possibly other notching procedures can solve this problem.

A short comment to the used evaluation equations should be given. In this work, the solutions for stress fields and stress intensity factors described in part I of the paper¹³ are used. In the standards the Newman and Raju equation¹² is used which is less precise than our equation. In the case of the measurements presented in this paper the differences between both equations are relatively small (between 0 and 7%), but it should be recognised, that depending on the Poisson's ratio of the investigated material and the crack geometry much higher differences may arise. This fact is even more relevant if the critical point at the crack front is point C.

In summary it can be stated, that the new method to determine the fracture toughness in the surface of balls can be recommended for wider use. Especially in the case of bearing balls it could be a good solution for a fair comparison between different materials.

Acknowledgements

Financial support by the Austrian Federal Government (in particular from Bundesministerium für Verkehr, Innovation und Technologie and Bundesministerium für Wirtschaft, Familie und Jugend) represented by Österreichische Forschungsförderungsgesellschaft mbH and the Styrian and the Tyrolean Provincial Government, represented by Steirische Wirtschaftsförderungsgesellschaft mbH and Standortagentur Tirol, within

the framework of the COMET Funding Programme is gratefully acknowledged.

References

1. ISO 23146. Fine ceramics (advanced ceramics, advanced technical ceramics) – Test methods for fracture toughness of monolithic ceramics – Single-edge V-notch beam (SEVNB) method; 2008.
2. ISO 24370. Fine ceramics (advanced ceramics, advanced technical ceramics) – Test method for fracture toughness of monolithic ceramics at room temperature by chevron-notched beam (CNB) method; 2005.
3. ISO 18756. Fine ceramics (advanced ceramics, advanced technical ceramics) – Determination of fracture toughness of monolithic ceramics at room temperature by the surface crack in flexure (SCF) method; 2003.
4. Munz D, Fett T. *Ceramics – mechanical properties, failure behaviour, materials selection*. Berlin: Springer; 2001.
5. Strobl S, Supancic P, Lube T, Danzer R. Surface crack in tension or in bending – a reassessment of the Newman and Raju formula in respect to fracture toughness measurements in Brittle materials. *J Eur Ceram Soc* 2012;**32**:1491–501.
6. Miyazaki H, Hyuga H, Yoshizawa Y, Hirao K, Ohji T. Fracture toughness test of silicon nitrides with different microstructures using Vickers indentations. *Ceram Eng Sci Proc* 2008;**28**:433–42.
7. Quinn GD, Kübler J, Gettings RJ. *Fracture toughness of advanced ceramics by the surface crack in flexure (SCF) method: A VAMAS round robin. VAMAS report No. 17. Report 1994*; 1994.
8. Miyazaki H, Hyuga H, Yoshizawa Y, Hirao K, Ohji T. Crack profiles under a Vickers indent in silicon nitride ceramics with various microstructures. *Ceram Int* 2010;**36**:173–9.
9. Jones SL, Norman CJ, Shahani R. Crack-profile shapes formed under a Vickers indent pyramid. *J Mater Sci Lett* 1987;**6**:721–3.
10. Lube T. Indentation crack profiles in silicon nitride. *J Eur Ceram Soc* 2001;**21**:211–8.
11. Newman JC, Raju IS. *Analysis of surface cracks in finite plates under tension or bending loads*. NASA. Report TP-1578; 1979.
12. Newman JC, Raju IS. An empirical stress-intensity factor equation for the surface crack. *Eng Fract Mech* 1981;**15**:185–92.
13. Strobl S, Supancic P, Lube T, Danzer R. Toughness measurement on ball specimens. Part I: Theoretical analysis. *J Eur Ceram Soc* 2012;**32**:1163–73.
14. ÖNORM M 6341. Rolling bearings—ceramic bearing balls—determination of the strength—notched ball test; 2013.
15. Supancic P, Danzer R, Harrer W, Wang Z, Witschnig S, Schöppl O. Strength tests on silicon nitride balls. *Key Eng Mater* 2009;**409**:193–200.
16. Supancic P, Danzer R, Wang Z, Witschnig S, Schöppl O. *The notched ball test – a new strength test for ceramic spheres. 9th International symposium on ceramic materials and components for energy and environmental applications*. Shanghai: The American Ceramic Society; 2009. p. 67–75.
17. Supancic P, Danzer R, Witschnig S, Polaczek E. *The strength of ceramic balls – the notched ball test. 18th European conference on fracture*; 2010. Dresden.
18. Supancic P, Danzer R, Witschnig S, Polaczek E, Morrell R. A new test to determine the tensile strength of brittle balls – the notched ball test. *J Eur Ceram Soc* 2009;**29**:2447–59.
19. EN 15335. Advanced technical ceramics – ceramic composites – determination of elastic properties by resonant beam method up to 2000 °C; 2007.
20. Lins W, Kaindl G, Peterlik H, Kromp K. A novel resonant beam technique to determine the elastic moduli in dependence on orientation and temperature up to 2000 °C. *Rev Sci Instrum* 1999;**70**:3052–8.
21. Migliori A, Sarrao JL. *Resonant ultrasonic spectroscopy*. New York, NY: Wiley Interscience; 1997.
22. Torres Y, Casellas D, Anglada M, Llanes L. Fracture toughness evaluation of hardmetals: influence of testing procedure. *Int J Refract Met Hard Mater* 2001;**19**:27–34.
23. Swab JJ, Quinn GD. Effect of precrack halos on fracture toughness determined by the surface crack in flexure method. *J Am Ceram Soc* 1998;**81**:2261–8.

24. Anstis GR, Chantikul P, Lawn BR, Marshall DB. A critical evaluation of indentation techniques for measuring fracture toughness: I, direct crack measurements. *J Am Ceram Soc* 1981;**64**:533–8.
25. ISO 14627. Fine ceramics (advanced ceramics, advanced technical ceramics) – test method for fracture resistance of silicon nitride materials for rolling bearing balls at room temperature by indentation fracture method; 2012.
26. Kaliszewski MS, Behrens G, Heuer AH, Shaw MC, Marshall DB, Dransmann GW, et al. Indentation studies on Y_2O_3 -stabilized ZrO_2 : I, development of indentation-induced cracks. *J Am Ceram Soc* 1994;**77**:1185–93.
27. Miyazaki H, Hyuga H, Hirao K, Ohji T. Comparison of fracture resistance as measured by the indentation fracture method and fracture toughness determined by the single-edge-precracked beam technique using silicon nitride ceramics with different microstructures. *J Eur Ceram Soc* 2007;**27**:2347–54.
28. Miyazaki H, Hyuga H, Yoshizawa Y, Hirao K, Ohji T. Relationship between fracture toughness determined by surface crack in flexure and fracture resistance measured by indentation fracture for silicon nitride ceramics with various microstructures. *Ceram Int* 2009;**35**:493–501.
29. Miyazaki H, Yoshizawa Y, Hirao K, Ohji T. Indentation fracture resistance test round robin on silicon nitride ceramics. *Ceram Int* 2010;**36**:899–907.
30. Niihara K, Morena R, Hasselman DPH. Further reply to “Comments on ‘elastic/plastic indentation damage in ceramics: the median/radial crack system’”. *J Am Ceram Soc* 1982;**65**:C-116.
31. Niihara K, Morena R, Hasselman DPH. Evaluation of K_{Ic} of brittle solids by the indentation method with low crack-to-indent ratios. *J Mater Sci Lett* 1982;**1**:13–6.
32. Quinn GD, Bradt RC. On the Vickers indentation fracture test. *J Am Ceram Soc* 2007;**90**:673–80.
33. *Standard specification for silicon nitride bearing balls*. American Society for Testing and Materials; 2008.
34. Park J-K, Yasuda K, Matsuo Y. Effect of crosshead speed on the fracture toughness of soda-lime glass, Al_2O_3 and Si_3N_4 ceramics determined by the surface crack in flexure (SCF) method. *J Mater Sci* 2001;**36**:2335–42.
35. Quinn GD, Salem JA. Effect of lateral cracks on fracture toughness determined by the surface-crack-in-flexure-method. *J Am Ceram Soc* 2003;**85**:873–80.
36. Damani R, Gstrein R, Danzer R. Critical notch root radius in SENB-S fracture toughness testing. *J Eur Ceram Soc* 1996;**16**:695–702.
37. Damani R, Schuster C, Danzer R. Polished notch modification of SENB-S fracture toughness testing. *J Eur Ceram Soc* 1997;**17**:1685–9.
38. Fünfschilling S, Fett T, Hoffmann MJ, Oberacker R, Jelitto H, Schneider GA, et al. Bridging stresses from *R*-curves of silicon nitrides. *J Mater Sci Lett* 2009;**44**:3900–4.
39. Anderson TL. *Fracture mechanics – fundamentals and applications*. Boca Raton, FL: CRC Press; 2005.
40. Fett T. *Stress intensity factors – T-stresses – weight functions (IKM 50)*. Karlsruhe: KIT Scientific Publishing; 2008.
41. Fett T. *Stress intensity factors – T-stresses – weight functions. Supplement volume (IKM 55)*. Karlsruhe: KIT Scientific Publishing; 2009.
42. Lube T, Witschnig S, Supancic P. Fracture toughness of ceramic balls. 18th European conference on fracture, Dresden; 2010.

Paper K

T. Lube, S. Rasche, T.G.T. Nindhia: "A fracture toughness test using the Ball-on-three-balls test", *Journal of the American Ceramic Society* **99** [1] (2016), 249–256, <http://www.dx.doi.org/10.1111/jace.13842>

Re-used under License 5715540363044, granted Jan 24, 2024, by John Wiley & Sons Inc.

A Fracture Toughness Test Using the Ball-on-Three-Balls Test

Tanja Lube,^{‡,†} Stefan Rasche,[‡] and Tjokorda Gde Tirta Nindhia^{‡,§}

[‡]Institut für Struktur- und Funktionskeramik, Montanuniversität Leoben, A-8700 Leoben, Austria

[§]Department of Mechanical Engineering, Udayana University, Jimbaran, Bali, Indonesia

A method for fracture toughness measurement of ceramics using small disks and plates is presented. Similar to the surface-crack-in-flexure (SCF) method a semielliptical surface crack is introduced centrally into one plane side of the specimen which is fractured in a ball-on-three-balls test. Finite element simulations are used to evaluate the stress intensity factor (SIF) for this loading geometry for a range of crack sizes and crack geometries. Empirical formulae for the geometric function are provided for evaluation of the test. The effect of position uncertainties is investigated using FEM and experiments. Other sources which may contribute to the measurement error are identified and quantified, resulting in recommendations for the practical realization of the test. A determination of the fracture toughness within $\pm 10\%$ measurement uncertainty is possible with specimens larger than 8 mm in diameter and thicker than 0.5 mm. With larger specimens an uncertainty comparable to other fracture toughness tests can be achieved. For precise measurements it is important to position the crack within $\pm 120 \mu\text{m}$ of the stress maximum, to know Poisson's ratio exactly and to test cracks that have the maximum SIF at their deepest point. A method how this can be achieved is presented.

I. Introduction

IN material development or situations where ceramics are prepared on laboratory scale (e.g., by various pressing routes), a convenient specimen shape is a rather thin cylindrical disk. There also exist ceramic components such as resistors,¹ watch glasses,² and others³ which are disk-shaped. This shape is also the prescribed form for biaxial strength tests of bio-ceramics.^{4,5} Often these parts are too small to cut standard bend bars for fracture toughness evaluation out of them. Since suitable, separately fabricated, bodies with larger dimensions may have different properties, a fracture toughness test method that uses residual stress-free indentation precracks and that can be applied directly to small disk- (or plate-) shaped parts would be extremely helpful. With such a method fracture toughness K_{Ic} instead of the poorly defined⁶ indentation fracture resistance K_{IFR} determined by the IF method^{7,8} will be accessible.

The ball-on-three-balls test (B3B test) is a favorable, high precision biaxial flexural strength testing method for small ceramic disks and plates.^{9–11} An advantage of this test is the possibility to test platelike components without special grinding procedure.

In Strobl et al.³ it was already shown, that the B3B test is also a good basis for fracture toughness testing. Similar to the surface-crack-in-flexure (SCF) method for bend bars^{12–14}

a sharp semielliptical surface crack was introduced into a B3B specimen. The crack size was measured on the fracture surfaces of the broken specimen. The critical stress intensity factor (SIF) along the crack front was evaluated with the help of a fracture mechanical three-dimensional finite element analysis. It was demonstrated for five different ceramic materials, that the obtained K_{Ic} results match very well the results determined with established methods. This new method we called B3B- K_{Ic} test.

A comparison of the three-dimensional stress field in the B3B test with the axisymmetric stress field found in ball on ring or punch on ring test was given in Rasche et al.¹⁵ There it was shown that the artificial crack is loaded by a almost axisymmetric stress field in the specimen center and therefore the SIF distribution along the crack front is almost symmetric too. But the position of the maximum can change with respect to the crack shape ratio, the crack size to specimen thickness ratio as well as the Poisson's ratio.

While in Strobl et al.³ only the maximum K_I value along the crack front was presented, we now investigate the position of the maximum. Furthermore, we proceed with an error analysis, which quantifies the effect of uncertainties of the crack's position.

The calculation of the SIF distribution along the crack front nowadays is an ordinary engineering problem thanks to available finite element software packages with fracture mechanical capabilities such as ANSYS or ABAQUS. Nevertheless, it might be a handicap for daily use of this new method outside research laboratories. More practical would be a formula which enables the test engineer to do the evaluation without the need to perform a finite element analysis. For this reason an easy-to-use empirical SIF formula is developed in this paper. It is based on a set of finite element calculations with systematically varied parameters.

II. Description of the B3B- K_{Ic} Test Method

The fracture toughness of ceramics can be determined when a crack of measurable size is introduced in a specimen of well-defined geometry which is then loaded until fracture under well-defined boundary conditions. These prerequisites are satisfied with the B3B- K_{Ic} method. It is already described in detail in Strobl et al.³ In the B3B strength test, we have a circular disk or a rectangular plate, which is supported by three balls in contact and loaded on the opposite side by a fourth ball of the same size. The loading ball is positioned centrally to the three supporting balls, see Fig. 1. Using a Knoop indentation a almost semicircular surface crack is introduced as a starter crack in the center of the specimen, opposite to the loading ball (Fig. 2). Residual stresses due to the plastic imprint are removed by a grinding procedure. A layer having the thickness of a minimum of one-sixth of the indent diagonal has to be removed from the surface.¹⁴ The ground specimen is put into the B3B testing jig such that the crack is situated on the tensile stressed side and located in one of the three symmetry planes. That means one surface point of the crack is directed toward one supporting ball, the

E. Lara-Curzio—contributing editor

Manuscript No. 37069. Received June 19, 2015; approved July 15, 2015.

[†]Author to whom correspondence should be addressed. e-mail: tanja.lube@unileoben.ac.at

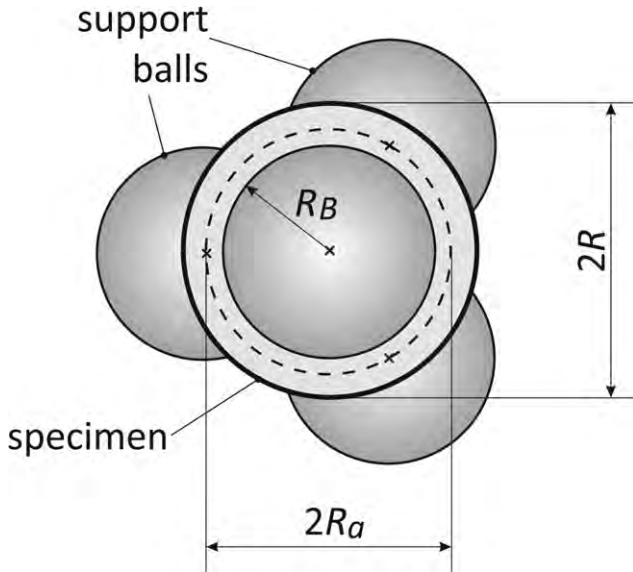


Fig. 1. Ball-on-three-balls test geometry with four equally sized balls of radius R_B . Specimen and loading ball are positioned centrally to the three supporting balls in contact.

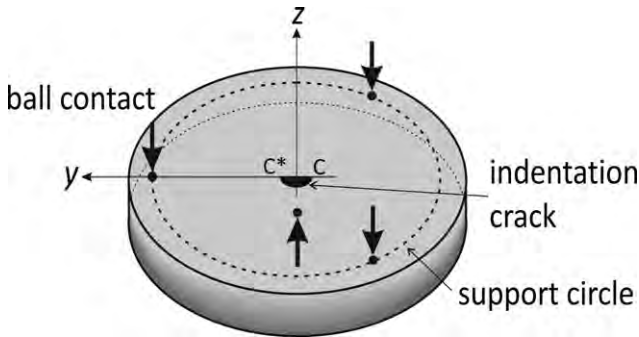


Fig. 2. Sketch of crack position in B3B-KIc test.

other surface point looks in the direction of the gap between the two remaining supporting balls.

Starting from a small preload the load is increased until fracture. The crack size is measured on both fracture surfaces of the broken specimen. It is assumed, that the crack shape can be modeled as semielliptical, Fig. 3, with crack depth a and crack width $2c$.

In the framework of linear elastic fracture mechanics the fracture toughness K_{Ic} can be evaluated with the Griffith/Irwin relation

$$K_{Ic} = \sigma_{B3B} Y \sqrt{\pi a} \quad (1)$$

where σ_{B3B} denotes the maximum tensile stress in the B3B strength test, which occurs in the center of the specimen opposite to the loading ball. The characteristic crack dimension a is the crack depth. The load independent geometric function Y depends on the specimen and crack geometry as well as on the Poisson's ratio ν of the tested material. For semicircular or semielliptical surface cracks which are of interest here, it varies with position along the crack front. Its maximum Y_{max} has to be used in Eq. (1). This maximum was calculated and plotted for certain parameter combinations and $\nu = 0.3$ in Strobl et al.³

σ_{B3B} can be expressed by the empirical formula⁹

$$\sigma_{B3B} = \frac{F}{t^2} \cdot f\left(\frac{t}{R}, \frac{R_a}{R}, \nu\right) \quad (2)$$

where the dimensionless factor f depends on the three dimensionless parameters t/R , R_a/R and ν , with the specimen

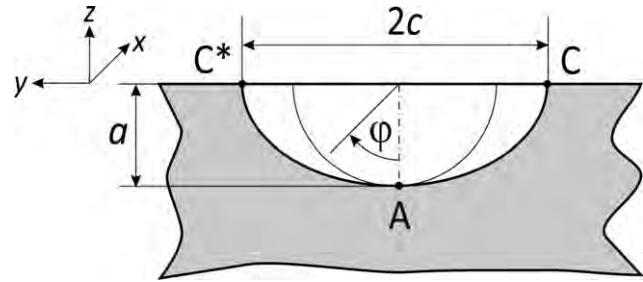


Fig. 3. Sketch of the semielliptical surface crack model, C is directed toward the gap between two support balls, C^* is directed to the contact point of the third support ball.

thickness t , the loading radius R_a and the specimen radius R . Although it is intended for circular disks, an effective specimen radius can be calibrated for rectangular plates.¹⁶ The loading radius is determined solely by the selection of the diameter D_B of the four balls, given by the relation: $R_a = D_B/\sqrt{3}$. Functions approximating f were already published by Börger et al.⁹ as well as by Danzer et al.¹⁷ In the Annex I we provide an even simpler function with less coefficients but high accuracy. So the remaining unknown is the geometric function Y , which depends on the following four dimensionless parameters:

$$Y = Y\left(\frac{a}{c}, \frac{a}{t}, \frac{t}{R_a}, \nu\right) \quad (3)$$

Y can be calculated with the help of finite element simulations and Eqs. (1) and (2):

$$Y = \frac{K_{I,FEM}}{\sigma_{B3B,fit} \sqrt{\pi a}} = \frac{K_{I,FEM} \cdot t^2}{F \cdot f\left(\frac{t}{R}, \frac{R_a}{R}, \nu\right) \cdot \sqrt{\pi a}} \quad (4)$$

The SIF varies along the crack front, which will be shown in more detail later. Due to the shape of the SIF curve it is sufficient to consider the values at two locations of the crack front, near the surface and near the deepest point, to obtain the values for Y_{max} . Then two geometric functions have to be evaluated to characterize the crack growth in the depth and at the surface. The one with the larger value has to be used in Eq. (1) to evaluate K_{Ic} .

III. Finite Element Simulations

(1) Modeling of the B3B Test with Surface Crack

A three-dimensional model of the B3B-KIc test was developed, using the commercial finite element package ABAQUS Standard (Release 6.13). The crack geometry is modeled as semielliptical. A focused mesh with singular crack tip elements (quarter point elements with collapsed element face at the crack front) is used. Although a half model would be sufficient to calculate the SIF for the ideal test geometry, because the crack is positioned in one of the three symmetry planes of the B3B test, a full model was developed to be able to consider deviations from the ideal crack position. Three types of position deviations are modeled:

1. Translation Δy tangential to the symmetry plane (in plane shift)
2. Translation Δx normal to the symmetry plane (out of plane shift)
3. Rotation α with the rotation axis parallel to the loading axis

Of course combinations of these deviations are possible. These position errors occur in real experiments but cannot be measured properly. Figure 4 shows the geometric model including the position errors Δx , Δy , and α .

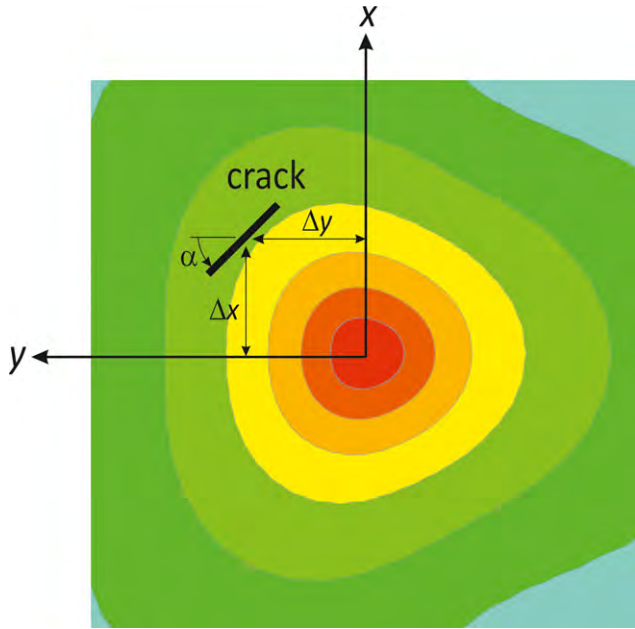


Fig. 4. Deviations from ideal crack position in the center of the specimen: normal shift (out of plane) Δx , tangential shift (in plane) Δy , and rotation α .

The finite element model is parameterized to give the opportunity to investigate separately and combined the influence of force, specimen geometry, crack geometry, and elastic constants.

The balls are modeled alternatively as rigid bodies or as point loads. We found that point loads lead to valid results, according to Saint-Venant's principle and preliminary finite element studies, as long as the specimen thickness is large compared to the size of the contact zone of the loading ball and the crack depth to thickness ratio a/t is 0.2 or less. This is true for the experiments we have conducted until now.

While half-circular cracks can easily be meshed with a focused mesh, semielliptical cracks are more complicated. They are not only curved, but also the radius of curvature changes along the crack front. With automatic meshing capabilities this would lead to a bad mesh quality, distorted elements with nonrectangular angles. This problem can be solved quite easily by adding datum planes, which are oriented normal to the crack front, and subsequently subdivisions of the crack tube geometry. With the help of these subdivisions a crack mesh can be created, which has ideal properties: the element faces are perpendicular to the crack front and all faces of the hexahedral elements are right-angled. Quadratic hexahedral elements with reduced integration (C3D20R) are used for the focused crack tip mesh. Automatic tetrahedral meshing (C3D10) is used for the surrounding volume. The different element types are tied automatically by ABAQUS at coincident nodes. This crack meshing is confined to a prism. A prism of same geometry is cut out from the specimen volume and replaced by the meshed prism containing the crack. The two bodies are connected with tie-contact. So the remaining specimen volume could be meshed with a quite coarse mesh seeding using quadratic hexahedral elements (C3D20R), see Fig. S1.

(2) Parametric Study

The parameters considered in the recent finite element analysis were defined by the following sets: $a/c = \{0.4, 0.5, 0.6, 0.7, 0.8\}$, $a/t = \{0.05, 0.10, 0.15, 0.2\}$, $t/R_a = \{0.1, 0.2, 0.3\}$, and $\nu = \{0.1, 0.2, 0.3, 0.4\}$, leading to 240 combinations. For reason of linear elasticity, the Young's modulus does not affect the SIF in a load-controlled simulation. The loading

radius R_a and the ratio R_a/R have been fixed to 8 mm and 0.8, respectively.

Figure 5 shows the SIF distribution along the crack front for two different semielliptical cracks with $a/c = 0.8$ and $a/c = 0.4$, respectively. Poisson's ratio is varied from 0.1 to 0.4, whereas $a/t = 0.15$ and $t/R_a = 0.2$ are held constant. Because of the trefoil symmetry of the stress field as shown in Fig. 4, the curves of $Y(\varphi)$ are slightly nonsymmetric about $\varphi = 0^\circ$. The extreme values Y_{\max} near point A, cp. Fig. 3, are up to 3° offset from $\varphi = 0^\circ$. The difference of $Y(0^\circ) = Y_0$ and the maximum near this point, $(Y_{\max} - Y_0)/Y_{\max}$ ranges from 0.00013% to 0.13% with a mean of 0.037% for the parameter range we investigated. Therefore, we will consider Y_0 for our further calculations. Near the intersection of the crack front with the specimen surface ($\varphi \pm 90^\circ$, points C and C*) the higher value always appears at C (negative values of φ), that is, at the position which points toward the gap between the two supporting balls.

Obviously Poisson's ratio influences not only the maximum value but also the shape of the curve. Generally, an increase in ν shifts Y to higher values. Shallow semielliptical cracks have the maximum at the deepest point. For almost semicircular cracks the maximum can always be found at the surface. The peak value moves below the surface with increasing Poisson's ratio at $\nu > 0.2$ and can reach almost the position of $\varphi = \pm 85^\circ$ for $\nu = 0.4$. This effect was obscured by the coarse mesh used for reasons of limited computational resources in previous works.¹⁸ In that study, from which the expression currently used in the analysis of beam bending SCF^{12,14} is taken, the element edge length spans a parametric angle range of 5° or more, whereas in our simulation the resolution is much finer with a span width of 2° or finer.

(3) Geometric Function Formulae for the B3B-KIc Test

For the evaluation of the B3B-KIc test, the geometric functions at the deepest point Y_0 and the peak value at or near the surface Y_{peak} are of interest. The SIFs needed for the evaluation, were calculated from the J-Integral values in the finite element results files, using

$$K_J = \sqrt{J \cdot E / (1 - \nu^2)} \quad (5)$$

Both geometric factors can be approximated with a quadratic response surface function where linear, quadratic, and interaction terms occur:

$$\begin{aligned} Y\left(\frac{a}{c}, \frac{a}{t}, \frac{t}{R_a}, \nu\right) = & c_0 + c_1 \left(\frac{a}{c}\right) + c_2 \left(\frac{a}{t}\right) + c_3 \left(\frac{t}{R_a}\right) + c_4 \nu \\ & + c_5 \left(\frac{a}{c}\right) \left(\frac{a}{t}\right) + c_6 \left(\frac{a}{c}\right) \left(\frac{t}{R_a}\right) + c_7 \left(\frac{a}{c}\right) \nu \\ & + c_8 \left(\frac{a}{t}\right) \left(\frac{t}{R_a}\right) + c_9 \left(\frac{a}{t}\right) \nu + c_{10} \left(\frac{t}{R_a}\right) \nu \\ & + c_{11} \left(\frac{a}{c}\right)^2 + c_{12} \left(\frac{a}{t}\right)^2 + c_{13} \left(\frac{t}{R_a}\right)^2 + c_{14} \nu^2 \end{aligned} \quad (6)$$

The fitted coefficients for the deepest point and the surface point are given in Tables I and II. The relative error of the fitted functions with respect to the finite element results, given as

$$\text{error} \left(\frac{a}{c}, \frac{a}{t}, \frac{t}{R_a}, \nu \right) = \frac{Y_{\text{fit}} \left(\frac{a}{c}, \frac{a}{t}, \frac{t}{R_a}, \nu \right) - Y_{\text{FEM}}}{Y_{\text{FEM}}} \quad (7)$$

was calculated and is between -0.00745 and 0.007435 with a mean of 5.96×10^{-5} for the deepest point and between

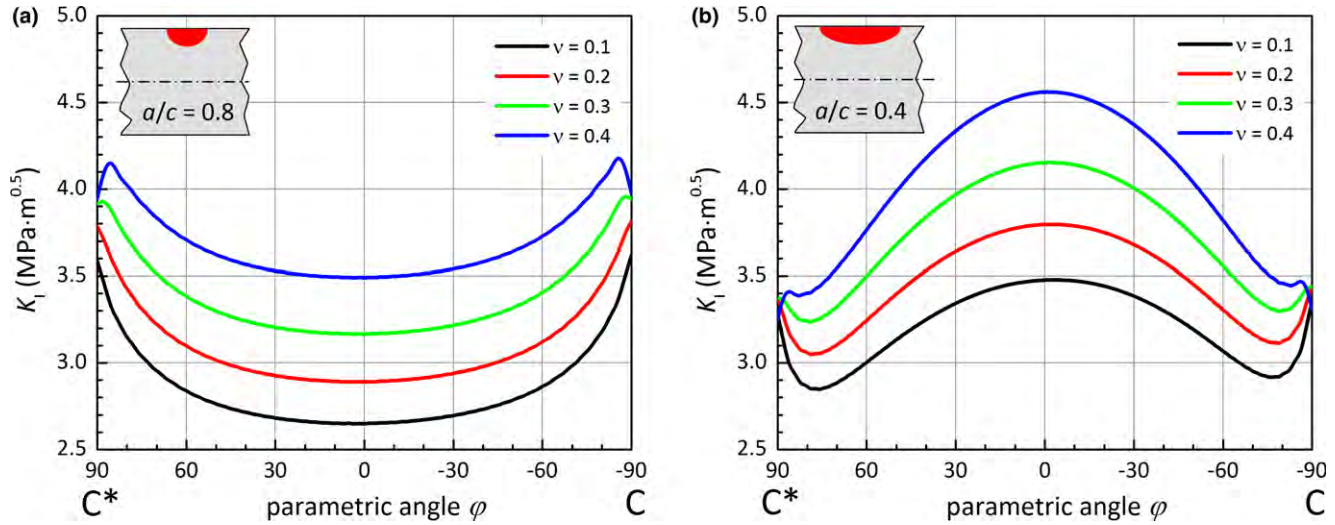


Fig. 5. K_I along crack front for $a/c = 0.8$ (left) and $a/c = 0.4$ (right) and varying Poisson's ratio; The ratios $a/t = 0.15$ and $t/R_a = 0.2$ are fixed.

Table I. Fit Coefficients of Eq. (6) for the Deepest Point, Y_{0° .

Linear terms		Interaction terms		Quadratic terms	
c_0	1.12614	c_5	0.253318	c_{11}	0.14092
c_1	-0.620484	c_6	0.0211878	c_{12}	1.77327
c_2	-1.6564	c_7	-0.0635111	c_{13}	0.105704
c_3	-0.0562209	c_8	-0.295002	c_{14}	0.277422
c_4	0.0772489	c_9	-0.157773		
		c_{10}	-0.062576		

Table II. Fit Coefficients of Eq. (6) for the Point Near the Surface, Y_{peak} .

Linear terms		Interaction terms		Quadratic terms	
c_0	0.593672	c_5	0.388541	c_{11}	-0.593958
c_1	0.715691	c_6	0.0510384	c_{12}	-0.15732
c_2	-0.51497	c_7	0.543851	c_{13}	0.157463
c_3	-0.0549222	c_8	-0.295276	c_{14}	0.139312
c_4	0.598183	c_9	-0.184307		
		c_{10}	-0.0915678		

-0.013779 and 0.016227 with a mean of 3.56×10^{-5} for the point near the surface, respectively.

V. Errors Associated with the B3B-KIc Test Method

Several sources for measurement errors can be identified for this test and are discussed below to estimate the possible accuracy of the new test method.

(1) Fracture Stress

Errors in the determination of the fracture stress due to force measurement, friction, and determination of the specimen thickness appear directly as errors in K_{Ic} and are similar to those which are present in a B3B-test without crack. They were thoroughly analyzed by Börger et al.¹⁰ and sum up to be approximately $\pm 1\%$.

(2) Poisson's Ratio

Both, the calculation of the fracture stress and the calculation of the geometric factor, require knowledge of Poisson's

ratio. It has already been recognized by Börger et al.¹⁰ that the influence of errors in Poisson's ratio on the stress in the B3B-test is smaller than $\pm 5\%$ for $\Delta\nu = \pm 0.05$ (which corresponds to an error of approximately 20% to 25% for usual values for a ceramic). Poisson's ratio has to be known to $\pm 5\%$ to limit the error in strength to $\pm 1\%$. The effect of an erroneous value of Poisson's ratio on the geometric factor Y is less than that on calculated stress (about 1/3 of that on stress). We can therefore assume that the error in B3B-KIc tests due to an erroneous Poisson's ratio can be kept smaller than $\pm 3\%$ in most practical cases. To keep the overall error small it is thus highly recommended to use an exact value for Poisson's ratio.

(3) Crack Size and Shape

The measurement of the crack size on the fracture surface is the crucial experimental step of the procedure. Errors arising from uncertainties in crack length measurement were analyzed previously by Quinn et al.^{19,20} for the standard SCF method on uniaxial bend bars. A similar analysis for the B3B-KIc test showed that their conclusions remain valid. Apparently, from the square root relation between K_{Ic} and a in Eq. (1), any error in crack depth a appears with half of its magnitude as error in K_{Ic} , that is, $\pm 10\%$ error in a results in $\pm 5\%$ error in K_{Ic} . But at the same time the geometric function is influenced in the opposite direction, so that the resulting error is reduced and only reaches the above-mentioned maximum in rare cases. Even an additional error of the same magnitude in surface crack length $2c$ never increases the total error to higher values. This trend does not depend on the size of the crack (a/t) or the shape of the crack (a/c).

Another source of error arises from the approximation of the true crack front shape (segment of an ellipse, surface angle $\chi \neq 90^\circ$) by a semiellipse ($\chi = 90^\circ$) with the same measured dimensions a and c , as depicted in Fig. 6. The error introduced by this simplification can be estimated for cracks in bend bars using the recently developed relation by Strobl et al.²¹ It turns out that the geometric function along the whole crack front is influenced by χ . Since the semiellipse always has a larger crack area, its geometric function is higher than the one for a segment of an ellipse. The simplification always leads to an overestimation of K_{Ic} . For small, shallow cracks which are critical near the deep point A, the effect is less pronounced. For such cracks the geometric function Y_{0° ($\chi \neq 90^\circ$) may be up to 4% smaller than the simplified valued $Y_{0^\circ}(\chi = 90^\circ)$ in rare unfavorable cases. Cracks which are critical near the surface of the

specimen (point C, large a/c ratio) are influenced significantly stronger.

We thus recommend to use shallow cracks with $Y_{0^\circ} > Y_{\text{peak}}$ in the B3B-KIc test. Such cracks can be obtained by grinding off a sufficient amount of material, usually more than the recommended 1/6th of the indent diagonal. A strategy how this amount can be estimated is presented in annex II.

Even though this analysis was made for cracks in a uniaxial bending stress field, it can be assumed that it remains valid as an upper limit for the B3B-KIc-test. In principle it is possible to include the effect of $\chi \neq 90^\circ$ into the modeling of the B3B-KIc-test, but often the precrack is not clear enough on the fracture surface to allow for a determination of χ , so that it does not seem to be worth the effort.

(4) Position and Orientation of the Crack

The calculations described in section 3 were performed for a crack that is exactly on the symmetry axis of the test which is centered with respect to the support circle, cp. Fig. 2. This ideal situation can be corrupted in actual tests because (i) the crack is not introduced in the correct position on the specimen, and (ii) the positioning of the specimen on the support balls is not perfect.

These positioning errors may result in a rotation of the crack away from symmetry axis (α), a shift along the symmetry axis (Δy), a shift away from the symmetry axis (Δx) or a combination of them as shown in Fig. 4. The effects of these three positioning errors on the maximum SIF along the crack front are shown in Fig. 7 for different crack sizes a/t . A rotation of the crack has only a negligible effect, see Fig. 7(a). A shift along the symmetry axis [Δy , Fig. 7(b)] leads to a reduction in the maximal SIF if the position of this maximum (at A) is not changed. It leads to an increase and a further decrease if the position of the maximum changes from point A to point C as is the case for $a/t = 0.2$. A shift away from the symmetry axis [Δx , Fig. 7(c)] dramatically decreases the SIF as the crack is moved away from the stress maximum. The effect is similar for all crack sizes.

Since most cases of positioning error result in a decrease in the SIF at the crack, we believe that the more probable error in this test is an overestimation of the measured K_{Ic} .

While, in general, the B3B (strength) test is very robust against positioning and geometry errors,¹⁰ this is not true for the B3B-KIc test. From the diagrams it can be concluded that any shift away from the ideal position should be less than 2% of the support radius R_a . This condition can be used to deduce a minimal specimen size which allows for fracture toughness measurements with a sufficient precision, as shown in annex II.

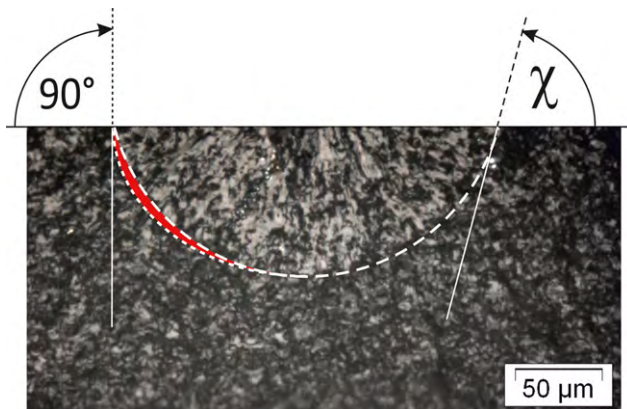


Fig. 6. Crack front modeled as semiellipse (dotted line, $\chi = 90^\circ$) or as segment of an ellipse (dashed line and $\chi \neq 90^\circ$) fitted to the same measured dimensions a and c .

VI. Experimental Validation

Experiments using the above described method were conducted on silicon nitride specimens (SL200, Ceramtec,

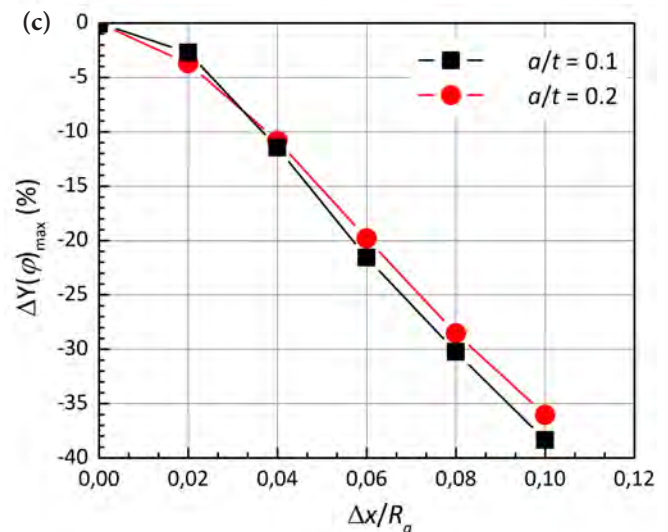
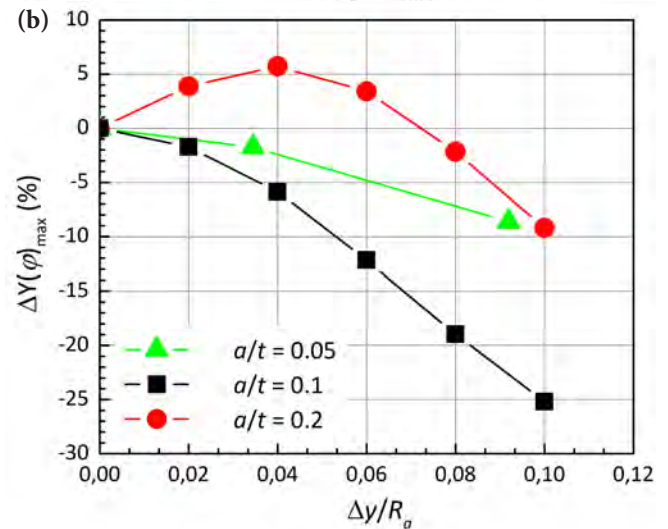
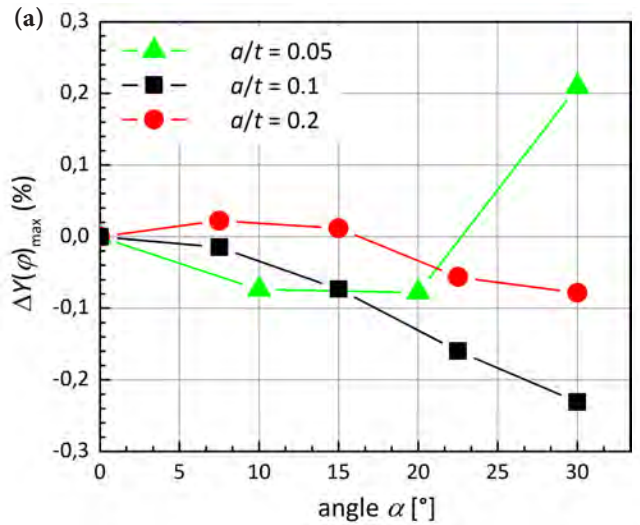


Fig. 7. The effect of (a) a rotation of the crack, (b) an in plane shift along the symmetry axis, and (c) an out of plane shift away from the symmetry axis on the maximum SIF along the crack front. Calculations were performed for various crack sizes a/t . The crack shape was set to $a/c = 0.5$ and Poisson's ratio $\nu = 0.3$, shifts are given relative to the support radius R_a .

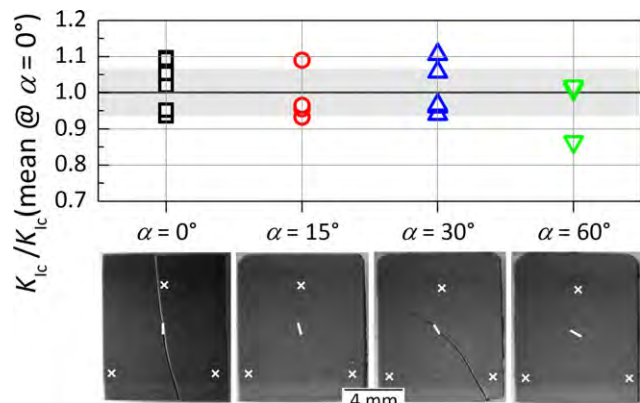


Fig. 8. Fracture toughness determined with cracks which were deliberately rotated by the angle α indicated in the plot. The lower part of the image shows the fractured specimens with the position of the supporting balls indicated by white \times and the position and orientation of the indentation crack by thick white lines. Note that $\alpha = 60^\circ$ is equivalent to $\alpha = 0^\circ$ because of symmetry.

$v = 0,268^{22}$). Rectangular plate specimens with $L = 10$ mm, $b = 8.4$ mm, and $t = 1$ mm were used. Different from round disks, the orientation of rectangular plate specimens with respect to the support balls is fixed, that is, the symmetry axis of the specimen is known before putting the specimen into the guide of the test device. It is thus easily possible to introduce indentation cracks with deliberate rotation α away from perfect alignment on the symmetry axis of the loading geometry or with a lateral offset, see Fig. 4. The magnitude of the rotation and offset can readily be determined prior to the test.

Indentation cracks were introduced using a Knoop indenter and loads of 10 or 20 kg, respectively. After indentation the cracks were decorated using fluorescent penetration dye. The amount of materials calculated using Eq. (AII.1) was ground off before the fracture test. For all specimens this amount was greater than 1/6th of the long indentation diagonal so that it was ensured that the “plastic zone” was completely removed. The crack dimension $2c$ was measured on the ground surfaces before the fracture test (measurement 1). Fracture tests were performed using balls with a diameter of $2R_B = 6.35$ mm, resulting in a support diameter of $2R_a = 7.332$ mm at a crosshead speed of 0.5 mm/min using a Zwick 010 testing equipment (Zwick GmbH & Co. KG, Ulm, Germany). Crack dimensions $2c$ and a were measured on the fracture surfaces immediately after the test using UV light (measurement 2) and, as a complimentary method, using stereo microscopy and grazing illumination (measurement 3). Only specimens with consistent measurements 1 to 3 were considered for evaluation. Fracture toughness was calculated using the maximum of Y obtained with the fitted expressions for Y_{0° and Y_{peak} , Eq. (6).

The results of these investigations are shown in Fig. 8. The results are normalized by the mean K_{Ic} determined at $\alpha = 0^\circ$. It is obvious that fracture toughness does not depend on the orientation of the crack with respect to the supporting balls, as predicted by the error analysis.

VII. Summary

A new fracture toughness test method for ceramics that uses small disks and plates with a centered, ground-off indentation precrack which are fractured in a ball-on-three-balls test is presented. A detailed analysis of the SIF along the crack front in the biaxial bending stress field is performed for a wide parameter range. A study of the effects of deviations from the ideal loading situation and an error analysis complement the simulations.

1. In the ideal case with the crack perfectly aligned and centered with respect to the stress field, only the mode

I SIF is of importance. As is the case for such cracks in pure uniaxial bending the SIF varies along the crack front and may have a maximum either at the deepest point of the crack or at or near the intersection point of the crack with the surface.

2. Simple polynomial fitting functions for the geometry function at two positions on the crack front are provided which allow for a quick calculation of K_I and facilitate practical application of the method.
3. The error analysis shows that measurement uncertainties stem from two main sources:
 - a). The errors inherent to the B3B-test, which are—to a great extent—due to inaccurate knowledge of Poisson’s ratio, and
 - b). The exact position of the crack in the stress field. Other than in the B3B-strength test, it plays an important role in the B3B- K_{Ic} test. A shift along or away from the symmetry axis results—in most cases—in an overestimation of the measured K_{Ic} , while a rotation causes no significant error.
4. From the error analysis specimen dimensions and requirements concerning the test practice which allow for a precise determination of fracture toughness are deduced. With disks of more than 8 mm in diameter and a thickness of at least 0.5 mm a measurement uncertainty of $\pm 10\%$ can be achieved if the crack is positioned within maximal ± 120 μm from the center of the stress maximum. An uncertainty comparable to that obtained with other common fracture toughness test methods can be reached with larger specimens. In any case Poisson’s ratio of the tested material should be known as exactly as possible and shallow cracks which are critical at their deepest point should be used. A method how this can be achieved is also presented.

Acknowledgments

Tjokorda Gde Tirta Nindhia acknowledges to support of ASEA-Uninet and the Ernst Mach-Nachbetreuungsstipendium (EZA, ICM-2014-07166) financed by the Austrian Federal Ministry of Science, Research and Economy (BMWFV).

Supporting Information

Additional Supporting Information may be found in the online version of this article:

Fig. S1. Focused mesh of the crack front region with hexahedrons and surrounding mesh with tetrahedrons for automatic volume meshing. Hexahedral elements (C3D20R, white) and tetrahedral elements (C3D10, gray) are tied automatically by ABAQUS with coincident nodes.

Fig. S2. Relative grinding depth versus the initial relative crack width for an initially semicircular crack $a_0/c_0 = 1$. Above the lines the maximum SIF occurs at the deepest point of the crack.

Annex I A New Empirical Formula for Geometric Factor f to Calculate the B3B Stress

A new empirical formula for the factor f in Eq. (2) is presented, which is simpler than the one reported by Danzer et al.,¹⁷ but has the same level of accuracy. The empirical fit is based on finite element calculations of the B3B strength test with the parameters t/R (from 0.05 to 0.5, in steps of 0.025), R_a/R (from 0.6 to 0.95, in steps of 0.025) and v (from 0.1 to 0.4, in steps of 0.05) and the following equation:

Table AI.1. Fitted Coefficients in Eq. (AI.1)

c_0	1.12613	c_5	-5.20337
c_1	-2.00184	c_6	0.253034
c_2	0.993698	c_7	5.58097
c_3	1.91891	c_8	1.12707
c_4	0.89157	c_9	-18.4977

$$f\left(\frac{t}{R}, \frac{R_a}{R}, \nu\right) = c_0 + c_1 \left(\frac{t}{R}\right) + c_2 \left(\frac{R_a}{R}\right) + c_3 \nu + c_4 \left(\frac{t}{R}\right)^2 + c_5 \left(\frac{t}{R}\right) \nu + c_6 \left(\frac{R_a}{R}\right) \nu + c_7 \left(\frac{t}{R}\right)^2 \nu + c_8 \exp\left(c_9 \left(\frac{t}{R}\right)\right) \quad (\text{AI.1})$$

The fitted coefficients are given in Table AI.1. The relative error of the fitted function with respect to the finite element results,

$$\text{error}\left(\frac{t}{R}, \frac{R_a}{R}, \nu\right) = \frac{f_{\text{fit}}\left(\frac{t}{R}, \frac{R_a}{R}, \nu\right) - f_{\text{FEM}}}{f_{\text{FEM}}} \quad (\text{AI.2})$$

was investigated resulting in values between -0.00871 and 0.010046 with an average of 1.89×10^{-7} . That means, the error due to fitting is expected to be less than 1%.

Annex II Hints for Practical Application

II.1 How Much to Grind off to Make Y_{0° the Maximum SIF Along the Crack Contour?

From a formal fracture mechanics viewpoint fracture starting from point C (i.e., the intersection point of the crack front with the specimen surface, cp. Fig. 3) is problematic. At this position the stress in front of the crack is no longer proportional to $r^{-1/2}$ (with r being the distance from the crack tip). Thus, the relation given in Eq. (1) is not strictly valid, too.^{23–25} It is not completely clear if valid fracture toughness results can be obtained with cracks for which $Y_{\text{peak}} > Y_{0^\circ}$.

Also, the simplification regarding the true crack shape (semiellipse instead of section of an ellipse) is less inaccurate if $Y_{0^\circ} > Y_{\text{peak}}$.

Our analysis of the stress intensity along the crack front showed that the situation where K_I (and Y) is maximal at/near point C may occur for certain combination of crack geometry (a/c) and specimen thickness (a/t). There is a tendency that cracks with a high ratio a/c are critical at point C. On the other hand, shallow cracks (small a/c) tend to have the maximum of K at point A. Such cracks can be obtained by grinding off enough material from the original specimen thickness. Using the expressions given in Eq. (6), the necessary material removal $\Delta t_{(A)}$ can be estimated which gives a crack geometry that fulfills $Y_{0^\circ} > Y_{\text{peak}}$. The magnitude of $\Delta t_{(A)}$ depends on the relative size of the starting crack directly after indentation (c_0/t_0), on the geometry of the starting crack (a_0/c_0) and on Poisson's ratio ν , see Fig. S2:

$$\Delta t_{(A)} = c_0 \left(-0.68912 - 0.652413 \nu + 1.17089 \frac{a_0}{c_0} + 1.4234 \frac{c_0}{t_0} - 1.90952 \left(\frac{c_0}{t_0} \right)^2 \right) \quad (\text{AII.1})$$

However, to ensure that the 'plastic zone' surrounding the indent is completely removed, which is an essential prerequisite for the validity of the test, the condition $\Delta t_{(pl)} \geq d/6$ also has to be fulfilled. We thus propose to use the relation

given in Eq. (AII.2) to determine the necessary amount of material removal Δt that satisfies both conditions:

$$\Delta t = \max(\Delta t_{(A)}, \Delta t_{(pl)}) \quad (\text{AII.2})$$

The surface crack length of the virgin indentation crack, c_0 , can be measured directly after indentation on the specimen surface. The quantity a_0/c_0 can be obtained from fracture surfaces of specimens with indentation cracks with no material ground off. According to literature²⁶ a_0/c_0 for Knoop indentation cracks is $0.8 \leq a_0/c_0 \leq 1.2$.

AII.2 Minimal Specimen Size for a Total Error Below $\pm 10\%$

The error analysis, Section V, showed that excessive measurement errors occur mainly if the indentation cracks are offset from the symmetry axis of the test setup. Any offset should preferably be below $0.02R_a$. The total errors decrease for cracks that are small compared to the support (or specimen) diameter. Taking into account typical crack sizes of indentation cracks, the possible accuracy of positioning of the cracks on the specimen, as well as of specimens in the guide of the test device and restrictions concerning valid specimen geometries for the B3B-test,^{9,17} it is possible to estimate a lower size limit for specimens which can be used for this measurement method.

Cracks can be positioned on the specimen with approximately $\pm 20 \mu\text{m}$ deviation or less from the ideal position provided the indentation device is equipped with a X–Y-stage and the specimens have a well-defined shape (no gross deviation from the circular shape or skewed angles in the case of rectangular plates). In addition, we have to consider that the guide which centers the specimen with respect to the support balls always has some clearance, which is in the order of $50\text{--}80 \mu\text{m}$. Specimens thus should have a minimal size with a diameter of approximately $2R > 8 \text{ mm}$, a thickness of $t > 0.5 \text{ mm}$ and contain cracks with a depth of $a \leq 50 \mu\text{m}$ (after grinding) and length $2c \geq 150 \mu\text{m}$. From our experience and literature^{3,19,27} such indentation cracks with a size of $2c = 70\text{--}400 \mu\text{m}$ and $a = 50\text{--}150 \mu\text{m}$ can be achieved in many ceramic materials. These findings are supported by the results presented for Al_2O_3 specimens by Rasche et al.¹⁵

References

- ¹S. Röhrig and P. Supancic, "New Self-Regulating Ceramic PTC Thermistor Heating Elements with Strongly Improved Performance," *Ceram. Forum Int.*, **89** [11–12] E25–9 (2012).
- ²P. Isler, "Watches: Mechanical Materials"; pp. 1–17 in *Encyclopedia of Materials: Science and Technology*, Second Edition, Edited by K. H. J. Buschow. Elsevier, Oxford, 2003.
- ³S. Strobl, S. Rasche, C. Krautgasser, E. Sharova, and T. Lube, "Fracture Toughness Testing of Small Ceramic Discs and Plates," *J. Eur. Ceram. Soc.*, **34** [6] 1637–42 (2014).
- ⁴ISO 13356, "Implants for Surgery — Ceramic Materials Based on Yttria-Stabilized Tetragonal Zirconia (Y-TZP)", 2008.
- ⁵ISO 6872, "Dentistry — Ceramic Materials", 2008.
- ⁶G. D. Quinn and R. C. Bradt, "On the Vickers Indentation Fracture Test," *J. Am. Ceram. Soc.*, **90** [3] 673–80 (2007).
- ⁷G. R. Anstis, P. Chantikul, B. R. Lawn, and D. B. Marshall, "A Critical Evaluation of Indentation Techniques for Measuring Fracture Toughness: I, Direct Crack Measurements," *J. Am. Ceram. Soc.*, **64** [9] 533–8 (1981).
- ⁸H. Miyazaki, H. Hyuga, Y. I. Yishizawa, K. Hirao, and T. Ohji, "Fracture Toughness Test of Silicon Nitrides with Different Microstructures Using Vickers Indentations," *Ceram. Eng. Sci. Proc.*, **28** [2] 433–42 (2008).
- ⁹A. Börger, P. Supancic, and R. Danzer, "The Ball on Three Balls Test for Strength Testing of Brittle Discs - Stress Distribution in the Disc," *J. Eur. Ceram. Soc.*, **22** [8] 1425–36 (2002).
- ¹⁰A. Börger, P. Supancic, and R. Danzer, "The Ball on Three Balls Test for Strength Testing of Brittle Discs - Part II: Analysis of Possible Errors in the Strength Determination," *J. Eur. Ceram. Soc.*, **24** [10–11] 2917–28 (2004).
- ¹¹R. Danzer, W. Harrer, P. Supancic, T. Lube, Z. Wang, and A. Börger, "The Ball on Three Balls Test - Strength and Failure Analysis of Different Materials," *J. Eur. Ceram. Soc.*, **27** [2–3] 1481–5 (2007).
- ¹²EN ISO 18756, "Fine Ceramics (Advanced Ceramics, Advanced Technical Ceramics) – Determination of Fracture Toughness of Monolithic Ceram-

ics at Room Temperature by the Surface Crack in Flexure (SCF) Method”, 2005.

¹³G. D. Quinn, J. J. Swab, and M. J. Motyka, “Fracture Toughness of a Toughened Silicon Nitride by ASTM C 1421,” *J. Am. Ceram. Soc.*, **86**[6] 1043–5 (2003).

¹⁴ASTM C 1421-10, Standard Test Methods for Determination of Fracture Toughness of Advanced Ceramics at Ambient Temperature.

¹⁵S. Rasche, S. Strobl, M. Kuna, R. Bermejo, and T. Lube, “Determination of Strength and Fracture Toughness of Small Ceramic Discs Using the Small Punch Test and the Ball-on-Three-Balls Test,” *Proc. Mater. Sci.*, **3**, 961–6 (2014).

¹⁶R. Danzer, P. Supancic, and W. Harrer, “Biaxial Tensile Strength Test for Brittle Rectangular Plates,” *J. Ceram. Soc. Jpn.*, **114** [11] 1054–60 (2006).

¹⁷R. Danzer, P. Supancic, and W. Harrer, “Der 4-Kugelversuch zur Ermittlung der Biaxialen Biegefestigkeit Spröder Werkstoffe (The Ball-on-Three-Balls Test for the Determination of Biaxial Bending Strength of Brittle Materials);” pp. 1–48 in *Technische Keramische Werkstoffe (Technical Ceramics)*, Vol. 113. Ergänzungslieferung (113. Supplement), Edited by J. Kriegesmann. HvB Verlag GbR., Ellerau, 2009.

¹⁸J. C. Newman and I. S. Raju, “An Empirical Stress-Intensity Factor Equation for the Surface Crack,” *Eng. Fract. Mech.*, **15** [1–2] 185–92 (1981).

¹⁹G. D. Quinn, J. Kübler, and R. J. Gettings, “Fracture Toughness of Advanced Ceramics by the Surface Crack in Flexure (SCF) Method: A VAMAS Round Robin”; VAMAS Report No. 17, http://www.vamas.org/documents/twa3/vamas_twa3_report_17.pdf, 1994.

²⁰G. D. Quinn, J. Kübler, and R. J. Gettings, “Fracture Toughness by the Surface Crack in Flexure (SCF) Method: Results of the VAMAS Round Robin,” *Ceram. Eng. Sci. Proc.*, **15** [5] 846–55 (1994).

²¹S. Strobl, P. Supancic, T. Lube, and R. Danzer, “Surface Crack in Tension or in Bending - A Reassessment of the Newman and Raju Formula in Respect to Fracture Toughness Measurements in Brittle Materials,” *J. Eur. Ceram. Soc.*, **32**, 1491–501 (2012).

²²T. Lube and J. Dusza, “A Silicon Nitride Reference Material - A Testing Program of ESIS TC6,” *J. Eur. Ceram. Soc.*, **27** [2–3] 1203–9 (2007).

²³T. Fett, *Stress Intensity Factors, T-Stresses, Weight Functions*, pp. 362, Vol. IKM 50. Karlsruher Institut für Technologie (KIT), Karlsruhe, 2008.

²⁴P. F. P. de Matos and D. Nowell, “The Influence of the Poisson’s Ratio and Corner Point Singularities in Three-Dimensional Plasticity-Induced Fatigue Crack Closure: A Numerical Study,” *Int. J. Fatigue*, **30** [10–11] 1930–43 (2008).

²⁵P. Hutar, L. Náhlík, and Z. Knésl, “The Effect of a Free Surface on Fatigue Crack Behaviour,” *Int. J. Fatigue*, **32** [8] 1265–9 (2010).

²⁶T. Lube, “Indentation Crack Profiles in Silicon Nitride,” *J. Eur. Ceram. Soc.*, **21** [2] 211–8 (2001).

²⁷J. J. Swab and G. D. Quinn, “Effect of Pre-crack “Halos” on Fracture Toughness Determined by the Surface Crack in Flexure Method,” *J. Am. Ceram. Soc.*, **81** [9] 2261–8 (1998). □